

Heterogeneous Semiconductors as Versatile Photocatalysts for Organic Synthesis

Inaugural-Dissertation
to obtain the academic degree
Doctor rerum naturalium (Dr. rer. nat.)

Submitted to the Department of Biology, Chemistry, Pharmacy
of Freie Universität Berlin

by
Susanne Reischauer

January 2022

This work was performed between February 2019 and December 2021 under the direction of Prof. Dr. Peter H. Seeberger and Dr. Bartholomäus Pieber in the Department of Biomolecular Systems, at the Max Planck Institute of Colloids and Interfaces.

1st reviewer: Prof. Dr. Peter H. Seeberger

2nd reviewer: Prof. Dr. Christian Müller

Date of oral defense: 6. April 2022

Acknowledgements

I am extremely grateful to my supervisor, Dr. Bartholomäus Pieber, for his outstanding support and scientific guidance throughout the last years. Thank you for the time and effort you have invested in my work. You taught me to always aim higher and that with ambition and hard work everything can be accomplished. I could not have wished for a better supervisor.

I also want to thank Prof. Dr. Peter Seeberger for giving me the opportunity to perform my dissertation in the Biomolecular Systems Department at Max Planck Institute of Colloids and Interfaces.

I am thankful to Prof. Dr. Christian Müller for kindly agreeing to review this thesis.

Many thanks to the Verband der Chemischen Industrie to support my thesis with a scholarship.

Many thanks to all my colleagues of the Biomolecular Systems department for the nice working environment, exchange of knowledge and fruitful discussion that contributed to the success of this thesis. Also thanks to Dorothee Böhme, Eva Settels and Olaf Niemeyer for excellent technical and organizational support. Special thanks goes to former and current members of the catalysis group - Cristian, Sebastian, Amiera, Lucia, Noah, Tommaso and Cosima - thanks for creating a great working environment. Especially, I would like to thank Cristian, Sebastian and Agata for their warm welcome, when I joined the institute and for their friendship and support over the years.

Ein großer Dank gilt auch Seba und Nicole! Danke für die zahlreichen Abenteuer, die wir zu viert erleben durften. Ich könnte mir keine besseren (fast) Nachbarn vorstellen.

Ich möchte mich auch bei Marion, Judith, Patrick, Laura und Lisi für eure langjährige Freundschaft bedanken. Egal wie viele Kilometer uns auch trennen, bei euch fühle ich mich immer angekommen.

A very special thanks goes to one of my closest friends, Ana. I cannot thank you enough for all your scientific support but especially for our friendship in the last years.

Ein großer Dank gilt natürlich, meiner besseren Hälfte Michi. Du bist mein Fels in der Brandung. Mit deiner unendlichen Geduld und liebevollen Art lässt du mich nie den Blick auf das Wesentliche verlieren. Danke für deine kompromisslose Unterstützung in den letzten Jahren. Ich freue mich auf unser nächstes großes Abenteuer „Amerika“.

Jedoch gilt mein größter Dank meiner Familie. Danken möchte ich all meinen Großeltern, die seit dem Anfang meines Studiums bei jedem meiner Schritte mitfiebern und mich immer unterstützen. Ganz Besonderes würde sich Reischauer-Opa freuen, wenn er meine Arbeit jetzt sehen könnte. Bedanken möchte ich mich auch bei meinen Schwestern - Isabella und Elisabeth. Bella, du hast mir gezeigt was kämpfen heißt und dass man alles erreichen kann, auch wenn die Hürden noch so groß sind. Lisi, danke für deine lebensfrohe und ausgelassene Art mit der du mich immer ansteckst. Zum Schluss gilt der größte Dank meinen Eltern. Ihr habt mir die Möglichkeit geben meine Träume zu verwirklichen und habt mich nicht nur finanziell, sondern auch emotional immer unterstützt. Durch eure kompromisslose und aufopfernde Liebe weiß ich welche Werte im Leben wirklich wichtig sind und dass ich an mich glauben kann.

List of Publications

Reischauer, S.; Pieber, B. Emerging Concepts in Photocatalytic Organic Synthesis. *iScience* **2021**, *24*, 102209.

Gisbertz, S.; **Reischauer, S.**; Pieber, B. Overcoming Limitations in Dual Photoredox/Nickel catalyzed C–N Cross-Couplings due to Catalyst Deactivation. *Nat. Catal.* **2020**, *3*, 611-620.

Schmermund, L.; **Reischauer, S.**; Bierbaumer, S.; Winkler, C.; Diaz-Rodriguez, A.; Edwards, L.; Kara, S.; Mielke, T.; Cartwright, J.; Grogan, G.; Pieber, B.; Kroutil, W. Chromoselective Photocatalysis Enables Stereocomplementary Biocatalytic Pathways. *Angew. Chem. Int. Ed.* **2021**, *60*, 6965-6969.

Reischauer, S.; Strauss, V.; Pieber, B.; Modular, self-assembling metallaphotocatalyst for cross couplings using the full visible-light spectrum. *ACS Catal.*, **2020**, *10*, 13269-13274.

Reischauer, S.; Pieber, B. Recyclable, bifunctional metallaphotocatalysts for C-S cross-couplings. *ChemPhotoChem* **2021**, *5*, 716-720.

Zhao Z., **Reischauer, S.**; Pieber, B., Delbianco M. Carbon dot/TiO₂ nanocomposites as photocatalysts for metallaphotocatalytic carbon–heteroatom cross-couplings. *Green Chem.*, **2021**, *23*, 4524-4530.

Table of Contents

Summary	1
Zusammenfassung	3
1 Introduction	5
1.1 General principles of photocatalysis	5
1.2 Metallaphotocatalyzed cross-couplings	9
1.3 Photocatalysts	11
1.4 Light as a parameter to control selectivity	19
1.5 Aim of the thesis	20
1.6 References	21
2 Emerging concepts in photocatalytic organic synthesis	27
2.1 Introduction	28
2.2 Photocatalysis in medicinal chemistry and the pharmaceutical industry	30
2.3 The wavelength matters	33
2.4 The energy and intensity of photons	37
2.5 Replacing elemental alkali metal reductants with light	40
2.6 Better, faster, scalable – technological aspects & developments	43
2.7 Photon-free photocatalysis	49
2.8 Summary and outlook	51
2.9 References	52
3 Overcoming limitations in dual photoredox/nickel catalyzed C–N cross-couplings due to catalyst deactivation	59
3.1 Introduction	61
3.2 Results and discussion	63
3.3 Conclusion	74
3.4 References	75

4	Chromoselective photocatalysis enables stereocomplementary biocatalytic pathways	79
4.1	Introduction	81
4.2	Results and discussion	81
4.3	Conclusion	87
4.4	References	88
5	Modular, self-assembling metallaphotocatalyst for cross couplings using the full visible-light spectrum	93
5.1	Introduction	95
5.2	Results and discussion	97
5.3	Conclusions	102
5.4	References	103
6	Recyclable, bifunctional metallaphotocatalysts for C-S cross-couplings	105
6.1	Introduction	107
6.2	Results and discussion	108
6.3	Conclusions	114
6.4	References	115
7	Carbon dot/TiO ₂ nanocomposites as photocatalysts for metallaphotocatalytic carbon-heteroatom cross-couplings	119
7.1	Introduction	121
7.2	Results and discussion	123
7.3	Conclusions	130
7.4	References	131
8	Discussion & Outlook	137
8.1	Discussion of the individual works	137
8.2	Outlook	142
8.3	Graphical summary of this thesis & outlook	143
8.4	References	144

Appendix	145
Supporting Information - Chapter 3	145
Supporting Information - Chapter 4	245
Supporting Information - Chapter 5	273
Supporting Information - Chapter 6	349
Supporting Information - Chapter 7	393
List of abbreviations	433

Statement of Authorship / Selbstständigkeitserklärung

I hereby certify that the herein presented dissertation was authored by myself and was completed using only the cited literature and sources. This thesis is submitted to the Department of Biology, Chemistry, Pharmacy of Freie Universität Berlin to obtain the academic degree Doctor rerum naturalium (Dr. rer. nat.) and has not been submitted for any other degree.

Hiermit versichere ich, dass ich die vorliegende Dissertation selbstständig und lediglich unter Benutzung der angegebenen Quellen und Hilfsmittel verfasst habe. Diese Arbeit wird beim Fachbereich Biologie, Chemie, Pharmazie der Freien Universität Berlin zur Erlangung des akademischen Grades Doctor rerum naturalium (Dr. rer. nat.) eingereicht und wurde für keinen anderen Abschluss eingereicht.

Potsdam, 06.01.2022

Susanne Reischauer

Summary

Visible-light is a powerful “reagent” for sustainable synthetic organic chemistry. In particular, the combination of photo- and nickel catalysis (metallaphotocatalysis) has emerged as a valuable strategy for carbon–carbon and carbon–heteroatom cross-couplings. This research field is dominated by expensive homogeneous noble metal complexes that can only convert a small portion of visible light (<500 nm) into chemical energy. The high-energy photons that excite the photocatalyst can result in unwanted side reactions and the homogenous nature of these does not allow for straightforward catalyst recycling.

Heterogeneous semiconductors that absorb visible light are a promising sustainable alternative to noble metal photocatalysts (Chapter 2).

Their potential for metallaphotocatalytic C–N cross-couplings was demonstrated (Chapter 3). This transformation suffers from deactivation of the nickel catalyst using homogeneous photocatalysts. The broad absorption range (up to 700 nm) of an organic, heterogeneous carbon nitride photocatalyst (CN-OA-m) allows controlling the rate of the bond-forming step by carefully selecting the wavelength thereby preventing catalyst deactivation. This is not only crucial for the reproducibility of such reactions, but also expands the scope to substrates that were previously unsuitable.

The redox potential of a carbon nitride photocatalyst can be tuned by changing the irradiation wavelength to generate electron holes with different oxidation potentials (Chapter 4). This was the key to design photo-chemo-enzymatic cascades that enable the synthesis of (*S*)- or (*R*)- 1-phenylethan-1-ol from ethylbenzene by choosing the irradiation wavelength and the enzyme co-catalyst.

In contrast to common photocatalysts that can be only excited using short wavelengths, abundant organic dyes absorb broadly across the entire visible-light spectrum. Inspired by dye-sensitized solar cells, the short-lived excited singlet states of such dyes were harnessed for light-mediated cross-coupling reactions (Chapter 5). Immobilization of a nickel catalyst on dye-sensitized titanium dioxide results in a material that catalyzes carbon–heteroatom and carbon–carbon bond formations. The modular approach of dye-sensitized metallaphotocatalysts (DSMPs) accesses the entire visible light spectrum and allows tackling selectivity issues resulting from low-wavelengths strategically. The concept overcomes current limitations of metallaphotocatalysis by unlocking the potential of dyes

that were previously unsuitable. However, recycling studies suffered from a gradual decrease of the yield due to leaching of the nickel catalyst and the dye from the surface of TiO₂. This was rationalized by the weak interaction between carboxylic acid anchoring groups and titanium dioxide. Therefore, recyclable, bifunctional materials for metallaphotocatalytic C–S cross-couplings were developed (Chapter 6). Key to the success was the permanent immobilization through phosphonic acid anchor groups. The optimized catalyst harvests a broad range of the visible light spectrum and requires a nickel loading of only ~0.1 mol%. Another robust alternative to organic dyes that does not suffer from photobleaching was realized, by immobilizing carbon dots on titanium dioxide (Chapter 7). The potential of these sustainable materials was demonstrated for various carbon–heteroatom cross-couplings.

Zusammenfassung

Sichtbares Licht ist ein leistungsstarkes „Reagenz“ für eine nachhaltige organische Synthesechemie. Insbesondere die Kombination von Photo- und Nickelkatalyse (Metallaphotokatalyse) hat sich als erfolgreiche Strategie für Kohlenstoff–Kohlenstoff und Kohlenstoff–Heteroatom Kreuzkupplungsreaktionen herausgestellt. Dieses Forschungsfeld wird von teuren homogenen Edelmetallkomplexen, die nur einen kleinen Teil des sichtbaren Lichtes absorbieren, dominiert. Die hochenergetischen Photonen, die für die Anregung des Photokatalysators benötigt werden, können zu unerwünschten Nebenreaktionen führen. Zusätzlich sind diese homogenen Katalysatoren nicht recycelbar.

Heterogene Halbleiter, die sichtbares Licht absorbieren, sind eine vielversprechende nachhaltige Alternative zu Edelmetall-Photokatalysatoren (Kapitel 2).

Das Potential dieser Materialien wurde für metallaphotokatalytischen C–N-Kreuzkupplungen demonstriert (Kapitel 3). Mit herkömmlichen Photokatalysatoren kommt es bei dieser Reaktion zu einer Deaktivierung des Nickelkatalysators. Der breite Absorptionsbereich (bis zu 700 nm) eines organischen, heterogenen Kohlenstoffnitrid-Photokatalysators (CN-OA-m) ermöglicht die Kontrolle der photokatalytischen Reaktion durch die Wahl der Wellenlänge λ , wodurch die Katalysatordeaktivierung verhindert werden kann. Dies ist nicht nur entscheidend für die Reproduzierbarkeit solcher Reaktionen, sondern erweitert den Anwendungsbereich der Reaktion auf Substrate, die bisher nicht zugänglich waren.

Weiters wurde gezeigt, dass das Redoxpotential eines Kohlenstoffnitrid-Photokatalysators durch Änderung der Bestrahlungswellenlänge beeinflusst werden kann. Durch unterschiedliche Lichtquellen, können Elektronenlöcher mit unterschiedlichen Oxidationspotentialen erzeugt werden (Kapitel 4). Dies war der Schlüssel zur Entwicklung von photo-chemo-enzymatischen Kaskaden, die, abhängig von der Einstrahlungswellenlänge und der Auswahl des Biokatalysators, eine enantioselektive Umwandlung von Ethylbenzen in (*S*)- oder (*R*)- 1-Phenylethan-1-ol ermöglichen.

Im Gegensatz zu herkömmlichen Photokatalysatoren, die nur mit kurzen Wellenlängen angeregt werden können, absorbieren organische Farbstoffe das gesamte Spektrum des sichtbaren Lichts. Inspiriert von farbstoffsensibilisierten Solarzellen wurde eine Methode entwickelt, um die kurzlebigen, angeregten Singulett-Zustände solcher Farbstoffe für

Kreuzkupplungsreaktionen zu nutzen (Kapitel 5). Die Immobilisierung eines Nickelkatalysators und eines Farbstoffes auf der Oberfläche von Titandioxid führt zu einem Material, das die Bildung von Kohlenstoff–Heteroatom und Kohlenstoff–Kohlenstoff Kreuzkupplungen katalysiert. Der modulare Ansatz dieser Metallaphotokatalysatoren kann das gesamte Spektrum des sichtbaren Lichts nutzen und ermöglicht es Selektivitätsprobleme, die bei kurzen Wellenlängen auftreten, strategisch zu lösen.

Recyclingstudien zeigten jedoch die stufenweise Abnahme der Ausbeute aufgrund des Auslaugens des Nickelkatalysators und des Farbstoffes. Dies deutet auf eine schwache Wechselwirkung zwischen den Carbonsäuregruppen des Farbstoffes und des Nickelkatalysators und Titandioxid hin. Daher wurden bifunktionelle Materialien für metallaphotokatalytische C–S-Kreuzkupplungen entwickelt, die ohne Verlust ihrer katalytischen Aktivität wiederverwendet werden können (Kapitel 6). Der Schlüssel zum Erfolg ist die permanente Immobilisierung durch Phosphonsäuregruppen. Der optimierte Katalysator absorbiert einen breiten Bereich des sichtbaren Lichtspektrums und benötigt nur kleine Mengen des Nickelkomplexes (~0,1 mol%). Eine Alternative zu organischen Farbstoffen, wurde mit Hilfe von Kohlenstoffquantenpunkten entwickelt (Kapitel 7).

Chapter 1

Introduction

This chapter provides the scientific background and notions necessary to understand the experimental studies and discussions within this thesis. Chapters 2 - 7 report the publications listed at page vii, reformatted but with unaltered content. For each publication, supporting information containing experimental details is included. Copies of NMR spectra of isolated compounds are excluded and available through the website of the Publisher. A discussion of the individual projects and their interpretation within the overall dissertation is given in Chapter 8.

1.1 General principles of photocatalysis

Nature has developed elegant ways to use solar light as an energy source for (bio)chemical processes, which inspired synthetic chemists to explore the use of light to facilitate chemical reactions. Traditionally, photochemical reactions were carried out using ultraviolet light,¹ but the high photon energies often cause selectivity problems. This has changed with the development of photocatalysts (PC) that can absorb visible light to reach an excited state that can activate substrates, reagents or co-catalysts.²

The electronic states of a molecule and transition between them are fundamental to understand photochemical reactions and are illustrated in a Jablonski diagram (Figure 1.1). Upon irradiation with a suitable wavelength, a chromophore is promoted from its ground state (S_0) to a non-equilibrium level, for example the first singlet excited state (S_1). Next, energy is dissipated through vibrational relaxation and the molecule reaches the lowest vibrational level of the singlet excited state. Relaxation to the ground state (S_0) typically occurs *via* fluorescence ($S_1 \rightarrow S_0$). Fluorescence is a transition between states of the same spin state ($S_1 \rightarrow S_0$) and occurs readily, resulting in short lifetimes of singlet states ($<10^{-10}$ to 10^{-7} s). Molecules with large spin-orbit coupling can alternatively undergo intersystem crossing (ISC; $S_1 \rightarrow T_1$) followed by phosphorescence ($T_1 \rightarrow S_0$). Intersystem crossing is a spin-forbidden, non-radiative transition between two isoenergetic vibrational levels belonging to electronic states of different spin multiplicity. Phosphorescence is a spin-

forbidden, radiative transition between two electronic states of different spin multiplicity. As a result, triplet states are long-lived (>100 ns).

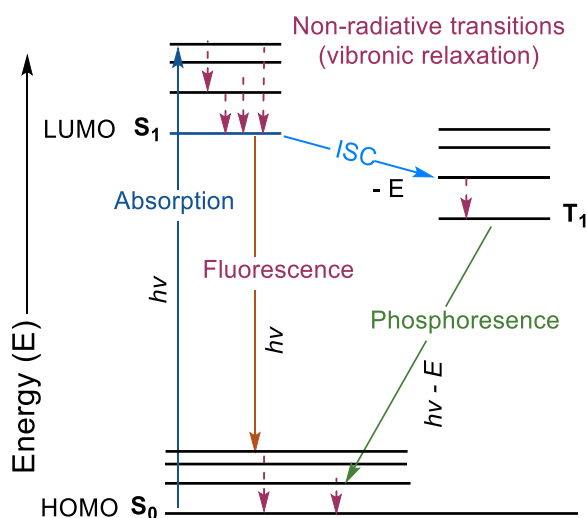


Figure 1.1. Jablonski diagram for the illustration of a molecule's electronic and vibronic states and the transition between the states.

Long excited state lifetimes are crucial for photocatalysts, because it enables the excited catalyst to engage in bimolecular processes in solution (Figure 1.2).³ Common photocatalysts for organic synthesis are organometallic chromophores, organic dyes and semiconductors that absorb visible light. Upon absorption of light, the PC reaches an excited state (PC^*) that can activate a target molecule (A, substrate or reagent) through energy or single electron transfer. Upon collision with A, PC^* relaxes to the ground state, and in the process generates a reactive intermediate of the target molecule (A^*). A^* then goes on to form the product either after or concurrent with its dissociation from PC. Thus, the lifetime of PC^* must be longer than time it takes to diffuse to A.

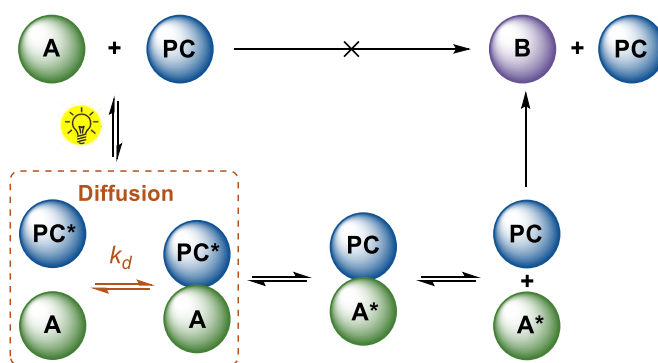


Figure 1.2. Key events to initiate reactions with a photocatalyst.

1.1.1 Energy transfer

Energy transfer (EnT) is defined as “the photophysical process in which an excited state of one molecular entity (the donor *D*) is deactivated to a lower-lying state by transferring energy to a second molecular entity (the acceptor *A*), which is thereby raised to a higher energy state.”⁴ In a photocatalytic reaction, the PC is the donor and a substrate, reagent, intermediate or a co-catalyst is the acceptor. Electron transfer can be rationalized by two different mechanisms: Förster resonance energy transfer and Dexter energy transfer (Figure 1.3).⁵

Förster energy resonance transfer (FRET) occurs through nonradiative dipole-dipole coupling of the donor and the acceptor. The donor relaxes to its ground state and the released energy is transferred through coulombic interactions (Figure 1.3, A). This phenomenon is used to measure molecular interactions, but is not suitable for most photocatalytic applications, especially in case of PCs that populate triplet excited states. This would require a $T_1 \rightarrow S_0$ transition of the PC and a $S_0 \rightarrow T_1$ transition of the substrate/reagent simultaneously to occur, which violates Wigner's spin conservation rules.⁵

Dexter energy transfer relies on two simultaneous electron transfer processes. In contrast to FRET, this requires an orbital overlap between the donor (PC) and the acceptor (Figure 1.3, B). Consequently, the efficiency of such reactions is limited by the rate of diffusion. The excited electron that populates the lowest unoccupied molecular orbital (LUMO) of the donor is transferred to the LUMO of the acceptor. Concomitantly, an electron from the highest occupied molecular orbital (HOMO) of the acceptor moves to the HOMO of the donor. The Dexter mechanism is responsible for the most photocatalytic organic transformations that take proceed *via* energy transfer mechanisms.

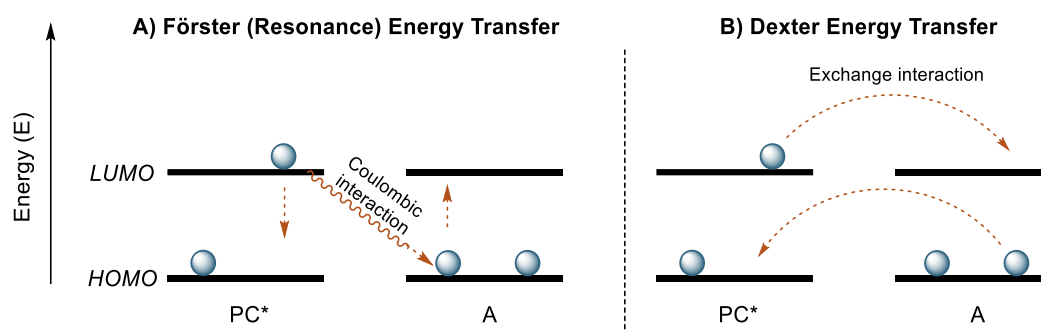


Figure 1.3. Förster (A) vs. Dexter EnT process (B).

1.1.2 Single electron transfer

The vast majority of photocatalytic reactions proceed *via* single electron transfer (SET) mechanisms (photoredox catalysis, PRC).⁶⁻⁷ Here, the excited photocatalyst is quenched by accepting or donating a single electron to a substrate, reagent or co-catalyst. This enables oxidative or reductive quenching cycles (Figure 1.4). In an oxidative quenching cycle, the excited photocatalyst (PC^*) first transfers an electron to an acceptor (A), which in turn generates a reducing species (PC^{ox}) that can subsequently accept an electron from a single electron donor (D) to close a catalytic cycle. Depending on reaction conditions, the inverse events occur to complete a reductive quenching cycle.

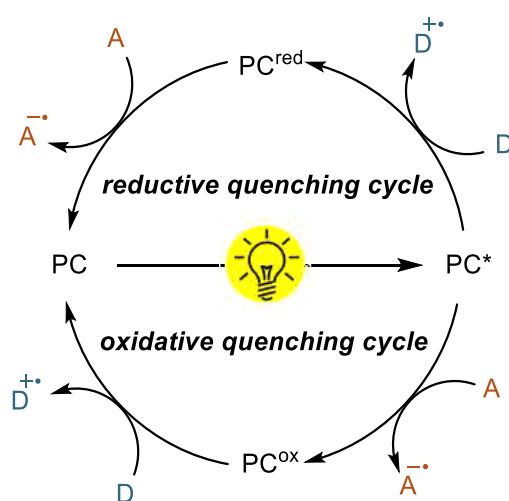


Figure 1.4. Reductive and oxidative quenching cycles in photoredox catalysis.

1.2 Metallaphotocatalyzed cross-couplings

Palladium-catalyzed cross-coupling reactions are among the most important reactions for constructing complex molecular scaffolds,⁸ but replacing palladium with a more sustainable metal is desirable. Nickel is an attractive alternative for palladium that exists in oxidation states that are crucial for such reactions and is much more abundant and therefore cheaper than noble metals. However, replacing palladium with nickel in cross-coupling reactions is challenging. Oxidative addition of an aryl halide to a Ni^0 complex and reaction with a nucleophile results in a thermodynamically stable Ni^{II} intermediate that does not form the desired carbon-heteroatom bond through reductive elimination.⁹ Destabilization of this Ni^{II} intermediate to trigger product formation requires strong bases, tailored ligands and/or high temperatures.¹⁰⁻¹² In 2014, the combination of photoredox and nickel catalysis was shown to efficiently perform such transformations under mild conditions with simple bipyridyl ligands.¹³⁻¹⁵ This approach is extensively studied for carbon-heteroatom (C-X) and carbon-carbon (C-C) cross-couplings.¹⁶⁻¹⁸

Depending on the substrates, different mechanisms were proposed in metallaphotocatalytic cross-couplings. In the case of the coupling of aryl halides with amines,¹⁹ sulfonamides²⁰ or carboxylic acids,²¹ energy transfer catalysis was suggested to turn over the nickel catalyst (Figure 1.5A).

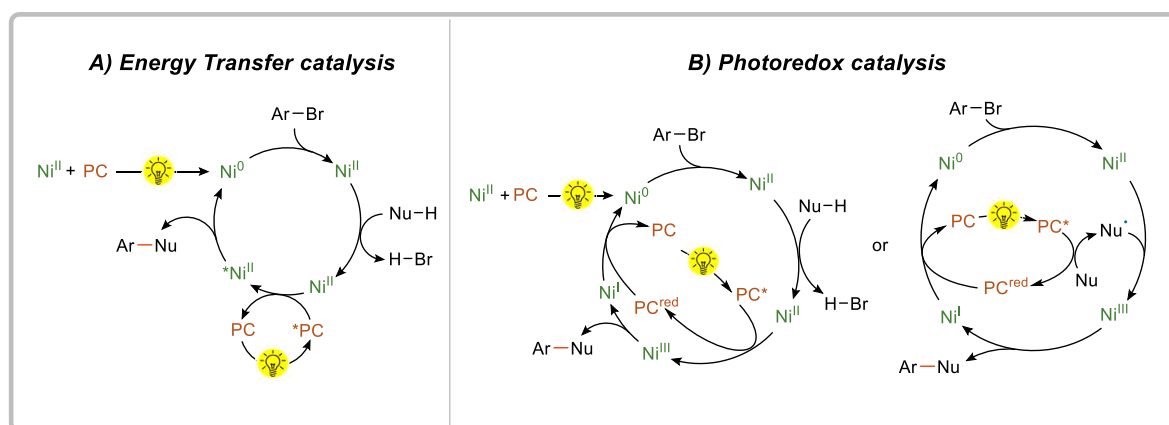


Figure 1.5. Activation of Ni^{II} intermediates with energy transfer catalysis (A) and photoredox catalysis for modulation of nickel oxidation state (B).

A fundamentally different mechanism was proposed for another amination²² protocol and the etherification²³ of aryl halides (Figure 1.5B). Here, oxidative addition is followed by

ligand exchange of the bromide with the respective nucleophile. Oxidation of the Ni^{II} species to Ni^{III} by the PC triggers reductive elimination of the desired product. The resulting Ni^{I} species is reduced by the PC to close both cycles. In the coupling of aryl halides with thiols and anilines,²⁴⁻²⁶ the photocatalyst was proposed to oxidize the nucleophile to produce a radical intermediate. This radical engages with a Ni^{II} species, which is generated by an oxidative addition of the aryl halide to Ni^0 . Reductive elimination of the formed Ni^{III} species releases the desired product and, after reduction of Ni^{I} to Ni^0 , the catalytic cycle is closed.

More recent studies, suggest that the role of the photocatalyst must be reconsidered. It has been hypothesized that carbon–heteroatom cross-couplings proceed *via* Ni^{I} - Ni^{III} sequences that are initiated by a reduction of the Ni^{II} pre-catalyst to the active Ni^{I} species. This hypothesis led to a photocatalyst-free coupling of aryl halides with carboxylic acids, alcohols and amines using Zn as a sub-stoichiometric reductant (Figure 1.6A).²⁷

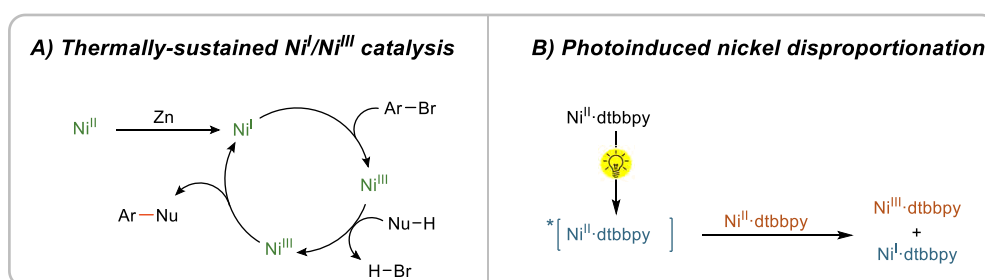


Figure 1.6. Thermally-sustained $\text{Ni}^{\text{I}}/\text{Ni}^{\text{III}}$ catalysis initiated by reduction with zinc (A), and photodisproportionation of nickel(II) complexes (B).

Another study showed that $\text{Ni}^{\text{II}}(\text{dtbbpy})$ aryl halide complexes (dtbbpy = 4,4'-di-*tert*-butyl-2,2'-bipyridyl) can absorb light through a metal-to-ligand charge transfer. Upon irradiation, Ni–aryl homolysis takes place to form a catalytically active Ni^{I} catalyst.²⁸⁻²⁹ This enables C–O and C–N cross-couplings by direct irradiation of nickel complexes with UV-light (Figure 1.6B).³⁰⁻³¹

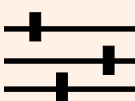
1.3 Photocatalysts

1.3.1 A wish list

In order to use light as a traceless, sustainable “reagent” an ideal photocatalyst should fulfill several requirements:³

Tunable redox potentials and excited state energies

Tunability



- redox potentials
- excited state energies

Depending on the reaction, the PC requires certain redox potentials or excited state energies to activate the substrate, reagent or co-catalyst. To adapt to the requirements of the reaction, these values should be tunable. For homogeneous organic and organometallic PCs, the introduction of electron donating or electron withdrawing groups can modify the redox potential. Heterogeneous photocatalysts can be tuned by structural modifications that alter the band structure.³²⁻³³

More specifically, the position of the valence and conduction band depend on several factors, such as the degree of crystallinity. In addition, surface complexation or doping can modify the electro- as well as photochemical properties of a photocatalyst. It is, however, important to note that changes of the electronic properties affect the optical properties of photocatalysts, such as absorbance. In addition, a reversible redox behavior is necessary.

Stability

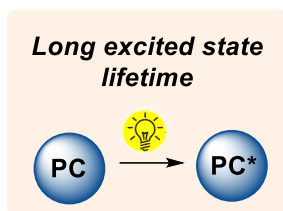
Stability



- thermal
- photo
- chemical

To ensure high turnover numbers, a photocatalyst has to be chemically, thermally and photochemically stable. Although most photocatalytic reactions are carried out without additional heating, some transformations can benefit from elevated temperatures under which no thermal degradations should occur. The photocatalyst should also not be destroyed by the highly reactive intermediates (radicals) it creates during a photocatalytic reaction. Most importantly, no degradation induced by photons (photobleaching) should occur.


Long excited state lifetime



Photocatalysts with short lifetimes may relax to the ground state before they collide with another species in solution. It is crucial that the lifetime of an excited photocatalyst is long enough to activate a target molecule in a diffusion-controlled process.

Absorption characteristics

Accessing long wavelengths




- Improved solar harvesting
- Better selectivity
- Chromoselective reactions

A strong absorbance over a broad range of wavelengths in the visible region (400-700 nm) is desirable for efficient use of (solar) light. Most organic molecules absorb only UV light. To prevent side reactions, an absorption overlap of the substrates and the catalyst should be avoided.³⁴ Accessing long wavelengths overcomes not only selectivity issues, but also enables biological applications,³⁵ increases the scalability of

reactions³⁶ and enables the opportunity to develop chromoselective reactions.³⁷

Preparation and sustainability

Simple synthesis



- 1-2 steps
- reproducible

The ideal synthesis of a photocatalyst is short, simple, scalable and reproducible. The precursors should be readily available. Common photocatalysts are based on expensive precious metal precursors, which is a drawback. Organic dyes are sustainable alternatives, but homogeneous photocatalysts are usually not recyclable. Heterogeneous photocatalysts are advantageous, because they can

be separated from the reaction mixture by filtration or centrifugation.

1.3.2 Organometallic complexes

To date, the vast majority of photocatalytic reactions are carried out using ruthenium or iridium polypyridyl complexes, which can undergo metal-to-ligand charge transfer to generate stable, long-lived excited states.⁷

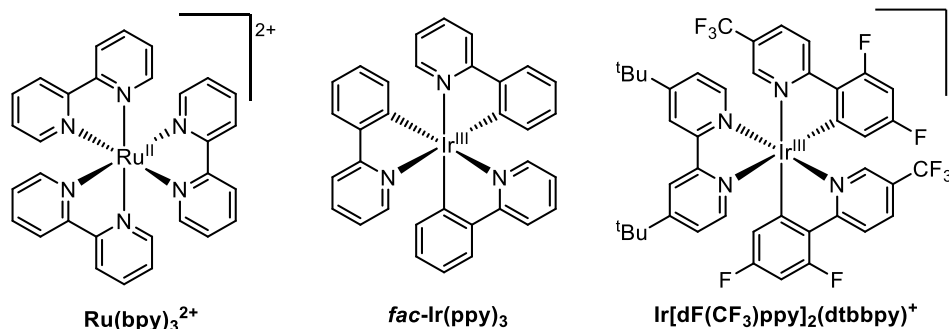


Figure 1.7. Structures of commonly used noble metal-based organometallic complexes.

Upon irradiation, an electron from the metal's t_{2g} -orbital is transferred to the π^* orbital of the ligand that is lower in energy than the e_g -orbital of the metal. This metal-to-ligand charge transfer (MLCT) transition results in a species in which the metal center has been oxidized and the ligand has undergone a single electron reduction. This singlet MLCT (S_1) immediately undergoes intersystem crossing (ISC), resulting in the lowest energy triplet MLCT state (T_1). The relaxation to the singlet ground state is a spin-forbidden process and such species have long excited state lifetimes (~ 1000 ns), suitable to participate in bimolecular ET or EnT processes. The versatility of these homogeneous photocatalysts derives from the ability to tailor their photochemical properties, by changing the metal and modifying the ligands in order to fulfill the needs of the respective chemical transformation.³ In addition, the solubility of a compound can be controlled by, for example, exchanging the counter ions. Recently, copper complexes have been investigated as photocatalysts, but are limited in their application compared to noble metal complexes.³⁸

1.3.3 Organic dyes

Organic dyes such as xanthenes, benzophenones, cyanoarenes,³⁹⁻⁴¹ acridinium salts⁴²⁻⁴³ and boron dipyrromethenes (BODIPY) are intensively studied as metal-free alternatives to transition metal complexes.⁴⁴

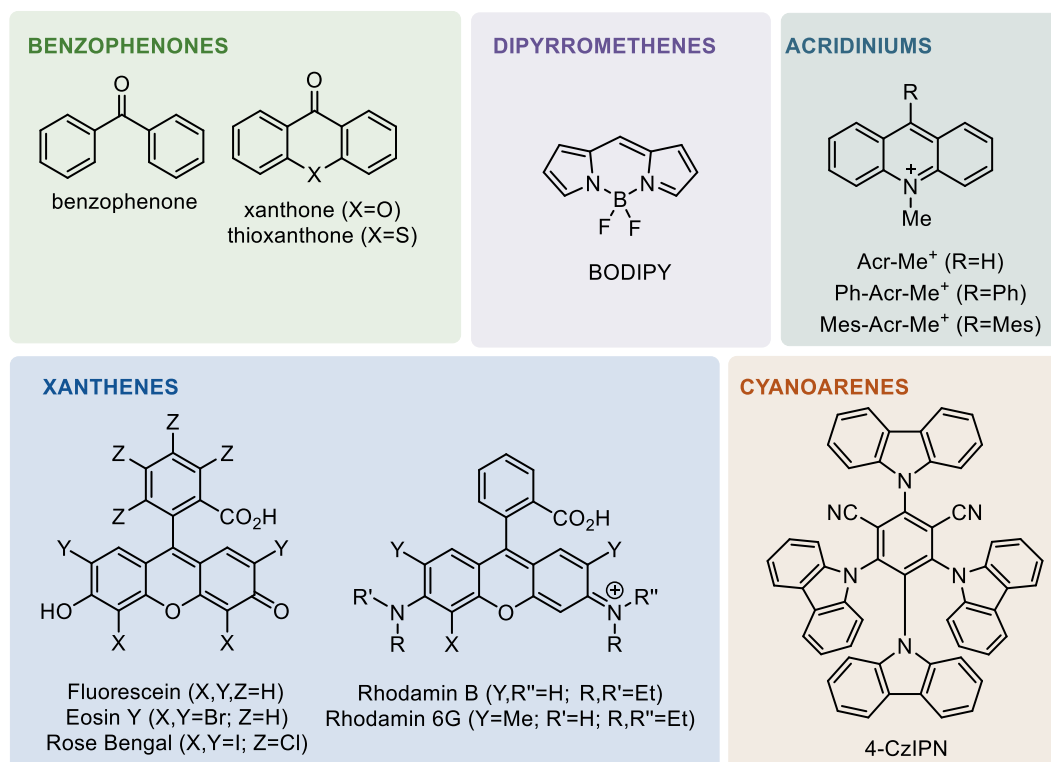


Figure 1.8. Structures of common organic dyes used as photocatalyst.

Many organic dyes are readily available or can be easily prepared and tuned by synthetic modifications. However, the short excited state lifetimes of most of these molecules are a major drawback.⁴⁴⁻⁴⁹ The majority of abundant organic dyes (e.g., fluorescein or rhodamine B) do not undergo intersystem crossing (Figure 1.9A). Upon excitation, they only reach short-lived singlet states, which quickly relax to the ground state *via* fluorescence. The collision of these singlet excited state species with another molecule in solution is statistically unlikely due to the limiting rate of diffusion, especially when the dye is present in catalytic amounts. Therefore, most of the current research using organic dyes as photocatalysts focuses on the design of photocatalysts that reach long-lived excited states.⁴⁹ Similar to organometallic complexes, some organic dyes such as cyanoarenes or eosin Y can reach long-lived triplet excited states through intersystem crossing (ISC) due to specific structural features, such as the heavy-atom effect,⁵⁰ or tailored electron densities (Figure

1.9B).⁵¹ In addition to their short excited state lifetimes, some organic dyes are prone to degradation.^{42, 52}

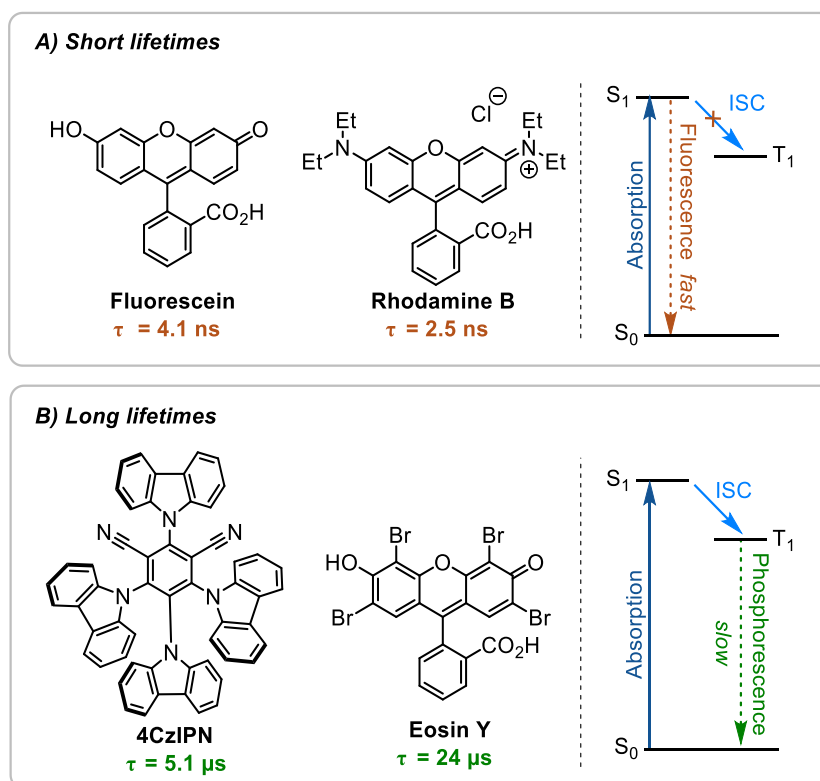


Figure 1.9. Selection of organic dyes that are suitable (A) or unsuitable (B) as photocatalysts due to their excited state lifetimes.

1.3.4 Summary of homogeneous photocatalysts

Redox potentials and selected photophysical properties of the discussed homogeneous photocatalysts are summarized below (Table 1.1).

Table 1.1. Photophysical and electrochemical properties of common photocatalysts.

<i>photocatalyst</i>	λ_{max} [nm]	τ [ns]	$E_{1/2}(PC^+/P^*)$ [V]	$E_{1/2}(P^*/P^{\cdot-})$ [V]	$E_{1/2}(PC^+/P)$ [V]	$E_{1/2}(P/P^{\cdot-})$ [V]	<i>Ref.</i>
<i>Ru(bpy)₃²⁺</i>	454	1100	-0.81	+0.77	+1.29	-1.33	7
<i>fac-Ir(ppy)₃</i>	375	1900	-1.73	+0.31	+0.77	-2.19	7
<i>Ir(ppy)₂(dtbbpy)⁺</i>	380	557	-0.96	+0.66	+1.21	-1.51	7
<i>Ir[dF(CF₃)ppy]₂(dtbbpy)⁺</i>	380	2300	-0.89	+1.21	+1.69	-1.37	7
<i>Cu(dap)₂⁺</i>	690	270	-1.43	-	+0.62	-	7
<i>4CzIPN</i>	365	5.1	-1.18	+1.43	+1.49	-1.24	39, 44
<i>Mes-Acr⁺</i>	425	6		2.06		-0.57	40, 44
<i>Fluorescein</i>	491	4.73		+0.83		-1.22	44
<i>Eosin Y</i>	520	2.1	-1.11	+0.83	+0.78	-1.06	39, 44
<i>Rose Bengal</i>	549	0.5	-0.99	+0.66	+0.78	-1.11	39, 44

All potentials are giving in volts versus the saturated calomel electrode (SCE)

1.3.5 Semiconductors

A suitable alternative to homogeneous photocatalysts are heterogeneous medium band gap semiconductors.⁵³ The energy difference between valence (VB) and conduction band (CB) enables the activation of such materials using visible light. When the semiconductor absorbs photons with sufficiently high energies, electrons are excited from the valence band (VB) into the conduction band (CB) thereby generating an oxidizing and a reducing species on a single particle at the same time. The electron holes in the VB (h^+) can oxidize electron donors whereas the electrons in the CB are able to reduce electron acceptors *via* single-electron transfer.

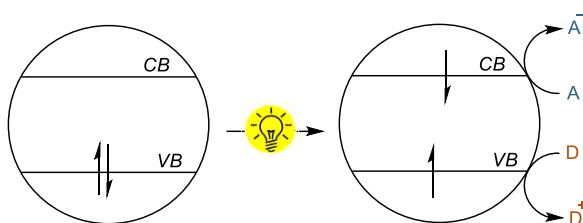


Figure 1.10. Charge separation in semiconductors upon light absorption.

A major benefit of semiconductors is their chemical and thermal stability and that they do not suffer from degradation during photocatalytic reactions. In addition, these heterogeneous catalysts can be typically easily recycled through filtration or centrifugation. Unfortunately, they often suffer from lower activity compared to homogenous catalysts.

Titanium dioxide (TiO₂)

Titanium dioxide has been used as a heterogeneous photocatalyst for multiple applications due to its high photoactivity and stability, as well as its low toxicity and abundance.⁵⁴ The large band gap energy of *ca.* 3.2 eV limits its absorbance to ultraviolet (UV) light.⁵⁵ Irradiation with UV light can cause selectivity issues through the direct activation of substrate or reagents. The absorbance of TiO₂ can be extended to visible light through the immobilization of sensitizers (dyes) on the surface of the metal oxide semiconductor.⁵⁶ This is used in dye-sensitized solar cells (DSSCs)⁵⁷ and dye-sensitized photocatalysts (DSPs) for H₂ production,⁵⁸ but rarely explored in organic synthesis.⁵⁹

Other inorganic semiconductors such as bismuth oxides, cadmium sulfide and cadmium selenide have smaller band gaps (2.1-2.8 eV) compared to TiO₂ and absorb visible light, but are only rarely applied in organic synthesis.⁵³

Carbon nitrides

The most common metal-free semiconductors used in photocatalysis are graphitic carbon nitrides (*g*-CN).⁵⁵⁻⁵⁶ These materials have a band gap of ~ 2.7 eV and are able to absorb visible light. In general, *g*-CN are organic polymers that consist of C and N and are easy to synthesize from cheap precursors, such as urea, cyanamide, or melamine through thermal polymerization. The band gap and position of the VB and CB can be modified by several factors such as the C/N ratio, the polymerization degree or the crystallinity that can be tailored *via* the synthetic approach.

Coming back to the “wish list” for photocatalysts, it can be concluded that an ideal candidate, that combines all the demands, does not exist yet. Each photocatalyst class has advantages, and disadvantages and the decision for the best material has to be made case-by-case considering the respective transformation.

The position of VB and CB, as well as the band gap of selected heterogeneous semiconductors are shown in Figure 1.11.

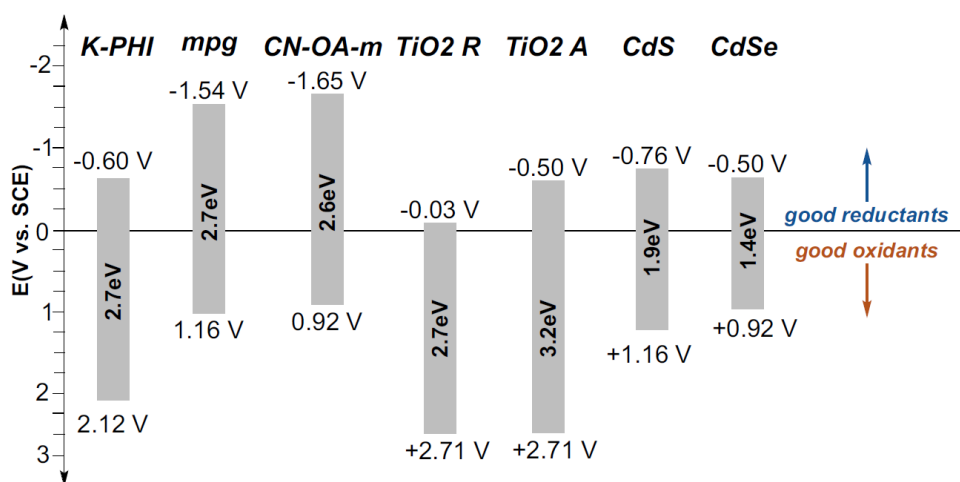


Figure 1.11. Band gap diagrams of heterogeneous photocatalysts.^{33, 60-61}

K-PHI = Potassium poly(heptazine imide), mpg = mesoporous graphitic carbon nitride, CN-OA-m = carbon nitride that is prepared through co-condensation of urea and oxamide, followed by post-calcination in a molten salt, TiO₂ R/A = titanium dioxide rutile/anatase, CdS = Cadmium sulfide, CdSe = cadmium selenide

1.4 Light as a parameter to control selectivity

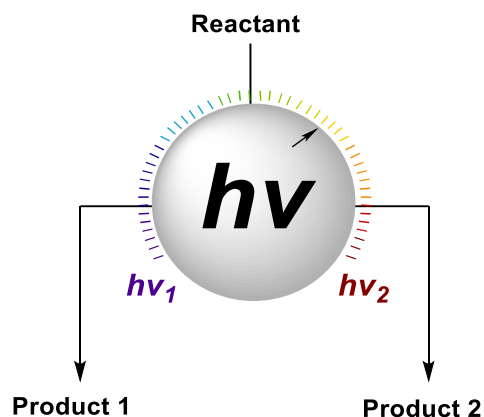


Figure 1.12. Light as a tool.

The main goal in synthetic chemistry is to find reaction conditions that maximize yield and selectivity. Traditionally, the selectivity of a reaction is often controlled by the stoichiometry of the reagents or changing reaction conditions such as temperature, pH, or the solvent. In photocatalysis, however, the wavelength and intensity of light are rarely used to influence the outcome of reactions.⁶²

Recently, it was shown that varying the irradiation wavelength also enables selective control between a one or two-fold substitution of 1,3,5-tribromobenzene with *N*-methylpyrrole using Rhodamin 6G (Rh-6G) as PC (Figure 1.13).³⁷ In presence of *N,N*-diisopropylethylamine (DIPEA), the radical anion Rh-6G^{•-} is formed upon irradiation with green light (530 nm). This species has a reduction potential of -1.0 V vs. SCE, which is sufficient to activate aryl bromides with relatively low reduction potentials, resulting in a selective monosubstitution. When blue light (455 nm) was used as irradiation source, the disubstituted products were obtained. This is possible, because at short wavelengths, Rh-6G^{•-} is again excited, forming Rh-6G^{•-*} (reduction potential ca -2.4 V vs. SCE), which can activate aryl bromides with rather high reduction potentials.

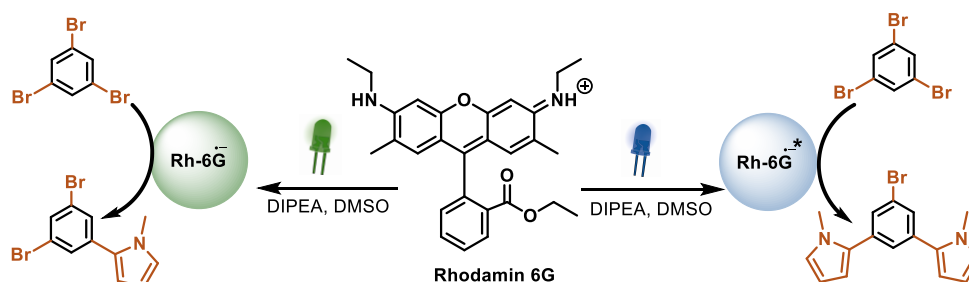


Figure 1.13. C-H arylation of *N*-methylpyrrole with 1,3,5-tribromobenzene.

1.5 Aim of the thesis

The aim of this doctoral thesis was to develop photocatalysts and methods that enable an efficient use of solar light and to study the influence of different wavelengths on photocatalytic reactions. A major focus of this doctoral study was the development of sustainable and efficient approaches using heterogeneous semiconductors.

First, a graphitic carbon nitride was used as a photocatalysts for the cross-coupling of aryl halides and amines. The semiconductor absorbs up to ~500 nm, which was key for developing robust conditions for challenging substrates. Specifically, the reaction of electron-rich aryl bromides suffered from severe reproducibility issues, which were overcome by controlling the rate of oxidative addition and reductive elimination *via* the substrate concentration and the wavelength, respectively.

The same catalyst enabled me and my collaborators to develop chromoselective reactions. I showed that a carbon nitrides can generate electron holes with different oxidation potentials depending on the irradiation wavelength. This allowed me to promote a photocatalytic reaction with green light selectively in the presence of a second substrate that is only photo-oxidized when high energetic blue light is used. By combining this approach with biocatalysis, the (*R*)- and (*S*)-enantiomer of 1-phenyl-ethan-1-ol derivatives were selectively synthesized from the respective ethylbenzenes in photo-biocatalytic cascade reactions.

In order to enable cross-coupling reactions with long wavelengths, I developed a strategy that was inspired by dye-sensitized solar cells. Key to success was the immobilization of an organic dye and a nickel complex on the surface of TiO₂. By studying different dyes and nickel complexes, I showed that such modular, self-assembling catalytic systems can harvest the entire visible light spectrum. More importantly, by studying different functional groups for the immobilization, I was able to attach the nickel complex and the dye permanently on the semiconductor. This resulted in a recyclable bifunctional catalyst for light-mediated cross-couplings.

1.6 References

1. Hoffmann, N., Photochemical Reactions as Key Steps in Organic Synthesis. *Chem. Rev.* **2008**, *108* (3), 1052-1103.
2. Scholes, G. D.; Fleming, G. R.; Olaya-Castro, A.; van Grondelle, R., Lessons from nature about solar light harvesting. *Nat. Chem.* **2011**, *3* (10), 763-774.
3. Arias-Rotondo, D. M.; McCusker, J. K., The photophysics of photoredox catalysis: a roadmap for catalyst design. *Chem. Soc. Rev.* **2016**, *45* (21), 5803-5820.
4. Verhoeven, J. W., Glossary of terms used in photochemistry. *Pure Appl. Chem.* **1996**, *68* (12).
5. Strieth-Kalthoff, F.; James, M. J.; Teders, M.; Pitzer, L.; Glorius, F., Energy transfer catalysis mediated by visible light: principles, applications, directions. *Chem. Soc. Rev.* **2018**, *47* (19), 7190-7202.
6. Shaw, M. H.; Twilton, J.; MacMillan, D. W. C., Photoredox Catalysis in Organic Chemistry. *J. Org. Chem.* **2016**, *81* (16), 6898-6926.
7. Prier, C. K.; Rankic, D. A.; MacMillan, D. W. C., Visible Light Photoredox Catalysis with Transition Metal Complexes: Applications in Organic Synthesis. *Chem. Rev.* **2013**, *113* (7), 5322-5363.
8. Johansson Seechurn, C. C. C.; Kitching, M. O.; Colacot, T. J.; Snieckus, V., Palladium-Catalyzed Cross-Coupling: A Historical Contextual Perspective to the 2010 Nobel Prize. *Angew. Chem. Int. Ed.* **2012**, *51* (21), 5062-5085.
9. Han, R.; Hillhouse, G. L., Carbon–Oxygen Reductive-Elimination from Nickel(II) Oxametallacycles and Factors That Control Formation of Ether, Aldehyde, Alcohol, or Ester Products. *J. Am. Chem. Soc.* **1997**, *119* (34), 8135-8136.
10. Wolfe, J. P.; Buchwald, S. L., Nickel-Catalyzed Amination of Aryl Chlorides. *J. Am. Chem. Soc.* **1997**, *119* (26), 6054-6058.
11. Ge, S.; Green, R. A.; Hartwig, J. F., Controlling First-Row Catalysts: Amination of Aryl and Heteroaryl Chlorides and Bromides with Primary Aliphatic Amines Catalyzed by a BINAP-Ligated Single-Component Ni(0) Complex. *J. Am. Chem. Soc.* **2014**, *136* (4), 1617-1627.
12. Tassone, J. P.; England, E. V.; MacQueen, P. M.; Ferguson, M. J.; Stradiotto, M., PhPAd-DalPhos: Ligand-Enabled, Nickel-Catalyzed Cross-Coupling of (Hetero)aryl

Electrophiles with Bulky Primary Alkylamines. *Angew. Chem. Int. Ed.* **2019**, *58* (8), 2485-2489.

13. Twilton, J.; Le, C.; Zhang, P.; Shaw, M. H.; Evans, R. W.; MacMillan, D. W. C., The merger of transition metal and photocatalysis. *Nat. Rev. Chem.* **2017**, *1*, 0052.

14. Skubi, K. L.; Blum, T. R.; Yoon, T. P., Dual Catalysis Strategies in Photochemical Synthesis. *Chem. Rev.* **2016**, *116* (17), 10035-10074.

15. Hopkinson, M. N.; Sahoo, B.; Li, J.-L.; Glorius, F., Dual Catalysis Sees the Light: Combining Photoredox with Organo-, Acid, and Transition-Metal Catalysis. *Chem. Eur. J.* **2014**, *20* (14), 3874-3886.

16. Milligan, J. A.; Phelan, J. P.; Badir, S. O.; Molander, G. A., Alkyl Carbon–Carbon Bond Formation by Nickel/Photoredox Cross-Coupling. *Angew. Chem. Int. Ed.* **2019**, *58* (19), 6152-6163.

17. Zhu, C.; Yue, H.; Jia, J.; Rueping, M., Nickel-Catalyzed C-Heteroatom Cross-Coupling Reactions under Mild Conditions via Facilitated Reductive Elimination. *Angew. Chem. Int. Ed.* **2021**, *60* (30), 17810-17831.

18. Zhu, C.; Yue, H.; Chu, L.; Rueping, M., Recent advances in photoredox and nickel dual-catalyzed cascade reactions: pushing the boundaries of complexity. *Chem. Sci.* **2020**, *11* (16), 4051-4064.

19. Kudisch, M.; Lim, C.-H.; Thordarson, P.; Miyake, G. M., Energy Transfer to Ni-Amine Complexes in Dual Catalytic, Light-Driven C–N Cross-Coupling Reactions. *J. Am. Chem. Soc.* **2019**, *141* (49), 19479-19486.

20. Kim, T.; McCarver, S. J.; Lee, C.; MacMillan, D. W. C., Sulfonamidation of Aryl and Heteroaryl Halides through Photosensitized Nickel Catalysis. *Angew. Chem. Int. Ed.* **2018**, *57* (13), 3488-3492.

21. Welin, E. R.; Le, C.; Arias-Rotondo, D. M.; McCusker, J. K.; MacMillan, D. W. C., Photosensitized, energy transfer-mediated organometallic catalysis through electronically excited nickel(II). *Science* **2017**, *355* (6323), 380-385.

22. Corcoran, E. B.; Pirnot, M. T.; Lin, S.; Dreher, S. D.; DiRocco, D. A.; Davies, I. W.; Buchwald, S. L.; MacMillan, D. W. C., Aryl amination using ligand-free Ni(II) salts and photoredox catalysis. *Science* **2016**, *353*, 279-283.

Chapter 1

23. Terrett, J. A.; Cuthbertson, J. D.; Shurtleff, V. W.; MacMillan, D. W. C., Switching on elusive organometallic mechanisms with photoredox catalysis. *Nature* **2015**, *524*, 330-334.
24. Oderinde, M. S.; Jones, N. H.; Juneau, A.; Frenette, M.; Aquila, B.; Tentarelli, S.; Robbins, D. W.; Johannes, J. W., Highly Chemoselective Iridium Photoredox and Nickel Catalysis for the Cross-Coupling of Primary Aryl Amines with Aryl Halides. *Angew. Chem. Int. Ed.* **2016**, *55* (42), 13219-13223.
25. Oderinde, M. S.; Frenette, M.; Robbins, D. W.; Aquila, B.; Johannes, J. W., Photoredox Mediated Nickel Catalyzed Cross-Coupling of Thiols With Aryl and Heteroaryl Iodides via Thiyl Radicals. *J. Am. Chem. Soc.* **2016**, *138* (6), 1760-1763.
26. Key, R. J.; Vannucci, A. K., Nickel Dual Photoredox Catalysis for the Synthesis of Aryl Amines. *Organometallics* **2018**, *37* (9), 1468-1472.
27. Sun, R.; Qin, Y.; Nocera, D. G., General Paradigm in Photoredox Nickel-Catalyzed Cross-Coupling Allows for Light-Free Access to Reactivity. *Angew. Chem. Int. Ed.* **2020**, *59* (24), 9527-9533.
28. Ting, S. I.; Garakyaraghi, S.; Taliaferro, C. M.; Shields, B. J.; Scholes, G. D.; Castellano, F. N.; Doyle, A. G., (3)d-d Excited States of Ni(II) Complexes Relevant to Photoredox Catalysis: Spectroscopic Identification and Mechanistic Implications. *J. Am. Chem. Soc.* **2020**, *142* (12), 5800-5810.
29. Shields, B. J.; Kudisch, B.; Scholes, G. D.; Doyle, A. G., Long-Lived Charge-Transfer States of Nickel(II) Aryl Halide Complexes Facilitate Bimolecular Photoinduced Electron Transfer. *J. Am. Chem. Soc.* **2018**, *140* (8), 3035-3039.
30. Li, G.; Yang, L.; Liu, J. J.; Zhang, W.; Cao, R.; Wang, C.; Zhang, Z.; Xiao, J.; Xue, D., Light-Promoted C-N Coupling of Aryl Halides with Nitroarenes. *Angew. Chem. Int. Ed.* **2021**, *60* (10), 5230-5234.
31. Yang, L.; Lu, H. H.; Lai, C. H.; Li, G.; Zhang, W.; Cao, R.; Liu, F.; Wang, C.; Xiao, J.; Xue, D., Light-Promoted Nickel Catalysis: Etherification of Aryl Electrophiles with Alcohols Catalyzed by a Ni(II) -Aryl Complex. *Angew. Chem. Int. Ed.* **2020**, *59* (31), 12714-12719.
32. Markushyna, Y.; Smith, C. A.; Savateev, A., Organic Photocatalysis: Carbon Nitride Semiconductors vs. Molecular Catalysts. *Eur. J. Org. Chem.* **2020**, *2020* (10), 1294-1309.

33. Savateev, A.; Antonietti, M., Heterogeneous Organocatalysis for Photoredox Chemistry. *ACS Catal.* **2018**, *8* (10), 9790-9808.
34. Marzo, L.; Pagire, S. K.; Reiser, O.; König, B., Visible-Light Photocatalysis: Does It Make a Difference in Organic Synthesis? *Angew. Chem. Int. Ed.* **2018**, *57* (32), 10034-10072.
35. Ravetz, B. D.; Pun, A. B.; Churchill, E. M.; Congreve, D. N.; Rovis, T.; Campos, L. M., Photoredox catalysis using infrared light via triplet fusion upconversion. *Nature* **2019**, *565* (7739), 343-346.
36. Ravetz, B. D.; Tay, N. E. S.; Joe, C. L.; Sezen-Edmonds, M.; Schmidt, M. A.; Tan, Y.; Janey, J. M.; Eastgate, M. D.; Rovis, T., Development of a Platform for Near-Infrared Photoredox Catalysis. *ACS Cent. Sci.* **2020**.
37. Ghosh, I.; König, B., Chromoselective Photocatalysis: Controlled Bond Activation through Light-Color Regulation of Redox Potentials. *Angew. Chem. Int. Ed.* **2016**, *55* (27), 7676-7679.
38. Hossain, A.; Bhattacharyya, A.; Reiser, O., Copper's rapid ascent in visible-light photoredox catalysis. *Science* **2019**, *364* (6439), eaav9713.
39. Shang, T. Y.; Lu, L. H.; Cao, Z.; Liu, Y.; He, W. M.; Yu, B., Recent advances of 1,2,3,5-tetrakis(carbazol-9-yl)-4,6-dicyanobenzene (4CzIPN) in photocatalytic transformations. *Chem Commun.* **2019**, *55* (38), 5408-5419.
40. Speckmeier, E.; Fischer, T. G.; Zeitler, K., A Toolbox Approach To Construct Broadly Applicable Metal-Free Catalysts for Photoredox Chemistry: Deliberate Tuning of Redox Potentials and Importance of Halogens in Donor–Acceptor Cyanoarenes. *J. Am. Chem. Soc.* **2018**, *140* (45), 15353-15365.
41. Luo, J.; Zhang, J., Donor–Acceptor Fluorophores for Visible-Light-Promoted Organic Synthesis: Photoredox/Ni Dual Catalytic C(sp³)–C(sp²) Cross-Coupling. *ACS Catal.* **2016**, *6* (2), 873-877.
42. Joshi-Pangu, A.; Lévesque, F.; Roth, H. G.; Oliver, S. F.; Campeau, L.-C.; Nicewicz, D.; DiRocco, D. A., Acridinium-Based Photocatalysts: A Sustainable Option in Photoredox Catalysis. *J. Org. Chem.* **2016**, *81* (16), 7244-7249.
43. Zilate, B.; Fischer, C.; Sparr, C., Design and application of aminoacridinium organophotoredox catalysts. *Chem. Commun.* **2020**, *56* (12), 1767-1775.

Chapter 1

44. Romero, N. A.; Nicewicz, D. A., Organic Photoredox Catalysis. *Chem. Rev.* **2016**, *116* (17), 10075-10166.
45. Fukuzumi, S.; Ohkubo, K., Selective photocatalytic reactions with organic photocatalysts. *Chem. Sci.* **2013**, *4* (2), 561-574.
46. Amos, S. G. E.; Garreau, M.; Buzzetti, L.; Waser, J., Photocatalysis with organic dyes: facile access to reactive intermediates for synthesis. *Beilstein J. Org. Chem.* **2020**, *16*, 1163-1187.
47. Bonardi, A.-H.; Dumur, F.; Noirbent, G.; Lalevée, J.; Gigmes, D., Organometallic vs organic photoredox catalysts for photocuring reactions in the visible region. *Beilstein J. Org. Chem.* **2018**, *14*, 3025-3046.
48. Bogdos, M. K.; Pinard, E.; Murphy, J. A., Applications of organocatalysed visible-light photoredox reactions for medicinal chemistry. *Beilstein J. Org. Chem.* **2018**, *14*, 2035-2064.
49. Vega-Peñaloza, A.; Mateos, J.; Companyó, X.; Escudero-Casao, M.; Dell'Amico, L., A Rational Approach to Organo-Photocatalysis: Novel Designs and Structure-Property Relationships. *Angew. Chem. Int. Ed.* **2021**, *60* (3), 1082-1097.
50. Zhao, J.; Wu, W.; Sun, J.; Guo, S., Triplet photosensitizers: from molecular design to applications. *Chem. Soc. Rev.* **2013**, *42* (12), 5323-5351.
51. Lu, J.; Pattengale, B.; Liu, Q.; Yang, S.; Shi, W.; Li, S.; Huang, J.; Zhang, J., Donor–Acceptor Fluorophores for Energy-Transfer-Mediated Photocatalysis. *J. Am. Chem. Soc.* **2018**, *140* (42), 13719-13725.
52. Romero, N. A.; Margrey, K. A.; Tay, N. E.; Nicewicz, D. A., Site-selective arene C–H amination via photoredox catalysis. *Science* **2015**, *349* (6254), 1326-1330.
53. Gisbertz, S.; Pieber, B., Heterogeneous Photocatalysis in Organic Synthesis. *ChemPhotoChem* **2020**, *4* (7), 456-475.
54. Schneider, J.; Matsuoka, M.; Takeuchi, M.; Zhang, J.; Horiuchi, Y.; Anpo, M.; Bahnemann, D. W., Understanding TiO₂ Photocatalysis: Mechanisms and Materials. *Chem. Rev.* **2014**, *114* (19), 9919-9986.
55. Riente, P.; Noël, T., Application of metal oxide semiconductors in light-driven organic transformations. *Catal. Sci. Tech.* **2019**, *9* (19), 5186-5232.
56. Zhang, L.; Cole, J. M., Anchoring Groups for Dye-Sensitized Solar Cells. *ACS Appl. Mater. Inter.* **2015**, *7* (6), 3427-3455.

57. Hagfeldt, A.; Boschloo, G.; Sun, L.; Kloo, L.; Pettersson, H., Dye-Sensitized Solar Cells. *Chem. Rev.* **2010**, *110* (11), 6595-6663.
58. Willkomm, J.; Orchard, K. L.; Reynal, A.; Pastor, E.; Durrant, J. R.; Reisner, E., Dye-sensitised semiconductors modified with molecular catalysts for light-driven H₂ production. *Chem. Soc. Rev.* **2016**, *45* (1), 9-23.
59. Franchi, D.; Amara, Z., Applications of Sensitized Semiconductors as Heterogeneous Visible-Light Photocatalysts in Organic Synthesis. *ACS Sustain. Chem. Eng.* **2020**, *8* (41), 15405-15429.
60. Babu, V. J.; Vempati, S.; Uyar, T.; Ramakrishna, S., Review of one-dimensional and two-dimensional nanostructured materials for hydrogen generation. *Phys. Chem. Chem. Phys.* **2015**, *17* (5), 2960-2986.
61. Markushyna, Y.; Schüßlbauer, C. M.; Ullrich, T.; Guldi, D. M.; Antonietti, M.; Savateev, A., Chromoselective Synthesis of Sulfonyl Chlorides and Sulfonamides with Potassium Poly(heptazine imide) Photocatalyst. *Angew. Chem. Int. Ed.* **2021**, *60* (37), 20543-20550.
62. Protti, S.; Ravelli, D.; Fagnoni, M., Wavelength dependence and wavelength selectivity in photochemical reactions. *Photochem. Photobiol. Sci.* **2019**, *18* (9), 2094-2101.

Chapter 2

Emerging concepts in photocatalytic organic synthesis

Reischauer, S.; Pieber, B.

iScience **2021**, *24*, 102209.

<https://doi.org/10.1016/j.isci.2021.102209>

Abstract

Visible light photocatalysis has become a powerful tool in organic synthesis that uses photons as traceless, sustainable reagents. Most of the activities in the field focus on the development of new reactions via common photoredox cycles, but recently a number of exciting new concepts and strategies entered less charted territories. We survey approaches that enable the use of longer wavelengths and show that the wavelength and intensity of photons are important parameters that enable tuning of the reactivity of a photocatalyst to control or change the selectivity of chemical reactions. In addition, we discuss recent efforts to substitute strong reductants, such as elemental lithium and sodium, by light, and technological advances in the field.

Specific contribution

I collected and organized the literature existing on the topic at the time (March 2021). I outlined a structure for the work, prepared figures, tables and schemes and wrote the manuscript. B. Pieber revised and corrected the manuscript.

2.1 Introduction

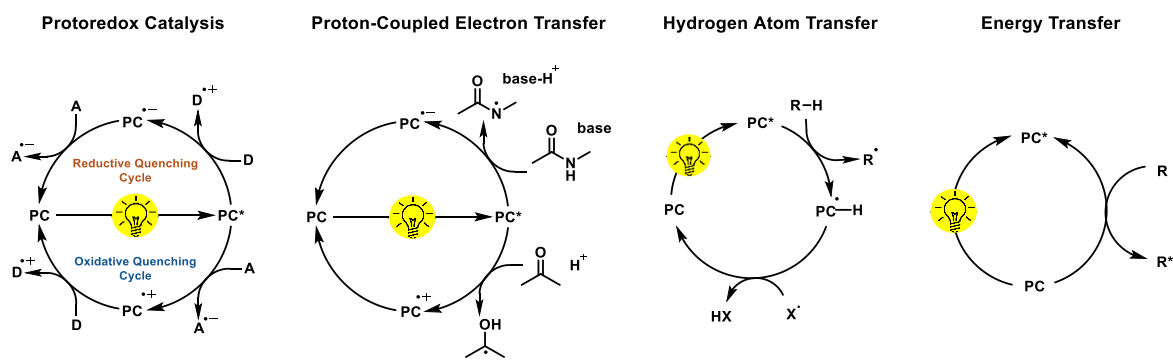
Using light to induce chemical reactions is attractive since photons are traceless reagents that provide energy to activate substrates, reagents or catalytic intermediates under mild conditions. Traditionally, photochemical reactions were carried out using ultraviolet light (UV) to excite substrates or reagents¹. The high energy of these light sources requires special equipment and often causes unselective reactions, which are difficult to predict and control. This has changed with the development of photocatalysts (PC) that can be activated with low-energy photons, paving the way for sustainable chemical synthesis that is driven by a non-hazardous and environmentally friendly reagent: visible-light.² Photocatalysts can initiate transformations via various mechanistic scenarios (Figure 2.1, A).³ In particular, visible light photoredox catalysis (PRC) has gained widespread recognition as a powerful tool in organic synthesis.⁴⁻⁵ Upon irradiation, an excited catalyst (PC*) accepts or donates a single electron, enabling oxidative or reductive quenching cycles depending on the substrates and reagents that are present in the reaction mixture. During an oxidative quenching cycle, the excited state catalyst reduces an electron acceptor (**A**), resulting in a strong oxidant (PC⁺). This oxidized form of the catalyst can accept an electron from a suitable donor (**D**) to close the catalytic cycle. Depending on reaction conditions, the inverse events can occur to complete a reductive quenching cycle. Redox events can be also accompanied by a concerted proton transfer (proton coupled electron transfer, PCET).⁶ Photocatalytic hydrogen atom transfer (HAT), on the contrary, proceeds through homolytic cleavage of C–H bonds by the photocatalyst, or after single electron transfer events.⁷ Moreover, a PC can also transfer its excited state energy to a substrate or reagent that is not able to absorb light at the given wavelength, thereby inducing a chemical reaction.⁸

Photocatalysis can be combined with “conventional” catalysis (dual catalysis) to enable reactions that are not possible using only one catalyst (Figure 2.1, B).⁹ Merging photocatalysis with transition metal catalysis (metallaphotocatalysis) enables selective carbon–heteroatom and carbon–carbon cross coupling reactions under mild conditions.¹⁰ Key to the success is the modulation of the oxidation state of transition metal complexes via single electron transfer (SET) processes, radical additions, or by photosensitization. This strategy is extensively studied using nickel complexes,¹⁰⁻¹¹ and was further expanded to a range of other transition metals,^{9, 12} including abundant first row metals such as cobalt,¹³ copper,¹⁴ and iron.¹⁵⁻¹⁶ Combining photo- and organocatalysis involves SET of an excited

Chapter 2

photocatalyst and, for example, enamine intermediates to enable the α -functionalization of aldehydes with high enantioselectivity.¹⁷ Catalytic amounts of Lewis acids form activated complexes with certain substrates, which can interact with a PC to trigger, for example, [2+2] photocycloadditions.¹⁸

A Mechanistic Pathways of Photocatalysis



B Dual Catalysis

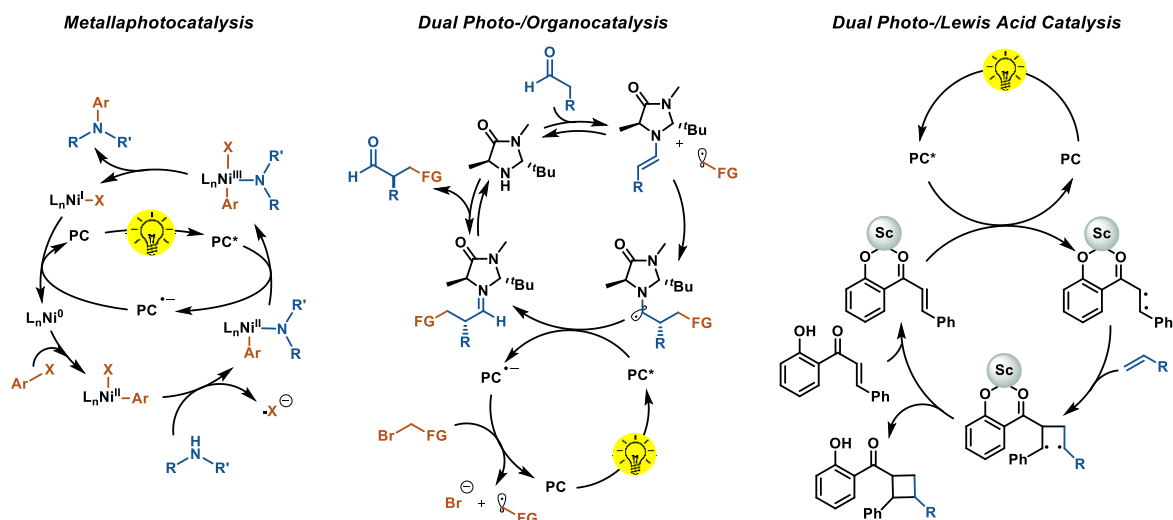


Figure 2.1. Different modes of photocatalysis (A) and selected examples for dual catalysis (B).

2.2 Photocatalysis in medicinal chemistry and the pharmaceutical industry

Although photocatalytic synthesis with visible light is a relatively young branch of organic chemistry, it quickly became an integral part of the synthetic chemists' toolbox. The advantages associated with visible light photocatalysis resulted in various applications in medicinal chemistry, including drug discovery, bioconjugation, late-stage C–H functionalization, and isotopic labelling (Figure 2.2).^{19–20}

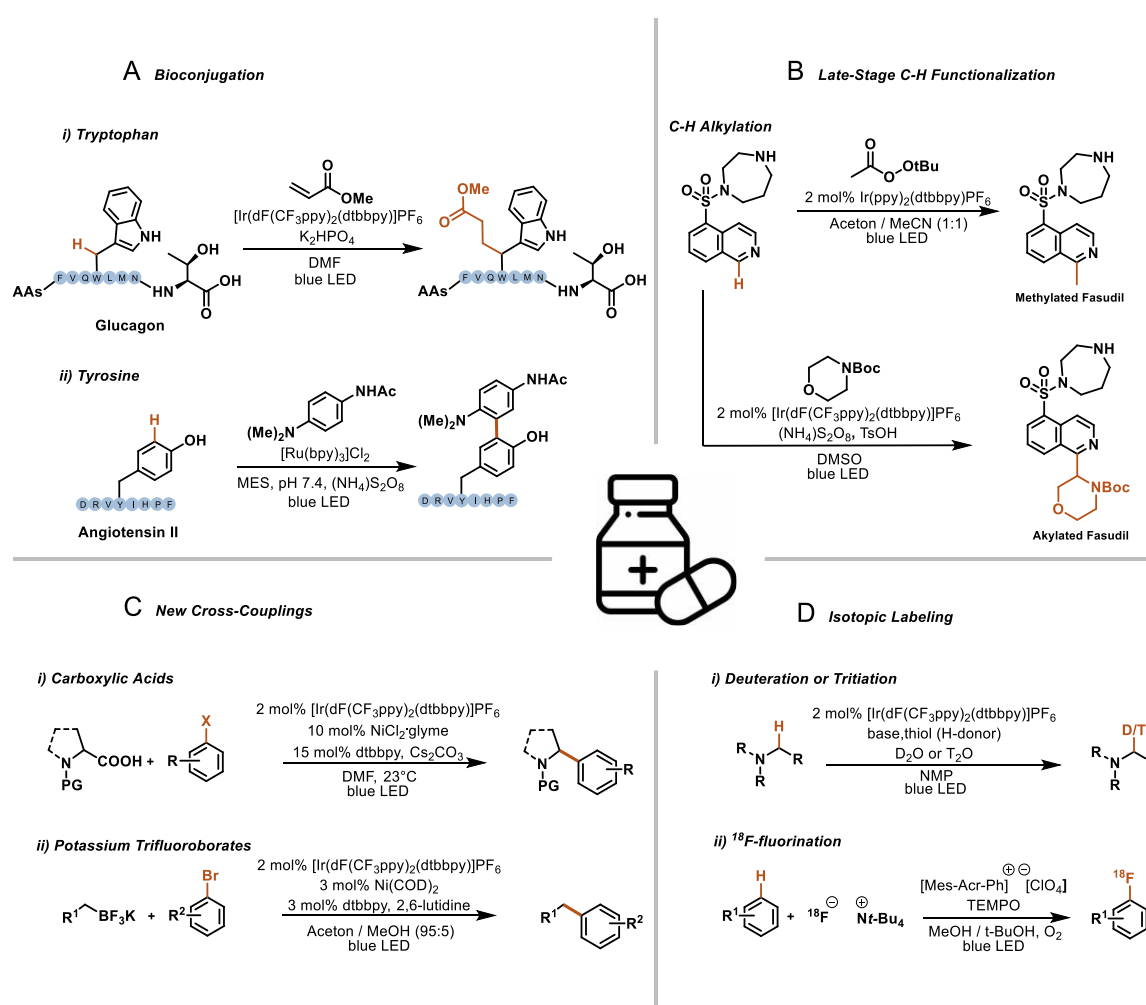


Figure 2.2. Representative examples of photocatalytic reactions of interest in medicinal chemistry. Bioconjugations (A). Late-stage C–H functionalizations (B). C_{sp3}–C_{sp2} cross-coupling reactions (C). Isotopic labeling (D).

Chemoselective peptide modifications are achieved through the selective photocatalytic activation of tryptophan to induce Michael-type additions (Figure 2.2, A).²¹ The method was validated on the peptide hormone glucagon resulting in 16% isolated yield of the desired conjugate. The low selectivity was a result of bis-conjugation (tryptophan and C-terminus), but remarkably, no conjugation on the His, Phe, Tyr, Arg, Met, Ser, Lys and Thr residues was observed.

Tyrosine residues were selectively modified using Ru(byp)₃Cl₂.²² The authors could also show that the tyrosine modification can be carried out on a specific protein in cell lysates. Therefore, the ruthenium PC was equipped with a ligand that binds selectively to the target protein. This enables local single electron transfer reactions on the target protein, whereas the tyrosine amino acids of other proteins in the lysate stay untouched.

Photocatalysis enabled the late stage alkylation of biologically active heterocycles (Figure 2.2, B). Methylation of Fasudil, an important rho-kinase inhibitor, was achieved via the generation of a methyl radical using *t*-butylperacetate and an iridium photocatalyst through a PCET mechanism.²³ In a similar vein, Fasudil was functionalized with *N*-Boc-protected morpholine. In this case, the generation of an α -amino radical enabled the direct cross-dehydrogenative-coupling via a Minisci-type addition.²⁴ In both cases, high-throughput experimentation (HTE) techniques were used to identify suitable catalytic cocktails.

Metallaphotocatalysis is at the forefront of light-mediated reactions and has a significant impact in small molecule synthesis (Figure 2.2, C). In traditional, palladium catalyzed transformations organometallic nucleophiles are coupled with aryl (pseudo)halides. These methods are effective for C_{sp2}-C_{sp2} couplings, but C_{sp3}-C_{sp2} are challenging due to low rates of oxidative addition and reductive elimination, as well as undesired side reactions via β -hydride elimination. In 2014, two independent publications showed that efficient C_{sp3}-C_{sp2} cross couplings can be achieved using dual photo/nickel catalysis via the photocatalytic generation of alkyl radicals from carboxylic acids,²⁵ or potassium trifluoroborates.²⁶ The radical adds to a Ni(II) complex that is formed via oxidative addition of an aryl halide with a Ni(0) catalyst. The resulting Ni(III) complex undergoes facile reductive elimination of the desired product and a final photocatalytic SET event regenerates the Ni(0) catalyst. A range of similar strategies for other alkyl radical

precursors,¹¹ and various carbon – heteroatom couplings²⁷ were developed that all have the potential to have a high impact in the synthesis of active pharmaceutical ingredients (APIs).

Understanding the metabolic fate of a drug candidate is a key factor during its development. One common technique to gain better understanding of the biological behavior is to label its molecular framework with stable isotopes. Late stage labeling of pharmaceutically active compounds with deuterium and tritium was recently realized via a photoredox mediated HAT reaction (Figure 2.2, D).²⁸ This method enables hydrogen-deuterium or hydrogen-tritium exchange reactions using isotopically labeled water (D₂O or T₂O) in a single step and was applied for several APIs. More recently, a direct arene C-H fluorination with ¹⁸F containing salts was realized using an acridinium photocatalyst.²⁹

In addition, a series of new strategies and concepts for light-mediated methodologies were developed that have the potential to open up new horizons in medicinal chemistry and industrial applications. These protocols access hitherto undisclosed reactions, enable new ways to control selectivities, and overcome limitations of current approaches. Here, we discuss these developments using selected examples. We begin our survey with methods that enable the use of long wavelengths, which is key for efficient solar harvesting. Thereafter, we discuss examples that show that the photons are not only a sustainable energy source to trigger reactions, but also enable controlling selectivities in reactions by changing the photon energy/intensity. Next, we survey strategies to generate catalyst species that have oxidation/reduction potentials beyond those which are accessible by “standard” photoredox cycles, and have the potential to serve as sustainable alternatives for reactions that, for example, require elemental sodium or lithium. Reaction technology is of utmost importance for reproducible and efficient photocatalytic reactions. In the last two chapters, we discuss some recent technological achievements for photocatalytic transformations using batch and continuous flow strategies.

2.3 The wavelength matters

Most photocatalytic reactions, including the examples described above, rely on a small set of photocatalysts, such as homogeneous iridium or ruthenium polypyridyl complexes,³⁰ a few organic dyes,³¹ and some semiconducting materials³² with suitable redox potentials or triplet energies, and long-lived excited states. One of the main drawbacks of these PCs is their limitation to highly energetic visible light (Figure 2.3).³³ Photocatalytic strategies that use the entire visible light spectrum would enable efficient solar harvesting and are key for performing sustainable photochemical reactions with sunlight instead of artificial light sources. Further, photochemical systems that are able to use near IR irradiation allow the activation of photocatalysts through barriers, such as skin and tissue, which bears high potential for biological and medical applications.³⁴ Many dyes absorb broadly across the visible light spectrum and their redox potentials and excited state energies are in theory suitable for photocatalysis, but these chromophores have low ISC rates, and therefore reach only short lived singlet excited states that are not suitable for photocatalysis.

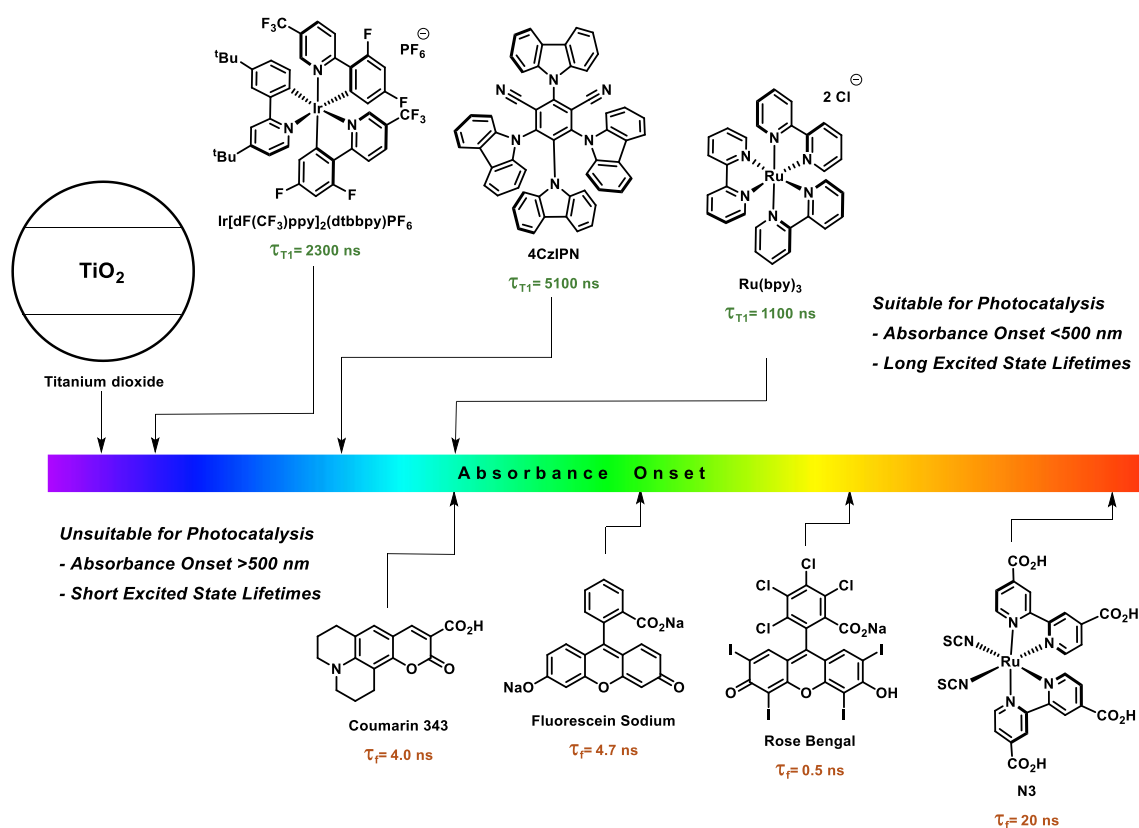


Figure 2.3. Onset of absorption of selected dyes and semiconductors. The suitability for photocatalysis depends on excited state lifetimes.

Chromophores with short excited lifetimes have shown enormous potential in other research areas. A plethora of organic dyes are used as sensitizers in dye-sensitized solar cells (DSSCs).³⁵ In DSSCs, the dyes are adsorbed or bound to the surface of a semiconducting material, such as TiO₂. Because of the resulting spatial proximity, even dyes with short excited state lifetimes efficiently inject electrons into the conduction band of the semiconductor. This results in charge-separated species that are sustained for several microseconds.³⁶ Compared to molecular PCs with long-lived excited states, only a few reports of dye-sensitized semiconductors as photocatalysts for organic synthesis were reported to date.³⁷

An intriguing example is the functionalization of TiO₂ nanoparticles with 6,7-dihydroxy-2-methylisoquinolium (DHMIQ), which results in a visible light PC that can catalyze the α -cyanation of tertiary amines (Figure 2.4, A).³⁸ DHMIQ is a combination of a chromophore and a catechol moiety that binds to the surface of the semiconductor. The redox active ligand was bound to spherical TiO₂ nanoparticles (NP), which were prepared *via* a hydrothermal synthesis of titanium(IV)butoxide with oleic acid via a post-synthetic ligand exchange. The resulting TiO₂-DHMIQ hybrid absorbs across the entire visible light spectrum and in the near infrared (NIR) region. The catalytic activity was shown for the aerobic cyanation of several tertiary amines using trimethylsilyl cyanide (TMSCN) in acetonitrile. A detailed study of all reaction conditions showed that traces of water lower the yield dramatically, presumably because of the formation of a hydration shell around the NPs that inhibits productive catalysis. The authors showed that the catalyst can be used with blue (462 nm), green (520 nm), yellow (592 nm), red (635 nm), and NIR (730 nm) irradiation for the title reaction.

More recently, the immobilization of a chromophore and a nickel complex on the surface of TiO₂ resulted in a single material that can be used for metallaphotocatalytic cross couplings.³⁹ These dye-sensitized metallaphotocatalysts (DSMPs) assemble *in situ* by adding a dye and a nickel complex, which both are equipped with a functional group that binds to the semiconducting material, and TiO₂ to a solution of the substrates and a base. The operational simplicity in combination with the high modularity of the three-component catalyst enabled a straightforward screening of suitable dyes and ligands for various cross couplings and different irradiation sources. The DSMP system was applied for C–O, C–S, C–N and C–C couplings using blue (440 nm), green (525 nm), and red (666 nm) light.

Chapter 2

During a series of control experiments, the authors showed that productive catalysis was also achieved when the semiconductor TiO₂ was replaced with insulating SiO₂ and Al₂O₃, but no product was formed in the absence of a support. These results in combination with spectroscopic studies indicated that two mechanisms are responsible for catalytic activity. In case of TiO₂, electrons are injected from the excited dye into the CB of TiO₂ and transferred to the nickel complex (“through-particle”). If insulating materials are used, the excited dye molecules directly transfer energy or electrons to the nickel complex (“on particle”). The latter process is, however, significantly less efficient compared to the “through-particle” mechanism, resulting in very long reaction times.

A more general approach to use long wavelengths for photocatalytic synthesis is triplet fusion upconversion (Figure 2.4, C).⁴⁰ This process involves a sensitizer ([Sen]) that absorbs low-energy photons to reach a triplet excited state (³[Sen]*), which transfers its energy to an annihilator ([An]) resulting in the triplet excited species ³[An]*. Two triplet excited annihilators (³[An]*) can undergo triplet fusion to generate a higher energy singlet exciton (¹[An]*) that decays via fluorescence by emitting a high energy photon. The annihilator furanyldiketopyrrolopyrrole (FDPP) was combined with the sensitizer palladium(II) octabutoxyphthalocyanine (PdPc) to convert NIR photons into orange light, which in turn can excite the organic PCs eosin Y and Rose Bengal.⁴¹ This catalytic cocktail was used for hydrodehalogenations, oxidations and radical cyclizations using NIR light as energy source. Tetratertbutylperylene (TTBP) and platinum(II) tetraphenyltetranaphthoporphyrin (PtTBTNB) were used to convert NIR into blue light to activate a ruthenium bipyridyl complex that catalyzes a [2+2] cyclization. TTBP and PtTBTNB also triggered the polymerization of methyl methacrylate (MMA) via NIR irradiation in the absence of an additional PC. Since NIR light penetrates through opaque media, the polymerization could be carried out by irradiating the reaction mixture through several materials, including pig skin. For similar reasons, this approach improved the scalability of the MMA polymerization significantly.

More recently, the use of NIR and deep red light was realized using Os(II) terpyridine complexes as photocatalysts (Figure 2.4, D).⁴² These transition metal complexes undergo a spin-forbidden S₀ → T₁ transition upon irradiation with long wavelengths. Strategic ligand design resulted in a library of osmium complexes with different redox potentials. Several examples, including polymerizations, cycloadditions, radical methylations, smiles reactions,

and metallaphotocatalytic transformations using NIR light showcased the broad applicability of this catalytic strategy. The extinction coefficients of Os(II) terpyridine complexes are lower compared to common PCs, which improves the scalability as showcased for an efficient photocatalytic trifluoromethylation on a mole scale in batch using a vessel with a large cross-sectional area.

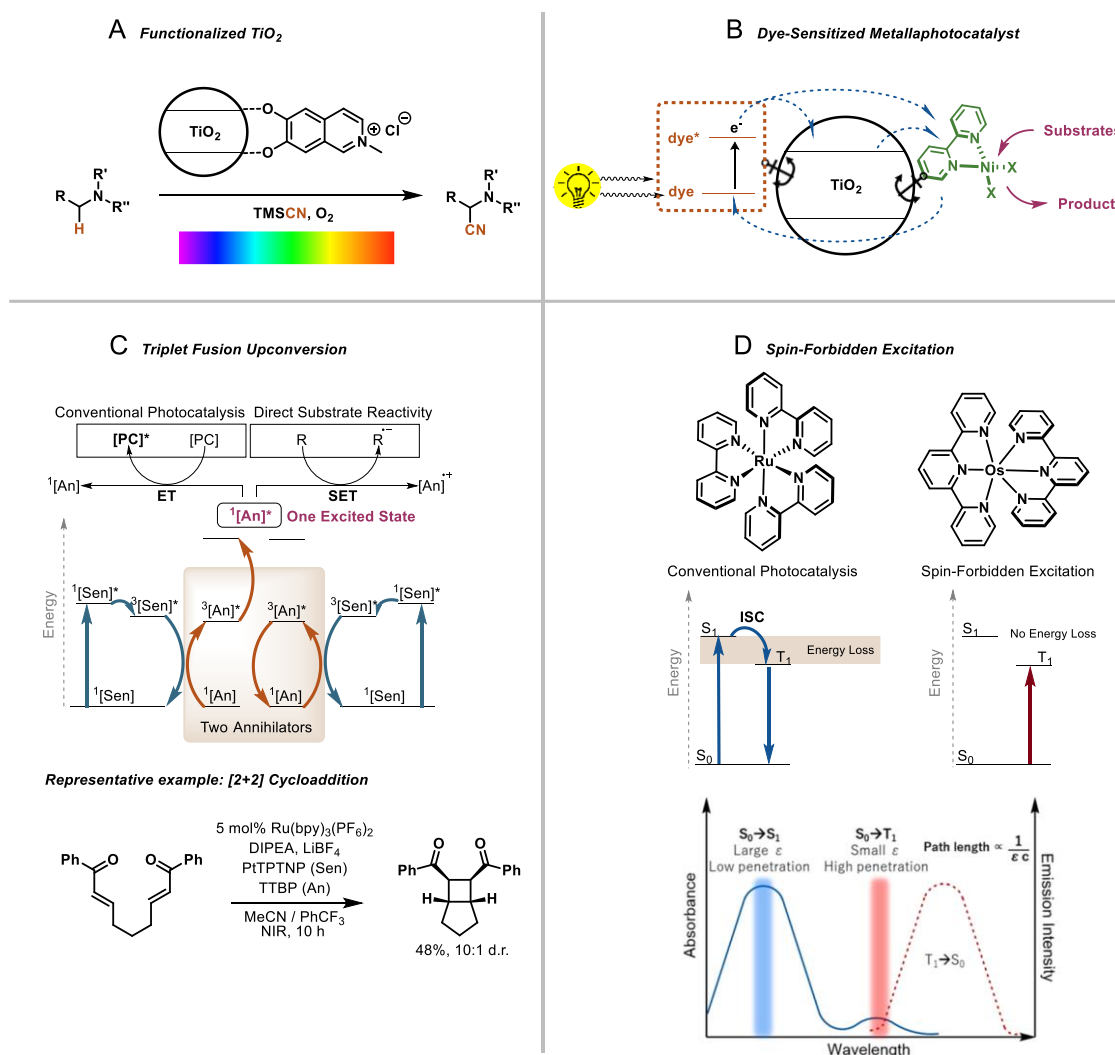


Figure 2.4. Strategies to access high wavelengths for photocatalytic synthesis. Functionalized TiO₂ with non-innocent ligands (A). Dye-sensitized metallaphotocatalysts (B). Triplet fusion upconversion (C). Spin-forbidden excitation of osmium complexes (D).

2.4 The energy and intensity of photons

Light is more than only a traceless, sustainable reagent. The energy and intensity of photons are overlooked parameters that can be used to tune photocatalytic activities and influence the selectivities, or even reactivity of a photocatalyst (Figure 2.5).⁴³ The water soluble iridium complex *fac*-tris[2-(5'-sulfonatophenyl)pyridine]iridate(III) pentahydrate (Irspyy) shows completely different reactivity depending on the intensity of blue light irradiation (Figure 2.5, A).⁴⁴ Low light intensity (one photon excitation) results in ³Irspyy that has a triplet energy of 2.65 eV and redox potentials that are suitable for various photoredox reactions. At high light intensities (two photon excitation), strongly reducing hydrated electrons (standard potential of -2.9 V vs. NHE) can be generated in aqueous solutions. By using a 447 nm continuous wave laser, this can be used to achieve different selectivities and reactivities for several transformations. Upon irradiation with low photon intensities, ³Irspyy induces the E-Z isomerization of 3-fluorocinammic acid via an energy transfer mechanism. When a lens is placed between the light source and the reaction mixture to concentrate the light intensity, the hydrogenation of the alkene was observed, which is initiated via a single electron reduction by hydrated electrons. Similarly, this method allowed to obtain either the hydrogen atom abstraction (low intensity) or the dimerization product (high intensity) of 4-(chloromethyl)benzoic acid.

As described in the previous section, the broad absorption of photocatalysts across the visible light spectrum improves solar harvesting, reduces the energy input using artificial light sources, and is beneficial for the scalability of light-mediated reactions. Moreover, the energy of photons can be used to control the activity of photochemical processes, thereby tuning the selectivity of a photocatalytic reaction. This was used to overcome substrate scope limitations and reproducibility issues in metallaphotocatalytic C–N cross couplings of cyclic secondary amines with electron poor aryl halides (Figure 2.5, B).⁴⁵ This limitation is a result of catalyst deactivation via the formation of nickel black, which was attributed to the accumulation of low valent nickel species due to the relatively slow oxidative addition in case of electron rich aryl halides. To avoid this problem, the relative rate of oxidative addition (OA) has to be equal or higher than the rate of reductive elimination (RE). By using a heterogeneous PC (CN-OA-m) that absorbs weakly at longer wavelengths, the rate of reductive elimination was significantly reduced using green light, which was sufficient to avoid catalyst deactivation in certain cases. Blue light irradiation could be used when the

rate of oxidative addition was increased using a high substrate concentration. These measures were, however, not successful in case of primary amines. For such substrates, the additive MTBD (7-methyl-1,5,7-triazabicyclo(4.4.0)dec-5-ene) was used to stabilize low valent nickel intermediates, thereby decelerating the rate of nickel black formation. Similarly, decelerating a photocatalytic reaction at longer wavelengths was key to achieve high selectivities for the light mediated benzyl ether deprotection with photoexcited 2,3-dichloro-5,6-dicyano-1,4-benzoquinone (DDQ).⁴⁶

More recently, it was shown that the oxidation potential of CN-OA-m differs depending on the irradiation wavelength (Figure 2.5, C).⁴⁷ Irradiation with blue light leads to π - π^* transitions that enable the oxidation of ethylbenzene to acetophenone, whereas no reaction was observed when n - π^* transitions were induced using green light was used. This phenomenon was used for photo-chemo-enzymatic cascades that give either the (*S*)- or the (*R*)-enantiomer of chiral benzylic alcohols. Green light irradiation of a cocktail consisting of CN-OA-m, an unspecific peroxygenase (UPO) from *Agrocybe aegerita*, and ethylbenzene in an aqueous buffer allows the selective formation of H₂O₂ that fuels the enantioselective biocatalytic hydroxylation of ethylbenzene to (*R*)-1-phenylethanol (99% ee). Blue light was used for the photocatalytic oxidation of the ethylbenzene to acetophenone, which in turn was reduced by an enantioselective alcohol dehydrogenase from *Rhodococcus ruber* to yield (*S*)-1-phenylethanol (93% ee).

Varying the irradiation wavelength also enables selective control between a one or two-fold substitution of 1,3,5-tribromobenzene with *N*-methylpyrrole using Rhodamin 6G (Rh-6G) as PC (Figure 2.5, D).⁴⁸ In presence of *N,N*-diisopropylethylamine (DIPEA), the radical anion Rh-6G^{•-} is formed upon irradiation with green light (530 nm). This species has a reduction potential of -1.0 V vs. SCE, which is sufficient to activate aryl bromides with relatively low reduction potentials, resulting in a selective monosubstitution. When blue light (455 nm) was used as irradiation source the disubstituted products were obtained. This is possible, because at short wavelengths, Rh-6G^{•-} is again excited, forming Rh-6G^{•-*} (reduction potential ca -2.4 V vs. SCE), which can activate aryl bromides with rather high reduction potentials.

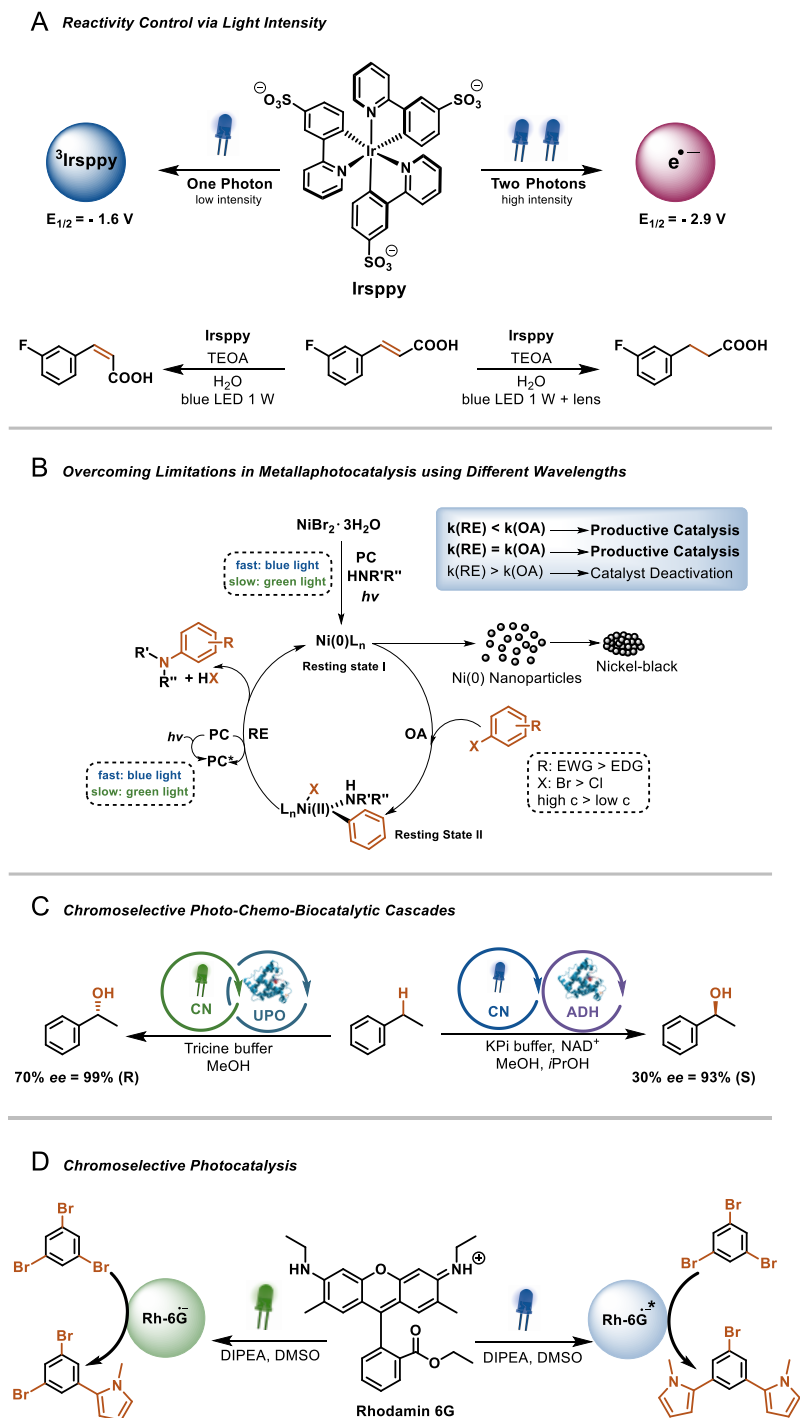


Figure 2.5. Accessing different photocatalytic activities by controlling the energy and intensity of photons. Reactivity control of an iridium photocatalyst through the light intensity (A). Overcoming limitations in metallaphotocatalysis using carbon nitride photocatalysis by changing the wavelength (B). Chromoselective photo-chemo-enzymatic cascade reactions with a carbon nitride photocatalyst (C). Chromoselective photocatalysis with Rhodamin 6G (D).

2.5 Replacing elemental alkali metal reductants with light

The wavelength dependent approach described above that generates Rh-6G^- or $\text{Rh-6G}^{\cdot-}$, which have different redox potentials, is not limited to this specific xanthene dye. Similar approaches can be used to generate highly reductive species from other organic PCs (Figure 2.6).⁴⁹ The common mechanistic feature of these strategies is that quenching of PC^* with a sacrificial electron donor (SED) generates a relatively stable intermediate that is able to absorb another photon (consecutive photoinduced electron transfer, ConPET). This results in excited states that are characterized by remarkably strong single electron reduction potentials that can be similar to elemental lithium (-3.28 V vs. SCE) and sodium (-2.95 V vs. SCE).

The first reported example used the perylene diimide *N,N*-bis(2,6-diisopropylphenyl)perylene-3,4,9,10-bis(dicarboximide) (PDI) as PC (Figure 2.6, A).⁵⁰ Perylene diimides are fluorescent dyes that absorb broadly across the visible light spectrum and are used as pigments, colorants, electronic materials and photoreceptors, with only a few applications in photocatalysis. Visible light excitation generates PDI^* , which is quenched by a SED yielding the moderately reducing PDI^- (-0.43 V vs. SCE). Absorption of a second photon generates $\text{PDI}^{\cdot-}$ that reduces several aryl iodides, bromides and chlorides in moderate to excellent yield. In presence of radical trapping agents, such as substituted pyrroles, the corresponding C–C coupling products were obtained.

More recently, a benzo[*ghi*]perylene monoimide (BPI) was shown to be also able to undergo ConPET, forming the excited radical anion $\text{BPI}^{\cdot-}$ (Figure 2.6, B).⁵¹ According to density functional theory calculations, this species is an extremely strong reductant (-2.43 to -4.28 V). In fact, the authors were able to show that BPI is able to reduce several arenes, including benzene ($E_{\text{red}} < -3.42$ V vs. SCE) to the corresponding 1,4-dienes in presence of NMe_4OH and 405 nm irradiation via a Birch type mechanism. Mechanistic investigations suggested that $\text{BPI}^{\cdot-}$ releases a solvated electron that is responsible for substrate reduction rather than a direct SET between the excited radical anion and the substrate. By adapting the reaction conditions, BPI ConPET catalysis was also demonstrated to enable reductive deoxygenations, selective olefin reductions, reductive cyclopropane ring-openings, and late stage dehalogenations.

Mesityl acridinium salts (Mes-Acr^+) are among the most potent PCs for oxidative reactions.³¹ Nicewicz and colleagues realized that the neutral acridine radical (Mes-Acr^\cdot),

which is formed after quenching of $^*\text{Mes-Acr}^+$ with Hünig's base, is relatively stable under oxygen-free conditions.⁵² Studies of the photophysical properties of this persistent radical revealed that absorption of a second photon (>350 nm) generates two new excited states, a lower-energy doublet and a twisted intramolecular charge-transfer state that have strong reduction potentials (-2.91 and -3.36 V vs. SCE, respectively). Based on this discovery, the authors developed protocols for the light-mediated reductive dehalogenation of aryl bromides and chlorides, and for the reductive detosylation of tosyl amines catalyzed by Mes-Acr-BF₄ (Figure 2.6, C). It is worth noting that ConPET pathways can be also realized using iridium complexes as photocatalysts.⁵³

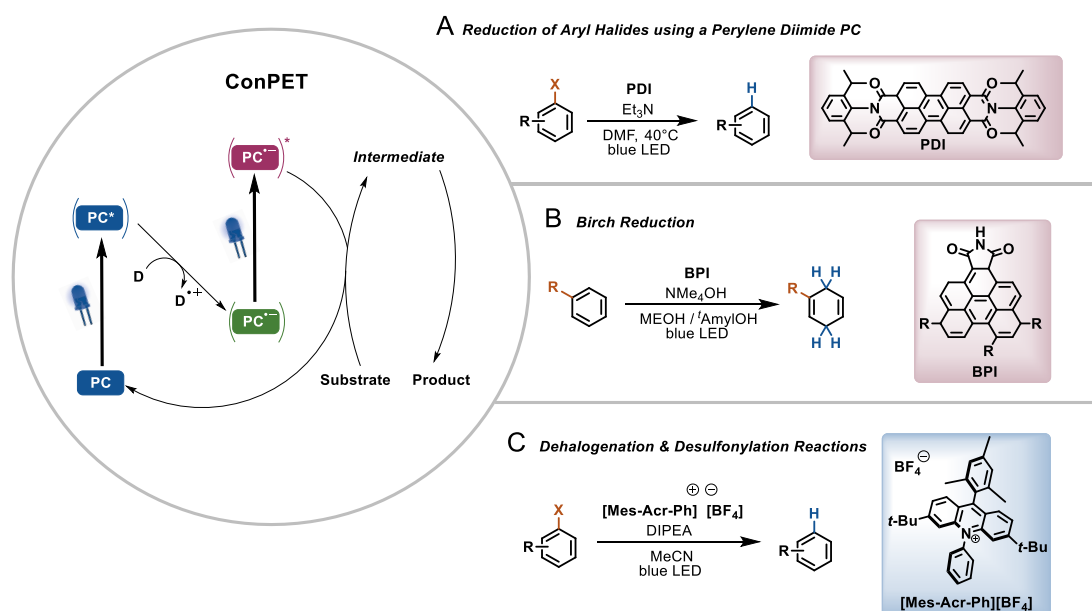


Figure 2.6. Accessing strong photoreductants via consecutive photoinduced electron transfer (ConPET). Reduction of aryl halides using a perylene diimide PC (A). Photocatalytic Birch-type reductions using BPI (B). Dehalogenation using a mesityl acridinium salt (C).

Polycyclic aromatic hydrocarbons (PAH), such as pyrene and triphenylene, generate strongly reducing radical anions upon irradiation with UV light and quenching of the excited state by a single electron donor. König and colleagues hypothesized that these excited states could be also accessible using visible light via an energy transfer from a PC to a polycyclic aromatic hydrocarbon (PAH, Figure 2.7).⁵⁴ Key to the success was the selection of a PAH/PC couple that has similar triplet energies, shows fast EnT from the PC to the PAH, and fast SET between PAH* and the sacrificial electron donor to generate the strongly reducing PAH radical anion. The authors identified that the combination of Ru(bpy)₃Cl₂, pyrene, and DIPEA as SED fulfills these requirements. Generation of the pyrene radical

anion enabled the C–H arylation of aryl (hetero)aryl bromides, chlorides or triflates, as well as light-mediated C–P couplings.

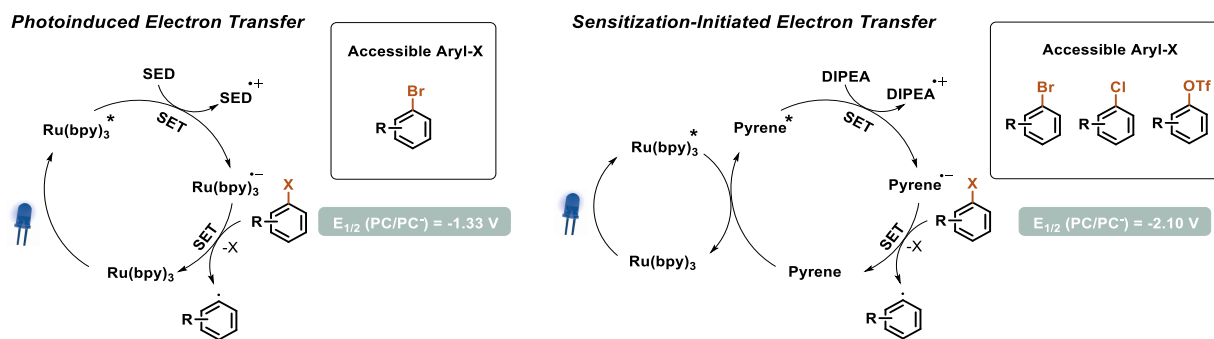


Figure 2.7. Photoinduced electron transfer (PET) versus Sensitization-initiated electron transfer (SenI-ET)

2.6 Better, faster, scalable – technological aspects & developments

The impact of visible light photocatalysis in academia and industry cannot be understated and the continuous advancements and developments of new concepts, catalysts, and strategies will likely increase the impact of such reactions for industrial processes in the future. Nevertheless, photocatalysis faces some problems that require the attention of practitioners in industrial and university settings.

First, the reported photocatalytic protocols can be difficult to reproduce, which renders the adaption of developed methods by other laboratories difficult. “Conventional” reactions require heating or cooling, which is in most cases easy to duplicate in other research laboratories. The reproducibility of photocatalytic transformations strongly depends on the experimental setup. Light-mediated reactions are usually carried out using LED lamps that often have different specifications, including emission spectra and photon outputs, which can have a dramatic influence on a photochemical transformation. The standardization of photochemical reactors using dedicated, commercial equipment might be an ideal solution,⁵⁵ but is unlikely to happen due to low prices of self-made setups. In an excellent comment, researchers from GSK, Pfizer, Merck and AbbVie, discussed problems related to photochemical setups and called for more accurate descriptions of light sources and reactor arrangements when reporting experimental procedures.⁵⁶

Second, photocatalytic transformations rely on efficient irradiation of the reaction mixture. Solvents, starting materials, products, photosensitizers, and photocatalysts, at the point of incident light, can all act as filters reducing the light intensity available for the rest of the reaction mixture. This attenuation effect of photon transport (Beer-Lambert law), becomes particularly problematic on larger scales. The Beer-Lambert law states the correlation between the absorption (A) and the molar extinction coefficient (ϵ) of the molecule(s), their concentration (c) and the optical path length of the light (l) (Equation 1).

$$A = \epsilon cl \quad (1)$$

This trade-off has serious implications, especially for scaling a photoreaction in batch. Continuous flow (micro)reactors are the technology of choice to overcome this bottleneck.⁵⁷⁵⁸ The narrow channel dimensions of flow reactors provide opportunities to ensure a uniform irradiation of the entire reaction mixture. Consequently, photochemical reactions can be substantially accelerated and scaled to higher quantities compared to batch reactors (Figure 2.8). Flow chemistry is also the technology of choice for transformations involving multiple phases. The high surface-area-to-volume ratios are a consequence of the small reactor size, leading to efficient mass transfer between two (or even three) phases. In case of gaseous reagents, flow reactors further offer the opportunity to control the stoichiometry of gasses with mass-flow controllers, and are easily pressurized, which increases the solubility of gasses in the reaction mixture.

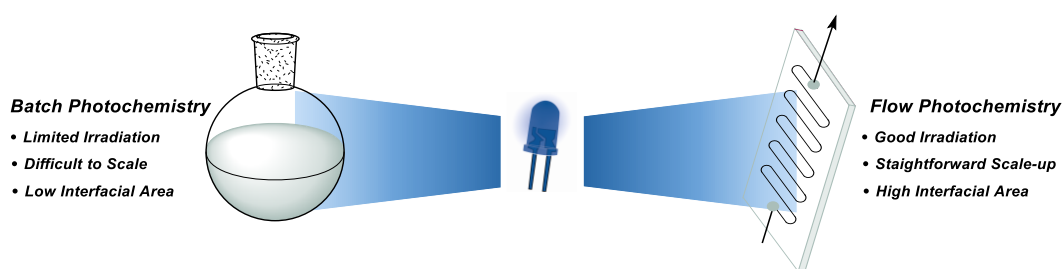


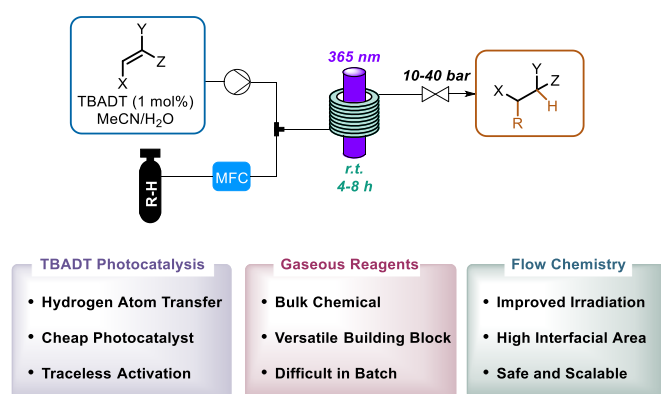
Figure 2.8. Photochemistry in batch and flow reactors

All of these advantages were recently combined in a photocatalytic gas/liquid process that enables the direct functionalization of light hydrocarbons via hydrogen atom transfer (HAT) (Figure 2.9, A).⁵⁹ A solution of the HAT catalyst tetrabutylammonium decatungstate (TBADT) and an olefin starting material in a suitable solvent was mixed with gaseous methane, ethane, propane, or isobutene and fed into a 365 nm flow photoreactor at back pressures of 10 to 45 bar. Upon irradiation, the excited PC abstracts a hydrogen atom from the respective alkane. The resulting nucleophilic C-centered radical undergoes a conjugate addition onto the olefin. A subsequent hydrogen back-donation results in the desired product and restores TBADT. This transformation is difficult to access in batch reactors as efficient irradiation and high pressures are crucial for product formation.

Similarly to the use of gaseous feedstock chemicals such as methane, the use of sunlight as energy source can greatly benefit from continuous flow chemistry. One approach to use sunlight efficiently combines continuous flow technology with luminescent solar

concentrators (LSCs, Figure 2.9, B).⁶⁰ LSCs are made by dispersing a luminophore in a waveguide, such as polymeric materials or glass. Light penetrates the surface of the waveguide and is absorbed by the luminophore. Re-emitted photons are guided and concentrated by total internal reflection towards the edge of the device. The adaption of this principle to continuous flow synthesis was realized using a chip based reactor made out of PDMS that was doped with the fluorescent dye Lumogen F red 305. This dye absorbs visible light from ~400-600 nm and re-emits light at ~600-700 nm. The emitted light perfectly overlaps with the absorption spectrum of methylene blue, a common triplet photosensitizer. The authors studied the singlet oxygen cycloaddition to 9,10-diphenylanthracene using sunlight during a cloudy day and showed that this reactor is significantly more efficient than non-doped reactors.

A C(sp³)-H Functionalization of Gaseous Alkanes using Flow-Photochemistry



B Flow-Photochemistry using Luminescent Solar Concentrators

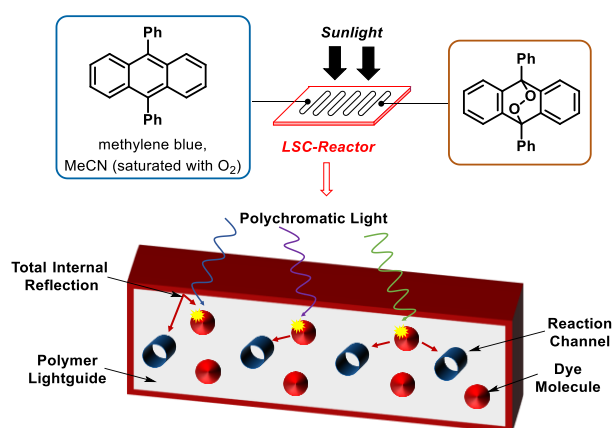


Figure 2.9. Flow-photocatalysis. C(sp³)-H functionalization of light hydrocarbons using photocatalysis in flow (A). Luminescent solar concentrator for energy efficient flow chemistry using sunlight (B).

Flow chemistry is, however, not the ultimate solution to all problems in (photo)chemical synthesis and has still several limitations. One of the biggest bottlenecks of flow chemistry is the handling of solid materials, such as heterogeneous photocatalysts which have advantages over homogeneous PCs.³² Packed bed reactors with heterogeneous catalysts embedded between filter units are unsuitable for opaque photocatalysts, because photons will be exclusively absorbed at the outer region while the inner particles are shielded. Efficient irradiation can be ensured by pumping a suspension through a coil reactor but the solid catalyst will settle, leading to a heterogeneous distribution, irreproducible results, or clogging.

This problem was recently tackled on laboratory scale by a system that generates serial micro-batch reactors (SMBRs, Figure 2.10, A).⁶¹ SMBRs are a series of small solid-liquid compartments, which contain all ingredients for the chemical transformation, and are separated by an inert gas spacer within a coil reactor tubing. This was realized by dosing a heterogeneous carbon nitride photocatalyst to a stable gas-liquid segmented flow. The resulting triphasic mixture can be conveniently pumped through an irradiated coil reactor that is submerged in a thermostatic bath to perform photocatalytic reactions. The natural Taylor flow mixes the slug to continuously re-suspend the material, ensuring efficient irradiation and reproducible processing. In this system, the reaction time can be adapted by changing the gas and/or liquid flow rate or the reactor volume while the catalyst stoichiometry can be varied by changing the rate of suspension dosing. The system was evaluated and optimized using the photocatalytic decarboxylative fluorination of phenoxyacetic acids and phenylacetic acid derivatives using Selectfluor and a carbon nitride photocatalyst made from cyanuric acid, melamine and barbituric acid (CMB-CN).

More recently, a the combination of an oscillatory pump and a microstructured plug flow photoreactor was shown to be also capable of processing heterogeneous photocatalysts (Figure 2.10, B).⁶² Careful tuning of the pulsation frequency and amplitude was crucial for controlling the residence time distribution. The nickel/carbon nitride catalyzed C–N cross coupling described above (Figure 2.5, B) was significantly intensified and was achieved in reaction times as low as 20 minutes. To demonstrate the scalability, a 4.5 hour experiment provided a model compound on a 12 g scale (2.67 g/h). Additionally, an intermediate of tetracaine, a local anesthetic, was synthesized on a gram scale.

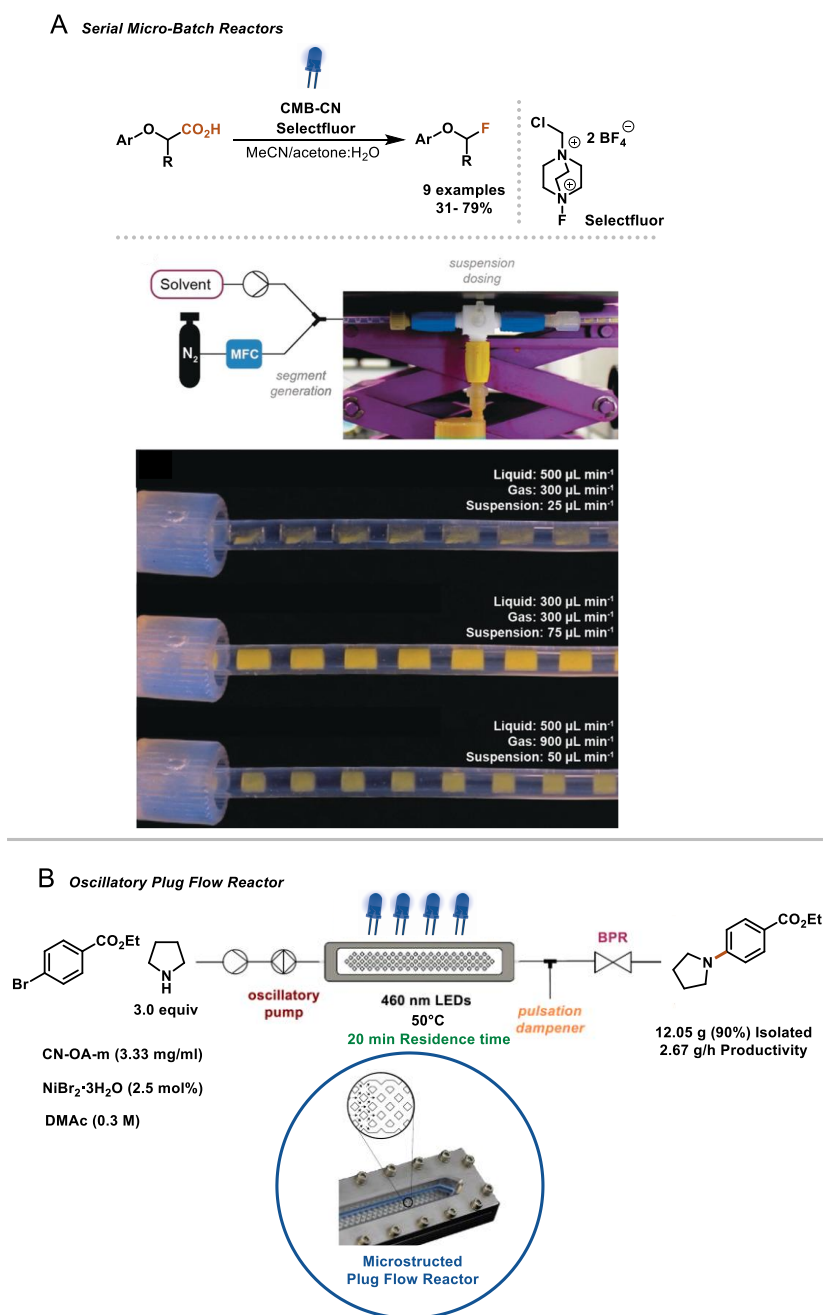


Figure 2.10. Heterogeneous Photocatalyst in Flow. Decarboxylative fluorination of phenoxy acid derivatives in flow with the use of serial micro-batch reactors (A). Dual nickel/carbon nitride amination using an oscillatory plug flow reactor (B).

A metallaphotocatalytic C-N cross coupling was also used as benchmark reaction for a continuous stirred tank reactor (CSTR) equipped with a continuous wave laser that achieves high productivities (Figure 2.11).⁶³ Continuous wave lasers have several advantages compared to standard LEDs, including the ability to measure the output power, the coherence of light, the ability to shape the beam, and a significantly higher intensity. The researchers coupled a 405 nm laser with an adjustable beam expander and studied the

reaction kinetics of a model C–N coupling using a homogeneous iridium complex as PC in combination with a nickel salt. During these studies, the authors realized that the optimal reaction performance is correlated to the concentration of the PC, the solution depth and the power density and can be entirely determined by the Beer-Lambert law. Coupling the laser setup with a CSTR and applying the optimized conditions allowed them to perform a continuous experiment over 32 h under steady-state conditions to produce 1.85 kg of the desired coupling product.

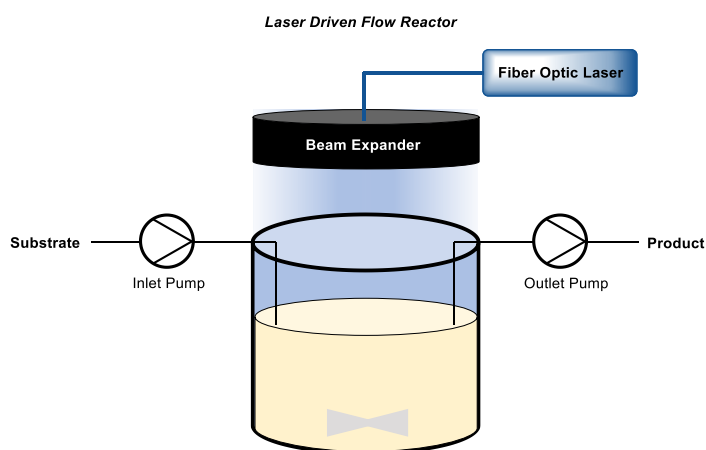


Figure 2.11. Continuous stirred tank reactor (CSTR) for large scale, laser-driven photocatalysis

2.7 Photon-free photocatalysis

The “unique” feature of many homogeneous photocatalysts is their ability to trigger redox events upon excitation through oxidative or reductive quenching cycles (Figure 2.1). Heterogeneous semiconductors, such as TiO₂ or carbon nitrides, are essentially operating by similar mechanisms. When a semiconductor absorbs photons with sufficiently high energy, electrons are excited from the valence band (VB) to the conduction band (CB), generating simultaneously an oxidizing and a reducing species on a single particle. The generated electron holes can oxidize electron donors whereas the electrons in the VB are able to reduce electron acceptors via single-electron transfer (Figure 2.12, A).

Ito and colleagues showed that electron-hole pairs can be also generated mechanochemically by generating an “excited-state” barium titanate via ball-milling (Figure 2.12, B).⁶⁴ Upon agitation, the piezoelectric material becomes temporarily highly polarized and generates an electrochemical potential that is suitable for the activation of redox active aryl diazonium salts, which was previously reported using, for example, TiO₂ photocatalysis.⁶⁵ The authors could show that ball milling of a mixture of aryldiazonium salts, BaTiO₃ and heterocycles, such as furan, thiophene, or protected pyrrole, results in C–C coupling products. Moreover, the borylation of aryldiazonium salts with bis(pinacolato)diboron was achieved via the same approach. The methodology was proven scalable during a gram scale synthesis. Recycling experiments further showed that BaTiO₃ can be reused three times before the catalytic activity decreases. This approach is an interesting alternative to photocatalysis that can be carried out in the absence of solvents and light, which overcomes some of the problems related to photochemistry. The method is also reported to be very robust as reactions were even induced by “wrapping all ingredients in weighing paper and striking it with a hammer” instead of dedicated ball milling equipment.

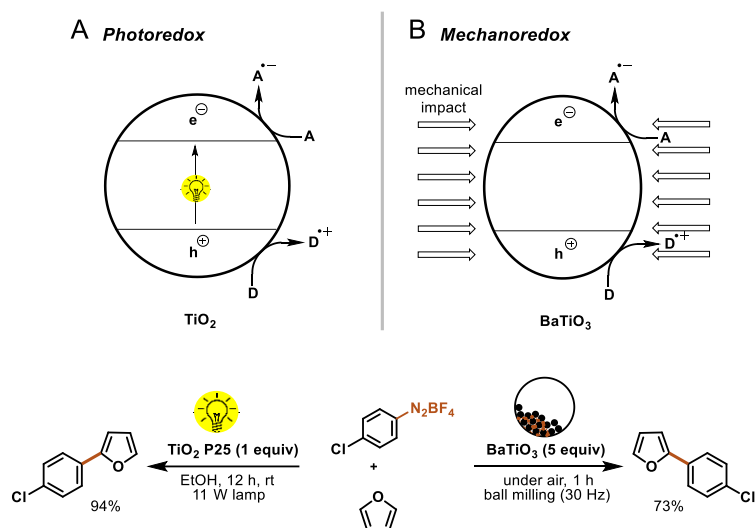


Figure 2.12. Comparison of photoredox catalysis (A) and mechano-redox catalysis (B).

2.8 Summary and outlook

In summary, it can be stated without any doubt that photocatalysis has already significantly expanded the organic chemists' toolbox and provides sustainable opportunities for synthesis in academia and industry. The steadily increasing amounts of hitherto undisclosed reactions that can be realized using visible light, such as replacing elemental alkali metal reductants, will certainly have a significant impact in industry and academia. The recent efforts to use the entire visible light spectrum for efficient photocatalysis might be a small step towards a chemical industry that was proposed more than hundred years ago, where "forests of glass tubes will extend over the plains and glass buildings will rise everywhere; inside of these will take place the photochemical processes that hitherto have been the guarded secret of the plants, but that will have been mastered by human industry which will know how to make them bear even more abundant fruit than nature".⁶⁶ It is, however, more realistic that artificial light sources will be the energy source of choice for most photocatalytic reactions in academia and industry, due to the better control over reaction conditions. Additionally, several recent examples indicate that the photon intensity and energy can be used as tunable reaction parameters that enable selectivity and reactivity control. Although this has been often overlooked in the past, we believe that the future will see more examples showcasing "chromoselective photocatalysis". Photochemistry tremendously benefits from technological developments including laser technology and flow chemistry, and interdisciplinary research programs between chemists and chemical engineers will be of utmost importance for the implementation of photocatalytic transformations in industrial setting.

2.9 References

1. Hoffmann, N., Photochemical Reactions as Key Steps in Organic Synthesis. *Chem. Rev.* **2008**, *108* (3), 1052-1103.
2. Crisenza, G. E. M.; Melchiorre, P., Chemistry glows green with photoredox catalysis. *Nat. Commun.* **2020**, *11* (1), 803.
3. Marzo, L.; Pagire, S. K.; Reiser, O.; König, B., Visible-Light Photocatalysis: Does It Make a Difference in Organic Synthesis? *Angew. Chem. Int. Ed.* **2018**, *57* (32), 10034-10072.
4. Schultz, D. M.; Yoon, T. P., Solar Synthesis: Prospects in Visible Light Photocatalysis. *Science* **2014**, *343* (6174), 1239176.
5. Shaw, M. H.; Twilton, J.; MacMillan, D. W. C., Photoredox Catalysis in Organic Chemistry. *J. Org. Chem.* **2016**, *81* (16), 6898-6926.
6. Gentry, E. C.; Knowles, R. R., Synthetic Applications of Proton-Coupled Electron Transfer. *Acc. Chem. Res.* **2016**, *49* (8), 1546-1556.
7. Capaldo, L.; Quadri, L. L.; Ravelli, D., Photocatalytic hydrogen atom transfer: the philosopher's stone for late-stage functionalization? *Green Chem.* **2020**, *22* (11), 3376-3396.
8. Strieth-Kalthoff, F.; James, M. J.; Teders, M.; Pitzer, L.; Glorius, F., Energy transfer catalysis mediated by visible light: principles, applications, directions. *Chem. Soc. Rev.* **2018**, *47* (19), 7190-7202.
9. Skubi, K. L.; Blum, T. R.; Yoon, T. P., Dual Catalysis Strategies in Photochemical Synthesis. *Chem. Rev.* **2016**, *116* (17), 10035-10074.
10. Twilton, J.; Le, C.; Zhang, P.; Shaw, M. H.; Evans, R. W.; MacMillan, D. W. C., The merger of transition metal and photocatalysis. *Nat. Rev. Chem.* **2017**, *1*, 0052.
11. Milligan, J. A.; Phelan, J. P.; Badir, S. O.; Molander, G. A., Alkyl Carbon–Carbon Bond Formation by Nickel/Photoredox Cross-Coupling. *Angew. Chem. Int. Ed.* **2019**, *58* (19), 6152-6163.
12. Hopkinson, M. N.; Sahoo, B.; Li, J.-L.; Glorius, F., Dual Catalysis Sees the Light: Combining Photoredox with Organo-, Acid, and Transition-Metal Catalysis. *Chem. Eur. J.* **2014**, *20* (14), 3874-3886.
13. Kojima, M.; Matsunaga, S., The Merger of Photoredox and Cobalt Catalysis. *Trends Chem.* **2020**, *2* (5), 410-426.

Chapter 2

14. Hossain, A.; Bhattacharyya, A.; Reiser, O., Copper's rapid ascent in visible-light photoredox catalysis. *Science* **2019**, *364* (6439), eaav9713.
15. Ouyang, X.-H.; Li, Y.; Song, R.-J.; Hu, M.; Luo, S.; Li, J.-H., Intermolecular dialkylation of alkenes with two distinct C(sp³)–H bonds enabled by synergistic photoredox catalysis and iron catalysis. *Sci. Adv.* **2019**, *5* (3), eaav9839.
16. Neumeier, M.; Chakraborty, U.; Schaarschmidt, D.; de la Pena O'Shea, V.; Perez-Ruiz, R.; Jacobi von Wangelin, A., Combined Photoredox and Iron Catalysis for the Cyclotrimerization of Alkynes. *Angew. Chem. Int. Ed.* **2020**, *59* (32), 13473-13478.
17. Nicewicz, D. A.; MacMillan, D. W. C., Merging Photoredox Catalysis with Organocatalysis: The Direct Asymmetric Alkylation of Aldehydes. *Science* **2008**, *322* (5898), 77-80.
18. Miller, Z. D.; Lee, B. J.; Yoon, T. P., Enantioselective Crossed Photocycloadditions of Styrenic Olefins by Lewis Acid Catalyzed Triplet Sensitization. *Angew. Chem. Int. Ed.* **2017**, *56* (39), 11891-11895.
19. Douglas, J. J.; Sevrin, M. J.; Stephenson, C. R. J., Visible Light Photocatalysis: Applications and New Disconnections in the Synthesis of Pharmaceutical Agents. *Org Process Res Dev.* **2016**, *20* (7), 1134-1147.
20. Li, P.; Terrett, J. A.; Zbieg, J. R., Visible-Light Photocatalysis as an Enabling Technology for Drug Discovery: A Paradigm Shift for Chemical Reactivity. *ACS Med. Chem. Lett.* **2020**.
21. Yu, Y.; Zhang, L.-K.; Buevich, A. V.; Li, G.; Tang, H.; Vachal, P.; Colletti, S. L.; Shi, Z.-C., Chemoselective Peptide Modification via Photocatalytic Tryptophan β -Position Conjugation. *J. Am. Chem. Soc.* **2018**, *140* (22), 6797-6800.
22. Sato, S.; Nakamura, H., Ligand-Directed Selective Protein Modification Based on Local Single-Electron-Transfer Catalysis. *Angew. Chem. Int. Ed.* **2013**, *52* (33), 8681-8684.
23. DiRocco, D. A.; Dykstra, K.; Krska, S.; Vachal, P.; Conway, D. V.; Tudge, M., Late-Stage Functionalization of Biologically Active Heterocycles Through Photoredox Catalysis. *Angew. Chem. Int. Ed.* **2014**, *53* (19), 4802-4806.
24. Grainger, R.; Heightman, T. D.; Ley, Steven V.; Lima, F.; Johnson, C. N., Enabling synthesis in fragment-based drug discovery by reactivity mapping: photoredox-mediated cross-dehydrogenative heteroarylation of cyclic amines. *Chem.* **2019**, *10* (8), 2264-2271.

25. Zuo, Z.; Ahneman, D. T.; Chu, L.; Terrett, J. A.; Doyle, A. G.; MacMillan, D. W. C., Merging photoredox with nickel catalysis: Coupling of α -carboxyl sp^3 -carbons with aryl halides. *Science* **2014**, *345* (6195), 437-440.
26. Tellis, J. C.; Primer, D. N.; Molander, G. A., Single-electron transmetalation in organoboron cross-coupling by photoredox/nickel dual catalysis. *Science* **2014**, *345* (6195), 433-436.
27. Zhu, C.; Yue, H.; Jia, J.; Rueping, M., Recent Advances in Nickel-Catalyzed C-Heteroatom Cross-Coupling Reactions under Mild Conditions via Facilitated Reductive Elimination. *Angew. Chem. Int. Ed.* **2012**, *60* (33), 17810-17831.
28. Loh, Y. Y.; Nagao, K.; Hoover, A. J.; Hesk, D.; Rivera, N. R.; Colletti, S. L.; Davies, I. W.; MacMillan, D. W. C., Photoredox-catalyzed deuteration and tritiation of pharmaceutical compounds. *Science* **2017**, *358* (6367), 1182-1187.
29. Chen, W.; Huang, Z.; Tay, N. E. S.; Giglio, B.; Wang, M.; Wang, H.; Wu, Z.; Nicewicz, D. A.; Li, Z., Direct arene C-H fluorination with $^{18}F^-$ via organic photoredox catalysis. *Science* **2019**, *364* (6446), 1170-1174.
30. Arias-Rotondo, D. M.; McCusker, J. K., The photophysics of photoredox catalysis: a roadmap for catalyst design. *Chem. Soc. Rev.* **2016**, *45* (21), 5803-5820.
31. Romero, N. A.; Nicewicz, D. A., Organic Photoredox Catalysis. *Chem. Rev.* **2016**, *116* (17), 10075-10166.
32. Gisbertz, S.; Pieber, B., Heterogeneous Photocatalysis in Organic Synthesis. *ChemPhotoChem* **2020**, *4*, 1-21.
33. Prier, C. K.; Rankic, D. A.; MacMillan, D. W. C., Visible Light Photoredox Catalysis with Transition Metal Complexes: Applications in Organic Synthesis. *Chem. Rev.* **2013**, *113* (7), 5322-5363.
34. Glaser, F.; Kerzig, C.; Wenger, O. S., Multi-Photon Excitation in Photoredox Catalysis: Concepts, Applications, Methods. *Angew. Chem. Int. Ed.* **2020**, *59* (26), 10266-10284.
35. Hagfeldt, A.; Boschloo, G.; Sun, L.; Kloo, L.; Pettersson, H., Dye-Sensitized Solar Cells. *Chem. Rev.* **2010**, *110* (11), 6595-6663.
36. Hagfeldt, A.; Graetzel, M., Light-Induced Redox Reactions in Nanocrystalline Systems. *Chem. Rev.* **1995**, *95* (1), 49-68.

Chapter 2

37. Franchi, D.; Amara, Z., Applications of Sensitized Semiconductors as Heterogeneous Visible-Light Photocatalysts in Organic Synthesis. *ACS Sustain. Chem. Eng.* **2020**, *8* (41), 15405-15429.
38. Nauth, A. M.; Schechtel, E.; Dören, R.; Tremel, W.; Opatz, T., TiO₂ Nanoparticles Functionalized with Non-innocent Ligands Allow Oxidative Photocyanation of Amines with Visible/Near-Infrared Photons. *J. Am. Chem. Soc.* **2018**, *140* (43), 14169-14177.
39. Reischauer, S.; Strauss, V.; Pieber, B., Modular, self-assembling metallaphotocatalyst for cross couplings using the full visible-light spectrum. *ACS Catal.* **2020**, *10* (22), 13269-13274.
40. Zhou, J.; Liu, Q.; Feng, W.; Sun, Y.; Li, F., Upconversion Luminescent Materials: Advances and Applications. *Chem. Rev.* **2015**, *115* (1), 395-465.
41. Ravetz, B. D.; Pun, A. B.; Churchill, E. M.; Congreve, D. N.; Rovis, T.; Campos, L. M., Photoredox catalysis using infrared light via triplet fusion upconversion. *Nature* **2019**, *565* (7739), 343-346.
42. Ravetz, B. D.; Tay, N. E. S.; Joe, C. L.; Sezen-Edmonds, M.; Schmidt, M. A.; Tan, Y.; Janey, J. M.; Eastgate, M. D.; Rovis, T., Development of a Platform for Near-Infrared Photoredox Catalysis. *ACS Cent. Sci.* **2020**.
43. Protti, S.; Ravelli, D.; Fagnoni, M., Wavelength dependence and wavelength selectivity in photochemical reactions. *Photochem. Photobiol. Sci.* **2019**, *18* (9), 2094-2101.
44. Kerzig, C.; Wenger, O. S., Reactivity control of a photocatalytic system by changing the light intensity. *Chem. Sci.* **2019**, *10* (48), 11023-11029.
45. Gisbertz, S.; Reischauer, S.; Pieber, B., Overcoming limitations in dual photoredox/nickel-catalysed C–N cross-couplings due to catalyst deactivation. *Nat. Catal.* **2020**, *3* (8), 611-620.
46. Cavedon, C.; Sletten, E. T.; Madani, A.; Niemeyer, O.; Seeberger, P. H.; Pieber, B., Visible-Light-Mediated Oxidative Debenzylation Enables the Use of Benzyl Ethers as Temporary Protecting Groups. *Org. Lett.* **2021**, *23* (2), 514-518.
47. Schmermund, L.; Reischauer, S.; Bierbaumer, S.; Winkler, C. K.; Diaz-Rodriguez, A.; Edwards, L. J.; Kara, S.; Mielke, T.; Cartwright, J.; Grogan, G.; Pieber, B.; Kroutil, W., Chromoselective Photocatalysis Enables Stereocomplementary Biocatalytic Pathways. *Angew. Chem. Int. Ed.* **2021**, *60* (13), 6965-6969.

48. Ghosh, I.; König, B., Chromoselective Photocatalysis: Controlled Bond Activation through Light-Color Regulation of Redox Potentials. *Angew. Chem. Int. Ed.* **2016**, *55* (27), 7676-7679.
49. Schmalzbauer, M.; Marcon, M.; König, B., Excited State Anions in Organic Transformations. *Angew. Chem. Int. Ed.* **2021**, *60* (12), 6270-6292.
50. Ghosh, I.; Ghosh, T.; Bardagi, J. I.; König, B., Reduction of aryl halides by consecutive visible light-induced electron transfer processes. *Science* **2014**, *346* (6210), 725-728.
51. Cole, J. P.; Chen, D.-F.; Kudisch, M.; Pearson, R. M.; Lim, C.-H.; Miyake, G. M., Organocatalyzed Birch Reduction Driven by Visible Light. *J. Am. Chem. Soc.* **2020**, *142* (31), 13573-13581.
52. MacKenzie, I. A.; Wang, L.; Onuska, N. P. R.; Williams, O. F.; Begam, K.; Moran, A. M.; Dunietz, B. D.; Nicewicz, D. A., Discovery and characterization of an acridine radical photoreductant. *Nature* **2020**, *580* (7801), 76-80.
53. Giedyk, M.; Narobe, R.; Weiß, S.; Touraud, D.; Kunz, W.; König, B., Photocatalytic activation of alkyl chlorides by assembly-promoted single electron transfer in microheterogeneous solutions. *Nat. Catal.* **2020**, *3* (1), 40-47.
54. Ghosh, I.; Shaikh, R. S.; König, B., Sensitization-Initiated Electron Transfer for Photoredox Catalysis. *Angew. Chem. Int. Ed.* **2017**, *56* (29), 8544-8549.
55. Le, C. C.; Wismer, M. K.; Shi, Z.-C.; Zhang, R.; Conway, D. V.; Li, G.; Vachal, P.; Davies, I. W.; MacMillan, D. W. C., A General Small-Scale Reactor To Enable Standardization and Acceleration of Photocatalytic Reactions. *ACS Cent. Sci.* **2017**, *3* (6), 647-653.
56. Bonfield, H. E.; Knauber, T.; Lévesque, F.; Moschetta, E. G.; Susanne, F.; Edwards, L. J., Photons as a 21st century reagent. *Nat. Commun.* **2020**, *11* (1), 804.
57. Plutschack, M. B.; Pieber, B.; Gilmore, K.; Seeberger, P. H., The Hitchhiker's Guide to Flow Chemistry. *Chem. Rev.* **2017**, *117* (18), 11796-11893.
58. Cambié, D.; Bottecchia, C.; Straathof, N. J. W.; Hessel, V.; Noël, T., Applications of Continuous-Flow Photochemistry in Organic Synthesis, Material Science, and Water Treatment. *Chem. Rev.* **2016**, *116* (17), 10276-10341.

Chapter 2

59. Laudadio, G.; Deng, Y.; van der Wal, K.; Ravelli, D.; Nuño, M.; Fagnoni, M.; Guthrie, D.; Sun, Y.; Noël, T., C(sp³)-H functionalizations of light hydrocarbons using decatungstate photocatalysis in flow. *Science* **2020**, *369* (6499), 92-96.
60. Cambié, D.; Zhao, F.; Hessel, V.; Debije, M. G.; Noël, T., A Leaf-Inspired Luminescent Solar Concentrator for Energy-Efficient Continuous-Flow Photochemistry. *Angew. Chem. Int. Ed.* **2017**, *56* (4), 1050-1054.
61. Pieber, B.; Shalom, M.; Antonietti, M.; Seeberger, P. H.; Gilmore, K., Continuous Heterogeneous Photocatalysis in Serial Micro-Batch Reactors. *Angew. Chem. Int. Ed.* **2018**, *57* (31), 9976-9979.
62. Rosso, C.; Gisbertz, S.; Williams, J. D.; Gemoets, H. P. L.; Debrouwer, W.; Pieber, B.; Kappe, C. O., An oscillatory plug flow photoreactor facilitates semi-heterogeneous dual nickel/carbon nitride photocatalytic C-N couplings. *React. Chem. Eng.* **2020**, *5* (3), 597-604.
63. Harper, K. C.; Moschetta, E. G.; Bordawekar, S. V.; Wittenberger, S. J., A Laser Driven Flow Chemistry Platform for Scaling Photochemical Reactions with Visible Light. *ACS Cent. Sci.* **2019**, *5* (1), 109-115.
64. Kubota, K.; Pang, Y.; Miura, A.; Ito, H., Redox reactions of small organic molecules using ball milling and piezoelectric materials. *Science* **2019**, *366* (6472), 1500-1504.
65. Zoller, J.; Fabry, D. C.; Rueping, M., Unexpected Dual Role of Titanium Dioxide in the Visible Light Heterogeneous Catalyzed C-H Arylation of Heteroarenes. *ACS Catal.* **2015**, *5* (6), 3900-3904.
66. Ciamician, G., THE PHOTOCHEMISTRY OF THE FUTURE. *Science* **1912**, *36* (926), 385-394.

Chapter 3

Overcoming Limitations in Dual Photoredox/Nickel catalyzed C–N Cross-Couplings due to Catalyst Deactivation

Gisbertz, S.; **Reischauer, S.**; Pieber, B.

Nat. Catal. **2020**, *3*, 611-620.

<https://doi.org/10.1038/s41929-020-0473-6>

Abstract

Dual photoredox/nickel catalyzed C–N cross-couplings suffer from low yields for electron-rich aryl halides. The formation of catalytically inactive nickel-black is responsible for this limitation and causes severe reproducibility issues. We demonstrate that catalyst deactivation can be avoided by using a carbon nitride photocatalyst. The broad absorption of the heterogeneous photocatalyst enables a wavelength dependent control of the rate of reductive elimination to prevent nickel-black formation during the coupling of cyclic, secondary amines and aryl halides. A second approach, that is applicable to a broader set of electron-rich aryl halides, is to run the reactions at high concentrations to increase the rate of oxidative addition. Less nucleophilic, primary amines can be coupled with electron-rich aryl halides by stabilizing low-valent nickel intermediates with a suitable additive. The developed protocols enable reproducible, selective C–N cross-couplings of electron-rich aryl bromides and can be also applied for electron-poor aryl chlorides.

Specific contribution

B. Pieber and S. Gisbertz conceived the research study. B. Pieber., S. Gisbertz and I designed all experiments. S. Gisbertz performed all synthetic experiment. S. Gisbertz and I carried out

characterizations of materials and studies on the Ni-black formation. B. Pieber, S. Gisbertz and I wrote the manuscript. B. Pieber revised and corrected the manuscript and directed the research study.

Supporting Information

All experimental procedures and analytical data are available in the supporting information in the appendix or through the website of the Publisher. DOI: [10.1038/s41929-020-0473-6](https://doi.org/10.1038/s41929-020-0473-6).

3.1 Introduction

The palladium-catalyzed formation of carbon–nitrogen bonds (Buchwald-Hartwig) ranks among the most widely applied reactions in synthetic chemistry.¹ Nickel is an attractive alternative to palladium due to its higher abundance, but the requirement of air-sensitive Ni(0) complexes, sophisticated ligands, as well as strong reductants, and bases for C–N bond formations have hampered its use.²⁻⁴ Air-stable nickel pre-catalysts have been developed, but still strong alkoxide bases and complex ligands are needed (Figure 3.1, a).⁵⁻⁹ In combination with electrochemistry, ligated Ni(II) salts catalyze the C–N cross-coupling under mild conditions (Figure 3.1, b).¹⁰⁻¹¹ Ligand-free Ni(II) salts were used together with UV light (365 nm),¹² or visible light photocatalysis *via* photoredox (PRC),¹³⁻¹⁷ or energy transfer (EnT)¹⁸⁻¹⁹ processes (Figure 3.1, c). Although synthetically attractive, electro- and photochemically mediated, nickel-catalyzed C–N couplings are limited to electron-poor aryl halides. Aryl halides that do not contain electron withdrawing groups are usually either unreactive,¹⁵ or give low yields,^{11-12, 16-17, 19} and only a few examples with a good isolated yield are reported (for a detailed analysis, see the Supplementary Information).¹³

Electro- and photochemically mediated methods rely on the initial reduction of the Ni(II) catalyst to a low valent (Ni⁰ or Ni^I) species, followed by oxidative addition that is slow for electron-rich aryl halides.^{11, 20} This bottleneck potentially leads to the accumulation of nickel(0) species that aggregate, resulting in catalyst deactivation. In the electrochemically driven, nickel-catalyzed aryl amination, nickel-black deposition was observed on the cathode and could be avoided by using Ni(bpy)₃Br₂ (bpy = 2,2' bipyridine) instead of a 1:1 mixture of NiBr₂·glyme and dtbbpy (4,4'-di-tert-butyl-2,2'-bipyridine), thereby expanding the scope to a few electron-rich heteroaryl halides.¹¹ Stabilizing bipyridine ligands are unsuitable for light-mediated, nickel-catalyzed C–N cross-couplings,¹²⁻¹⁷ but catalyst deactivation or nickel-black formation was not reported. It is, however, well known that Ni(II) salts – in presence of amines as sacrificial electron donors (SED) – can be used intentionally for the photochemical preparation of Ni(0) nanoparticles (Figure 3.1, d).²¹⁻²³

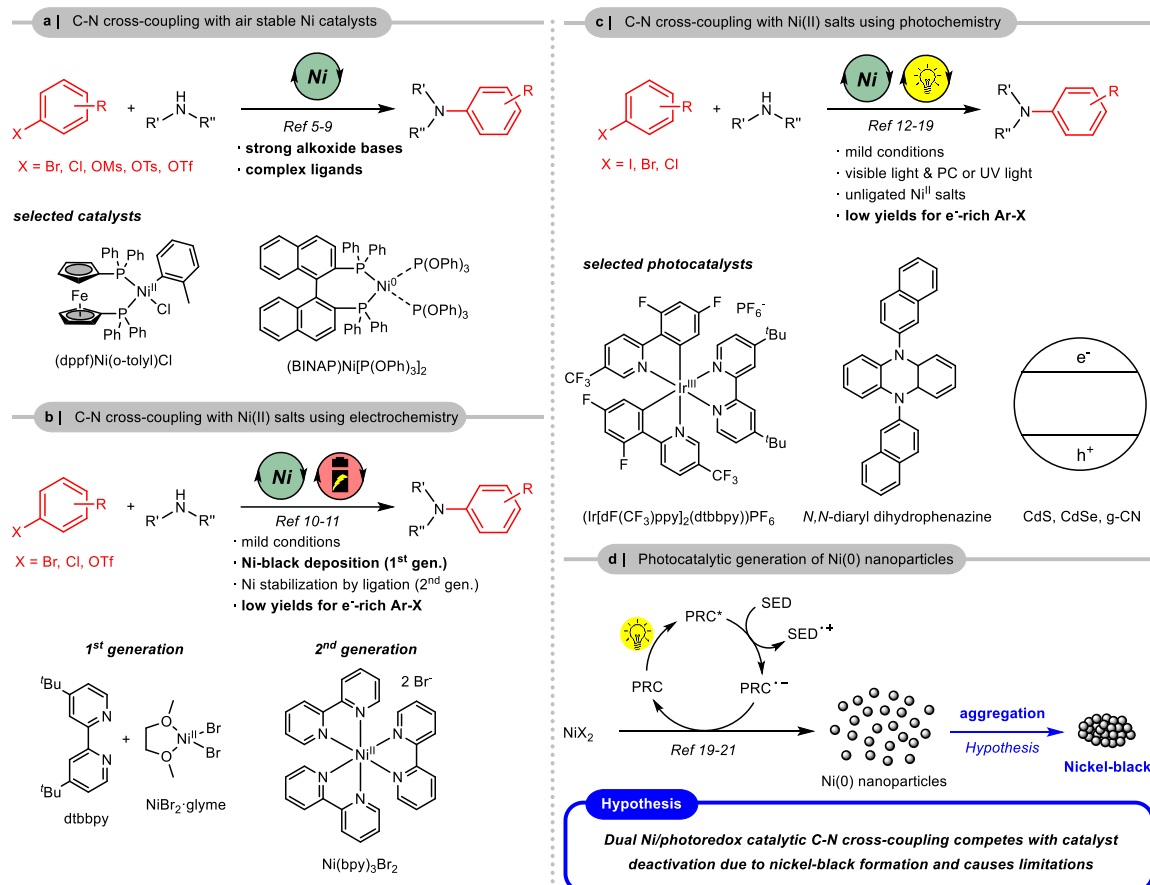
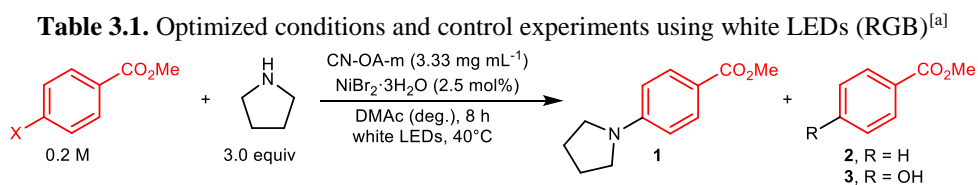


Figure 3.1. Nickel catalyzed C–N cross-coupling reactions. **a**, air stable Ni precatalysts require strong bases and sophisticated ligands. **b**, electrochemically enabled, Ni-catalyzed aminations and; **c**, photochemically driven, Ni-catalyzed aminations are limited to electron-poor aryl halides. **d**, photocatalytic reduction of Ni(II) salts is used for nanoparticle formation potentially leads to nickel-black formation in catalysis.

Here, we show that catalyst deactivation *via* nickel-black formation is responsible for the low yields when electron-rich aryl bromides are used in dual photoredox/nickel catalyzed C–N cross-couplings. Deposition of the catalytically inactive, low-valent nickel species further deactivates a heterogeneous photocatalyst, hampering its recyclability. We demonstrate that nickel-black formation can be avoided by i) decelerating the light-mediated reductive elimination, ii) enhancing the oxidative addition or, iii) stabilizing low-valent nickel intermediates. The resulting protocols enable selective and reproducible couplings of amines with electron-poor, -neutral, and -rich aryl halides, and allow for recycling of the heterogeneous photocatalyst.

3.2 Results and discussion

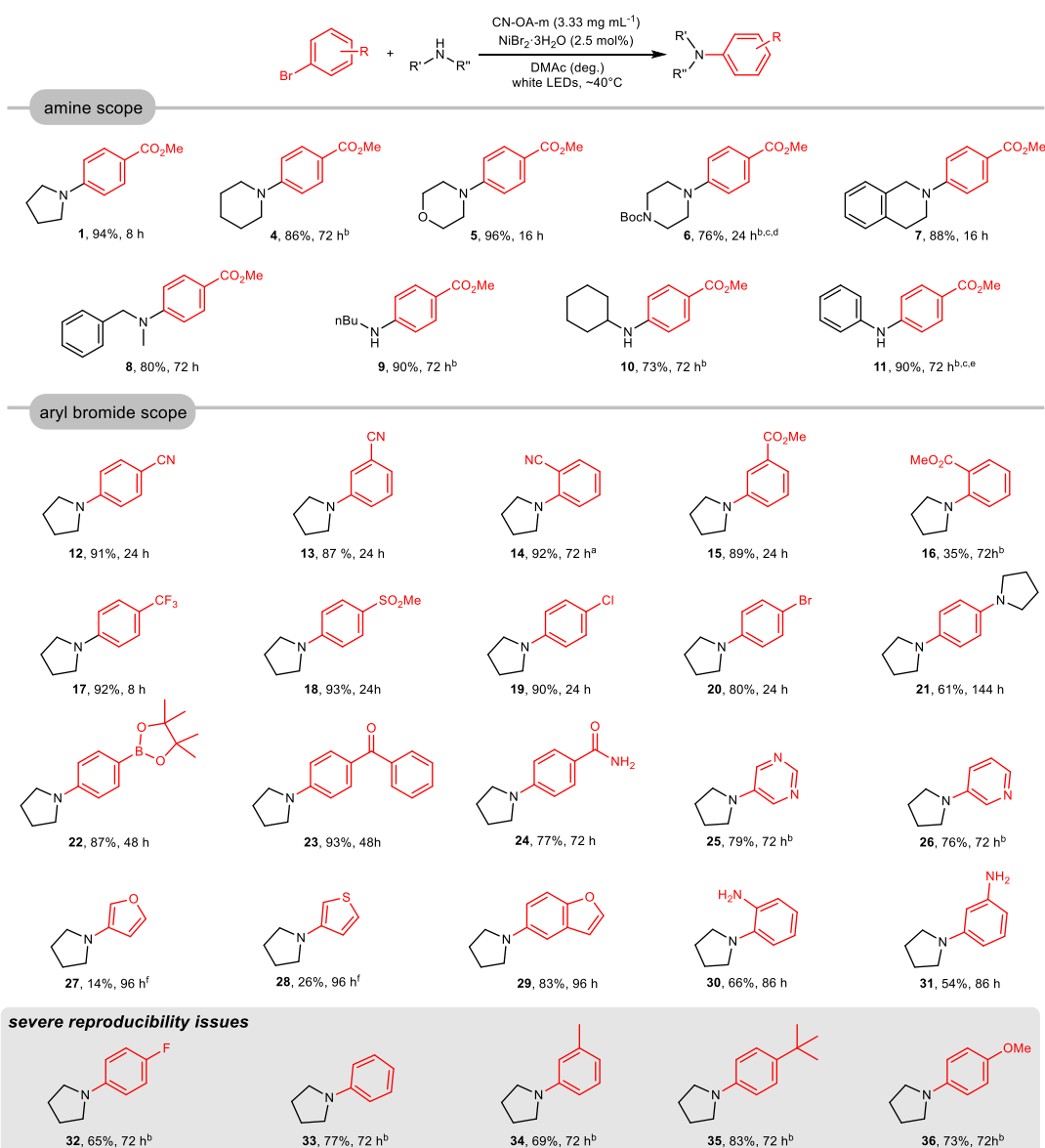
Our investigations started by optimizing the dual nickel/photoredox catalyzed amination of methyl 4-bromobenzoate with pyrrolidine using the carbon nitride CN-OA-m as photocatalyst (Table 3.1). This heterogeneous material has a broader optical absorption in the visible region compared to most other known CN materials and can be easily prepared on gram scale *via* co-condensation of urea and oxamide followed by post-calcination in a molten salt (see Supplementary Information).²⁴⁻²⁶ Nearly quantitative formation of the desired alkyl aryl amine (**1**) was obtained within 8 h when CN-OA-m (3.33 mg mL⁻¹), NiBr₂·3H₂O (2.5 mol%) and three equivalents of the amine were used without any additional base in dimethylacetamide (DMAc) as solvent (Table 3.1, Entry 1-2).²⁷ The reaction was easily scaled up by increasing the reaction time, affording **1** on a gram scale within 14 hours (see Supplementary Information).²⁸



Entry	X	Conditions	Conversion [%] ^b	1 [%] ^c	2 [%] ^c	3 [%] ^c
1	Br	as shown	quant.	98	2	n.d.
2	Br	1.66 mg mL ⁻¹ CN-OA-m	quant.	96	2	1
3	I	as shown	quant.	99	1	n.d.
4	Cl	168 h	76	72	4	n.d.
5	OTf	72 h	75	67	5	2
6	Br	no CN-OA-m	5	n.d.	2	1
7	Br	no NiBr ₂ ·3H ₂ O	5	n.d.	n.d.	n.d.
8	Br	no light	<1	n.d.	n.d.	n.d.
9	Br	no degassing	10	10	n.d.	n.d.

^aReaction conditions: methyl 4-bromobenzoate (1.2 mmol), pyrrolidine (3.6 mmol), NiBr₂·3H₂O (2.5 mol%), CN-OA-m (20 mg), DMAc (anhydrous, 6 mL), white LEDs (RGB) at 40 °C for 8 h. ^bConversion aryl halide determined by ¹H-NMR using 1,3,5-trimethoxybenzene as internal standard. ^cNMR yields were determined by ¹H-NMR using 1,3,5-trimethoxybenzene as internal standard. n.d. = not detected. dtbbpy = 4,4'-di-*tert*-butyl-2,2'-bipyridine.

Aside from aryl bromides, aryl iodides coupled with similar efficiency and selectivity (Entry 3). The optimized protocol further enabled C–N couplings using aryl chlorides and aryl triflates, but these reactions did not go to completion (Entry 4-5). Control studies in the absence of CN-OA-m, NiBr₂·3H₂O and light did not result in the formation of the desired product, and the presence of oxygen significantly decreased the reaction rate (Entry 6-9). With the optimized conditions in hand, the versatility of the semi-heterogeneous catalytic system was evaluated (Table 3.2). The reaction of methyl 4-bromobenzoate with cyclic secondary amines generally gave high yields for the corresponding aryl amines (**1**, **4-7**). A secondary amine with low steric hindrance also resulted in the desired aryl amine (**8**), but the majority of acyclic secondary amines did not react under these conditions (see Supplementary Information). Aliphatic and aromatic primary amines reacted efficiently (**9-11**). Aryl halides containing electron-withdrawing groups coupled with high selectivity; nitriles (**12-14**), carbonyl groups (**1**, **15**, **23-24**), trifluoromethyl- (**15**) as well as methylsulfonyl-groups (**16**), halides (**17-18**), boronic acid pinacol esters (**22**), and electron-poor heteroaromatic bromides (**25**, **26**) were tolerated in the dual catalytic amination. 1,4-Dibromobenzene can undergo selective mono- (**20**) or di-amination (**21**) by varying the reaction time and stoichiometry of the amine coupling partner. Similar to related C–O bond formations,²⁴⁻²⁵ a carbonyl-group in the 2-position only gave moderate yield (**16**). Low reactivity was observed for electron-rich heterocycles (**27**, **28**). Notably, good isolated yields were obtained for the C–N coupling of pyrrolidine with a range of electron-rich aryl bromides (**29-36**).²⁹ However, in the case of 1-bromo-4-fluorobenzene (**32**),³⁰ bromobenzene (**33**), 3-bromotoluene (**34**), 1-bromo-4-*tert*-butylbenzene (**35**), and 4-bromoanisole (**36**) these values are not representative, as these substrates suffered from severe reproducibility issues. These reactions frequently resulted in low yields and the heterogeneous PRC became black, whereas almost no color change was observed in case of aryl halides that do not suffer from these reproducibility issues. High amounts of deposited nickel were detected on the recovered, black carbon nitride material by ICP-OES analysis, indicating nickel-black formation (see Supplementary Information).

Table 3.2. Scope of the semi-heterogeneous amination of amines and aryl bromides.^[a]

^aReaction conditions: aryl bromide (1.2 mmol), amine (3.6 mmol), CN-OA-m (20 mg), NiBr₂·3H₂O (30 μmol), DMAc (anhydrous, 6.0 mL), white LEDs at 40 °C. Isolated yields are reported. For experimental details, see the Supplementary Information. ^b5 mol% NiBr₂·3H₂O were used. ^c10 mol% pyrrolidine were added. ^dThe reaction was carried out on a 0.6 mmol scale. ^e3 equivalents *N*-*tert*-butylisopropylamine were added. ^fYield was determined by ¹H-NMR using 1,3,5-trimethoxybenzene as internal standard.

Deactivation of metal catalysts *via* deposition is a common problem in palladium catalysis (Pd-black formation) and can be addressed by avoiding high concentrations of Pd(0) species that agglomerate.³¹ In light-mediated, nickel catalyzed C–N cross-couplings, a Ni(0) complex was proposed to be the catalytically active species that is initially formed *via* a photoredox-catalyzed hydrogen atom transfer (HAT).²⁰ We assumed that, in the case of electron-rich aryl halides, slow oxidative addition results in the accumulation of unstabilized Ni(0) that aggregate. Since the heterogeneous photocatalyst absorbs only weakly above 450 nm,²⁵ we assumed that the formation of nickel-black can be decelerated using higher wavelengths. As anticipated, when a mixture of pyrrolidine and CN-OA-m in DMAc was irradiated with green light (520 nm), nickel black formation was significantly slower than with blue light (450 nm, see Supplementary Information). To our delight, the coupling of pyrrolidine and 1-bromo-4-fluorobenzene was highly selective and reproducible using 520 nm LEDs (Method B), and the desired compound (**32**) was obtained in 85-91% in six parallel experiments (Figure 3.2, a). The same set of experiments using blue LEDs (~450 nm, Method A) exhibited large variations in yield. While five experiments gave 60-70% of **32**, only 5-6% of the desired amine were formed for two reactions where the reaction mixture turned black. Careful analysis of the heterogeneous material recovered from the low yielding reactions identified the nature and quantity of the deposited Ni species (see Supplementary Information). ICP-OES analysis showed a Ni concentration of 126 mg g⁻¹ for the reaction irradiated with blue light and only 36 mg g⁻¹ for the material after an experiment using green LEDs. Elemental analysis *via* energy-dispersive X-ray spectroscopy (EDX) is in agreement with these results. X-ray powder diffraction (XRD) confirmed the deposition of low valent nickel species, with a significantly higher concentration on the material irradiated with blue light. High resolution X-ray photoelectron spectroscopy (XPS) for core levels of Ni2p_{3/2} spectrum of the recovered CN-OA-m from experiments using 450 nm LEDs (Method A) showed two main deconvoluted peaks located at 853.7 (±0.02) eV and 852.5 (±0.02) eV that can be assigned to the binding energy of Ni(II) and Ni(0) species.

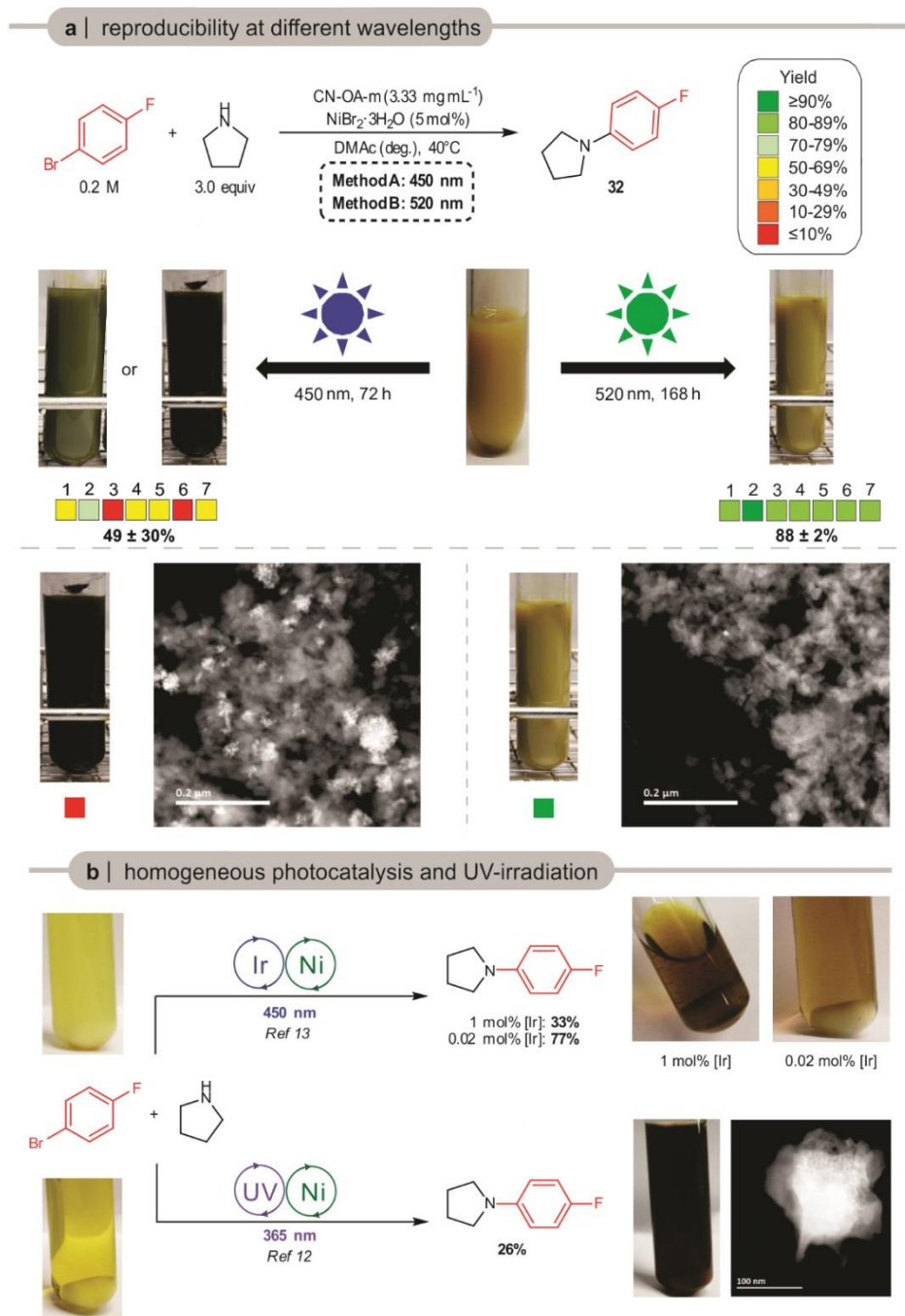


Figure 3.2. Catalyst deactivation during the reaction of 4-bromofluorobenzene with pyrrolidine. a, Reproducibility using blue (450 nm) and green (520 nm) LED irradiation. The reaction mixture turned dark green or black and suffered from severe reproducibility issues at 450 nm, whereas almost no color change and reproducible results were obtained at 520 nm. HAADF-STEM images show nickel particle agglomerates (bright spots) on CN-OA-m recovered the experiment using blue light and almost no agglomerates when 520 nm were used. **c,** Nickel-black formation was also observed using the homogeneous $(\text{Ir}[\text{dF}(\text{CF}_3)\text{ppy}]_2(\text{dtbbpy}))\text{PF}_6$ ($= [\text{Ir}]$) photocatalyst and in the PRC-free reaction using UV light. For experimental details, see the Supplementary Information.

Only Ni(II) was detected on the material recovered from experiments using 520 nm LEDs (Method B) by XPS. Scanning transmission electron microscopy (STEM) was used to visualize nickel particles on the surface of the recovered CN-OA-m from both methods. High-angle annular dark-field (HAADF) images show a high amount of nickel particles that agglomerated (nickel-black) on the CN-OA-m recovered from experiments using 450 nm LEDs (Method A), whereas the material from experiments using 520 nm LEDs (Method B) contained almost no agglomerates (Figure 3.2, a).

Nickel-black formation was also shown to be responsible for low yields using other light-mediated protocols for the same model reaction (Figure 3.2, b). A reaction with 1 mol% of the homogeneous PRC (Ir[dF(CF₃)ppy]₂(dtbbpy))PF₆,¹⁷ resulted in low selectivity towards the desired coupling product (**32**, 33% yield), and small amounts of a black precipitate were formed during the reaction. Decreasing the amount of (Ir[dF(CF₃)ppy]₂(dtbbpy))PF₆ to 0.02 mol% increased the yield of **32** significantly (77%) and no particle formation was observed. Here, the amount of the PRC plays a crucial role to avoid nickel-black formation and the optimal catalyst loading needs to be determined for each substrate individually. The PRC-free, UV light-mediated protocol¹² resulted in no more than 26% of **32** and a black precipitate was formed in high amounts (Figure 3.2, c). STEM imaging and EDX spectroscopy confirmed that these solids consist of nickel and organic matter that is presumably resulting from substrate/product degradation by the high-energy light source (see Supplementary Information for details).

The dual carbon nitride/nickel catalyzed protocol using green light (520 nm, Method B) did also enable selective, reproducible C–N cross-couplings of bromobenzene (**33**), and 3-bromotoluene (**34**) with pyrrolidine, but did not eliminate catalyst deactivation issues in the cases of 1-bromo-4-*tert*-butylbenzene (**35**), and 4-bromoanisole (**36**) (Figure 3.3, a). Although almost quantitative product formation was observed in some cases, the reactions sometimes gave low yields and black reaction mixtures. In the case of 1-bromo-4-*tert*-butylbenzene, for example, six parallel reactions using 450 nm (Method A) gave 52-70% of the desired product (**35**), whereas up to 92% as well as only 28 % were obtained under identical conditions using 520 nm (Method B). Efforts to increase the reproducibility and to minimize the nickel-black formation by changing the light intensity, distance between the reaction mixture and light source, varying the amount of both catalysts, changing the solvent or nickel catalyst, and adding MTBD (7-Methyl-1,5,7-triazabicyclo(4.4.0)dec-5-ene)¹⁷ or

dtbbpy to stabilize intermediate nickel species were not successful. We hypothesized that the formation of Ni(0) agglomerates can be addressed by increasing the concentration of the reaction mixture for two reasons. First, a higher concentration would increase the rate of oxidative addition, thus minimizing the accumulation of Ni(0) species. Second, catalyst deactivation might not only be accelerated by higher photon energies, but also a competitive binding of the amine and the solvent (DMAc) with low-valent nickel intermediates. In palladium catalysis, for example, PdArylXL_n intermediates were reported to form complexes with various solvents, including DMAc, that undergo β-hydride elimination followed by the formation of Pd(0) and Aryl-H.³² Although pyrrolidine was shown to be the primary ligand in light-mediated, nickel catalyzed aminations,²⁰ the high excess of DMAc potentially results in solvent-catalyst interactions that could contribute to Ni-black formation. Indeed, running the reaction at 1.2 M instead of 0.2 M resulted in reproducible reactions and the desired products (**32-36**) were obtained in high yields, even at 450 nm (Method C). These results could not be further improved using 520 nm irradiation, suggesting that the nickel-black formation can be outpaced at high concentrations independent of the photon energy in our semi-heterogeneous catalytic system (see Supplementary Information).³³

A reinvestigation of the coupling of methyl 4-chlorobenzoate with pyrrolidine was carried out using all protocols (see Supplementary Information). The standard protocol (Method A) afforded the desired coupling product (**1**) in 65% within seven days. Longer irradiation did not result in higher yields and only increased the amount of the dehalogenated side product, indicating complete catalyst deactivation.

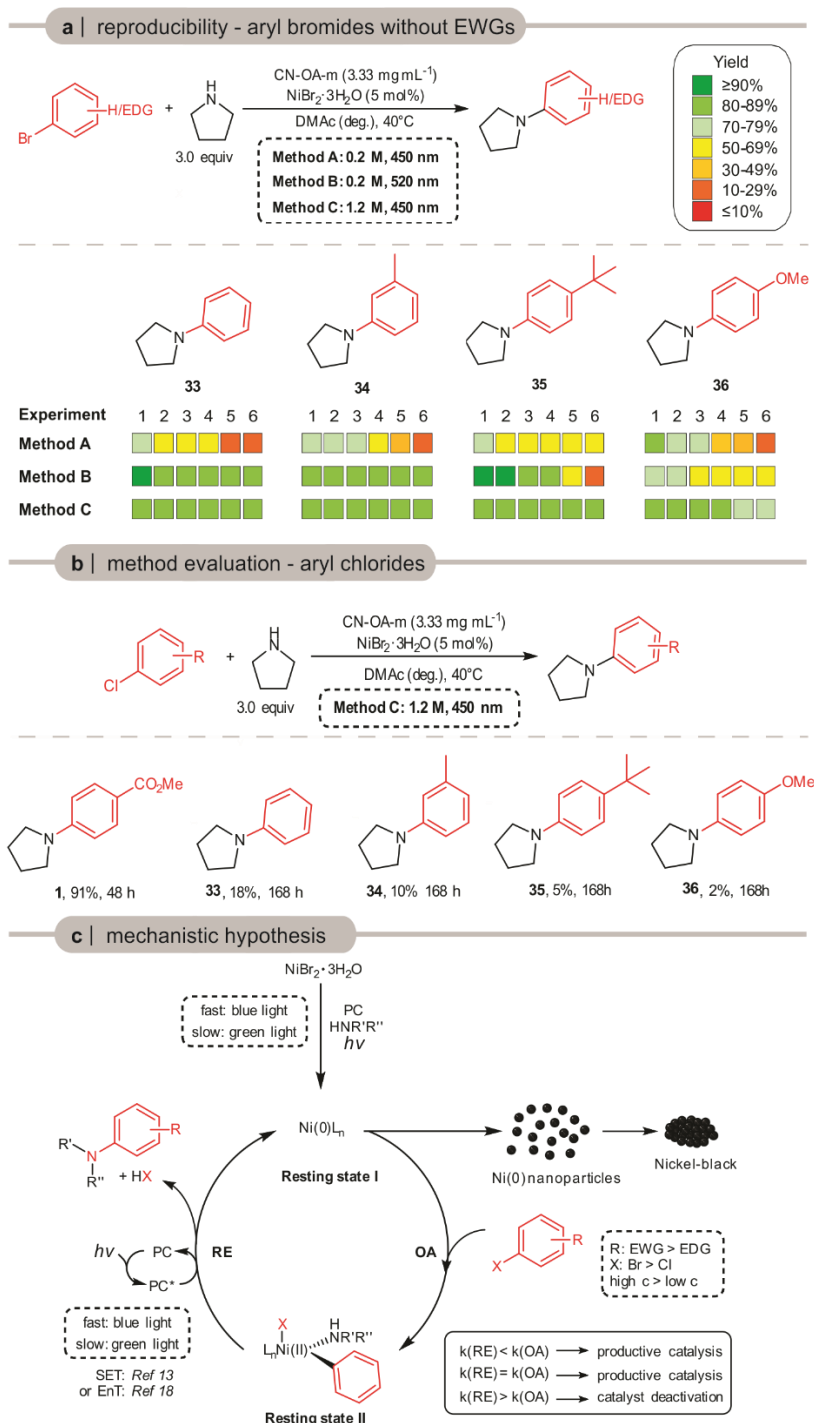


Figure 3.3. Evaluation of different protocols for coupling aryl bromides and aryl chlorides with pyrrolidine. **a**, Reproducibility study for aryl bromides without electron withdrawing groups using different C–N coupling protocols. NMR yields are reported **b**, Evaluation of Method C for the coupling of aryl halides and pyrrolidine. ^aIsolated yield. ^bNMR-yield **c**, Simplified mechanism of productive catalysis and catalyst deactivation. The reductive elimination (RE) likely follows either a three-step photoredox (N(II)-N(III)-N(I)-N(0));¹⁷ or a two-step energy transfer (Ni(II)-Ni(II)*-Ni(0)) process.¹⁸⁻¹⁹

With green light (Method B), 83% of **1** was obtained within 14 days. The optimized method using 450 nm LEDs and a lower amount of solvent (Method C) significantly enhanced the C–N coupling and resulted in 92% of **1** within two days (Figure 3.3, b). When the best conditions (Method C) were applied for electron-neutral, and -rich aryl chlorides, a clear trend was observed (Figure 3.3, b). Chlorobenzene gave 18% of **33** within 168 hours, and substrates with electron-donating substituents gave even lower yields. In all cases the formation of nickel black was observed.

Taking all experiments together, we propose that catalyst deactivation is avoided when the relative rate of oxidative addition (OA) is equal or higher than the relative rate of reductive elimination (RE), avoiding accumulation of Ni(0) species (Resting state **I**, Figure 3.3, c). This is (under all conditions) the case for activated (electron-poor) aryl bromides. In case of 4-bromobenzene and 3-bromotoluene, the rate of RE (and the initial formation of Ni(0)) was sufficiently decelerated by using green light (slow OA, slow RE). At higher concentrations, the rate of OA is increased significantly, resulting in efficient productive catalysis for all tested, electron-rich aryl bromides (fast OA, fast RE). For non-activated, electron-rich aryl chlorides OA becomes too slow and Ni(0) accumulation cannot be avoided under the conditions reported herein.

Next, we sought to study if the deposition of nickel-black also affects the recyclability of CN-OA-m by altering its photocatalytic activity. During the coupling of pyrrolidine with methyl 4-bromobenzoate using white (RGB) LEDs, the reaction mixture became greenish-brown (Figure 3.4, a). ICP-OES analysis of the heterogeneous material showed a nickel content of $\sim 14 \text{ mg g}^{-1}$. The formation of product decreased significantly when the heterogeneous PRC was recycled (Figure 3.4, b).³⁴ Further, the yellow PRC turned dark green to black and the amount of deposited Ni rose to $\sim 61 \text{ mg g}^{-1}$ over five recycling experiments. At higher wavelengths (520 nm, Method B), the model reaction required 48 h instead of 8 h for full conversion (Figure 3.4, a). Although the reaction mixture did not change its color, the amount of deposited Ni was similar to the white LED experiment ($\sim 14 \text{ mg g}^{-1}$). The photocatalyst did, however, not lose its catalytic activity during five recycling experiments and was recovered as a yellow solid that contained a lower amount of deposited nickel ($\sim 39 \text{ mg g}^{-1}$) compared to the white light experiment (Figure 3.4, b).

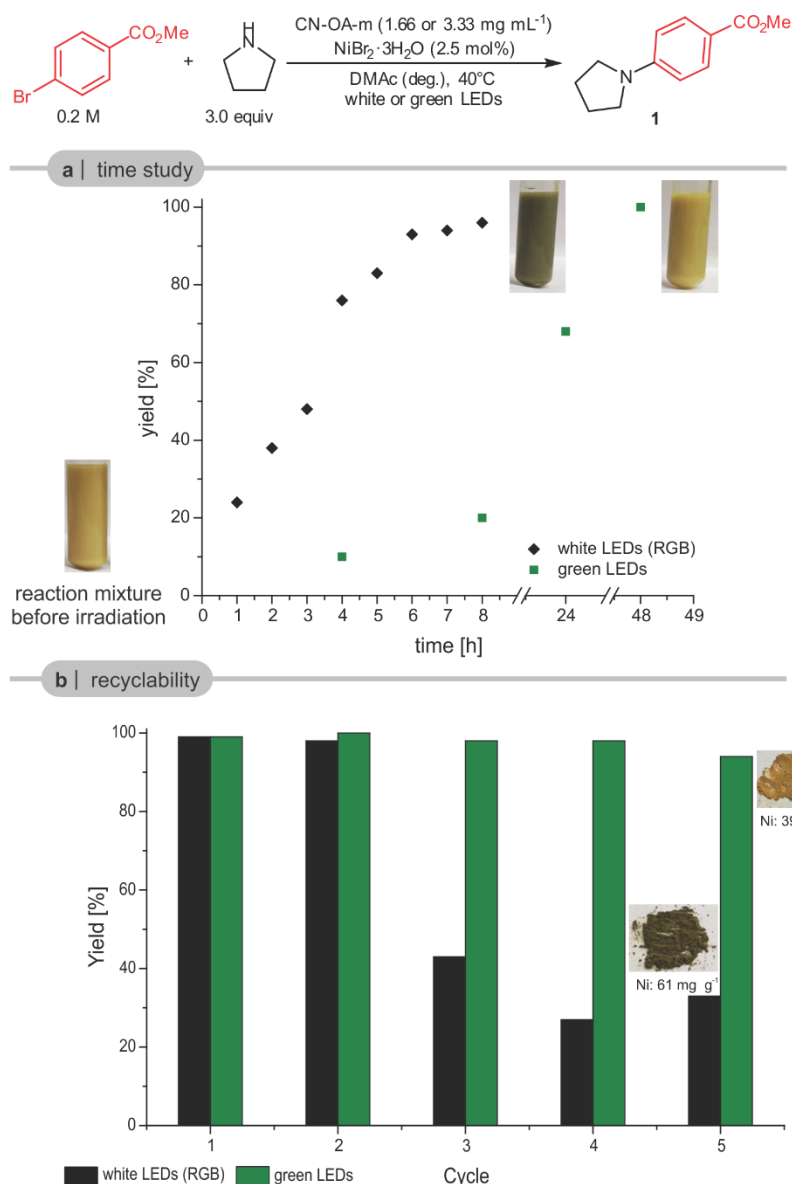


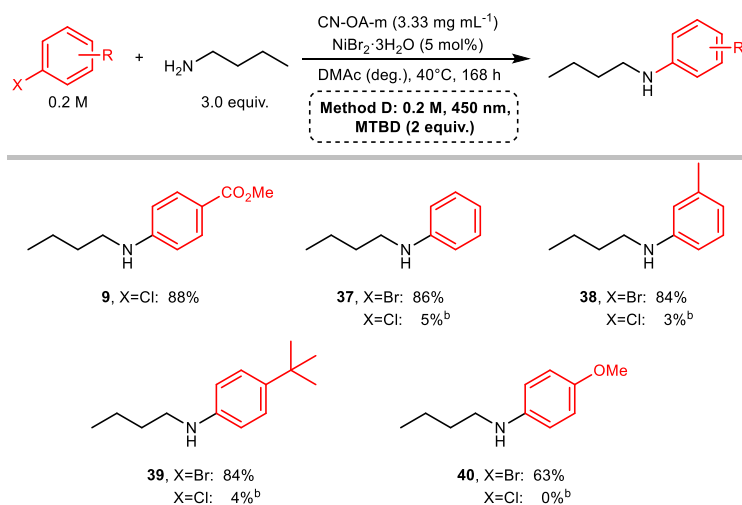
Figure 3.4. Reduction of catalyst deactivation using higher wavelengths. **a**, Time study for the coupling of methyl 4-bromobenzoate and pyrrolidine using white (RGB) and green (~520 nm) LED irradiation. The heterogeneous photocatalyst turned green using white light (RGB) irradiation whereas no color change was observed when green light (~520 nm) was used. **b**, The recyclability of CN-OA-m is excellent using green (~520 nm) LEDs. Deactivation of the PRC by nickel-black depositions was observed using white (RGB) LEDs. For experimental details, see the Supplementary Information.

Scanning transmission electron microscopy (STEM) of CN-OA-m from both recycling studies showed a significant amount of nickel agglomerates (nickel-black) for CN-OA-m from the experiments using white LEDs, whereas almost no agglomerates were detected on the semiconductor recovered from the recycling study using green LEDs (see Supplementary Information).

Finally, we sought to determine if deactivation of the nickel catalyst could also be avoided when less nucleophilic, primary amines are used. These substrates are usually less efficient

and give lower yields than cyclic, secondary amines, even with electron-deficient aryl bromides.^{12-13, 18-19, 28} By studying the cross-coupling of *n*-butylamine with 1-bromo-4-*tert*-butylbenzene, we observed only 8% of the desired product (**39**) during a 16 h experiment using blue light (Method A, see Supplementary Information). Notably, running the reaction at higher concentrations decreased the yield, indicating that low-valent Ni(*n*-butylamine)_n species are rather inefficient towards OA and a higher concentration in this case might even accelerate catalyst deactivation. Increasing the temperature from 40 to 60 °C resulted in up to 42% of the desired coupling product (**39**), but concomitant deactivation of the nickel catalyst was observed. Switching to green light or performing the reaction at 80 °C did not improve these result.

The above described strategies to accelerate OA or decelerate RE were not successful. It was previously reported that the addition of DBU and MTBD has a positive effect on the reaction outcome with primary amines, but the reason for that remains unclear.^{15, 17} We assumed that coordination of these additives to the active, low valent nickel species i) might activate the low-valent nickel complex towards OA, and ii) has a stabilizing effect that would increase the lifetime of resting state **I** by inhibiting nickel-black formation. We could ultimately prove this stabilizing affect during control experiments in the absence of aryl halides (see Supplementary Information). When NiBr₂·3H₂O was irradiated in the presence of pyrrolidine with blue light, Ni-black was rapidly formed. However, the formation of nickel black takes significantly longer in the presence of MTBD. Further, a comparison of the coupling of 1-bromo-4-*tert*-butylbenzene with *n*-butylamine with and without additives showed a higher catalytic activity when MTBD was added. After a short optimization, we obtained conditions that enabled the coupling of electron-poor aryl bromides with *n*-butylamine in good to excellent selectivity at 40°C (Table 3.3). This method was also applicable for an electron-poor aryl chloride, but, similar to the coupling with pyrrolidine, deactivated aryl chlorides remain a limitation.

Table 3.3. Semi-heterogeneous amination of primary amines and aryl halides.^[a]

^aReaction conditions: aryl halide (1.2 mmol), *n*-butylamine (3.6 mmol), CN-OA-m (20 mg), NiBr₂·3H₂O (60 μmol), 7-Methyl-1,5,7-triazabicyclo[4.4.0]dec-5-ene (MTBD) (2.4 mmol), DMAc (anhydrous, 6.0 mL), blue LEDs at 40 °C. Isolated yields are reported. ^bYield was determined by ¹H-NMR using 1,3,5-trimethoxybenzene as internal standard.

3.3 Conclusion

The formation of nickel-black limits the applicability of light-mediated, nickel catalyzed C–N cross-couplings. In particular, aryl bromides lacking electron-withdrawing groups suffer from reproducibility problems due to deactivation of the nickel catalyst. Deposition of nickel particles (nickel-black) not only deactivates the homogeneous nickel catalyst, but also the heterogeneous carbon nitride photocatalyst. Careful studies using dual carbon nitride/nickel catalysis showed that nickel-black formation likely results from a slow oxidative addition in case of electron-rich aryl bromides, leading to accumulation of low-valent nickel species that agglomerate. We showed that this issue can be overcome by i) decreasing the rate of the reductive elimination, ii) increasing the rate of oxidative addition, and iii) stabilizing low-valent nickel intermediates with a suitable additive. Our strategies enable reproducible, highly selective C–N cross-couplings of electron-rich, -neutral and -poor aryl bromides with primary and cyclic, secondary amines and can even be used for efficient reactions of electron-poor aryl chlorides.

3.4 References

1. Roughley, S. D.; Jordan, A. M., The Medicinal Chemist's Toolbox: An Analysis of Reactions Used in the Pursuit of Drug Candidates. *J. Med. Chem.* **2011**, *54* (10), 3451-3479.
2. Wolfe, J. P.; Buchwald, S. L., Nickel-Catalyzed Amination of Aryl Chlorides. *J. Am. Chem. Soc.* **1997**, *119* (26), 6054-6058.
3. Ge, S.; Green, R. A.; Hartwig, J. F., Controlling First-Row Catalysts: Amination of Aryl and Heteroaryl Chlorides and Bromides with Primary Aliphatic Amines Catalyzed by a BINAP-Ligated Single-Component Ni(0) Complex. *J. Am. Chem. Soc.* **2014**, *136* (4), 1617-1627.
4. Tassone, J. P.; England, E. V.; MacQueen, P. M.; Ferguson, M. J.; Stradiotto, M., PhPAd-DalPhos: Ligand-Enabled, Nickel-Catalyzed Cross-Coupling of (Hetero)aryl Electrophiles with Bulky Primary Alkylamines. *Angew. Chem. Int. Ed.* **2019**, *58* (8), 2485-2489.
5. Kelly, R. A.; Scott, N. M.; Díez-González, S.; Stevens, E. D.; Nolan, S. P., Simple Synthesis of CpNi(NHC)Cl Complexes (Cp = Cyclopentadienyl; NHC = N-Heterocyclic Carbene). *Organometallics* **2005**, *24* (14), 3442-3447.
6. Park, N. H.; Teverovskiy, G.; Buchwald, S. L., Development of an Air-Stable Nickel Precatalyst for the Amination of Aryl Chlorides, Sulfamates, Mesylates, and Triflates. *Org. Lett.* **2014**, *16* (1), 220-223.
7. Kampmann, S. S.; Skelton, B. W.; Wild, D. A.; Koutsantonis, G. A.; Stewart, S. G., An Air-Stable Nickel(0) Phosphite Precatalyst for Primary Alkylamine C–N Cross-Coupling Reactions. *Eur. J. Org. Chem.* **2015**, *2015* (27), 5995-6004.
8. Shields, J. D.; Gray, E. E.; Doyle, A. G., A Modular, Air-Stable Nickel Precatalyst. *Org. Lett.* **2015**, *17* (9), 2166-2169.
9. McGuire, R. T.; Paffile, J. F. J.; Zhou, Y.; Stradiotto, M., Nickel-Catalyzed C–N Cross-Coupling of Ammonia, (Hetero)anilines, and Indoles with Activated (Hetero)aryl Chlorides Enabled by Ligand Design. *ACS Catal.* **2019**, *9* (10), 9292-9297.
10. Li, C.; Kawamata, Y.; Nakamura, H.; Vantourout, J. C.; Liu, Z.; Hou, Q.; Bao, D.; Starr, J. T.; Chen, J.; Yan, M.; Baran, P. S., Electrochemically Enabled, Nickel-Catalyzed Amination. *Angew. Chem. Int. Ed.* **2017**, *56* (42), 13088-13093.
11. Kawamata, Y.; Vantourout, J. C.; Hickey, D. P.; Bai, P.; Chen, L.; Hou, Q.; Qiao, W.; Barman, K.; Edwards, M. A.; Garrido-Castro, A. F.; deGruyter, J. N.; Nakamura, H.;

Knouse, K.; Qin, C.; Clay, K. J.; Bao, D.; Li, C.; Starr, J. T.; Garcia-Irizarry, C.; Sach, N.; White, H. S.; Neurock, M.; Minter, S. D.; Baran, P. S., Electrochemically Driven, Ni-Catalyzed Aryl Amination: Scope, Mechanism, and Applications. *J. Am. Chem. Soc.* **2019**, *141* (15), 6392-6402.

12. Lim, C.-H.; Kudisch, M.; Liu, B.; Miyake, G. M., C–N Cross-Coupling via Photoexcitation of Nickel–Amine Complexes. *J. Am. Chem. Soc.* **2018**, *140* (24), 7667-7673.

13. Du, Y.; Pearson, R. M.; Lim, C.-H.; Sartor, S. M.; Ryan, M. D.; Yang, H.; Damrauer, N. H.; Miyake, G. M., Strongly Reducing, Visible-Light Organic Photoredox Catalysts as Sustainable Alternatives to Precious Metals. *Chem. Eur. J.* **2017**, *23* (46), 10962-10968.

14. Caputo, J. A.; Frenette, L. C.; Zhao, N.; Sowers, K. L.; Krauss, T. D.; Weix, D. J., General and Efficient C–C Bond Forming Photoredox Catalysis with Semiconductor Quantum Dots. *J. Am. Chem. Soc.* **2017**, *139* (12), 4250-4253.

15. Liu, Y.-Y.; Liang, D.; Lu, L.-Q.; Xiao, W.-J., Practical heterogeneous photoredox/nickel dual catalysis for C–N and C–O coupling reactions. *Chem. Commun.* **2019**, *55* (33), 4853-4856.

16. Ghosh, I.; Khamrai, J.; Savateev, A.; Shlapakov, N.; Antonietti, M.; König, B., Organic semiconductor photocatalyst can bifunctionalize arenes and heteroarenes. *Science* **2019**, *365* (6451), 360-366.

17. Corcoran, E. B.; Pirnot, M. T.; Lin, S.; Dreher, S. D.; DiRocco, D. A.; Davies, I. W.; Buchwald, S. L.; MacMillan, D. W. C., Aryl amination using ligand-free Ni(II) salts and photoredox catalysis. *Science* **2016**, *353* (6296), 279-283.

18. Escobar, R. A.; Johannes, J. W., A Unified and Practical Method for Carbon–Heteroatom Cross-Coupling using Nickel/Photo Dual Catalysis. *Chem. Eur. J.* **2020**, *26* (23), 5168-5173.

19. Kudisch, M.; Lim, C.-H.; Thordarson, P.; Miyake, G. M., Energy Transfer to Ni–Amine Complexes in Dual Catalytic, Light-Driven C–N Cross-Coupling Reactions. *J. Am. Chem. Soc.* **2019**, *141* (49), 19479-19486.

20. Qi, Z.-H.; Ma, J., Dual Role of a Photocatalyst: Generation of Ni(0) Catalyst and Promotion of Catalytic C–N Bond Formation. *ACS Catal.* **2018**, *8* (2), 1456-1463.

21. Wang, C.; Cao, S.; Fu, W.-F., A stable dual-functional system of visible-light-driven Ni(ii) reduction to a nickel nanoparticle catalyst and robust in situ hydrogen production. *Chem. Commun.* **2013**, *49* (96), 11251-11253.

Chapter 3

22. Rodríguez, J. L.; Valenzuela, M. A.; Pola, F.; Tiznado, H.; Poznyak, T., Photodeposition of Ni nanoparticles on TiO₂ and their application in the catalytic ozonation of 2,4-dichlorophenoxyacetic acid. *J. Mol. Catal. A: Chem.* **2012**, 353-354, 29-36.
23. Indra, A.; Menezes, P. W.; Kailasam, K.; Hollmann, D.; Schröder, M.; Thomas, A.; Brückner, A.; Driess, M., Nickel as a co-catalyst for photocatalytic hydrogen evolution on graphitic-carbon nitride (sg-CN): what is the nature of the active species? *Chem. Commun.* **2016**, 52 (1), 104-107.
24. Cavedon, C.; Madani, A.; Seeberger, P. H.; Pieber, B., Semiheterogeneous Dual Nickel/Photocatalytic (Thio)etherification Using Carbon Nitrides. *Org. Lett.* **2019**, 21 (13), 5331-5334.
25. Pieber, B.; Malik, J. A.; Cavedon, C.; Gisbertz, S.; Savateev, A.; Cruz, D.; Heil, T.; Zhang, G.; Seeberger, P. H., Semi-heterogeneous Dual Nickel/Photocatalysis using Carbon Nitrides: Esterification of Carboxylic Acids with Aryl Halides. *Angew. Chem. Int. Ed.* **2019**, 58 (28), 9575-9580.
26. Zhang, G.; Li, G.; Lan, Z.-A.; Lin, L.; Savateev, A.; Heil, T.; Zafeiratos, S.; Wang, X.; Antonietti, M., Optimizing Optical Absorption, Exciton Dissociation, and Charge Transfer of a Polymeric Carbon Nitride with Ultrahigh Solar Hydrogen Production Activity. *Angew. Chem. Int. Ed.* **2017**, 56 (43), 13445-13449.
27. Bulky, secondary amines such as N-tert-butylisopropylamine and 2,2,6,6-tetramethylpiperidine do not couple with aryl halides and can be used as a base if 1.5 equivalents of pyrrolidine are used (see Supplementary Information).
28. Rosso, C.; Gisbertz, S.; Williams, J. D.; Gemoets, H. P. L.; Debrouwer, W.; Pieber, B.; Kappe, C. O., An oscillatory plug flow photoreactor facilitates semi-heterogeneous dual nickel/carbon nitride photocatalytic C–N couplings. *React. Chem. Eng.* **2020**, 5 (3), 597-604.
29. Interestingly, although 2- and 3-bromoaniline (30 & 31) gave good yields, only a very low amount of the desired product (<5%) was formed when 4-bromoaniline was used (see Supplementary Information).
30. The strong resonance donating effect of fluorine appears sufficient to counteract the inductive withdrawing effect in dual photoredox/nickel catalyzed cross-couplings resulting in low reactivity (see Refs. 22-23).

31. Crabtree, R. H., Deactivation in Homogeneous Transition Metal Catalysis: Causes, Avoidance, and Cure. *Chem. Rev.* **2015**, *115* (1), 127-150.
32. Molina de la Torre, J. A.; Espinet, P.; Albéniz, A. C., Solvent-Induced Reduction of Palladium-Aryls, a Potential Interference in Pd Catalysis. *Organometallics* **2013**, *32* (19), 5428-5434.
33. It has to be noted that a higher concentration does not increase the yield in case of $(\text{Ir}[\text{dF}(\text{CF}_3)\text{ppy}]_2(\text{dtbbpy}))\text{PF}_6$.
34. When no $\text{NiBr}_2 \cdot 3\text{H}_2\text{O}$ is added to the recovered CN-OA-m material containing deposited nickel, only trace amounts of the C-N coupling product were observed (see Supplementary Information).

Chapter 4

Chromoselective Photocatalysis Enables Stereocomplementary Biocatalytic Pathways

Schmermund, L.; **Reischauer, S.**; Bierbaumer, S.; Winkler, C.; Diaz-Rodriguez, A.; Edwards, L.; Kara, S.; Mielke, T.; Cartwright, J.; Grogan, G.; Pieber, B.; Kroutil, W.

Angew. Chem. Int. Ed. **2021**, *60*, 6965-6969.

<https://doi.org/10.1002/anie.202100164>

Abstract

Controlling the selectivity of a chemical reaction with external stimuli is common in thermal processes, but rare in visible-light photocatalysis. Here we show that the redox potential of a carbon nitride photocatalyst (CN-OA-m) can be tuned by changing the irradiation wavelength to generate electron holes with different oxidation potentials. This tuning was the key to realizing photo-chemo-enzymatic cascades that give either the (S)- or the (R)-enantiomer of phenylethanol. In combination with an unspecific peroxygenase from *Agroclybe aegerita*, green light irradiation of CN-OA-m led to the enantioselective hydroxylation of ethylbenzene to (R)-1-phenylethanol (99% e.e.). In contrast, blue light irradiation triggered the photocatalytic oxidation of ethylbenzene to acetophenone, which in turn was enantioselectively reduced with an alcohol dehydrogenase from *Rhodococcus ruber* to form (S)-1-phenylethanol (93% e.e.).

Specific contribution

L. Schmermund and W. Kroutil conceived the research study. L. Schmermund, W. Kroutil, B. Pieber and I designed all experiments. L. Schmermund, S. Bierbaumer and I performed all synthetic experiment. I synthesized the photocatalyst. C. Winkler built the photoreactor. T. Mielke, J. Cartwright, G. Grogan, A. Diaz-Rodriguez and L. Edwards provided the enzyme and reference compounds. L. Schmermund wrote the manuscript with contribution from S. Reischauer, B. Pieber and W. Kroutil.

Supporting Information

All experimental procedures and analytical data are available in the supporting information in the appendix or through the website of the Publisher. DOI: [10.1002/anie.202100164](https://doi.org/10.1002/anie.202100164).

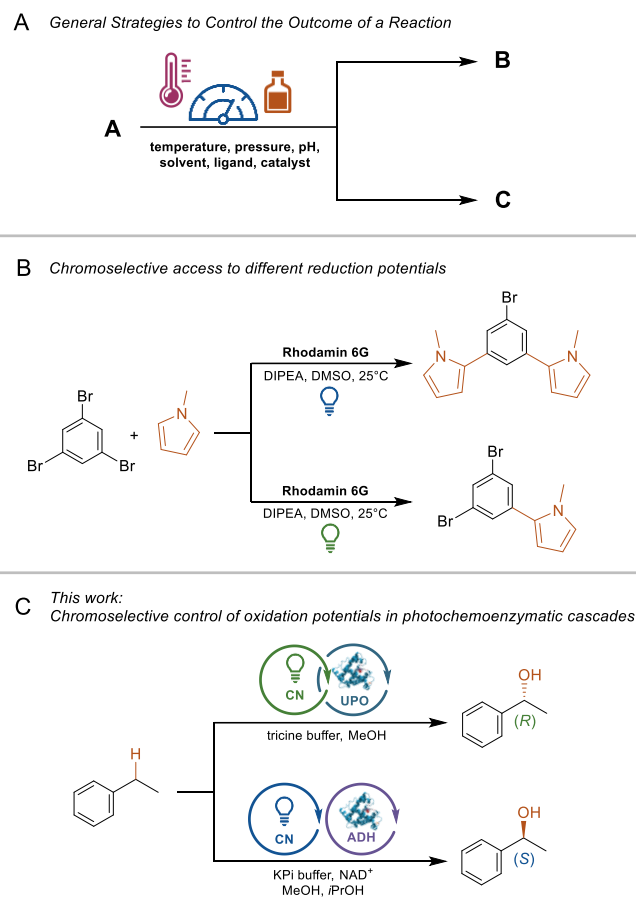
4.1 Introduction

Many parameters influence the selectivity of a chemical reaction.¹⁻² For instance, catalytic reactions can be controlled by varying the catalyst/coordinated ligands, directing groups³⁻⁶ or by tuning external parameters (Scheme 4.1, A).^{1, 7} The selectivity of photochemical reactions varies with different wavelengths,⁸ but examples that use this for visible-light photocatalysis are rare.⁹⁻¹³

In one example, selective control between either a one- or two-fold substitution of 1,3,5-tribromobenzene with *N*-methylpyrrole using Rhodamin 6G (Rh-6G) as photocatalyst was demonstrated (Scheme 4.1, B)⁹ This selectivity switch is explained by the chromoselective generation of two photocatalytic species that differ in their reduction potential. Green light irradiation results in a common photoredox cycle and the expected mono-substituted product. In case of blue light, the Rh-6G radical anion, which is formed after quenching of Rh-6G* with a sacrificial electron donor, can absorb a second photon, resulting in the highly reducing Rh-6G^{•-} species that enables the formation of the di-substituted product.⁹

4.2 Results and discussion

Here we show that electron holes with different oxidation potentials can be generated using a heterogeneous carbon nitride (CN) catalyst by changing the incident photon energy. The combination of this strategy with two enantioselective biocatalysts¹⁴ allowed us to selectively produce the (*S*)- or (*R*)-enantiomer of a chiral alcohol in photo-chemo-enzymatic reaction sequences (Scheme 4.1C).



Scheme 4.1. A) General approaches to control the outcome of a chemical reaction; B) Chromoselective control in photocatalytic C-H-arylations⁹; C) This study: Chromoselective control of the stereochemical outcome of photo-chemo-enzymatic reactions.

We recently realized that the choice of the wavelength is crucial for high selectivities in metallophotocatalytic cross couplings using a heterogeneous carbon nitride material, which is made from urea and oxamide in molten salt (CN-OA-m).^{10, 13, 15} While this can be rationalized by a purely kinetic effect, there is also evidence that a wavelength-controlled generation of excited species with different oxidation potentials could be responsible for this phenomenon. CN-OA-m has a strong absorption up to ~460 nm and a comparably weaker absorption band up to ~700 nm, which were ascribed as the π - π^* and n - π^* electron transitions, respectively (Figure 4.1, A).¹⁶ The selective induction of the n - π^* electron transition using long wavelengths (525 nm) should result in electron holes with a lower oxidation potential compared to irradiation using blue light (440 nm). The choice of the wavelength should not affect the reduction potential of the electron that is promoted into the valence band. Although such a behavior was previously suggested,¹⁶ there is, to the best of

our knowledge, no report that applies this concept for controlling the selectivity of chemical reactions.

We hypothesized that such a strategy would allow us to induce a photocatalytic reaction of a substrate with green light selectively in the presence of a second compound that is only photo-oxidized when shorter wavelengths are used. The photocatalytic aerobic oxidation of benzylic sp^3 C-H bonds, which is feasible with other members of the carbon nitride family and blue light irradiation,¹⁷⁻¹⁸ served as a model reaction for our initial studies. In a series of experiments, we were indeed able to show that only blue light results in the desired carbonyl products and no reaction occurs at longer wavelengths (Figure 4.1, B).

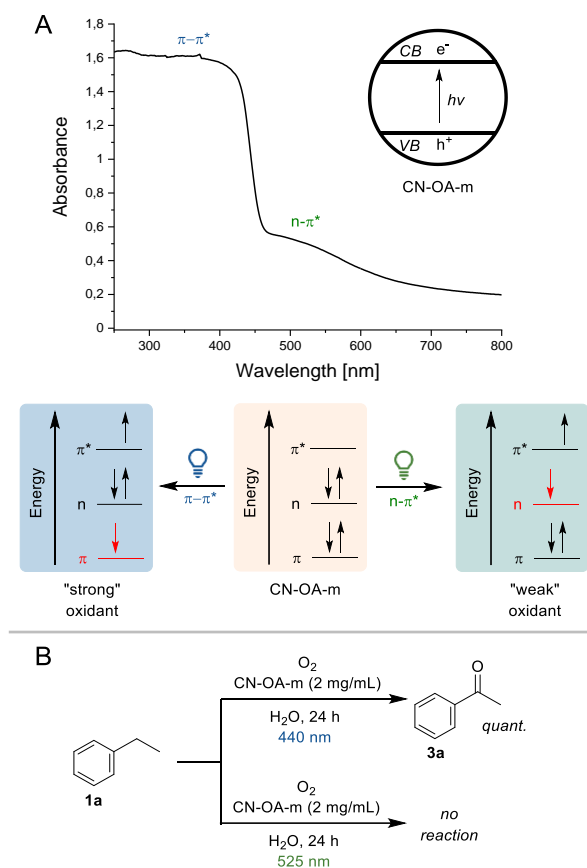


Figure 4.1. Chromoselective generation of excited CN-OA-m species with different oxidation potentials. A) Switching between π - π^* and n - π^* electron transitions using different wavelengths. B) The oxidation of ethylbenzene **1a** to acetophenone **3a** is only possible using blue light.

Carbon nitrides are used to catalyse the formation of O_2 and H_2 via water oxidation¹⁹ and the production of hydrogen peroxide from oxygen and alcohols, which requires the reduction of O_2 .²⁰⁻²³ Hydrogen peroxide can then be used as stoichiometric oxidant in the enantioselective

hydroxylation of ethylbenzene derivatives catalysed by the unspecific peroxygenase (UPO)²⁴⁻²⁷ from *A. aegerita*²⁸⁻²⁹ (*AaeUPO*) acting as chiral catalyst.³⁰⁻⁴⁰

We hypothesized that a chromoselective activation of CN-OA-m with green light enables the selective formation of H₂O₂ in the presence of ethylbenzene (**1**) and the *AaeUPO*, which in turn catalyses the asymmetric hydroxylation of **1** (Figure 4.2). Performing the reaction in tricine buffer using 528 nm LEDs indeed resulted in a high selectivity towards (*R*)-1-phenylethanol formation [(*R*)-**2a**, up to 3.8 mM, 98% *e.e.*] with low amounts (3%) of acetophenone (**3a**). When the same reaction was carried out using shorter wavelengths, **3a** became the main product, thus supporting our hypothesis. Ketone (**3a**) formation was also the preferred reaction in the presence of blue light in phosphate buffer. It is worth to note, that the type of buffer had a significant influence on the outcome on the reaction, whereby the molecular reason needs to be clarified.

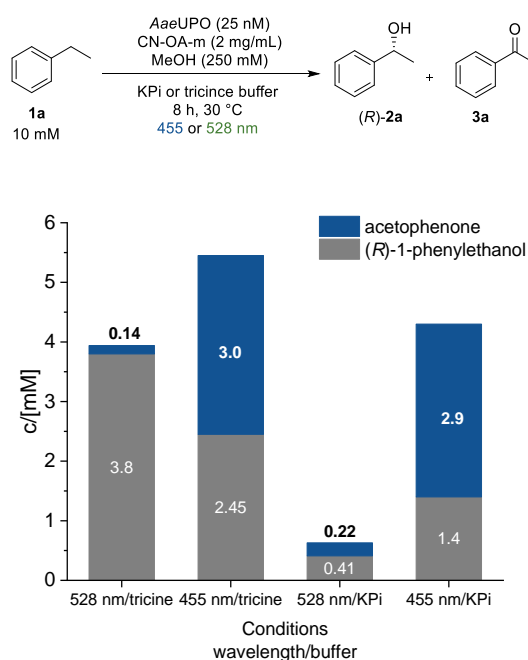


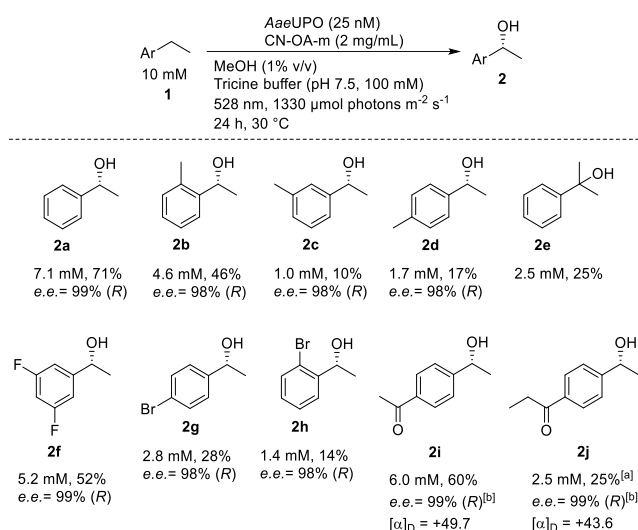
Figure 4.2. Influence of different wavelengths and buffers on the photoenzymatic hydroxylation of ethylbenzene; reaction conditions: *AaeUPO* (25 nM), ethylbenzene (10 mM), CN-OA-m (2 mg mL⁻¹), MeOH (250 mM), KPi (100 mM, pH 7.5) or tricine (100 mM, pH 7.5), 455 nm (1440 μmol photons m⁻² s⁻¹) or 528 nm (1330 μmol photons m⁻² s⁻¹), 30 °C, 8 h.

It was previously shown that UPOs are deactivated in the presence of blue light, a photocatalyst and O₂ due to the generation of reactive oxygen species (ROS) that harm the enzyme.⁴¹⁻⁴² Consequently, one might expect that green light might be less harmful to the

UPO and lead to higher conversions in comparison to blue light. To investigate this aspect, UPO and CN-OA-m were incubated for one hour in the presence of oxygen and green or blue light, before **1a** was added (Figure S4.10). The mixture incubated at longer wavelengths indeed led to a higher conversion for the asymmetric hydroxylation after addition of **1a**.

The milder conditions subsequently allowed an extension of the substrate scope for *Aae*UPO (Scheme 4.2). Nine additional substrates were converted with high stereoselectivity (>98% *e.e.*) to the corresponding alcohols with concentrations of 1.0–6.0 mM. None of these ethylbenzene derivatives has been transformed with *Aae*UPO using an *in situ* H₂O₂ generation system before.

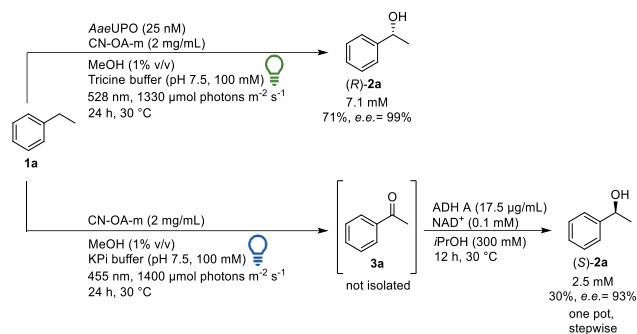
Ethylbenzenes bearing a methyl-substituent in the *ortho*- or *meta*-position were hydroxylated with 99% regioselectivity at the ethyl group to give the desired chiral alcohols (*R*)-**2b-c**. This ability to distinguish between a methyl and an ethyl group has not been reported before. A possible explanation for this selectivity might be a preferred formation of the secondary intermediate radical over the primary radical. Acetophenone substituted with ethyl in the *para*-position (**1i**) allowed to access a bi-functionalised chiral hydroxyketone **2i**, which is otherwise difficult to make. The same is true for **2j**.



Scheme 4.2. Substrate scope of *Aae*UPO using H₂O₂ generated by CN-OA-m under green light irradiation; Absolute configurations were determined by reference material; [a] (*R*)-enantiomer determined by measurement of the specific rotation (20 °C, *c* 1.00, CHCl₃) and comparison to literature; [b] based on external calibration curves of **2i**.

Recycling experiments further showed that CN-OA-m can be reused by centrifugation and one washing step with water. CN-OA-m was reused three times after drying at room temperature. Transferring the photo-chemo-enzymatic hydroxylation from a total volume of 1 mL in 1.5 mL glass vials successfully to a larger scale (7 mL volume, 10 mL tubes) in another photoreactor (provided by GlaxoSmithKline, S5),⁴³⁻⁴⁴ showed the robustness and reproducibility of the approach. The hydroxylation of **1a** worked equally well giving up to 7.5 mM of (*R*)-**2a**.

Recently, photo-chemo-biocatalytic cascades were reported combining a photoredox oxidation of ethylbenzene with an enzymatic reduction.⁴⁵⁻⁴⁶ In a related approach a photo-chemo-biocatalytic cascade that yields the corresponding (*S*)-enantiomers was set up by taking advantage of the chromoselective activation of CN-OA-m (Scheme 4.3). The blue-light mediated oxidation of **1a** to **3a** proceeded smoothly in KPi buffer. The resulting ketone (**3a**) was stereoselectively reduced using an alcohol dehydrogenase (ADH-A) from *Rhodococcus ruber* in presence of NAD⁺ as cofactor.⁴⁷ The optimized two-step one-pot procedure led to 2.5 mM (*S*)-**2a** with an *e.e.* of 93%. The lower *e.e.* obtained in the photochemo-enzymatic cascade compared to previous reports by ADH-A (*e.e.* 99%),⁴⁸ can be explained by the formation of a small amount of *rac*-1-phenylethanol during the photocatalytic reaction under blue light irradiation (Table S4.1). This cascade represents a stereocomplementary pathway compared to the pathway with *Aae*UPO using the same photocatalyst. Interestingly, it was noticed that MeOH was not required for the reaction to hydroxylate ethylbenzene with *Aae*UPO. Without MeOH the same concentration of product was detected. Thus, the reaction is possible without a sacrificial electron donor like MeOH or formate, which is in contrast to some examples reported in literature.^{30, 49} For practical reasons, MeOH was still used since it simplified the preparation of stock solutions of the hydrophobic substrates. To test whether the cascade can also be transferred to other substrates, *para*- and *ortho*-bromo substituted ethylbenzene (**1g**, **1h**) were investigated: Using the blue-light pathway, (*S*)-**2g** was obtained with an *e.e.* of >99% (1 mM) and (*S*)-**2h** with an *e.e.* of 94% (1.4 mM).



Scheme 4.3. Light-driven enantioselective oxyfunctionalizations of **1a** by using chromoselective CN-OA-m and *AaeUPO* or *ADH-A*.

To the best of our knowledge this is the first example in which it was possible to utilize the same photocatalyst to either oxidize an organic substrate or to provide *in situ* formed H_2O_2 without photocatalytic oxidation of the substrate, all controlled only by the choice of the wavelength.

4.3 Conclusion

In summary, we showed that electron holes with different oxidation potentials can be generated using a carbon nitride material by simply changing the photon energy. In the presence of blue light this enables the oxidation of ethylbenzene to acetophenone in an aqueous solution. Using green light, the organic substrate does not react and only H_2O_2 is formed. This was the key for designing chromoselective photo-chemo-enzymatic cascade reactions. Selective hydrogen peroxide generation enabled the hydroxylation of ethylbenzene to give (*R*)-1-phenylethanol (*R*)-**2a** using an UPO, whereas the photocatalytic oxidation to acetophenone was coupled with an enantioselective reduction to (*S*)-1-phenylethanol (*S*)-**2a** by an ADH. Additionally, low energy photons (green light) increased the stability of UPO compared to blue light, which permitted the expansion of the substrate scope of this enzyme. Controlling the outcome of a photocatalytic reaction merely through the choice of wavelength employed presents exciting new options in reaction design and could be an important new tool for controlling reactivity and stereoselection in organic synthesis.

4.4 References

1. Gaich, T.; Winterfeldt, E., *Directed Selectivity in Organic Synthesis: A Practical Guide*. 1st ed.; Wiley-VCH Verlag GmbH & Co. KGaA: Weinheim, 2014.
2. Statham, G., The Manipulation of Chemical Reactions: Probing the Limits of Interventionism. *Synthese* **2017**, *194*, 4815-4838.
3. Fleming, I.; Barbero, A.; Walter, D., Stereochemical Control in Organic Synthesis Using Silicon-Containing Compounds. *Chem. Rev.* **1997**, *97*, 2063-2192.
4. Sambiagio, C.; Schönbauer, D.; Blicke, R.; Dao-Huy, T.; Pototschnig, G.; Schaaf, P.; Wiesinger, T.; Zia, M. F.; Wencel-Delord, J.; Besset, T.; Maes, B. U. W.; Schnürch, M., A comprehensive overview of directing groups applied in metal-catalysed C–H functionalisation chemistry. *Chem. Soc. Rev.* **2018**, *47*, 6603-6743.
5. Rousseau, G.; Breit, B., Removable Directing Groups in Organic Synthesis and Catalysis. *Angew. Chem. Int. Ed.* **2011**, *50* (11), 2450-2494.
6. Huang, Z.; Dong, G., Site-Selectivity Control in Organic Reactions: A Quest To Differentiate Reactivity among the Same Kind of Functional Groups. *Acc. Chem. Res.* **2017**, *50*, 465-471.
7. Jurczak, J., Application of high pressure in organic synthesis. *Physica B+C* **1986**, *139-140*, 709-716.
8. Protti, S.; Ravelli, D.; Fagnoni, M., Wavelength dependence and wavelength selectivity in photochemical reactions. *Photochem. Photobiol. Sci.* **2019**, *18* (9), 2094-2101.
9. Ghosh, I.; König, B., Chromoselective Photocatalysis: Controlled Bond Activation through Light-Color Regulation of Redox Potentials. *Angew. Chem. Int. Ed.* **2016**, *55*, 7676-7679.
10. Gisbertz, S.; Reischauer, S.; Pieber, B., Overcoming limitations in dual photoredox/nickel-catalysed C–N cross-couplings due to catalyst deactivation. *Nat. Catal.* **2020**, *3* (8), 611-620.
11. Cavedon, C.; Sletten, E. T.; Madani, A.; Niemeyer, O.; Seeberger, P. H.; Pieber, B., Visible Light-Mediated Oxidative Debenzylation. *Org. Lett.* **2021**, *23*, 514–518.
12. Martínez-Gualda, A. M.; Cano, R.; Marzo, L.; Pérez-Ruiz, R.; Luis-Barrera, J.; Mas-Ballesté, R.; Fraile, A.; de la Peña O’Shea, V. A.; Alemán, J., Chromoselective access to Z- or E- allylated amines and heterocycles by a photocatalytic allylation reaction. *Nat. Commun.* **2019**, *10*, 2634.

Chapter 4

13. Cavedon, C.; Sletten, E. T.; Madani, A.; Niemeyer, O.; Seeberger, P. H.; Pieber, B., Visible-Light-Mediated Oxidative Debenzylation Enables the Use of Benzyl Ethers as Temporary Protecting Groups. *Org. Lett.* **2021**, *23* (2), 514-518.
14. Winkler, C. K.; Schrittwieser, J. H.; Kroutil, W., Power of Biocatalysis for Organic Synthesis. *ACS Centr. Sci.* **2021**.
15. Pieber, B.; Malik, J. A.; Cavedon, C.; Gisbertz, S.; Savateev, A.; Cruz, D.; Heil, T.; Zhang, G.; Seeberger, P. H., Semi-heterogeneous Dual Nickel/Photocatalysis using Carbon Nitrides: Esterification of Carboxylic Acids with Aryl Halides. *Angew. Chem. Int. Ed.* **2019**, *58*, 9575-9580.
16. Zhang, G.; Li, G.; Lan, Z.-A.; Lin, L.; Savateev, A.; Heil, T.; Zafeiratos, S.; Wang, X.; Antonietti, M., Optimizing Optical Absorption, Exciton Dissociation, and Charge Transfer of a Polymeric Carbon Nitride with Ultrahigh Solar Hydrogen Production Activity. *Angew. Chem. Int. Ed.* **2017**, *56* (43), 13445-13449.
17. Geng, P.; Tang, Y.; Pan, G.; Wang, W.; Hu, J.; Cai, Y., A g-C₃N₄-Based Heterogeneous Photocatalyst for Visible Light Mediated Aerobic Benzylic C–H Oxygenations. *Green Chem.* **2019**, *21* (22), 6116-6122.
18. Zhang, W.; Bariotaki, A.; Smonou, I.; Hollmann, F., Visible-Light-Driven Photooxidation of Alcohols using Surface-Doped Graphitic Carbon Nitride. *Green Chem.* **2017**, *19* (9), 2096-2100.
19. Ong, W. J.; Tan, L. L.; Ng, Y. H.; Yong, S. T.; Chai, S. P., Graphitic Carbon Nitride (g-C₃N₄)-Based Photocatalysts for Artificial Photosynthesis and Environmental Remediation: Are We a Step Closer To Achieving Sustainability? *Chem. Rev.* **2016**, *116* (12), 7159-329.
20. Shiraishi, Y.; Kanazawa, S.; Kofuji, Y.; Sakamoto, H.; Ichikawa, S.; Tanaka, S.; Hirai, T., Sunlight-Driven Hydrogen Peroxide Production from Water and Molecular Oxygen by Metal-Free Photocatalysts. *Angew. Chem. Int. Ed.* **2014**, *53* (49), 13454-13459.
21. Shiraishi, Y.; Kanazawa, S.; Sugano, Y.; Tsukamoto, D.; Sakamoto, H.; Ichikawa, S.; Hirai, T., Highly Selective Production of Hydrogen Peroxide on Graphitic Carbon Nitride (g-C₃N₄) Photocatalyst Activated by Visible Light. *ACS Catal.* **2014**, *4* (3), 774-780.
22. Wei, Z.; Liu, M.; Zhang, Z.; Yao, W.; Tan, H.; Zhu, Y., Efficient Visible-Light-Driven Selective Oxygen Reduction to Hydrogen Peroxide by Oxygen-Enriched Graphitic Carbon Nitride Polymers. *Energy Environ. Sci.* **2018**, *11* (9), 2581-2589.

23. Zeng, X.; Liu, Y.; Kang, Y.; Li, Q.; Xia, Y.; Zhu, Y.; Hou, H.; Uddin, M. H.; Gengenbach, T. R.; Xia, D.; Sun, C.; McCarthy, D. T.; Deletic, A.; Yu, J.; Zhang, X., Simultaneously Tuning Charge Separation and Oxygen Reduction Pathway on Graphitic Carbon Nitride by Polyethylenimine for Boosted Photocatalytic Hydrogen Peroxide Production. *ACS Catal.* **2020**, *10* (6), 3697-3706.
24. Wang, Y.; Lan, D.; Durrani, R.; Hollmann, F., Peroxygenases en Route to Becoming Dream Catalysts. What are the Opportunities and Challenges? *Curr. Opin. Chem. Biol.* **2017**, *37*, 1-9.
25. Faiza, M.; Huang, S.; Lan, D.; Wang, Y., New Insights on Unspecific Peroxygenases: Superfamily Reclassification and Evolution. *BMC Evol. Biol.* **2019**, *19* (1), 76.
26. Hofrichter, M.; Ullrich, R., Oxidations Catalyzed by Fungal Peroxygenases. *Curr. Opin. Chem. Biol.* **2014**, *19*, 116-125.
27. Hobisch, M.; Holtmann, D.; Gomez de Santos, P.; Alcalde, M.; Hollmann, F.; Kara, S., Recent Developments in the Use of Peroxygenases – Exploring Their High Potential in Selective Oxyfunctionalisations. *Biotechnol. Adv.* **2020**, 107615.
28. Molina-Espeja, P.; Garcia-Ruiz, E.; Gonzalez-Perez, D.; Ullrich, R.; Hofrichter, M.; Alcalde, M., Directed Evolution of Unspecific Peroxygenase from *Agrocybe aegerita*. *Appl. Environ. Microbiol.* **2014**, *80* (11), 3496–3507.
29. Molina-Espeja, P.; Ma, S.; Mate, D. M.; Ludwig, R.; Alcalde, M., Tandem-Yeast Expression System for Engineering and Producing Unspecific Peroxygenase. *Enzyme Microb. Technol.* **2015**, *73-74*, 29–33.
30. Zhang, W.; Burek, B. O.; Fernandez-Fueyo, E.; Alcalde, M.; Bloh, J. Z.; Hollmann, F., Selective Activation of C-H Bonds in a Cascade Process Combining Photochemistry and Biocatalysis. *Angew. Chem. Int. Ed.* **2017**, *56*, 15451-15455.
31. Schmermund, L.; Jurkaš, V.; Özgen, F. F.; Barone, G. D.; Büchenschütz, H. C.; Winkler, C. K.; Schmidt, S.; Kourist, R.; Kroutil, W., Photo-Biocatalysis: Biotransformations in the Presence of Light. *ACS Catal.* **2019**, *9*, 4115-4144.
32. Burek, B. O.; Bormann, S.; Hollmann, F.; Bloh, J. Z.; Holtmann, D., Hydrogen Peroxide Driven Biocatalysis. *Green Chem.* **2019**, *21* (12), 3232–3249.
33. Willot, S. J. P.; Fernández-Fueyo, E.; Tieves, F.; Pesic, M.; Alcalde, M.; Arends, I. W. C. E.; Park, C. B.; Hollmann, F., Expanding the Spectrum of Light-Driven Peroxygenase Reactions. *ACS Catal.* **2019**, *9*, 890-894.

Chapter 4

34. Tieves, F.; Willot, S. J.-P.; van Schie, M. M. C. H.; Rauch, M. C. R.; Younes, S. H. H.; Zhang, W.; Dong, J.; Gomez de Santos, P.; Robbins, J. M.; Bommarius, B.; Alcalde, M.; Bommarius, A. S.; Hollmann, F., Formate Oxidase (FOx) from *Aspergillus oryzae*: One Catalyst Enables Diverse H₂O₂-Dependent Biocatalytic Oxidation Reactions. *Angew. Chem. Int. Ed.* **2019**, *58* (23), 7873–7877.
35. Ni, Y.; Fernández-Fueyo, E.; Baraibar, A. G.; Ullrich, R.; Hofrichter, M.; Yanase, H.; Alcalde, M.; van Berkel, W. J. H.; Hollmann, F., Peroxygenase-Catalyzed Oxyfunctionalization Reactions Promoted by the Complete Oxidation of Methanol. *Angew. Chem. Int. Ed.* **2016**, *55* (2), 798–801.
36. Choi, D. S.; Ni, Y.; Fernández-Fueyo, E.; Lee, M.; Hollmann, F.; Park, C. B., Photoelectroenzymatic Oxyfunctionalization on Flavin-Hybridized Carbon Nanotube Electrode Platform. *ACS Catal.* **2017**, *7* (3), 1563–1567.
37. Churakova, E.; Kluge, M.; Ullrich, R.; Arends, I.; Hofrichter, M.; Hollmann, F., Specific Photobiocatalytic Oxyfunctionalization Reactions. *Angew. Chem. Int. Ed.* **2011**, *50*, 10716-10719.
38. Hobisch, M.; van Schie, M. M. C. H.; Kim, J.; Andersen, K. R.; Alcalde, M.; Kourist, R.; Park, C. B.; Hollmann, F.; Kara, S., Solvent-Free Photobiocatalytic Hydroxylation of Cyclohexane. *ChemCatChem* **2020**, *12* (16), 4009-4013.
39. Yoon, J.; Kim, J.; Tieves, F.; Zhang, W.; Alcalde, M.; Hollmann, F.; Park, C. B., Piezobiocatalysis: Ultrasound-Driven Enzymatic Oxyfunctionalization of C–H Bonds. *ACS Catal.* **2020**, 5236–5242.
40. Zhang, W.; Fernandez-Fueyo, E.; Ni, Y.; van Schie, M.; Gacs, J.; Renirie, R.; Wever, R.; Mutti, F. G.; Rother, D.; Alcalde, M.; Hollmann, F., Selective Aerobic Oxidation Reactions Using a Combination of Photocatalytic Water Oxidation and Enzymatic Oxyfunctionalisations. *Nat. Catal.* **2018**, *1*, 55-62.
41. Bormann, S.; Gomez Baraibar, A.; Ni, Y.; Holtmann, D.; Hollmann, F., Specific Oxyfunctionalisations Catalysed by Peroxygenases: Opportunities, Challenges and Solutions. *Catal. Sci. Technol.* **2015**, *5*, 2038-2052.
42. Burek, B. O.; Boer, S. R. d.; Tieves, F.; Zhang, W.; van Schie, M.; Bormann, S.; Alcalde, M.; Holtmann, D.; Hollmann, F.; Bahnemann, D. W.; Bloh, J. Z., Photoenzymatic Hydroxylation of Ethylbenzene Catalyzed by Unspecific Peroxygenase: Origin of Enzyme

Inactivation and the Impact of Light Intensity and Temperature. *ChemCatChem* **2019**, *11* (13), 3093–3100.

43. Bonfield, H. E.; Williams, J. D.; Ooi, W. X.; Leach, S. G.; Kerr, W. J.; Edwards, L. J., A Detailed Study of Irradiation Requirements Towards an Efficient Photochemical Wohl-Ziegler Procedure in Flow. *ChemPhotoChem* **2018**, *2*, 938-944.

44. Bonfield, H. E.; Mercer, K.; Diaz-Rodriguez, A.; Cook, G. C.; McKay, B. S. J.; Slade, P.; Taylor, G. M.; Ooi, W. X.; Williams, J. D.; Roberts, J. P. M.; Murphy, J. A.; Schmermund, L.; Kroutil, W.; Mielke, T.; Cartwright, J.; Grogan, G.; Edwards, L. J., The Right Light: De Novo Design of a Robust Modular Photochemical Reactor for Optimum Batch and Flow Chemistry. *ChemPhotoChem* **2020**, *4* (1), 45-51.

45. Betori, R. C.; May, C. M.; Scheidt, K. A., Combined Photoredox/Enzymatic C-H Benzylic Hydroxylations. *Angew. Chem. Int. Ed.* **2019**, *58* (46), 16490–16494.

46. Peng, Y.; Li, D.; Fan, J.; Xu, W.; Xu, J.; Yu, H.; Lin, X.; Wu, Q., Enantiocomplementary C–H Bond Hydroxylation Combining Photo-Catalysis and Whole-Cell Biocatalysis in a One-Pot Cascade Process. *Eur. J. Org. Chem.* **2020**, *2020* (7), 821-825.

47. Edegger, K.; Gruber, C. C.; Poessl, T. M.; Wallner, S. R.; Lavandera, I.; Faber, K.; Niehaus, F.; Eck, J.; Oehrlein, R.; Hafner, A.; Kroutil, W., Biocatalytic Deuterium- and Hydrogen-Transfer using Over-Expressed ADH-‘A’: Enhanced Stereoselectivity and 2H-Labeled Chiral Alcohols. *Chem. Commun.* **2006**, (22), 2402-2404.

48. Stampfer, W.; Kosjek, B.; Moitzi, C.; Kroutil, W.; Faber, K., Biocatalytic Asymmetric Hydrogen Transfer. *Angew. Chem. Int. Ed.* **2002**, *41* (6), 1014-7.

49. van Schie, M. M. C. H.; Zhang, W.; Tieves, F.; Choi, D. S.; Park, C. B.; Burek, B. O.; Bloh, J. Z.; Arends, I. W. C. E.; Paul, C. E.; Alcalde, M.; Hollmann, F., Cascading g-C₃N₄ and Peroxygenases for Selective Oxyfunctionalization Reactions. *ACS Catal.* **2019**, *9*, 7409-7417.

Chapter 5

Modular, self-assembling metallaphotocatalyst for cross couplings using the full visible-light spectrum

Reischauer, S.; Strauss, V.; Pieber, B.;

ACS Catal., **2020**, *10*, 13269-13274.

<https://doi.org/10.1021/acscatal.0c03950>

Abstract

The combination of nickel- and photocatalysis has unlocked a variety of cross couplings. These protocols rely on a few photocatalysts that can only convert a small portion of visible light (<500 nm) into chemical energy. The high-energy photons that excite the photocatalyst can result in unwanted side reactions. Dyes that absorb a much broader spectrum of light are not applicable due to their short-lived excited states. Here we describe a self-assembling catalyst system that overcomes this limitation. Immobilization of a nickel catalyst on dye-sensitized titanium dioxide results in a material that catalyzes carbon-heteroatom and carbon-carbon bond formations. The modular approach of dye-sensitized metallaphotocatalysts (DSMPs) accesses the entire visible light spectrum and allows tackling selectivity issues resulting from low-wavelengths strategically. The concept overcomes current limitations of metallaphotocatalysis by unlocking the potential of dyes that were previously unsuitable.

Specific contribution

Together with B. Pieber, I conceived the idea behind this project. I verified its feasibility and prepared catalysts and reagents. After optimizing the reactions, I studied the recycling of the catalyst and evaluated scope and limitations of this protocol. V. Strauss performed the spectrophotometric titrations. I wrote the manuscript and B. Pieber revised and corrected the manuscript.

Supporting Information

All experimental procedures and analytical data are available in the supporting information in the appendix or through the website of the Publisher. DOI: [10.1021/acscatal.0c03950](https://doi.org/10.1021/acscatal.0c03950).

5.1 Introduction

The combination of photo- and nickel catalysis (metallaphotocatalysis) has emerged as a powerful strategy for carbon–carbon and carbon–heteroatom cross couplings (Figure 5.1A).¹⁻³ Key to the success are redox or photosensitization events between a nickel- and a photocatalyst (PC). Applicable PCs are iridium and ruthenium polypyridyl complexes,² or carbazolyl dicyanobenzenes,⁴ with tailored redox potentials or triplet energies, and long-lived excited states (Figure 5.1B). These PCs are limited to short excitation wavelengths that can cause unwanted side-reactions.⁵ These could be avoided in a metallaphotocatalytic system that harvests longer wavelengths. Current approaches towards photocatalysis with low photon energies require complex catalytic cocktails that enable photon upconversion,⁶ osmium complexes as PCs,⁷ or multi-photon excitation processes.⁵

The use of abundant dyes that absorb broadly across the visible-light spectrum is highly desirable. The redox potentials and triplet energies of many commodity chemicals, such as fluorescein, rose bengal, or coumarins are in theory suitable for metallaphotocatalysis,⁸ but their short excited state lifetime render a diffusion-limited interaction with a nickel catalyst in a homogeneous solution unlikely (Figure 5.1B). These dyes are, however, able to sensitize metal oxide semiconductors, such as TiO₂, in dye-sensitized solar cells (DSSCs),⁹ or dye-sensitized photocatalysts (DSPs) for light-driven H₂ production.¹⁰ The carboxylic acid groups of the dyes bind to the surface hydroxyl groups of TiO₂. This facilitates electron injection into the conduction band of the semiconductor upon photoexcitation. This results in a charge-separated species that is sustained for several microseconds.¹¹

We wondered whether immobilization of a suitable nickel complex on dye-sensitized TiO₂ accesses a bifunctional material that serves as metallaphotocatalyst (Figure 5.1 C). We hypothesized that such a system overcomes limitations related to short excited state lifetimes and diffusion-controlled energy or single electron transfer events due to the close spatial proximity between the PC and the nickel catalyst. The proposed, modular design of dye-sensitized metallaphotocatalysts (DSMPs) allows selecting dyes/wavelengths and nickel complexes depending on the respective application.

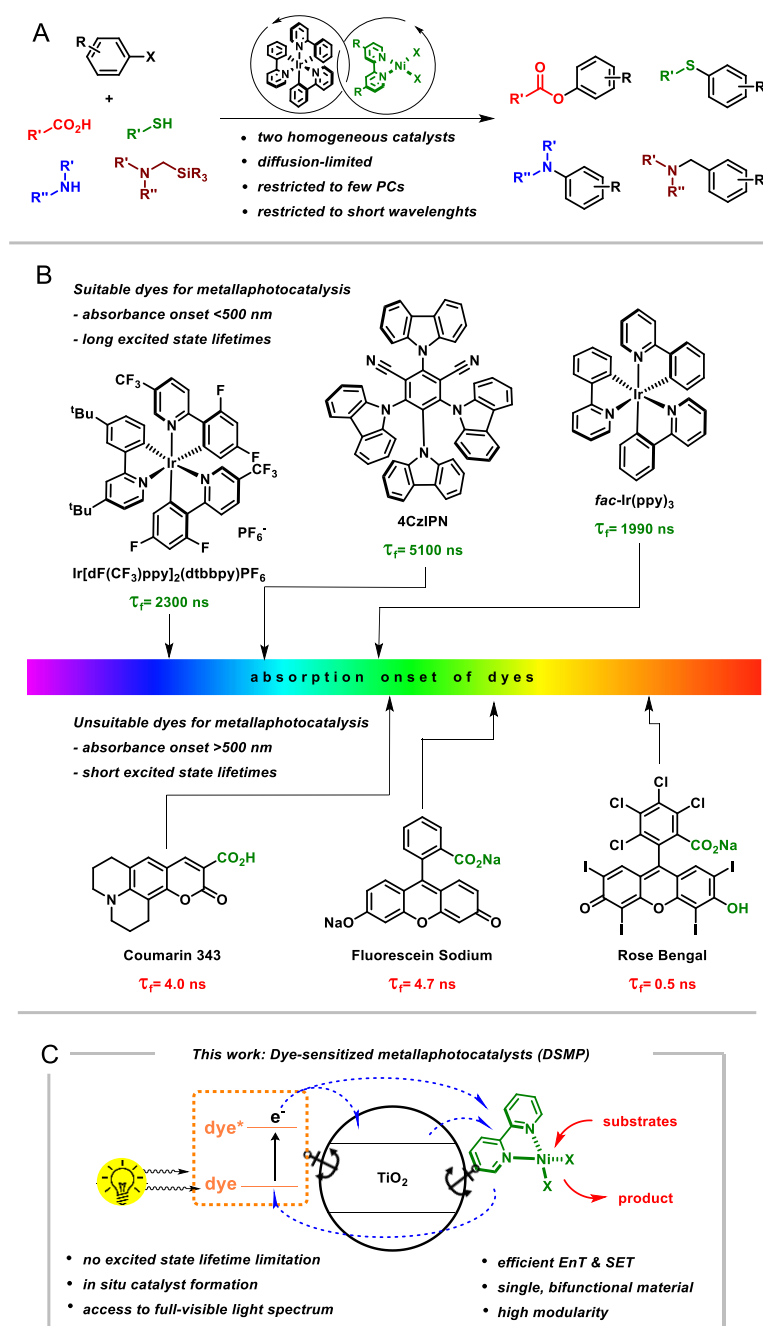


Figure 5.1. Working hypothesis towards a modular, heterogeneous metallaphotocatalyst. Cross-coupling reactions using homogeneous metallaphotocatalysis (A). Onset of absorption of photocatalysts. The suitability for homogeneous metallaphotocatalysis depends on excited state lifetime (B). Dye-sensitized metallaphotocatalysts (DSMP) are proposed to overcome excited state lifetime limitations (C).

5.2 Results and discussion

Our investigations started with the *O*-arylation of carboxylic acids that was reported using the PC Ir(ppy)₃ (ppy = 2-phenylpyridine) and a nickel bipyridine complex. The cross-coupling proceeds *via* an energy transfer (EnT) mechanism,¹²⁻¹³ and is feasible using semiconductors that absorb blue light,¹⁴⁻¹⁶ but does not work using simple organic dyes.⁴ We first tested if anchoring of a nickel complex on TiO₂ P25 results i) in an active, heterogeneous metallaphotocatalyst, and ii) improves the reaction yield due to permanent spatial proximity of the PC and the nickel catalyst using near-UV light. A ligand equipped with carboxylic acid groups (dcbpy = 2,2'-bipyridine-4,4'-dicarboxylic acid) indeed gave a higher yield of the C–O cross coupling product **1** than a ligand that lacks functionalities capable of binding to the semiconductor's surface (dtbbpy = 4,4'-di-*tert*-butyl-2,2'-dipyridyl) (Figure 5.2A). Next, dyes that contain a suitable anchoring group were studied as sensitizers using green light (525 nm). Fluorescein sodium (NaFluo) showed the best results (see Supplementary Information). The C–O coupling was also feasible at higher wavelengths (666 nm) using the ruthenium dye N3 that has an excited state lifetime of 20 ns.⁹ The DSMPs self-assemble *in situ*. An *ex situ* preparation of the DSMPs was carried out to characterize the bifunctional materials (Figure 5.2B). The UV–Vis spectra of the materials confirmed immobilization of the dyes on the metal oxide, and inductively coupled plasma - optical emission spectrometry (ICP-OES) corroborated anchoring of the nickel complex.

The *in situ* DSMP approach resulted in a highly selective formation of **1** using blue (440 nm), green (525 nm), or red (666 nm) light (Figure 5.2C). A high catalytic activities was obtained when the amount of dye (1.25 mol%) and NiCl₂·dcbpy (10 mol%) exceeded the loading that was determined using *ex situ* DSMP preparation. This is rationalized by a dynamic equilibrium between immobilized and unbound NiCl₂·dcbpy as well as dye molecules, which also contribute to productive catalysis in the course of the bulk experiment¹⁰. Reducing the amount of dye (0.1 mol%) or NiCl₂·dcbpy (1 mol%) still resulted in almost quantitative yield of the desired ester. When the dye and the nickel complex are used in such low amounts no product formation was observed. We assume that high loadings of either NiCl₂·dcbpy or the dye are sufficient for the formation of a monolayer on TiO₂ and the resulting close spatial proximity of NaFluo and the nickel complex is responsible for the catalytic activity. It has to be noted that also the substrates and the base are likely to bind to the surface of TiO₂, which could contribute to the performance of the catalytic system. No

product formation was observed in the absence of TiO_2 P25, the dye, dcbpy, nickel salt, or light. In agreement with previously reported protocols for metallaphotocatalyzed C-O arylation of carboxylic acids,¹²⁻¹⁶ the substrate scope is limited to electron-poor aryl halides (see SI).

The DSMP approach also enabled metallaphotocatalyzed C-S¹⁷, C-N¹⁸, and C-C¹⁹ bond formations that proceed *via* single electron transfer processes (SET) (Fig. 2D). Since the C-S¹⁷ and C-C¹⁹ couplings proceed via a single electron oxidation of the substrate and a single electron reduction of a nickel complex, we assume that the affinity of the substrates to the semiconductors' surface has a positive effect on the catalytic activity.

The modular design principle and the self-assembling strategy facilitated a straightforward optimization of dyes, nickel salts, and ligands resulting in selective cross-couplings using blue (440 nm), green (525 nm), and red (666 nm) light. With regards to the C-C coupling, 68% of the desired product (**4**) were obtained using blue light, which is similar to the homogeneous metallaphotocatalysis system.¹⁹ Reactions at higher wavelengths, not accessible with the original, homogeneous approach, resulted in a higher selectivity.

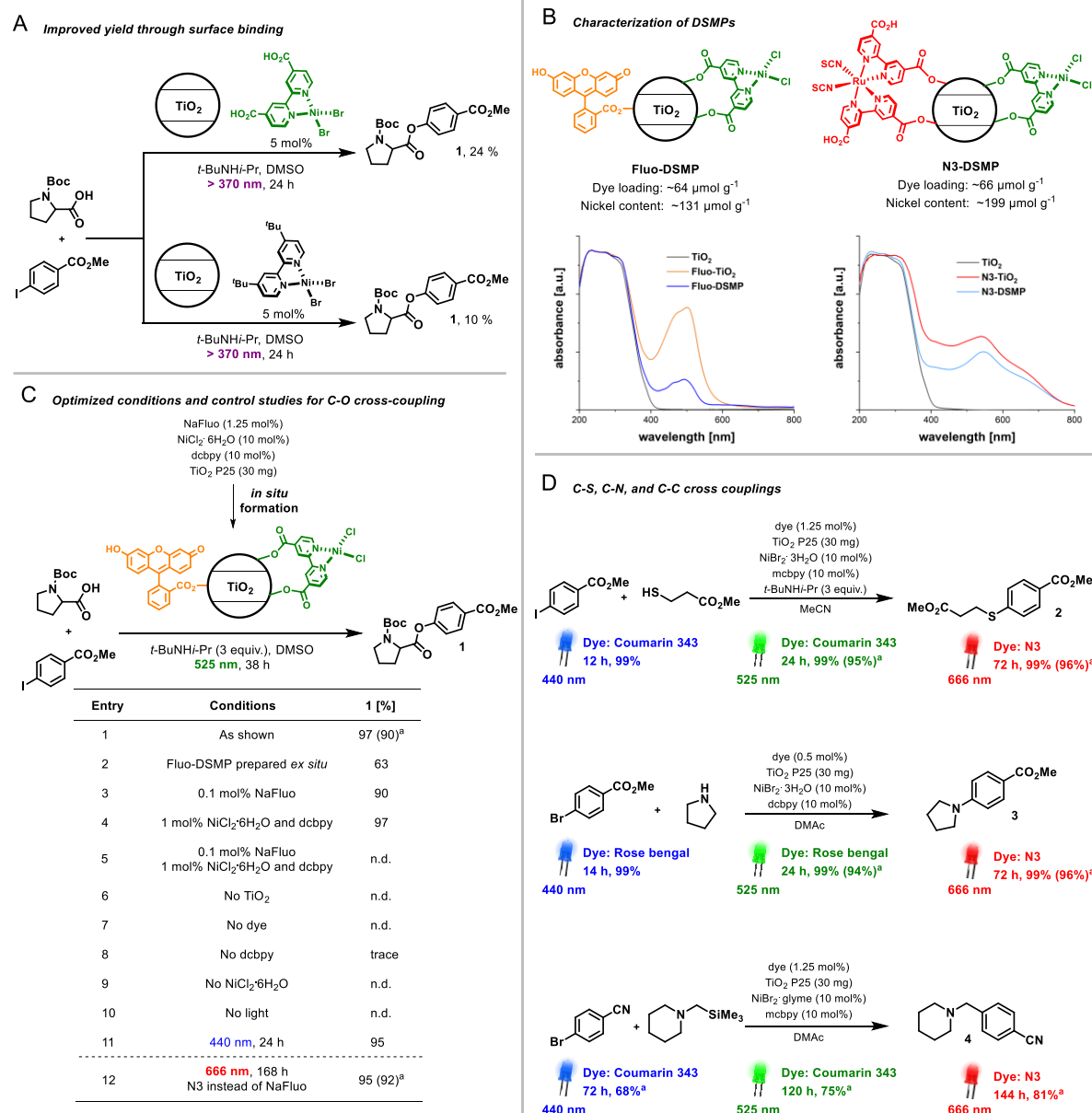


Figure 5.2. Self-assembling, modular metallaphotocatalysts enable cross-couplings using the entire visible-light spectrum. Anchoring of nickel complexes on TiO₂ P25 improves yield due to permanent spatial proximity (A). UV-Vis spectra and nickel/dye loadings of two representative DSMPs (B). Optimized conditions and control experiments for the *O*-arylation of carboxylic acids using DSMPs (C). C-S, C-N, and C-C cross coupling catalyzed by DSMPs using blue, green, or red light (D). Yields were determined by ¹H-NMR using 1,3,5-trimethoxybenzene as internal standard if not stated otherwise. ^aIsolated yields. DSMP = dye-sensitized metallaphotocatalyst n.d. = not detected. dcbpy = 2,2'-bipyridine-4,4'-dicarboxylic acid. mcbpy = 4'-methyl-2,2'-bipyridine-4-carboxylic acid. glyme = 1,2-dimethoxyethane. NaFluo = fluorescein sodium

The dynamic equilibrium between immobilized and unbound molecules is responsible for leaching of nickel and fluorescein during catalyst recycling studies and caused a gradual decrease of the yield of **1** (Figure 5.3A). Addition of either NaFluo or the

nickel salt restored the catalytic activity, which is in agreement with the experiments using low amounts of either the dye or the nickel complex (Figure 5.2C). This indicated that the amount of immobilized dye molecules and nickel complexes have to be above a certain limit to observe catalytic activity. We therefore questioned if only the close proximity of the dye molecules and the nickel complex is responsible for productive catalysis, and TiO₂ P25 only acts as support. In other words, an “on-particle” rather than a “through-particle” mechanism could be responsible for overcoming the short excited state lifetime (Figure 5.3B). To test this hypothesis, we substituted TiO₂ P25 with the insulating metal oxides (MO) SiO₂ and Al₂O₃ that only enable binding of the dye and the nickel complex and observed product formation for all cross-couplings, but with significantly lower efficiency compared to TiO₂ P25 (Figure 5.3C). A second set of experiments was carried out using a nickel complex that is not able to bind to the surface of metal oxides. Here, only experiments with the semiconductor TiO₂ P25 gave productive catalysis. This confirms that dye sensitization leads to a charge-separated species that is sufficiently long-lived to turn over a homogeneous nickel catalyst in a semi-heterogeneous, diffusion-controlled reaction. Spectrophotometric titrations unveiled the electronic communication between the excited dye and the immobilized nickel complex “through” a semiconductor. Static fluorescence quenching of fluorescein-sensitized TiO₂ P25 was observed with a nickel complex that binds to the semiconductor’s surface (NiCl₂-dcbpy). NiCl₂-dtbbpy showed solely dynamic quenching (Figure 5.3D). Titration experiments with fluorescein bound to SiO₂ instead of TiO₂ P25 displayed dynamic quenching behavior in case of both nickel complexes, and significantly lower quenching rates. Taking all results together, we assumed that a combination of “on-particle” and “through-particle” processes is responsible for the high catalytic activity of DSMPs with TiO₂ P25.

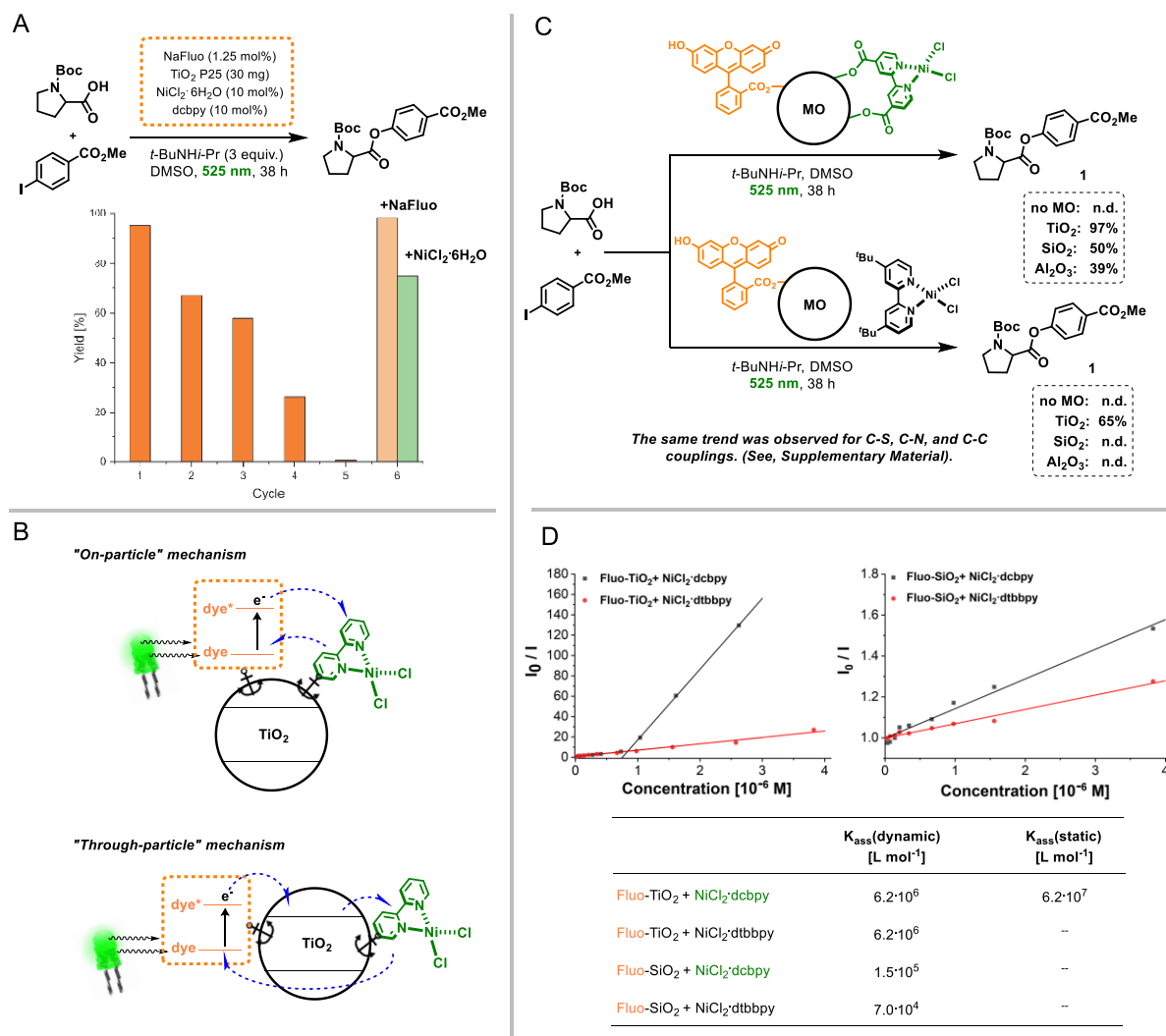


Figure 5.3. Mechanistic investigations. Recycling experiments showed that catalytic inactive materials still contain nickel complexes and dye molecules (A). DSMPs might work *via* an “on-particle” and/or “through-particle” mechanism (B). Experiments using insulating metal oxides and diffusion controlled metallaphotocatalysis (C). Spectrophotometric titrations show static quenching for DSMPs, whereas solely dynamic quenching was observed in other systems (D). MO = metal oxide. dcbpy = 2,2'-bipyridine-4,4'-dicarboxylic acid. dtbbpy = 4,4'-di-*tert*-butyl-2,2'-bipyridine. Fluo = fluorescein.

In addition, we sought to compare the selectivity of DSMPs with homogenous metallaphotocatalysis systems in the C–O arylation of (*E*)-cinnamic acid with 4-iodobenzotrifluoride (Figure 5.4). The resulting coupling product (*E*-5) is prone to subsequent photocatalytic isomerization or cycloadditions that could lead to low selectivities.²⁰⁻²¹ We indeed observed significant amounts of the undesired *Z*-isomer (*Z*-5) when Ir(ppy)₃ was used as PCs using 440 nm irradiation. Other Ir complexes gave even worse results (see Supplementary Information). Control experiments showed that *E*-5 is also slowly converted to *Z*-5 at 440 nm in the absence of a PC (see Supplementary Information).

The selectivity was, however, not improved using Ir(ppy)₃ and 525 nm irradiation, because the triplet energy of the PC is not wavelength-dependent. The *E-Z* isomerization was also observed when the reaction was catalyzed by a DSMP at 440 nm, but was totally suppressed by switching to higher wavelengths, resulting in a selective formation of **E-5**.

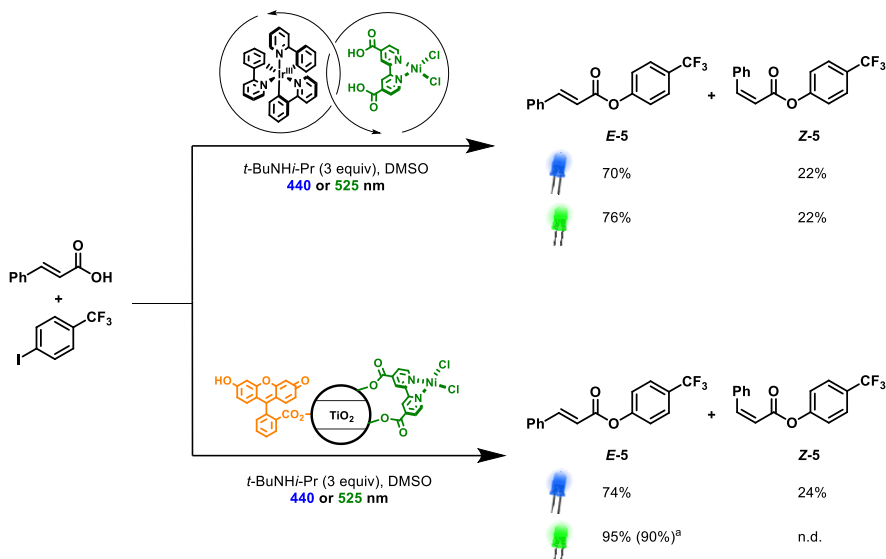


Figure 5.4. C–O arylation of (*E*)-cinnamic acid with 4-iodobenzotrifluoride with different metallaphotocatalyst systems. Yields were determined by ¹H-NMR using 1,3,5-trimethoxybenzene as internal standard if not stated otherwise. ^aIsolated yield in parentheses.

5.3 Conclusion

The DSMP concept overcomes the constraint of long excited state lifetimes of PCs for metallaphotocatalysis and unlocks the potential of many dyes that were previously unsuitable. Many cross couplings can be carried out using the entire visible light spectrum and selectivity issues can be tackled strategically. The simplicity and modularity of DSMPs suggest that the present approach will complement existing methods.

5.4 References

1. Milligan, J. A.; Phelan, J. P.; Badir, S. O.; Molander, G. A., Alkyl Carbon–Carbon Bond Formation by Nickel/Photoredox Cross-Coupling. *Angew. Chem. Int. Ed.* **2019**, *58* (19), 6152-6163.
2. Twilton, J.; Le, C.; Zhang, P.; Shaw, M. H.; Evans, R. W.; MacMillan, D. W. C., The merger of transition metal and photocatalysis. *Nat. Rev. Chem.* **2017**, *1*, 0052.
3. Cavedon, C.; Seeberger, P. H.; Pieber, B., Photochemical Strategies for Carbon–Heteroatom Bond Formation. *Eur. J. Org. Chem.* **2020**, *2020* (10), 1379-1392.
4. Lu, J.; Pattengale, B.; Liu, Q.; Yang, S.; Shi, W.; Li, S.; Huang, J.; Zhang, J., Donor–Acceptor Fluorophores for Energy-Transfer-Mediated Photocatalysis. *J. Am. Chem. Soc.* **2018**, *140* (42), 13719-13725.
5. Glaser, F.; Kerzig, C.; Wenger, O. S., Multi-Photon Excitation in Photoredox Catalysis: Concepts, Applications, Methods. *Angew. Chem. Int. Ed.* **2020**, *59* (26), 10266-10284.
6. Ravetz, B. D.; Pun, A. B.; Churchill, E. M.; Congreve, D. N.; Rovis, T.; Campos, L. M., Photoredox catalysis using infrared light via triplet fusion upconversion. *Nature* **2019**, *565* (7739), 343-346.
7. Ravetz, B. D.; Tay, N. E. S.; Joe, C., L.; Sezen-Edmonds, M.; Schmidt, M. A.; Tan, Y.; Janey, J. M.; Eastgate, M.; Rovis, T., Development of a Platform for Near-Infrared Photoredox Catalysis **2020**, *6* (11), 2053–2059.
8. Romero, N. A.; Nicewicz, D. A., Organic Photoredox Catalysis. *Chem. Rev.* **2016**, *116* (17), 10075-10166.
9. Hagfeldt, A.; Boschloo, G.; Sun, L.; Kloo, L.; Pettersson, H., Dye-Sensitized Solar Cells. *Chem. Rev.* **2010**, *110* (11), 6595-6663.
10. Willkomm, J.; Orchard, K. L.; Reynal, A.; Pastor, E.; Durrant, J. R.; Reisner, E., Dye-sensitized semiconductors modified with molecular catalysts for light-driven H₂ production. *Chem. Soc. Rev.* **2016**, *45* (1), 9-23.
11. Hagfeldt, A.; Graetzel, M., Light-Induced Redox Reactions in Nanocrystalline Systems. *Chem. Rev.* **1995**, *95* (1), 49-68.
12. Welin, E. R.; Le, C.; Arias-Rotondo, D. M.; McCusker, J. K.; MacMillan, D. W. C., Photosensitized, energy transfer-mediated organometallic catalysis through electronically excited nickel(II). *Science* **2017**, *355* (6323), 380-385.

13. Tian, L.; Till, N. A.; Kudisch, B.; MacMillan, D. W. C.; Scholes, G. D., Transient Absorption Spectroscopy Offers Mechanistic Insights for an Iridium/Nickel-Catalyzed C–O Coupling. *J. Am. Chem. Soc.* **2020**, *142* (10), 4555-4559.
14. Zhu, X.; Lin, Y.; San Martin, J.; Sun, Y.; Zhu, D.; Yan, Y., Lead halide perovskites for photocatalytic organic synthesis. *Nat. Commun.* **2019**, *10* (1), 2843.
15. Pieber, B.; Malik, J. A.; Cavedon, C.; Gisbertz, S.; Savateev, A.; Cruz, D.; Heil, T.; Zhang, G.; Seeberger, P. H., Semi-heterogeneous Dual Nickel/Photocatalysis using Carbon Nitrides: Esterification of Carboxylic Acids with Aryl Halides. *Angew. Chem. Int. Ed.* **2019**, *58* (28), 9575-9580.
16. Malik, J. A.; Madani, A.; Pieber, B.; Seeberger, P. H., Evidence for Photocatalyst Involvement in Oxidative Additions of Nickel-Catalyzed Carboxylate O-Arylations. *J. Am. Chem. Soc.* **2020**, *142* (25), 11042-11049.
17. Oderinde, M. S.; Frenette, M.; Robbins, D. W.; Aquila, B.; Johannes, J. W., Photoredox Mediated Nickel Catalyzed Cross-Coupling of Thiols With Aryl and Heteroaryl Iodides via Thiyl Radicals. *J. Am. Chem. Soc.* **2016**, *138* (6), 1760-1763.
18. Corcoran, E. B.; Pirnot, M. T.; Lin, S.; Dreher, S. D.; DiRocco, D. A.; Davies, I. W.; Buchwald, S. L.; MacMillan, D. W. C., Aryl amination using ligand-free Ni(II) salts and photoredox catalysis. *Science* **2016**, *353*, 279-283.
19. Remeur, C.; Kelly, C. B.; Patel, N. R.; Molander, G. A., Aminomethylation of Aryl Halides Using α -Silylamines Enabled by Ni/Photoredox Dual Catalysis. *ACS Catal.* **2017**, *7* (9), 6065-6069.
20. Lei, T.; Zhou, C.; Huang, M.-Y.; Zhao, L.-M.; Yang, B.; Ye, C.; Xiao, H.; Meng, Q.-Y.; Ramamurthy, V.; Tung, C.-H.; Wu, L.-Z., General and Efficient Intermolecular [2+2] Photodimerization of Chalcones and Cinnamic Acid Derivatives in Solution through Visible-Light Catalysis. *Angew. Chem. Int. Ed.* **2017**, *56* (48), 15407-15410.
21. Shu, P.; Xu, H.; Zhang, L.; Li, J.; Liu, H.; Luo, Y.; Yang, X.; Ju, Z.; Xu, Z., Synthesis of (Z)-Cinnamate Derivatives via Visible-Light-Driven E-to-Z Isomerization. *SynOpen* **2019**, *03* (04), 103-107.

Chapter 6

Recyclable, bifunctional metallaphotocatalysts for C-S cross-couplings

Reischauer, S.; Pieber, B.

ChemPhotoChem, 2021, 5, 716-720.

<https://doi.org/10.1002/cptc.202100062>

CC BY Lizenz: <https://creativecommons.org/licenses/by/4.0/>

Abstract

Metallaphotocatalytic cross-couplings are typically carried out by combining homogeneous or heterogeneous photocatalysts with a soluble nickel complex. Attempts to realize recyclable catalytic systems use immobilized iridium complexes to harvest light. We present bifunctional, materials for metallaphotocatalytic C–S cross couplings that can be reused without losing their catalytic activity. Key to the success is the permanent immobilization of a nickel complex on the surface of a heterogeneous semiconductor through phosphonic acid anchors. The optimized catalyst harvests a broad range of the visible light spectrum and requires a nickel loading of only ~0.1 mol%.

Specific contribution

Together with B. Pieber, I conceived the idea behind this project. I verified its feasibility and prepared catalysts and reagents. After optimizing the reactions, I studied the recycling of the catalyst and evaluated scope and limitations of this protocol. I wrote the manuscript and B. Pieber revised and corrected the manuscript.

Supporting Information

All experimental procedures and analytical data are available in the supporting information in the appendix or through the website of the Publisher. DOI: [10.1002/cptc.202100062](https://doi.org/10.1002/cptc.202100062).

6.1 Introduction

Visible-light is a powerful reagent in organic synthesis.¹⁻⁴ In particular, the merger of photo- and nickel catalysis (metallaphotocatalysis) has emerged as an attractive strategy to achieve carbon–carbon and carbon–heteroatom bond formations under mild conditions.⁵⁻⁷ The cross-coupling of thiols with (hetero)aryl halides, for example, was carried out by combining a nickel catalyst with an iridium, or ruthenium polypyridyl complex as photoredox catalyst (Figure 6.1, A).⁸⁻¹⁰ Similar C–S cross-couplings were also reported using an organic photocatalyst.¹¹

A semi-heterogeneous method using a carbon nitride material as photocatalyst was developed to partially recycle the catalytic system (Figure 6.1, B).¹²⁻¹³

More recently, a bifunctional polymeric catalyst was prepared using building units that were functionalized with an iridium polypyridyl photocatalyst and a nickel complex.¹⁴ Metal leaching during recycling experiments resulted in a gradual decrease of the yield. Heterogeneous metal-organic frameworks that can be reused in C–S bond formations were synthesized by coordinating iridium- and nickel complexes to zirconium¹⁵ or hafnium clusters.¹⁶ However, these bifunctional catalysts are difficult to prepare and rely on immobilized noble-metal complexes as photocatalysts.

We recently developed a self-assembling catalyst system, in which a nickel complex and a dye adsorb to the surface of TiO₂ (dye-sensitized metallaphotocatalysts, DSMPs) that catalyses several cross-couplings.¹⁷ Key to the success was that the nickel complex and the dye are equipped with carboxylic acid groups that bind to the semiconductor's surface. However, recycling studies suffered from a gradual decrease of the yield due to leaching of the nickel catalyst and the dye because of the weak interaction between carboxylic acid groups and TiO₂.¹⁸

Various functional groups are known to bind to the surface of semiconducting materials and are intensively studied for dye-sensitized solar cells (DSSCs).¹⁹ Carboxylic acids are commonly used, because this functional group enables facile electron injection from the excited dye into the conduction band of the semiconductor.²⁰⁻²¹ Phosphonic acid groups have a significantly higher adsorption strength than carboxylic acids,^{18, 22} but their low electron injection rates make them often unsuitable for DSSCs.²³

6.2 Results and discussion

Here we demonstrate that the strong interaction of phosphonic acid moieties with the surface of semiconducting materials accesses recyclable metallaphotocatalysts for C–S cross-couplings (Figure 6.1, C).¹⁷

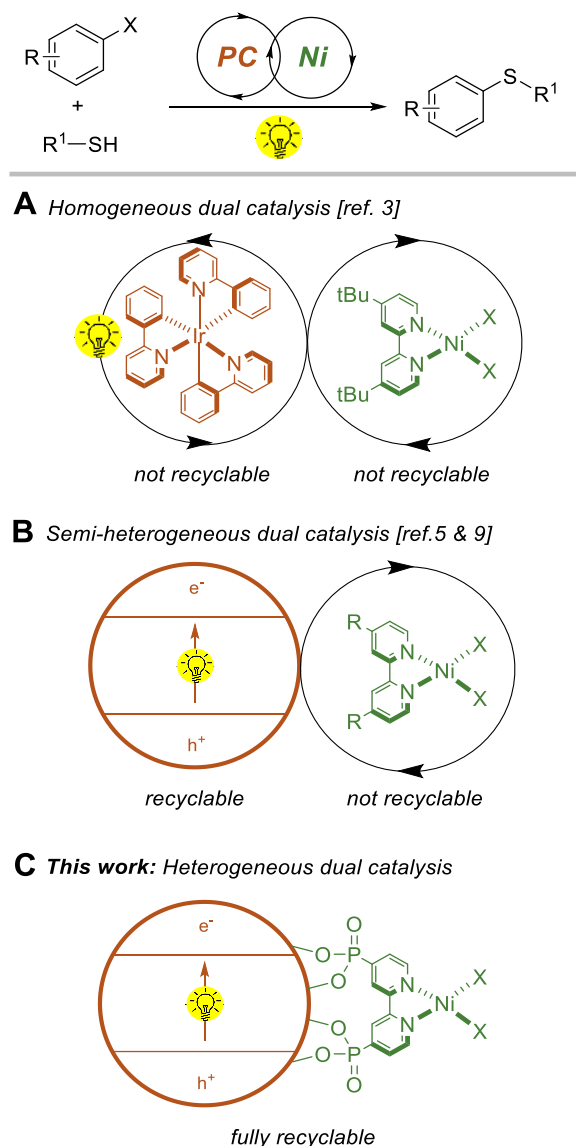


Figure 6.1. Catalytic systems for metallaphotocatalytic C–S cross-couplings

Our investigations started by studying different semiconductors as photocatalysts in the metallaphotocatalytic cross-coupling of methyl 4-iodobenzoate and 2-mercaptoethanol in presence of catalytic amounts of $\text{NiBr}_2 \cdot 3\text{H}_2\text{O}$, a bipyridine ligand that is equipped with phosphonic acid groups (dpbpy = [2,2'-bipyridine]-4,4'-diyl diphosphonic acid), and a base (Table 6.1). Using blue light (440 nm), two carbon nitride materials (CN-OA-m²⁴ and mpg-

CN²⁵), TiO₂ P25, dye-sensitized TiO₂ P25 (pre-functionalized with a ruthenium dye that contains a phosphonic acid anchoring group (Ru(bpy)₂(dpbpy)–TiO₂)²⁶), and CdS resulted in the formation of the desired coupling product (Entry 1-5). Bismuth oxide was unsuitable as photocatalyst (Entry 6-7).

We also studied this reaction at longer wavelengths (Entry 8-14), because the high energy of blue light potentially causes deactivation of nickel catalysts through the formation of nickel black,²⁷ and can lead to undesired side reactions.^{17, 28} Quantitative product formation was observed at 525 nm using CN-OA-m, (Entry 8). In addition, Ru(bpy)₂(dpbpy)–TiO₂ also catalysed the desired reaction and resulted in 69 % of the desired coupling product (Entry 11). All other tested semiconductors showed low catalytic activities using green light.

Table 6.1. Semiconductor screening for C–S cross-couplings using a nickel complex that contains phosphonic acid groups.^[a]

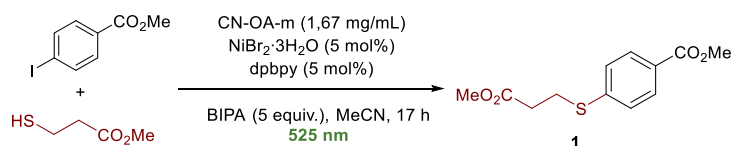
440 nm			525 nm		
Entry	Semiconductor	1 [%] ^[b]	Entry	Semiconductor	1 [%] ^[b]
1	CN-OA-m	99	8	CN-OA-m	99
2	mpg-CN	99	9	mpg-CN	4
3	TiO ₂	38	10	TiO ₂	5
4	Ru(bpy) ₂ (dpbpy)–TiO ₂	99	11	Ru(bpy) ₂ (dpbpy)–TiO ₂	69
5	CdS	45	12	CdS	20
6	Bi ₂ O ₃	n.d.	13	Bi ₂ O ₃	n.d.
7	Bi ₂ O ₃ nanopowder	n.d.	14	Bi ₂ O ₃ nanopowder	n.d.

[a] Reaction conditions: methyl 4-iodobenzoate (190.3 μmol), methyl 3-mercaptopropionate (380.5 μmol), Ru(bpy)₂(dpbpy) (2.4 μmol), NiBr₂·3H₂O (19.0 μmol), dpbpy (19.0 μmol), semiconductor (30 mg) and BIPA (951.5 μmol) in MeCN (3 mL). [b] Determined by ¹H-NMR using 1,3,5-trimethoxybenzene as internal standard. dpbpy = [2,2'-bipyridine]-4,4'-diylidiphosphonic acid, BIPA = *N*-tert-butylisopropylamine, bpy = 2,2'-bipyridine, n.d. = not detected.

Next, we sought to optimize the two most promising catalytic systems. In case of CN-OA-m, a careful investigation of all reaction parameters showed that 1.67 mg/mL of the semiconductor in combination with 5 mol% of NiBr₂·3H₂O and dpbpy are sufficient to quantitatively form the desired product within 17 h using 525 nm LEDs (Table 6.2, Entry 1). Under the same conditions, methyl 4-bromobenzoate resulted in low amounts of **1** (Table 6.2, Entry 2). When Ru(bpy)₂(dpbpy)–TiO₂ was used as photocatalyst, a longer reaction time in combination with a higher loading of the nickel complex was necessary, but the high

selectivity towards the desired product was maintained (Entry 3). Control studies showed that no reaction occurred in the absence of CN-OA-m, dpbpy, the base, or light (Entry 4-7). Only small amounts of the coupling product were formed without the Ni^{II} salt, or in the presence of oxygen (Entry 8-9). Using a 440 nm irradiation source, full conversion was obtained after 3 h (Entry 10).

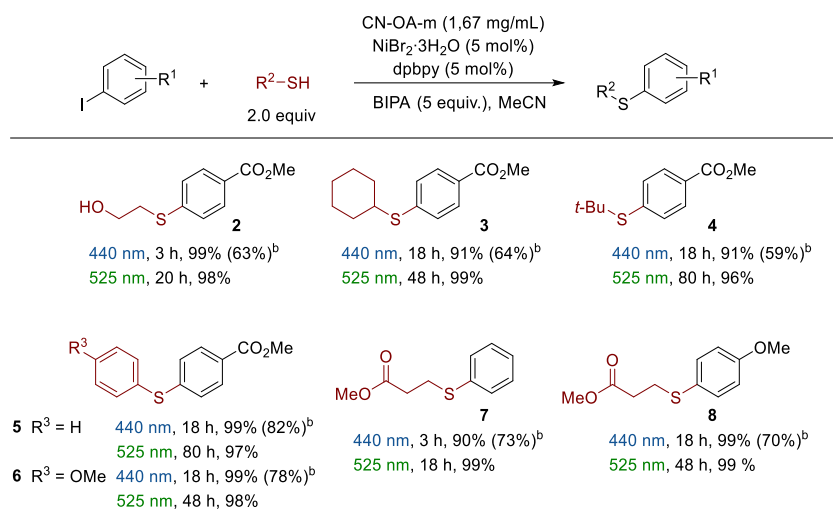
Table 6.2. Optimized conditions and control studies.^[a]



Entry	Conditions	1 [%] ^[b]
1	As shown	99 (94) ^[c]
2	methyl 4-bromobenzoate	11
3	Ru(bpy) ₂ (dpbpy)-TiO ₂ instead of CN-OA-m ^[d]	99
4	No CN-OA-m	n.d.
5	No dpbpy	n.d.
6	No BIPA	n.d.
7	No light	n.d.
8	No NiBr ₂ ·3H ₂ O	10
9	no degassing	4
10	440 nm, 3 h	99

[a] Reaction conditions: methyl 4-iodobenzoate (190.3 μmol), methyl 3-mercaptopropionate (380.5 μmol), NiBr₂·3H₂O (9.5 μmol), dpbpy (9.5 μmol), CN-OA-m (5 mg) and BIPA (951.5 μmol) in MeCN (3 mL). [b] Determined by ¹H-NMR using 1,3,5-trimethoxybenzene as internal standard. [c] Isolated yield in parantheses. [d] Carried out with 10 mg/mL TiO₂ P25, Ru(bpy)₂(dpbpy) (2.4 μmol), NiBr₂·3H₂O (19 μmol), dpbpy (19 μmol), BIPA (951.5 μmol) in MeCN (3 mL) within 24 h. dpbpy = [2,2'-bipyridine]-4,4'-diylidiphosphonic acid, BIPA = *N*-tert-Butylisopropylamine, bpy = 2,2'-bipyridine, n.d. = not detected.

The optimized conditions were evaluated for a small set of thiols and aryl iodides using blue and green light irradiation (Table 6.3). When 2-mercaptoethanol was used, a selective C–S bond formation (**2**), with no detectable amount of the corresponding C–O coupling product was obtained. The catalytic cocktail was also applicable for selective couplings of secondary, tertiary and aromatic thiols with methyl 4-iodobenzoate (**3-6**). Moreover, the protocol is not limited to electron-rich aryl iodides, and excellent yields were obtained for the when iodobenzene (**7**) and 4-iodoanisole (**8**) were used.

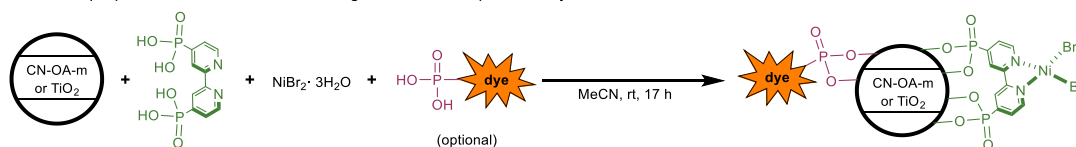
Table 6.3. Scope.^[a]

[a] Reaction conditions: methyl 4-iodobenzoate (190.3 μ mol), methyl 3-mercaptopropionate (380.5 μ mol), NiBr₂·3H₂O (9.5 μ mol), dpbpy (9.5 μ mol), CN-OA-m (5 mg) and BIPA (951.5 μ mol) in MeCN (3 mL). Yields were determined by ¹H-NMR using 1,3,5-trimethoxybenzene as internal standard. [b] Isolated yield in parantheses. dpbpy = [2,2'-bipyridine]-4,4'-diylidiphosphonic acid, BIPA = *N*-tert-Butylisopropylamine.

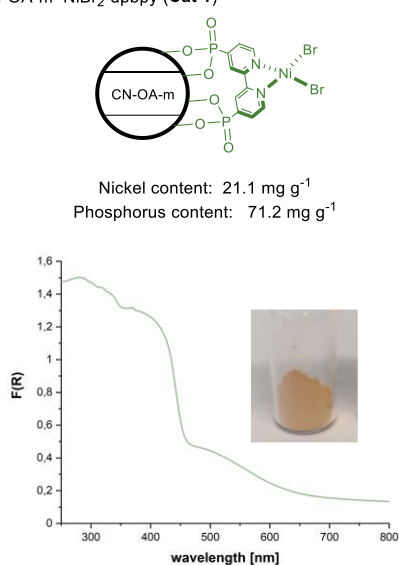
Similar to the previously reported DSMPs, in which the nickel complex and a dye were equipped with carboxylic acid groups,¹⁷ the catalytic system reported herein self-assembles *in situ*. To characterize the functional heterogeneous catalysts, an *ex situ* preparation was carried out (Figure 6.2). Therefore, the respective semiconductor material was dispersed in MeCN, followed by addition of dpbpy, the nickel salt and the dye (optional) (Figure 6.2, A). The mixture was stirred overnight and the resulting material was isolated by centrifugation, washing and lyophilisation (see SI for details). Inductive coupled plasma - optical emission spectroscopy (ICP-OES) was used to study the amount of nickel, phosphorus and ruthenium. In case of the functionalized carbon nitride material (**Cat 1**), a nickel loading of 21.1 mg g⁻¹ (corresponding to 1 mol% NiBr₂·3H₂O) and a phosphorus content of 71.2 mg g⁻¹ (corresponding to 3 mol% dpbpy) was determined. For the variant using dye-sensitized TiO₂ (**Cat 2**), a nickel loading of 4.18 mg g⁻¹ (corresponding to 1 mol% NiBr₂·3H₂O), a Ru loading of 4.59 mg g⁻¹ (corresponding to 0.7 mol% Ru(bpy)₂(dpbpy)) and a phosphorus content of 32.2 mg g⁻¹ (corresponds to 8.2 mol% dpbpy as ligand in the nickel salt and Ru(bpy)₂(dpbpy)) was measured. The significant difference in the nickel loadings were further confirmed by energy-dispersive X-ray spectroscopy (EDX) analysis (Table S6.11 and S6.13), and is likely responsible for the different catalytic activity of the functionalized materials in the model reaction. The UV-Vis spectrum of the functionalized carbon nitride confirms its absorption up to ~700 nm (Figure 6.2, B), which is similar to the non-

functionalized CN-OA-m (Figure S6.6).²⁴ TiO₂ functionalized with the ruthenium dye and the nickel complex broadly absorbs across the visible light spectrum (Figure 6.2, C). Scanning electron microscopy (SEM) analysis of both materials showed that the porous surface of CN-OA-m and TiO₂ P25 was not altered during the immobilization (Figure S6.7 and S6.10).

A *Ex situ* preparation of bifunctional, heterogeneous metallaphotocatalysts



B CN-OA-m–NiBr₂·dppby (Cat 1)



C Ru(bpy)₂(dppby)–TiO₂–NiBr₂·dppby (Cat 2)

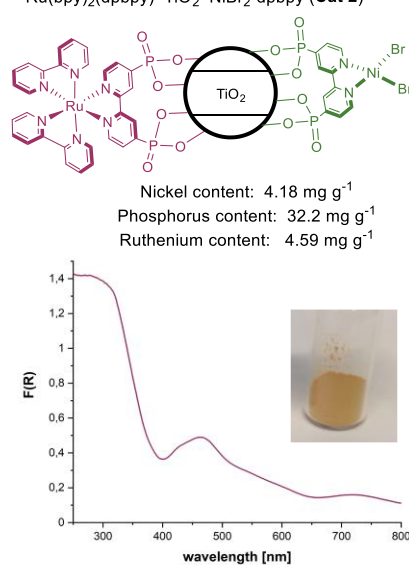


Figure 6.2. Preparation (A) and characterization (B, C) of fully heterogeneous metallaphotocatalysts.

Next, we studied the recyclability of the bifunctional materials using blue (440 nm) and green (525 nm) light (Figure 6.3, A). In all cases, the first experiment was carried out through *in situ* catalyst formation using the conditions reported in Table 6.2. After the respective reaction time, the heterogeneous catalyst was separated, washed and reused without adding additional nickel salt or ligand. To our delight, both catalytic systems could be recycled multiple times without losing their activity using both wavelengths. This provides evidence that the ligand binds permanently to the surface of the semiconductor, and that the nickel atoms strongly coordinate to the ligand.

A more detailed investigation was carried out using the functionalized carbon nitride material (Figure 6.3, B). The heterogeneous catalyst was reused ten times and analyzed after each experiment by ICP-OES. After the first experiment, a nickel loading of 2.65 mg g⁻¹

and a phosphorus content of 52.2 mg g^{-1} was determined, which indicates that 2.2 % of the ligand and 0.1 % of the nickel salt that were initially added to the reaction mixture were still immobilized (for details, see Table S6.21). The amount of nickel and phosphorus did not further decrease during the subsequent cycles, and the catalytic activity was maintained. This shows that both species are permanently immobilized on the surface of the semiconductor and that the catalytic system only requires ~0.1 mol% of the nickel salt and ~1.9 mol% of the ligand. Indeed, a control experiment using this nickel and ligand loading through the *in situ* method gave quantitative product formation within 17 h (Table S6.23).

Unfortunately, the heterogeneous materials was not applicable for the metallaphotocatalytic C–O cross coupling of carboxylic acids with aryl halides,²⁹ or the C–C coupling of α -silylamines with aryl halides (Table S6.24 and S6.25).³⁰ Control experiments using iridium polypyridyl complexes instead of the heterogeneous semiconductor also gave no product formation in these reactions, which indicates a detrimental effect of the phosphonic acid groups of the nickel complex in these transformations. Product formation (25%) was observed for the C–C cross coupling reaction of potassium benzyltrifluoroborates with aryl halides using mpg-CN³¹ in combination with NiBr₂·3H₂O and dpbpy (Table S6.27), but attempts to optimize the reaction or to recycle the catalyst failed, presumably due to the formation of nickel black.²⁷

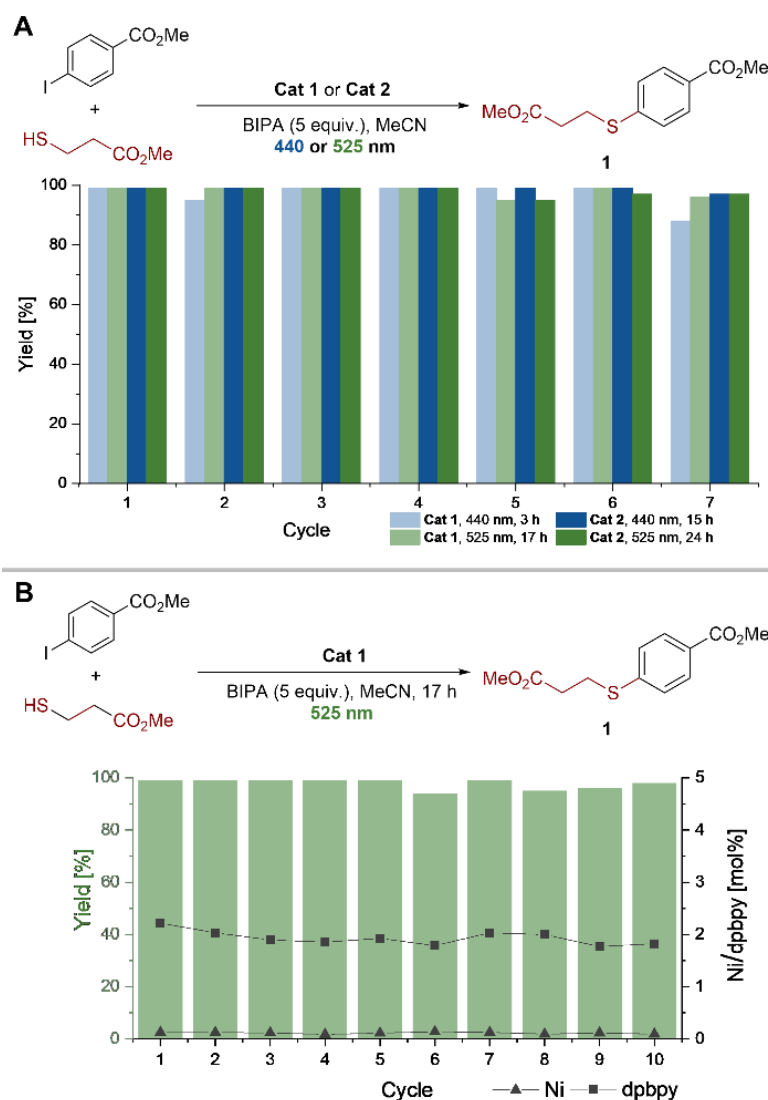


Figure 6.3. Recycling studies of **Cat 1** and **Cat 2** with blue and green light irradiation (**A**) and recycling studies including ICP-OES analysis using **Cat 1** with green light irradiation (**B**).

6.3 Conclusion

In conclusion, we have shown that a self-assembling heterogeneous material for metallaphotocatalytic C–S cross-couplings can be obtained by mixing a carbon nitride material or dye-sensitized TiO₂ with a nickel complex that is functionalized with phosphonic acid groups. The final catalyst shows high activity even though the nickel content is only 0.1 mol% and absorbs broadly across the visible light spectrum. The catalyst can be recycled at least ten times maintaining its catalytic activity. Improved ligand designs to expand the applicability of this concept to other cross-couplings are currently evaluated in our laboratory.

6.4 References

1. Marzo, L.; Pagire, S. K.; Reiser, O.; König, B., Visible-Light Photocatalysis: Does It Make a Difference in Organic Synthesis? *Angew. Chem. Int. Ed.* **2018**, *57* (32), 10034-10072.
2. Arias-Rotondo, D. M.; McCusker, J. K., The photophysics of photoredox catalysis: a roadmap for catalyst design. *Chem. Soc. Rev.* **2016**, *45* (21), 5803-5820.
3. Prier, C. K.; Rankic, D. A.; MacMillan, D. W. C., Visible Light Photoredox Catalysis with Transition Metal Complexes: Applications in Organic Synthesis. *Chem. Rev.* **2013**, *113* (7), 5322-5363.
4. Schultz, D. M.; Yoon, T. P., Solar Synthesis: Prospects in Visible Light Photocatalysis. *Science* **2014**, *343* (6174), 985.
5. Milligan, J. A.; Phelan, J. P.; Badir, S. O.; Molander, G. A., Alkyl Carbon–Carbon Bond Formation by Nickel/Photoredox Cross-Coupling. *Angew. Chem. Int. Ed.* **2019**, *58* (19), 6152-6163.
6. Zhu, C.; Yue, H.; Jia, J.; Rueping, M., Recent Advances in Nickel-Catalyzed C-Heteroatom Cross-Coupling Reactions under Mild Conditions via Facilitated Reductive Elimination. *Angew. Chem. Int. Ed.* **2021**, *60* (33), 17810-17831.
7. Zhu, C.; Yue, H.; Chu, L.; Rueping, M., Recent advances in photoredox and nickel dual-catalyzed cascade reactions: pushing the boundaries of complexity. *Chem. Sci.* **2020**, *11* (16), 4051-4064.
8. Oderinde, M. S.; Frenette, M.; Robbins, D. W.; Aquila, B.; Johannes, J. W., Photoredox Mediated Nickel Catalyzed Cross-Coupling of Thiols With Aryl and Heteroaryl Iodides via Thiyl Radicals. *J. Am. Chem. Soc.* **2016**, *138* (6), 1760-1763.
9. Jouffroy, M.; Kelly, C. B.; Molander, G. A., Thioetherification via Photoredox/Nickel Dual Catalysis. *Org. Lett.* **2016**, *18* (4), 876-879.
10. Vara, B. A.; Li, X.; Berritt, S.; Walters, C. R.; Petersson, E. J.; Molander, G. A., Scalable thioarylation of unprotected peptides and biomolecules under Ni/photoredox catalysis. *Chem. Sci.* **2018**, *9* (2), 336-344.
11. Santandrea, J.; Minozzi, C.; Cruché, C.; Collins, S. K., Photochemical Dual-Catalytic Synthesis of Alkynyl Sulfides. *Angew. Chem. Int. Ed.* **2017**, *56* (40), 12255-12259.

12. Cavedon, C.; Madani, A.; Seeberger, P. H.; Pieber, B., Semiheterogeneous Dual Nickel/Photocatalytic (Thio)etherification Using Carbon Nitrides. *Org. Lett.* **2019**, *21* (13), 5331-5334.
13. Cavedon, C.; Seeberger, P. H.; Pieber, B., Photochemical Strategies for Carbon–Heteroatom Bond Formation. *Eur. J. Org. Chem.* **2020**, *10* (10), 1379-1392.
14. Pan, Y.; Zhang, N.; Liu, C.-H.; Fan, S.; Guo, S.; Zhang, Z.-M.; Zhu, Y.-Y., Boosting Photocatalytic Activities for Organic Transformations through Merging Photocatalyst and Transition-Metal Catalyst in Flexible Polymers. *ACS Catal.* **2020**, *10* (20), 11758-11767.
15. Zhu, Y.-Y.; Lan, G.; Fan, Y.; Veroneau, S. S.; Song, Y.; Micheroni, D.; Lin, W., Merging Photoredox and Organometallic Catalysts in a Metal–Organic Framework Significantly Boosts Photocatalytic Activities. *Angew. Chem. Int. Ed.* **2018**, *57* (43), 14090-14094.
16. Lan, G.; Quan, Y.; Wang, M.; Nash, G. T.; You, E.; Song, Y.; Veroneau, S. S.; Jiang, X.; Lin, W., Metal–Organic Layers as Multifunctional Two-Dimensional Nanomaterials for Enhanced Photoredox Catalysis. *J. Am. Chem. Soc.* **2019**, *141* (40), 15767-15772.
17. Reischauer, S.; Strauss, V.; Pieber, B., Modular, Self-Assembling Metallaphotocatalyst for Cross-Couplings Using the Full Visible-Light Spectrum. *ACS Catal.* **2020**, *10* (22), 13269-13274.
18. Zeininger, L.; Portilla, L.; Halik, M.; Hirsch, A., Quantitative Determination and Comparison of the Surface Binding of Phosphonic Acid, Carboxylic Acid, and Catechol Ligands on TiO₂ Nanoparticles. *Chem. Eur. J.* **2016**, *22* (38), 13506-13512.
19. Zhang, L.; Cole, J. M., Anchoring Groups for Dye-Sensitized Solar Cells. *ACS Appl. Mater. Interfaces* **2015**, *7* (6), 3427-3455.
20. Baktash, A.; Khoshnevisan, B.; Sasani, A.; Mirabbaszadeh, K., Effects of carboxylic acid and phosphonic acid anchoring groups on the efficiency of dye sensitized solar cells: A computational study. *Org. Electron.* **2016**, *33*, 207-212.
21. Ambrosio, F.; Martsinovich, N.; Troisi, A., Effect of the Anchoring Group on Electron Injection: Theoretical Study of Phosphonated Dyes for Dye-Sensitized Solar Cells. *J. Phys. Chem. C* **2012**, *116* (3), 2622-2629.
22. Kuriki, R.; Yamamoto, M.; Higuchi, K.; Yamamoto, Y.; Akatsuka, M.; Lu, D.; Yagi, S.; Yoshida, T.; Ishitani, O.; Maeda, K., Robust Binding between Carbon Nitride Nanosheets

and a Binuclear Ruthenium(II) Complex Enabling Durable, Selective CO₂ Reduction under Visible Light in Aqueous Solution. *Angew. Chem. Int. Ed.* **2017**, *56* (17), 4867-4871.

23. Guerrero, G.; Alauzun, J. G.; Granier, M.; Laurencin, D.; Mutin, P. H., Phosphonate coupling molecules for the control of surface/interface properties and the synthesis of nanomaterials. *Dalton Trans.* **2013**, *42* (35), 12569-12585.

24. Zhang, G.; Li, G.; Lan, Z.-A.; Lin, L.; Savateev, A.; Heil, T.; Zafeiratos, S.; Wang, X.; Antonietti, M., Optimizing Optical Absorption, Exciton Dissociation, and Charge Transfer of a Polymeric Carbon Nitride with Ultrahigh Solar Hydrogen Production Activity. *Angew. Chem. Int. Ed.* **2017**, *56* (43), 13445-13449.

25. Goettmann, F.; Fischer, A.; Antonietti, M.; Thomas, A., Chemical Synthesis of Mesoporous Carbon Nitrides Using Hard Templates and Their Use as a Metal-Free Catalyst for Friedel–Crafts Reaction of Benzene. *Angew. Chem. Int. Ed.* **2006**, *45* (27), 4467-4471.

26. Neuthe, K.; Bittner, F.; Stiemke, F.; Ziem, B.; Du, J.; Zellner, M.; Wark, M.; Schubert, T.; Haag, R., Phosphonic acid anchored ruthenium complexes for ZnO-based dye-sensitized solar cells. *Dyes Pigments* **2014**, *104*, 24-33.

27. Gisbertz, S.; Reischauer, S.; Pieber, B., Overcoming limitations in dual photoredox/nickel-catalysed C–N cross-couplings due to catalyst deactivation. *Nat. Catal.* **2020**, *3* (8), 611-620.

28. Cavedon, C.; Sletten, E. T.; Madani, A.; Niemeyer, O.; Seeberger, P. H.; Pieber, B., Visible-Light-Mediated Oxidative Debenzylation Enables the Use of Benzyl Ethers as Temporary Protecting Groups. *Org. Lett.* **2021**, *23* (2), 514-518.

29. Welin, E. R.; Le, C.; Arias-Rotondo, D. M.; McCusker, J. K.; MacMillan, D. W. C., Photosensitized, energy transfer-mediated organometallic catalysis through electronically excited nickel(II). *Science* **2017**, *355* (6323), 380-385.

30. Remeur, C.; Kelly, C. B.; Patel, N. R.; Molander, G. A., Aminomethylation of Aryl Halides Using α -Silylamines Enabled by Ni/Photoredox Dual Catalysis. *ACS Catal.* **2017**, *7* (9), 6065-6069.

31. Tellis, J. C.; Primer, D. N.; Molander, G. A., Single-electron transmetalation in organoboron cross-coupling by photoredox/nickel dual catalysis. *Science* **2014**, *345* (6195), 433-436.

Chapter 7

Carbon dot/TiO₂ nanocomposites as photocatalysts for metallaphotocatalytic carbon–heteroatom cross-couplings

Zhao Z., Reischauer, S.; Pieber, B., Delbianco M.

Green Chem., **2021**, 23, 4524-4530.

<https://doi.org/10.1039/D1GC01284C>

Abstract

Carbon dots have been immobilized on titanium dioxide to generate photocatalysts for pollutant degradation and water splitting. Here we demonstrate that these nanocomposites are valuable photocatalysts for metallaphotocatalytic carbon–heteroatom cross-couplings. These sustainable materials show a large applicability, high photostability, excellent reusability and broadly absorb across the visible-light spectrum.

Specific contribution

M. Delbianco and B. Pieber conceived the idea behind this project. Z. Zhao prepared and characterized the carbon dots. I verified its feasibility in photocatalytical reactions. Z. Zhao and I designed and carried out all the photocatalytical experiments. Z. Zhao wrote the manuscript with contribution of S. Reischauer. M. Delbianco and B. Pieber revised and corrected the manuscript.

Supporting Information

All experimental procedures and analytical data are available in the supporting information in the appendix or through the website of the Publisher. DOI: [10.1039/D1GC01284C](https://doi.org/10.1039/D1GC01284C).

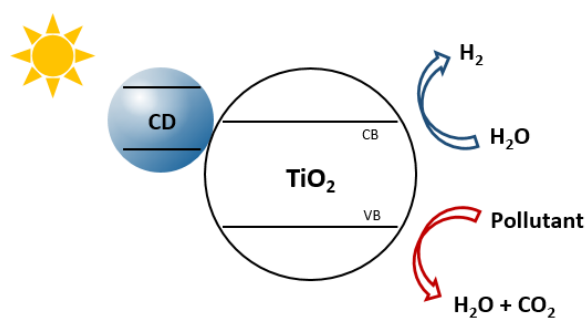
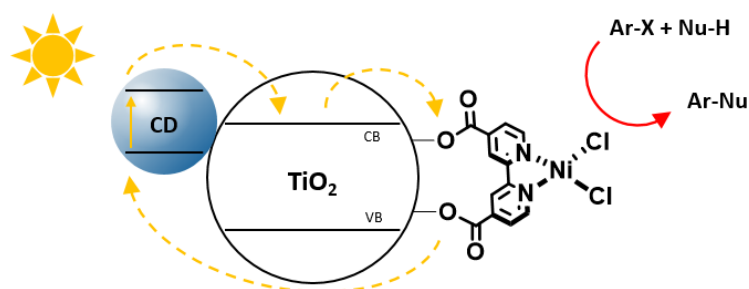
7.1 Introduction

Carbon dots (CDs) are quasi-spherical fluorescent carbon-based materials with a size of typically less than 10 nm.¹⁻⁵ CDs are easily prepared through top-down or bottom-up approaches from a variety of carbon sources that permit to adjust their chemical compositions and tune their photoluminescence (PL) properties.⁶⁻⁷ Their chemical inertness and biocompatibility has prompted applications in sensing, bioimaging, and nanomedicine.⁷⁻¹¹ Moreover, the surface functional groups enabled applications as sustainable nano-organocatalysts for synthetic transformations. The superficial carboxylic acid, hydroxy, or amino functionalities were exploited in acid-base, hydrogen bond, or amine-catalysed reactions.¹²⁻¹⁵

CDs are also promising metal-free photocatalysts for pollutant degradation, H₂ evolution and CO₂ conversion, owing to their photostability, light-harvesting ability and electron-transfer efficiency.¹⁶⁻¹⁹ The high solubility of CDs in water makes them a suitable alternative to hydrophobic organic materials, such as carbon nitride and graphite.²⁰ This feature permitted to use CDs in combination with nickel catalysis for H₂ evolution in aqueous solution.²¹⁻²²

However, due to their short PL lifetimes,²³⁻²⁴ examples of CDs as photocatalysts for selective organic synthesis are scarce¹⁴⁻¹⁵ when compared to common photocatalysts, such as ruthenium (Ru) and iridium (Ir) polypyridyl complexes that have long-lived triplet excited states.²⁵⁻²⁷ To overcome the problems associated with the short-lived excited states, CDs can be immobilized on heterogeneous semiconductors such as titanium dioxide to generate a composite material that absorbs visible-light and generates a long-lived charge-separated species.²⁸⁻³⁰ Still, the applications of such composites remained limited to water splitting, CO₂ reduction, and pollutant degradation (Figure 7.1A).³¹⁻³³

The combination of a photo- and a nickel catalyst (termed metallaphotocatalysis) triggers many important carbon–heteroatom and carbon–carbon cross-couplings using light as sustainable energy source.³⁴ Suitable photocatalysts for these reactions range from ruthenium and iridium polypyridyl complexes and organic dyes to heterogeneous semiconductors.³⁴ Moreover, nickel complexes and photocatalysts were combined in bifunctional heterogeneous materials, such as metal-organic frameworks,³⁵⁻³⁶ or organic polymers.³⁷

A CD/TiO₂ nanocomposites for water splitting and pollutant degradation**B** This work: CD/TiO₂ nanocomposites as photocatalysts for cross-couplings

- *Low economic cost and toxicity*
- *Facile nanocomposite preparation*
- *Excellent stability*
- *Broad absorption of visible-light*

Figure 7.1. Schematic representation of CD/TiO₂ nanocomposites as photocatalysts for water splitting, pollutant degradation (A) and metallaphotocatalytic carbon–heteroatom cross-couplings (B).

Titanium dioxide can be sensitized with organic dyes to serve as a visible light photocatalyst for selective organic transformations.³⁸⁻³⁹ Recently, it was shown that the immobilization of a Ni(II) catalyst and an organic dye on the surface of metal oxides provides a heterogeneous catalytic system for metallaphotocatalytic carbon–carbon and carbon–heteroatom cross-couplings that overcomes the problems associated with short-lived singlet excited states of organic dyes.⁴⁰ Following this seminal work, we show that CDs are a valuable alternative to organic dyes in such catalytic systems due to i) their low economic cost and toxicity, ii) their facile immobilization on semiconductors, iii) their broad absorption across the visible-light spectrum, and iv) their superior photo- and chemical stability (Figure 7.1B).^{21, 30}

7.2 Results and discussion

Preparation of CD1/TiO₂ nanocomposite

Carbohydrates are an attractive carbon source for CD synthesis owing to their low cost, high solubility in water, easy carbonisation at relatively low temperatures, and presence of heteroatoms.⁴¹ We therefore began our investigations by preparing **CD1** from glucosamine hydrochloride (GlcN·HCl), following a microwave-based carbonisation method (Figure 7.2A).⁴² Doping with β -alanine (β -Ala) ensured a high amount of surface carboxylic acid groups (Figure S7.6 and S7.7).⁴² The zeta potential in the range of -11.1 to +18.7 mV suggested the presence of several functional groups (carboxylic acids, alcohols, and amino groups) on the surface of **CD1** (Figure S7.8).⁴²⁻⁴³

Transmission electron microscopy (TEM) confirmed a spherical shape of the CD nanoparticles with a diameter of about 4 nm (Figure 7.2B and Figure S7.2). The X-ray diffraction (XRD) profile showed a single broad peak ($2\theta = 23^\circ$), indicating the amorphous structure of **CD1** (Figure S7.9). A colloidal solution of **CD1** in H₂O emitted blue light under UV light irradiation ($\lambda_{\text{ex}} = 366$ nm) (Figure S7.3). Spectroscopic analysis showed an absorption peak at 276 nm (Figure S7.5) and a PL emission maximum at ~460 nm ($\lambda_{\text{ex}} = 360$ nm, Figure S7.4). A PL lifetime of 4.45 ns was measured by fitting the PL decay curve of **CD1** (Figure S7.10).

CD1 was immobilized on the surface of TiO₂ P25 by stirring a mixture of the two components in water (mass ratio 1:1; Figure 7.2A). The resulting brown powder (**CD1**/TiO₂) was analysed by scanning electron microscopy (SEM) and energy dispersive X-ray spectroscopy (EDX) (Figure S7.15). The morphology and size of the nanocomposites remained similar to unfunctionalized TiO₂. The increased carbon content confirmed the immobilization of **CD1**. UV-Vis spectroscopy of the resulting material confirmed its extended absorption in the visible-light region (Figure 7.2C).

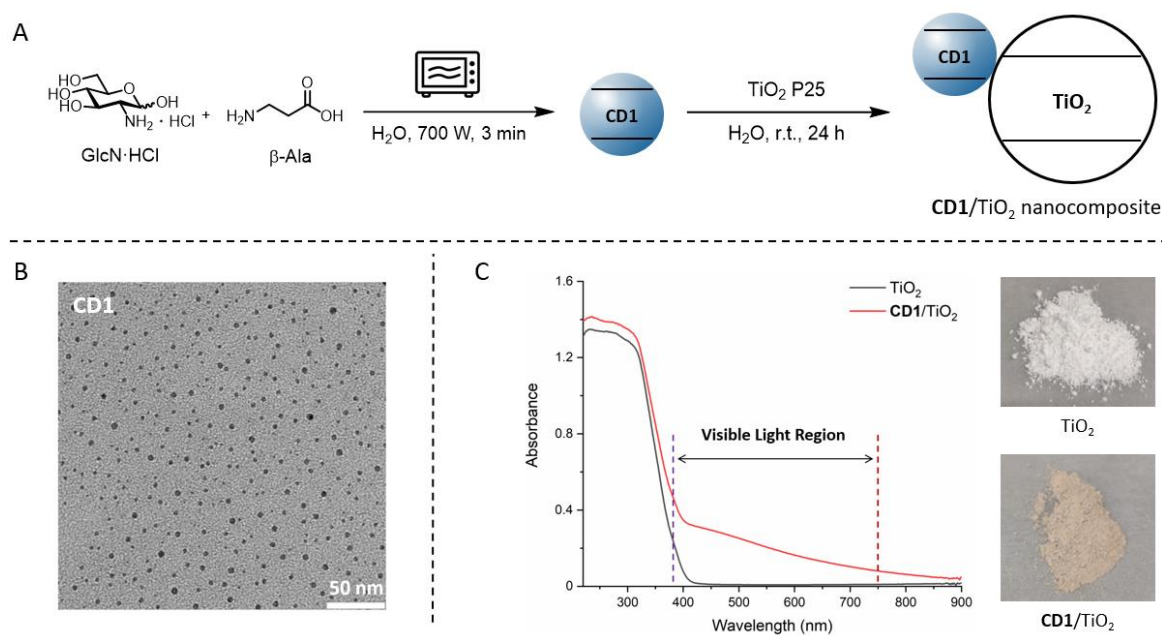


Figure 7.2. Schematic representation of the preparation of **CD1** and **CD1/TiO₂** nanocomposite (A). TEM image of **CD1** (B). UV-Vis absorption (solid state) and photographs of TiO₂ and **CD1/TiO₂** nanocomposite (C). GlcN·HCl = Glucosamine hydrochloride. β-Ala = β-Alanine.

Applicability of CD1/TiO₂ as photocatalyst

The applicability of **CD1/TiO₂** as photocatalyst for metallaphotocatalytic cross-couplings was tested for the C–O arylation of **N-(tert-butoxycarbonyl)-L-proline** (Boc-Pro-OH) with methyl 4-iodobenzoate using visible-light (Figure 7.3A).^{40, 44} A Ni(II) complex that contains carboxylic acid groups was employed to bind to the nanocomposite. The selective formation of 83% of the desired ester product (**1**) was observed when the reaction was irradiated with blue (440 nm) light for 24 h (Entry 1). Control experiments confirmed the necessity of TiO₂, **CD1**, and the carboxylic acid functionalized ligand 2,2'-bipyridine-4,4'-dicarboxylic acid (dcbpy) (Entries 2-5).

A previous report that used molecular dyes with short excited state lifetimes instead of **CD1** showed that insulating materials, such as SiO₂, can be used instead of TiO₂ for the same reaction.⁴⁰ In this case, it was proposed that the close proximity between dye molecules and the nickel complex is responsible for productive catalysis. Using a **CD1/SiO₂** nanocomposite, we only observed a modest yield of 7% of the desired product (Entry 6), suggesting that an electronic communication between the excited

CD and the immobilized nickel complex “through” a semiconducting material is crucial.

Using **CD1**/TiO₂ an almost quantitative formation of **1** required 40 h (Entry 7). The broad absorption of the nanocomposite also enabled cross-coupling at longer wavelengths (525 nm), albeit with longer reaction times (Entry 8). It is worth noting that **CD1**/TiO₂ is also highly active using very low loadings (Table 6), and that the nanocomposite is bench-stable and does not lose its catalytic activity upon storage at room temperature for 26 weeks (Table 5).

To our delight, **CD1**/TiO₂ served as an active photocatalyst for a range of metallaphotocatalytic carbon–heteroatom cross-couplings.³⁴ Moderate to excellent yields were obtained for the coupling of aryl halides with an alcohol, a thiol, a sodium sulfonate, and a sulfonamide using slightly adapted conditions (Figure 7.3B).

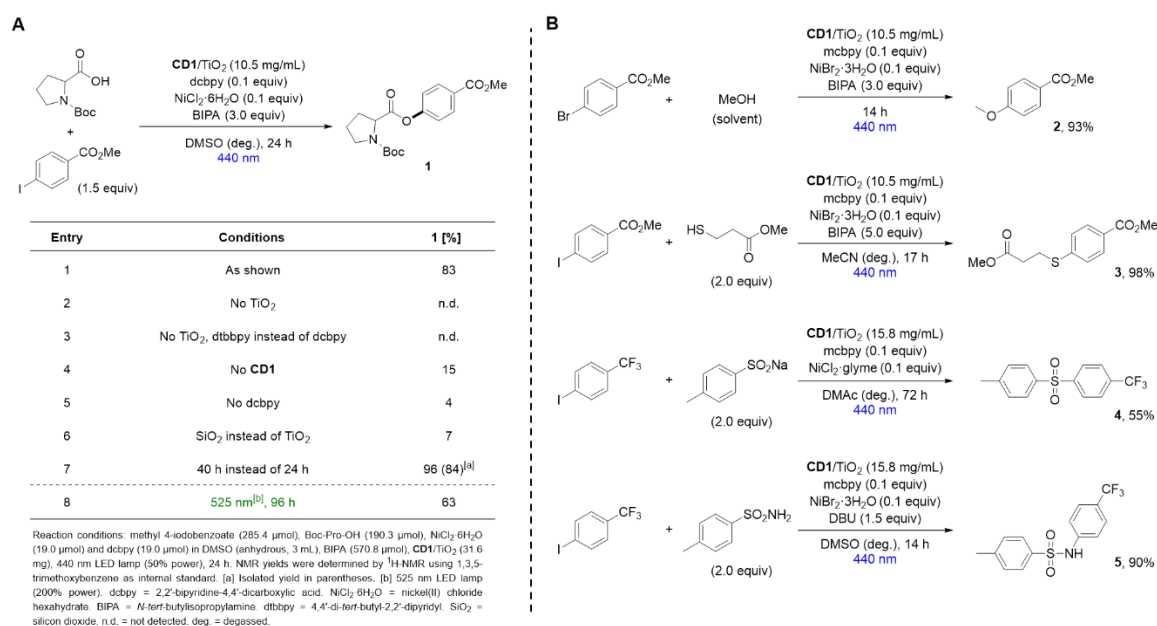


Figure 7.3. Optimized conditions and control experiments for the cross-coupling of Boc-Pro-OH with methyl 4-iodobenzoate using **CD1**/TiO₂ nanocomposite (A). Application of **CD1**/TiO₂ as photocatalyst for C–O, C–S, and C–N cross-couplings (B).

Photostability and recyclability studies

Next, we sought to compare the photostability of the **CD1**/TiO₂ nanocomposite with TiO₂ that was functionalized with the organic dye fluorescein (Fluo/TiO₂) (Figure 7.4). The functionalized semiconductors were pre-irradiated with blue light for a defined amount of time and subsequently used as photocatalysts in the metallaphotocatalytic C–O arylation of Boc-Pro-OH. The photocatalytic performance of **CD1**/TiO₂ remained unchanged even after 72 h exposure to light. In contrast, Fluo/TiO₂ suffered from significantly lower yields after 6 h irradiation. The yield obtained with the Fluo/TiO₂ photocatalyst did not decrease linearly with the irradiation time, but seemed to reach a plateau after 6–12 h pre-irradiation. We assume that the prolonged irradiation could promote the formation of fluorescein degradation products that still serve as a sensitizer.⁴⁵⁻⁴⁶

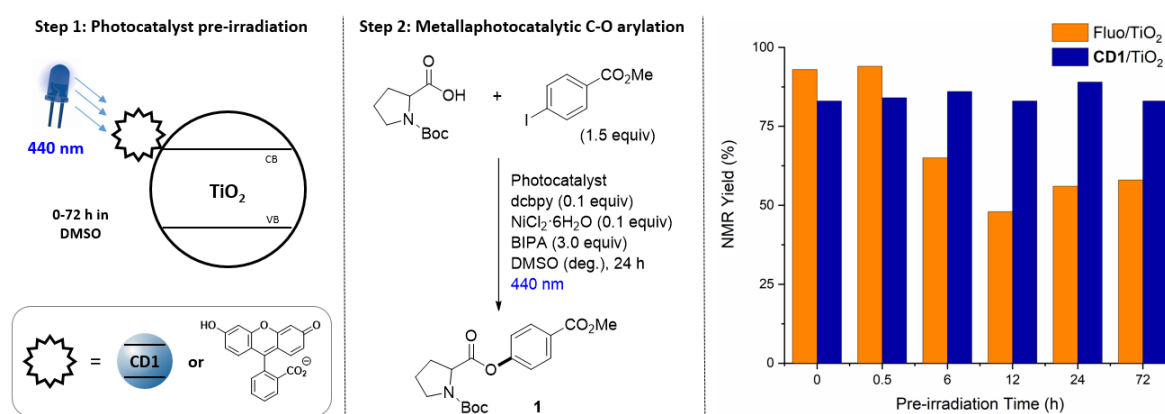


Figure 7.4. Photobleaching experiments to compare the photostability of **CD1**/TiO₂ and Fluo/TiO₂. The two photocatalysts were pre-irradiated with blue light and then used in the metallaphotocatalytic C–O arylation. Yields were determined *via* ¹H-NMR using 1,3,5-trimethoxybenzene as internal standard. Fluo = fluorescein.

The nanocomposite was characterized before and after the catalytic reaction (Table 3). Inductively coupled plasma - optical emission spectrometry (ICP-OES) revealed the presence of nickel in the **CD1**/TiO₂ nanocomposite after the C–O cross-coupling (Figure 7.3A, Entry 7). This indicated that the nickel complex remained immobilized on **CD1**/TiO₂, prompting us to explore the recyclability of the bifunctional heterogeneous catalyst (Figure 7.5). Recyclability experiments were performed using the reaction conditions reported in Figure 7.3A (Entry 1). After each cycle, the heterogeneous material was separated, washed and reused in the next C–O cross-coupling. Excellent catalytic performances were observed even after four recycling cycles. Importantly, the addition of nickel salt or nickel complex

after each cross-coupling cycle, which was previously required in a related approach,⁴⁰ was not only unnecessary, but significantly decreased the catalytic activity. This may be ascribed to Ni accumulation and formation of nickel-black upon irradiation by high-energy light (Figure S7.28).⁴⁷

Overall, these results underscore the potential of **CD1**/TiO₂ nanocomposites as a robust, cheap, and green photocatalyst for applications in organic chemistry.

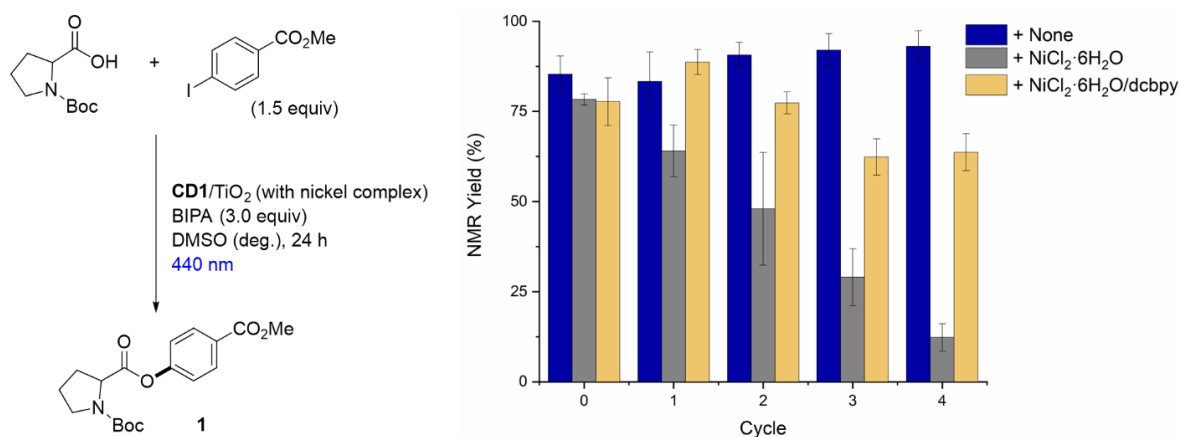


Figure 7.5. Reusability of **CD1**/TiO₂ nanocomposite decorated with a nickel complex in the metallaphotocatalytic C–O arylation.

Screening of different CD photosensitizers

Having demonstrated the potential of **CD1** as photosensitizer for dual photoredox/Ni catalysis, we assessed the effect of different carbon sources and doping agents on the photocatalytic reaction (Fig. 6A). A first set of CDs was synthesized maintaining GlcN·HCl as the carbon source and screening different doping agents. 1,3-Diaminobenzene, l-cysteine (l-Cys), poly(ethylene glycol) (average M_n 400) (PEG), and glycine (Gly) were tested. Each compound was selected to introduce respectively aromatic groups,⁴⁸ sulphur atoms, polymers to enhance surface passivation,⁴⁹ or aminoacid analogues of β -Ala. A second set of CDs was based on β -Ala as doping agent and different carbon sources. Three monosaccharides (glucose (Glc), *N*-acetyl-glucosamine (GlcNAc), galactose (Gal)), a disaccharide (D-lactose (Lac)) and a polysaccharide (pullulan) were tested to explore the influence of chain length and sugar structure on the photocatalytic performance. All CD precursors resulted in spherical nanoparticles with diameters smaller than 10 nm (Figure

S7.11). Most CDs showed similar photophysical properties, with the exception of **CD2** that emitted bright green light under UV light irradiation ($\lambda_{\text{ex}} = 366 \text{ nm}$) (Figure S7.11-13) and had an absorption maximum at 363 nm (Figure S7.16). All CDs were immobilized on TiO₂ P25 to prepare nine CD/TiO₂ nanocomposites able to absorb light in the visible region (Figure 7.6B and Figure S7.18). While most UV-Vis spectra share a similar profile, **CD2/TiO₂** nanocomposites exhibit a strong absorption band with a maximum at 466 nm. The photocatalytic performances of all nanocomposites were compared (Figure 7.6C). Despite the broad and intense absorption in the visible range, **CD2/TiO₂** resulted in low yields, whereas all other nanocomposites showed good to excellent results. For a fair comparison it should be noted that, even though all nanocomposites were prepared starting with an initial 1:1 mass ratio of CD:TiO₂, differences in immobilization might play a role in the photocatalytic results.

These results show that the system is highly flexible and that CD photosensitizers can be prepared from several starting materials, without affecting the catalytic performances. For example, excellent results were obtained for **CD9** and **CD10** prepared using lactose and pullulan as carbon source, respectively. These materials are highly abundant and cheap (lactose is a waste product of the dairy industry that is produced at >6 million ton scale every year) suggesting the possibility of turning naturally sourced polysaccharides from waste materials into valuable catalysts. Fine tuning of the elemental composition and its effect on the photocatalytic reaction will be explored in follow up studies.

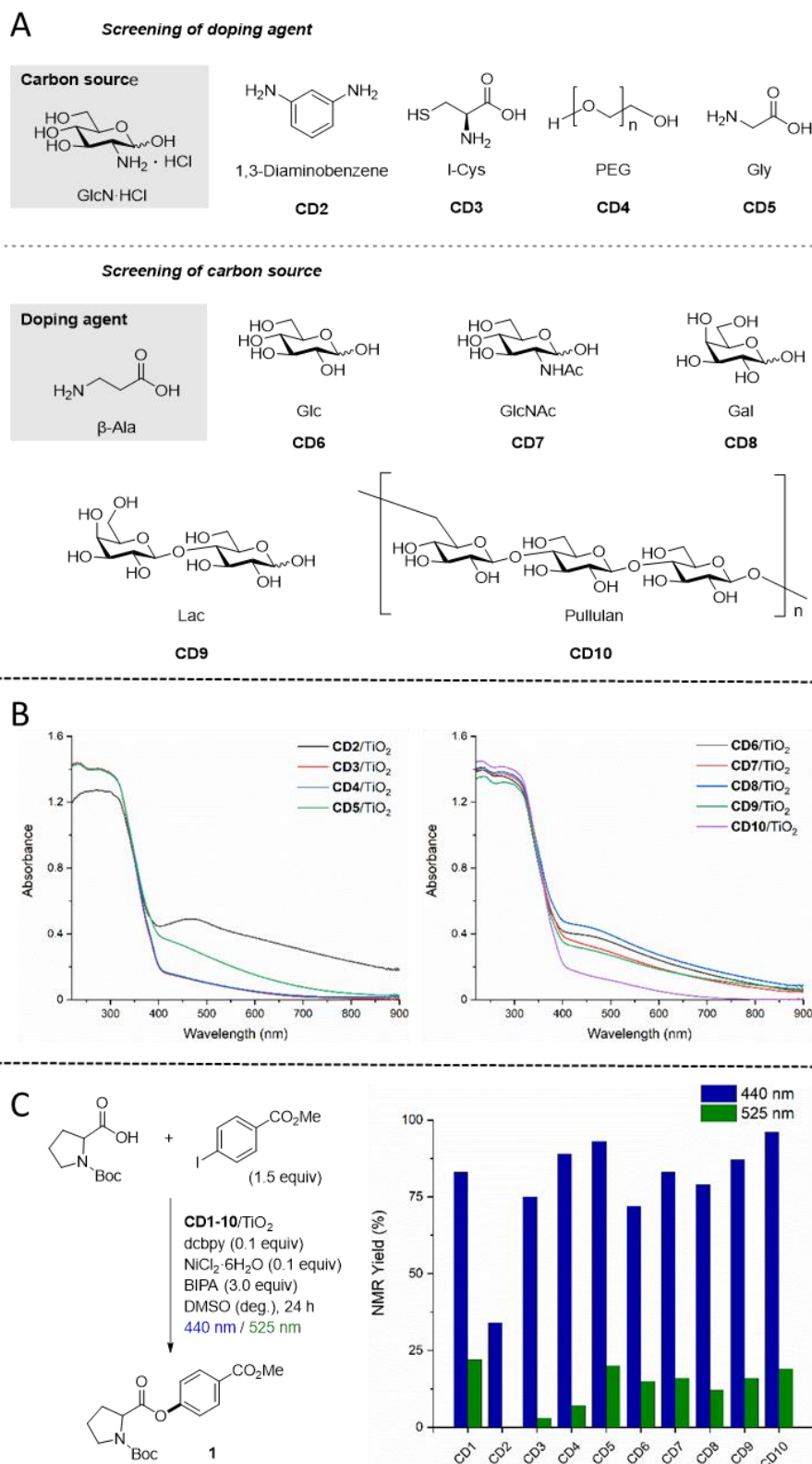


Figure 7.6. Chemical structures of carbon sources and doping agents used for CD synthesis (A). UV-Vis absorption spectra (solid state) of CD/TiO₂ nanocomposites (B). Evaluation of different CD/TiO₂ nanocomposites as photocatalyst for the metallaphotocatalytic C–O arylation of Boc-Pro-OH with methyl 4-iodobenzoate (C).

7.3 Conclusion

Carbohydrate-based CDs were immobilized on TiO₂ to prepare nanocomposites, offering a cheap and robust alternative to organic dyes. This approach allowed us to overcome the issues associated with the short excited state lifetime of CDs. We demonstrated that CDs are valuable photocatalysts for metallaphotocatalytic carbon–heteroatom cross-couplings. High conversions were observed under irradiation by either blue or green light. Photobleaching experiments confirmed that the catalytic performances of the CD/TiO₂ nanocomposites are not affected by long-time light irradiation prior to their use in catalytic reactions. Recycling experiments showed the excellent reusability of this catalytic system in C–O cross-coupling reactions. CDs could be prepared from different carbohydrate sources and doping agents, without significant difference in the catalytic performance. This is particularly important in the perspective of using polysaccharide waste materials to generate valuable photocatalysts.

7.4 References

1. Electrophoretic Analysis and Purification of Fluorescent Single-Walled Carbon Nanotube Fragments. *J. Am. Chem. Soc.* **2004**, 12736-12737.
2. Hutton, G. A. M.; Martindale, B. C. M.; Reisner, E., Carbon dots as photosensitisers for solar-driven catalysis. *Chem. Soc. Rev.* **2017**, *46* (20), 6111-6123.
3. Wu, Z. L.; Liu, Z. X.; Yuan, Y. H., Carbon dots: materials, synthesis, properties and approaches to long-wavelength and multicolor emission. *J. Mater. Chem. B* **2017**, *5* (21), 3794-3809.
4. Zhan, J.; Geng, B.; Wu, K.; Xu, G.; Wang, L.; Guo, R.; Lei, B.; Zheng, F.; Pan, D.; Wu, M., A solvent-engineered molecule fusion strategy for rational synthesis of carbon quantum dots with multicolor bandgap fluorescence. *Carbon* **2018**, *130*, 153-163.
5. Vallan, L.; Urriolabeitia, E. P.; Ruiperez, F.; Matxain, J. M.; Canton-Vitoria, R.; Tagmatarchis, N.; Benito, A. M.; Maser, W. K., Supramolecular-Enhanced Charge Transfer within Entangled Polyamide Chains as the Origin of the Universal Blue Fluorescence of Polymer Carbon Dots. *J. Am. Chem. Soc.* **2018**, *140* (40), 12862-12869.
6. Lim, S. Y.; Shen, W.; Gao, Z., Carbon quantum dots and their applications. *Chem. Soc. Rev.* **2015**, *44* (1), 362-81.
7. Jiang, K.; Sun, S.; Zhang, L.; Lu, Y.; Wu, A.; Cai, C.; Lin, H., Red, green, and blue luminescence by carbon dots: full-color emission tuning and multicolor cellular imaging. *Angew. Chem. Int. Ed.* **2015**, *54* (18), 5360-3.
8. Shen, Z.; Zhang, C.; Yu, X.; Li, J.; Wang, Z.; Zhang, Z.; Liu, B., Microwave-assisted synthesis of cyclen functional carbon dots to construct a ratiometric fluorescent probe for tetracycline detection. *J. Mat. Chem. C* **2018**, *6* (36), 9636-9641.
9. Zhi, B.; Cui, Y.; Wang, S.; Frank, B. P.; Williams, D. N.; Brown, R. P.; Melby, E. S.; Hamers, R. J.; Rosenzweig, Z.; Fairbrother, D. H.; Orr, G.; Haynes, C. L., Malic Acid Carbon Dots: From Super-resolution Live-Cell Imaging to Highly Efficient Separation. *ACS Nano*. **2018**, *12* (6), 5741-5752.
10. Sri, S.; Kumar, R.; Panda, A. K.; Solanki, P. R., Highly Biocompatible, Fluorescence, and Zwitterionic Carbon Dots as a Novel Approach for Bioimaging Applications in Cancerous Cells. *ACS Appl. Mater. Interfaces* **2018**, *10* (44), 37835-37845.
11. Zhao, H.; Duan, J.; Xiao, Y.; Tang, G.; Wu, C.; Zhang, Y.; Liu, Z.; Xue, W., Microenvironment-Driven Cascaded Responsive Hybrid Carbon Dots as a Multifunctional

Theranostic Nanoplatfrom for Imaging-Traceable Gene Precise Delivery. *Chem. Mater.* **2018**, *30* (10), 3438-3453.

12. Majumdar, B.; Mandani, S.; Bhattacharya, T.; Sarma, D.; Sarma, T. K., Probing Carbocatalytic Activity of Carbon Nanodots for the Synthesis of Biologically Active Dihydro/Spiro/Glyco Quinazolinones and Aza-Michael Adducts. *J. Org. Chem.* **2017**, *82* (4), 2097-2106.

13. Pei, X.; Xiong, D.; Wang, H.; Gao, S.; Zhang, X.; Zhang, S.; Wang, J., Reversible Phase Transfer of Carbon Dots between an Organic Phase and Aqueous Solution Triggered by CO₂. *Angew. Chem. Int. Ed.* **2018**, *57* (14), 3687-3691.

14. Han, Y.; Huang, H.; Zhang, H.; Liu, Y.; Han, X.; Liu, R.; Li, H.; Kang, Z., Carbon Quantum Dots with Photoenhanced Hydrogen-Bond Catalytic Activity in Aldol Condensations. *ACS Catal.* **2014**, *4* (3), 781-787.

15. Filippini, G.; Amato, F.; Rosso, C.; Ragazzon, G.; Vega-Peñaloza, A.; Companyó, X.; Dell'Amico, L.; Bonchio, M.; Prato, M., Mapping the Surface Groups of Amine-Rich Carbon Dots Enables Covalent Catalysis in Aqueous Media. *Chem* **2020**, *6* (11), 3022-3037.

16. Hu, S.; Tian, R.; Wu, L.; Zhao, Q.; Yang, J.; Liu, J.; Cao, S., Chemical regulation of carbon quantum dots from synthesis to photocatalytic activity. *Chem.--Asian J.* **2013**, *8* (5), 1035-41.

17. Yang, P.; Zhao, J.; Wang, J.; Cui, H.; Li, L.; Zhu, Z., Multifunctional Nitrogen-Doped Carbon Nanodots for Photoluminescence, Sensor, and Visible-Light-Induced H₂ Production. *ChemPhysChem* **2015**, *16* (14), 3058-63.

18. Wu, J.; Ma, S.; Sun, J.; Gold, J. I.; Tiwary, C.; Kim, B.; Zhu, L.; Chopra, N.; Odeh, I. N.; Vajtai, R.; Yu, A. Z.; Luo, R.; Lou, J.; Ding, G.; Kenis, P. J.; Ajayan, P. M., A metal-free electrocatalyst for carbon dioxide reduction to multi-carbon hydrocarbons and oxygenates. *Nat Commun* **2016**, *7*, 13869.

19. Cao, L.; Sahu, S.; Anilkumar, P.; Bunker, C. E.; Xu, J.; Fernando, K. A.; Wang, P.; Gulians, E. A.; Tackett, K. N., 2nd; Sun, Y. P., Carbon nanoparticles as visible-light photocatalysts for efficient CO₂ conversion and beyond. *J. Am. Chem. Soc.* **2011**, *133* (13), 4754-7.

20. Li, H.; He, X.; Kang, Z.; Huang, H.; Liu, Y.; Liu, J.; Lian, S.; Tsang, C. H.; Yang, X.; Lee, S. T., Water-soluble fluorescent carbon quantum dots and photocatalyst design. *Angew. Chem. Int. Ed.* **2010**, *49* (26), 4430-4.

21. Martindale, B. C.; Hutton, G. A.; Caputo, C. A.; Reisner, E., Solar hydrogen production using carbon quantum dots and a molecular nickel catalyst. *J. Am. Chem. Soc.* **2015**, *137* (18), 6018-25.
22. Liu, Y.; Zhao, Y.; Wu, Q.; Wang, X.; Nie, H.; Zhou, Y.; Huang, H.; Shao, M.; Liu, Y.; Kang, Z., Charge storage of carbon dot enhances photo-production of H₂ and H₂O₂ over Ni₂P/carbon dot catalyst under normal pressure. *Chem. Eng. J.* **2021**, *409*, 128184.
23. Zhou, Z.; Tian, P.; Liu, X.; Mei, S.; Zhou, D.; Li, D.; Jing, P.; Zhang, W.; Guo, R.; Qu, S.; Rogach, A. L., Hydrogen Peroxide-Treated Carbon Dot Phosphor with a Bathochromic-Shifted, Aggregation-Enhanced Emission for Light-Emitting Devices and Visible Light Communication. *Adv. Sci.* **2018**, *5* (8), 1800369.
24. Li, S.; Ji, K.; Zhang, M.; He, C.; Wang, J.; Li, Z., Boosting the photocatalytic CO₂ reduction of metal-organic frameworks by encapsulating carbon dots. *Nanoscale* **2020**, *12* (17), 9533-9540.
25. Schultz, D. M.; Yoon, T. P., Solar synthesis: prospects in visible light photocatalysis. *Science* **2014**, *343* (6174), 1239176.
26. Prier, C. K.; Rankic, D. A.; MacMillan, D. W., Visible light photoredox catalysis with transition metal complexes: applications in organic synthesis. *Chem. Rev.* **2013**, *113* (7), 5322-63.
27. Marzo, L.; Pagire, S. K.; Reiser, O.; König, B., Visible-Light Photocatalysis: Does It Make a Difference in Organic Synthesis? *Angew. Chem. Int. Ed.* **2018**, *57* (32), 10034-10072.
28. Surface-Binding Forms of Carboxylic Groups on Nanoparticulate TiO₂ Surface Studied by the Interface-Sensitive Transient Triplet-State Molecular Probe. *J. Phys. Chem. B* **2003**, 4356-4363.
29. Agrawal, S.; English, N. J.; Thampi, K. R.; MacElroy, J. M., Perspectives on ab initio molecular simulation of excited-state properties of organic dye molecules in dye-sensitised solar cells. *Phys. Chem. Chem. Phys.* **2012**, *14* (35), 12044-56.
30. Xu, L.; Bai, X.; Guo, L.; Yang, S.; Jin, P.; Yang, L., Facial fabrication of carbon quantum dots (CDs)-modified N-TiO_{2-x} nanocomposite for the efficient photoreduction of Cr(VI) under visible light. *Chem. Eng. J.* **2019**, *357*, 473-486.
31. Shi, R.; Li, Z.; Yu, H.; Shang, L.; Zhou, C.; Waterhouse, G. I. N.; Wu, L. Z.; Zhang, T., Effect of Nitrogen Doping Level on the Performance of N-Doped Carbon Quantum

Dot/TiO₂ Composites for Photocatalytic Hydrogen Evolution. *ChemSusChem* **2017**, *10* (22), 4650-4656.

32. Zhang, J.; Zhang, X.; Dong, S.; Zhou, X.; Dong, S., N-doped carbon quantum dots/TiO₂ hybrid composites with enhanced visible light driven photocatalytic activity toward dye wastewater degradation and mechanism insight. *J. Photochem. Photobiol.* **2016**, *325*, 104-110.

33. Facile microwave assisted synthesis of N-rich carbon quantum dots/dualphase TiO₂ heterostructured nanocomposites with high activity in CO₂ photoreduction. *Appl. Catal. B.* **2018**, *231*, 269–276.

34. Zhu, C.; Yue, H.; Jia, J.; Rueping, M., Nickel-Catalyzed C-Heteroatom Cross-Coupling Reactions under Mild Conditions via Facilitated Reductive Elimination. *Angew. Chem. Int. Ed.* **2021**, *60* (33), 17810-17831.

35. Lan, G.; Quan, Y.; Wang, M.; Nash, G. T.; You, E.; Song, Y.; Veroneau, S. S.; Jiang, X.; Lin, W., Metal–Organic Layers as Multifunctional Two-Dimensional Nanomaterials for Enhanced Photoredox Catalysis. *J. Am. Chem. Soc.* **2019**, *141* (40), 15767-15772.

36. Zhu, Y.-Y.; Lan, G.; Fan, Y.; Veroneau, S. S.; Song, Y.; Micheroni, D.; Lin, W., Merging Photoredox and Organometallic Catalysts in a Metal–Organic Framework Significantly Boosts Photocatalytic Activities. *Angew. Chem. Int. Ed.* **2018**, *57* (43), 14090-14094.

37. Pan, Y.; Zhang, N.; Liu, C.-H.; Fan, S.; Guo, S.; Zhang, Z.-M.; Zhu, Y.-Y., Boosting Photocatalytic Activities for Organic Transformations through Merging Photocatalyst and Transition-Metal Catalyst in Flexible Polymers. *ACS Catal.* **2020**, *10* (20), 11758-11767.

38. Franchi, D.; Amara, Z., Applications of Sensitized Semiconductors as Heterogeneous Visible-Light Photocatalysts in Organic Synthesis. *ACS Sustain. Chem. Eng.* **2020**, *8* (41), 15405-15429.

39. Gisbertz, S.; Pieber, B., Heterogeneous Photocatalysis in Organic Synthesis. *ChemPhotoChem* **2020**, *4* (7), 456-475.

40. Reischauer, S.; Strauss, V.; Pieber, B., Modular, Self-Assembling Metallaphotocatalyst for Cross-Couplings Using the Full Visible-Light Spectrum. *ACS Catal.* **2020**, *10* (22), 13269-13274.

41. Hill, S.; Galan, M. C., Fluorescent carbon dots from mono- and polysaccharides: synthesis, properties and applications. *Beilstein J. Org. Chem.* **2017**, *13*, 675-693.

42. Hill, S. A.; Benito-Alifonso, D.; Davis, S. A.; Morgan, D. J.; Berry, M.; Galan, M. C., Practical Three-Minute Synthesis of Acid-Coated Fluorescent Carbon Dots with Tuneable Core Structure. *Sci Rep* **2018**, 8 (1), 12234.
43. Hill, S. A.; Benito-Alifonso, D.; Morgan, D. J.; Davis, S. A.; Berry, M.; Galan, M. C., Three-minute synthesis of sp³ nanocrystalline carbon dots as non-toxic fluorescent platforms for intracellular delivery. *Nanoscale* **2016**, 8 (44), 18630-18634.
44. Pieber, B.; Malik, J. A.; Cavedon, C.; Gisbertz, S.; Savateev, A.; Cruz, D.; Heil, T.; Zhang, G.; Seeberger, P. H., Semi-heterogeneous Dual Nickel/Photocatalysis using Carbon Nitrides: Esterification of Carboxylic Acids with Aryl Halides. *Angew. Chem. Int. Ed.* **2019**, 58 (28), 9575-9580.
45. U. Kriiger and R. Memming, *Ber. Bunsenges. Phys. Chem.*, **1974**, 78, 670.
46. Zheng, Q.; Lavis, L. D., Development of photostable fluorophores for molecular imaging. *Curr. Opin. Chem. Biol.* **2017**, 39, 32-38.
47. Overcoming limitations in dual photoredox/ nickel-catalysed C–N cross-couplings due to catalyst deactivation. *Nat. Catal.* **2020**, 3, 611–620.
48. Hill, S. A.; Sheikh, S.; Zhang, Q.; Sueiro Ballesteros, L.; Herman, A.; Davis, S. A.; Morgan, D. J.; Berry, M.; Benito-Alifonso, D.; Galan, M. C., Selective photothermal killing of cancer cells using LED-activated nucleus targeting fluorescent carbon dots. *Nano. Adv.* **2019**, 1 (8), 2840-2846.
49. Li, L.; Dong, T., Photoluminescence tuning in carbon dots: surface passivation or/and functionalization, heteroatom doping. *J. Mat. Chem. C* **2018**, 6 (30), 7944-7970.

Chapter 8

Discussion & Outlook

8.1 Discussion of the individual works

Light has a high potential to serve as a sustainable energy source for chemical reactions. Visible-light photocatalysis has become a powerful strategy for organic synthesis. In particular, the merger of photo- and transition metal catalysis (metallaphotocatalysis) has emerged as an attractive concept to achieve carbon–carbon and carbon–heteroatom bond formations under mild conditions. In contrast to conventional cross coupling reactions, abundant metals like nickel can be utilized for bond formations using that strategy. Key to success are photoredox or photosensitization events between a nickel complex and a photocatalyst. These reactions are mainly studied using homogeneous iridium- or ruthenium polypyridyl complexes as photocatalysts, which are not recyclable, expensive and are limited to short excitation wavelengths. Only a few tailored organic dyes are available as alternatives, but have limited applicability.

During my doctoral studies, I developed sustainable approaches for photochemistry using recyclable, heterogeneous semiconductors. Specifically, I studied their application as photocatalysts for metallaphotocatalysis and investigated a wavelength dependent activation of semiconductors to control the selectivity in organic reactions. Further, I surveyed approaches in photocatalysis that enable the use of long wavelengths, show the importance of the intensity of photons, substitute strong reductants, and benefit from technological advances (*iScience* **2021**, 24, 102209 - Chapter 2).¹

8.1.1 Semi-heterogeneous dual nickel/photocatalytic C–N cross-couplings using graphitic carbon nitrides (Chapter 3)

Light is more than just a traceless, sustainable reagent. The energy and intensity of photons are overlooked parameters that can be used to tune the activity of photocatalysts. This was used to overcome substrate scope limitations and reproducibility issues in the metallaphotocatalytic C–N cross coupling of amines and electron rich aryl halides (Figure 8.2) (*Nature Catal.* **2020**, *3*, 611-620 - Chapter 3).²

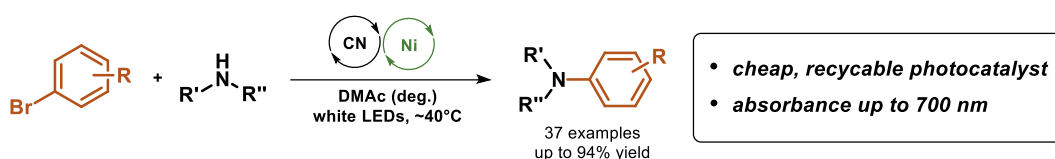


Figure 8.1. Semi-heterogeneous amination with carbon nitride and nickel catalysis

We identified that this limitation is a result of catalyst deactivation *via* the formation of nickel black. Together with my colleagues, I realized that this results from the accumulation of low valent nickel species due to slow oxidative addition of electron rich aryl halides (Figure 8.3). We assumed that productive catalysis requires that the relative rate of oxidative addition (OA) needs to be equal or higher than the rate of reductive elimination (RE). Using the graphitic carbon nitride CN-OA-m that absorbs longer wavelengths than most common photocatalysts, the rate of reductive elimination could be reduced using photons with low energy (green light). This was sufficient to avoid catalyst deactivation in certain cases. More energetic photons (blue light) could be used by increasing the rate of oxidative addition using high substrate concentrations, and by stabilizing the low valent nickel intermediate with a suitable additive.

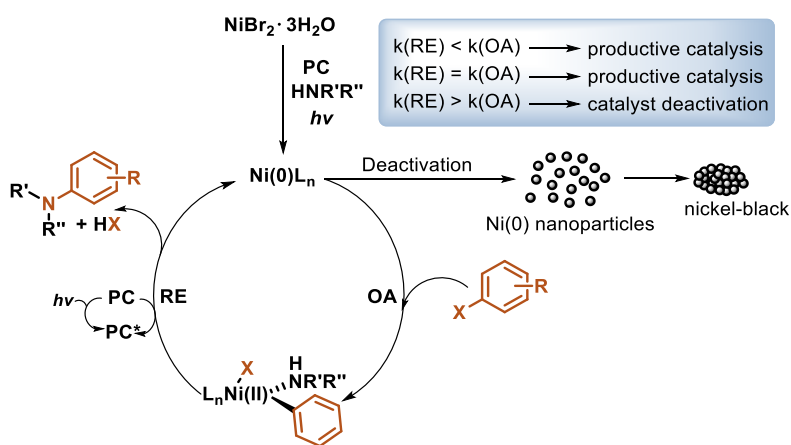


Figure 8.2. Wavelength-dependent control of the reaction rate. Overcoming limitations in metallaphotocatalysis using carbon nitride photocatalysis.

8.1.2 Chromoselective photocatalysis merged with biocatalysis (Chapter 4)

The wavelength dependent reactivity of CN-OA-m in the example described in Chapter 3 was initially rationalized by a purely kinetic effect (lower absorbance at long wavelengths results in low reaction rates). My alternative hypothesis was that different wavelengths induce different transitions in the semiconducting material, which eventually results in different redox potentials. I could indeed show that it is possible to generate electron holes with different oxidation potentials in the same material depending on the wavelength. Blue light induces π - π^* transitions that generate a strongly oxidizing species, whereas green light irradiation results exclusively in n - π^* transitions that generate a weaker oxidant. This was key to design photo-chemo-enzymatic cascade reactions that enable the selective synthesis of the (*S*)- or the (*R*)-enantiomer of phenylethanol from ethylbenzene (Figure 8.4) (*Angew. Chem. Int. Ed.* **2021**, 60, 6965-6969 - Chapter 4).³ Green light irradiation of CN-OA-m was used to form hydrogen peroxide, which was used by an unspecific peroxygenase from *Agroclybe aegerita*, for the enantioselective hydroxylation of ethylbenzene to (*R*)-1-phenylethan-1-ol (99% ee). Blue light irradiation triggered the photocatalytic oxidation of ethylbenzene to acetophenone, which was enantioselectively reduced with an alcohol dehydrogenase from *Rhodococcus ruber* to form (*S*)-1-phenylethan-1-ol (93% ee).

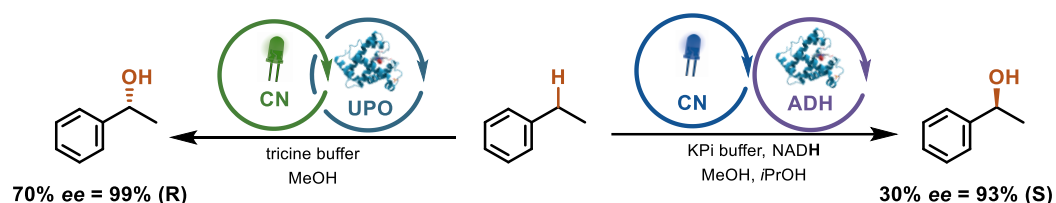


Figure 8.3. Accessing different photocatalytic activities by controlling the energy of photons. Chromoselective photo-chemo-enzymatic cascade reactions with a carbon nitride photocatalyst.

8.1.3 Dye-sensitized metallaphotocatalysts (Chapter 5-7)

In contrast to common photocatalysts that can be only excited using short wavelengths, abundant organic dyes absorb broadly across the entire visible-light spectrum. Methods that enable the use of such dyes as photocatalysts could be key for efficient solar harvesting in organic synthesis. This would improve the scalability and could tackle selectivity issues.

Unfortunately, most organic dyes only reach singlet excited-states with short lifetimes that hamper the activation of a substrate, reagent or co-catalyst in solution due to the limiting rate of diffusion. Inspired by dye-sensitized solar cells, I developed an approach to use excited singlet states of dyes for light-mediated cross-coupling reactions (*ACS Catal.*, **2020**, 10, 13269-13274 - Chapter 5).⁴ Key to success was the immobilization of a nickel complex and a dye on the semiconductor surface (Figure 8.5). Upon excitation, the dye can transfer electrons to the heterogeneous semiconductor, resulting in a charge-separated species that fuels the attached nickel complex to induce the desired couplings. This modular approach accesses the entire visible light spectrum and allows to strategically tackle selectivity issues resulting from short wavelengths.

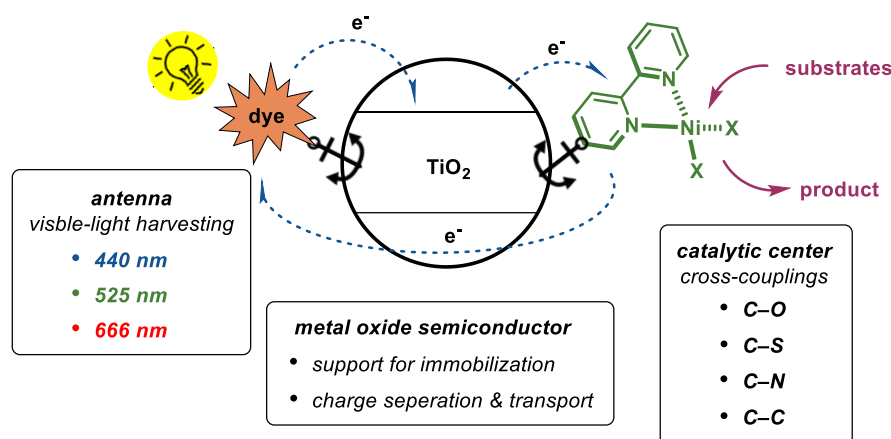


Figure 8.4. Modular, self-assembling metallaphotocatalyst for cross couplings using the full visible-light spectrum.

However, recycling studies showed a gradual decrease of the yield due to leaching of the nickel catalyst and the dye. This was rationalized by the weak interaction between the carboxylic acid anchoring groups and titanium dioxide. This was overcome by permanently immobilizing nickel complexes on the surface of a heterogeneous semiconductor through phosphonic acid anchors (Figure 8.6) (*ChemPhotoChem*, **2021**, 5, 716-720 - Chapter 6).⁵ The optimized, recyclable catalyst requires a nickel loading of only ~0.1 mol% for selective C–S cross couplings.

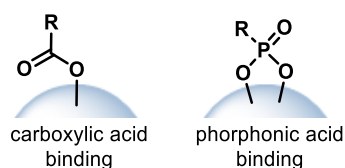


Figure 8.5. Binding modes of carboxylic and phosphonic acid on semiconductor surface

A drawback of organic dyes is photobleaching. To address this issue, I developed an alternative approach by immobilizing carbon dots on titanium dioxide in a collaborative effort with experts in carbohydrate-based materials (Figure 8.7). (*Green Chem.*, **2021**, 23, 4524-4530 Chapter 7).⁶

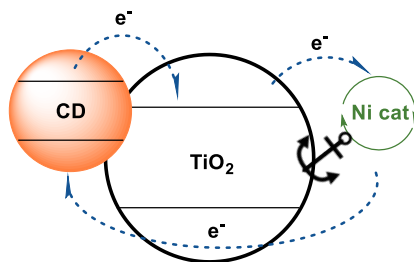


Figure 8.6. Carbon dot/titanium dioxide nanocomposites as photocatalysts for metallaphotocatalytic carbon-heteroatom cross-couplings.

8.2 Outlook

The combination of photo- and nickel catalysis emerged as an alternative to palladium catalysis for cross-couplings. However, the photocatalysts typically used in dual nickel/photoredox catalysis are homogeneous noble metal based complexes rendering the sustainability of these protocols low. In the first part of my thesis I showed, that these photocatalyst can be replaced by a recyclable heterogeneous carbon nitride semiconductor. The main drawback of this system was dependence on a homogenous nickel catalyst that is not recyclable. I developed a modular, self-assembling catalyst system for cross-coupling reactions, which was inspired by dye-sensitized solar cells. By studying different functionalities and organic dyes, I showed that these bifunctional photocatalysts for light-mediated nickel catalyzed cross-couplings are recyclable and absorb across the entire visible-light spectrum. The results of these studies led to the next generation of light mediated nickel catalysis currently investigated in our group.⁷ By decorating a nickel bipyridine complex with carbazole groups, a nickel complex that does not require an exogenous photocatalyst was developed. A recyclable variant of that homogenous photocatalyst was obtained by developing a polymeric ligand that induces light-mediated carbon–heteroatom cross-couplings. This concept is promising towards sustainable light-mediated cross-coupling reactions, but still suffers from various drawbacks, such as low catalytic activity for aryl bromides and no catalytic activity in carbon–carbon bond formations.

I envision that modifications of the carbazole substituent will allow tuning of the electrochemical properties and thereby broaden the scope and the applicability of this approach. I showed in several projects that the wavelength is an often overlooked parameter in light mediated synthesis that bears a lot of potentials. Systematic structure–activity studies will lead to better light-harvesting properties of these catalysts to improve the scalability, selectivity and reproducibility of these new class of nickel catalysts.

8.3 Graphical summary of this thesis & outlook

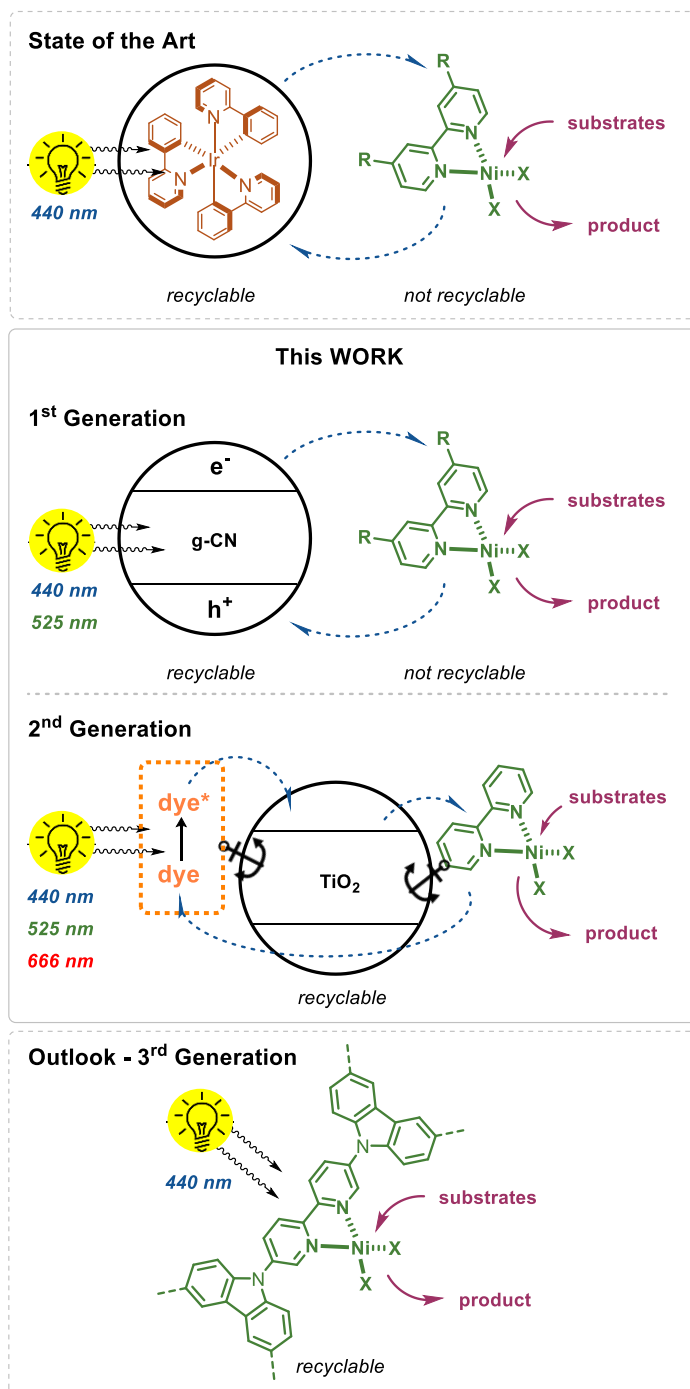


Figure 8.7. Graphical summary of this thesis and outlook.

8.4 References

1. Reischauer, S.; Pieber, B., Emerging concepts in photocatalytic organic synthesis. *iScience* **2021**, *24* (3), 102209.
2. Gisbertz, S.; Reischauer, S.; Pieber, B., Overcoming limitations in dual photoredox/nickel-catalysed C–N cross-couplings due to catalyst deactivation. *Nat. Catal.* **2020**, *3* (8), 611-620.
3. Schmermund, L.; Reischauer, S.; Bierbaumer, S.; Winkler, C. K.; Diaz-Rodriguez, A.; Edwards, L. J.; Kara, S.; Mielke, T.; Cartwright, J.; Grogan, G.; Pieber, B.; Kroutil, W., Chromoselective Photocatalysis Enables Stereocomplementary Biocatalytic Pathways. *Angew. Chem. Int. Ed.* **2021**, *60*, 6965-6969.
4. Reischauer, S.; Strauss, V.; Pieber, B., Modular, Self-Assembling Metallaphotocatalyst for Cross-Couplings Using the Full Visible-Light Spectrum. *ACS Catal.* **2020**, *10* (22), 13269-13274.
5. Reischauer, S.; Pieber, B., Recyclable, Bifunctional Metallaphotocatalysts for C–S Cross-Coupling Reactions. *ChemPhotoChem* **2021**, *5* (8), 716-720.
6. Zhao, Z.; Reischauer, S.; Pieber, B.; Delbianco, M., Carbon dot/TiO₂ nanocomposites as photocatalysts for metallaphotocatalytic carbon–heteroatom cross-couplings. *Green Chem.* **2021**, *23* (12), 4524-4530.
7. Cavedon, C.*; Gisbertz, S.*; Vogl, S.; Richter, N.; Schrottke, S.; Teutloff, C.; Seeberger, P. H.; Thomas, A.; Pieber, B. *ChemRxiv. Preprint*. August 4, **2021**.

Supporting Information - Chapter 3

Overcoming Limitations in Dual Photoredox/Nickel catalyzed C–N Cross-Couplings due to Catalyst Deactivation

Gisbertz, S.; **Reischauer, S.**; Pieber, B.

Nat. Catal. **2020**, *3*, 611-620.

<https://doi.org/10.1038/s41929-020-0473-6>

3.5 Supporting information

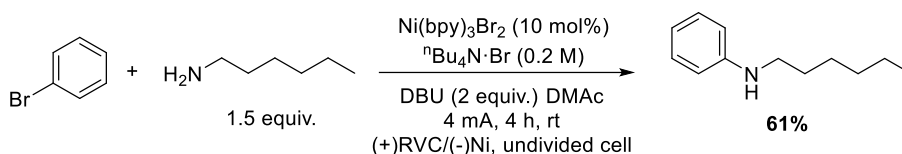
3.5.1 General remarks

Substrates, reagents, and solvents were purchased from commercial suppliers and used without further purification. Methyl 4-(trifluoromethylsulfonyloxy)benzoate,¹ methyl 4-(tosyloxy)benzoate², methyl 4-((methylsulfonyl)oxy)benzoate³ and *N-tert*-butylisopropylamine (BIPA)⁴ were prepared according to literature procedures. ¹H-, ¹³C- and ¹⁹F-NMR spectra were obtained using a Varian 400 spectrometer (400 MHz, Agilent), an Ascend™ 400 spectrometer (400 MHz, cryoprobe, Bruker) and a Varian 600 spectrometer (600 MHz, Agilent) at 298 K, and are reported in ppm relative to the residual solvent peaks. Peaks are reported as: s = singlet, d = doublet, t = triplet, q = quartet, m = multiplet or unresolved, with coupling constants in Hz. Analytical thin layer chromatography (TLC) was performed on pre-coated TLC-sheets, ALUGRAM Xtra SIL G/UV₂₅₄ sheets (Macherey-Nagel) and visualized with 254 nm light or staining solutions followed by heating. Purification of final compounds was carried out by flash chromatography on the Reveleris X2 Flash Chromatography System from GRACE using prepacked columns with 40 μm silica gel. Silica 60 M (0.04-0.063 mm) silica gel (Sigma Aldrich) was used for dry loading of the crude compounds on the flash chromatography system. Centrifugation was carried out using an Eppendorf 5430 centrifuge. High-resolution mass spectral data were obtained using a HR-EI-MS (Waters Autospec Premier) and a Waters XEVO G2-XS 4K spectrometer with the XEVO G2-XS QTOF capability kit. Emission spectra of LED lamps were recorded using 10 in. (24.5 cm) integrating sphere (Labsphere, Inc. Model LMS 1050) equipped with a diode array detector (International Light, Model RPS900). The UV/Vis spectrum of Ir(ppy)₂(dtbbpy)PF₆ was recorded using a UVmini-1240 spectrometer (Shimadzu). Inductively coupled plasma - optical emission spectrometry (ICP-OES) was carried out using a Horiba Ultra 2 instrument equipped with photomultiplier tube detection. FTIR spectra were recorded on a Thermo Scientific Nicolet iD5 spectrometer. Diffuse reflectance UV/Vis spectra of powders were recorded on a Shimadzu UV-2600 spectrometer equipped with an integrating sphere. For XRD measurements, a Bruker D8 Advanced X-ray diffractometer with Cu Kα radiation was used. Scanning electron microscopy (SEM) images were obtained on a LEO 1550-Gemini microscope. Energy-dispersive X-ray (EDX) investigations were conducted on a Link ISIS-300 system (Oxford Microanalysis Group)

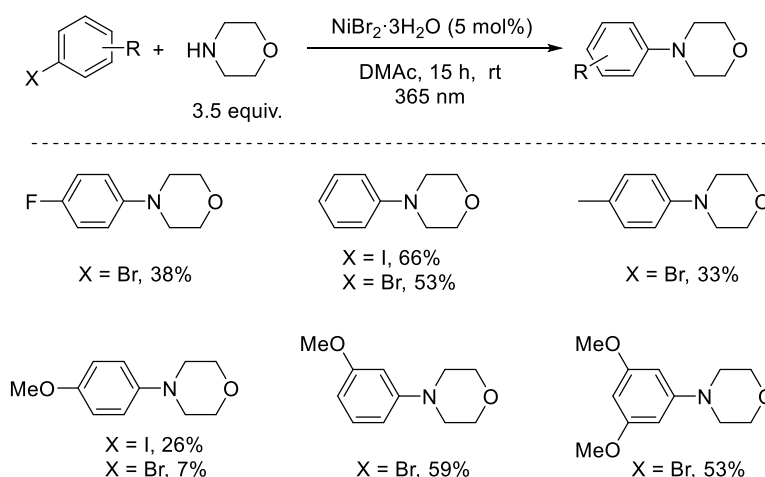
equipped with a Si(Li) detector and an energy resolution of 133 eV. X-ray photoelectron spectroscopic (XPS) measurements were carried out with a CISSY set-up, equipped with a SPECS XR 50 X-ray gun with Mg K α excitation radiation (1254.6 eV) and combined with a lens analyzer module (CLAM) under ultra-high vacuum (UHV, 1.5×10^{-8} Pa). The calibration was performed using the Au 4f $_{7/2}$ (84.0 eV) binding energy scale as reference. Quantitative analysis and deconvolution were achieved using “peakfit” and “Igor” software with Lorentzian-Gaussian functions and Shirley background deletion in photoemission spectra. The STEM images were acquired using a double-corrected Jeol ARM200F, equipped with a cold field emission gun. For the investigation, the acceleration voltage was set to 200 kV, the emission was put to 5 μ A and a condenser aperture with a diameter of 20 μ m was used. With these settings, the microscope reaches a lattice resolution below 1 Å. The STEM specimens were prepared by dissolving a powder sample of the material in ethanol, sonicating the solution for 15 minutes and finally dropping a few drops onto a copper TEM grid coated with holey carbon film. Once the solution had dried off, the specimens were investigated.

3.5.2 Literature analysis: aryl halides without electron withdrawing groups

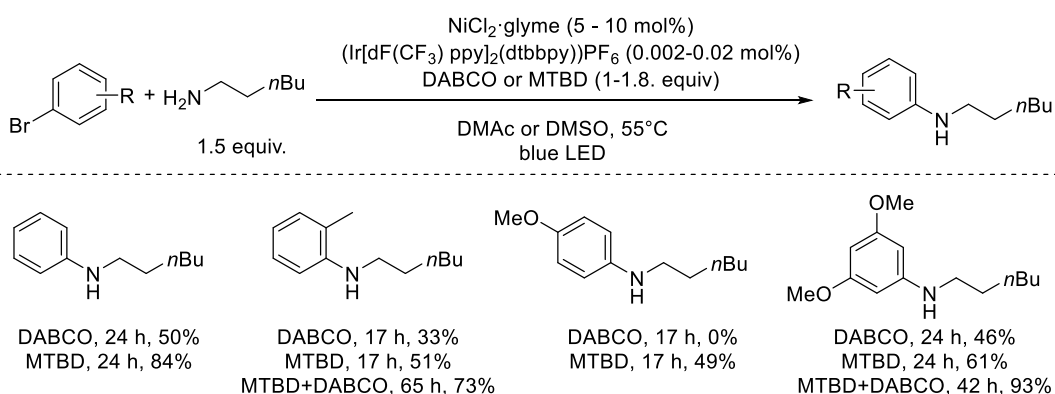
a) Electrochemically driven, Ni-catalyzed amination⁵



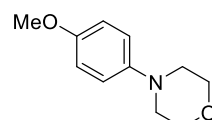
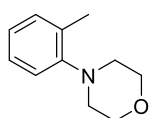
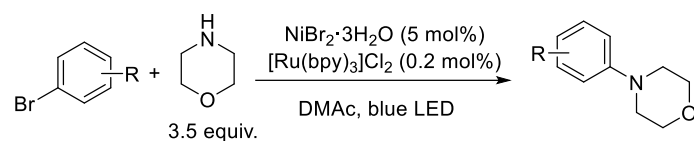
b) UV-light mediated, Ni-catalyzed amination⁶



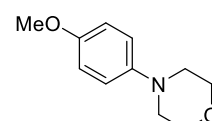
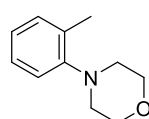
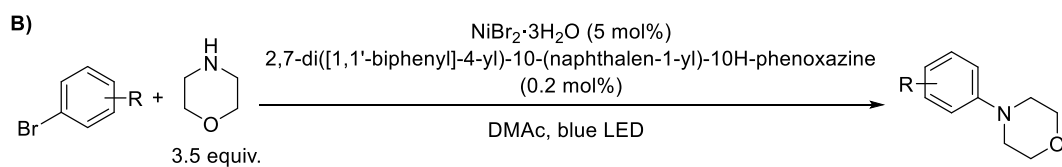
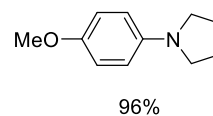
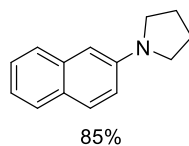
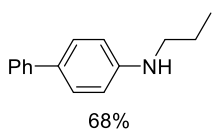
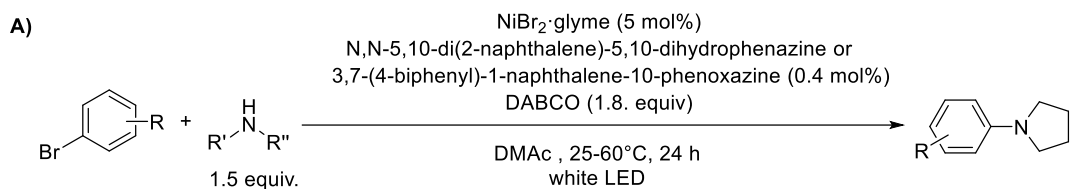
c) Dual nickel/photo catalyzed amination using $(\text{Ir}[\text{dF}(\text{CF}_3)\text{ppy}]_2(\text{dtbbpy}))\text{PF}_6$ ⁷

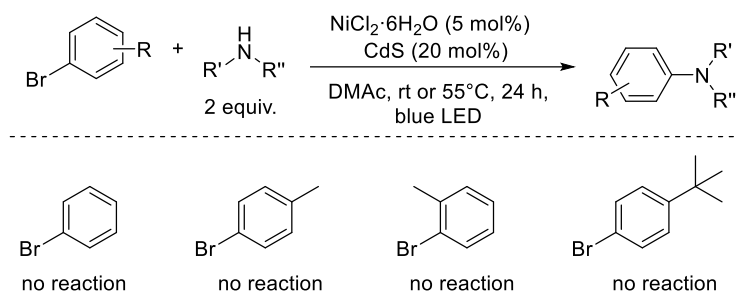
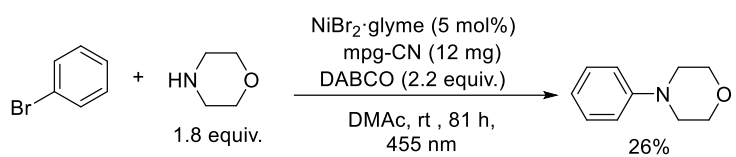


d) Dual nickel/photo catalyzed amination using [Ru(ppy)₃]Cl₂⁸

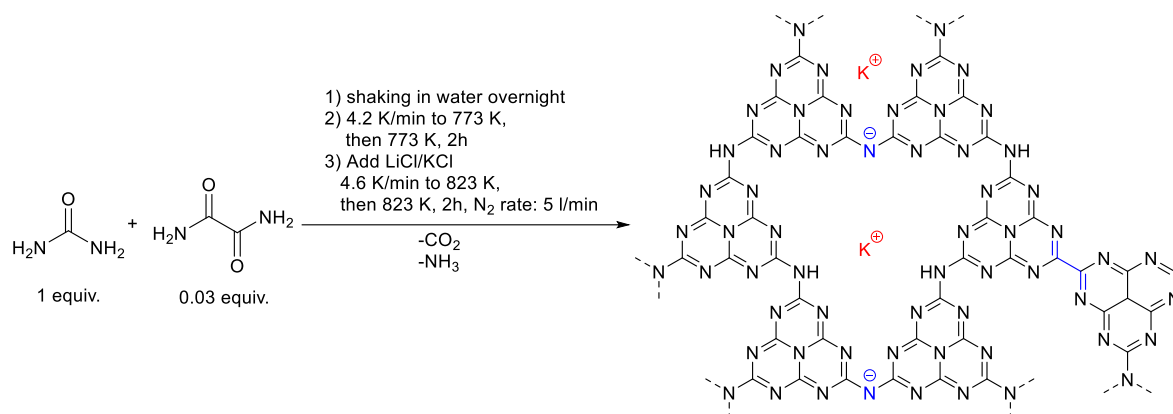


e) Dual nickel/photoredox catalyzed amination using organic dyes⁸⁻⁹



f) Dual nickel/photoredox catalyzed amination using CdS¹⁰g) Dual nickel/photoredox catalyzed amination using mpg-CN¹¹

3.5.3 Preparation of CN-OA-m



Scheme S3.1. Synthesis of CN-OA-m.

The synthesis for CN-OA-m was carried out using a slightly adapted version of the literature procedure (Scheme 3.1)¹²: For each batch of the photocatalyst, urea (10 g, 166.5 mmol) and oxamide (0.5 g, 5.7 mmol) were mixed in 10 ml of DI water to generate a homogeneous mixture. After drying at 373 K, the resulting solids were grinded, transferred into a crucible with a cover and heated up in an air-oven with a heating rate of 4.3 K/min to 773 K. After keeping the mixture for 2h at 773 K, the sample was allowed to cool to room temperature. Subsequently, KCl (3.3 g, 44.3 mmol) and LiCl (2.7 g, 63.7 mmol) were added and the solids were grinded to obtain a homogeneous mixture which was heated in an inert atmosphere (N₂ flow: 5 mL/min) to 823 K with a heating rate of 4.6 K/min. After keeping the mixture for 2 h at 823 K, the sample was allowed to cool to room temperature and the resulting solids were collected on a filter paper and washed with H₂O (3 x 100 mL). The resulting yellow material was dried at 373 K (average yield per batch: ~425 mg). All analytical data (FTIR, UV/Vis, XRD, SEM, etc.; see Section 3.4.8) are in full agreement with those published in the literature.¹²

The UV/Vis spectrum of CN-OA-m shows a strong absorption up to ~460 nm and a comparably weaker absorption band up to ~700 nm (Figure S3.1, A) which are attributed to the π - π^* electron transition of the sp^2 hybridization of C and N in the heptazine framework and n - π^* electron transition involving the lone pairs of the edge nitrogen atoms in the heptazine units, respectively.¹² The capability of harvesting low energy light is therefore superior compared to Ir and Ru photocatalysts (see Figure S3.1, B for the UV/Vis spectrum of Ir[dF(CF₃)ppy]₂(dtbbpy)PF₆ as a representative example) which have only a low

absorption band between 400 and 500 nm in the visible region, which corresponds to the metal-to-ligand charge transfer transition.

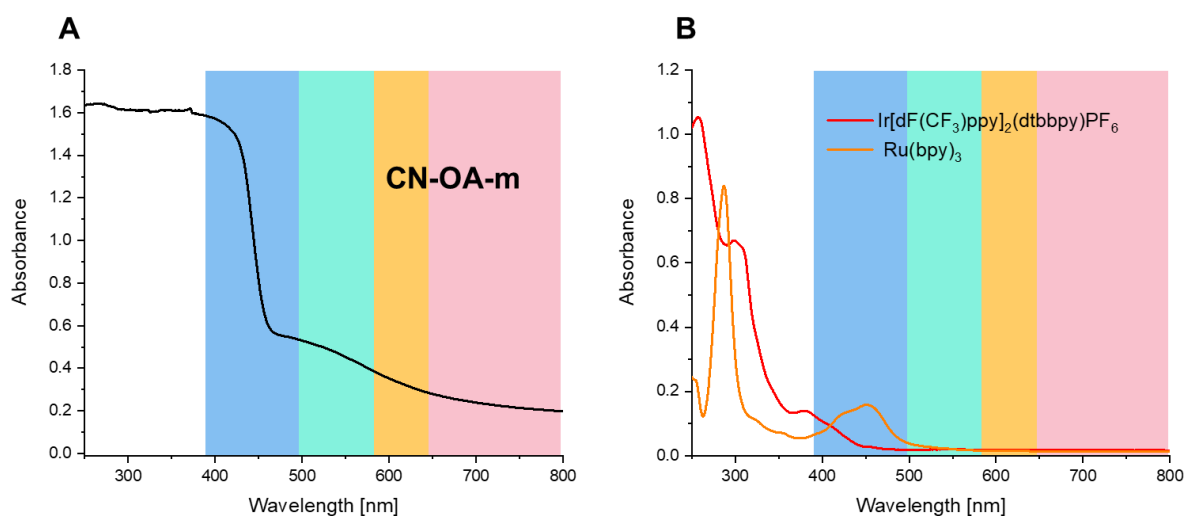


Figure S3.1. UV/VIS-absorption spectra of CN-OA-m (A) and Ir[dF(CF₃)ppy]₂(dtbbpy)PF₆ (B).

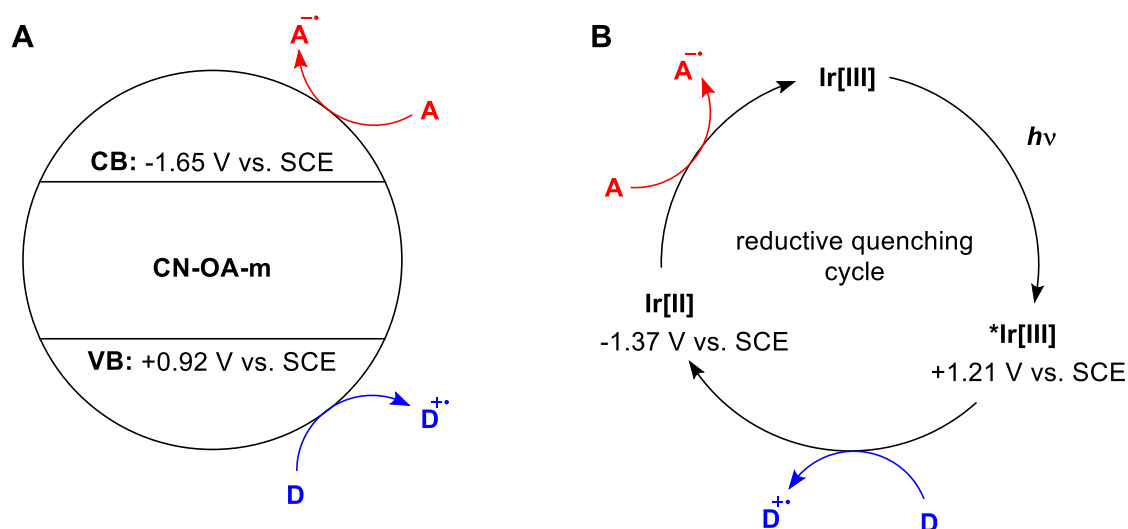


Figure S3.2. Comparison of the photoredox properties of CN-OA-m (A) and Ir[dF(CF₃)ppy]₂(dtbbpy)PF₆ (=Ir[III]) during an reductive quenching cycle (B). The photoredox properties of CN-OA-m were originally measured against Ag/AgCl¹² and were converted for better comparison. The half-reaction reduction potential for the oxidation of representative Ni[II] to Ni[III] complexes was, to the best of our knowledge not reported. For bpy(Ni(II)(Mes)OMe), however, $E_{\text{red}}^{1/2}$ was determined to be +0.71 V vs Ag/AgCl (0.67 V vs. SCE),¹³ which is thermodynamically feasible for both photocatalysts. It has to be noted that the reaction might also be triggered by energy transfer instead of than single transfer.

3.5.4 Setup for photochemical reactions

A flexible, red/green/blue LED strip¹⁴ (RGB, 5m, 24 W/strip; Tween Light, BAHAG AG, Germany) was wrapped around a 115 mm borosilicate crystallization dish (Figure S3.3, A). Blue, green, red or white (illumination of all three LED colors - red/green/blue) light was used at full power for all experiments (For emission spectra of a single diode, see Figure S3.4). The evaporating dish was filled with ethylene glycol and the temperature was set to 40°C to maintain a constant temperature. The sealed, cylindrical reaction vessels (16 x 100 mm) were placed at the same distance from the LED strip during all experiments (Figure S3.3, A). All reactions were performed with a stirring speed of 600 (1 mL) or 1400 rpm (3 or 6 mL). For large scale aminations a flexible, red/green/blue LED strip (RGB, 5m, 24 W/strip; Tween Light, BAHAG AG, Germany) was wrapped around a 115mm borosilicate beaker (Figure S3.3, B). The scale-up reaction was performed in a sealed, cylindrical reaction vessel (25 x 140 mm) with a stirring speed of 700 rpm and without additional heating (Figure S3.3, B).

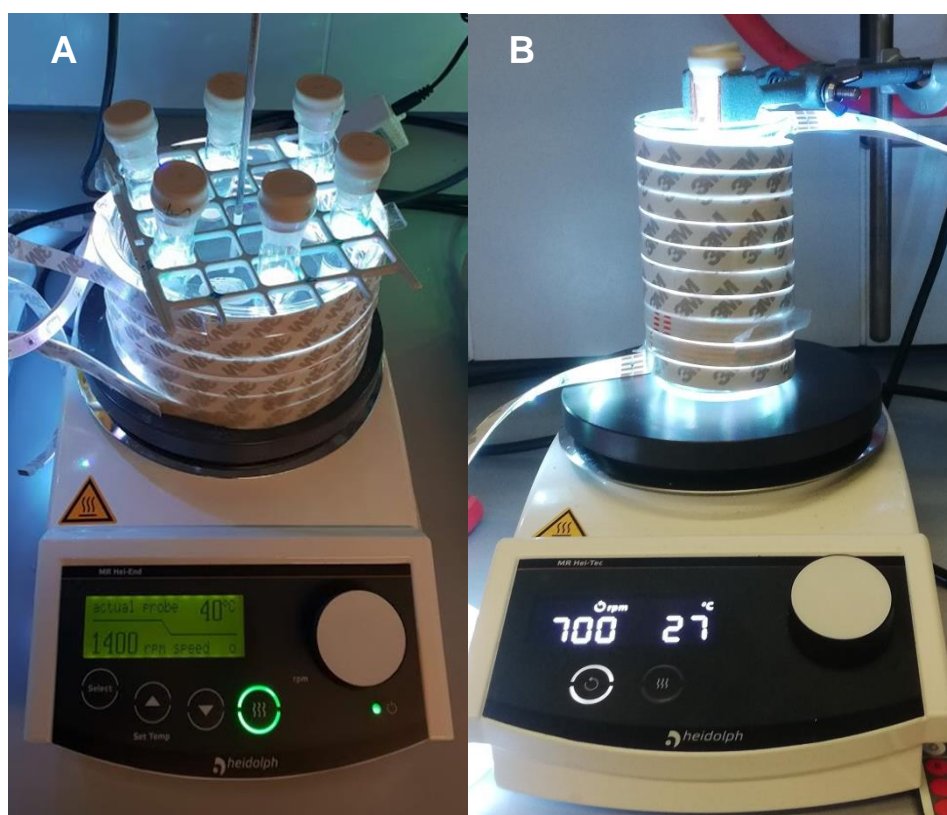


Figure S3.3. Experimental setup for general photochemical reactions (A) and for the scale-up reaction (B).

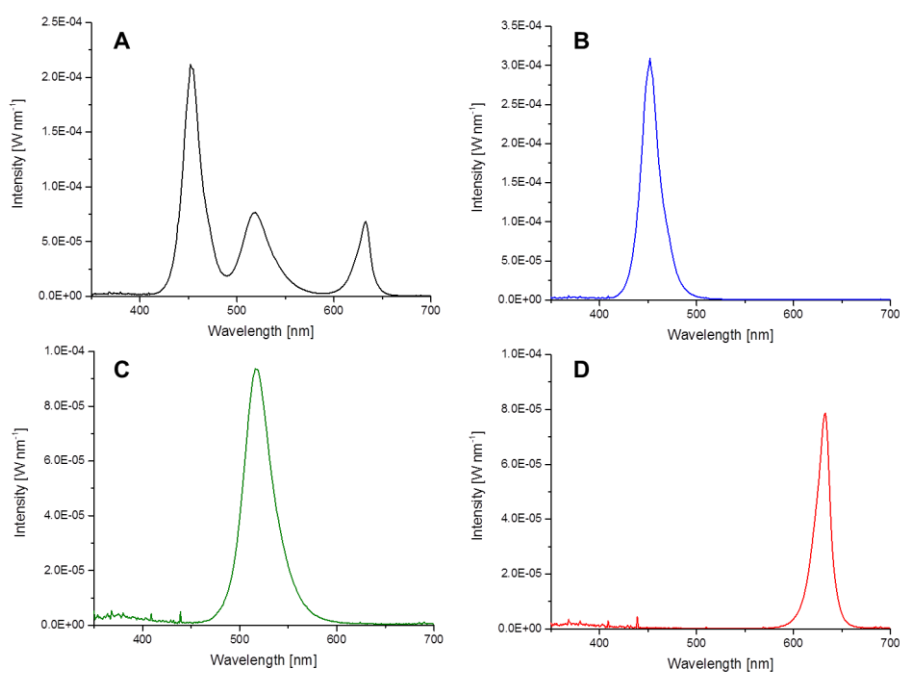


Figure S3.4. Emission spectra of the LED strips used for photochemical reactions. All experiments were carried out at maximum power. **A:** white light (RGB). **B:** blue light only. **C:** green light only. **D:** red light only.

A Kessil[®] PR 160-370nm lamp,¹⁵ a stir plate and a fan for cooling was used for UV-light experiments (Figure S3.5, A). All experiments were carried out with maximum lamp power. The sealed reaction vessels (16 x 100 mm) were placed at the same distance (4 cm) from the light source during all experiments. All reactions were performed with vigorous stirring.

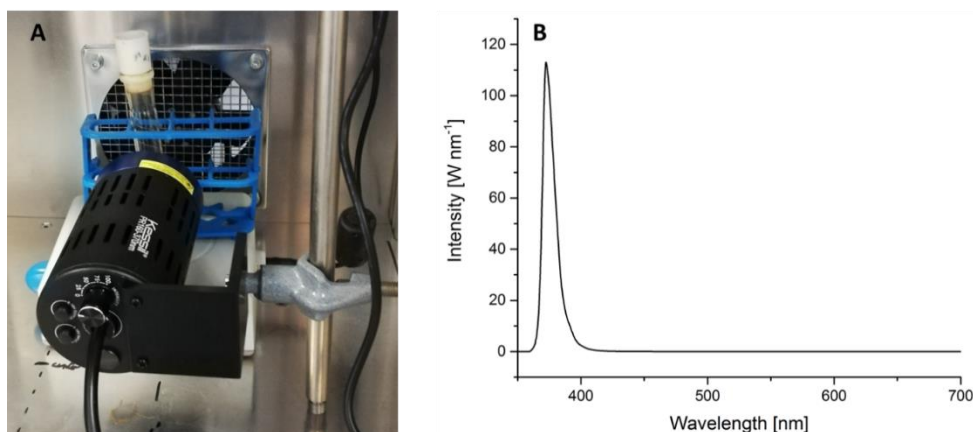
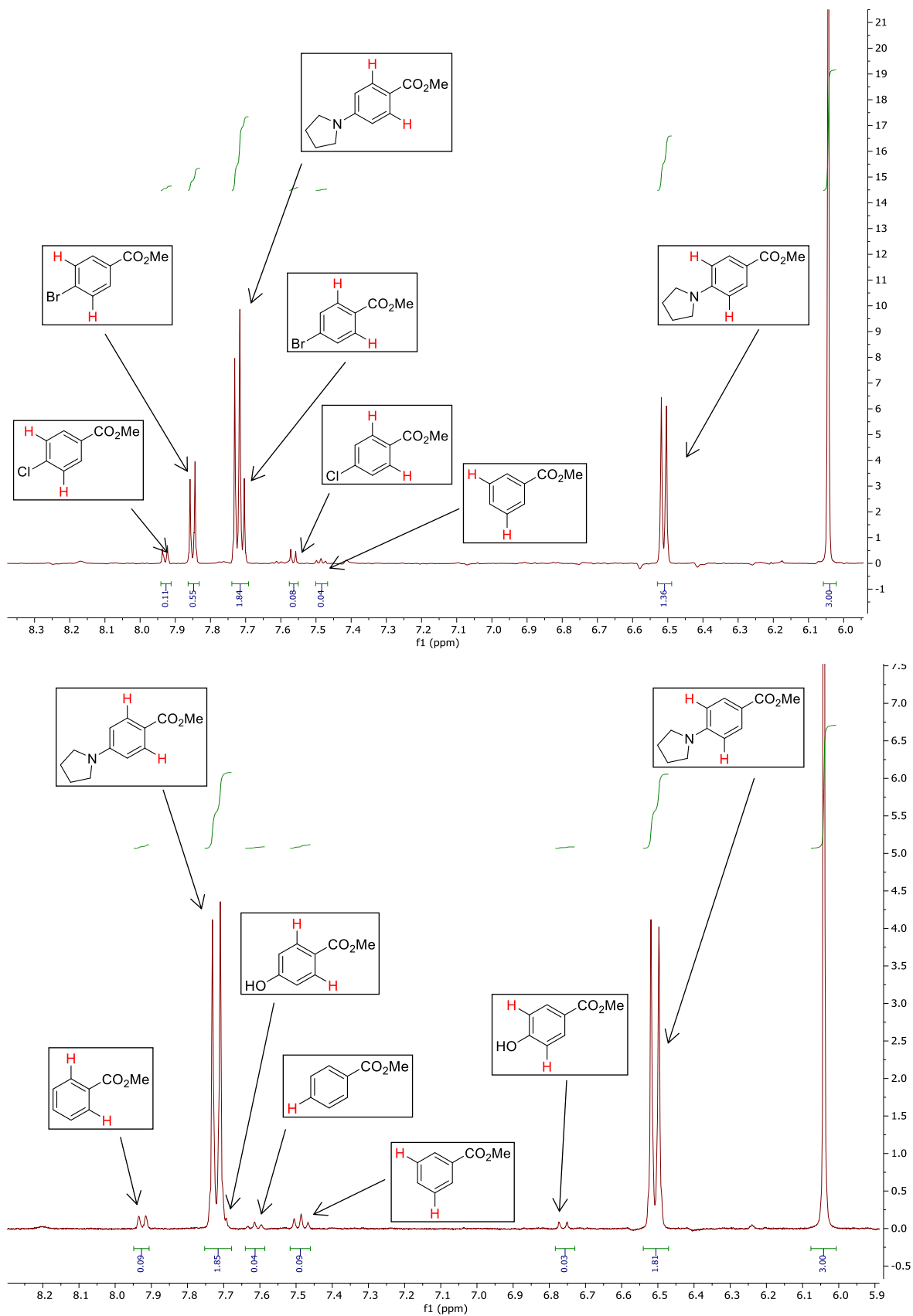


Figure S3.5. A: Picture of the Set-up for UV-light experiments **B:** Emission spectra of the Kessil[®] PR 160-370nm lamp used for photochemical reactions. All experiments were carried out at maximum power.

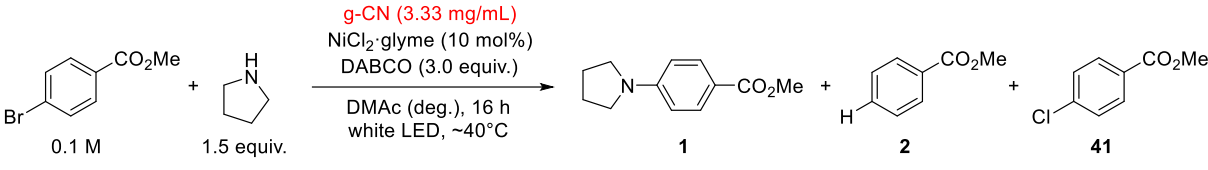
3.5.5 Reaction optimization

3.5.5.1 General experimental procedure for screening experiments

An oven dried vial (16 x 100 mm) equipped with a stir bar was charged with methyl 4-bromobenzoate (0.3 mmol, 64.5 mg, 1 equiv.), the base (0.9 mmol, 3.0 equiv.), the Ni^{II} catalyst (30 μ mol, 10 mol%) and the carbon nitride material (10 mg). Subsequently, pyrrolidine (0.45 mmol, 37.0 μ L, 1.5 equiv.) and the solvent (anhydrous, 3 mL) were added and the vial was sealed with a septum and Parafilm. The reaction mixture was sonicated for 5-10 min followed by stirring for 5 min until a fine dispersion of the solids was achieved and the mixture was then degassed by bubbling N₂ for 10 min. The mixture was irradiated in the photoreactor at 40 °C with rapid stirring (1400 rpm). After the respective reaction time, one equivalent of 1,3,5-trimethoxybenzene (0.3 mmol, 50.5 mg) was added. An aliquot of the reaction mixture (~300 μ L) was filtered, diluted with DMSO-d₆ and subjected to ¹H-NMR analysis. (Alternatively, 1.5 mL CDCl₃ and 3 mL H₂O were added and the vial was sealed and vigorously shaken. After phase separation, the CDCl₃ layer was carefully removed using a syringe, filtered, and analyzed by ¹H-NMR.) For representative NMR spectra, see Figure S3.6.

Figure S3.6. Examples of $^1\text{H-NMR}$ spectra for determining NMR yields.

3.5.5.2 Screening of carbon nitride material

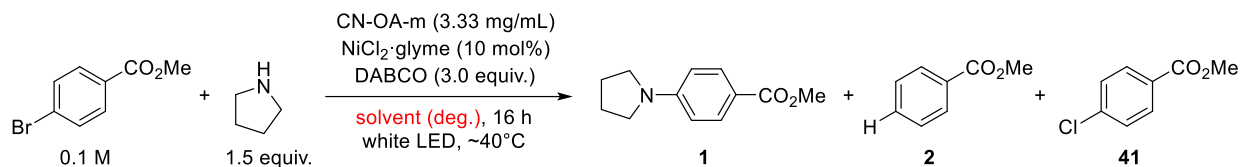
Table S3.1. Screening of carbon nitride materials.^a


Entry	CN catalyst	Conversion [%] ^b	1 [%] ^c	2 [%] ^c	41 [%] ^c
1	CN-OA-m	73	65	2	5
2	CMB _{0.05} -CN	25	21	2	trace
3	mpg-CN	23	19	trace	trace
4	PHIK	18	14	trace	trace
5	CNS ₆₀₀	9	6	trace	trace

^aReaction conditions: methyl 4-bromobenzoate (0.3 mmol), pyrrolidine (0.45 mmol), NiCl₂·glyme (10 mol%), DABCO (0.9 mmol), carbon nitride (10 mg), DMAc (anhydrous, 3 mL), white LEDs at 40 °C for 16h. ^bConversion of methyl 4-bromobenzoate determined by ¹H-NMR using 1,3,5-trimethoxybenzene as internal standard. ^cNMR yields determined by ¹H-NMR using 1,3,5-trimethoxybenzene as internal standard.

Several carbon nitride materials were tested: Mesoporous graphitic carbon nitride (mpg-CN),¹⁶ a modified carbon nitride derived from a cyanuric acid/melamide/barbituric acid complex (CMB_{0.05}-CN),¹⁷ a sulfur-doped material (CNS₆₀₀),¹⁸ a strongly oxidizing potassium poly(heptazine imide) (K-PHI),¹⁹ and a carbon nitride derivative prepared *via* co-condensation of urea and oxamide followed by post-calcination in a molten salt (CN-OA-m),¹² all using white LED (RGB) irradiation at a constant temperature of 40 °C.

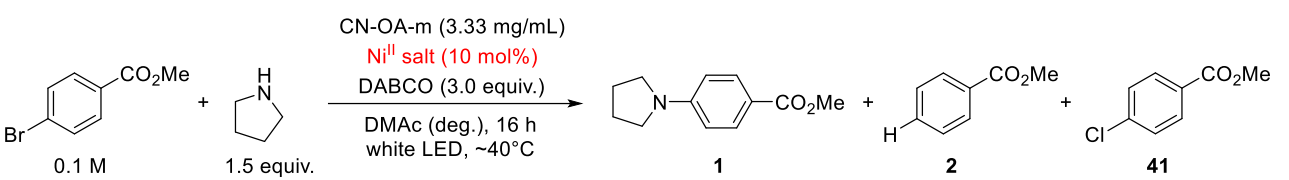
3.5.5.3 Solvent screening

Table S3.2. Solvent screening.^a

Entry	Solvent	Conversion [%] ^b	1 [%] ^c	2 [%] ^c	41 [%] ^c
1	DMAc	74	66	2	4
2	DMSO	28	24	trace	trace
3	DMF	n.d.o ^d	18	trace	trace
4	MeCN	19	14	trace	trace
5	diglyme	15	11	trace	trace
6	toluene	6	6	trace	trace
7	DCM	11	trace	trace	trace

^aReaction conditions: methyl 4-bromobenzoate (0.3 mmol), pyrrolidine (0.45 mmol), NiCl₂·glyme (10 mol%), DABCO (0.9 mmol), CN-OA-m (10 mg), solvent (anhydrous, 3 mL), white LEDs at 40 °C for 16h. ^bConversion of methyl 4-bromobenzoate determined by ¹H-NMR using 1,3,5-trimethoxybenzene as internal standard. ^cNMR yields determined by ¹H-NMR using 1,3,5-trimethoxybenzene as internal standard. ^d not detected due to overlapping peaks.

3.5.5.4 Screening of Ni^{II} sourcesTable S3.3. Screening Ni^{II} sources.^a

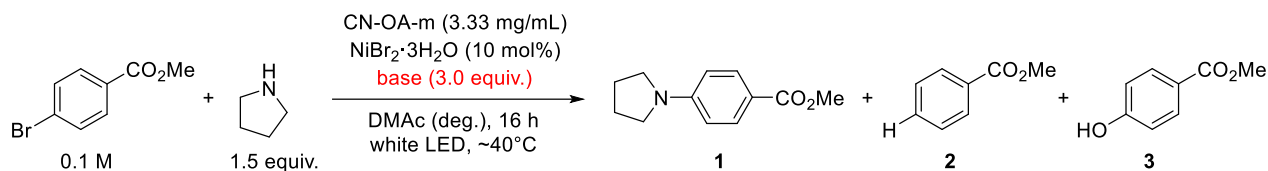


Entry	Ni ^{II} catalyst	Conversion [%] ^b	1 [%] ^c	2 [%] ^c	41 [%] ^c	Price [€ mol ⁻¹] ^d
1	NiI ₂	90	86	2	n.d.	2063
2	NiBr ₂ ·glyme	87	80	3	n.d.	10431
3	NiCl ₂	85	76	4	5	110
4	NiBr ₂	74	72	trace	n.d.	411
5	NiBr ₂ ·3H ₂ O	71	68	3	n.d.	116
6	NiCl ₂ ·glyme	74	66	trace	9	4161
7	Ni(ClO ₄) ₂ ·6H ₂ O	62	59	trace	n.d.	171
8	Ni(NO ₃) ₂ ·6H ₂ O	52	52	trace	n.d.	49
9	Ni(OTf) ₂	55	51	3	n.d.	12917
10	NiCl ₂ ·6H ₂ O	45	35	4	2	71
11	Ni(BF ₄) ₂ ·6H ₂ O	24	23	2	n.d.	223
12	Ni(TMHD) ₂	10	5	2	n.d.	35294
13	Ni(OAc) ₂ ·4H ₂ O	9	5	4	n.d.	28
14	Ni(SO ₄) ₂ ·6H ₂ O	9	4	2	n.d.	41
15	Ni(acac) ₂	3	n.d.	trace	n.d.	620

^aReaction conditions: methyl 4-bromobenzoate (0.3 mmol), pyrrolidine (0.45 mmol), Ni^{II} catalyst (10 mol%), DABCO (0.9 mmol), CN-OA-m (10 mg), DMAc (anhydrous, 3 mL), white LEDs at 40 °C for 16h. ^bConversion of methyl 4-bromobenzoate determined by ¹H-NMR using 1,3,5-trimethoxybenzene as internal standard. ^cNMR yields determined by ¹H-NMR using 1,3,5-trimethoxybenzene as internal standard. ^dPrices according to Sigma Aldrich (Merck)^x.

NiBr₂·3H₂O gave the best combination of price, selectivity (chloride formation in case of NiCl₂), activity and handling (NiI₂ and NiBr₂ are highly hygroscopic).

3.5.5.5 Base screening

Table S3.4. Base screening.^a

Entry	Base	Conversion [%] ^b	1 [%] ^c	2 [%] ^c	3 [%] ^c
1	TMP ^d	quant.	91	3	2
2	BIPA ^e	90	89	trace	n.d. ^f
3	DABCO ^g	71	68	3	trace
4	K ₂ HPO ₄	68	63	4	trace
5	dimethylaniline	59	62	n.d.	n.d.
6	CaCO ₃	65	61	trace	trace
7	2,6-lutidine	62	60	3	n.d.
8	without base	65	58	4	trace
9	tetramethylguanidine	53	43	n.d.	n.d.
10	DIPEA ^h	49	42	6	n.d.
11	Et ₃ N	42	35	5	trace
12	DMAP ⁱ	43	31	6	trace
13	K ₃ PO ₄	33	21	trace	trace
14	DBU ^j	27	19	trace	trace
15	Na ₂ CO ₃	17	14	trace	trace
16	NaHCO ₃	14	8	4	trace
17	NaO <i>t</i> Bu	29	5	trace	trace
19	NaOH	quant.	n.d.	n.d.	n.d.

Supporting Information - Chapter 3

20	K ₂ CO ₃	8	n.d.	trace	n.d.
21	NaH ₂ PO ₄	10	n.d.	n.d.	n.d.
18	KOH	quant.	4	n.d.	n.d.
22	LiOH	43	n.d.	n.d.	n.d.
23	Cs ₂ CO ₃	11	n.d.	5	trace
24	CsF	7	n.d.	trace	n.d.
25	CsOAc	2	n.d.	n.d.	n.d.
26	HMDS ^k	quant.	n.d.	n.d.	n.d.

^aReaction conditions: methyl 4-bromobenzoate (0.3 mmol), pyrrolidine (0.45 mmol), NiBr₂·3H₂O (10 mol%), base (0.9 mmol), CN-OA-m (10 mg), DMAc (anhydrous, 3 mL), white LEDs at 40 °C for 16h.

^bConversion of methyl 4-bromobenzoate determined by ¹H-NMR using 1,3,5-trimethoxybenzene as internal standard. ^cNMR yields determined by ¹H-NMR using 1,3,5-trimethoxybenzene as internal standard.

^d2,2,6,6-tetramethylpiperidin ^e*N-tert*-butylisopropylamine. ^fnot detected. ^g1,4-diazabicyclo[2.2.2]octane.

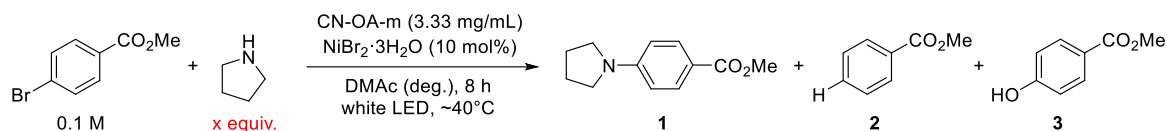
^h*N,N*-diisopropylethylamine. ⁱ4-(dimethylamino)pyridine. ^j1,8-diazabicyclo[5.4.0]undec-7-ene.

^kGexamethylidisilazane

N-tert-butylisopropylamine (BIPA) and 2,2,6,6-tetramethylpiperidine (TMP) gave best results. No C-N coupling between the aryl halide and these secondary, sterically hindered amines was observed. The absence of a base resulted in 58% yield indicating that the amine substrate can play several roles simultaneously (substrate, ligand, base). All other tested bases did not significantly increase the yield compared to the base-free method.

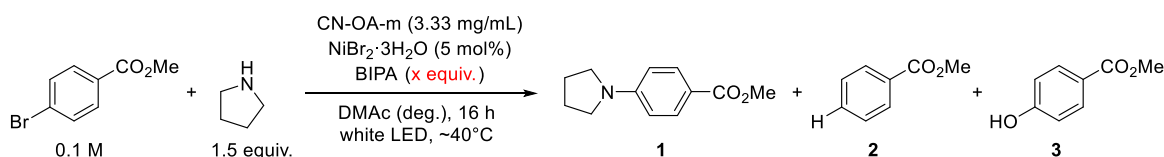
3.5.5.6 Screening of conditions

Table S3.5. Screening of amine equivalents for the base-free method.



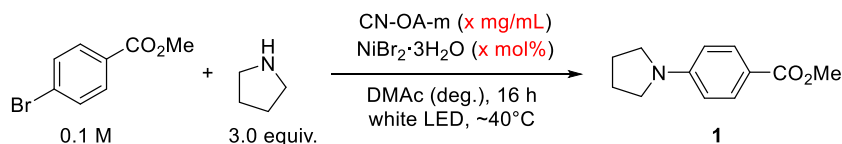
Entry	Pyrrolidine [equiv.]	Conversion	1	2	3
		[%] ^b	[%] ^c	[%] ^c	[%] ^c
1	1	33	24	4	1
2	1.5	53	43	6	1
3	2.0	67	59	7	1
4	2.5	91	83	6	2
5	3.0	quant.	94	5	2
6	3.5	quant.	92	6	3

^aReaction conditions: methyl 4-bromobenzoate (0.3 mmol), pyrrolidine (x equiv.), NiBr₂·3H₂O (10 mol%), CN-OA-m (10 mg), DMAc (anhydrous, 3 mL), white LEDs at 40 °C for 8 h. ^bConversion of methyl 4-bromobenzoate determined by ¹H-NMR using 1,3,5-trimethoxybenzene as internal standard. ^cNMR yields determined by ¹H-NMR using 1,3,5-trimethoxybenzene as internal standard.

Table S3.6. Screening of base (BIPA) equivalents for reactions with 1.5 equiv. pyrrolidine.^a

Entry	BIPA [equiv.]	Conversion	1	2	3
		[%] ^b	[%] ^c	[%] ^c	[%] ^c
1	-	65	58	5	n.d. ^d
2	0.5	68	58	5	3
3	1	87	81	4	2
4	1.5	91	82	5	n.d.
5	2.0	92	84	5	n.d.

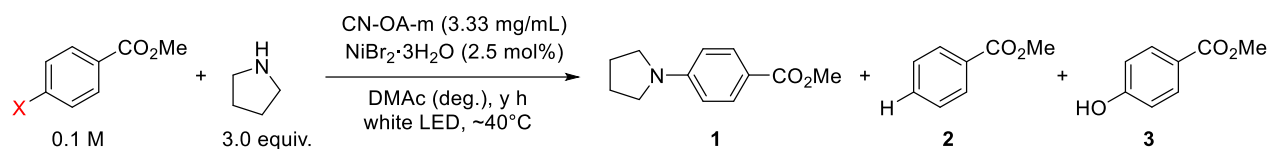
^aReaction conditions: methyl 4-bromobenzoate (0.3 mmol), pyrrolidine (0.45 mmol), NiBr₂·3H₂O (5 mol%), CN-OA-m (10 mg), BIPA (0-2 equiv.), DMAc (anhydrous, 3 mL), white LEDs at 40 °C for 16 h. ^bConversion of methyl 4-bromobenzoate determined by ¹H-NMR using 1,3,5-trimethoxybenzene as internal standard. ^cNMR yields determined by ¹H-NMR using 1,3,5-trimethoxybenzene as internal standard. ^dnot detected.

Table S3.7. Effect of the amount of NiBr₂·3H₂O and CN-OA-m on the yield of **1**.^a

Entry	NiBr ₂ ·3H ₂ O [mol%]	CN-OA-m	Conversion	1 [%] ^c
		[g/mL]	[%] ^b	
1	10	3.33	quant.	95
2	5	3.33	quant.	98
3	5	1.66	quant.	97
4	2.5	1.66	quant.	98
5	1	1.66	47	47
6	2.5	0.88	56	56

^aReaction conditions: methyl 4-bromobenzoate (0.3 mmol), pyrrolidine (0.9 mmol), NiBr₂·3H₂O (y mol%), base (0.9 mmol), CN-OA-m (x mg), DMAc (anhydrous, 3 mL), white LEDs at 40 °C for 16h. ^bConversion of methyl 4-bromobenzoate determined by ¹H-NMR using 1,3,5-trimethoxybenzene as internal standard. ^cNMR yields determined by ¹H-NMR using 1,3,5-trimethoxybenzene as internal standard.

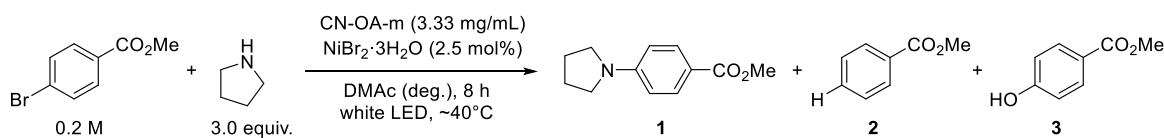
3.5.5.7 Screening of aryl (pseudo)halides

Table S3.8. Screening of aryl (pseudo)halides.^a

Entry	X	Time [h]	Conversion [%] ^b	1 [%] ^c	2 [%] ^c	3 [%] ^c
1	I	8	quant.	99	1	n.d.
2	Br	8	quant.	98	2	1
3	Cl	168	76	72	4	n.d.
4	OTf	72	75	67	5	2
5	OTs	16	2	n.d.	n.d.	n.d.
6	OMs	16	5	n.d.	n.d.	4

^aReaction conditions: aryl (pseudo)halide (0.3 mmol), pyrrolidine (0.9 mmol), NiBr₂·3H₂O (2.5 mol%), CN-OA-m (10 mg), DMAc (anhydrous, 3 mL), white LEDs at 40 °C for x h. ^bConversion of methyl 4-bromobenzoate determined by ¹H-NMR using 1,3,5-trimethoxybenzene as internal standard. ^cNMR yields determined by ¹H-NMR using 1,3,5-trimethoxybenzene as internal standard. ^dnot detected.

3.5.5.8 Control studies

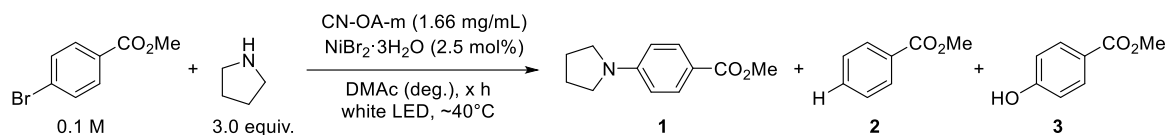
Table S3.9. Control studies.^a

Entry	Deviation from standard conditions	Conversion [%] ^b	1 [%] ^c	2 [%] ^c	3 [%] ^c
1	None	quant.	98	2	n.d. ^d
2	dtbbpy ^e (2.5 mol%) as ligand	48	45	2	n.d.
3	No CN-OA-m	5	n.d.	2	1
4	No NiBr ₂ ·3H ₂ O	5	n.d.	n.d.	n.d.
5	No light	<1	n.d.	n.d.	n.d.
6	No degassing	10	10	n.d.	n.d.

^aReaction conditions: methyl 4-bromobenzoate (1.2 mmol), pyrrolidine (3.6 mmol), NiBr₂·3H₂O (2.5 mol%), CN-OA-m (20 mg), DMAc (anhydrous, 6 mL), white LEDs at 40 °C for 8 h. ^bConversion of methyl 4-bromobenzoate determined by ¹H-NMR using 1,3,5-trimethoxybenzene as internal standard. ^cNMR yields determined by ¹H-NMR using 1,3,5-trimethoxybenzene as internal standard. ^dnot detected. ^e4,4'-Di-tert-butyl-2,2'-bipyridyl.

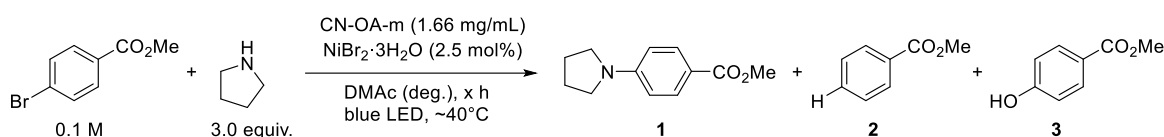
3.5.5.9 Time/Wavelength study

Table S3.10. Time study using white light.



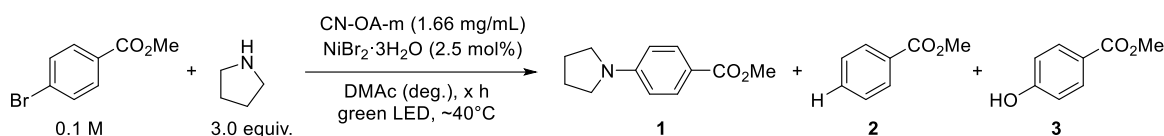
Entry	Time [h]	Conversion [%] ^b	1 [%] ^c	2 [%] ^c	3 [%] ^c
1	1	25	24	n.d. ^d	n.d.
2	2	39	38	n.d.	n.d.
3	3	48	48	trace	n.d.
4	4	77	76	1	n.d.
5	5	87	83	2	n.d.
6	6	91	91	2	n.d.
7	7	97	94	3	n.d.
8	8	quant.	96	2	1

^aReaction conditions: methyl 4-bromobenzoate (0.6 mmol), pyrrolidine (1.8 mmol), NiBr₂·3H₂O (2.5 mol%), CN-OA-m (10 mg), DMAc (anhydrous, 6 mL), white LEDs at 40 °C for x h. ^bConversion of methyl 4-bromobenzoate determined by ¹H-NMR using 1,3,5-trimethoxybenzene as internal standard. ^cNMR yields determined by ¹H-NMR using 1,3,5-trimethoxybenzene as internal standard. ^dnot detected.

Table S3.11. Time study using blue light.

Entry	Time [h]	Conversion [%] ^b	1 [%] ^c	2 [%] ^c	3 [%] ^c
1	2	51	51	n.d. ^d	n.d.
2	4	77	80	trace	n.d.
3	5.5	quant.	>99	trace	n.d.

^aReaction conditions: methyl 4-bromobenzoate (0.6 mmol), pyrrolidine (1.8 mmol), NiBr₂·3H₂O (2.5 mol%), CN-OA-m (10 mg), DMAc (anhydrous, 6 mL), blue LEDs at 40 °C for x h. ^bConversion of methyl 4-bromobenzoate determined by ¹H-NMR using 1,3,5-trimethoxybenzene as internal standard. ^cNMR yields determined by ¹H-NMR using 1,3,5-trimethoxybenzene as internal standard. ^dnot detected.

Table S3.12. Time study using green light.

Entry	Time [h]	Conversion [%] ^b	1 [%] ^c	2 [%] ^c	3 [%] ^c
1	4	10	10	n.d. ^d	n.d.
2	8	21	20	n.d.	n.d.
3	24	69	68	n.d.	n.d.
4	48	quant.	>99	n.d.	n.d.

^aReaction conditions: methyl 4-bromobenzoate (0.6 mmol), pyrrolidine (1.8 mmol), NiBr₂·3H₂O (2.5 mol%), CN-OA-m (10 mg), DMAc (anhydrous, 6 mL), green LEDs at 40 °C for x h. ^bConversion of methyl 4-bromobenzoate determined by ¹H-NMR using 1,3,5-trimethoxybenzene as internal standard. ^cNMR yields determined by ¹H-NMR using 1,3,5-trimethoxybenzene as internal standard. ^dnot detected.

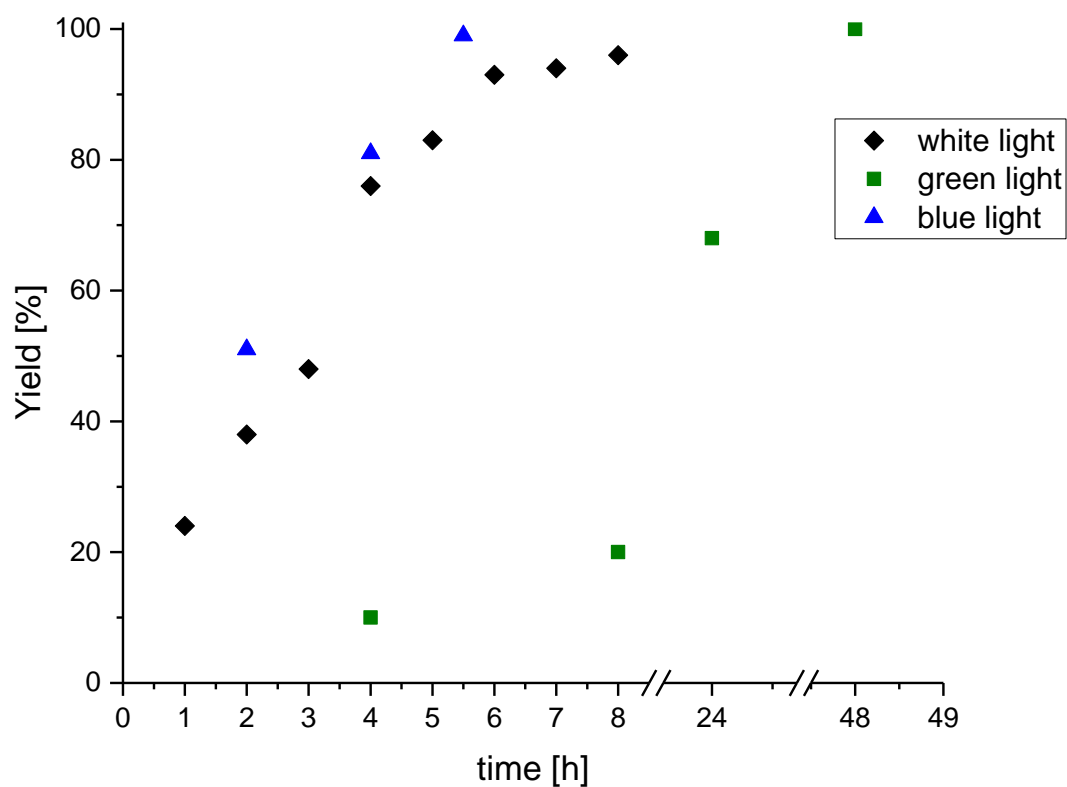


Figure S3.7. Time study using blue, green and white light for model reaction.

For ICP-OES experiments, the reaction mixture was centrifuged at 3000 rpm for 20 min and the liquid phase was carefully separated and analyzed by $^1\text{H-NMR}$. The carbon nitride was washed with DMAc (anhydrous, 6 mL, followed by centrifugation at 3000 rpm for 20 min and separation of the liquid phase), water (6 mL, followed by centrifugation at 3000 rpm for 20 min and separation of the liquid phase) and lyophilized (overnight) before analysis.

Table S3.13. ICP-OES measurements of the nickel content on the new and recovered CN-OA-m after 8 h white light and 48 h green light standard reaction.

Sample	Ni [mg/g CN]	% adsorbed Ni
CN-OA-m new	0.117	/
CN-OA-m white light standard reaction 1	14.2	16.1
CN-OA-m green light standard reaction	13.8	15.7



Figure S3.8. Fresh CN-OA-m (A), CN-OA-m after 8 h white light irradiation for standard reaction (B) and CN-OA-m after 48 h green light irradiation for standard reaction (C).

Note: Although 1.66 mg mL^{-1} of CN-OA-m is suitable for the C-N cross-coupling, a higher loading (3.33 mg mL^{-1}) was used for further experiments in order to obtain enough material for material characterization (ICP-OES, EDX, SEM, TEM, etc).

3.5.6 Recycling studies

An oven dried vial (13 x 80 mm) equipped with a stir bar was charged with CN-OA-m (20 mg), 4-bromomethylbenzoate (258.0 mg, 1.2 mmol, 1.0 equiv.) and NiBr₂·3H₂O (8.2 mg, 30 μmol, 2.5 mol%). Subsequently, pyrrolidine (256.0 mg, 295.6 μl, 3.6 mmol, 3.0 equiv.) and DMAc (anhydrous, 6 mL) were added and the vial was sealed with a septum and Parafilm. The reaction mixture was sonicated for 5-10 min followed by stirring for 5 min until fine dispersion of the solids was achieved and the mixture was then degassed by bubbling N₂ for 10 min. The mixture was irradiated in the photoreactor (white light or green light) at 40 °C with rapid stirring (1400 rpm). After the respective reaction time, one equivalent of 1,3,5-trimethoxybenzene (202.0 mg, 1.2 mmol) was added and the mixture was stirred for 5 min. The reaction mixture was centrifuged at 3000 rpm for 20 min and the liquid phase was carefully separated and analyzed by ¹H-NMR. The carbon nitride was washed with DMAc (anhydrous, 6 mL, followed by centrifugation at 3000 rpm for 20 min and separation of the liquid phase), lyophilized (overnight) and reused in the next reaction.

Table S3.14. Reusability of CN-OA-m using white light.^a

Reaction scheme: Methyl 4-bromobenzoate (0.2 M) + Pyrrolidine (3.0 equiv.) $\xrightarrow[\text{DMAc (deg.), 16 h, white LED, } \sim 40^\circ\text{C}]{\text{CN-OA-m (3.33 mg/mL), NiBr}_2\cdot\text{3H}_2\text{O (2.5 mol\%)}}$ Methyl 4-(pyrrolidin-2-yl)benzoate (1)

Cycle	1 [%] ^b
1	99
2	98
3	43
4	27
5	33

^aReaction conditions: methyl 4-bromobenzoate (1.2 mmol), pyrrolidine (3.6 mmol), NiBr₂·3H₂O (2.5 mol%), CN-OA-m (20 mg - reused), DMAc (anhydrous, 6 mL), white LEDs at 40 °C for 16h. ^bNMR yields determined by ¹H-NMR using 1,3,5-trimethoxybenzene as internal standard.

Table S3.15. Reusability of CN-OA-m without additional NiBr₂·3H₂O using white light.^a

Cycle	1 [%] ^b
1	99
2 ^c	1

^aReaction conditions: methyl 4-bromobenzoate (1.2 mmol), pyrrolidine (3.6 mmol), NiBr₂·3H₂O (2.5 mol%), CN-OA-m (20 mg - reused), DMAc (anhydrous, 6 mL), white LEDs at 40 °C for 16h. ^bNMR yields determined by ¹H-NMR using 1,3,5-trimethoxybenzene as internal standard. ^cNo NiBr₂·3H₂O added.

Table S3.16. Reusability of CN-OA-m using green light.^a

Cycle	1 [%] ^b
1	99
2	99
3	98
4	98
5	94

^aReaction conditions: methyl 4-bromobenzoate (1.2 mmol), pyrrolidine (3.6 mmol), NiBr₂·3H₂O (2.5 mol%), CN-OA-m (20 mg - reused), DMAc (anhydrous, 6 mL), green LEDs at 40 °C for 48h. ^bNMR yields determined by ¹H-NMR using 1,3,5-trimethoxybenzene as internal standard.

Table S3.17. ICP-OES measurements of the nickel content on recovered CN-OA-m after white light and green light recyclability tests.

Sample	Ni [mg/g CN]	% adsorbed Ni
CN-OA-m white light recyclability tests	60.5	13.7
CN-OA-m green light recyclability tests	38.8	8.8

**Figure S3.9.** Fresh CN-OA-m (A), CN-OA-m after recyclability tests with white light irradiation (B) and CN-OA-m after recyclability tests with green light irradiation (C).

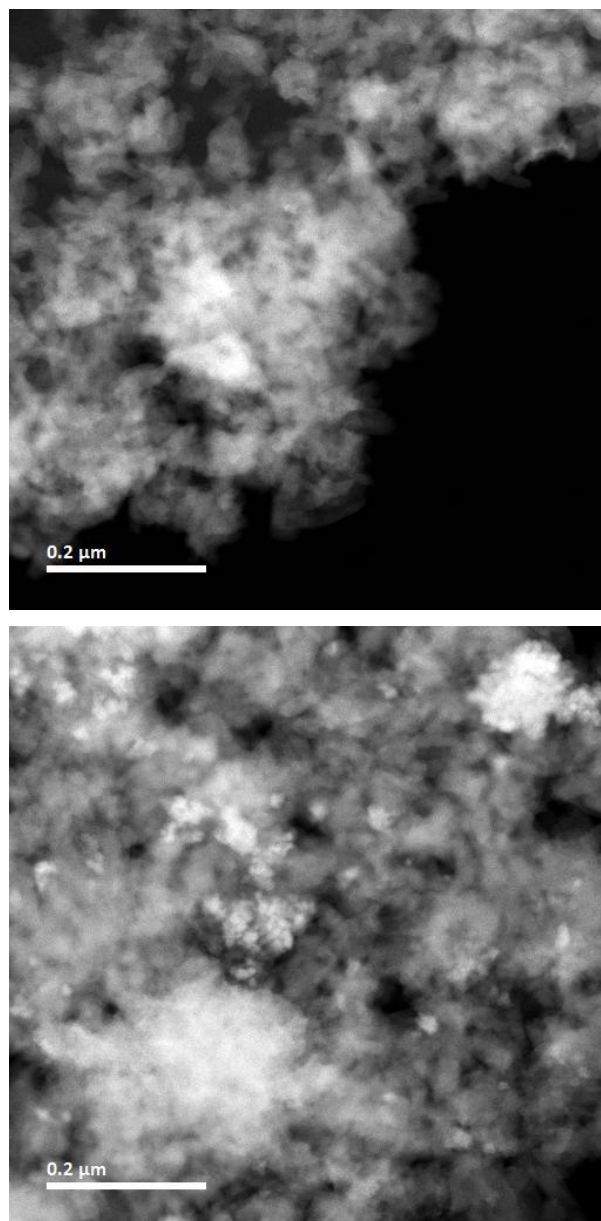


Figure S3.10. HAADF-STEM brightfield images show almost no nickel particle agglomerates (bright spots) on CN-OA-m after recyclability tests with green light irradiation (left) and a significant amount of agglomerates after recyclability tests with white light irradiation (right).

3.5.7. Scale-up of amination

An oven dried vial (25 x 140 mm) (Figure S3.11, A) equipped with a stir bar was charged with NiBr₂·3H₂O (54.5 mg, 0.2 mmol, 2.5 mol%), methyl 4-bromobenzoate (1.720 g, 8.0 mmol, 1 equiv.) and CN-OA-m (133.3 mg). Subsequently, pyrrolidine (1.706 g, 1.97 ml, 24.0 mmol, 3 equiv.) and DMAc (anhydrous, 6 mL) were added and the vial was sealed with a septum and parafilm. The reaction mixture was sonicated for 10 min and the mixture was then degassed by bubbling N₂ for 30 min and stirring the reaction mixture. The mixture was irradiated in a beaker wrapped with a LED-band (Figure S3.3, B) at ~40°C with rapid stirring (700 rpm). The completion of the reaction (14 h) was confirmed by taking an aliquot and measuring ¹H-NMR of the crude mixture in DMSO-d₆. The catalyst was removed by centrifugation (3000 rpm, 20 min) and the liquid phase was diluted with H₂O (200 mL) and extracted with ethyl acetate (3 x 200 mL). The combined organic phases were washed with H₂O (200 mL), a sat. NaHCO₃ solution (200 ml), and brine (200 mL), dried over Na₂SO₄ and concentrated. The crude product was purified by flash column chromatography (SiO₂, Hexane/EtOAc; gradient 0-5% ethyl acetate in hexane; 2. Isocratic 5% ethyl acetate in hexane)) on a Grace™ Reveleris™ system using a 24 g cartridge to afford (1-(4-methylbenzoate)pyrrolidine) (**1**) in 93 % (1.5338 g, 7.47 mmol) as a white solid (Figure S3.12).

¹H NMR (400 MHz, CDCl₃) δ 7.88 (d, *J* = 8.7 Hz, 2H), 6.46 (d, *J* = 8.7 Hz, 2H), 3.83 (s, 3H), 3.40 – 3.09 (m, 4H), 2.05 – 1.86 (m, 4H). ¹³C NMR (101 MHz, Chloroform-*d*) δ = 167.57, 150.79, 131.31, 116.16, 110.62, 51.37, 47.47, 25.41. HRMS (ESI-TOF) *m/z* calcd. for C₁₂H₁₆NO₂ [(M+H)⁺]: 206.1176; found: 206.116.

These data are in full agreement with those previously published in the literature.²⁰



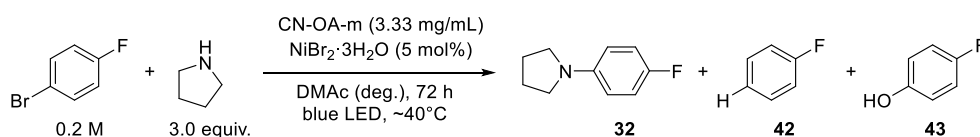
Figure S3.11. Vessel dimensions of vial for scale-up reaction (A) and vial for “standard scale” reactions (B).



Figure S3.12. Isolated product (1-(4-methylbenzoate)pyrrolidine) (**1**) from 8 mmol scale.

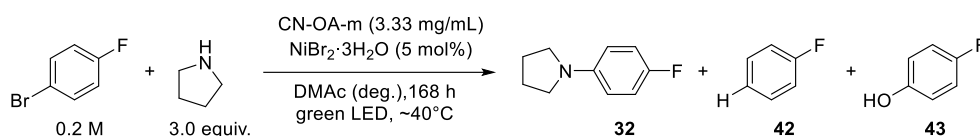
3.5.8 Studies on the reaction of 4-bromofluorobenzene with pyrrolidine.

Method A: Dual CN-OA-m/Ni catalysis with irradiation at 450 nm

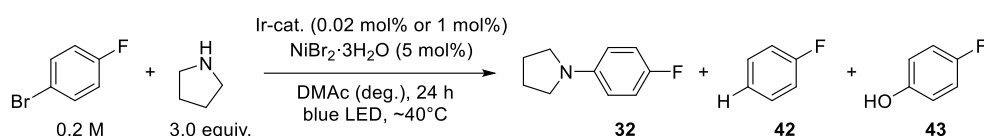


An oven dried vial (19 x 80 mm) equipped with a stir bar was charged with the CN-OA-m (20 mg), 4-bromofluorobenzene (210.0 mg, 131.8 μ l, 1.2 mmol, 1.0 equiv.) and NiBr₂·3H₂O (16.4 mg, 60 μ mol, 5.0 mol%). Subsequently, pyrrolidine (256.0 mg, 295.6 μ l, 3.6 mmol, 3.0 equiv.) and DMAc (anhydrous, 6 mL) were added and the vial was sealed with a septum and Parafilm. The reaction mixture was sonicated for 5-10 min followed by stirring for 5 min until fine dispersion of the solids was achieved and the mixture was then degassed by bubbling N₂ for 10 min. The mixture was irradiated in the photoreactor (blue light function of RGB LED strip) at 40 °C with rapid stirring (1400 rpm). After 72 h, one equivalent of 1,3,5-trimethoxybenzene (1.2 mmol) was added and the mixture was stirred for 5 min. An aliquot of the reaction mixture (~300 μ L) was filtered, diluted with DMSO-d₆ and subjected to ¹H-NMR analysis.

Method B: Dual CN-OA-m/Ni catalysis with irradiation at 520 nm



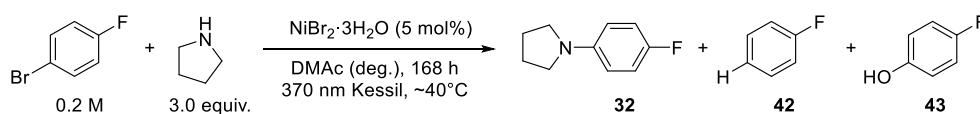
An oven dried vial (19 x 80 mm) equipped with a stir bar was charged with the CN-OA-m (20 mg), 4-bromofluorobenzene (210.0 mg, 131.8 μ l, 1.2 mmol, 1.0 equiv.) and (16.4 mg, 60 μ mol, 5.0 mol%). Subsequently, pyrrolidine (256.0 mg, 295.6 μ l, 3.6 mmol, 3.0 equiv.) and DMAc (anhydrous, 6 mL) were added and the vial was sealed with a septum and Parafilm. The reaction mixture was sonicated for 5-10 min followed by stirring for 5 min until fine dispersion of the solids was achieved and the mixture was then degassed by bubbling N₂ for 10 min. The mixture was irradiated in the photoreactor (green light function of RGB LED strip) at 40 °C with rapid stirring (1400 rpm). After 168 h, one equivalent of 1,3,5-trimethoxybenzene (1.2 mmol) was added and the mixture was stirred for 5 min. An aliquot of the reaction mixture (~300 μ L) was filtered, diluted with DMSO-d₆ and subjected to ¹H-NMR analysis.

Method “Ir”: Dual Ir/Ni catalysis with irradiation at 420 nm

Ir1: An oven dried vial (19 x 80 mm) equipped with a stir bar was charged with 4-bromofluorobenzene (210.0 mg, 131.8 μ l, 1.2 mmol, 1.0 equiv.) and NiBr₂·3H₂O (16.4 mg, 60 μ mol, 5.0 mol%) and a solution of Ir[dF(CF₃)ppy]₂(dtbbpy)PF₆ (0.27 mg, 0.02 mol%) in DMAc (48 μ l). Subsequently, pyrrolidine (256.0 mg, 295.6 μ l, 3.6 mmol, 3.0 equiv.) and DMAc (anhydrous, 6 mL) were added and the vial was sealed with a septum and Parafilm.

Ir2: An oven dried vial (19 x 80 mm) equipped with a stir bar was charged with 4-bromofluorobenzene (52.5 mg, 33.0 μ l, 0.3 mmol, 1.0 equiv.), NiBr₂·3H₂O (4.1 mg, 15 μ mol, 5.0 mol%) and a solution of Ir [dF(CF₃)ppy]₂(dtbbpy)PF₆ (3.37 mg, 1 mol%) in DMAc (600 μ l). Subsequently, pyrrolidine (64.0 mg, 73.9 μ l, 0.9 mmol, 3.0 equiv.) and DMAc (anhydrous, 2.4 mL) were added and the vial was sealed with a septum and Parafilm. The reaction mixture was sonicated for 5-10 min followed by stirring for 5 min and the mixture was then degassed by bubbling N₂ for 10 min. The mixture was irradiated in the photoreactor (blue light function of LED-band) at 40 °C with rapid stirring (1400 rpm). After 24 h, one equivalent of 1,3,5-trimethoxybenzene (Ir1: 202.0 mg, 1.2 mmol/ Ir2: 50.5 mg, 0.3 mmol) was added and the mixture was stirred for 5 min. An aliquot of the reaction mixture (~300 μ L) was filtered, diluted with DMSO-d₆ and subjected to ¹H-NMR analysis.

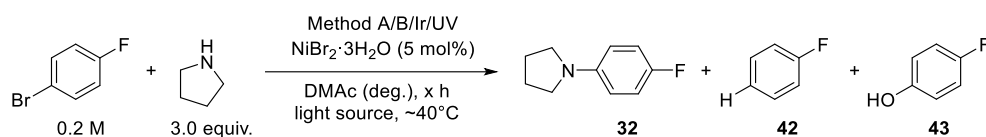
Note: In case if procedure C2, the formation of small amounts of black particles was observed after the reaction.

Method “UV”: Ni catalysis with irradiation at 370 nm

An oven dried vial (19 x 80 mm) equipped with a stir bar was charged 4-bromofluorobenzene (210.0 mg, 131.8 μ l, 1.2 mmol, 1.0 equiv.) and NiBr₂·3H₂O (16.4 mg, 60 μ mol, 5.0 mol%). Subsequently, pyrrolidine (256.0 mg, 295.6 μ l, 3.6 mmol, 3.0 equiv.) and DMAc (anhydrous, 6 mL) were added and the vial was sealed with a septum and Parafilm. The reaction mixture was sonicated for 5-10 min followed by stirring for 5 min and the mixture was then degassed by bubbling N₂ for 10 min. The mixture was irradiated with UV light using the Kessil[®] PR 160-370 nm lamp with rapid stirring (~800 rpm) and cooling by a fan. After 3 h (UV1), 15 h (UV2), 72 h (UV3) and 168 h (UV4) one equivalent of 1,3,5-trimethoxybenzene (202.0 mg, 1.2 mmol) was added and the mixture was stirred for 5 min. An aliquot of the reaction mixture (~300 μ L) was filtered, diluted with DMSO-d₆ and subjected to ¹H-NMR analysis.

Note: The color of the reaction solution changed from yellowish to black and a significant amount of black particles was formed.

The reaction mixtures of procedure A, B, and UV were centrifuged at 3000 rpm for 20 min. The carbon nitride from the blue (procedure A) and green light experiment (procedure B) and the black particles formed during the UV-light experiment (procedure UV) were washed with DMAc (anhydrous 6 mL, followed by centrifugation at 3000 rpm for 20 min and separation of the liquid phase) and acetone (6 mL, followed by centrifugation at 3000 rpm for 20 min and separation of the liquid phase), lyophilized (overnight) and subjected to FTIR, UV-Vis, XRD, , ICP-OES, EDX, XPS as well as SEM and TEM analysis. For comparison, an unused sample of CN-OA-m from the same batch was also analyzed.

Table S3.18. Coupling of 4-bromofluorobenzene and pyrrolidine using different light sources and catalysts.

Entry	Procedure	Conversion [%] ^a	32 [%] ^b	42 [%] ^b	43 [%] ^b
1	A	93	70	6	9
2	A	92	69	7	8
3	A	91	68	6	9
4	A	92	63	7	6
5	A	87	60	7	9
6	A	18	6	2	n.d. ^c
7	A	22	5	n.d.	3
8	B	quant.	91	5	2
9	B	quant.	89	1	10
10	B	quant.	89	9	1
11	B	99	86	9	2
12	B	quant.	88	1	10
13	B	97	86	2	9
14	B	quant.	84	9	n.d.
15	Ir1	quant.	77	7	4
16	Ir2	79	33	20	13
17	UV1	18	7	3	n.d.
18	UV2	39	17	9	4
19	UV3	94	26	32	16
20	UV4	quant.	10	23	9

^aConversion of 4-bromofluorobenzene determined by ¹H-NMR using 1,3,5-trimethoxybenzene as internal standard. ^bNMR yields determined by ¹H-NMR using 1,3,5-trimethoxybenzene as internal standard. ^cnot detected.

3.5.8.1 Powder X-ray diffraction (XRD) and X-ray photoelectron spectroscopy (XPS)

The powder X-ray diffraction spectra (PXRD) of the black material generated during the UV-light experiment (Table S3.19, Entry 17) showed diffraction peaks at 44° , 51° and 76° that could be assigned to the (1 1 1), (2 0 0), (2 2 0) planes of nickel(0) (Figure S3.9). Spectra of the recovered CN-OA-m (Table S3.13, Entry 7 & 8) materials show a characteristic peak at 27.4° , which corresponds to the in-planar structural packing and inter-planar stacking peaks of the aromatic systems of CN-OA-m. Nickel(0) (diffraction peaks at 44° , 51° and 76°) was detected in the material recovered from experiment using blue LEDs (Method A), and, although in significantly lower quantity, in the material recovered from the experiment using green LEDs (Method B).

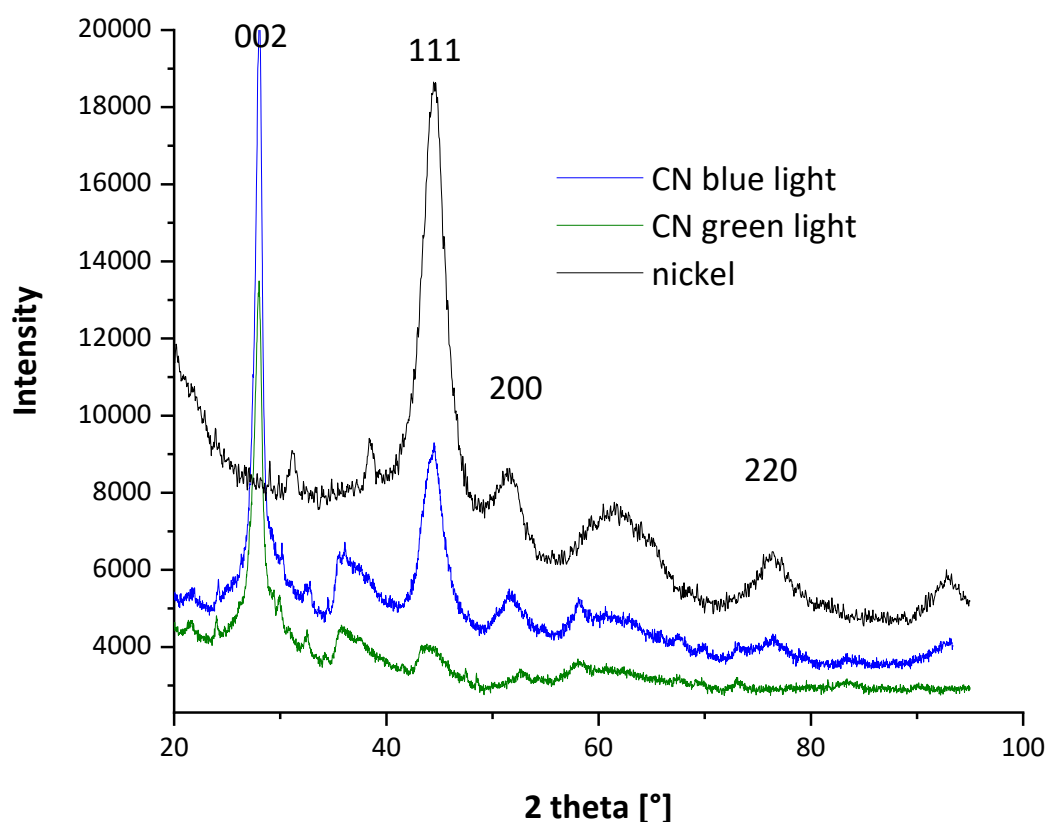


Figure S3.13. XRD measurements of the material generated by UV-light (black line), CN-OA-m after method A with blue light irradiation (blue line) and CN-OA-m after method B with green light irradiation (green line).

XPS scans of the solid material generated during UV light experiments and CN-OA-m recovered from the experiments using blue (Method A) and green LED (Method B) irradiation confirmed the presence of nickel in both samples (Figure S3.14). High-resolution XPS analysis spectra for core levels of Ni2p confirm the presence of Ni²⁺ and Ni⁰ at 854.6 (± 0.02) eV and 852.3 (± 0.02) eV, for CN-OA-m recovered from method A (blue light) and the material generated during UV light irradiation (Figure S3.14, A). Only Ni²⁺ (854.6 (± 0.02) eV) species were detected in the CN-OA-m sample recovered from the experiment using method B (green light). The high-resolution XPS spectra of the C 1s core level spectra shows typical C-C and N-C=N bonding signals for all CN-OA-m samples (Figure S3.114, B). The N 1s spectra contain two main peaks that are typical for carbon nitrides and can be assigned to i) sp² bonded nitrogen in tri-s-triazine groups (C-N=C), and ii) sp³ amino groups (C-NH) for all CN-OA-m samples. The calculated elemental composition indicates a two times higher concentration of nickel on CN-OA-m recovered from method A (blue light) compared to CN-OA-m recovered from method B (green light) (Table S3.19).

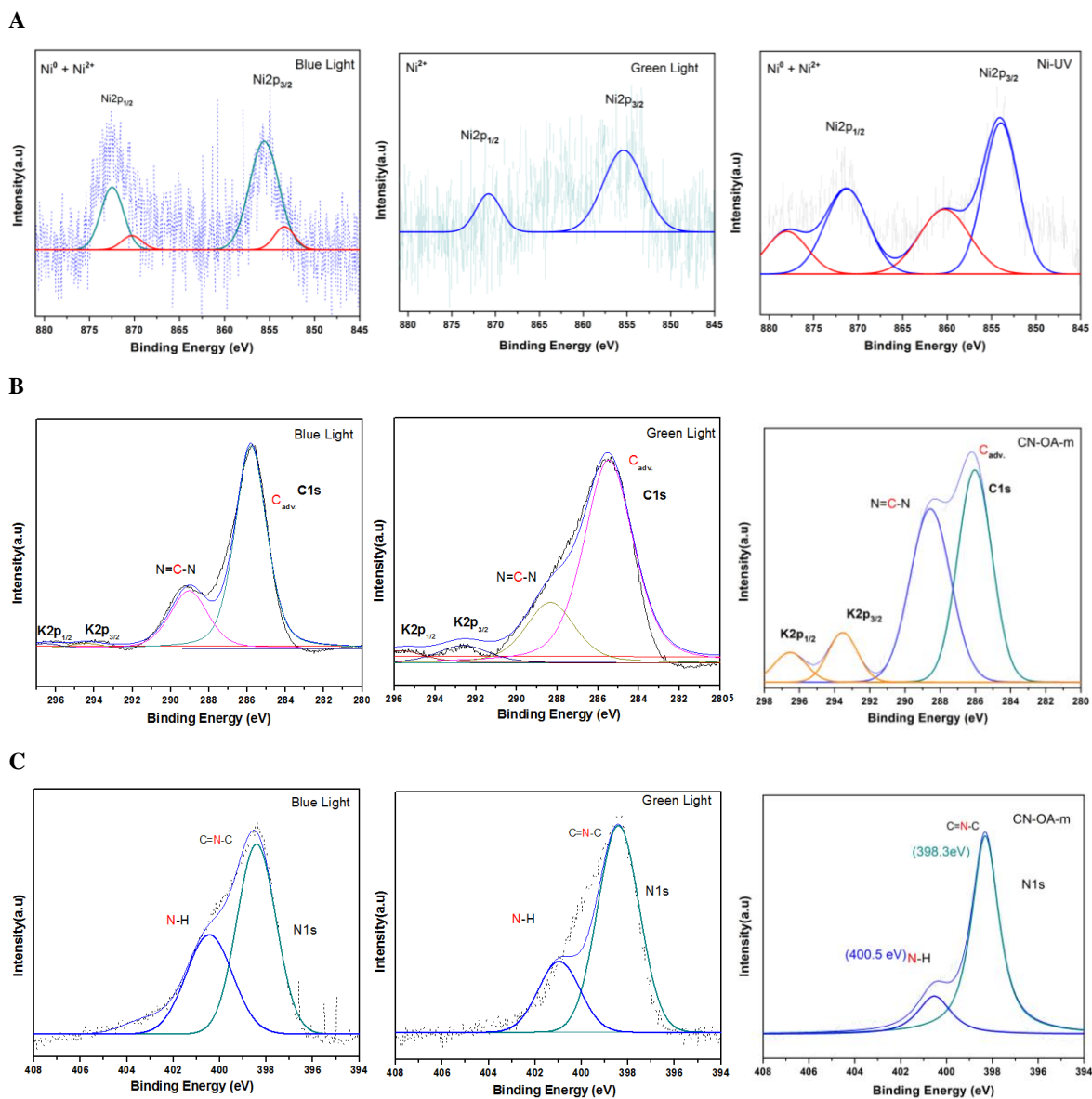


Figure S3.14. **A)** High-resolution XPS analysis spectra for core levels of Ni $2p_{3/2}$: CN-OA-m recovered from experiments using method A (blue light) and method B (green light), and the heterogeneous material generated during UV-light experiments (Ni-UV). **B)** High-resolution XPS analysis spectra for core levels of C $1s$: CN-OA-m recovered from experiments using method A (blue light) and method B (green light), and unused CN-OA-m. **C)** High-resolution XPS analysis spectra for core levels of N $1s$: CN-OA-m recovered from experiments using method A (blue light) and method B (green light), and unused CN-OA-m. has been deconvoluted using *Lorentzian-Gaussian* peak fitting functions with Shirley background deletion.

Table S3.19. XPS Elemental composition of CN-OA-m and CN-OA-m recovered from experiments using method A and B.

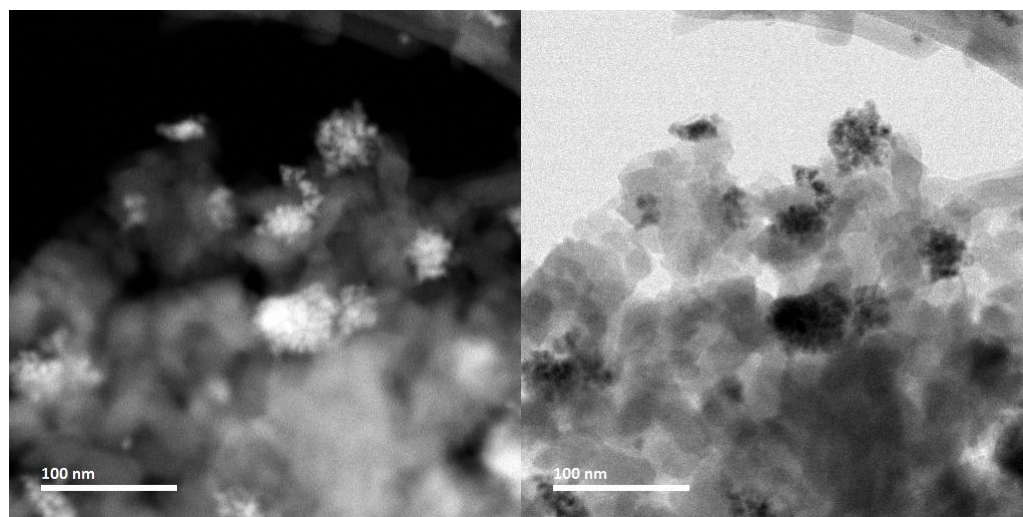
Sample	% w/w N	% w/w C	% w/w K	% w/w Ni
CN-OA-m	57.257	41.191	1.552	---
CN-OA-m blue light^a	61.094	37.718	0.365	0.822
CN-OA-m green light^b	59.021	39.983	0.709	0.377

^aSample recovered from experiment described in Table S3.18, Entry 7. ^bSample recovered from experiment described in Table S3.18, Entry 8.

3.5.8.2 Scanning transmission electron microscopy (STEM)

3.5.8.2.1 CN-OA-m recovered from method A (blue LEDs) and method B (green LEDs)

Scanning transmission electron microscopy (STEM) was used to visualize nickel particles on the surface of the recovered CN-OA-m. High-angle annular dark-field (HAADF) images show round- to oval-shaped particles with sizes ranging 10-20 nm. The polycrystalline particle consist of smaller ones (1-5 nm), which agglomerated on the surface (Figure S3.15 and S3.16). The images show the porous structure of CN-OA-m containing particles that show a diffraction pattern indicating Ni-species deposition. The exact lattice of a selected nickel particle is shown in higher resolution. The STEM images of CN-OA-m recovered from experiments using method B (green LED) (Figure S3.16) show a significantly lower amount of (agglomerated) nickel particles compared to using method A (blue LED, Figure 3.19). This confirms the results obtained using XRD (Figure S3.13), XPS (Figure S3.14), EDX (Table S3.20) and ICP-OES (Table S3.21) analysis.



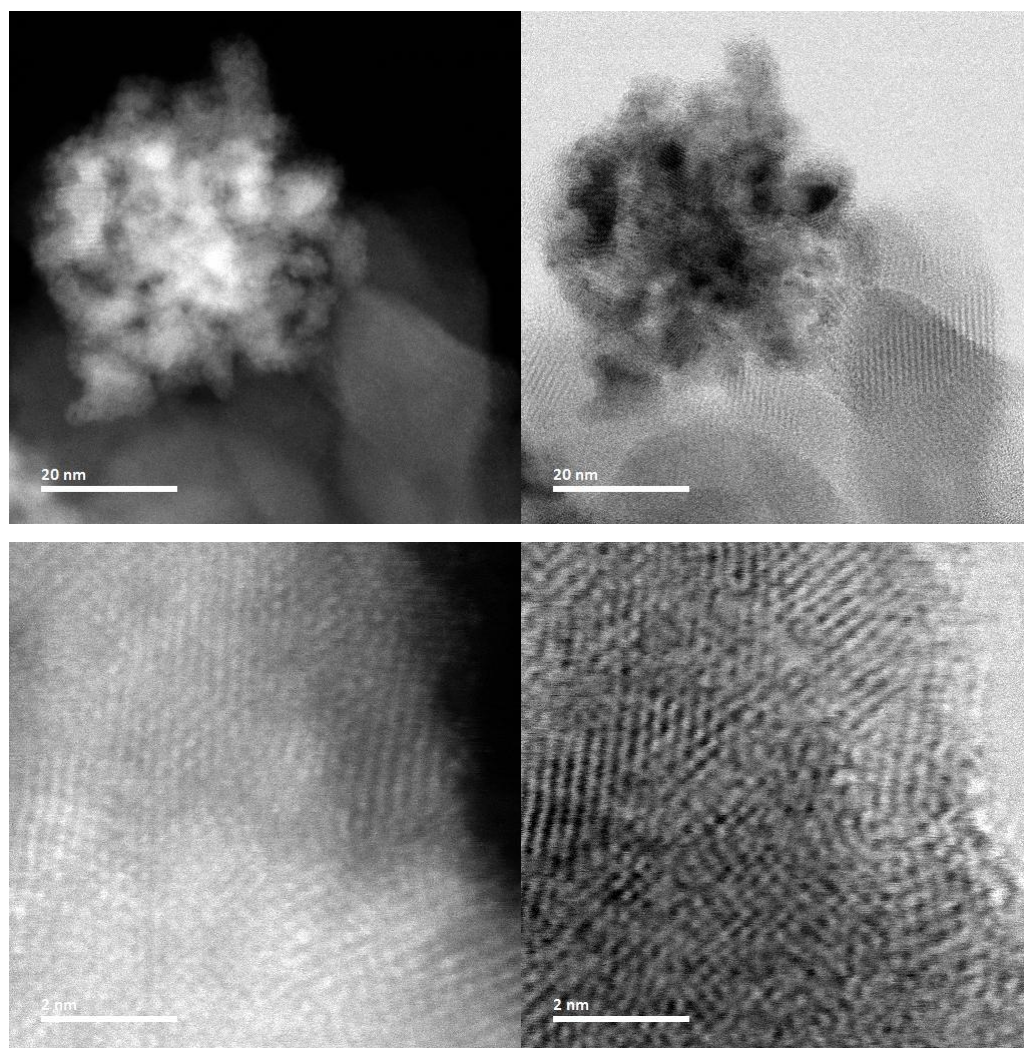


Figure S3.15. HAADF-STEM brightfield (left)/darkfield (right) images showing nickel particles (bright spots in brightfield and dark spots in darkfield) on CN-OA-m recovered from the experiment using method A (blue LED).

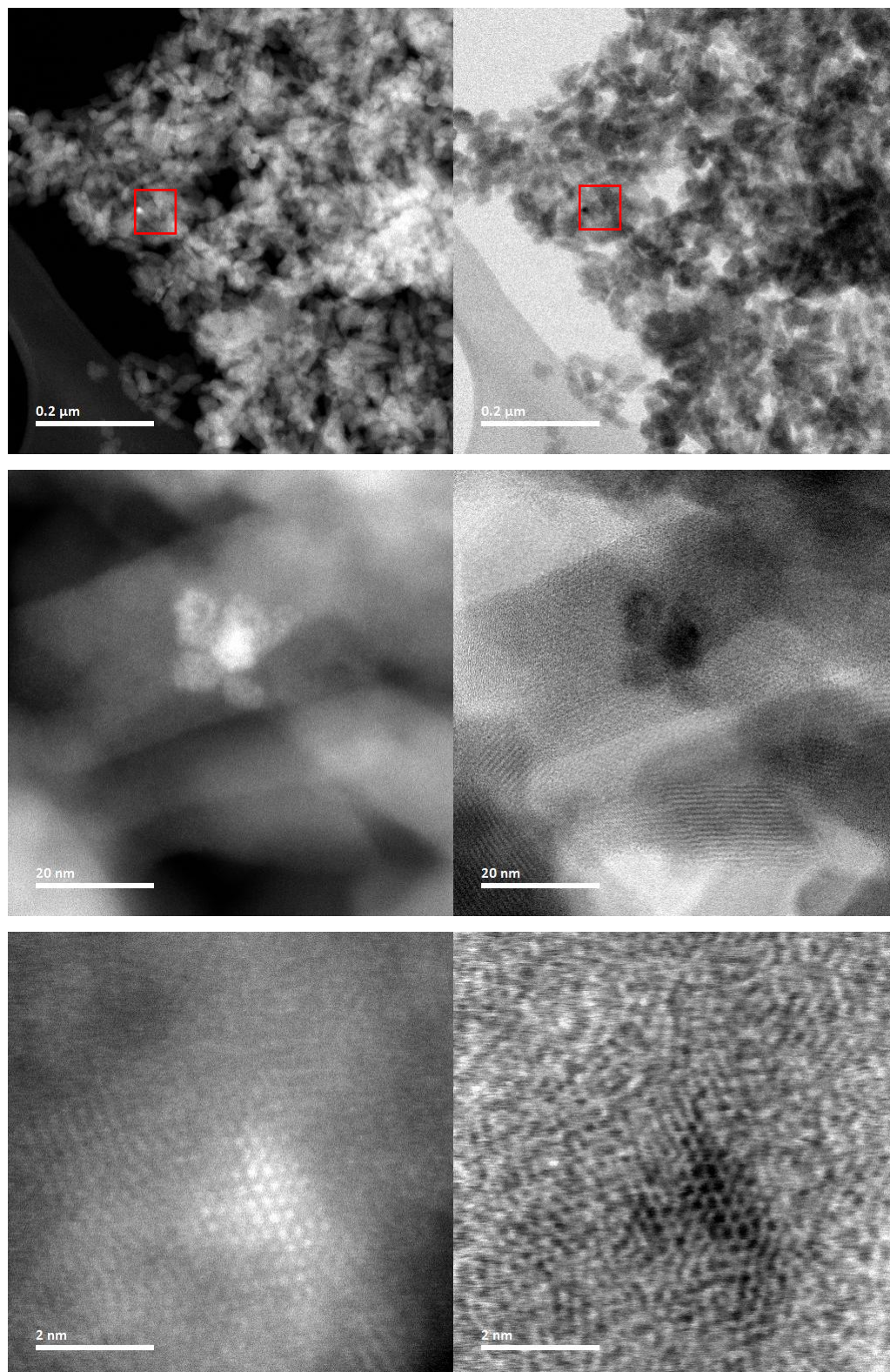


Figure S3.16. HAADF-STEM brightfield (left)/darkfield (right) showing a nickel particle (bright spot in brightfield and dark spot in darkfield) on CN-OA-m recovered from the experiment using method B (green LED).

3.5.8.2.2 Heterogeneous material generated during experiments using the UV method (photocatalyst-free and UV-light)

The STEM image shows the solid material formed using method C (UV-light). Although the particle mainly consists of nickel, lighter elements can be additionally identified. EDX analysis (Table S3.20) shows the presence of carbon, indicating that agglomerated nickel species incorporate organic materials. This is in agreement with the low mass-balance observed during these reactions (e.g. Table S3.18, Entry 20), suggesting substrate/product degradation presumably by the high energy light source.

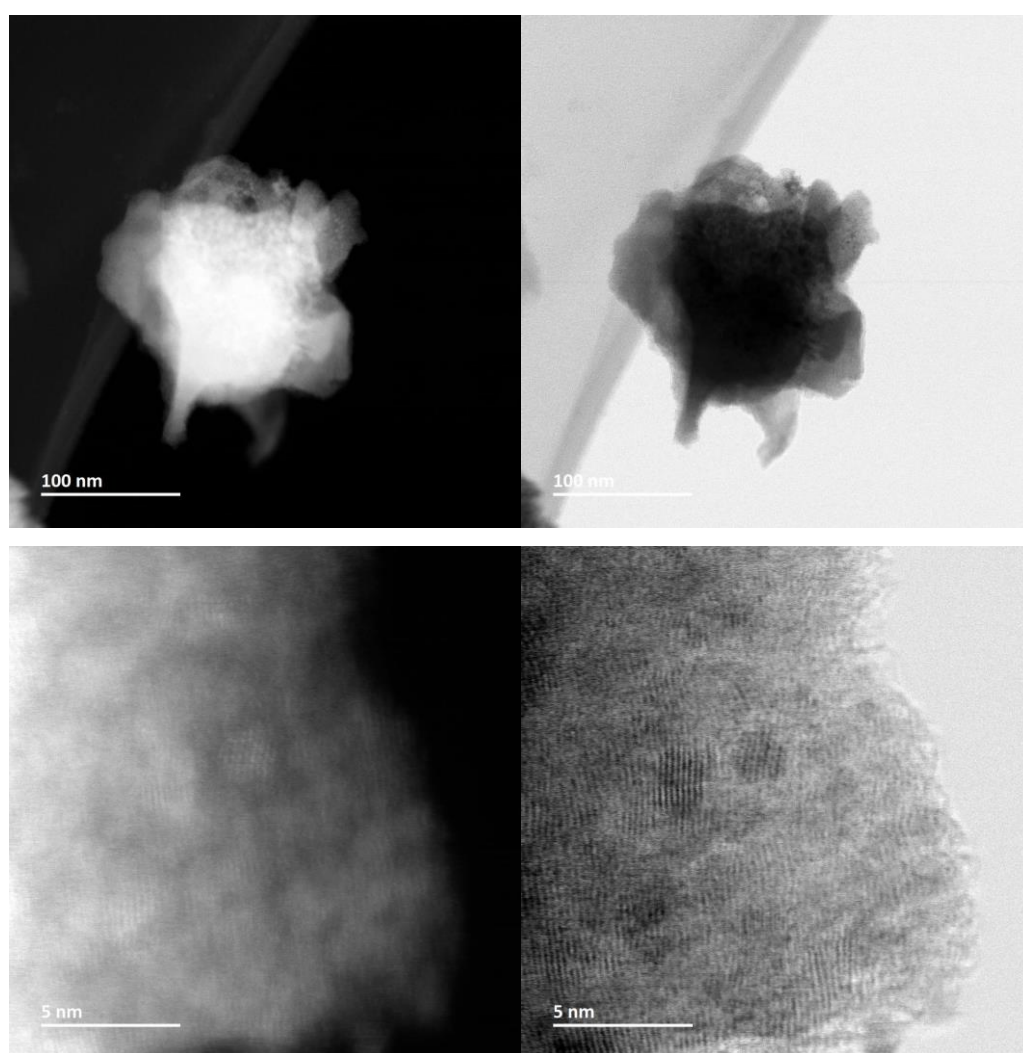


Figure S3.17. HAADF-STEM brightfield (left)/darkfield (right) images of nickel particles (bright spots in brightfield and dark spots in darkfield) after UV-light method (photocatalyst-free).

3.5.8.3 Scanning electron microscopy (SEM)

SEM images of the new and recovered CN-OA-m samples showed a porous texture that was not altered during the catalytic transformation (Figure S3.18).

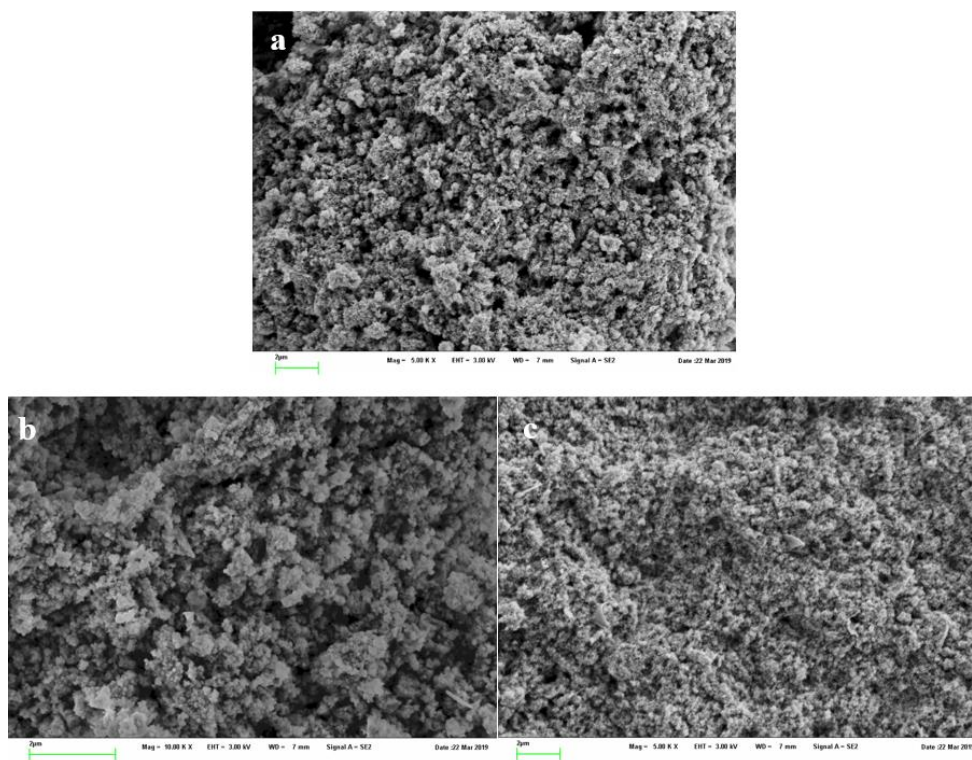


Figure S3.18. SEM images of CN-OA-m new (A), CN-OA-m recovered from the cross-coupling using blue light (Table S3.18, Entry 7) (B), and CN-OA-m recovered from the cross-coupling using green light (Table S3.18, Entry 8) (C).

3.5.8.4 Energy-dispersive X-ray spectroscopy (EDX) and inductively coupled plasma atomic emission spectroscopy (ICP-OES)

Elemental analysis via EDX (Table S3.20) and ICP-OES (Table S3.21) analysis of the recovered CN-OA-m samples shows a 3 times higher Ni concentration for the blue light experiment. The material from the blue light experiment contains ~12-14 w/w % Ni suggesting that ~70% of the homogeneous nickel catalyst were deposited on the CN-OA-m during the model reaction. The material from the green light experiment contains ~3-4 w/w % Ni suggesting that ~70% of the homogeneous nickel catalyst were deposited on the CN-OA-m during the model reaction.

Table S3.20. EDX elemental composition acquired from new and recovered CN-OA-m.

Sample	% w/w N	% w/w C	% w/w O	% w/w K	% w/w Ni
CN-OA-m	42.56	37.59	3.65	1.06	0.05
CN-OA-m from Method A (blue light)^a	36.25	30.27	7.16	8.60	13.90
CN-OA-m from Method B (green light)^b	47.19	29.46	7.79	8.86	3.38
Solid from UV-experiment^c	22.8	21.00	18.92	-	26.71

^aSample recovered from experiment described in Table S3.18, Entry 7. ^bSample recovered from experiment described in Table S3.18, Entry 8. ^cSample recovered from experiment described in Table S3.18, Entry 17.

Table S3.21. ICP-OES measurements of the nickel content on the new and recovered CN-OA-m.

Sample	Ni [mg/g CN]	% absorbed Ni
CN-OA-m new	0.69	0.39
CN-OA-m from Method A (blue light)^a	126	71.2
CN-OA-m from Method B (green light)^b	35.5	20.1

^aSample recovered from experiment described in Table S3.18, Entry 7.

^bSample recovered from experiment described in Table S3.18, Entry 8.

3.5.8.5 Fourier-transform infrared spectroscopy (FTIR) and Ultraviolet-visible spectroscopy (UV-VIS)

FTIR spectra of the new and recovered CN-OA-m samples were identical (Figure S3.19).

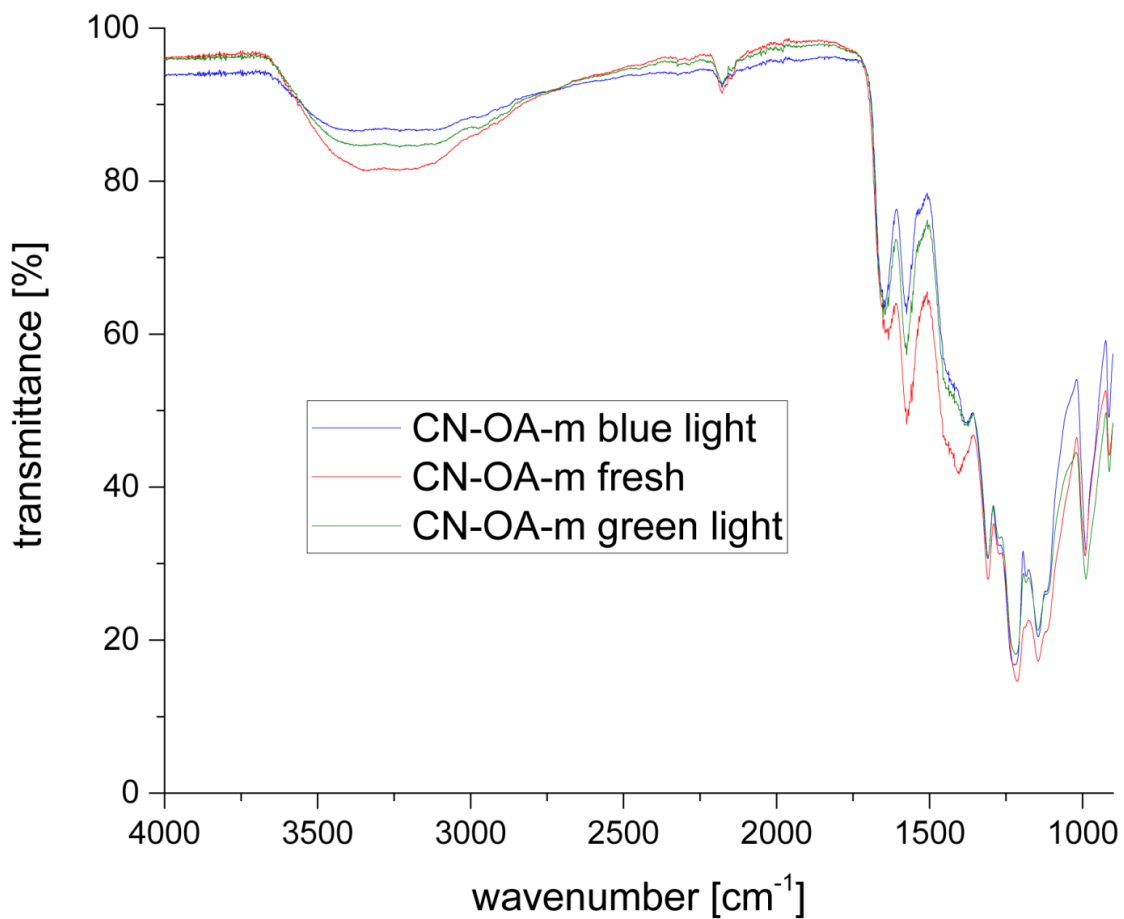


Figure S3.19. FTIR spectra of CN-OA-m new (red), CN-OA-m recovered from the cross-coupling using blue light (blue), and CN-OA-m recovered from the cross-coupling using green light (green).

The UV-Vis spectra of the CN-OA-m recovered from the cross-coupling using green light and CN-OA-m recovered from the cross-coupling using blue showed an increased absorption in the visible region (>460 nm) compared to a unused CN-OA-m sample.

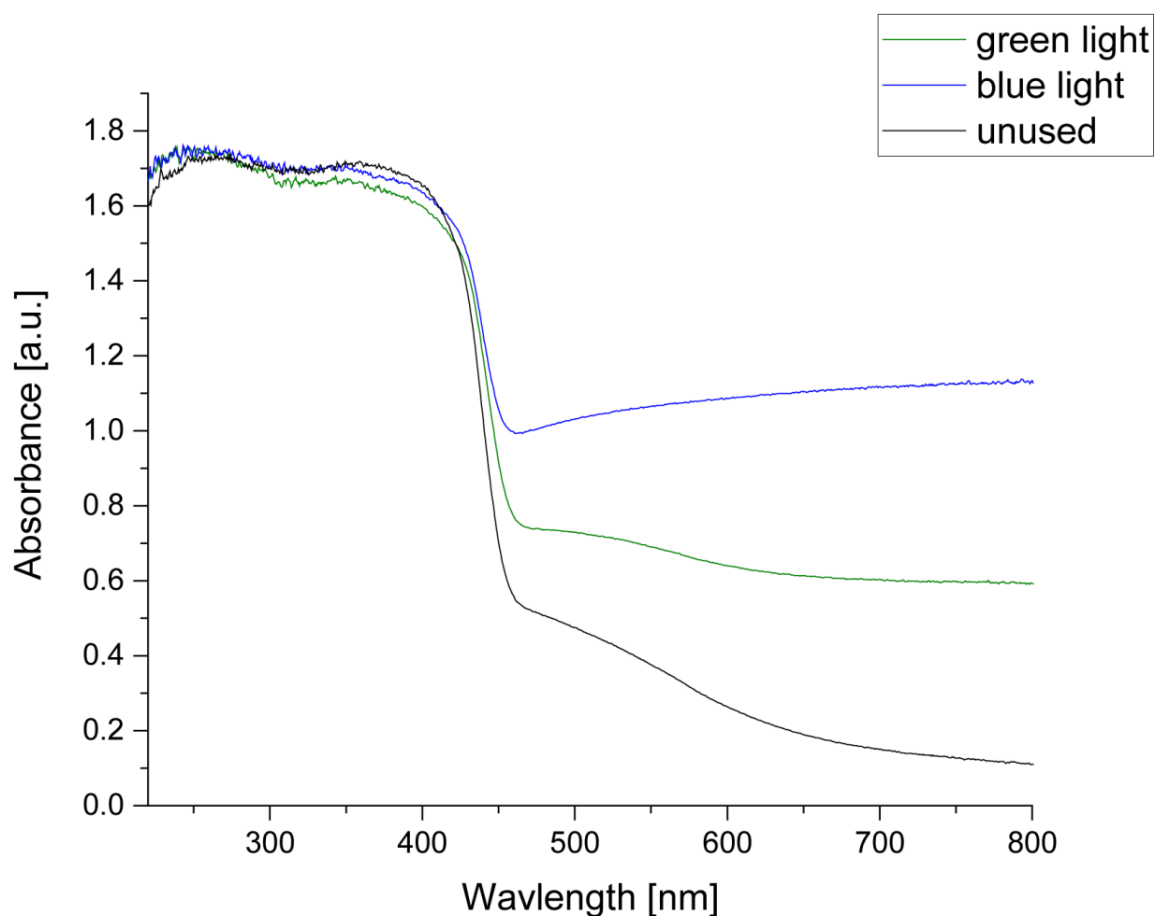
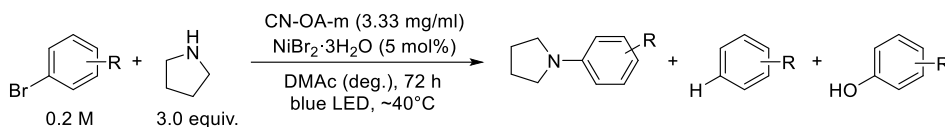


Figure S3.20. UV/Vis absorption spectra of CN-OA-m new (grey), CN-OA-m recovered from the cross-coupling using blue light (blue), and CN-OA-m recovered from the cross-coupling using green light (green).

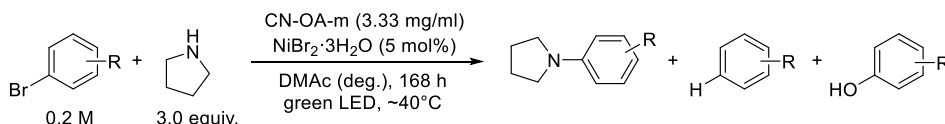
3.5.9 Studies on the reaction of bromobenzene, 3-bromotoluene, 1-bromo-4-*tert*-butylbenzene, and 4-bromoanisole with pyrrolidine.

Method A: Dual CN-OA-m/Ni catalysis with irradiation at 450 nm

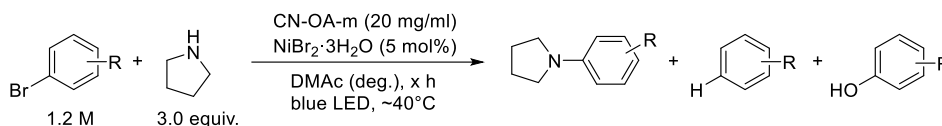


An oven dried vial (19 x 80 mm) equipped with a stir bar was charged with the CN-OA-m (20 mg), aryl bromide (1.2 mmol, 1.0 equiv.) and NiBr₂·3H₂O (16.4 mg, 60 μmol, 5.0 mol%). Subsequently, pyrrolidine (256.0 mg, 295.6 μl, 3.6 mmol, 3.0 equiv.) and DMAc (anhydrous, 6 mL) were added and the vial was sealed with a septum and Parafilm. The reaction mixture was sonicated for 5-10 min followed by stirring for 5 min until fine dispersion of the solids was achieved and the mixture was then degassed by bubbling N₂ for 10 min. The mixture was irradiated in the photoreactor (blue light function of RGB LED strip) at 40 °C with rapid stirring (1400 rpm). After 72 h, one equivalent of 1,3,5-trimethoxybenzene (1.2 mmol) was added and the mixture was stirred for 5 min. An aliquot of the reaction mixture (~300 μL) was filtered, diluted with DMSO-d₆ and subjected to ¹H-NMR analysis.

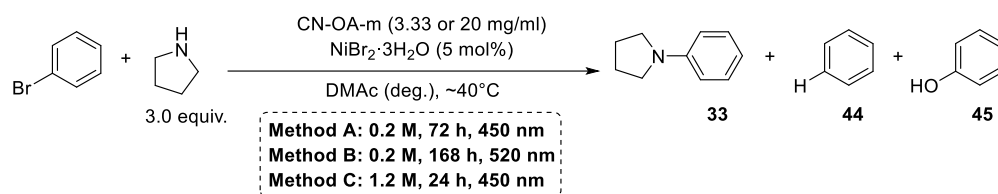
Method B: Dual CN-OA-m/Ni catalysis with irradiation at 520 nm



An oven dried vial (19 x 80 mm) equipped with a stir bar was charged with the CN-OA-m (20 mg), aryl bromide (1.2 mmol, 1.0 equiv.) and NiBr₂·3H₂O (16.4 mg, 60 μmol, 5.0 mol%). Subsequently, pyrrolidine (256.0 mg, 295.6 μl, 3.6 mmol, 3.0 equiv.) and DMAc (anhydrous, 6 mL) were added and the vial was sealed with a septum and Parafilm. The reaction mixture was sonicated for 5-10 min followed by stirring for 5 min until fine dispersion of the solids was achieved and the mixture was then degassed by bubbling N₂ for 10 min. The mixture was irradiated in the photoreactor (green light function of RGB LED strip) at 40 °C with rapid stirring (1400 rpm). After 168 h, one equivalent of 1,3,5-trimethoxybenzene (1.2 mmol) was added and the mixture was stirred for 5 min. An aliquot of the reaction mixture (~300 μL) was filtered, diluted with DMSO-d₆ and subjected to ¹H-NMR analysis.

Method C: Dual CN-OA-m/Ni catalysis with irradiation at 450 nm and higher concentration (1.2 M)

An oven dried vial (19 x 80 mm) equipped with a stir bar was charged with the CN-OA-m (20 mg), aryl bromide (1.2 mmol, 1.0 equiv.) and NiBr₂·3H₂O (16.4 mg, 60 μmol, 5.0 mol%). Subsequently, pyrrolidine (256.0 mg, 295.6 μl, 3.6 mmol, 3.0 equiv.) and DMAc (anhydrous, 1 mL) were added and the vial was sealed with a septum and Parafilm. The reaction mixture was sonicated for 5-10 min followed by stirring for 5 min until fine dispersion of the solids was achieved and the mixture was then degassed by bubbling N₂ for 10 min. The mixture was irradiated in the photoreactor (blue light function of RGB LED strip) at 40 °C with moderate stirring (600 rpm). After respective reaction time, one equivalent of 1,3,5-trimethoxybenzene (202.0 mg, 1.2 mmol) was added and the mixture was stirred for 5 min. An aliquot of the reaction mixture (~300 μL) was filtered, diluted with DMSO-d₆ and subjected to ¹H-NMR analysis.

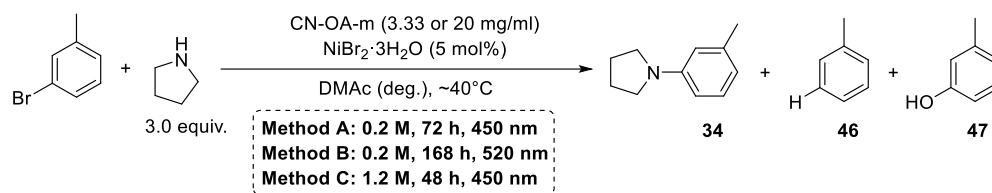
Table S3.22. Coupling of bromobenzene and pyrrolidine using methods A-C.

Entry	Procedure	Conversion [%] ^a	33 [%] ^b	44 [%] ^b	45 [%] ^b
1	A	quant.	74	8	11
2	A	quant.	68	11	10
3	A	quant.	67	11	12
4	A	quant.	66	10	11
5	A	67	44	7	6
6	A	56	32	5	4
<hr/>					
7	B	quant.	94	4	3
8	B	quant.	93	4	3
9	B	quant.	91	5	5
10	B	quant.	90	4	4
11	B	quant.	88	4	5
12	B	quant.	87	4	5
<hr/>					
13	C	quant.	86	8	4
14	C	quant.	85	7	3
15	C	99	85	8	3
16	C	quant.	85	9	3
17	C	quant.	84	8	3
18	C	quant.	84	9	3
19	C ^d	quant.	85	5	2
20	C ^d	quant.	82	5	1

^aConversion of bromobenzene determined by ¹H-NMR using 1,3,5-trimethoxybenzene as internal standard.

^bNMR yields determined by ¹H-NMR using 1,3,5-trimethoxybenzene as internal standard. ^cnot detected.

^dCarried out using 520 nm LEDs and 168 h reaction time.

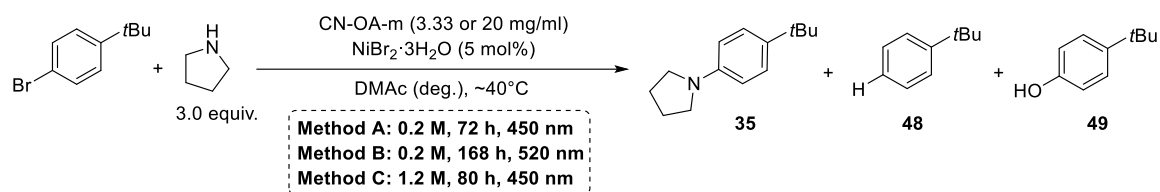
Table S3.23. Coupling of 3-bromotoluene and pyrrolidine using methods A-C.

Entry	Procedure	Conversion [%] ^a	34 [%] ^b	46 [%] ^b	47 [%] ^b
1	A	quant.	74	17	6
2	A	quant.	72	17	6
3	A	quant.	72	18	4
4	A	quant.	61	18	12
5	A	64	31	12	9
6	A	52	20	13	8
<hr/>					
7	B	quant.	93	5	4
8	B	quant.	86	10	4
9	B	quant.	85	10	5
10	B	quant.	84	10	5
11	B	quant.	84	10	7
12	B	quant.	83	10	6
<hr/>					
13	C	quant.	85	14	2
14	C	quant.	84	14	3
15	C	quant.	83	14	3
16	C	quant.	83	14	3
17	C	quant.	82	15	3
18	C	quant.	81	16	3
19	C ^d	quant.	80	6	0

^aConversion of 3-bromotoluene determined by ¹H-NMR using 1,3,5-trimethoxybenzene as internal standard.

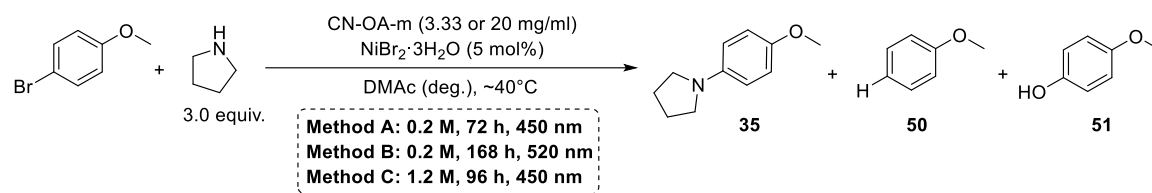
^bNMR yields determined by ¹H-NMR using 1,3,5-trimethoxybenzene as internal standard. ^cnot detected.

^dCarried out using 520 nm LEDs and 168 h reaction time.

Table S3.24. Coupling of 1-bromo-4-*tert*-butylbenzene and pyrrolidine using methods A-C.

Entry	Procedure	Conversion [%] ^a	35 [%] ^b	48 [%] ^b	49 [%] ^b
1	A	98	70	13	9
2	A	99	69	17	7
3	A	quant.	67	14	8
4	A	88	57	16	9
5	A	82	53	15	9
6	A	90	52	13	7
7	B	quant.	92	5	3
8	B	96	90	4	2
9	B	94	87	3	3
10	B	91	85	3	2
11	B	57	50	4	2
12	B	30	28	1	2
13	C	quant.	82	9	2
14	C	quant.	80	9	1
15	C	quant.	80	9	2
16	C	quant.	80	9	2
17	C	quant.	80	9	3
18	C	quant.	80	10	3
19	C ^d	91	82	4	0

^aConversion of 1-bromo-4-*tert*-butylbenzene determined by ¹H-NMR using 1,3,5-trimethoxybenzene as internal standard. ^bNMR yields determined by ¹H-NMR using 1,3,5-trimethoxybenzene as internal standard. ^cnot detected. ^dCarried out using 520 nm LEDs and 72 h reaction time.

Table S3.25. Coupling of 4-bromoanisole and pyrrolidine using methods A-C.

Entry	Procedure	Conversion [%] ^a	35 [%] ^b	50 [%] ^b	51 [%] ^b
1	A	86	80	6	n.d. ^c
2	A	91	78	12	2
3	A	90	72	10	5
4	A	66	53	8	2
5	A	43	32	4	2
6	A	13	4	n.d.	2
7	B	82	77	7	0
8	B	83	77	6	0
9	B	76	68	6	0
10	B	68	60	4	4
11	B	68	60	4	3
12	B	58	52	4	2
13	C	quant.	81	8	5
14	C	quant.	80	11	5
15	C	quant.	80	11	5
16	C	quant.	80	8	4
17	C	quant.	79	11	4
18	C	quant.	77	9	6
19	C ^d	quant.	84	8	1
20	C ^d	quant.	83	8	0

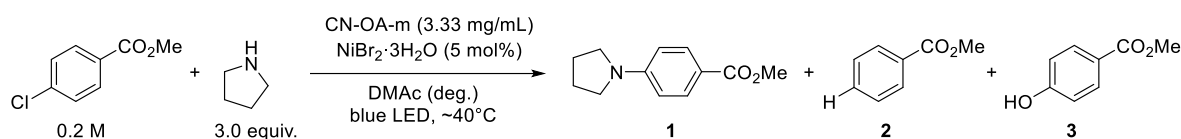
^aConversion of 4-bromoanisole determined by ¹H-NMR using 1,3,5-trimethoxybenzene as internal standard.

^bNMR yields determined by ¹H-NMR using 1,3,5-trimethoxybenzene as internal standard. ^cnot detected.

^dCarried out using 520 nm LEDs and 168 h reaction time.

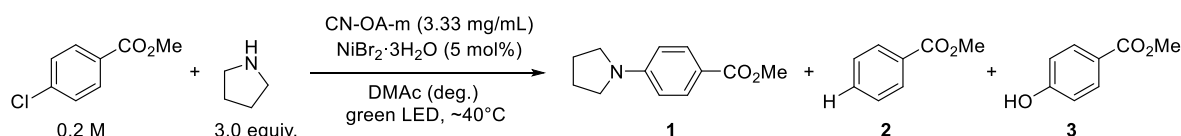
3.5.10 Studies on the reaction of pyrrolidine with aryl chlorides

Method A: Dual CN-OA-m/Ni catalysis with irradiation at 450 nm

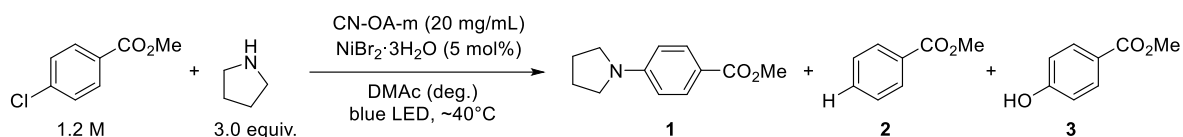


An oven dried vial (19 x 80 mm) equipped with a stir bar was charged with the CN-OA-m (20 mg), methyl 4-chloromethylbenzoate (204.7 mg, 1.2 mmol, 1.0 equiv.) and NiBr₂·3H₂O (16.4 mg, 60 μmol, 5.0 mol%). Subsequently, pyrrolidine (64.0 mg, 295.6 μl, 3.6 mmol, 3.0 equiv.) and DMAc (anhydrous, 6 mL) were added and the vial was sealed with a septum and Parafilm. The reaction mixture was sonicated for 5-10 min followed by stirring for 5 min until fine dispersion of the solids was achieved and the mixture was then degassed by bubbling N₂ for 10 min. The mixture was irradiated in the photoreactor (blue light of LED-band) at 40 °C with rapid stirring (1400 rpm). After respective reaction time, one equivalent of 1,3,5-trimethoxybenzene (202.0 mg, 1.2 mmol) was added and the mixture was stirred for 5 min. An aliquot of the reaction mixture (~300 μL) was filtered, diluted with DMSO-d₆ and subjected to ¹H-NMR analysis.

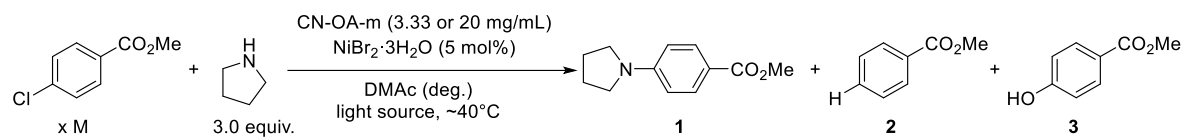
Method B: Dual CN-OA-m/Ni catalysis with irradiation at 520 nm



An oven dried vial (19 x 80 mm) equipped with a stir bar was charged with the CN-OA-m (20 mg), methyl 4-chloromethylbenzoate (204.7 mg, 1.2 mmol, 1.0 equiv.) and NiBr₂·3H₂O (16.4 mg, 60 μmol, 5.0 mol%). Subsequently, pyrrolidine (64.0 mg, 295.6 μl, 3.6 mmol, 3.0 equiv.) and DMAc (anhydrous, 6 mL) were added and the vial was sealed with a septum and Parafilm. The reaction mixture was sonicated for 5-10 min followed by stirring for 5 min until fine dispersion of the solids was achieved and the mixture was then degassed by bubbling N₂ for 10 min. The mixture was irradiated in the photoreactor (blue light of LED-band) at 40 °C with rapid stirring (1400 rpm). After respective reaction time, one equivalent of 1,3,5-trimethoxybenzene (202.0 mg, 1.2 mmol) was added and the mixture was stirred for 5 min. An aliquot of the reaction mixture (~300 μL) was filtered, diluted with DMSO-d₆ and subjected to ¹H-NMR analysis.

Method C: Dual CN-OA-m/Ni catalysis with irradiation at 450 nm and higher concentration (1.2 M)

An oven dried vial (19 x 80 mm) equipped with a stir bar was charged with the CN-OA-m (20 mg), methyl 4-chloromethylbenzoate (204.7 mg, 1.2 mmol, 1.0 equiv.) and NiBr₂·3H₂O (16.4 mg, 60 μmol, 5.0 mol%). Subsequently, pyrrolidine (64.0 mg, 295.6 μl, 3.6 mmol, 3.0 equiv.) and DMAc (anhydrous, 1 mL) were added and the vial was sealed with a septum and Parafilm. The reaction mixture was sonicated for 5-10 min followed by stirring for 5 min until fine dispersion of the solids was achieved and the mixture was then degassed by bubbling N₂ for 10 min. The mixture was irradiated in the photoreactor (blue light or green function of LED-band) at 40 °C with moderate stirring (600 rpm). After respective reaction time, one equivalent of 1,3,5-trimethoxybenzene (202.0 mg, 1.2 mmol) was added and the mixture was stirred for 5 min. An aliquot of the reaction mixture (~300 μL) was filtered, diluted with DMSO-d₆ and subjected to ¹H-NMR analysis.

Table S3.26. Coupling of methyl 4-chlorobenzoate and pyrrolidine using methods A-C.

Entry	Method	Time [days]	Conversion [%] ^a	1 [%] ^b	2 [%] ^b	3 [%] ^b
1	A	3	47	37	2	n.d. ^c
2	A	7	78	65	7	3
3	A	14	91	65	16	7
4	B	3	59	41	1	12
5	B	7	76	72	4	n.d.
6	B	14	89	83	n.d.	9
7	C	1	79	75	3	1
8	C	2	97	92	3	2
9	C	3	97	89	4	2
10	C	4	99	89	3	2

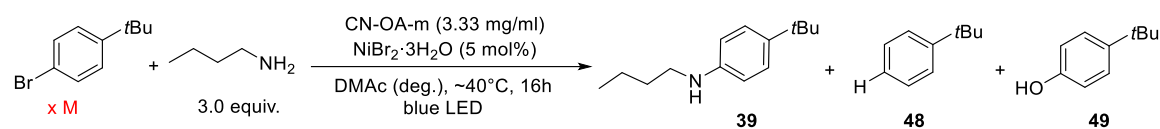
^aConversion of methyl 4-chlorobenzoate determined by ¹H-NMR using 1,3,5-trimethoxybenzene as internal standard. ^bNMR yields determined by ¹H-NMR using 1,3,5-trimethoxybenzene as internal standard. ^cnot detected

Table S3.27. NMR-Yields for the coupling of electroneutral and electron-rich aryl chlorides with pyrrolidine at 40 °C and blue LED irradiation using method C.

Aryl chloride				
Yield ^a	18%	10%	5%	2%

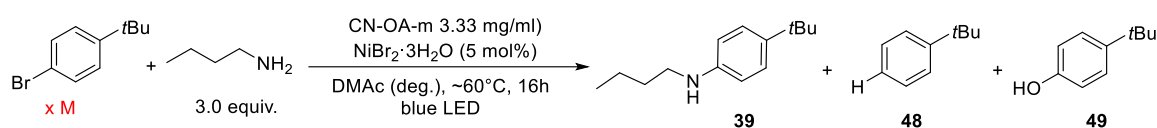
^aNMR yields determined by ¹H-NMR using 1,3,5-trimethoxybenzene as internal standard.

3.5.11 Studies on the coupling of *n*-butylamine with aryl halides

Table S3.28. Coupling of 1-bromo-4-*tert*-butylbenzene and *n*-butylamine using different concentrations at 40 °C and blue light.

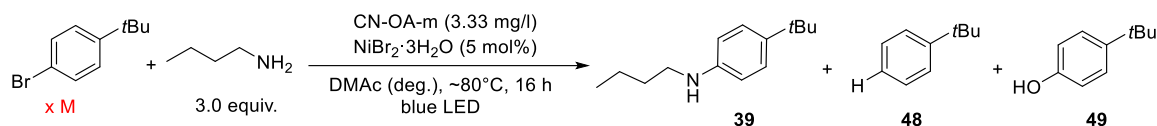
Entry	Concentration [mol/L]	Conversion [%] ^a	39 [%] ^b	48 [%] ^b	49 [%] ^b
1	0.2	8	8	n.d. ^c	n.d.
2	0.4	6	6	n.d.	n.d.
3	0.6	4	4	n.d.	n.d.
4	0.8	3	3	n.d.	n.d.
5	1.2	2	2	n.d.	n.d.

^aConversion of 1-bromo-4-*tert*-butylbenzene determined by ¹H-NMR using 1,3,5-trimethoxybenzene as internal standard. ^bNMR yields determined by ¹H-NMR using 1,3,5-trimethoxybenzene as internal standard. ^cnot detected.

Table S3.29. Coupling of 1-bromo-4-*tert*-butylbenzene and *n*-butylamine using different concentrations at 60 °C and blue light.

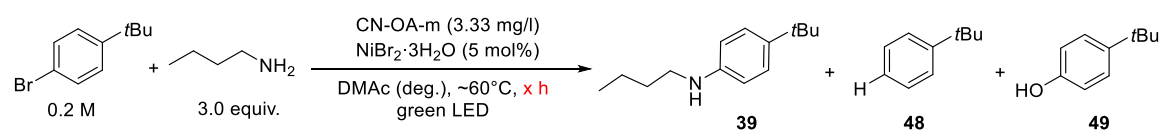
Entry	Concentration [mol/L]	Conversion [%] ^a	39 [%] ^b	48 [%] ^b	49 [%] ^b
1	0.2	22	20	2	n.d. ^c
2	0.4	15	13	2	n.d.
3	0.6	11	10	1	n.d.
4	0.8	9	8	1	n.d.
5	1.2	7	6	1	n.d.

^aConversion of 1-bromo-4-*tert*-butylbenzene determined by ¹H-NMR using 1,3,5-trimethoxybenzene as internal standard. ^bNMR yields determined by ¹H-NMR using 1,3,5-trimethoxybenzene as internal standard. ^cnot detected.

Table S3.30. Coupling of 1-bromo-4-*tert*-butylbenzene and *n*-butylamine using different concentrations at 80 °C.

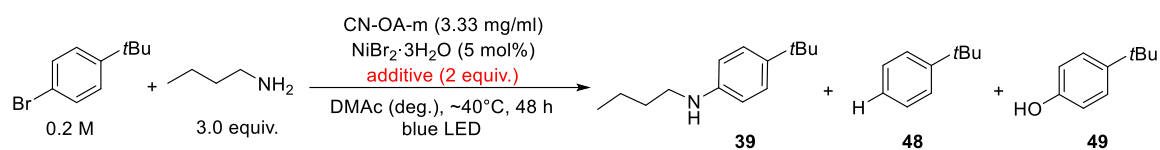
Entry	Concentration [mol/L]	Conversion [%] ^a	39 [%] ^b	48 [%] ^b	49 [%] ^b
1	0.2	26	26	n.d. ^c	n.d.
2	0.4	14	12	2	n.d.
3	0.6	10	10	n.d.	n.d.
4	0.8	15	15	n.d.	n.d.
5	1.2	6	4	2	n.d.

^aConversion of 1-bromo-4-*tert*-butylbenzene determined by ¹H-NMR using 1,3,5-trimethoxybenzene as internal standard. ^bNMR yields determined by ¹H-NMR using 1,3,5-trimethoxybenzene as internal standard. ^cnot detected.

Table S3.31. Coupling of 1-bromo-4-*tert*-butylbenzene and *n*-butylamine at 60 °C and green light irradiation.

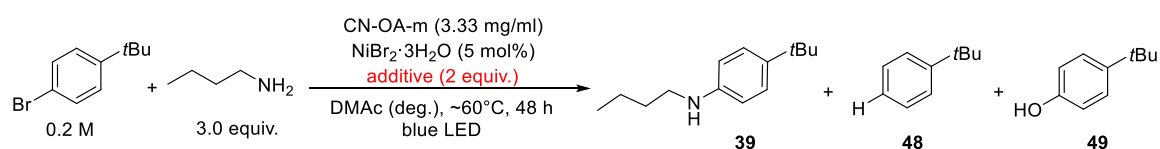
Entry	Time [h]	Conversion [%] ^a	37 [%] ^b	45 [%] ^b	46 [%] ^b
1	72	20	20	n.d. ^c	n.d.
2	96	20	20	n.d.	n.d.

^aConversion of 1-bromo-4-*tert*-butylbenzene determined by ¹H-NMR using 1,3,5-trimethoxybenzene as internal standard. ^bNMR yields determined by ¹H-NMR using 1,3,5-trimethoxybenzene as internal standard. ^cnot detected.

Table S3.32. Additive screening for the coupling of 1-bromo-4-*tert*-butylbenzene and *n*-butylamine at 40 °C.

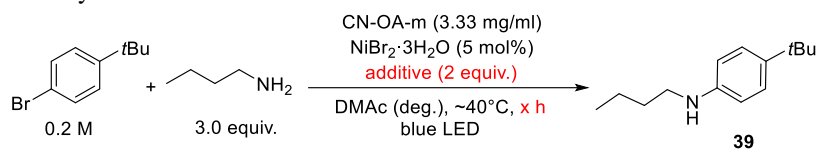
Entry	base	Conversion [%] ^a	39 [%] ^b	48 [%] ^b	49 [%] ^b
1	MTBD ^c	51	48	2	n.d. ^d
2	DABCO ^e	20	20	n.d.	n.d.
3	none	14	14	n.d.	n.d.
4	quinuclidine ^f	14	14	n.d.	n.d.
6	Pyrrolidine ^g	14	13	1	n.d.
7	DBU ^h	11	10	1	n.d.
5	BIPA ⁱ	10	9	1	n.d.










^aConversion of 1-bromo-4-*tert*-butylbenzene determined by ¹H-NMR using 1,3,5-trimethoxybenzene as internal standard. ^bNMR yields determined by ¹H-NMR using 1,3,5-trimethoxybenzene as internal standard. ^c7-Methyl-1,5,7-triazabicyclo[4.4.0]dec-5-ene. ^dnot detected. ^e1,4-diazabicyclo[2.2.2]octane. ^f1-Azabicyclo[2.2.2]octane. ^g10 mol%. ^h1,8-Diazabicyclo(5.4.0)undec-7-ene. ⁱ*N*-*tert*-butylisopropylamine.

Table S3.33. Additive screening for the coupling of 1-bromo-4-*tert*-butylbenzene and *n*-butylamine at 60 °C.

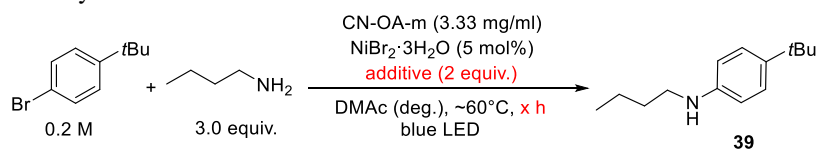
Entry	base	Conversion [%] ^a	39 [%] ^b	48 [%] ^b	49 [%] ^b
1	MTBD ^c	62	55	6	n.d. ^d
2	DABCO ^e	64	49	9	5
3	none	46	39	7	n.d.

^aConversion of 1-bromo-4-*tert*-butylbenzene determined by ¹H-NMR using 1,3,5-trimethoxybenzene as internal standard. ^bNMR yields determined by ¹H-NMR using 1,3,5-trimethoxybenzene as internal standard. ^c7-Methyl-1,5,7-triazabicyclo[4.4.0]dec-5-ene. ^dnot detected. ^e1,4-diazabicyclo[2.2.2]octane.

Table S3.34. Time study using no additive, DABCO, and MTBD for the coupling of 1-bromo-4-*tert*-butylbenzene and *n*-butylamine at 40 °C and blue LED irradiation. ^a

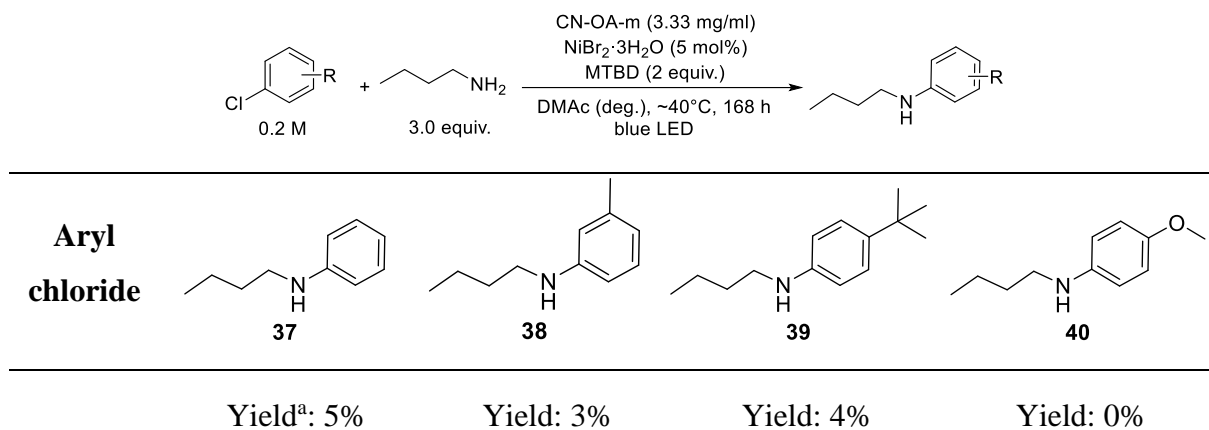
additive	48 h	96 h	168 h
none	 Yield: 14%	 Yield: 16%	 Yield: 18%
DABCO ^b	 Yield: 20%	 Yield: 35%	 Yield: 37%
MTBD ^c	 Yield: 48%	 Yield: 72%	 Yield: 85%

^aNMR yields determined by ¹H-NMR using 1,3,5-trimethoxybenzene as internal standard. ^b1,4-diazabicyclo[2.2.2]octane. ^c7-Methyl-1,5,7-triazabicyclo[4.4.0]dec-5-ene.

Table S3.35. Time study using no additive, DABCO and MTBD for the coupling of 1-bromo-4-*tert*-butylbenzene and *n*-butylamine at 60 °C and blue LED irradiation. ^a

additive		48 h		96 h		168 h
none		Yield: 39%		Yield: 30%		Yield: 42%
DABCO ^b		Yield: 49%		Yield: 42%		Yield: 35%
MTBD ^c		Yield: 55%		Yield: 50%		Yield: 38%

^aNMR yields determined by ¹H-NMR using 1,3,5-trimethoxybenzene as internal standard. ^b1,4-diazabicyclo[2.2.2]octane. ^c7-Methyl-1,5,7-triazabicyclo[4.4.0]dec-5-ene.

Table S3.36. NMR-Yields for the coupling of electro-neutral and electron-rich aryl chlorides with *n*-butylamine using MTBD at 40 °C and blue LED irradiation.

^aNMR yields determined by ¹H-NMR using 1,3,5-trimethoxybenzene as internal standard. ^b MTBD= 7-Methyl-1,5,7-triazabicyclo[4.4.0]dec-5-ene.

3.5.12 Nickel-black formation: Time studies in absence of aryl halides

General procedure. An oven dried vial (19 x 80 mm) equipped with a stir bar was charged with CN-OA-m (20 mg), and $\text{NiBr}_2 \cdot 3\text{H}_2\text{O}$ (0.06 mmol). Subsequently, the amine (3.6 mmol) (and - in case of additive experiments - 7-Methyl-1,5,7-triazabicyclo[4.4.0]dec-5-ene (MTBD, 2.4 mmol), or 1,4-diazabicyclo[2.2.2]octane (DABCO, 2.4 mmol)) and DMAc (anhydrous, Method A, B, and D: 6 mL, Method C: 1 mL) were added and the vial was sealed with a septum and Parafilm. The reaction mixture was sonicated for 5-10 min until fine dispersion of the solids was achieved and the mixture was then degassed by bubbling N_2 for 10 min. The mixture was irradiated in the photoreactor (blue (450 nm) or green (520 nm) light at 40 or 60°C. Pictures of the reaction mixtures were taken regularly to study the rate of Ni-black formation.

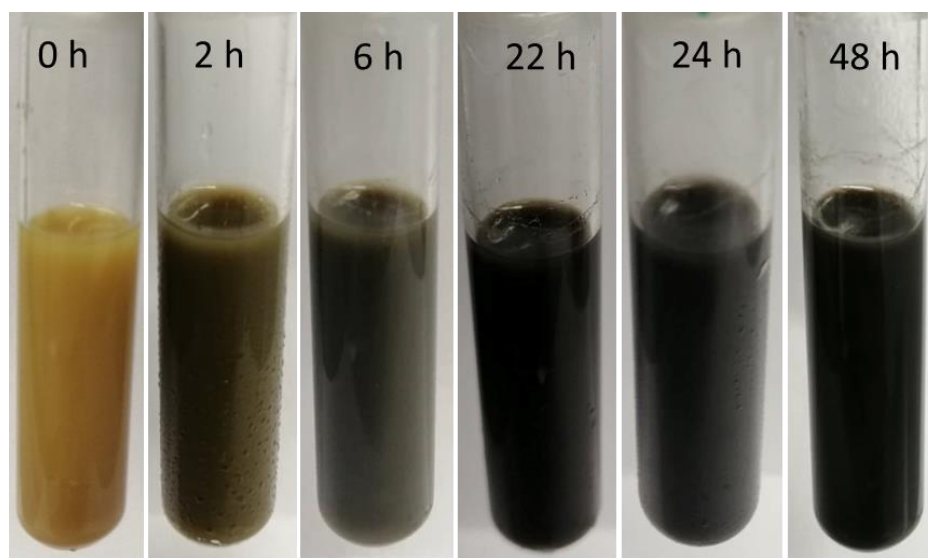
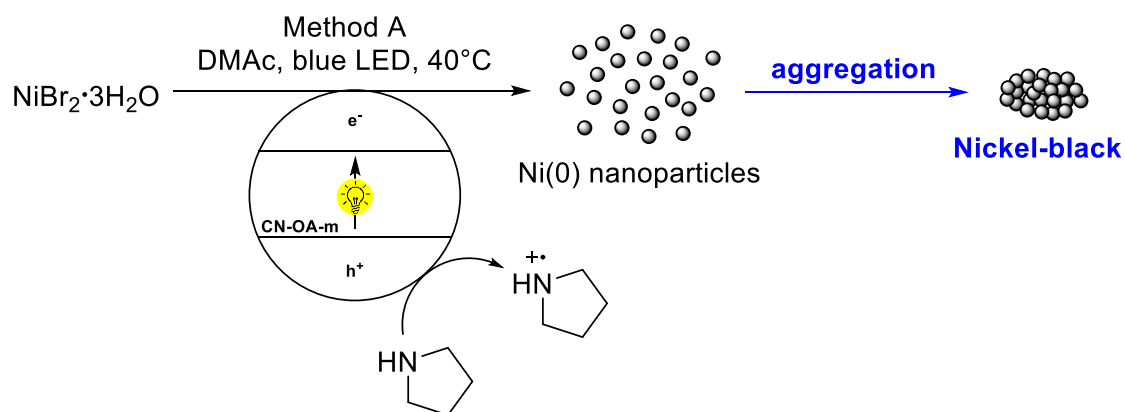


Figure S3.21. Time-dependent discoloration of the solution for method A due to nickel particle formation over time using $\text{NiBr}_2 \cdot 3\text{H}_2\text{O}$ as nickel source, CN-OA-m as photoredox catalyst (PRC) and pyrrolidine as single electron donor (SED) in DMAc (0.2M) under blue light irradiation at 40 °C.

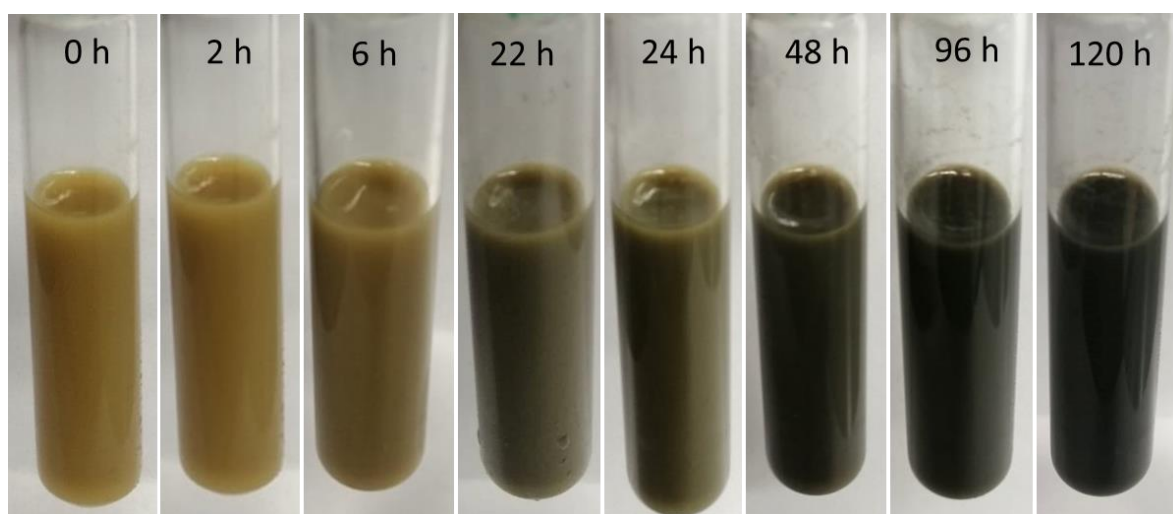
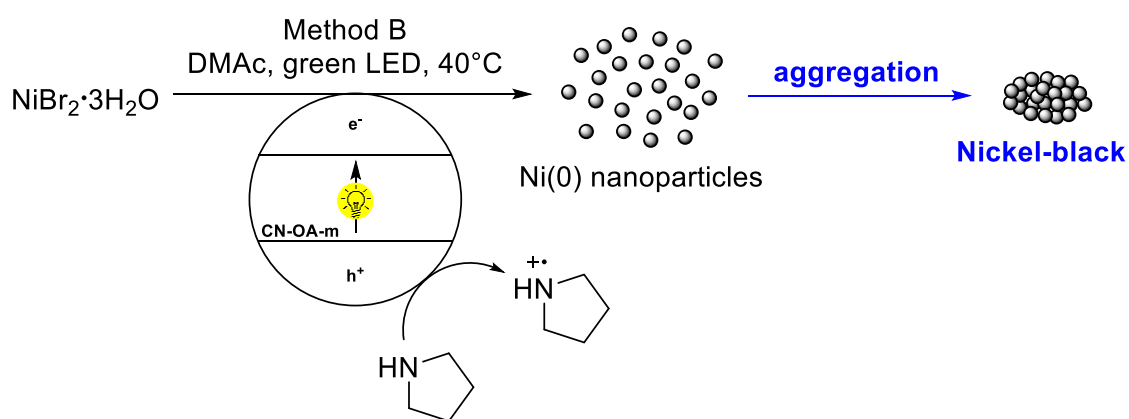


Figure S3.22. Time-dependent discoloration of the solution for method B due to nickel particle formation over time using $\text{NiBr}_2 \cdot 3\text{H}_2\text{O}$ as nickel source, CN-OA-m as photoredox catalyst (PRC) and pyrrolidine as single electron donor (SED) in DMAc (0.2M) under green light irradiation at 40 °C.

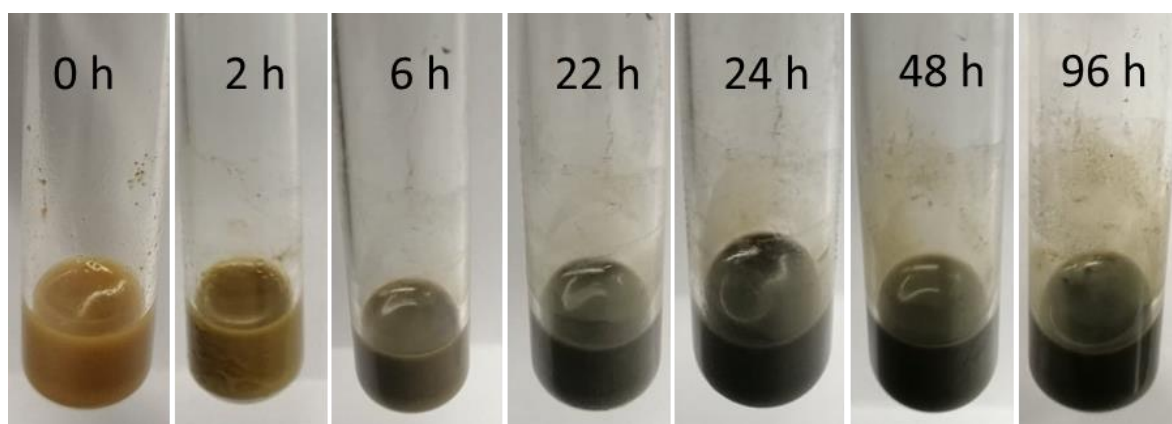
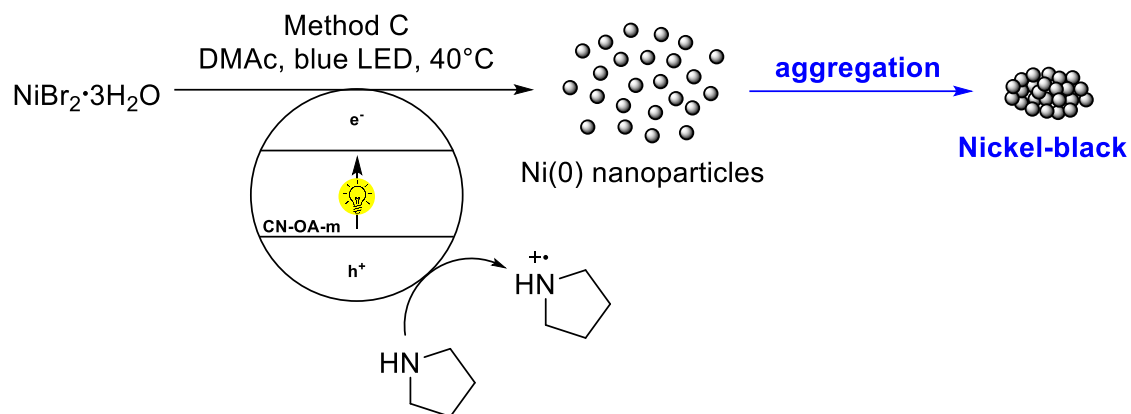


Figure S3.23. Time-dependent discoloration of the solution for method C due to nickel particle formation over time using $\text{NiBr}_2 \cdot 3\text{H}_2\text{O}$ as nickel source, CN-OA-m as photoredox catalyst (PRC) and pyrrolidine as single electron donor (SED) in DMAc (1.2 M) under blue light irradiation at 40 °C.

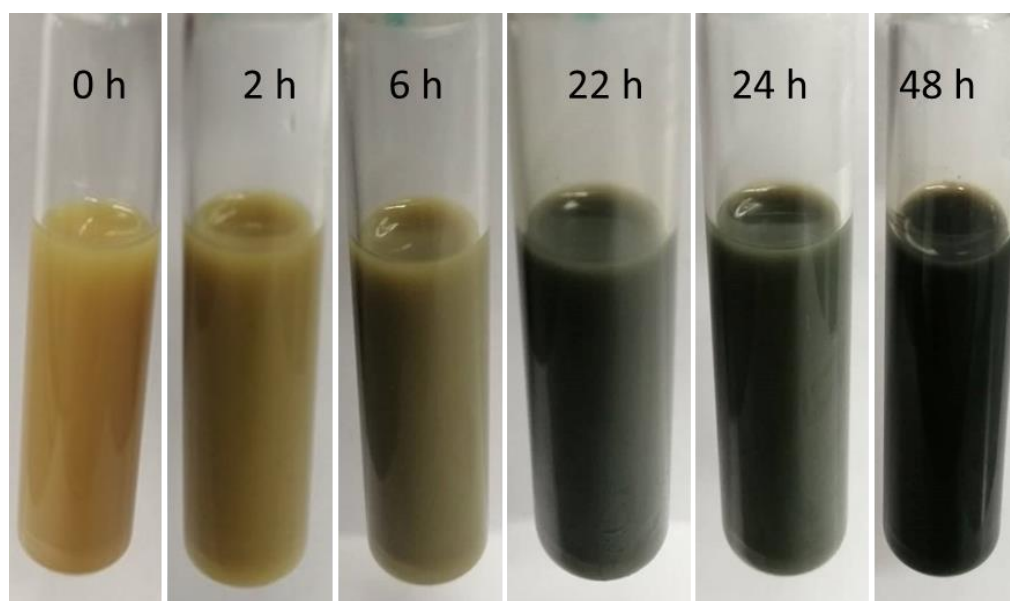
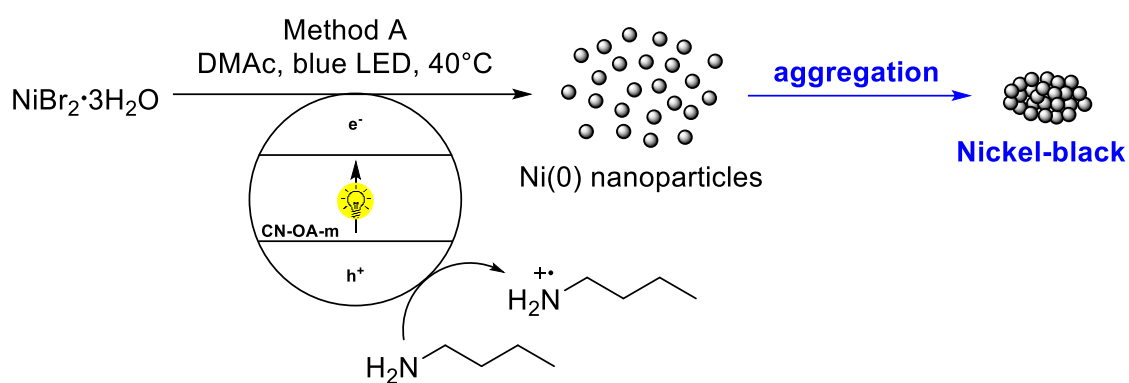


Figure S3.24. Time-dependent discoloration of the solution for method A due to nickel particle formation over time using $\text{NiBr}_2 \cdot 3\text{H}_2\text{O}$ as nickel source, CN-OA-m as photoredox catalyst (PRC) and n-butylamine as single electron donor (SED) in DMAc (0.2M) under blue light irradiation at 40 °C.

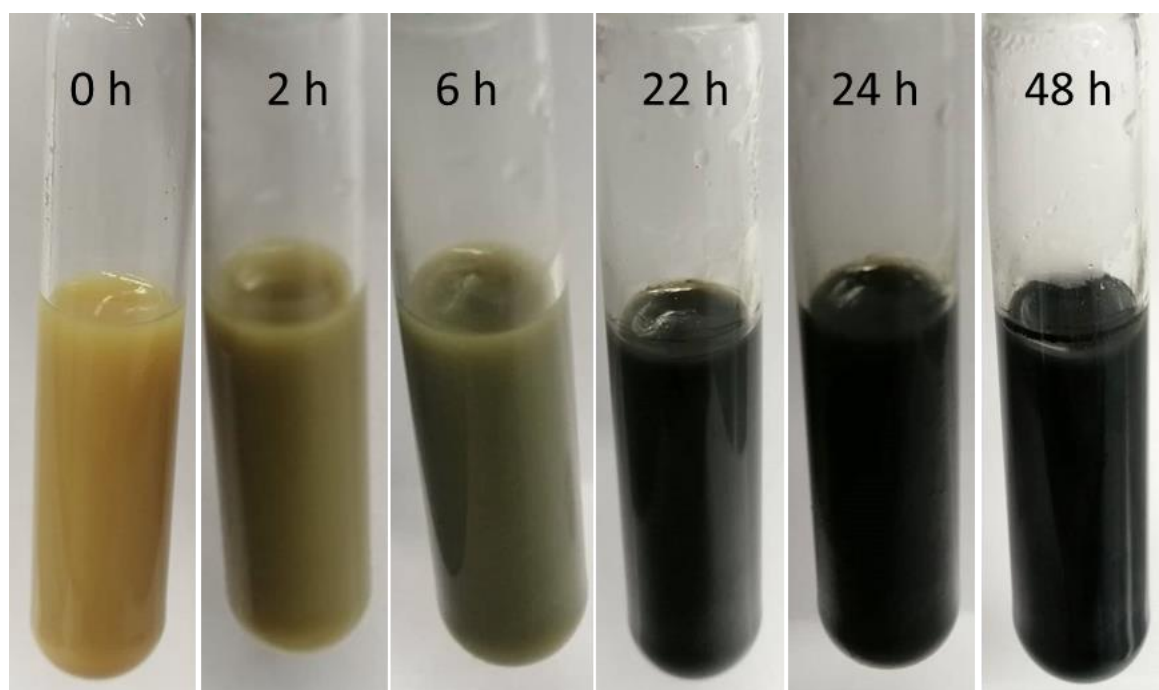
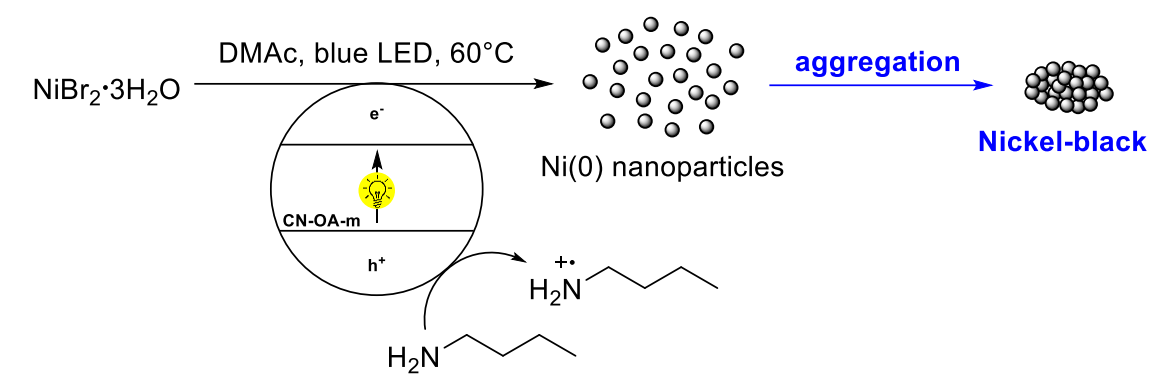


Figure S3.25. Time-dependent discoloration of the solution for method A due to nickel particle formation over time using $\text{NiBr}_2 \cdot 3\text{H}_2\text{O}$ as nickel source, CN-OA-m as photoredox catalyst (PRC) and n-butylamine as single electron donor (SED) in DMAc (0.2M) under blue light irradiation at 60 °C.

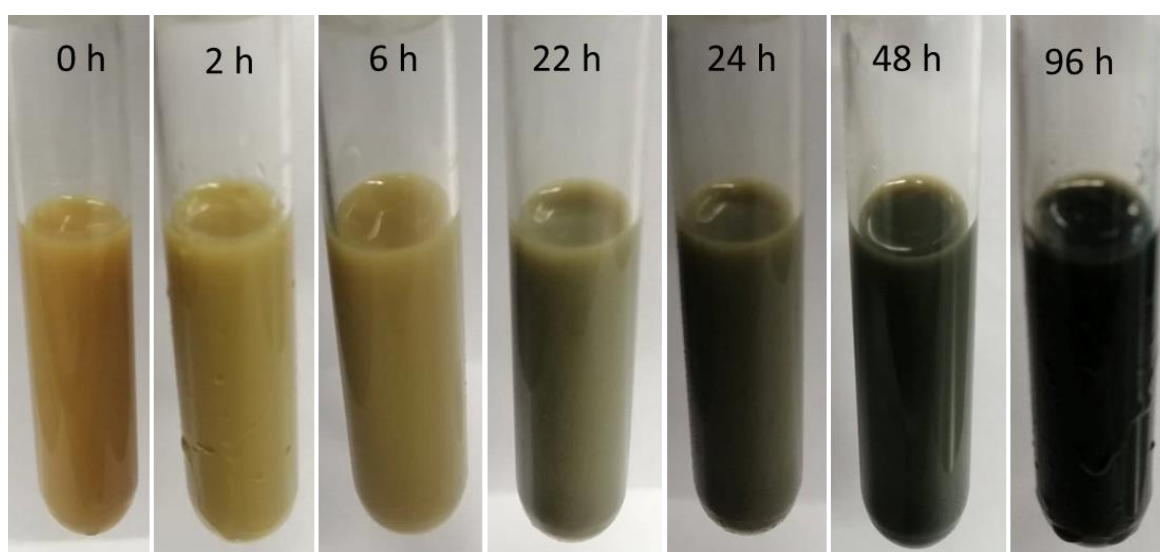
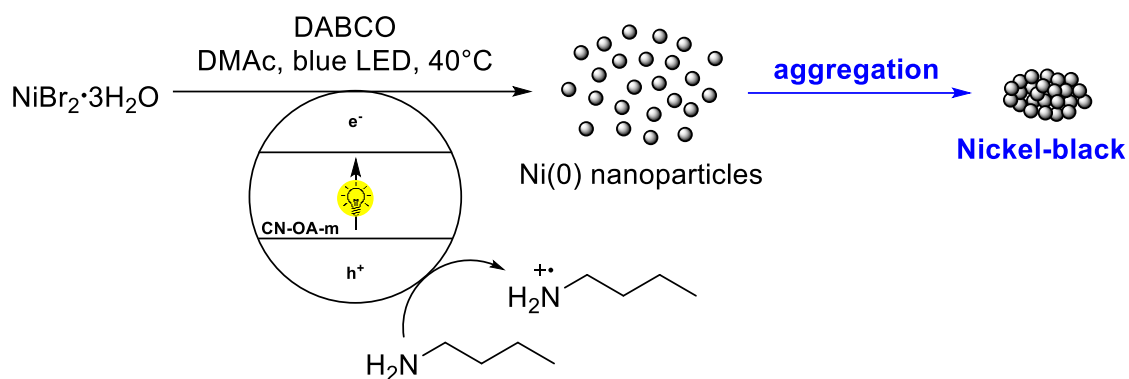


Figure S3.26. Time-dependent discoloration of the solution for method A due to nickel particle formation over time using $\text{NiBr}_2 \cdot 3\text{H}_2\text{O}$ as nickel source, CN-OA-m as photoredox catalyst (PRC) and *n*-butylamine and DABCO as single electron donor (SED) in DMAc (0.2M) under blue light irradiation at 40 °C.

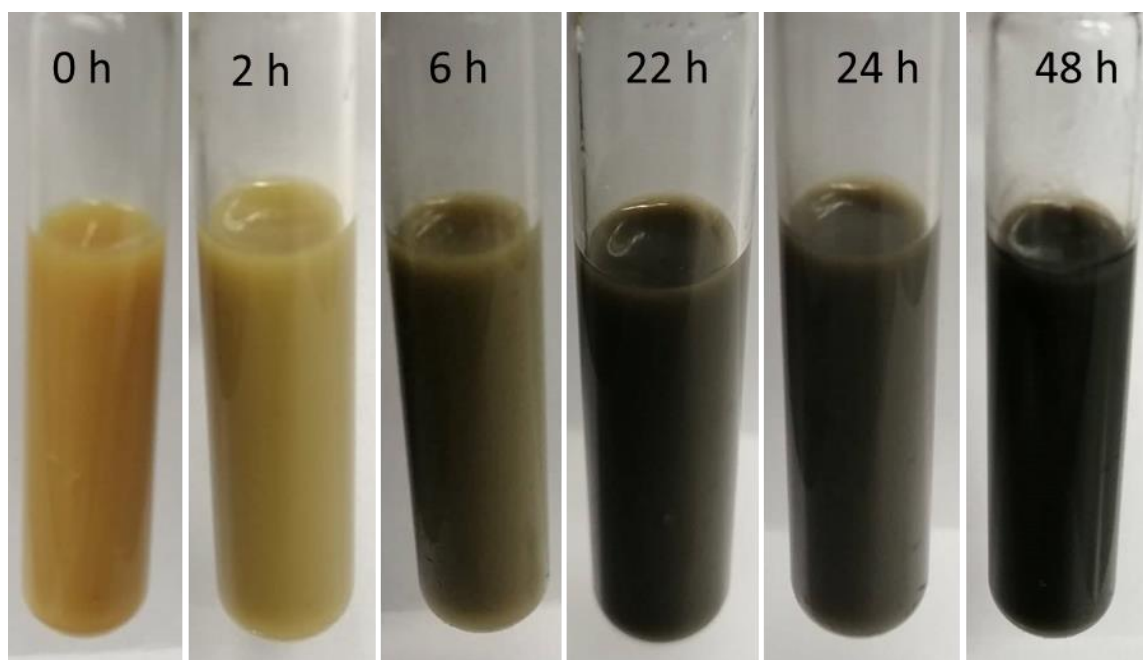
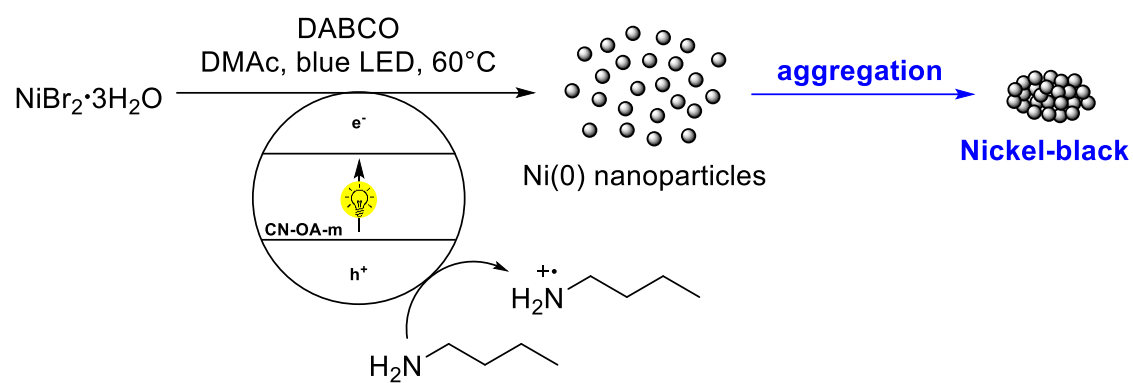


Figure S3.27. Time-dependent discoloration of the solution for method A due to nickel particle formation over time using $\text{NiBr}_2 \cdot 3\text{H}_2\text{O}$ as nickel source, CN-OA-m as photoredox catalyst (PRC) and n-butylamine and DABCO as single electron donor (SED) in DMAC (0.2M) under blue light irradiation at 60 °C.

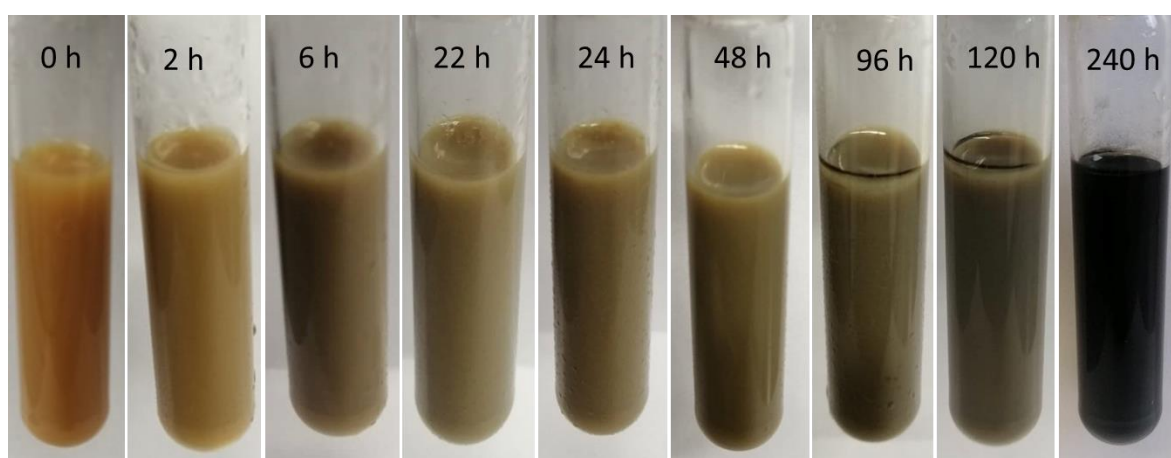
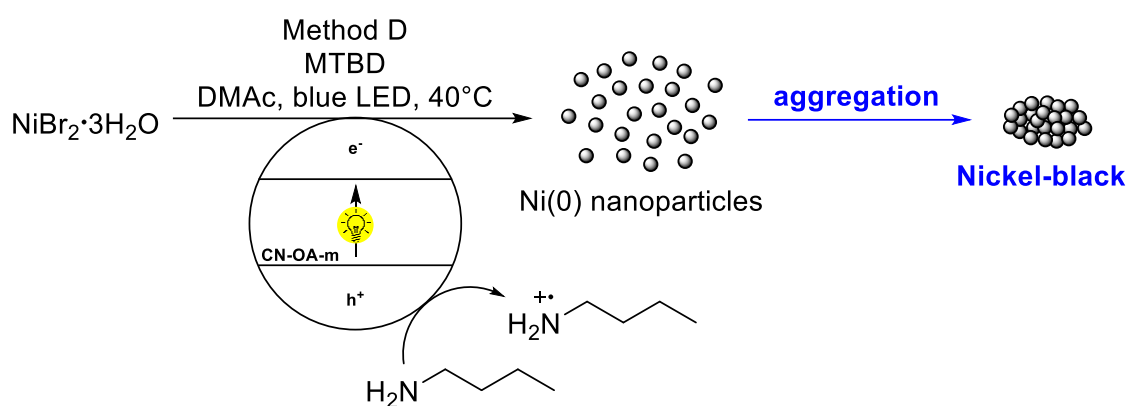


Figure S3.28. Time-dependent discoloration of the solution for method A due to nickel particle formation over time using $\text{NiBr}_2 \cdot 3\text{H}_2\text{O}$ as nickel source, CN-OA-m as photoredox catalyst (PRC) and n-butylamine and MTBD as single electron donor (SED) in DMAc (0.2M) under blue light irradiation at 40 °C.

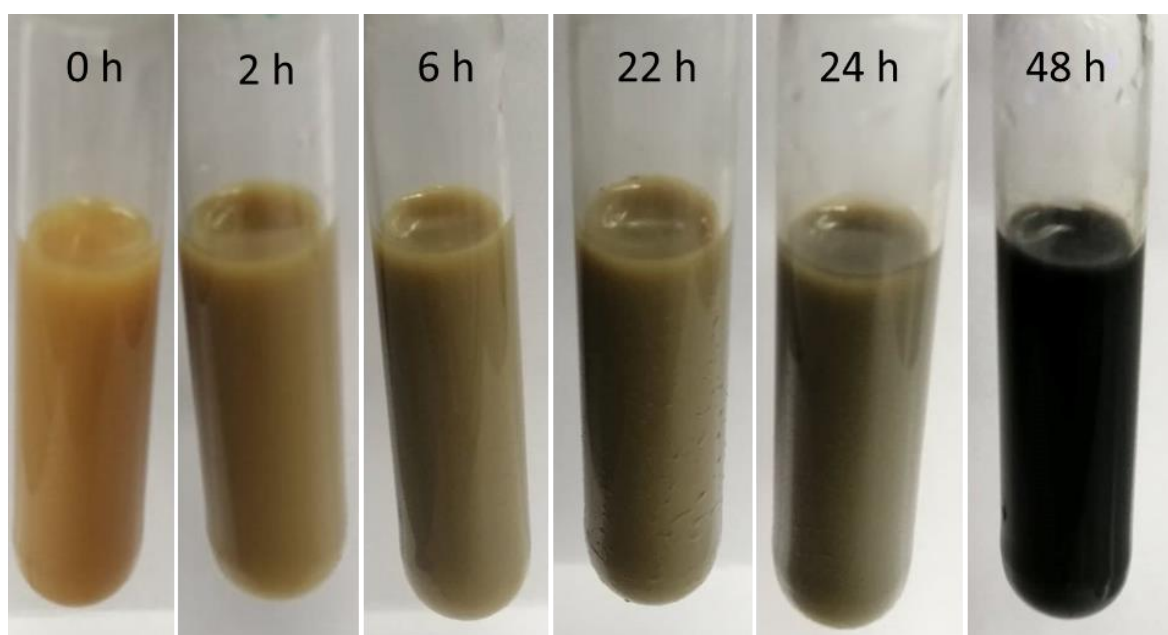
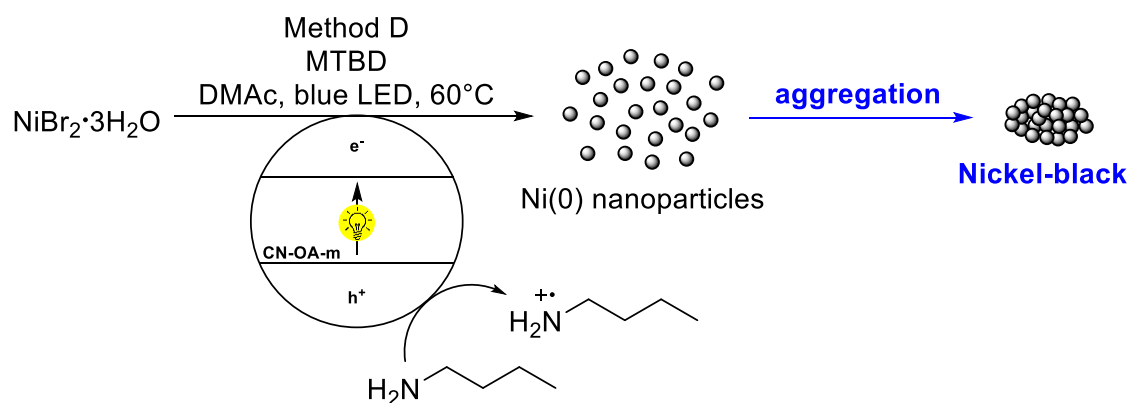
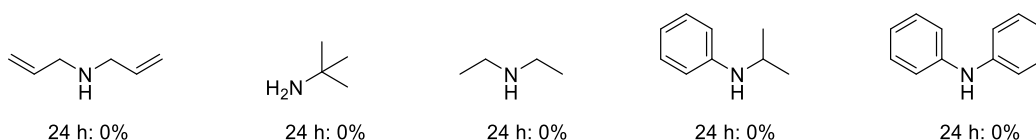


Figure S3.29. Time-dependent discoloration of the solution for method A due to nickel particle formation over time using $\text{NiBr}_2 \cdot 3\text{H}_2\text{O}$ as nickel source, CN-OA-m as photoredox catalyst (PRC) and n-butylamine and MTBD as single electron donor (SED) in DMAc (0.2M) under blue light irradiation at 60 °C.

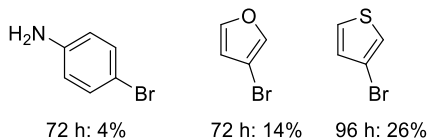
3.5.13 Scope and limitations

General experimental procedure (Table 3.2). An oven dried vial (13 x 95 mm) equipped with a stir bar was charged with NiBr₂·3H₂O (8.2 mg, 30 μmol, 2.5 mol%), aryl bromide (1.2 mmol, 1 equiv.) and CN-OA-m (20 mg). Subsequently, the amine (3.6 mmol, 3 equiv.) and DMAc (anhydrous, 6 mL) were added and the vial was sealed with a septum and parafilm. The reaction mixture was sonicated for 5-10 min and the mixture was then degassed by bubbling N₂ for 10 min. The mixture was irradiated in the batch reactor (described above) at 40°C with rapid stirring (1400 rpm). After the respective reaction time, one equivalent of 1,3,5-trimethoxybenzene (202.0 mg, 1.2 mmol, internal standard) was added. An aliquot (~300 μL) of the reaction mixture was diluted with DMSO-d₆ and subjected to ¹H-NMR analysis. The liquid phase was diluted with H₂O (40 mL) and extracted with ethyl acetate (3 x 30 mL). The combined organic phases were washed with H₂O (40 mL), NaHCO₃ solution (40 ml) and brine (40 mL), dried over Na₂SO₄ and concentrated. The crude product was purified by flash column chromatography (SiO₂, Hexane/EtOAc, dichloromethane/EtOAc or dichloromethane/MeOH) on a Grace™ Reveleris™ system using a 12 g cartridge to afford the desired product. The final product was characterized by ¹H-NMR, ¹³C-NMR, ¹⁹F-NMR and HRMS (ESI-TOF).

Unsuccessful amines for the coupling with methyl 4-bromobenzoate (with NMR-yields)



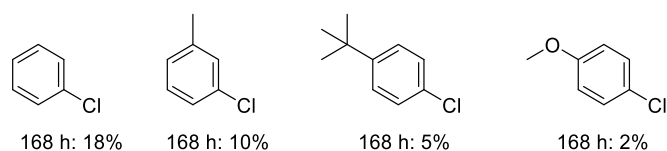
Unsuccessful aryl bromides for the coupling with pyrrolidine (with NMR-yields)



Method B: Coupling of pyrrolidine with electron-neutral aryl bromides and aryl bromides with weakly electron donating substituents (Figure 3.2 & 3.3). An oven dried vial (19 x 80 mm) equipped with a stir bar was charged with the CN-OA-m (20 mg), aryl bromide (1.2 mmol, 1.0 equiv.) and NiBr₂·3H₂O (16.4 mg, 60 μmol, 5.0 mol%). Subsequently, pyrrolidine (256.0 mg, 295.6 μl, 3.6 mmol, 3.0 equiv.) and DMAc (anhydrous, 6 mL) were added and the vial was sealed with a septum and Parafilm. The reaction mixture was sonicated for 5-10 min followed by stirring for 5 min until fine dispersion of the solids was achieved and the mixture was then degassed by bubbling N₂ for 10 min. The mixture was irradiated in the photoreactor (green light function of RGB LED strip) at 40 °C with rapid stirring (1400 rpm). After 168 h, one equivalent of 1,3,5-trimethoxybenzene (1.2 mmol) was added and the mixture was stirred for 5 min. An aliquot of the reaction mixture (~300 μL) was filtered, diluted with DMSO-d₆ and subjected to ¹H-NMR analysis. The combined organic phases were washed with H₂O (40 mL), NaHCO₃ solution (40 ml) and brine (40 mL), dried over Na₂SO₄ and concentrated. The crude product was purified by flash column chromatography (SiO₂, Hexane/EtOAc, dichloromethane/EtOAc or dichloromethane/MeOH) on a Grace™ Reveleris™ system using a 12 g cartridge to afford the desired product. The final product was characterized by ¹H-NMR, ¹³C-NMR, ¹⁹F-NMR and HRMS (ESI-TOF).

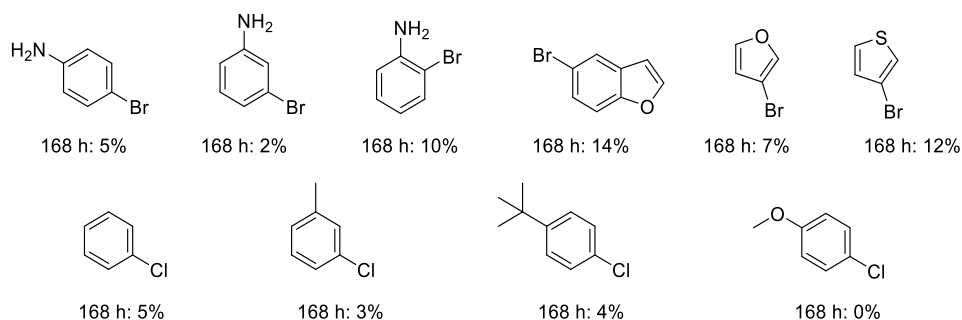
Method C: Coupling of pyrrolidine with electron-rich aryl bromides and electron-deficient aryl chlorides (Figure 3.3). An oven dried vial (19 x 80 mm) equipped with a stir bar was charged with the CN-OA-m (20 mg), aryl bromide (1.2 mmol, 1.0 equiv.) and NiBr₂·3H₂O (16.4 mg, 60 μmol, 5.0 mol%). Subsequently, pyrrolidine (256.0 mg, 295.6 μl, 3.6 mmol, 3.0 equiv.) and DMAc (anhydrous, 1 mL) were added and the vial was sealed with a septum and Parafilm. The reaction mixture was sonicated for 5-10 min followed by stirring for 5 min until fine dispersion of the solids was achieved and the mixture was then degassed by bubbling N₂ for 10 min. The mixture was irradiated in the photoreactor (blue light function of RGB LED strip) at 40 °C with moderate stirring (600 rpm). After respective reaction time, one equivalent of 1,3,5-trimethoxybenzene (202.0 mg, 1.2 mmol) was added and the mixture was stirred for 5 min. An aliquot of the reaction mixture (~300 μL) was filtered, diluted with DMSO-d₆ and subjected to ¹H-NMR analysis. The combined organic phases were washed with H₂O (40 mL), NaHCO₃ solution (40 ml) and brine (40 mL), dried over Na₂SO₄ and concentrated. The crude product was purified by flash column chromatography (SiO₂, Hexane/EtOAc, dichloromethane/EtOAc or dichloromethane/MeOH) on a Grace™ Reveleris™ system using a 12 g cartridge to afford the desired product. The final product was characterized by ¹H-NMR, ¹³C-NMR, ¹⁹F-NMR and HRMS (ESI-TOF).

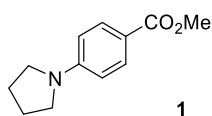
Unsuccessful aryl halides for the coupling with pyrrolidine



Method D: Coupling of *n*-butylamine with aryl bromides and aryl chlorides (Table 3.3).

An oven dried vial (19 x 80 mm) equipped with a stir bar was charged with the CN-OA-m (20 mg), aryl bromide (1.2 mmol, 1.0 equiv.) and NiBr₂·3H₂O (16.4 mg, 60 μmol, 5.0 mol%). Subsequently, pyrrolidine (256.0 mg, 295.6 μl, 3.6 mmol, 3.0 equiv.) and DMAc (anhydrous, 1 mL) were added and the vial was sealed with a septum and Parafilm. The reaction mixture was sonicated for 5-10 min followed by stirring for 5 min until fine dispersion of the solids was achieved and the mixture was then degassed by bubbling N₂ for 10 min. The mixture was irradiated in the photoreactor (blue light function of RGB LED strip) at 40 °C with moderate stirring (600 rpm). After respective reaction time, one equivalent of 1,3,5-trimethoxybenzene (202.0 mg, 1.2 mmol) was added and the mixture was stirred for 5 min. An aliquot of the reaction mixture (~300 μL) was filtered, diluted with DMSO-d₆ and subjected to ¹H-NMR analysis. The combined organic phases were washed with H₂O (40 mL), NaHCO₃ solution (40 ml) and brine (40 mL), dried over Na₂SO₄ and concentrated. The crude product was purified by flash column chromatography (SiO₂, Hexane/EtOAc, dichloromethane/EtOAc or dichloromethane/MeOH) on a Grace™ Reveleris™ system using a 12 g cartridge to afford the desired product. The final product was characterized by ¹H-NMR, ¹³C-NMR, ¹⁹F-NMR and HRMS (ESI-TOF).

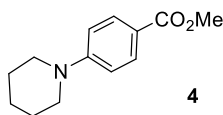
Unsuccessful aryl halides for the coupling with *n*-butylamine (with NMR-yields).



1-(4-methylbenzoate)pyrrolidine. From pyrrolidine (256.0 mg, 295.6 μ l, 3.6 mmol, 3.0 equiv.) and 4-bromomethylbenzoate (258.0 mg, 1.2 mmol, 1.0 equiv.) or 4-chloromethylbenzoate (204.7 mg, 1.2 mmol, 1.0 equiv.) using 1 ml instead of 6 ml DMAc. Reaction time: 8 h (Br) and 48 h (Cl). Purification with flash chromatography (1. gradient 0-5% ethyl acetate in hexane; 2. Isocratic 5% ethyl acetate in hexane) afforded the title compound (231.1 mg, 1.13 mmol, 94%) for aryl bromide and (224.6 mg, 1.09 mmol, 91%) for aryl chloride as a white solid.

^1H NMR (400 MHz, Chloroform-*d*) δ 7.88 (d, J = 8.7 Hz, 2H), 6.46 (d, J = 8.7 Hz, 2H), 3.83 (s, 3H), 3.40 – 3.09 (m, 4H), 2.05 – 1.86 (m, 4H). ^{13}C NMR (101 MHz, Chloroform-*d*) δ = 167.58, 150.79, 131.32, 116.17, 110.62, 51.37, 47.47, 25.41. HRMS (ESI-TOF) m/z calcd. for $\text{C}_{12}\text{H}_{16}\text{NO}_2$ [(M+H) $^+$]: 206.1176; found: 206.1158.

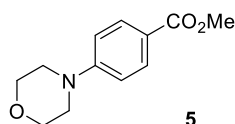
These data are in full agreement with those previously published in the literature.²⁰



Methyl 4-(piperidin-1-yl)benzoate. From piperidine (306.5 mg, 356.4 μ l, 3.6 mmol, 3.0 equiv.) and 4-bromomethylbenzoate (258.0 mg, 1.2 mmol, 1.0 equiv.). Reaction time: 72 h. Double amount of $\text{NiBr}_2 \cdot 3\text{H}_2\text{O}$ (16.4 mg, 60 μ mol, 5.0 mol%) was used. Purification with flash chromatography (1. gradient 0-5% ethyl acetate in hexane; 2. Isocratic 5% ethyl acetate in hexane) afforded the title compound (225.8 mg, 1.03 mmol, 86%) as a white solid.

^1H NMR (600 MHz, Chloroform-*d*) δ 7.87 (d, J = 9.1 Hz, 2H), 6.82 (d, J = 9.0 Hz, 2H), 3.83 (s, 3H), 3.28 (m, 4H), 1.67 – 1.56 (m, 6H). ^{13}C NMR (151 MHz, Chloroform-*d*) δ 167.18, 154.46, 131.19, 118.61, 113.52, 51.49, 48.73, 25.35, 24.32. HRMS (ESI-TOF) m/z calcd. for $\text{C}_{13}\text{H}_{18}\text{NO}_2$ [(M+H) $^+$]: 220.1332 ; found: 220.1340.

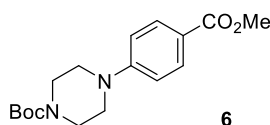
These data are in full agreement with those previously published in the literature.²¹



Methyl 4-morpholinobenzoate. From morpholine (313.6 mg, 313.6 μ l, 3.6 mmol, 3.0 equiv.) and 4-bromomethylbenzoate (258.0 mg, 1.2 mmol, 1.0 equiv.). Reaction time: 16 h. Purification with flash chromatography (gradient 0-2% ethyl acetate in DCM; 2. Isocratic 2% ethyl acetate in DCM) afforded the title compound (255.5 mg, 1.15 mmol, 96%) as a white solid.

^1H NMR (400 MHz, Chloroform-*d*) δ 7.93 (d, $J = 9.0$ Hz, 2H), 6.86 (d, $J = 9.0$ Hz, 2H), 3.92 – 3.72 (m, 7H), 3.26 (d, $J = 5.1$ Hz, 4H). ^{13}C NMR (101 MHz, Chloroform-*d*) δ 167.04, 154.15, 131.21, 120.34 113.50, 66.59, 51.71, 47.72. HRMS (ESI-TOF) m/z calcd. for $\text{C}_{12}\text{H}_{16}\text{NO}_3$ [(M+H) $^+$]: 222.1125; found: 222.1139.

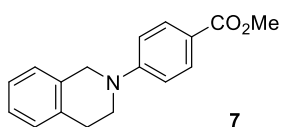
These data are in full agreement with those previously published in the literature.²²



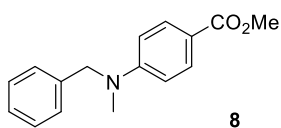
tert-Butyl 4-(4-(methoxycarbonyl)phenyl)piperazine-1-carboxylate. From *tert*-butyl piperazine-1-carboxylate (335.3 mg, 1.8 mmol, 3.0 equiv.) and 4-bromomethylbenzoate (129.0 mg, 0.6 mmol, 1.0 equiv.) using 5 mol% $\text{NiBr}_2 \cdot 3\text{H}_2\text{O}$ (8.2 mg, 60 μ mol) and pyrrolidine (4.3 mg, 4.9 μ l, 0.06 mmol, 10 mol%) as additive. Reaction time: 24 h. Purification with flash chromatography (1. gradient 0-3% ethyl acetate in DCM; 2. Isocratic 3% ethyl acetate in DCM) afforded the title compound (146.2 mg, 0.45 mmol, 76%) as a white solid. The pyrrolidine-coupled side-product was formed in 10% yield, as determined by analysis of the crude mixture by ^1H NMR spectroscopy.

^1H NMR (400 MHz, Chloroform-*d*) δ 7.92 (d, $J = 8.9$ Hz, 2H), 6.85 (d, $J = 8.9$ Hz, 2H), 3.86 (s, 3H), 3.57 (m, 4H), 3.29 (m, 4H), 1.48 (s, 9H). ^{13}C NMR (101 MHz, Chloroform-*d*) δ 167.48, 155.09, 154.41, 131.69, 120.63, 114.42, 80.56, 52.15, 47.98, 43.46, 28.92, 28.78. HRMS (ESI-TOF) m/z calcd. for $\text{C}_{17}\text{H}_{25}\text{N}_2\text{O}_4$ [(M+H) $^+$]: 321.1809; found: 321.1818

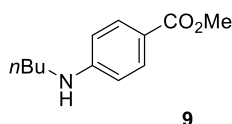
These data are in full agreement with those previously published in the literature.²¹



Methyl 4-(3,4-dihydroisoquinolin-2(1H)-yl)benzoate. From 1,2,3,4-tetrahydroisoquinoline (479.5 mg, 456.7 μ l, 3.6 mmol, 3.0 equiv.) and 4-bromomethylbenzoate (258.0 mg, 1.2 mmol, 1.0 equiv.). Reaction time: 16 h. Purification with flash chromatography (1. gradient 0-5% ethyl acetate in hexane; 2. Isocratic 5% ethyl acetate in hexane) afforded the title compound (281.6 mg, 1.06 mmol, 88%) as a white solid. ^1H NMR (600 MHz, Chloroform-*d*) δ 7.97 (d, $J = 9.0$ Hz, 2H), 7.23 – 7.13 (m, 4H), 6.86 (d, $J = 9.0$ Hz, 2H), 4.49 (s, 2H), 3.88 (s, 3H), 3.62 (t, $J = 5.9$ Hz, 2H), 2.97 (t, $J = 5.8$ Hz, 2H). ^{13}C NMR (151 MHz, Chloroform-*d*) δ 167.29, 153.00, 135.02, 133.80, 131.36, 128.22, 126.73, 126.51, 126.37, 118.29, 112.10, 51.56, 49.01, 44.78, 29.04. HRMS (ESI-TOF) m/z calcd. for $\text{C}_{17}\text{H}_{18}\text{NO}_2$ [(M+H) $^+$]: 268.1332; found: 268.1344. These data are in full agreement with those previously published in the literature.²³



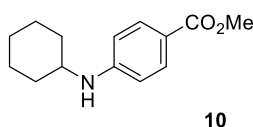
Methyl 4-(benzyl(methyl)amino)benzoate. From *N*-methylbenzylamine (438.6 mg, 467.1 μ l, 3.6 mmol, 3.0 equiv.) and 4-bromomethylbenzoate (258.0 mg, 1.2 mmol, 1.0 equiv.). Reaction time: 72 h. Purification with flash chromatography (1.gradient 0-4% ethyl acetate in hexane; 2. Isocratic 4% ethyl acetate in hexane) afforded the title compound (245.4 mg, 0.96 mmol, 80%) as a white solid. ^1H NMR (400 MHz, Chloroform-*d*) δ 7.92 (d, $J = 9.1$ Hz, 2H), 7.34 (t, $J = 7.2$ Hz, 2H), 7.28 (d, $J = 7.2$ Hz, 1H), 7.20 (d, $J = 7.1$ Hz, 2H), 6.71 (d, $J = 9.1$ Hz, 2H), 4.62 (s, 2H), 3.86 (s, 3H), 3.12 (s, 3H). ^{13}C NMR (101 MHz, Chloroform-*d*) δ 167.39, 152.75, 137.79, 131.43, 128.78, 127.20, 126.46, 117.37, 110.88, 55.92, 51.52, 38.69. HRMS (ESI-TOF) m/z calcd. for $\text{C}_{16}\text{H}_{18}\text{NO}_2$ [(M+H) $^+$]: 256.1332; found: 256.1344. These data are in full agreement with those previously published in the literature.²⁴



Methyl 4-(butylamino)benzoate. From *n*-butylamine (263.3 mg, 355.8 μ l, 3.6 mmol, 3.0 equiv.) and 4-bromomethylbenzoate (258.0 mg, 1.2 mmol, 1.0 equiv.) or 4-chloromethylbenzoate (204.7 mg, 1.2 mmol, 1.0 equiv.) and 7-Methyl-1,5,7-triazabicyclo[4.4.0]dec-5-ene (MTBD) (367.8 mg, 344.7 μ l, 2.4 mmol, 2.0 equiv.) using 5 mol% NiBr₂·3H₂O (16.4 mg, 60 μ mol,). Reaction time: 72 h (9-Br) and 168 h (9-Cl). Purification with flash chromatography (1. gradient 0-8% ethyl acetate in hexane; 2. Isocratic 8% ethyl acetate in hexane) afforded the title compounds (223.2 mg, 1.08 mmol, 90%) from aryl bromide and (219.6 mg, 1.06 mmol, 88%) from aryl chloride as a white solid.

¹H NMR (400 MHz, Chloroform-*d*) δ 7.85 (d, *J* = 8.6 Hz, 2H), 6.52 (d, *J* = 8.6 Hz, 2H), 4.21 (brs, 1H), 3.83 (s, 3H), 3.16 – 3.07 (m, 2H), 1.63 – 1.52 (m, 2H), 1.41 (h, *J* = 7.3, 6.9 Hz, 2H), 0.94 (td, *J* = 7.3, 1.0 Hz, 3H). ¹³C NMR (101 MHz, Chloroform-*d*) δ 167.45, 152.17, 131.61, 118.05, 111.45, 51.57, 43.19, 31.42, 20.29, 13.92. HRMS (ESI-TOF) *m/z* calcd. for C₁₂H₁₈NO₂ [(M+H)⁺]: 208.1332; found: 208.1342.

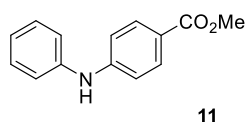
These data are in full agreement with those previously published in the literature.²⁵



Methyl 4-(cyclohexylamino)benzoate. From cyclohexylamine (357.0 mg, 415.4 μ l, 3.6 mmol, 3.0 equiv.) and 4-bromomethylbenzoate (258.0 mg, 1.2 mmol, 1.0 equiv.) using 5 mol% NiBr₂·3H₂O (16.4 mg, 60 μ mol,). Reaction time: 72 h. Purification with flash chromatography (1. gradient 0-5% ethyl acetate in hexane; 2. Isocratic 5% ethyl acetate in hexane) afforded the title compound (203.2 mg, 0.87 mmol, 73%) as a white solid.

¹H NMR (400 MHz, Chloroform-*d*) δ 7.82 (d, *J* = 8.8 Hz, 2H), 6.51 (d, *J* = 8.9 Hz, 2H), 4.01 (brs, 1H), 3.83 (s, 3H), 3.30 (m, 1H), 2.06 – 2.00 (m, 2H), 1.81 – 1.73 (m, 2H), 1.69 – 1.61 (m, 1H), 1.42 – 1.32 (m, 2H), 1.28 – 1.13 (m, 3H). ¹³C NMR (101 MHz, Chloroform-*d*) δ 167.36, 151.10, 131.60, 117.56, 111.59, 51.47, 51.24, 33.10, 25.73, 24.87. HRMS (ESI-TOF) *m/z* calcd. for C₁₄H₂₀NO₂ [(M+H)⁺]: 234.1489; found: 234.1500.

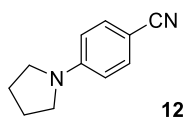
These data are in full agreement with those previously published in the literature.²⁶



Methyl 4-(butylamino)benzoate. From aniline (335.5 mg, 329.2 μ l, 3.6 mmol, 3.0 equiv.) and 4-bromomethylbenzoate (258.0 mg, 1.2 mmol, 1.0 equiv.) using 5 mol% NiBr₂·3H₂O (8.2 mg, 60 μ mol) and pyrrolidine (4.3 mg, 4.9 μ l, 0.06 mmol, 10 mol) as well as *N*-tert-butylisopropylamine (BIPA) (414.8 mg, 570.6 μ l, 3.6 mmol, 3.0 equiv.) as additives. Reaction time: 72 h. Purification with flash chromatography (1. gradient 0-10% ethyl acetate in hexane; 2. Isocratic 10% ethyl acetate in hexane) afforded the title compound (246.7 mg, 1.09 mmol, 90%) as a white solid. The pyrrolidine-coupled side-product was formed in 2% yield, as determined by analysis of the crude mixture by ¹H NMR spectroscopy.

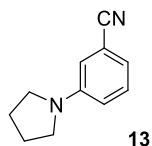
¹H NMR (400 MHz, Chloroform-*d*) δ 7.93 (d, *J* = 8.1 Hz, 2H), 7.34 (m, 2H), 7.18 (d, *J* = 7.7 Hz, 2H), 7.07 (t, *J* = 7.4 Hz, 1H), 6.99 (d, *J* = 8.6 Hz, 2H), 6.19 (brs, 1H), 3.88 (s, 3H). ¹³C NMR (101 MHz, Chloroform-*d*) δ 167.08, 148.16, 140.88, 131.50, 129.51, 123.07, 120.94, 120.42, 114.56, 51.77. HRMS (ESI-TOF) *m/z* calcd. for C₁₄H₁₄NO₂ [(M+H)⁺]: 228.1019; found: 228.1033.

These data are in full agreement with those previously published in the literature.²⁷



1-(4-benzonitrile)pyrrolidine. From pyrrolidine (256.0 mg, 295.6 μ l, 3.6 mmol, 3.0 equiv.) and 4-bromobenzonitrile (218.4 mg, 1.2 mmol, 1.0 equiv.). Reaction time: 24 h. Purification with flash chromatography (1. gradient 0-5% ethyl acetate in hexane; 2. Isocratic 5% ethyl acetate in hexane) afforded the title compound (189.6mg, 1.11 mmol, 92%) as a white solid. ¹H NMR (400 MHz, Chloroform-*d*) δ 7.42 (d, *J* = 8.8 Hz, 2H), 6.48 (d, *J* = 8.9 Hz, 2H), 3.32 – 3.28 (m, 4H), 2.09 – 1.94 (m, 4H). ¹³C NMR (101 MHz, Chloroform-*d*) δ = 150.00, 133.43, 121.11, 111.47, 96.38, 47.51, 25.44. HRMS (ESI-TOF) *m/z* calcd. for C₁₁H₁₃N₂ [(M+H)⁺]: 173.1074; found: 173.1081.

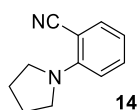
These data are in full agreement with those previously published in the literature.²⁸



1-(3-benzonitrile)pyrrolidine. From pyrrolidine (256.0 mg, 295.6 μ l, 3.6 mmol, 3.0 equiv.) and 3-bromobenzonitrile (218.4 mg, 1.2 mmol, 1.0 equiv.). Reaction time: 24 h. No internal standard (1,3,5-trimethoxybenzene was used) due to poor separation from the product during flash chromatography. Purification with flash chromatography (1. gradient 0-5% ethyl acetate in hexane; 2. Isocratic 5% ethyl acetate in hexane) afforded the title compound (180.4 mg, 1.05 mmol, 87%) as a white solid.

^1H NMR (400 MHz, Chloroform-*d*) δ 7.30 – 7.23 (m, 1H), 6.90 (m, 1H), 6.77 – 6.69 (m, 2H), 3.34 – 3.23 (m, 4H), 2.13 – 1.99 (m, 4H). ^{13}C NMR (101 MHz, Chloroform-*d*) δ 147.62, 129.73, 119.95, 118.50, 115.78, 114.24, 112.63, 47.55, 25.46. HRMS (ESI-TOF) *m/z* calcd. for $\text{C}_{11}\text{H}_{13}\text{N}_2$ [(M+H) $^+$]: 173.1074; found: 173.1080

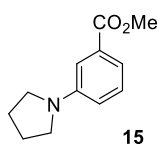
These data are in full agreement with those previously published in the literature.²⁹



1-(2-benzonitrile)pyrrolidine. From pyrrolidine (256.0 mg, 295.6 μ l, 3.6 mmol, 3.0 equiv.) and 2-bromobenzonitrile (218.4 mg, 1.2 mmol, 1.0 equiv.) using 5 mol% $\text{NiBr}_2 \cdot 3\text{H}_2\text{O}$ (8.2 mg, 60 μ mol). Reaction time: 72 h. No internal standard (1,3,5-trimethoxybenzene was used) due to poor separation from the product during flash chromatography. Purification with flash chromatography (eluents: 1. gradient 0-5% ethyl acetate in hexane; 2. Isocratic 5% ethyl acetate in hexane) afforded the title compound (190.5 mg, 1.11 mmol, 92%) as a colorless oil.

^1H NMR (400 MHz, Chloroform-*d*) δ 7.42 (m, 1H), 7.31 (m, 1H), 6.67 – 6.59 (m, 2H), 3.63 – 3.53 (m, 4H), 2.03 – 1.94 (m, 4H). ^{13}C NMR (101 MHz, Chloroform-*d*) δ 150.04, 135.72, 133.40, 121.51, 115.86, 114.24, 94.27, 49.81, 25.76. HRMS (ESI-TOF) *m/z* calcd. for $\text{C}_{11}\text{H}_{13}\text{N}_2$ [(M+H) $^+$]: 173.1074; found: 173.1081

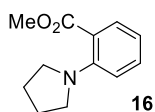
These data are in full agreement with those previously published in the literature.¹



1-(3-methylbenzoate)pyrrolidine. From pyrrolidine (256.0 mg, 295.6 μ l, 3.6 mmol, 3.0 equiv.) and 3-bromomethylbenzoate (258.0 mg, 1.2 mmol, 1.0 equiv.). Reaction time: 24 h. No internal standard (1,3,5-trimethoxybenzene was used) due to poor separation from the product during flash chromatography. Purification with flash chromatography (1. gradient 0-5% ethyl acetate in hexane; 2. Isocratic 5% ethyl acetate in hexane) afforded the title compound (218.4 mg, 1.06 mmol, 89%) as a colorless oil.

^1H NMR (400 MHz, Chloroform-*d*) δ 7.32 (d, $J = 7.6$ Hz, 1H), 7.25 (t, $J = 7.8$ Hz, 1H), 7.22 – 7.91 (s, 1H), 6.71 (m, 1H), 3.89 (s, 3H), 3.29 (t, $J = 6.6$ Hz, 4H), 2.00 (t, $J = 6.6$ Hz, 4H). ^{13}C NMR (101 MHz, Chloroform-*d*) δ 167.89, 147.78, 130.73, 129.02, 116.39, 115.93, 112.38, 52.00, 47.70, 25.48. HRMS (ESI-TOF) m/z calcd. for $\text{C}_{12}\text{H}_{16}\text{NO}_2$ [(M+H) $^+$]: 206.17556; found: 206.1185.

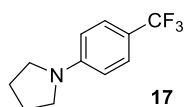
These data are in full agreement with those previously published in the literature.²²



1-(2-methylbenzoate)pyrrolidine. From pyrrolidine (256.0 mg, 295.6 μ l, 3.6 mmol, 3.0 equiv.) and 2-bromomethylbenzoate (258.0 mg, 1.2 mmol, 1.0 equiv.) using 5 mol% $\text{NiBr}_2 \cdot 3\text{H}_2\text{O}$ (8.2 mg, 60 μ mol). Reaction time: 72 h. No internal standard (1,3,5-trimethoxybenzene was used) due to poor separation from the product during flash chromatography. Purification with flash chromatography (1. gradient 0-5% ethyl acetate in hexane; 2. Isocratic 5% ethyl acetate in hexane) afforded the title compound (87.2 mg, 0.42 mmol, 35%) as a colourless oil.

^1H NMR (400 MHz, Chloroform-*d*) δ 7.57 (m, 1H), 7.31 (t, $J = 8.7$ Hz, 1H), 6.79 (m, 1H), 6.71 (t, $J = 7.4$ Hz, 1H), 3.88 (s, 3H), 3.28 – 3.19 (m, 4H), 1.99 – 1.88 (m, 4H). ^{13}C NMR (101 MHz, Chloroform-*d*) δ 169.57, 147.93, 131.79, 131.08, 117.09, 115.63, 113.95, 52.00, 50.87, 25.88. HRMS (ESI-TOF) m/z calcd. for $\text{C}_{12}\text{H}_{16}\text{NO}_2$ [(M+H) $^+$]: 206.17556; found: 206.1185.

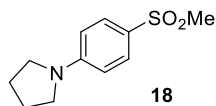
These data are in full agreement with those previously published in the literature.³⁰



1-(4-(trifluoromethyl)phenyl)pyrrolidine. From pyrrolidine (256.0 mg, 295.6 μ l, 3.6 mmol, 3.0 equiv.) and 4-bromobenzotrifluoride (270.0 mg, 168.0 μ l, 1.2 mmol, 1.0 equiv.). Reaction time: 8 h. Purification with flash chromatography (1. gradient 0-3% ethyl acetate in hexane; 2. Isocratic 3% ethyl acetate in hexane) afforded the title compound (238.2 mg, 1.11 mmol, 92%) as a white solid.

^1H NMR (400 MHz, Chloroform-*d*) δ 7.48 (d, J = 8.7 Hz, 2H), 6.58 (d, J = 8.7 Hz, 2H), 3.37 – 3.27 (m, 4H), 2.10 – 2.00 (m, 4H). ^{13}C NMR (101 MHz, Chloroform-*d*) δ 149.76, 126.38 (q, J = 3.7 Hz), 125.42 (q, J = 269.9 Hz), 116.56 (q, J = 32.5 Hz), 110.84, 47.53, 25.48. ^{19}F NMR (376 MHz, Chloroform-*d*) δ -60.58(s, 3F). HRMS (ESI-TOF) m/z calcd. for $\text{C}_{11}\text{H}_{13}\text{F}_3\text{N}$ [(M+H) $^+$]: 216.0922 ; found: 216.1008.

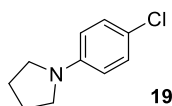
These data are in full agreement with those previously published in the literature.³¹



1-(4-(methylsulfonyl)phenyl)pyrrolidine. From pyrrolidine (256.0 mg, 295.6 μ l, 3.6 mmol, 3.0 equiv.) and 4-bromophenyl methylsulfone (282.1 mg, 1.2 mmol, 1.0 equiv.). Reaction time: 24 h. Purification with flash chromatography (1. gradient 0-2% ethyl acetate in DCM; 2. Isocratic 2% ethyl acetate in DCM) afforded the title compound (251.0 mg, 1.11 mmol, 93%) as a white solid.

^1H NMR (600 MHz, Chloroform-*d*) δ 7.65 (d, J = 8.9 Hz, 2H), 6.51 (d, J = 9.0 Hz, 2H), 3.30 – 3.24 (m, 4H), 2.94 (s, 3H), 2.05 – 1.93 (m, 4H). ^{13}C NMR (151 MHz, Chloroform-*d*) δ 150.89, 129.02, 125.04, 110.98, 47.61, 45.13, 25.39. HRMS (ESI-TOF) m/z calcd. for $\text{C}_{11}\text{H}_{16}\text{NO}_2\text{S}$ [(M+H) $^+$]: 226.0897; found: 226.0907.

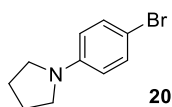
These data are in full agreement with those previously published in the literature.³²



1-(4-chlorophenyl)pyrrolidine. From pyrrolidine (256.0 mg, 295.6 μ l, 3.6 mmol, 3.0 equiv.) and 4-bromochlorobenzene (229.7 mg, 1.2 mmol, 1.0 equiv.). Reaction time: 24 h. Purification with flash chromatography (1. gradient 0-2% ethyl acetate in hexane; 2. Isocratic 2% ethyl acetate in hexane) afforded the title compound (196.8 mg, 1.08 mmol, 90%) as a white solid.

^1H NMR (600 MHz, Chloroform-*d*) δ 7.17 (d, J = 8.9 Hz, 2H), 6.48 (d, J = 8.9 Hz, 2H), 3.28 – 3.18 (m, 4H), 2.06 – 1.97 (m, 4H). ^{13}C NMR (151 MHz, Chloroform-*d*) δ 146.49, 128.81, 120.04, 112.61, 47.73, 25.48. HRMS (ESI-TOF) m/z calcd. for $\text{C}_{10}\text{H}_{13}\text{ClN}$ [(M+H) $^+$]: 182.0731; found: 182.0738.

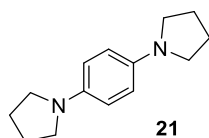
These data are in full agreement with those previously published in the literature.²⁰



1-(4-bromophenyl)pyrrolidine. From pyrrolidine (256.0 mg, 295.6 μ l, 3.6 mmol, 3.0 equiv.) and 1,4-dibromobenzene (283.1 mg, 1.2 mmol, 1.0 equiv.). Reaction time: 24 h. Purification with flash chromatography (1. gradient 0-2% ethyl acetate in hexane; 2. Isocratic 2% ethyl acetate in hexane) afforded the title compound (218.4 mg, 0.97 mmol, 80%) as a white solid.

^1H NMR (400 MHz, Chloroform-*d*) δ 7.28 (d, J = 8.9 Hz, 2H), 6.42 (d, J = 8.9 Hz, 2H), 3.29 – 3.16 (m, 4H), 2.05 – 1.96 (m, 4H). ^{13}C NMR (101 MHz, Chloroform-*d*) δ 146.82, 131.68, 113.19, 107.08, 47.68, 25.50. HRMS (ESI-TOF) m/z calcd. for $\text{C}_{10}\text{H}_{13}\text{BrN}$ [(M+H) $^+$]: 226.0226; found: 226.0231.

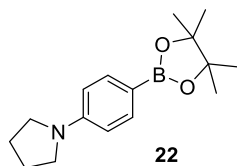
These data are in full agreement with those previously published in the literature.³³



1-di(4-pyrrolidin-1-yl)benzene. From pyrrolidine (853.3 mg, 985.3 μ l, 12.0 mmol, 10 equiv.) and 1,4-dibromobenzene (283.1 mg, 1.2 mmol, 1.0 equiv.). Reaction time: 144 h. Purification with flash chromatography (1. gradient 0-5% ethyl acetate in hexane; 2. Isocratic 5% ethyl acetate in hexane) afforded the title compound (157.3 mg, 0.73 mmol, 61%) as a white solid. For analysis via NMR spectroscopy, the final product was treated with deuterated trifluoro acetic acid in D_2O .

1H NMR (400 MHz, deuterium oxide) δ 7.17 (s, 4H), 3.20 (m, 8H), 1.68 (m, 8H). ^{13}C NMR (101 MHz, deuterium oxide) δ 143.24, 126.02, 61.01, 25.62. HRMS (ESI-TOF) m/z calcd. for $C_{14}H_{21}N_2$ [(M+H) $^+$]: 217.1700; found: 217.1709

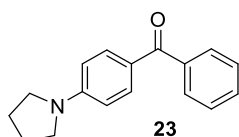
These data are in full agreement with those previously published in the literature.³⁴



1-(4-(4,4,5,5-tetramethyl-1,3,2-dioxaborolan-2-yl)phenyl)pyrrolidine. From pyrrolidine (256.0 mg, 295.6 μ l, 3.6 mmol, 3.0 equiv.) and 4-bromomethyl-phenylboronic acid pinacol ester (339.6 mg, 1.2 mmol, 1.0 equiv.). Reaction time: 48 h. No internal standard (1,3,5-trimethoxybenzene was used) due to poor separation from the product during flash chromatography. Purification with flash chromatography (1. gradient 0-10% ethyl acetate in hexane; 2. Isocratic 2% ethyl acetate in hexane) afforded the title compound (284.3 mg, 1.04 mmol, 87%) as a white solid.

1H NMR (400 MHz, Chloroform-*d*) δ 7.70 (d, J = 8.6 Hz, 2H), 6.55 (d, J = 8.6 Hz, 2H), 3.39 – 3.17 (m, 4H), 2.13 – 1.92 (m, 4H), 1.35 (s, 12H). ^{13}C NMR (101 MHz, Chloroform-*d*) δ 150.00, 136.24, 113.94, 110.93, 83.06, 47.40, 25.46, 24.88. HRMS (ESI-TOF) m/z calcd. for $C_{16}H_{25}BNO_2$ [(M+H) $^+$]: 274.1973; found: 274.1987.

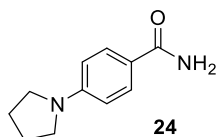
These data are in full agreement with those previously published in the literature.³⁵



phenyl(4-(pyrrolidin-1-yl)phenyl)methanone. From pyrrolidine (256.0 mg, 295.6 μ l, 3.6 mmol, 3.0 equiv.) and 4-bromobenzophenone (313.3 mg, 1.2 mmol, 1.0 equiv.). Reaction time: 48 h. Purification with flash chromatography (1. gradient 0-5% ethyl acetate in hexane; 2. Isocratic 5% ethyl acetate in hexane) afforded the title compound (281.9 mg, 1.12 mmol, 93%) as a white solid.

^1H NMR (600 MHz, Chloroform-*d*) δ 7.78 (d, J = 8.9 Hz, 2H), 7.72 – 7.66 (m, 2H), 7.49 (t, J = 7.4 Hz, 1H), 7.45 – 7.37 (m, 2H), 6.51 (d, J = 8.9 Hz, 2H), 3.38 – 3.27 (m, 4H), 2.02 – 1.95 (m, 4H). ^{13}C NMR (151 MHz, Chloroform-*d*) δ 195.01, 150.88, 139.51, 132.90, 130.95, 129.37, 127.97, 124.20, 110.63, 47.58, 25.42. HRMS (ESI-TOF) m/z calcd. for $\text{C}_{17}\text{H}_{17}\text{NO}$ [($\text{M}+\text{H}$) $^+$]: 252.1383; found: 252.1394.

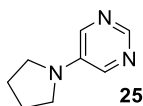
These data are in full agreement with those previously published in the literature.³⁶



1-(4-benzamide)pyrrolidine. From pyrrolidine (256.0 mg, 295.6 μ l, 3.6 mmol, 3.0 equiv.) and 4-bromobenzamide (240.0 mg, 1.2 mmol, 1.0 equiv.). Reaction time: 72 h. Purification with flash chromatography (1. gradient 0-5% methanol in DCM; 2. Isocratic 5% methanol in DCM) afforded the title compound (175.0 mg, 0.92 mmol, 77%) as a white solid.

^1H NMR (400 MHz, DMSO-*d*₆) δ 7.69 (d, J = 8.8 Hz, 2H), 7.58 – 7.52 (brs, 1H), 6.86 – 6.80 (brs, 1H), 6.47 (d, J = 8.8 Hz, 2H), 3.23 (s, 4H), 1.92 (s, 4H). ^{13}C NMR (101 MHz, DMSO-*d*₆) δ 168.05, 149.49, 129.08, 120.24, 110.47, 47.22, 25.01. HRMS (ESI-TOF) m/z calcd. for $\text{C}_{11}\text{H}_{15}\text{N}_2\text{O}$ [($\text{M}+\text{H}$) $^+$]: 191.1179; found: 191.1188.

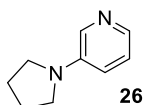
These data are in full agreement with those previously published in the literature.³⁷



5-(4-pyrrolidin-1-yl)pyrimidine. From pyrrolidine (256.0 mg, 295.6 μ l, 3.6 mmol, 3.0 equiv.) and 5-bromopyrimidine (190.8 mg, 1.2 mmol, 1.0 equiv.) using 5 mol% NiBr₂·3H₂O (16.4 mg, 60 μ mol). Reaction time: 72 h. Purification with flash chromatography (1. gradient 0-50% ethyl acetate in hexane with 1% Et₃N; 2. Isocratic 50% ethyl acetate in hexane with 1% Et₃N) afforded the title compound (141.3 mg, 0.95 mmol, 79%) as a colorless solid.

¹H NMR (400 MHz, Chloroform-*d*) δ 8.47 (s, 1H), 7.97 (s, 2H), 3.32 – 3.16 (m, 4H), 2.06 – 1.90 (m, 4H). ¹³C NMR (101 MHz, Chloroform-*d*) δ 146.60, 141.09, 139.35, 46.84, 25.27. HRMS (ESI-TOF) *m/z* calcd. for C₈H₁₂N₃ [(M+H)⁺]: 150.1026 ; found: 150.1033.

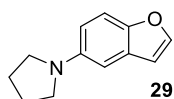
These data are in full agreement with those previously published in the literature.³⁸



3-(pyrrolidin-1-yl)pyridine. From pyrrolidine (256.0 mg, 295.6 μ l, 3.6 mmol, 3.0 equiv.) and 3-bromopyridine (189.6 mg, 115.6 μ l, 1.2 mmol, 1.0 equiv.) using 5 mol% NiBr₂·3H₂O (16.4 mg, 60 μ mol). Reaction time: 72 h. Purification with flash chromatography (1. gradient 0-40% ethyl acetate in hexane with 1% Et₃N; 2. Isocratic 40% ethyl acetate in hexane with 1% Et₃N) afforded the title compound (135.2 mg, 0.91 mmol, 76%) as a colorless oil.

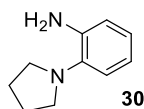
¹H NMR (400 MHz, Chloroform-*d*) δ 7.96 – 7.81 (m, 2H), 7.03 (m, 1H), 6.72 (m, 1H), 3.21 (m, 4H), 2.00 – 1.87 (m, 4H). ¹³C NMR (101 MHz, Chloroform-*d*) δ 143.68, 136.74, 134.23, 123.49, 117.60, 47.19, 25.32. HRMS (ESI-TOF) *m/z* calcd. for C₉H₁₃N₂ [(M+H)⁺]: 149.1074 ; found: 149.1081

These data are in full agreement with those previously published in the literature.³⁹



1-(benzofuran-5-yl)pyrrolidine. From pyrrolidine (256.0 mg, 295.6 μ l, 3.6 mmol, 3.0 equiv.) and 5-bromobenzofuran (236.4 mg, 150.3 μ l, 1.2 mmol, 1.0 equiv.) using 5 mol% NiBr₂·3H₂O (16.4 mg, 60 μ mol). Reaction time: 96 h. No internal standard (1,3,5-trimethoxybenzene was used) due to poor separation from the product during flash chromatography. Purification with flash chromatography (1. gradient 0-2% ethyl acetate in hexane; 2. Isocratic 2% ethyl acetate in hexane) afforded the title compound (188.5 mg, 1.01 mmol, 84%) as a colourless oil.

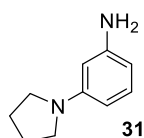
¹H NMR (600 MHz, Chloroform-*d*) δ 7.61 (d, *J* = 2.2 Hz, 1H), 7.47 (d, *J* = 8.9 Hz, 1H), 6.79 (d, *J* = 2.5 Hz, 1H), 6.74 (d, *J* = 2.2 Hz, 1H), 6.71 (dd, *J* = 8.9, 2.5 Hz, 1H), 3.37 (m, 4H), 2.18 – 2.02 (m, 4H). ¹³C NMR (151 MHz, Chloroform-*d*) δ 148.33, 145.31, 145.25, 128.51, 111.58, 110.69, 106.67, 102.17, 48.76, 25.66. HRMS (EI-TOF) *m/z* calcd. for C₁₂H₁₃NO [(M*)⁺]: 187.0997 ; found: 187.0982



2-(pyrrolidin-1-yl)aniline. From pyrrolidine (256.0 mg, 295.6 μ l, 3.6 mmol, 3.0 equiv.) and 2-bromoaniline (206.4 mg, 135.8 μ l, 1.2 mmol, 1.0 equiv.) using 5 mol% NiBr₂·3H₂O (16.4 mg, 60 μ mol). Reaction time: 86 h. Purification with flash chromatography (1. gradient 0-10% ethyl acetate in hexane with 1% Et₃N; 2. Isocratic 10% ethyl acetate in hexane with 1% Et₃N) afforded the title compound (128.6 mg, 0.79 mmol, 66%) as a colorless oil.

¹H NMR (600 MHz, Chloroform-*d*) δ 7.04 (dd, *J* = 7.9, 1.4 Hz, 1H), 6.93 (td, *J* = 7.5, 1.4 Hz, 1H), 6.78 (m, 2H), 3.88 (brs, 2H), 3.15 – 2.98 (m, 4H), 2.03 – 1.80 (m, 4H). ¹³C NMR (151 MHz, Chloroform-*d*) δ 141.59, 137.93, 123.65, 118.85, 118.78, 115.66, 51.09, 24.35. HRMS (EI-TOF) *m/z* calcd. for C₁₀H₁₄N₂ [(M*)⁺]: 162.1157; found: 162.1164

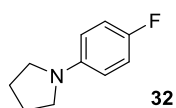
These data are in full agreement with those previously published in the literature.⁴⁰



3-(pyrrolidin-1-yl)aniline. From pyrrolidine (256.0 mg, 295.6 μ l, 3.6 mmol, 3.0 equiv.) and 3-bromoaniline (206.4 mg, 130.6 μ l, 1.2 mmol, 1.0 equiv.) using 5 mol% NiBr₂·3H₂O (16.4 mg, 60 μ mol). Reaction time: 86 h. Purification with flash chromatography (1. gradient 0-3% ethyl acetate in hexane; 2. Isocratic 3% ethyl acetate in hexane; 3. Gradient 3-10% ethyl acetate in hexane; 4. Isocratic 10% ethyl acetate in hexane) afforded the title compound (104.3 mg, 0.64 mmol, 54%) as a slidely brownish oil.

¹H NMR (600 MHz, Chloroform-*d*) δ 7.02 (t, *J* = 8.0 Hz, 1H), 6.05 (m, 2H), 5.92 (t, *J* = 2.3 Hz, 1H), 3.57 (brs, 2H), 3.32 – 3.22 (m, 4H), 2.03 – 1.92 (m, 4H). ¹³C NMR (151 MHz, Chloroform-*d*) δ 148.97, 147.28, 129.79, 103.09, 102.81, 98.39, 47.43, 25.31. HRMS (EI-TOF) *m/z* calcd. for C₁₀H₁₄N₂ [(M)⁺]: 162.1157; found: 162.1151

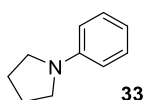
These data are in full agreement with those previously published in the literature.⁴¹



1-(4-fluorophenyl)pyrrolidine. From pyrrolidine (256.0 mg, 295.6 μ l, 3.6 mmol, 3.0 equiv.) and 4-bromofluorobenzene (210.0 mg, 131.8 μ l, 1.2 mmol, 1.0 equiv.) using 5 mol% NiBr₂·3H₂O (16.4 mg, 60 μ mol). Reaction time: 72 h. Purification with flash chromatography (1. gradient 0-3% ethyl acetate in hexane; 2. Isocratic 3% ethyl acetate in hexane) afforded the title compound (128.8 mg, 0.78 mmol, 65 %) as a white solid.

¹H NMR (400 MHz, Chloroform-*d*) δ 6.99 – 6.89 (m, 2H), 6.52 – 6.44 (m, 2H), 3.30 – 3.19 (m, 4H), 2.05 – 1.96 (m, 4H). ¹³C NMR (101 MHz, Chloroform-*d*) δ 154.81 (d, *J* = 233.3 Hz), 144.78, 115.48 (d, *J* = 22.0 Hz), 112.05 (d, *J* = 7.1 Hz), 48.10, 25.50. ¹⁹F NMR (564 MHz, Chloroform-*d*) δ -131.00 (s, 1F). HRMS (ESI-TOF) *m/z* calcd. for C₁₀H₁₃FN [(M+H)⁺]: 166.1027 ; found: 166.1033.

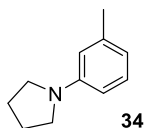
These data are in full agreement with those previously published in the literature.³³



1-phenylpyrrolidine. From pyrrolidine (256.0 mg, 295.6 μ l, 3.6 mmol, 3.0 equiv.) and bromobenzene (188.4 mg, 125.6 μ l, 1.2 mmol, 1.0 equiv.) using 5 mol% NiBr₂·3H₂O (16.4 mg, 60 μ mol). Reaction time: 72 h. Purification with flash chromatography (1. gradient 0-2% ethyl acetate in hexane; 2. Isocratic 2% ethyl acetate in hexane) afforded the title compound (136.9 mg, 0.93 mmol, 77%) as a colourless oil.

¹H NMR (400 MHz, Chloroform-*d*) δ 7.35 (m, 2H), 6.78 (t, *J* = 7.3 Hz, 1H), 6.69 (d, *J* = 8.0 Hz, 2H), 3.43 – 3.30 (m, 4H), 2.13 – 2.05 (m, 4H). ¹³C NMR (101 MHz, Chloroform-*d*) δ 148.04, 129.25, 115.49, 111.77, 47.71, 25.61. HRMS (ESI-TOF) *m/z* calcd. for C₁₀H₁₄N [(M+H)⁺]: 148.1121; found: 148.1122.

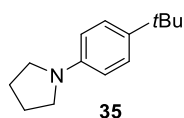
These data are in full agreement with those previously published in the literature.²⁰



1-(m-tolyl)pyrrolidine. From pyrrolidine (256.0 mg, 295.6 μ l, 3.6 mmol, 3.0 equiv.) and 3-bromotoluene (188.4 mg, 145.6 μ l, 1.2 mmol, 1.0 equiv.) using 5 mol% NiBr₂·3H₂O (16.4 mg, 60 μ mol). Reaction time: 72 h. Purification with flash chromatography (1. gradient 0-2% ethyl acetate in hexane; 2. Isocratic 2% ethyl acetate in hexane) afforded the title compound (134.0 mg, 0.93 mmol, 69%) as a colorless oil.

¹H NMR (400 MHz, Chloroform-*d*) δ 7.24-7.16 (t, *J* = 8.8 Hz, 1H), 6.58 (d, *J* = 7.4 Hz, 1H), 6.51 – 6.44 (m, 2H), 3.35 (m, 4H), 2.41 (s, 3H), 2.11 – 2.00 (m, 4H). ¹³C NMR (101 MHz, Chloroform-*d*) δ 148.13, 138.86, 129.09, 116.44, 112.45, 108.99, 47.68, 25.56, 21.98. HRMS (ESI-TOF) *m/z* calcd. for C₁₁H₁₆N [(M+H)⁺]: 162.1278; found: 162.1282.

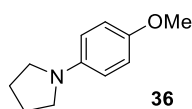
These data are in full agreement with those previously published in the literature.³¹



1-(4-(tert-butyl)phenyl)pyrrolidine. From pyrrolidine (256.0 mg, 295.6 μ l, 3.6 mmol, 3.0 equiv.) and 4-bromotertbutylbenzene (255.7 mg, 208.8 μ l, 1.2 mmol, 1.0 equiv.) using 5 mol% $\text{NiBr}_2 \cdot 3\text{H}_2\text{O}$ (16.4 mg, 60 μ mol). Reaction time: 72 h. Purification with flash chromatography (1. gradient 0-3% ethyl acetate in hexane; 2. Isocratic 3% ethyl acetate in hexane) afforded the title compound (203.2 mg, 1.00 mmol, 83%) as a white solid.

^1H NMR (400 MHz, Chloroform-*d*) δ 7.37 (d, $J = 7.0$ Hz, 2H), 6.64 (d, $J = 7.0$ Hz, 2H), 3.42 – 3.30 (m, 4H), 2.11 – 2.02 (m, 4H), 1.40 (s, 9H). ^{13}C NMR (101 MHz, Chloroform-*d*) δ 145.94, 138.03, 125.99, 111.43, 47.79, 33.82, 31.70, 25.56. HRMS (ESI-TOF) m/z calcd. for $\text{C}_{14}\text{H}_{22}\text{N}$ [(M+H) $^+$]: 204.1747; found: 204.1759.

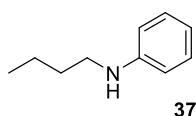
These data are in full agreement with those previously published in the literature.²⁰



1-(4-methoxyphenyl)pyrrolidine. From pyrrolidine (256.0 mg, 295.6 μ l, 3.6 mmol, 3.0 equiv.) and 4-bromoanisole (224.4 mg, 150.2 μ l, 1.2 mmol, 1.0 equiv.) using 5 mol% $\text{NiBr}_2 \cdot 3\text{H}_2\text{O}$ (16.4 mg, 60 μ mol). Reaction time: 72 h. No internal standard (1,3,5-trimethoxybenzene was used) due to poor separation from the product during flash chromatography. Purification with flash chromatography (1. gradient 0-5% ethyl acetate in hexane; 2. Isocratic 5% ethyl acetate in hexane) afforded the title compound (154.7 mg, 0.87 mmol, 73%) as a white solid.

^1H NMR (400 MHz, Chloroform-*d*) δ 6.88 (d, $J = 8.1$ Hz, 2H), 6.57 (d, $J = 8.1$ Hz, 2H), 3.78 (s, 3H), 3.32 – 3.18 (m, 4H), 2.07 – 1.94 (m, 4H). ^{13}C NMR (101 MHz, Chloroform-*d*) δ 150.75, 143.25, 115.01, 112.59, 56.01, 48.24, 25.41. HRMS (ESI-TOF) m/z calcd. for $\text{C}_{11}\text{H}_{16}\text{NO}$ [(M+H) $^+$]: 178.1227; found: 178.1236

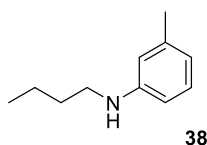
These data are in full agreement with those previously published in the literature.²⁰



N-butylaniline. From *n*-butylamine (263.3 mg, 355.8 μ l, 3.6 mmol, 3.0 equiv.), 7-Methyl-1,5,7-triazabicyclo[4.4.0]dec-5-ene (MTBD) (367.8 mg, 344.7 μ l, 2.4 mmol, 2.0 equiv.) and bromobenzene (188.4 mg, 125.6 μ l, 1.2 mmol, 1.0 equiv.) using 5 mol% NiBr₂·3H₂O (16.4 mg, 60 μ mol.). Reaction time: 168 h. Purification with flash chromatography (1. gradient 0-2% ethyl acetate in hexane; 2. Isocratic 2% ethyl acetate in hexane) afforded the title compound (154.6 mg, 1.04 mmol, 86%) as a colourless oil.

¹H NMR (400 MHz, Chloroform-*d*) δ 7.20 (dd, *J* = 7.4, 7.6 Hz, 2H), 6.72 (t, *J* = 7.4 Hz, 1H), 6.64 (d, *J* = 7.6 Hz, 2H), 3.65 (brs, 1H), 3.14 (t, *J* = 7.1 Hz, 1H), 1.71 – 1.56 (m, 1H), 1.47 (dq, *J* = 9.4, 7.3 Hz, 1H), 0.99 (t, *J* = 7.3 Hz, 2H). ¹³C NMR (101 MHz, Chloroform-*d*) δ 148.51, 129.33, 117.30, 112.90, 43.87, 31.74, 20.42, 14.04. HRMS (EI-TOF) *m/z* calcd. for C₁₀H₁₅N [(M*)⁺]: 149.1204; found: 149.1203

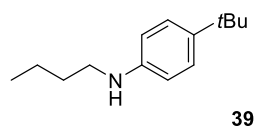
These data are in full agreement with those previously published in the literature.⁴²



N-butyl-3-methylaniline. From *n*-butylamine (263.3 mg, 355.8 μ l, 3.6 mmol, 3.0 equiv.), 7-Methyl-1,5,7-triazabicyclo[4.4.0]dec-5-ene (MTBD) (367.8 mg, 344.7 μ l, 2.4 mmol, 2.0 equiv.) and 3-bromotoluene (205.2 mg, 145.6 μ l, 1.2 mmol, 1.0 equiv.) using 5 mol% NiBr₂·3H₂O (16.4 mg, 60 μ mol.). Reaction time: 168 h. Purification with flash chromatography (1. gradient 0-2% ethyl acetate in hexane; 2. Isocratic 2% ethyl acetate in hexane) afforded the title compound (163.7 mg, 1.00 mmol, 84%) as a colourless oil.

¹H NMR (400 MHz, Chloroform-*d*) δ 7.18 – 7.05 (m, 1H), 6.58 (d, *J* = 7.5 Hz, 1H), 6.54 – 6.44 (m, 2H), 3.72 (brs, 1H), 3.15 (t, *J* = 7.1 Hz, 2H), 2.33 (s, 3H), 1.72 – 1.58 (m, 2H), 1.55 – 1.38 (m, 2H), 1.01 (t, *J* = 7.3 Hz, 3H). ¹³C NMR (101 MHz, Chloroform-*d*) δ 148.52, 139.05, 129.18, 118.26, 113.69, 110.09, 43.90, 31.75, 21.73, 20.41, 14.02. HRMS (EI-TOF) *m/z* calcd. for C₁₁H₁₈N [(M+H)⁺]: 163.1361; found: 163.1360

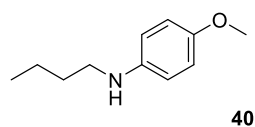
These data are in full agreement with those previously published in the literature.⁴²



4-(tert-butyl)-N-butylaniline. From *n*-butylamine (263.3 mg, 355.8 μ l, 3.6 mmol, 3.0 equiv.), 7-Methyl-1,5,7-triazabicyclo[4.4.0]dec-5-ene (MTBD) (367.8 mg, 344.7 μ l, 2.4 mmol, 2.0 equiv.) and 4-bromotertbutylbenzene (255.7 mg, 208.8 μ l, 1.2 mmol, 1.0 equiv.) using 5 mol% NiBr₂·3H₂O (16.4 mg, 60 μ mol,). Reaction time: 168 h. Purification with flash chromatography (1. gradient 0-2% ethyl acetate in hexane; 2. Isocratic 2% ethyl acetate in hexane) afforded the title compound (206.4 mg, 1.01 mmol, 84%) as a colourless oil.

¹H NMR (600 MHz, Chloroform-*d*) δ 7.35 (d, *J* = 8.8 Hz, 2H), 6.70 (d, *J* = 8.8 Hz, 2H), 3.61 (s, 1H), 3.24 (t, *J* = 7.2 Hz, 2H), 1.77 – 1.70 (m, 2H), 1.62 – 1.53 (m, 2H), 1.44 (s, 9H), 1.11 (t, *J* = 7.4 Hz, 3H). ¹³C NMR (151 MHz, Chloroform-*d*) δ 146.36, 139.92, 126.09, 112.51, 44.02, 33.94, 31.91, 31.69, 20.45, 14.06. HRMS (EI-TOF) *m/z* calcd. for C₁₄H₂₃N [(M*)⁺]: 205.1830; found: 205.1834

These data are in full agreement with those previously published in the literature.⁴²



N-butyl-4-methoxyaniline. From *n*-butylamine (263.3 mg, 355.8 μ l, 3.6 mmol, 3.0 equiv.), 7-Methyl-1,5,7-triazabicyclo[4.4.0]dec-5-ene (MTBD) (367.8 mg, 344.7 μ l, 2.4 mmol, 2.0 equiv.) and 4-bromoanisole (224.4 mg, 150.2 μ l, 1.2 mmol, 1.0 equiv.) using 5 mol% NiBr₂·3H₂O (16.4 mg, 60 μ mol,). Reaction time: 168 h. Purification with flash chromatography (1. gradient 0-4% ethyl acetate in hexane; 2. Isocratic 4% ethyl acetate in hexane) afforded the title compound (135.7 mg, 0.76 mmol, 63%) as a colourless oil.

¹H NMR (600 MHz, Chloroform-*d*) δ 6.79 (d, *J* = 8.9 Hz, 2H), 6.61 (d, *J* = 8.9 Hz, 2H), 3.75 (s, 3H), 3.57 (s, 1H), 3.07 (t, *J* = 7.1 Hz, 2H), 1.67 – 1.54 (m, 2H), 1.51 – 1.35 (m, 2H), 0.96 (t, *J* = 7.3 Hz, 3H). ¹³C NMR (151 MHz, Chloroform-*d*) δ 152.24, 142.66, 115.01, 114.37, 55.95, 45.01, 31.82, 20.45, 14.06. HRMS (EI-TOF) *m/z* calcd. for C₁₁H₁₇NO [(M*)⁺]: 179.1310; found: 179.1303

These data are in full agreement with those previously published in the literature.⁴²

Copies of NMR spectra of isolated compounds

Copies of NMR spectra of isolated compounds are available in the Supporting Information through the website of the Publisher. DOI: [10.1038/s41929-020-0473-6](https://doi.org/10.1038/s41929-020-0473-6)

3.5.14 References

1. Yu, P.; Morandi, B., Nickel-Catalyzed Cyanation of Aryl Chlorides and Triflates Using Butyronitrile: Merging Retro-hydrocyanation with Cross-Coupling. *Angew. Chem. Int. Ed.* **2017**, *56* (49), 15693-15697.
2. Wang, J.; Zhao, J.; Gong, H., Nickel-catalyzed methylation of aryl halides/tosylates with methyl tosylate. *Chem. Commun.* **2017**, *53* (73), 10180-10183.
3. Mori, A.; Mizusaki, T.; Ikawa, T.; Maegawa, T.; Monguchi, Y.; Sajiki, H., Mechanistic Study of a Pd/C-Catalyzed Reduction of Aryl Sulfonates Using the Mg–MeOH–NH₄OAc System. *Chem. Eur. J.* **2007**, *13* (5), 1432-1441.
4. Brown, H. C.; Kanth, J. V. B.; Dalvi, P. V.; Zaidlewicz, M., Molecular Addition Compounds. 15. Synthesis, Hydroboration, and Reduction Studies of New, Highly Reactive tert-Butyldialkylamine–Borane Adducts. *J. Org. Chem.* **1999**, *64* (17), 6263-6274.
5. Kawamata, Y.; Vantourout, J. C.; Hickey, D. P.; Bai, P.; Chen, L.; Hou, Q.; Qiao, W.; Barman, K.; Edwards, M. A.; Garrido-Castro, A. F.; deGruyter, J. N.; Nakamura, H.; Knouse, K.; Qin, C.; Clay, K. J.; Bao, D.; Li, C.; Starr, J. T.; Garcia-Irizarry, C.; Sach, N.; White, H. S.; Neurock, M.; Minter, S. D.; Baran, P. S., Electrochemically Driven, Ni-Catalyzed Aryl Amination: Scope, Mechanism, and Applications. *J. Am. Chem. Soc.* **2019**, *141* (15), 6392-6402.
6. Lim, C.-H.; Kudisch, M.; Liu, B.; Miyake, G. M., C–N Cross-Coupling via Photoexcitation of Nickel–Amine Complexes. *J. Am. Chem. Soc.* **2018**, *140* (24), 7667-7673.
7. Corcoran, E. B.; Pirnot, M. T.; Lin, S.; Dreher, S. D.; DiRocco, D. A.; Davies, I. W.; Buchwald, S. L.; MacMillan, D. W. C., Aryl amination using ligand-free Ni(II) salts and photoredox catalysis. *Science* **2016**, *353* (6296), 279-283.
8. Kudisch, M.; Lim, C.-H.; Thordarson, P.; Miyake, G. M., Energy Transfer to Ni-amine Complexes in Dual Catalytic, Light-driven C–N Cross-Coupling Reactions. *J. Am. Chem. Soc.* **2019**, *141* (49), 19479–19486.
9. Du, Y.; Pearson, R. M.; Lim, C.-H.; Sartor, S. M.; Ryan, M. D.; Yang, H.; Damrauer, N. H.; Miyake, G. M., Strongly Reducing, Visible-Light Organic Photoredox Catalysts as Sustainable Alternatives to Precious Metals. *Chem. Eur. J.* **2017**, *23* (46), 10962-10968.

10. Liu, Y.-Y.; Liang, D.; Lu, L.-Q.; Xiao, W.-J., Practical heterogeneous photoredox/nickel dual catalysis for C–N and C–O coupling reactions. *Chem. Commun.* **2019**, 55 (33), 4853-4856.
11. Ghosh, I.; Khamrai, J.; Savateev, A.; Shlapakov, N.; Antonietti, M.; König, B., Organic semiconductor photocatalyst can bifunctionalize arenes and heteroarenes. *Science* **2019**, 365 (6451), 360-366.
12. Zhang, G.; Li, G.; Lan, Z.-A.; Lin, L.; Savateev, A.; Heil, T.; Zafeiratos, S.; Wang, X.; Antonietti, M., Optimizing Optical Absorption, Exciton Dissociation, and Charge Transfer of a Polymeric Carbon Nitride with Ultrahigh Solar Hydrogen Production Activity. *Angew. Chem. Int. Ed.* **2017**, 56 (43), 13445-13449.
13. Terrett, J. A.; Cuthbertson, J. D.; Shurtleff, V. W.; MacMillan, D. W. C., Switching on elusive organometallic mechanisms with photoredox catalysis. *Nature* **2015**, 524, 330-334.
14. https://www.bauhaus.info/led-baender/tween-light-led-band/p/22517610?gclid=EAIaIQobChMIoLWto9zl3wIVTZSyCh3YDweqEAQYASABEgJmRfD_BwE&s_kwcid=AL!5677!3!190027496787!!!g!462716337331!&pla_prpaid=462716337331&ef_id=EAIaIQobChMIoLWto9zl3wIVTZSyCh3YDweqEAQYASABEgJmRfD_BwE:G:s&pla_adgrid=41635814775&pla_campid=225980581&pla_prch=online&pla_prid=22517610&cid=PSEGoo225980581_41635814775&pla_adt=pla (Germany; 2019 October 16).
15. <https://www.kessil.com/photoreaction/index.php> (Germany, March 2020)
16. Goettmann, F.; Fischer, A.; Antonietti, M.; Thomas, A., Chemical Synthesis of Mesoporous Carbon Nitrides Using Hard Templates and Their Use as a Metal-Free Catalyst for Friedel–Crafts Reaction of Benzene. *Angew. Chem. Int. Ed.* **2006**, 45 (27), 4467-4471.
17. Shalom, M.; Guttentag, M.; Fettkenhauer, C.; Inal, S.; Neher, D.; Llobet, A.; Antonietti, M., In Situ Formation of Heterojunctions in Modified Graphitic Carbon Nitride: Synthesis and Noble Metal Free Photocatalysis. *Chem. Mater.* **2014**, 26 (19), 5812-5818.
18. Zhang, J.; Sun, J.; Maeda, K.; Domen, K.; Liu, P.; Antonietti, M.; Fu, X.; Wang, X., Sulfur-mediated synthesis of carbon nitride: Band-gap engineering and improved functions for photocatalysis. *Energy Environ. Sci.* **2011**, 4 (3), 675-678.
19. Savateev, A.; Pronkin, S.; Epping, J. D.; Willinger, M. G.; Wolff, C.; Neher, D.; Antonietti, M.; Dontsova, D., Potassium Poly(heptazine imides) from Aminotetrazoles:

Shifting Band Gaps of Carbon Nitride-like Materials for More Efficient Solar Hydrogen and Oxygen Evolution. *ChemCatChem* **2017**, *9* (1), 167-174.

20. Hamid, M. H.; Allen, C. L.; Lamb, G. W.; Maxwell, A. C.; Maytum, H. C.; Watson, A. J.; Williams, J. M., Ruthenium-catalyzed N-alkylation of amines and sulfonamides using borrowing hydrogen methodology. *J. Am. Chem. Soc.* **2009**, *131* (5), 1766-74.

21. Sandtorv, A. H.; Stuart, D. R., Metal-free Synthesis of Aryl Amines: Beyond Nucleophilic Aromatic Substitution. *Angew. Chem. Int. Ed.* **2016**, *55* (51), 15812-15815.

22. Urgaonkar, S.; Xu, J.-H.; Verkade, J. G., Application of a New Bicyclic Triaminophosphine Ligand in Pd-Catalyzed Buchwald–Hartwig Amination Reactions of Aryl Chlorides, Bromides, and Iodides. *J. Org. Chem.* **2003**, *68* (22), 8416-8423.

23. Lin, S.-X.; Sun, G.-J.; Kang, Q., A visible-light-activated rhodium complex in enantioselective conjugate addition of α -amino radicals with Michael acceptors. *Chem. Commun.* **2017**, *53* (54), 7665-7668.

24. Wolfe, J. P.; Buchwald, S. L., Scope and Limitations of the Pd/BINAP-Catalyzed Amination of Aryl Bromides. *J. Org. Chem.* **2000**, *65* (4), 1144-1157.

25. Xie, X.; Zhang, T. Y.; Zhang, Z., Synthesis of Bulky and Electron-Rich MOP-type Ligands and Their Applications in Palladium-Catalyzed C–N Bond Formation. *J. Org. Chem.* **2006**, *71* (17), 6522-6529.

26. Liu, K.-J.; Zeng, X.-L.; Zhang, Y.; Wang, Y.; Xiao, X.-S.; Yue, H.; Wang, M.; Tang, Z.; He, W.-M., Palladium-Catalyzed Reductive Coupling of Nitroarenes with Phenols leading to N-Cyclohexylanilines. *Synthesis* **2018**, *50* (23), 4637-4644.

27. Suárez-Pantiga, S.; Hernández-Ruiz, R.; Virumbrales, C.; Pedrosa, M. R.; Sanz, R., Reductive Molybdenum-Catalyzed Direct Amination of Boronic Acids with Nitro Compounds. *Angew. Chem. Int. Ed.* **2019**, *58* (7), 2129-2133.

28. Desmarets, C.; Schneider, R.; Fort, Y., Nickel(0)/Dihydroimidazol-2-ylidene Complex Catalyzed Coupling of Aryl Chlorides and Amines. *J. Org. Chem.* **2002**, *67* (9), 3029-3036.

29. Wolfe, J. P.; Tomori, H.; Sadighi, J. P.; Yin, J.; Buchwald, S. L., Simple, Efficient Catalyst System for the Palladium-Catalyzed Amination of Aryl Chlorides, Bromides, and Triflates. *J. Org. Chem.* **2000**, *65* (4), 1158-1174.

30. Yoshida, H.; Morishita, T.; Ohshita, J., Direct Access to Anthranilic Acid Derivatives via CO₂ Incorporation Reaction Using Arynes. *Org. Lett.* **2008**, *10* (17), 3845-3847.

31. Brenner, E.; Schneider, R.; Fort, Y., Nickel-catalysed couplings of aryl chlorides with secondary amines and piperazines. *Tetrahedron* **1999**, *55* (44), 12829-12842.
32. Johnson, T. C.; Elbert, Bryony L.; Farley, A. J. M.; Gorman, T. W.; Genicot, C.; Lallemand, B.; Pasau, P.; Flasz, J.; Castro, J. L.; MacCoss, M.; Dixon, D. J.; Paton, R. S.; Schofield, C. J.; Smith, M. D.; Willis, M. C., Direct sulfonylation of anilines mediated by visible light. *Chem. Sci.* **2018**, *9* (3), 629-633.
33. Hollmann, D.; Bähn, S.; Tillack, A.; Parton, R.; Altink, R.; Beller, M., A novel salt-free ruthenium-catalyzed alkylation of aryl amines. *Tetrahedron Lett.* **2008**, *49* (40), 5742-5745.
34. Ju, Y.; Varma, R. S., An Efficient and Simple Aqueous N-Heterocyclization of Aniline Derivatives: Microwave-Assisted Synthesis of N-Aryl Azacycloalkanes. *Org. Lett.* **2005**, *7* (12), 2409-2411.
35. Lim, S.; Song, D.; Jeon, S.; Kim, Y.; Kim, H.; Lee, S.; Cho, H.; Lee, B. C.; Kim, S. E.; Kim, K.; Lee, E., Cobalt-Catalyzed C–F Bond Borylation of Aryl Fluorides. *Org. Lett.* **2018**, *20* (22), 7249-7252.
36. Wolfe, J. P.; Buchwald, S. L., Palladium-Catalyzed Amination of Aryl Triflates. *J. Org. Chem.* **1997**, *62* (5), 1264-1267.
37. Lakshminarayana, N.; Prasad, Y. R.; Gharat, L.; Thomas, A.; Narayanan, S.; Raghuram, A.; Srinivasan, C. V.; Gopalan, B., Synthesis and evaluation of some novel dibenzo[b,d]furan carboxylic acids as potential anti-diabetic agents. *Eur. J. Med. Chem.* **2010**, *45* (9), 3709-3718.
38. Charles, M. D.; Schultz, P.; Buchwald, S. L., Efficient Pd-Catalyzed Amination of Heteroaryl Halides. *Org. Lett.* **2005**, *7* (18), 3965-3968.
39. Maiti, D.; Fors, B. P.; Henderson, J. L.; Nakamura, Y.; Buchwald, S. L., Palladium-catalyzed coupling of functionalized primary and secondary amines with aryl and heteroaryl halides: two ligands suffice in most cases. *Chem. Sci.* **2011**, *2* (1), 57-68.
40. Perez Garcia, P. M.; Di Franco, T.; Epenoy, A.; Scopelliti, R.; Hu, X., From Dimethylamine to Pyrrolidine: The Development of an Improved Nickel Pincer Complex for Cross-Coupling of Nonactivated Secondary Alkyl Halides. *ACS Catal.* **2016**, *6* (1), 258-261.

41. Wang, Y.; Ling, J.; Zhang, Y.; Zhang, A.; Yao, Q., N-(1-Oxy-2-picolyl)oxalamic Acid as an Efficient Ligand for Copper-Catalyzed Amination of Aryl Iodides at Room Temperature. *Eur. J. Org. Chem.* **2015**, 2015 (19), 4153-4161.
42. Afanasenko, A.; Elangovan, S.; Stuart, M. C. A.; Bonura, G.; Frusteri, F.; Barta, K., Efficient nickel-catalysed N-alkylation of amines with alcohols. *Catal. Sci. Technol.* **2018**, 8 (21), 5498-5505.

Supporting Information - Chapter 4

Chromoselective Photocatalysis Enables Stereocomplementary Biocatalytic Pathways

Schmermund, L.; **Reischauer, S.**; Bierbaumer, S.; Winkler, C.; Diaz-Rodriguez, A.;
Edwards, L.; Kara, S.; Mielke, T.; Cartwright, J.; Grogan, G.; Pieber, B.; Kroutil, W.
Angew. Chem. Int. Ed. **2021**, *60*, 6965-6969.

<https://doi.org/10.1002/anie.202100164>

4.5 Supporting information

4.5.1 General remarks

General reagents, substrates and solvents were purchased and used as supplied from Sigma-Aldrich (Merck KGaA), TCI, Alfa Aesar, Thermo Fisher Scientific, AmBeed, Enamine and Lancaster. The CN-OA-m photocatalyst was produced by co-condensation of urea and oxamide followed post-calcination in a molten salt according to a literature procedure.¹⁻² For the **thin layer chromatography (TLC)** Merck TLC silica gel 60 F₂₅₄ plates were used. The compounds were visualized by using UV-light (254 nm/366 nm) or basic aqueous potassium permanganate stain (2.5 g NaHCO₃, 0.67 g KMnO₄, 0.2 mL acetic acid, 200 mL), followed by heating with a heat gun. **Flash column chromatography** was used to purify crude products. The purification was performed using silica gel 60 M (particle size 40-63 μm / 230-400 mesh) from Merck as stationary phase under excess pressure. **¹H-NMR spectra** were recorded on AV II 300 MHz spectrometer from Bruker Physics in chloroform-*d*₁ (CDCl₃). The chemical shift δ is indicated in parts per million (ppm) relative to the internal standard trimethylsilane ($\delta = 0$ ppm). The spectra were calibrated using the residual proton signal of the solvent CDCl₃ at 7.26 ppm internal references.³ The coupling constants (*J*) are given in Hz. The following abbreviations were used to designate multiplicities in the recorded spectra: s (singlet), d (doublet), t (triplett), q (quartet), quint (quintet) and m (multiplet). **¹³C-NMR spectra** were recorded on AV-300 (75.5 MHz) spectrometer from Bruker Physics in CDCl₃. The chemical shift δ is indicated in parts per million (ppm) relative to the internal standard trimethylsilane ($\delta = 0$ ppm). The spectra were calibrated using the carbon signal of the solvent CDCl₃ at 77.16 ppm.³ For **gas chromatography (GC)** an Agilent GC7890A system with FID-detector (heater 300 °C, H₂-flow 28 mL/min, Air-flow 350 mL/min, makeup flow 25 mL/min; Date Rate/min peak width 50 Hz/0.004 min) was used. For general measurements a 30 m CP WAX 52CB column (Varian) with 0.25 μm inner diameter was used. Heater was at 250 °C, 0.60 bar, gas saver 15 mL/min after 2 min. For determination of optical purities, a 25 m CP-ChiraSil-DEX CB column (Agilent Technologies) with 0.032 μm inner diameter was used. Heater was at 220 °C, 0.17 bar, gas saver 15 mL/min after 2 min. **Optical rotation** values were measured on a Perkin Elmer Polarimeter 341. **Transmission electron microscopy (TEM)** was performed on a CM200F EG (Philips) microscope, operated at 200 kV. **Scanning electron**

microscopy (SEM) images were obtained on a LEO 1550-Gemini microscope. **Energy-dispersive X-ray (EDX)** investigations were conducted on a Link ISIS-300 system (Oxford Microanalysis Group) equipped with a Si(Li) detector and an energy resolution of 133 eV.

4.5.2 Photoreactor Set Up for Initial Studies of the Oxidation of Ethylbenzene using CN-OA-m

Experiments using blue light were carried out using a Kessil PR160-440 LED (Fig. 4.3). Two sealed reaction vessels were placed on a stirring plate 4.5 cm away from a single lamp. To avoid heating of the reaction mixture, a fan was used for cooling. All reactions were performed with maximum stirring speed.

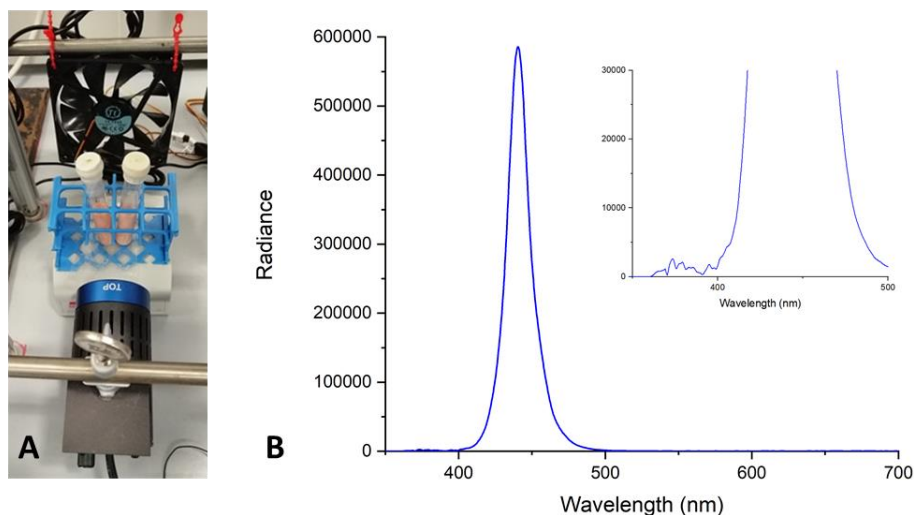


Figure S4.1. Setup for blue light experiments (A); Emission spectra of the Kessil PR160-440 (B).

Experiments using green light were carried out using a Kessil PR160-525 LED (Fig. 4.4). Two sealed reaction vessels were placed on a stirring plate 4.5 cm away from a single lamp. To avoid heating of the reaction mixture, a fan was used for cooling. All reactions were performed with maximum stirring speed.

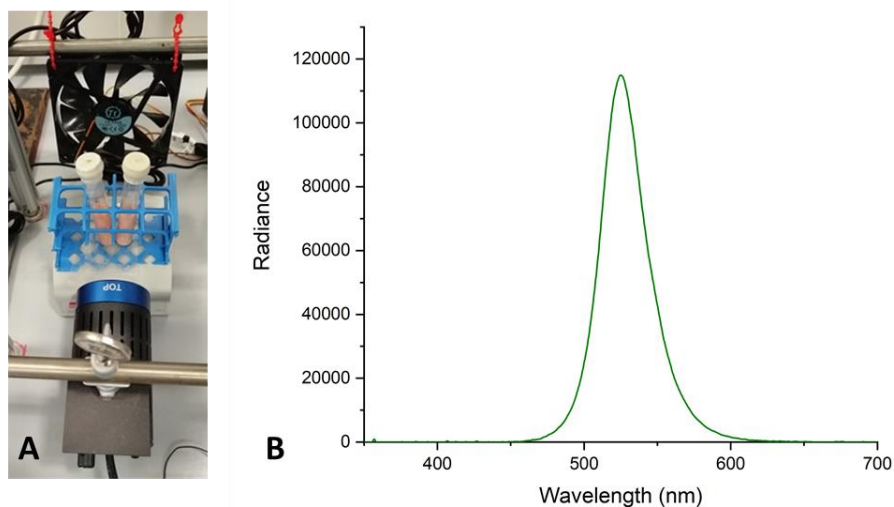


Figure S4.2. Setup for green light experiments (A). Emission spectra of the Kessil PR160-525 (B).

Photoreactor for Photo-Chemo-Enzymatic Reactions in Glass Vials

For reactions performed in crimp glass vials (1.5 mL, Merck, Fig. 4.5) a self-built photoreactor (Fig. 4.6) was used. The glass vials were closed with crimp seals (Merck) and placed in the photoreactor for irradiation.

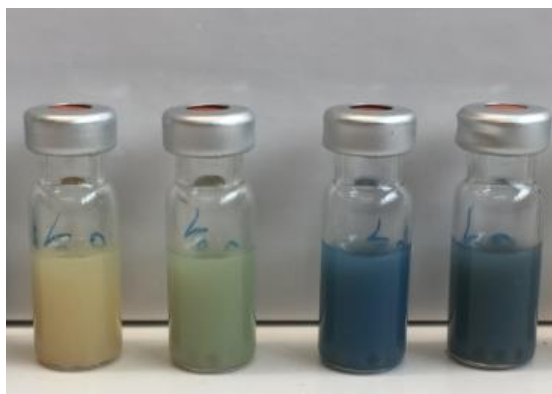


Figure S4.3. Crimp glass vial (1.5 mL) used for biotransformations with CN-OA-m and UPO (total volume 1 mL).

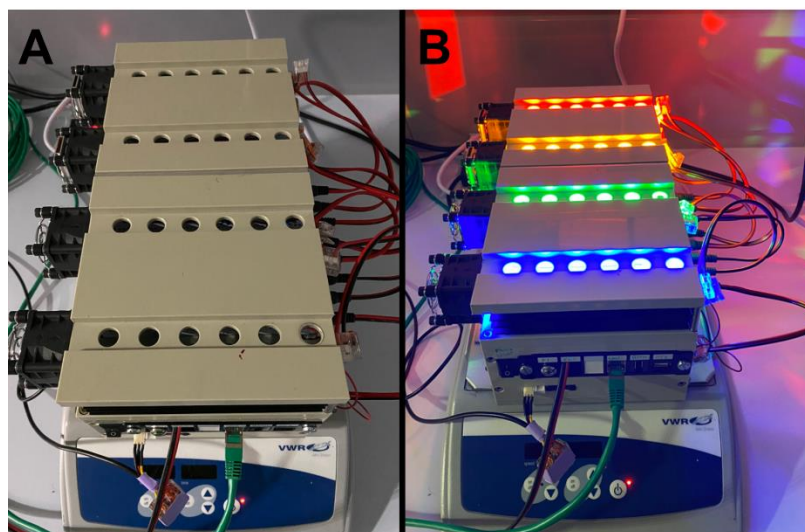


Figure S4.4. Photoreactor used for the CN-OA-m/UPO system; A) Photoreactor off; B) Photoreactor on: The reactor has four rows with six reactions slots (24 in total) for 1.5 mL glass vials. Every row has two LED stripes (Lumitronix, PowerBar V3 LED-Modul Aluminium 12x Osram Oslon SSL LEDs) and every glass vial is irradiated by two LED lamps. The LED stripes are interchangeable allowing to perform reactions at different wavelengths (white light >450 nm, 405 nm, 455 nm, 470 nm, 528 nm, 590 nm). Temperature and light intensity are independently adjustable for each LED row. Shaking was performed at 500 rpm. The emission spectra and specification sheets of the LED lamps are given by the supplier.

GSK Photoreactor for Photo-Chemo-Enzymatic Reactions in Microwave Tubes

For reactions performed in microwave reaction vials (Biotage, Microwave Reaction Kit, 2-10 mL) a photoreactor⁴⁻⁵ provided by GSK (electronics designed by Pacer Components Ltd. Pangbourne, UK; housing machined by Rosper Engineering Co., Harlow, UK) was used (Fig. 4.7). A stirring bar was added, the microwave reaction vials were closed with crimp seals and placed in the photoreactor for irradiation. The emission spectra of the LED stripes used for photochemoenzymatic reactions and the characterization of the photoreactor can be found in the provided literature.⁴⁻⁵



Figure S4.5. Photoreactor used for the CN-OA-m/UPO system; A) Complete photoreactor unit with control panel unit (left) and reactor and cooling unit (right); B) Reactor unit on a magnetic stirrer with microwave reaction vials: The reactor has three slots for microwave reaction vials. A magnetic stirrer is used to stir the reaction (500 rpm). The photoreactor is controlled by a control unit allowing to adjust the temperature, light intensity (25-500 mA), and wavelength. Six different wavelengths can be used for reactions (365 nm, 385 nm, 405 nm, 420 nm, 455 nm and 528 nm).

4.5.3 Expression of *Aae*UPO and ADH-A

Expression of *Aae*UPO

Expression, isolation and lyophilisation of *Aae*UPO were performed as described in Reference.⁵

Expression and Purification of ADH-A

For the expression of ADH-A (ADH-A-pET21a-strep, internal number pEG518), LB-medium (700 mL) containing the ampicillin (100 µg/mL) was inoculated in a 2 L baffled flask with 1% *Escherichia coli* BL21(DE3)/pEG518. The culture was incubated at 30 °C and 120 rpm until an OD₆₀₀ of 5 was reached. Then induction was performed by adding IPTG (2 mM). Further incubation took place at 20 °C and 120 rpm for 24 h. Afterwards, the cell suspension was centrifuged (5000 rpm, 20 min, 4 °C), the supernatant discarded, and the pellets were resuspended in Tris buffer (15 mL, 50 mM TRIS/HCl, pH 7.5). The suspension was centrifuged (8 °C, 4500 rpm, 20 min), the supernatant was discarded and the pellet either lysed (50 mM Tris/HCl, 150 mM NaCl, 20 mM imidazole, pH 7.5) or shock frozen in liquid nitrogen and stored at -20 °C till further use.

To purify the protein the harvested cells were resuspended in lysis buffer (10 mL/g pellet, 50 mM Tris/HCl, 150 mM NaCl, 20 mM imidazole, pH 7.5) and lysed on ice by sonication (3x, 2 min 30 sec, 30% amplitude, 2.0 sec pulse on, 4.0 sec pulse off, 1 min pause, Digital sonifier, Branson). The cell suspension was centrifuged (20 min, 18000 rpm, 4 °C) and the clear slightly yellow cell free extract (CFE) was filtered (0.45 µm syringe filter) and stored on ice for protein purification.

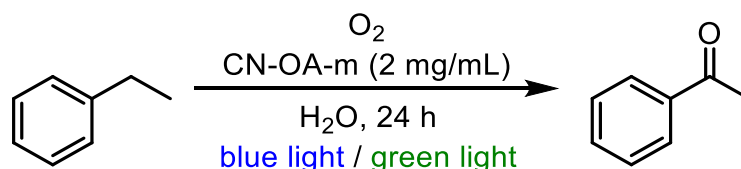
The ADH-A bearing a strep-Tag were purified by strep-tactin affinity chromatography (Strep-Tactin®XT Superflow® Column, IBA) with gravity flow.

The purification was performed at 4 °C. The column was equilibrated with 2 CV buffer W (100 mM Tris/HCl, 150 mM NaCl, pH 8) before the filtered CFE was loaded onto the column and the flow through collected for SDS-PAGE-sample. The column was then 5x washed with 1 CV buffer W. Then, the protein was eluted by applying 8x 0.5 CV Buffer BXT (100 mM Tris/HCl, 150 mM NaCl, 50 mM biotin, pH 8). After finished elution the column was regenerated with 4 CV 10 mM sodium hydroxide (NaOH). NaOH was removed immediately by washing the column 2x with 4 CV Buffer W. The column was stored at 4 °C.

To exchange the buffer a Sephadex G-25 PD10 desalting column (GE Healthcare) was equilibrated with KP_i buffer. The concentrated protein solution (2.5 mL) was loaded onto the column and eluted with KP_i buffer (exactly 3.5 mL). The final enzyme solution was aliquoted and stored at $-20\text{ }^\circ\text{C}$.

4.5.4 Photocatalytic Oxidation of Ethylbenzene and *rac*-1-phenylethanol using CN-OA-m with Different Wavelengths

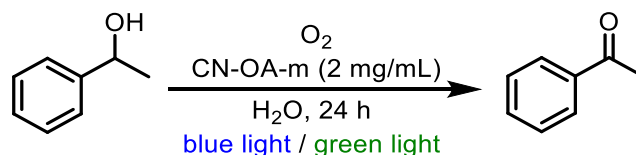
Table S4.1. Photocatalytic reaction of ethylbenzene in the presence of CN-OA-m.



Entry ^[a]	additive	light	Ratio ethylbenzene: acetophenone ^[b]
1	MeOH	blue	1:1
2	MeOH	green	1:0
3	-	blue	0:1
4	-	green	1:0

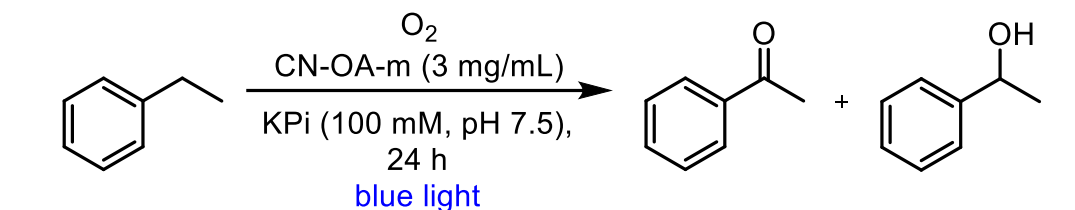
[a] Reaction conditions: ethylbenzene (180 μ mol), 12 mg CN-OA-m in water (3 mL) or water and MeOH (1:1), 440 nm blue LED or 525 nm green LED (50% power) at 21 $^{\circ}$ C for 24 h; [b] Determined by 1 H-NMR after extraction of the entire reaction mixture with $CDCl_3$.

Table S4.2. Photocatalytic reaction of *rac*-1-phenylethanol in the presence of CN-OA.



Entry	additive	light	Ratio <i>rac</i> -1-phenylethanol: acetophenone ^[b]
1	MeOH	blue	1:0.19
2	MeOH	green	1:traces
3	-	blue	1:1.8
4	-	green	1:0.05

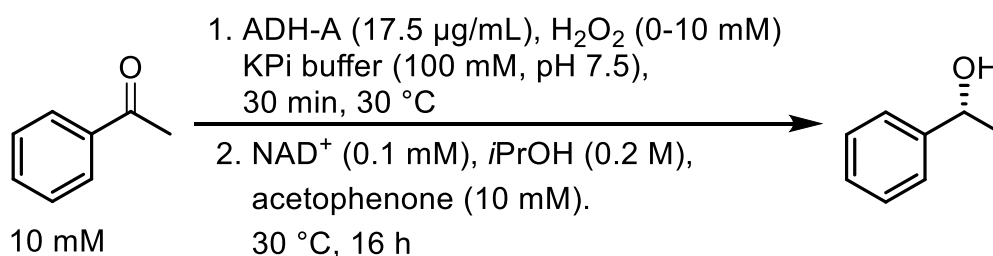
[a] Reaction conditions: *rac*-1-phenylethanol (180 μ mol), 12 mg CN-OA-m in water (3 mL) or water and MeOH (1:1), 440 nm blue LED or 525 nm green LED (50% power) at 21 $^{\circ}$ C for 24 h. [b] Determined by 1 H-NMR after extraction of the entire reaction mixture with $CDCl_3$.

Table S4.3. Photocatalytic reaction of ethylbenzene in the presence of CN-OA-m in the photoreactor used for photo-chemo-enzymatic reactions.

Entry ^[a]	additive	light	acetophenone ^[b]	1-phenylethanol ^[b]
1	MeOH	blue	2.7 mM	0.3 mM

[a] Reaction conditions: ethylbenzene (10 mM), CN-OA-m (3 mg/mL), MeOH (1% v/v), KPi buffer (100 mM, pH 7.5), LED 455 nm, 1998 $\mu\text{mol photons m}^{-2} \text{s}^{-1}$, 30 °C, 24 h. [b] GC yield.

4.5.5 ADH-A Catalysed Reduction of Acetophenone under the Presence of Hydrogen Peroxide

Table S4.4. ADH-A catalysed reduction of acetophenone in the presence of hydrogen peroxide.

Entry ^[a]	CH_2O_2	C_1 -phenylethanol ^[b]	<i>ee</i> ^[c]
1	10	8.9 mM	>99% (<i>S</i>)
2	2	8.7 mM	>99% (<i>S</i>)
3	0	9.0 mM	>99% (<i>S</i>)

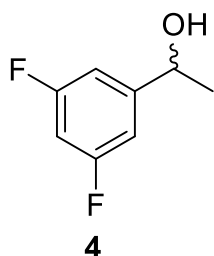
[a] Reaction conditions: 1) H_2O_2 (0, 2, 10 mM), ADH-A (17.5 $\mu\text{g/mL}$), KPi buffer (100 mM, pH 7.5), 30 °C, 30 min; 2) acetophenone (10 mM), NAD^+ (0.1 mM), *i*PrOH (0.2 M), KPi buffer (100 mM, pH 7.5), 30 °C, 16 h; [b] GC yield; [c] Determined by GC.

4.5.6 Experimental Procedures

Experimental Procedure for the Synthesis of Racemic Reference Compounds

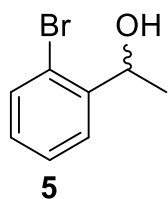
The respective ketone (1.0 eq) was dissolved in EtOH (10 mL). Then the solution was cooled to 0 °C with an ice water bath and sodium borohydride (1.5 eq) was added in one portion. The reaction was stirred for 10 min at 0 °C. Afterwards, the ice water bath was removed, and the reaction was stirred for 50 min at rt (the product formation was monitored by TLC). After complete consumption of the starting material the reaction was cooled to 0 °C with an ice water bath. Then water (3 mL) was added dropwise over 3 min followed by a dropwise addition of hydrochloric acid (37 wt.%, 3 mL) over 3 min. The ice water bath was removed, the reaction was stirred for 10 min at 21 °C and brine (10 mL) was added. The reaction was extracted with EtOAc (3x10 mL), the combined organic phases were dried over Na₂SO₄ and the solvent was removed under reduced pressure. The obtained crude product was purified by flash column chromatography.

rac-1-(3,5-difluorophenyl)ethan-1-ol



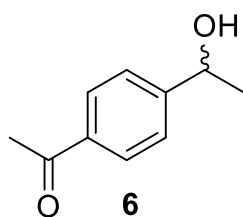
Batch: 1-ethyl-3,5-difluorobenzene (104 mg, 0.67 mmol, 1.0 eq) and sodium borohydride (37.8 mg, 1.0 mmol, 1.5 eq). The obtained crude product was purified via flash column chromatography (cyclohexane/EtOAc 8/1 to 4/1) to give **4** as a colourless oil (98.0 mg, 0.62 mmol, 93%).

R_f = 0.30 (cyclohexane/EtOAc 4/1); **¹H NMR** (300 MHz, CDCl₃) δ 6.9 (qt, *J* = 6.7, 2.2 Hz, 2H), 6.69 (tt, *J* = 8.9, 2.3 Hz, 1H), 4.88 (q, *J* = 6.5 Hz, 1H), 1.47 (d, *J* = 6.5 Hz, 3H) ppm; **¹³C NMR** (75 MHz, CDCl₃) δ 164.9 (d, *J* = 12.6 Hz), 161.6 (d, *J* = 12.6 Hz), 150.1 (t, *J* = 8.2 Hz), 108.3 (d, *J* = 25.1 Hz), 108.3 (d, *J* = 9.3 Hz), 102.7 (t, *J* = 25.4 Hz), 69.6, 25.4 ppm.⁶

rac-1-(2-bromophenyl)ethan-1-ol

Batch: 1-bromo-2-ethylbenzene (162 mg, 0.82 mmol, 1.0 eq) and sodium borohydride (46.3 mg, 1.22 mmol, 1.5 eq). The obtained crude product was purified via flash column chromatography (cyclohexane/EtOAc 8/1 to 4/1) to give **5** as a colourless oil (153 mg, 0.77 mmol, 94%).

R_f = 0.13 (cyclohexane/EtOAc 4/1); $^1\text{H NMR}$ (300 MHz, CDCl_3) δ 7.59 (dd, J = 7.8, 1.5 Hz, 1H), 7.51 (d, J = 8.0 Hz, 1H), 7.34 (t, J = 7.5 Hz, 1H), 7.12 (td, J = 7.7, 1.6 Hz, 1H), 5.24 (q, J = 6.4 Hz, 1H), 1.48 (d, J = 6.4 Hz, 3H) ppm; $^{13}\text{C NMR}$ (75 MHz, CDCl_3) δ 144.7, 132.8, 128.8, 128.0, 126.8, 121.9, 69.3, 23.7 ppm.⁷

rac-1-(4-(1-hydroxyethyl)phenyl)ethan-1-one

Batch: 1-(4-ethylphenyl)ethan-1-one (200 mg, 1.23 mmol, 1.0 eq) and sodium borohydride (23.3 mg, 0.62 mmol, 0.5 eq). The obtained crude product was purified via flash column chromatography (cyclohexane/EtOAc 7/1 to 3/1) to give **6** as a colourless oil (90.0 mg, 0.055 mmol, 89%).

R_f = 0.30 (cyclohexane/EtOAc 4/1); $^1\text{H NMR}$ (300 MHz, CDCl_3) δ 7.91 (d, J = 8.3 Hz, 2H), 7.44 (d, J = 8.3 Hz, 2H), 4.95 (q, J = 6.5 Hz, 1H), 2.57 (s, 3H), 1.49 (d, J = 6.5 Hz, 3H) ppm;⁸ $^{13}\text{C NMR}$ (75 MHz, CDCl_3) δ 198.1, 151.4, 136.3, 128.7, 125.6, 77.2, 26.8, 25.4 ppm.

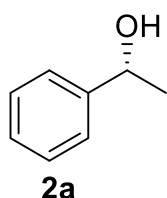
Experimental Procedure for Photo-Chemo-Enzymatic Hydroxylations**General Procedure for Photo-Chemo-Enzymatic Hydroxylations with CN-OA-m and UPO in Glass Vials**

A crimp glass vial (1.5 mL) was charged with CN-OA-m (2.0 mg, 2.0 mg/mL) and five glass beads (1.0 mm, Merck). Then tricine buffer (840 μL , 100 mM, pH 7.5) was added and the mixture was sonicated in an ultrasonic bath (5 s) to ensure a fine distribution of the CN-OA-m. Then the substrate (10 mM, 10 μmol) dissolved in MeOH (1 M stock solution, 10.0 μL

were used) and the *Aae*UPO (150 μ L, 2.2 U/mg, 25 nM) from a stock solution (6 mg/mL *Aae*UPO in tricine buffer 6 mg/mL) were added. The crimp vial was sealed, and the glass vial was irradiated in the photoreactor (528 nm, 1330 μ mol photons $m^{-2} s^{-1}$) for 24 h at 30 °C and 500 rpm. Afterwards, the reaction was extracted with EtOAc (1x 400 μ L and 1x 400 μ L + 10 mM 1-octanol) and the combined organic phases were dried over Na_2SO_4 . The extracts were analyzed by GC.

For isolation and purification of the product 10-20 glass vial reactions were combined. The combined reactions were extracted with EtOAc (2x12 mL), the combined organic phase was dried over Na_2SO_4 and the solvent was removed under reduced pressure. The obtained crude product was purified via flash column chromatography.

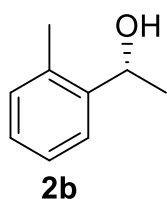
(*R*)-1-phenylethan-1-ol



Substrate: ethylbenzene (10 mM, 10 μ M). The obtained crude product was purified via flash column chromatography (cyclohexane/EtOAc 7/1 to 4/1) to give **2a** as a colourless oil (9.3 mg, 78.0 μ mol, 25%).

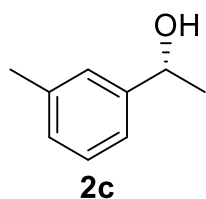
R_f = 0.40 (cyclohexane/EtOAc 4/1); 1H NMR (300 MHz, $CDCl_3$) δ 7.42–7.24 (m, 5H), 4.90 (q, J = 6.5 Hz, 1H), 1.50 (d, J = 6.5 Hz, 3H) ppm,⁹⁻¹⁰ *e.e.* = 99%.

(*R*)-1-(*o*-tolyl)ethan-1-ol



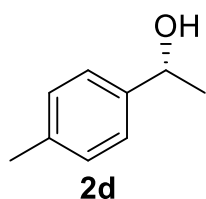
Substrate: 1-ethyl-2-methylbenzene (10 mM, 10 μ M). The obtained crude product was purified via flash column chromatography (cyclohexane/EtOAc 7/1 to 4/1) to give **2b** as a colourless oil (10.2 mg, 75.0 μ mol, 36%).

R_f = 0.32 (cyclohexane/EtOAc 4/1); 1H NMR (300 MHz, $CDCl_3$) δ 7.56–7.49 (m, 1H), 7.29–7.11 (m, 3H), 5.14 (q, J = 6.4 Hz, 1H), 2.35 (s, 3H), 1.47 (d, J = 6.4 Hz, 3H) ppm,¹¹ *e.e.* = 98%.

(R)-1-(*m*-tolyl)ethan-1-ol

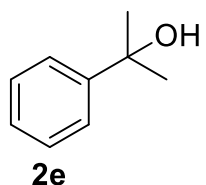
Substrate: 1-ethyl-3-methylbenzene (10 mM, 10 μ M). The obtained crude product was purified via flash column chromatography (cyclohexane/EtOAc 7/1 to 4/1) to give **2c** as a colourless oil (1.6 mg, 11.7 μ mol, 4.9%).

R_f = 0.35 (cyclohexane/EtOAc 4/1); $^1\text{H NMR}$ (300 MHz, CDCl_3) δ 7.28–7.14 (m, 1H), 7.09 (d, J = 7.3 Hz, 3H), 4.87 (q, J = 6.5 Hz, 3H), 2.36 (s, 9H), 1.49 (d, J = 6.5 Hz, 9H) ppm,¹⁰ *e.e.* = 98%.

(R)-1-(*p*-tolyl)ethan-1-ol

Substrate: 1-ethyl-4-methylbenzene (10 mM, 10 μ M). The obtained crude product was purified via flash column chromatography (cyclohexane/EtOAc 7/1 to 4/1) to give **2d** as a colourless oil (2.1 mg, 17.5 μ mol, 8.3%).

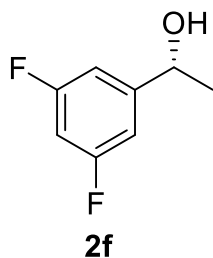
R_f = 0.35 (cyclohexane/EtOAc 4/1); $^1\text{H NMR}$ (300 MHz, CDCl_3) δ 7.29 (s, 5H), 7.16 (d, J = 7.9 Hz, 2H), 4.88 (q, J = 6.4 Hz, 1H), 2.35 (s, 3H), 1.49 (d, J = 6.4 Hz, 3H) ppm,⁹⁻¹⁰ *e.e.* = 98%.

2-phenylpropan-2-ol

Substrate: cumene (10 mM, 10 μ M). The obtained crude product was purified via flash column chromatography (cyclohexane/EtOAc 7/1 to 4/1) to give **2e** as a colourless oil (7.0 mg, 51.0 μ mol, 25.0%).

R_f = 0.34 (cyclohexane/EtOAc 5/1); $^1\text{H NMR}$ (300 MHz, CDCl_3) δ 7.53–7.47 (m, 1H), 7.35 (t, J = 7.5 Hz, 1H), 7.28–7.21 (m, 1H), 1.59 (s, 3H) ppm.¹²

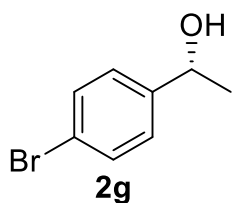
(R)-1-(3,5-difluorophenyl)ethan-1-ol



Substrate: 1-ethyl-3,5-difluorobenzene (10 mM, 10 μ M). The obtained crude product was purified via flash column chromatography (cyclohexane/EtOAc 7/1 to 4/1) to give **2f** as a colourless oil (10.1 mg, 64.0 μ mol, 30%).

R_f = 0.26 (cyclohexane/EtOAc 5/1); $^1\text{H NMR}$ (300 MHz, CDCl_3) δ 6.93–6.83 (m, 2H), 6.73–6.66 (m, 1H), 4.88 (q, J = 6.5 Hz, 1H), 1.48 (d, J = 6.5 Hz, 3H) ppm, $e.e.$ = 98%.

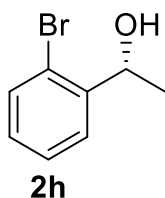
(R)-1-(4-bromophenyl)ethan-1-ol



Substrate: 1-bromo-4-ethylbenzene (10 mM, 10 μ M). The obtained crude product was purified via flash column chromatography (cyclohexane/EtOAc 7/1 to 4/1) to give **2g** as a colourless oil (5.1 mg, 25.4 μ mol, 11%).

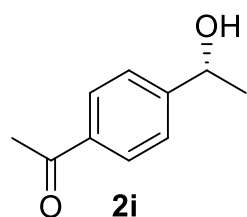
R_f = 0.32 (cyclohexane/EtOAc 4/1); $^1\text{H NMR}$ (300 MHz, CDCl_3) δ 7.47 (d, J = 8.4 Hz, 2H), 7.24 (d, J = 6.7 Hz, 2H), 4.86 (q, J = 6.4 Hz, 1H), 1.47 (d, J = 6.5 Hz, 3H) ppm,⁷ $e.e.$ = 98%.

(R)-1-(2-bromophenyl)ethan-1-ol



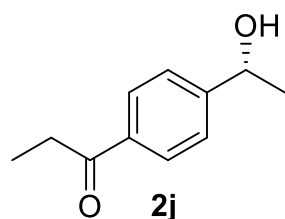
Substrate: 1-bromo-2-ethylbenzene (10 mM, 10 μ M). The obtained crude product was purified via flash column chromatography (cyclohexane/EtOAc 7/1 to 4/1) to give **2h** as a colourless oil (2.1 mg, 10.0 μ mol, 5.0%).

R_f = 0.46 (cyclohexane/EtOAc 4/1); $^1\text{H NMR}$ (300 MHz, CDCl_3) δ 7.60 (dd, J = 7.8, 1.5 Hz, 1H), 7.51 (d, J = 8.0 Hz, 1H), 7.35 (t, J = 7.2 Hz, 1H), 7.13 (td, J = 7.7, 1.6 Hz, 1H), 5.25 (q, J = 6.4 Hz, 1H), 1.49 (d, J = 6.4 Hz, 3H) ppm,⁷ $e.e.$ = 98%.

(R)-1-(4-(1-hydroxyethyl)phenyl)ethan-1-one

Substrate: 1-(4-ethylphenyl)ethan-1-one (10 mM, 10 μ M). The obtained crude product was purified via flash column chromatography (cyclohexane/EtOAc 6/1 to 4/1) to give **2i** as a colourless solid (10.5 mg, 64.0 μ mol, 30.5%).

R_f = 0.13 (cyclohexane/EtOAc 4/1); $^1\text{H NMR}$ (300 MHz, CDCl_3) δ 7.93 (d, J = 8.2 Hz, 2H), 7.46 (d, J = 8.3 Hz, 2H), 4.96 (q, J = 6.5 Hz, 1H), 2.59 (s, 3H), 1.50 (d, J = 6.5 Hz, 3H) ppm,⁸ **optical rotation:** $[\alpha]_{\text{D}}^{20}$ = +49.7 (CHCl_3 , c = 1.00), lit.: $[\alpha]_{\text{D}}^{20}$ = +41.7 (CHCl_3 , c = 0.69);¹³ $[\alpha]_{\text{D}}^{20}$ = -42.6 (CHCl_3 , c = 1.00, *S*-enantiomer);¹⁴ *e.e.* = 99%.

(R)-1-(4-(1-hydroxyethyl)phenyl)propan-1-one

Substrate: 1-(4-ethylphenyl)propan-1-one (10 mM, 10 μ M). The obtained crude product was purified via flash column chromatography (cyclohexane/EtOAc 6/1 to 3/1) to give **2j** as a colourless solid (9.80 mg, 54.9 μ mol, 26.1%).

R_f = 0.3 (cyclohexane/EtOAc 4/1); $^1\text{H NMR}$ (300 MHz, CDCl_3) δ 7.94 (d, J = 8.3 Hz, 2H), 7.46 (d, J = 8.3 Hz, 2H), 4.96 (q, J = 6.5 Hz, 1H), 2.99 (q, J = 7.2 Hz, 2H), 1.50 (d, J = 6.5 Hz, 3H), 1.22 (t, J = 7.3 Hz, 3H) ppm; **optical rotation:** $[\alpha]_{\text{D}}^{20}$ = +41.9 (CHCl_3 , c = 0.92), *e.e.* = 98%.

General Procedure for Photo-Chemo-Enzymatic Cascade Reactions with CN-OA-m and ADH.

A crimp glass vial (1.5 mL) was charged with CN-OA-m (3.0 mg, 3.0 mg/mL) and five glass beads (1.0 mm, Merck). Then phosphate buffer (990 μ L, 100 mM, pH 7.5) was added and the mixture was sonicated in an ultrasonic bath (5 s) to ensure a fine distribution of the CN-OA-m. Then the substrate (10 mM, 10 μ mol) dissolved in MeOH (1 M stock solution, 10.0 μ L were used) was added, the crimp vial was sealed and the glass vial was irradiated in

the photoreactor (455 nm, 1998 $\mu\text{mol photons m}^{-2} \text{s}^{-1}$) for 24 h at 30 °C and 500 rpm. Afterwards, the reaction was transferred to an Eppendorf tube (1.5 mL). Then isopropanol (15 μL , 194 μmol), NAD^+ (0.25 mg, 0.38 μmol) and ADH A (10 μL , 0.018 μg , stock: 1.75 $\mu\text{g/mL}$, 46 U/mg) were added and the reaction was incubated for 24 h at 30 °C and 600 rpm. Subsequently, the reaction was extracted with EtOAc (1x400 μL and 1x400 μL + 10 mM 1-octanol) and the combined organic phases were dried over Na_2SO_4 . The extracts were analysed by GC.

Photocatalytic Oxidation of Ethylbenzene with CN-OA-m in the Photoreactor for Photo-Chemo-Enzymatic Reactions

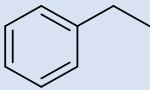
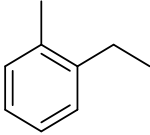
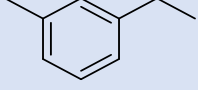
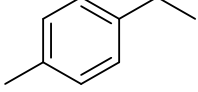
A crimp glass vial (1.5 mL) was charged with CN-OA-m (3.0 mg, 3.0 mg/mL) and five glass beads (1.0 mm, Merck). Then phosphate buffer (990 μL , 100 mM, pH 7.5) was added and the mixture was sonicated in an ultrasonic bath (5 s) to ensure a fine distribution of the CN-OA-m. Then the substrate (10 mM, 10 μmol) dissolved in MeOH (1 M stock solution, 10.0 μL were used) was added, the crimp vial was sealed and the glass vial was irradiated in the photoreactor (455 nm, 1998 $\mu\text{mol photons m}^{-2} \text{s}^{-1}$) for 24 h at 30 °C and 500 rpm. Subsequently, the reaction was extracted with EtOAc (1x400 μL and 1x400 μL + 10 mM 1-octanol) and the combined organic phases were dried over Na_2SO_4 . The extracts were analysed by GC.

ADH-A Catalysed Reduction of Acetophenone in the Presence of Hydrogen Peroxide

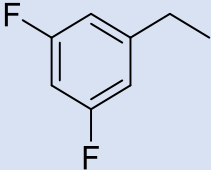
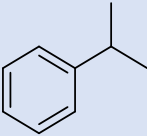
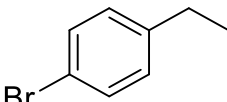
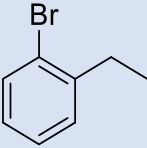
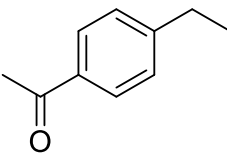
ADH-A (15 μL , 17.5 $\mu\text{g/mL}$) was added to phosphate buffer (100 mM, pH 7.5) containing hydrogen peroxide (0, 2 or 10 mM). The solution was incubated in a thermo shaker (30 min, 30 °C, 600 rpm). Afterwards, isopropanol (15 μL , 194 μmol), NAD^+ (0.25 mg, 0.38 μmol) and acetophenone (1.17 μL , 10 mM) were added and the reaction was incubated for 16 h at 30 °C and 600 rpm. Subsequently, the reaction was extracted with EtOAc (1x400 μL and 1x400 μL + 10 mM 1-octanol) and the combined organic phases were dried over Na_2SO_4 . The extracts were analysed by GC.

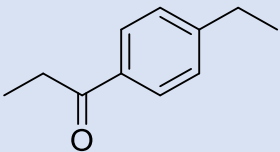
4.5.7 GC Analytics

Table S4.5. Information about the GC measurements.

Substrate	Column ^[a]	Retention time T_R /[min]	Temperature program
 ethylbenzene	Quantification: Column A Enantiomeric excess: Column B	Quantification: ethylbenzene 1.79 acetophenone 5.95 1-phenylethanol 6.72 Enantiomeric excess: (<i>R</i>)-1-phenylethanol 8.96 (<i>S</i>)-1-phenylethanol 9.40	Quantification: 70 °C hold 2 min, 20 °C/min to 140 °C hold 1 min, 20 °C/min to 250 °C hold 2.5 min. Enantiomeric excess: 70 °C hold 0.5 min, 20 °C/min to 120 °C hold 8 min, 20 °C/min to 180 °C hold 1 min.
 1-ethyl-2-methylbenzene	Quantification: Column A Enantiomeric excess: Column B	Quantification: 1-ethyl-2-methylbenzene 2.66 1-(<i>o</i> -tolyl)ethan-1-one 6.13 1-(<i>o</i> -tolyl)ethan-1-ol 7.72 (2-ethylphenyl)methanol 8.58 Enantiomeric excess: (<i>R</i>)-1-(<i>o</i> -tolyl)ethan-1-ol 13.01 (<i>S</i>)-1-(<i>o</i> -tolyl)ethan-1-ol 13.92	Quantification: 70 °C hold 2 min, 20 °C/min to 140 °C hold 1 min, 20 °C/min to 200 °C hold 4 min, 10 °C/min to 210 °C hold 4 min, 20 °C/min to 250 °C hold 2 min. Enantiomeric excess: 70 °C hold 0.5 min, 20 °C/min to 120 °C hold 8 min, 20 °C/min to 140 °C hold 3 min, 20 °C/min to 160 °C hold 3 min, 20 °C/min to 180 °C hold 3 min.
 1-ethyl-3-methylbenzene	Quantification: Column A Enantiomeric excess: Column B	Quantification: 1-ethyl-2-methylbenzene 2.37 1-(<i>m</i> -tolyl)ethan-1-one 6.74 1-(<i>m</i> -tolyl)ethan-1-ol 7.45 (3-ethylphenyl)methanol 8.54 Enantiomeric excess: (<i>R</i>)-1-(<i>m</i> -tolyl)ethan-1-ol 12.00 (<i>S</i>)-1-(<i>m</i> -tolyl)ethan-1-ol 12.28	Quantification: 70 °C hold 0.5 min, 20 °C/min to 120 °C hold 1 min, 20 °C/min to 200 °C hold 4 min, 10 °C/min to 210 °C hold 4 min, 20 °C/min to 250 °C hold 2 min. Enantiomeric excess: 70 °C hold 0.5 min, 20 °C/min to 120 °C hold 8 min, 20 °C/min to 140 °C hold 3 min, 20 °C/min to 160 °C hold 3 min, 20 °C/min to 180 °C hold 3 min.
 1-ethyl-4-methylbenzene	Quantification: Column A Enantiomeric excess: Column B	Quantification: 1-ethyl-2-methylbenzene 2.36 1-(<i>p</i> -tolyl)ethan-1-one 6.70 1-(<i>p</i> -tolyl)ethan-1-ol 7.46 (4-ethylphenyl)methanol 8.56 Enantiomeric excess: (<i>R</i>)-1-(<i>p</i> -tolyl)ethan-1-ol 11.46 (<i>S</i>)-1-(<i>p</i> -tolyl)ethan-1-ol 11.99	Quantification: 70 °C hold 2 min, 20 °C/min to 140 °C hold 1 min, 20 °C/min to 200 °C hold 4 min, 10 °C/min to 210 °C hold 4 min, 20 °C/min to 250 °C hold 2 min. Enantiomeric excess: 70 °C hold 0.5 min, 20 °C/min to 120 °C hold 8 min, 20 °C/min to 140 °C hold 3 min, 20 °C/min to 160 °C hold 3 min, 20 °C/min to 180 °C hold 3 min.
	Quantification: Column A	Quantification: 1-ethyl-3,5-difluorobenzene 1.85	Quantification:

Supporting Information - Chapter 4

 1-ethyl-3,5-difluorobenzene	Enantiomeric excess: Column B	1-(3,5-difluorophenyl)ethan-1-one 5.15 1-(3,5-difluorophenyl)ethan-1-ol 7.08 Enantiomeric excess: (R)-1-(3,5-difluorophenyl)ethan-1-ol 13.70 (S)-1-(3,5-difluorophenyl)ethan-1-ol 14.01	70 °C hold 2 min, 20 °C/min to 140 °C hold 1 min, 20 °C/min to 200 °C hold 4 min, 10 °C/min to 210 °C hold 4 min, 20 °C/min to 250 °C hold 2 min. Enantiomeric excess: 70 °C hold 0.5 min, 20 °C/min to 110 °C hold 6 min, 10 °C/min to 115 °C hold 4 min, 10 °C/min to 120 °C hold 3 min, 20 °C/min to 180 °C hold 1 min.
Substrate	Column^[a]	Retention time T_R/[min]	Temperature program
 cumene	Quantification: Column A	Quantification: cumene 1.92 2-phenylpropan-2-ol 6.31	Quantification: 70 °C hold 2 min, 20 °C/min to 140 °C hold 1 min, 20 °C/min to 250 °C hold 2.5 min.
 1-bromo-4-ethylbenzen	Quantification: Column A Enantiomeric excess: Column B	Quantification: 1-bromo-4-ethylbenzen 4.88 1-(4-bromophenyl)ethan-1-one 8.94 1-(4-bromophenyl)ethan-1-ol 9.95 Enantiomeric excess: (R)-1-(4-bromophenyl)ethan-1-ol 13.03 (S)-1-(4-bromophenyl)ethan-1-ol 13.41	Quantification: 70 °C hold 2 min, 20 °C/min to 140 °C hold 1 min, 20 °C/min to 200 °C hold 4 min, 10 °C/min to 210 °C hold 4 min, 20 °C/min to 250 °C hold 2 min. Enantiomeric excess: 70 °C hold 0.5 min, 20 °C/min to 140 °C hold 6 min, 20 °C/min to 160 °C hold 6 min, 20 °C/min to 180 °C hold 1 min.
 1-bromo-2-ethylbenzen	Quantification: Column A Enantiomeric excess: Column B	Quantification: 1-bromo-2-ethylbenzen 4.62 1-(2-bromophenyl)ethan-1-one 8.46 1-(2-bromophenyl)ethan-1-ol 9.44 Enantiomeric excess: (R)-1-(2-bromophenyl)ethan-1-ol 12.45 (S)-1-(2-bromophenyl)ethan-1-ol 13.46	Quantification: 70 °C hold 2 min, 20 °C/min to 140 °C hold 1 min, 20 °C/min to 200 °C hold 4 min, 10 °C/min to 210 °C hold 4 min, 20 °C/min to 250 °C hold 2 min. Enantiomeric excess: 70 °C hold 0.5 min, 20 °C/min to 140 °C hold 6 min, 20 °C/min to 160 °C hold 6 min, 20 °C/min to 180 °C hold 1 min.
 1-(4-ethylphenyl)ethan-1-one	Quantification: Column A Enantiomeric excess: Column B	Quantification: 1-(4-ethylphenyl)ethan-1-one 7.63 1,1'-(1,4-phenylene)bis(ethan-1-one) 11.14 1-(4-(1-hydroxyethyl)phenyl)ethan-1- one 12.84 Enantiomeric excess:	Quantification: 70 °C hold 2 min, 20 °C/min to 140 °C hold 1 min, 20 °C/min to 200 °C hold 4 min, 10 °C/min to 210 °C hold 4 min, 20 °C/min to 250 °C hold 2 min. Enantiomeric excess: 70 °C hold 0.5 min, 20 °C/min to 120 °C hold 8 min, 20 °C/min to 140 °C hold 3 min, 20 °C/min to 160 °C hold 3 min, 20 °C/min to 180 °C hold 3 min.

		<p>(<i>R</i>)-1-(4-(1-hydroxyethyl)phenyl)ethan-1-one 21.34</p> <p>(<i>S</i>)-1-(4-(1-hydroxyethyl)phenyl)ethan-1-one 21.55</p>	
 <p>1-(4-ethylphenyl)propan-1-one</p>	<p>Quantification: Column A</p> <p>Enantiomeric excess: Column B</p>	<p>Quantification:</p> <p>1-(4-ethylphenyl)propan-1-one 8.07 1-(4-acetylphenyl)propan-1-one 11.67 1-(4-(1-hydroxyethyl)phenyl)propan-1-one 13.55</p> <p>Enantiomeric excess:</p> <p>(<i>R</i>)-1-(4-(1-hydroxyethyl)phenyl)propan-1-one 22.98 (<i>S</i>)-1-(4-(1-hydroxyethyl)phenyl)propan-1-one 23.21*</p>	<p>Quantification:</p> <p>70 °C hold 2 min, 20 °C/min to 140 °C hold 1 min, 20 °C/min to 200 °C hold 4 min, 10 °C/min to 210 °C hold 4 min, 20 °C/min to 250 °C hold 2 min.</p> <p>Enantiomeric excess:</p> <p>70 °C hold 0.5 min, 20 °C/min to 120 °C hold 8 min, 20 °C/min to 140 °C hold 3 min, 20 °C/min to 160 °C hold 3 min, 20 °C/min to 180 °C hold 6 min, 20 °C/min to 200 °C hold 3 min.</p>

[a] Column A CP WAX 52CB; column B CP-ChiraSil-DEX CB; *no reference material for the (*S*)-enantiomer; 5 mM 1-octanol were used as internal standard.

4.5.8 Additional Experiments

Influence of the MeOH Concentration

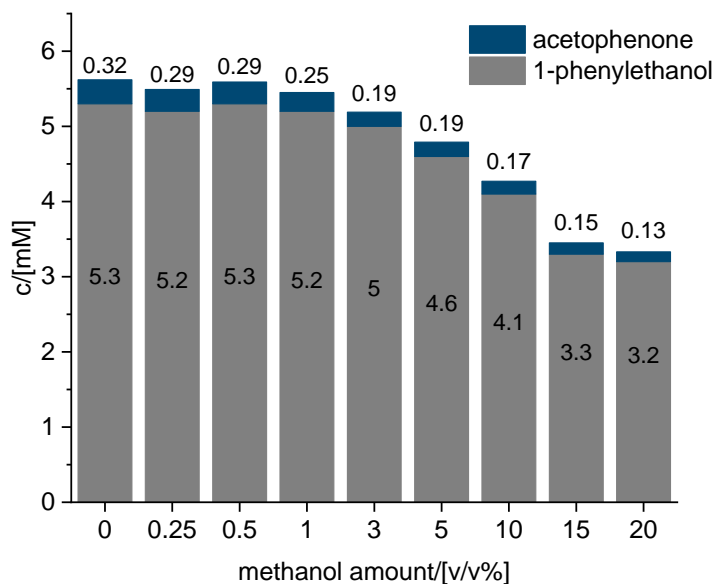


Figure S4.6. Influence of the MeOH concentration on the photoenzymatic hydroxylation of ethylbenzene; reaction conditions: *Aae*UPO (25 nm), ethylbenzene (10 mM), CN-OA-m (2.0 mg/mL), MeOH (0-20% v/v), tricine buffer (100 mM, pH 7.5), 528 nm ($1330 \mu\text{mol photons m}^{-2} \text{s}^{-1}$), 30 °C, 24 h.

Influence of the Enzyme Concentration

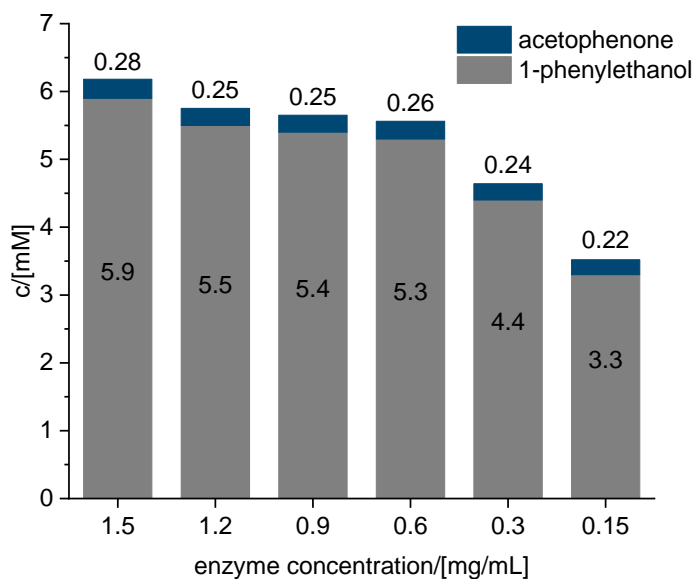


Figure S4.7. Influence of the enzyme concentration on the photoenzymatic hydroxylation of ethylbenzene; reaction conditions: *Aae*UPO (1.5-0.15 mg/mL), ethylbenzene (10 mM), CN-OA-m (2.0 mg/mL), MeOH (250 mM), tricine buffer (100 mM, pH 7.5), 528 nm ($1330 \mu\text{mol photons m}^{-2} \text{s}^{-1}$), 30 °C, 24 h.

Influence of the Amount of CN-OA-m

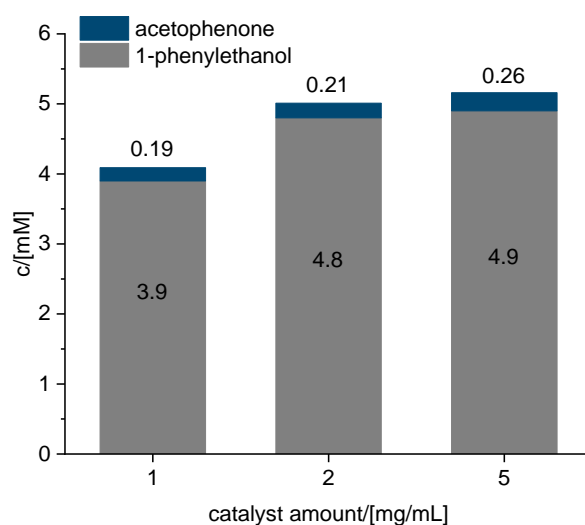


Figure S4.8. Influence of the CN-OA-m concentration on the photoenzymatic hydroxylation of ethylbenzene; reaction conditions: *Aae*UPO (25 nM), ethylbenzene (10 mM), CN-OA-m (1.0-5.0 g/mL), MeOH (250 mM), tricine buffer (100 mM, pH 7.5), 528 nm (1330 $\mu\text{mol photons m}^{-2} \text{s}^{-1}$), 30 °C, 24 h.

Influence of the Light Intensity

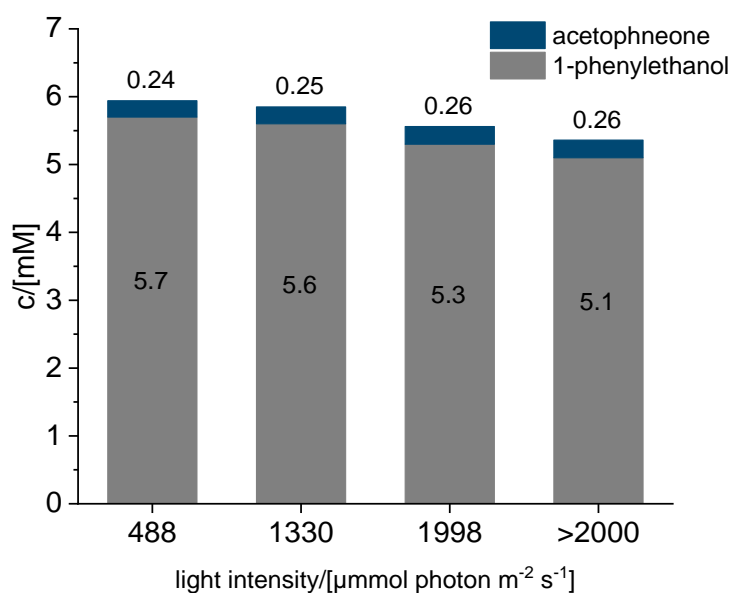


Figure S4.9. Influence of the light intensity on the photoenzymatic hydroxylation of ethylbenzene; reaction conditions: *Aae*UPO (25 nM), ethylbenzene (10 mM), CN-OA-m (2.0 mg/mL), MeOH (250 mM), tricine buffer (100 mM, pH 7.5), 528 nm (488->2000 $\mu\text{mol photons m}^{-2} \text{s}^{-1}$), 30 °C, 24 h.

*Aae*UPO Stability under Different Wavelengths

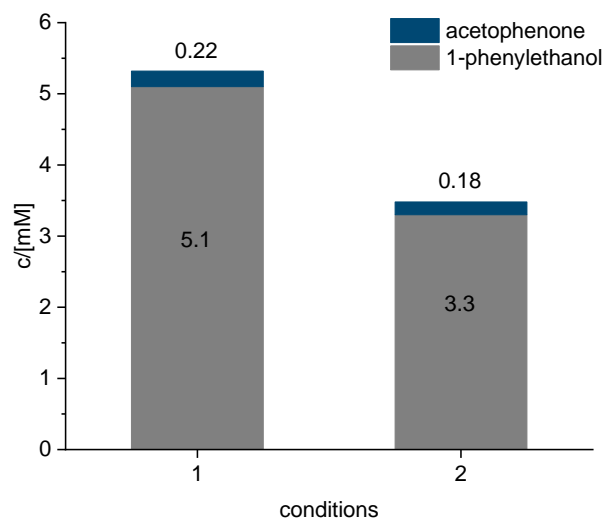


Figure S4.10. Influence of the wavelength on the photoenzymatic hydroxylation of ethylbenzene; 1) Incubation of *Aae*UPO in tricine buffer at 528 nm for 1 h (without substrate); 2) Incubation of *Aae*UPO in tricine buffer at 455 nm for 1 h (without substrate); After pre-incubation, ethylbenzene (10 mM) was added and the reactions were incubated at 528 nm for further 24 h; reaction conditions: *Aae*UPO (25 nM), ethylbenzene (10 mM), CN-OA-m (2.0 mg/mL), MeOH (250 mM), tricine buffer (100 mM, pH 7.5), 528 nm ($1330 \mu\text{mol photons m}^{-2} \text{s}^{-1}$), 30 °C, 24 h.

Reuse of CN-OA-m

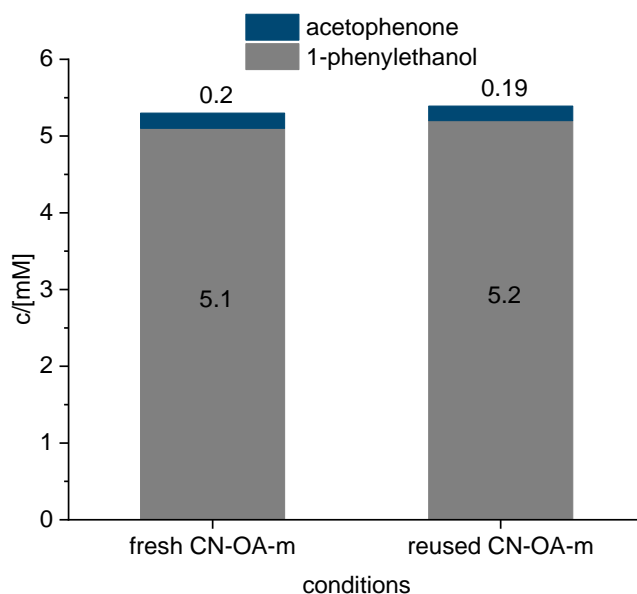


Figure S4.11. Influence of reused CN-OA-m on the photoenzymatic hydroxylation of ethylbenzene; reaction conditions: *Aae*UPO (25 nM), ethylbenzene (10 mM), CN-OA-m (2.0 mg/mL), MeOH (250 mM), tricine buffer (100 mM, pH 7.5), 528 nm ($1330 \mu\text{mol photons m}^{-2} \text{s}^{-1}$), 30 °C, 24 h.

4.5.9 Comparison of CN-OA-m before and after the Photo-Chemo-Enzymatic Reaction with AaeUPO

Table S4.6. EDX elemental composition acquired from new and recovered CN-OA-m.

Sample	% w/w N	% w/w C	% w/w O	% w/w K	% w/w Fe
CN-OA-m	45.91	38.47	5.64	9.51	0.01
CN-OA-m recovered	57.34	30.97	7.94	1.91	0.03

The SEM, as well as the TEM images, show the same morphology and no altering during the catalytic transformation

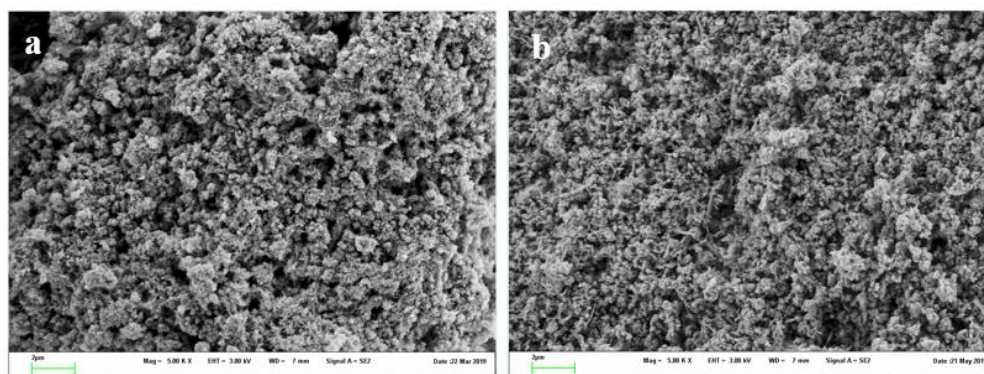


Figure S4.12. a) SEM images of CN-OA-m new; b) recovered CN-OA-m.

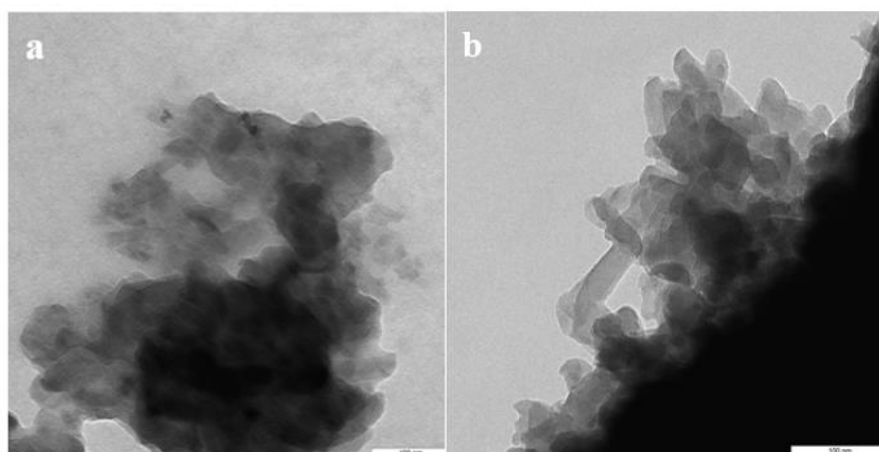


Figure S4.13. a) TEM images of CN-OA-m new; b) recovered CN-OA-m.

DNA and Protein Sequences

5`-

catatgGCCAGCTGGAGTCATCCGCAGTTTGAAAAAGGCGCCGAGTTTATGAAAGCAGTGCAGTAT
ACCGAAATTGGCAGTGAACCGGTTGTTGTTGATATTCCGACCCCGACCCCGGGCCCGGGTAAAA
TTCTGCTGAAAGTGACCGCAGCAGGCCTGTGCCATAGTGATATTTTTGTGATGGATATGCCGGC
AGCACAGTATGCATACGGTCTGCCGCTGACCCTGGGTCATGAAGGTGTGGGTACCGTTGCCGAA
CTGGGCGAAGGTGTGACCGGTTTTGGTGTGGGTGACGCCGTTGCAGTTTATGGCCCGTGGGGCT
GCGGTGCATGTCATGCATGCGCACGCGGCCGCGAAAATTATTGTACCCGTGCAGCAGATCTGGG
TATTACCCCGCCGGGCCTGGGCAGCCCTGGTAGCATGGCTGAATATATGATTGTTGATAGCGCC
CGTCATCTGGTTCCGATTGGCGATCTGGATCCGGTGGCCGCCGCCCTCTGACAGATGCTGGTCT
GACCCCGTATCATGCAATTAGCCGTGTTCTGCCGCTGCTGGGTCCGGGTAGCACCCGCAGTGGTT
ATTGGTGTGGTGGCCTGGGTCATGTTGGTATTCAGATTCTGCGTGCCGTGAGTGCCGCACGCGT
GATTGCCGTGGATCTGGATGATGATCGTCTGGCCCTGGCCCGTGAAGTTGGTGCCGATGCAGCC
GTTAAAAGTGGTGCAGGCGCCCGCATGCAATTCGTGAACTGACCGGTGGTCAGGGCGCAACC
GCCGTTTTTGATTTTGTGGCGCACAGAGCACCATTGATACCGCACAGCAGGTTGTTGCCGTGG
ATGGTCATATTAGCGTGGTTGGCATTTCATGCAGGCGCCCATGCCAAAGTTGGTTTCTTTATGATT
CCGTTTGGTGCAAGCGTTGTGACCCCGTATTGGGGTACCCGTAGCGAACTGATGGAAGTTGTGG
CACTGGCACGTGCCGGTTCGTCTGGATATTCATACCGAAACCTTTACCCTGGATGAAGGCCCGGC
CGCATATCGCCGCTGCGTGAAGGTAGTATTCGCGGTCGTGGCGTGGTTGTTCCGTAActcgag-3`

DNA sequence of ADH-A with strep-tag sequence and restriction sites (*Nde*I and *Xho*I).

HMASWSHPQFEKGAEFMKAVQYTEIGSEPVVVDIPTPTPGPGEILLKVTAAGLCHSDIFVMDMPAA
QYAYGLPLTLGHEGVGTVAELGEGVTGFGVGDAAVYGPWGCACHACARGRENYCTRAADLGI
TPPGLGSPGSMAEYMIVDSARHLVPIGDLDPVAAAPLTDAGLTPYHAISRVLPLLGPGSTAVVIGVG
GLGHVGIQILRAVSAARVIAVDLDDRLALAREVGADAAVKSGAGAADAIRELTGGQGATAVFDF
VGAQSTIDTAQQVVAVDGHISVVGIIHAGAHAKVGGFMIPFGASVVTPYWGTRSELMEVVALARAG
RLDIHTETFTLDEGPAA YRRLREGSIRGRGVVVP-

Protein sequence of ADH-A and fused strep-tag (yellow).

Copies of GC chromatogram of the isolated and purified compounds

Copies of GC chromatogram of the isolated and purified compounds are available in the Supporting Information through the website of the Publisher. DOI: [10.1002/anie.202100164](https://doi.org/10.1002/anie.202100164)

4.5.10 References

1. Pieber, B.; Malik, J. A.; Cavedon, C.; Gisbertz, S.; Savateev, A.; Cruz, D.; Heil, T.; Zhang, G.; Seeberger, P. H., Semi-heterogeneous Dual Nickel/Photocatalysis using Carbon Nitrides: Esterification of Carboxylic Acids with Aryl Halides. *Angew. Chem. Int. Ed.* **2019**, *58*, 9575-9580.
2. Zhang, G.; Li, G.; Lan, Z.-A.; Lin, L.; Savateev, A.; Heil, T.; Zafeiratos, S.; Wang, X.; Antonietti, M., Optimizing Optical Absorption, Exciton Dissociation, and Charge Transfer of a Polymeric Carbon Nitride with Ultrahigh Solar Hydrogen Production Activity. *Angew. Chem. Int. Ed.* **2017**, *56* (43), 13445-13449.
3. Fulmer, G. R.; Miller, A. J. M.; Sherden, N. H.; Gottlieb, H. E.; Nudelman, A.; Stoltz, B. M.; Bercaw, J. E.; Goldberg, K. I., NMR Chemical Shifts of Trace Impurities: Common Laboratory Solvents, Organics, and Gases in Deuterated Solvents Relevant to the Organometallic Chemist. *Organometallics* **2010**, *29* (9), 2176-2179.
4. Bonfield, H. E.; Williams, J. D.; Ooi, W. X.; Leach, S. G.; Kerr, W. J.; Edwards, L. J., A Detailed Study of Irradiation Requirements Towards an Efficient Photochemical Wohl-Ziegler Procedure in Flow. *ChemPhotoChem* **2018**, *2*, 938-944.
5. Bonfield, H. E.; Mercer, K.; Diaz-Rodriguez, A.; Cook, G. C.; McKay, B. S. J.; Slade, P.; Taylor, G. M.; Ooi, W. X.; Williams, J. D.; Roberts, J. P. M.; Murphy, J. A.; Schmermund, L.; Kroutil, W.; Mielke, T.; Cartwright, J.; Grogan, G.; Edwards, L. J., The Right Light: De Novo Design of a Robust Modular Photochemical Reactor for Optimum Batch and Flow Chemistry. *ChemPhotoChem* **2020**, *4* (1), 45-51.
6. Xiao, J.; Wong, Z. Z.; Lu, Y. P.; Loh, T. P., Hexahydropyrrolo[2,3-b]indoles: A New Class of Structurally Rigid Tricyclic Skeleton for Oxazaborolidine-Catalyzed Asymmetric Borane Reduction. *Adv. Synth. Catal.* **2010**, *352*, 1107-1112.
7. Du, D.-M.; Fang, T.; Xu, J.; Zhang, S.-W., Structurally Well-Defined, Recoverable C3-Symmetric Tris(β -hydroxy phosphoramidate)-Catalyzed Enantioselective Borane Reduction of Ketones. *Org. Lett.* **2006**, *8*, 1327-1330.
8. Holland, H. L.; Bergen, E. J.; Chenchiah, P. C.; Khan, S. H.; Munoz, B.; Ninniss, R. W.; Richards, D., Side chain hydroxylation of aromatic compounds by fungi.: 1. Products and stereochemistry. *Can. J. Chem.* **1987**, *65*, 502-507.

9. Hatano, M.; Miyamoto, T.; Ishihara, K., 3,3'-Diphosphoryl-1,1'-bi-2-naphthol-Zn(II) Complexes as Conjugate Acid-Base Catalysts for Enantioselective Dialkylzinc Addition to Aldehydes. *J. Org. Chem.* **2006**, *71*, 6474-6484.
10. Zhang, B.; Wang, H.; Lin, G.-Q.; Xu, M.-H., Ruthenium(II)-Catalyzed Asymmetric Transfer Hydrogenation Using Unsymmetrical Vicinal Diamine-Based Ligands: Dramatic Substituent Effect on Catalyst Efficiency. *Eur. J. Org. Chem.* **2011**, *2011*, 4205-4211.
11. Moteki, S. A.; Takacs, J. M., Exploiting Self-Assembly for Ligand-Scaffold Optimization: Substrate-Tailored Ligands for Efficient Catalytic Asymmetric Hydroboration. *Angew. Chem. Int. Ed.* **2008**, *47*, 894-897.
12. Hatano, M.; Ito, O.; Suzuki, S.; Ishihara, K., Zinc(II)-Catalyzed Addition of Grignard Reagents to Ketones. *J. Org. Chem.* **2010**, *75*, 5008-5016.
13. Yamada, S.; Misono, T.; Iwai, Y.; Masumizu, A.; Akiyama, Y., New Class of Pyridine Catalyst Having a Conformation Switch System: Asymmetric Acylation of Various sec-Alcohols. *J. Org. Chem.* **2006**, *71*, 6872-6880.
14. Fernández-Mateos, E.; Maciá, B.; Yus, M., Catalytic enantioselective addition of organoaluminum reagents to aldehydes. *Tetrahedron: Asymmetry* **2012**, *23*, 789-794.

Supporting Information - Chapter 5

Modular, self-assembling metallaphotocatalyst for cross couplings using the full visible-light spectrum

Reischauer, S.; Strauss, V.; Pieber, B.;

ACS Catal., **2020**, *10*, 13269-13274.

<https://doi.org/10.1021/acscatal.0c03950>

5.5 Supporting information

5.5.1 General remarks

Substrates, reagents, and solvents were purchased from commercial suppliers and used without further purification. Titanium dioxide Aeroxide P25 (Acros), silicon dioxide (10-20 nm particle size; Aldrich), and aluminum oxide, basic (50-200 μm , 60 \AA ; Acros) were used. 2,2'-Bipyridine-4,4'-diphosphonic acid,¹ 4,4'-di(p-carboxyphenyl)-2,2'-bipyridine,² *N*-tert-butylisopropylamine (BIPA),³ and 1-((trimethylsilyl)methyl)piperidine⁴ were prepared according to literature procedures. LED lamps for photocatalytic experiments were purchased from Kessil Lightning⁵. ¹H-, ¹³C-, and ¹⁹F spectra were recorded on a Varian 400 spectrometer (400 MHz, Agilent), a AscendTM 400 spectrometer (400 MHz, cryoprobe, Bruker) and a Varian 600 spectrometer (600 MHz, Agilent) at 298 K, and are reported in ppm relative to the residual solvent peaks. Peaks are reported as: s = singlet, d = doublet, t = triplet, q = quartet, m = multiplet or unresolved, with coupling constants in Hz. Analytical thin layer chromatography (TLC) was performed on pre-coated TLC-sheets, ALUGRAM Xtra SIL G/UV₂₅₄ sheets (Macherey-Nagel) and visualized with 254 nm light or staining solutions followed by heating. Purification of final compounds was carried out by flash chromatography on the Reveleris X2 Flash Chromatography System from GRACE using prepacked columns with 40 μm silica gel. Silica 60 M (0.04-0.063 mm) silica gel (Sigma Aldrich) was used for dry loading of the crude compounds on the flash chromatography system. Centrifugation was carried out using an Eppendorf 5430 centrifuge. UV/Vis spectra of liquid samples were recorded using a UV-1900 spectrometer (Shimadzu). Diffuse reflectance UV/Vis spectra of powders were recorded on a Shimadzu UV-2600 spectrometer equipped with an integrating sphere. Inductively coupled plasma - optical emission spectrometry (ICP-OES) was carried out using a Horiba Ultra 2 instrument equipped with a photomultiplier tube detection system. FTIR spectra were recorded on a Thermo Scientific Nicolet iD5 spectrometer. High-resolution mass spectral data were obtained using a Waters XEVO G2-XS 4K spectrometer with the XEVO G2-XS QTOF capability kit (ESI) and a Micromass GC-TOF micro (Water Inc.) (EI). Spectrophotometric titrations were carried out in 10 mm OS cuvettes. Prior to the measurements, the optical density of the TiO₂ or SiO₂ dispersions were adjusted to ~0.1 at 505 nm for comparability and to reduce the influence of inner filter effects. UV-vis-NIR absorption measurements were performed with a Specord

210 plus from Analytik Jena. Fluorescence measurements were performed with a Fluoromax 4 from Horiba.

5.5.1.1 440 nm setup

Experiments using blue light were carried out using a Kessil PR160-440 LED (Figure S5.1). Two sealed reaction vessels were placed on a stirring plate 4.5 cm away from a single lamp. To avoid heating of the reaction mixture, a fan was used for cooling. All reactions were performed with maximum stirring speed. The LED also emits light below 400 nm, which enabled the excitation of pure titanium dioxide Aeroxide P25 for initial experiments (see Figure S5.1A in the manuscript)

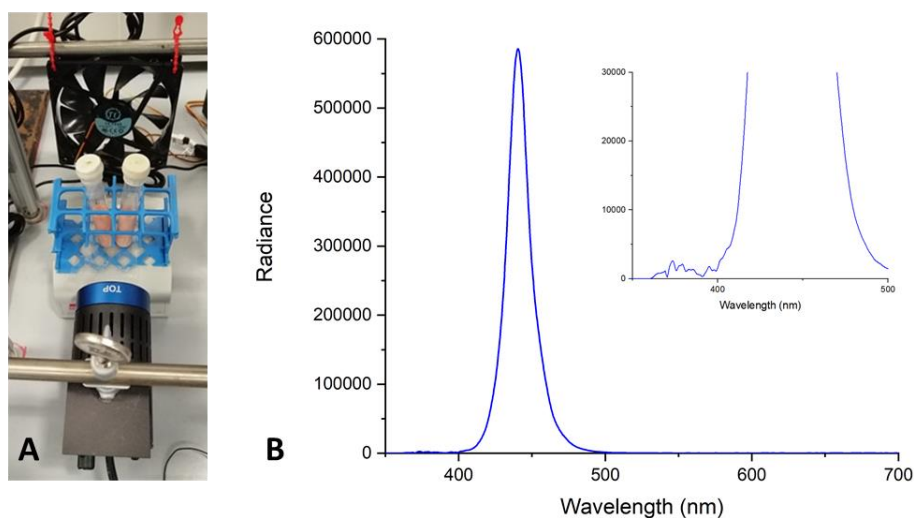


Figure S5.1. Setup for blue light experiments (A). Emission spectra of the Kessil PR160-440 (B)

5.5.1.2 525 nm setup

Experiments using green light were carried out using a Kessil PR160-525 LED (Figure S5.2). Two sealed reaction vessels were placed on a stirring plate 4.5 cm away from a single lamp. To avoid heating of the reaction mixture, a fan was used for cooling. All reactions were performed with maximum stirring speed.

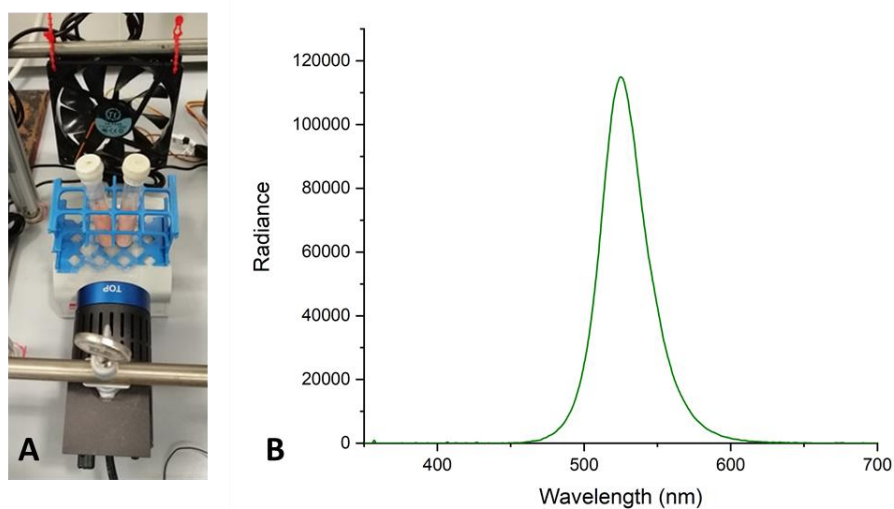


Figure S5.2. Setup for green light experiments (A). Emission spectra of the Kessil PR160-525 (B).

5.5.1.3 666 nm setup

Experiments using red light were carried out using a Kessil H160 Tuna Flora LED in “red” mode (Figure S5.3). Two sealed reaction vessels were placed between two lamps on a stirring plate (4.5 cm distance from each lamp). To avoid heating of the reaction mixture, a fan was used for cooling. All reactions were performed with maximum stirring speed.

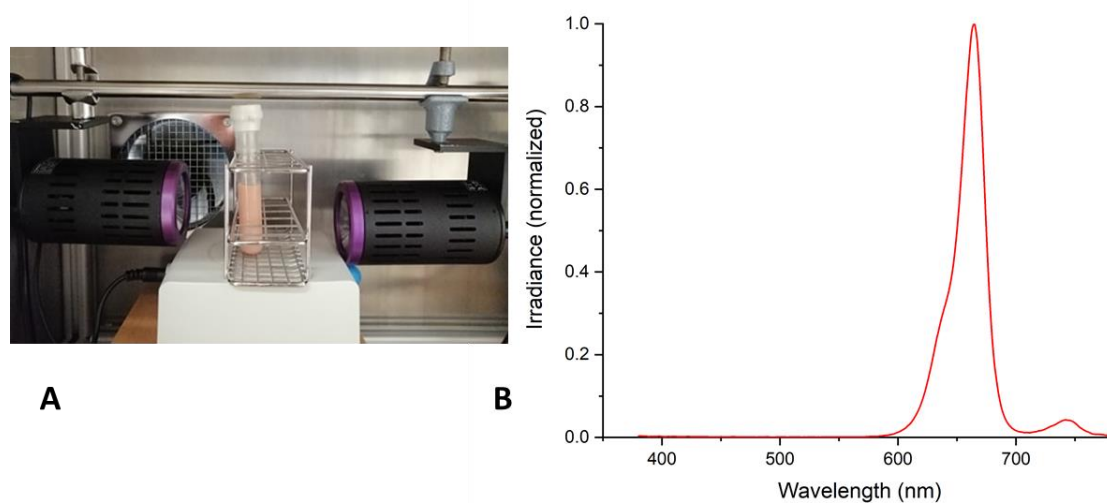


Figure S5.3. A Setup for red light experiments (A). Emission spectra of the Kessil H160 Tuna Flora LED in “red” mode (B).

5.5.2 *Ex situ* preparation and characterization of DSMPs

General experimental procedure for the *ex situ* preparation of DSMPs. TiO₂ Aeroxide P25 (30 mg) was dispersed in 3 mL DMSO and sonicated for 5 min. The respective dye (2.4 μmol), NiCl₂·6H₂O (19.0 μmol) and 2,2'-bipyridine-4,4'-dicarboxylic acid (dcbpy, 19.0 μmol) were added and the mixture was again sonicated for 10 min. The mixture was stirred overnight and the solid material was separated by centrifugation. After washing with DMSO and separation by centrifugation (2x), the DMSP was lyophilized overnight.

The experimental procedure was also modified to immobilize only the dye (dye-TiO₂), or the nickel complex (TiO₂-NiCl₂·dcbpy) on TiO₂ Aeroxide P25.

5.5.2.1 Fluo-TiO₂-NiCl₂·dcbpy

Fluorescein sodium (NaFluo) was used as dye (**Fehler! Verweisquelle konnte nicht gefunden werden.** S5.4). The amount of immobilized fluorescein (Fluo, ~64 μmol g⁻¹) was determined by UV/Vis spectrometry. The solution of the dye in DMSO was measured before and after (supernatant) the immobilization process and the amount of immobilized dye was determined using a calibration curve.

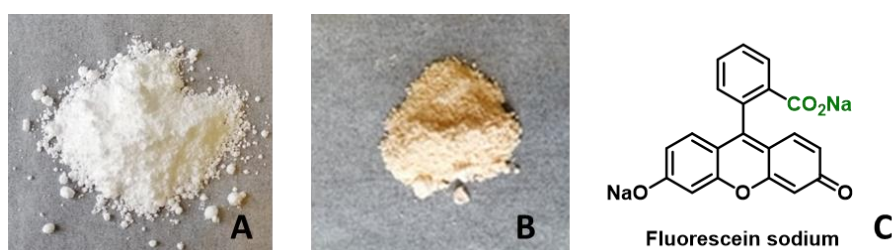
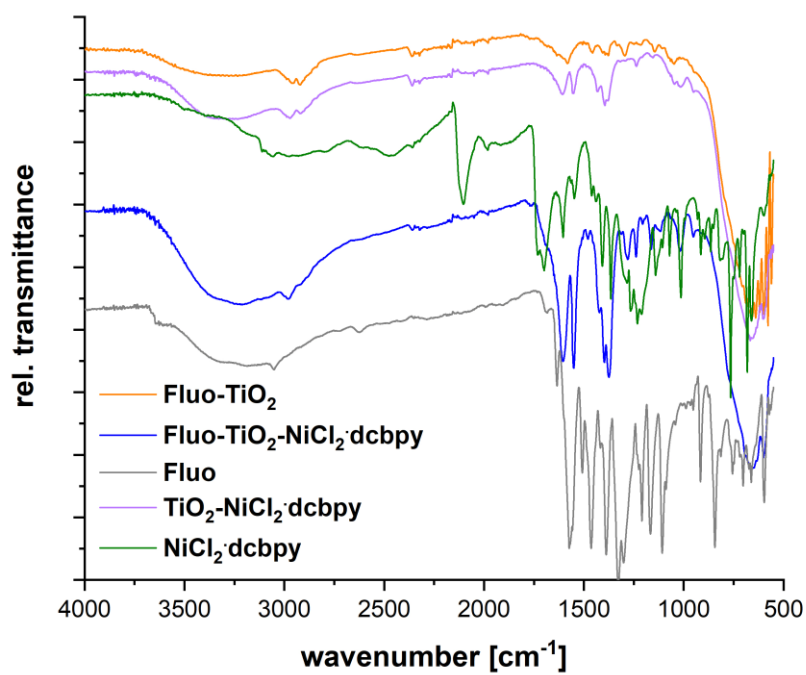


Figure S5.4. Fluo-TiO₂-NiCl₂·dcbpy. Unfunctionalized TiO₂ Aeroxide P25 (A) and Fluo-TiO₂-NiCl₂·dcbpy (B). Structure of fluorescein sodium (C). The functionalities that bind to the surface hydroxyl groups of TiO₂ are marked in green.

Table S5.1. Nickel content of Fluo-TiO₂-NiCl₂·dcbpy and reference samples determined by ICP-OES analysis

Sample	Ni [mg/g catalyst]
Fluo-TiO ₂ -NiCl ₂ ·dcbpy	6.50
TiO ₂	0.02
TiO ₂ -NiCl ₂ ·dcbpy	5.45

**Figure S5.5.** FTIR spectra of Fluo-TiO₂-NiCl₂·dcbpy and reference samples.

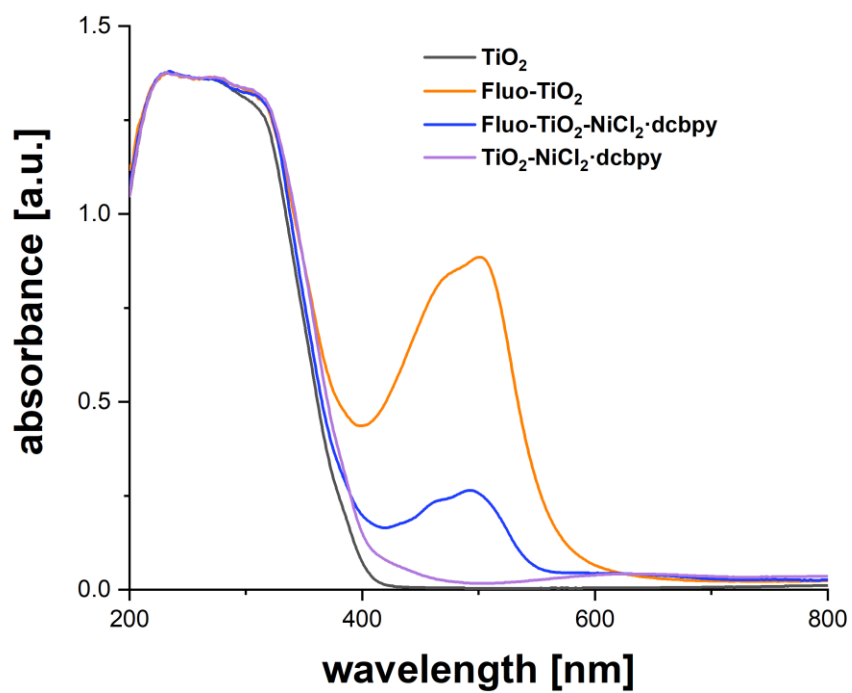


Figure S5.6 Diffuse reflectance UV/Vis spectra of $\text{Fluo-TiO}_2\text{-NiCl}_2\cdot\text{dcbpy}$ and reference samples.

5.5.2.2 N3-TiO₂-NiCl₂·dcbpy

The ruthenium complex N3 was used as dye (Figure S5.17). The amount of immobilized N3 (~66 μmol g⁻¹) was determined by UV/Vis spectrometry. The solution of the dye in DMSO was measured before and after (supernatant) the immobilization process and the amount of immobilized dye was determined using a calibration curve.

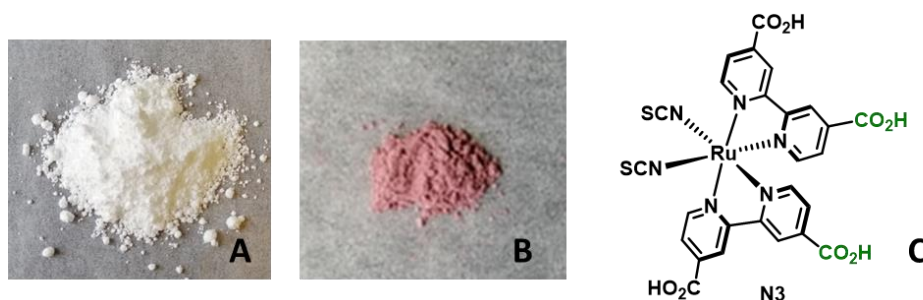


Figure S5.7 N3-TiO₂-NiCl₂·dcbpy. Unfunctionalized TiO₂ Aerioxide P25 (A) and N3-TiO₂-NiCl₂·dcbpy (B). Structure of N3 (C). The functionalities that bind to the surface hydroxyl groups of TiO₂ are marked in green.

Table S5.2. Nickel content of N3-TiO₂-NiCl₂·dcbpy and reference samples determined by ICP-OES analysis

Sample	Ni [mg/g catalyst]
N3-TiO ₂ -NiCl ₂ ·dcbpy	11.3
TiO ₂	0.02
TiO ₂ -NiCl ₂ ·dcbpy	5.45

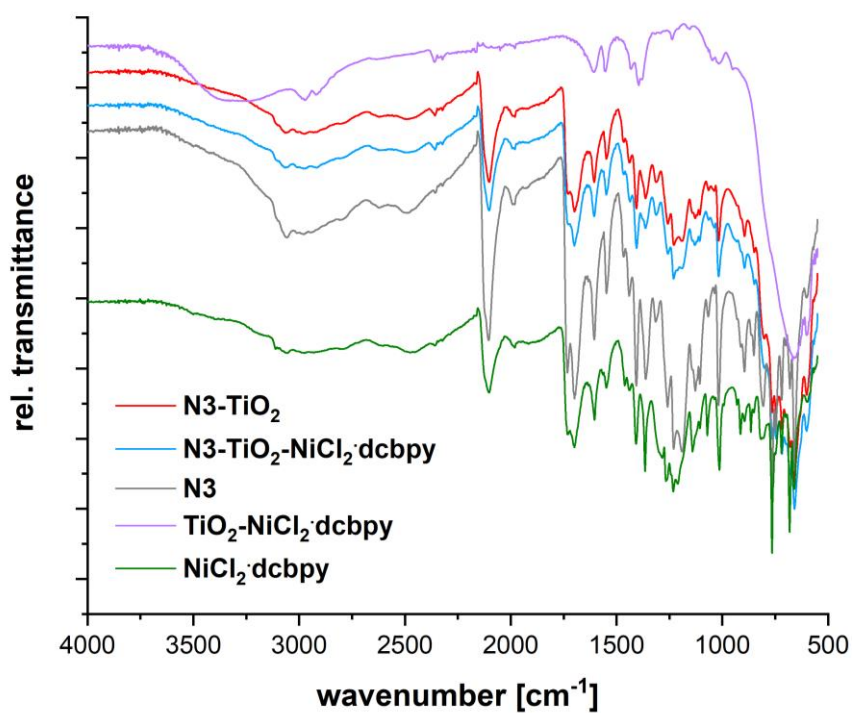


Figure S5.8. FTIR spectra of N3-TiO₂-NiCl₂·dcbpy and reference samples.

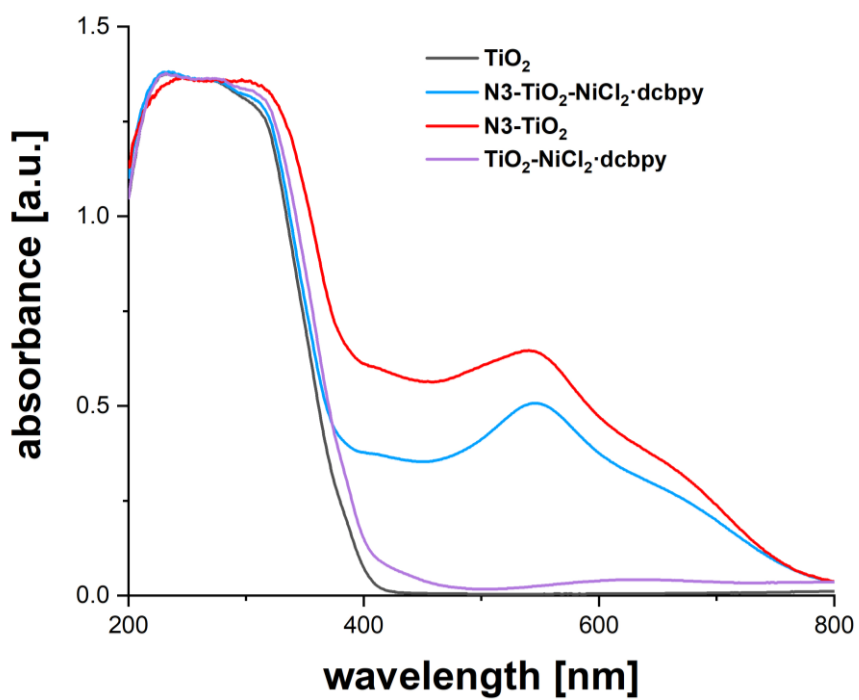


Figure S5.9 Diffuse reflectance UV/Vis spectra of N3-TiO₂-NiCl₂·dcbpy and reference samples.

5.5.3 C-O cross-coupling

5.5.3.1 Optimization studies using *in situ* generated DSMPs.

General experimental procedure for screening experiments *via in situ* DSMP preparation. An oven dried vial (19 x 100 mm) equipped with a stir bar was charged with TiO₂ P25, methyl 4-iodobenzoate, *N*-Boc proline (*N*-(*tert*-Butoxycarbonyl)-L-proline), a dye, a Ni^{II} salt and the ligand. Subsequently, the solvent (anhydrous, 3 mL) and *N*-*tert*-butylisopropylamine were added and the vial was sealed with a septum and Parafilm. The reaction mixture was sonicated for 5-10 min followed by stirring for 5 minutes to obtain a fine dispersion. The mixture was then degassed by bubbling argon for 10 min. The mixture was irradiated with the respective LED lamps with rapid stirring (1400 rpm). After the respective reaction time, one equivalent of 1,3,5-trimethoxybenzene was added. An aliquot of the reaction mixture (~200 μL) was filtered, diluted with DMSO-d₆ and subjected to ¹H-NMR analysis. For a representative NMR spectrum, see Figure S5.10.

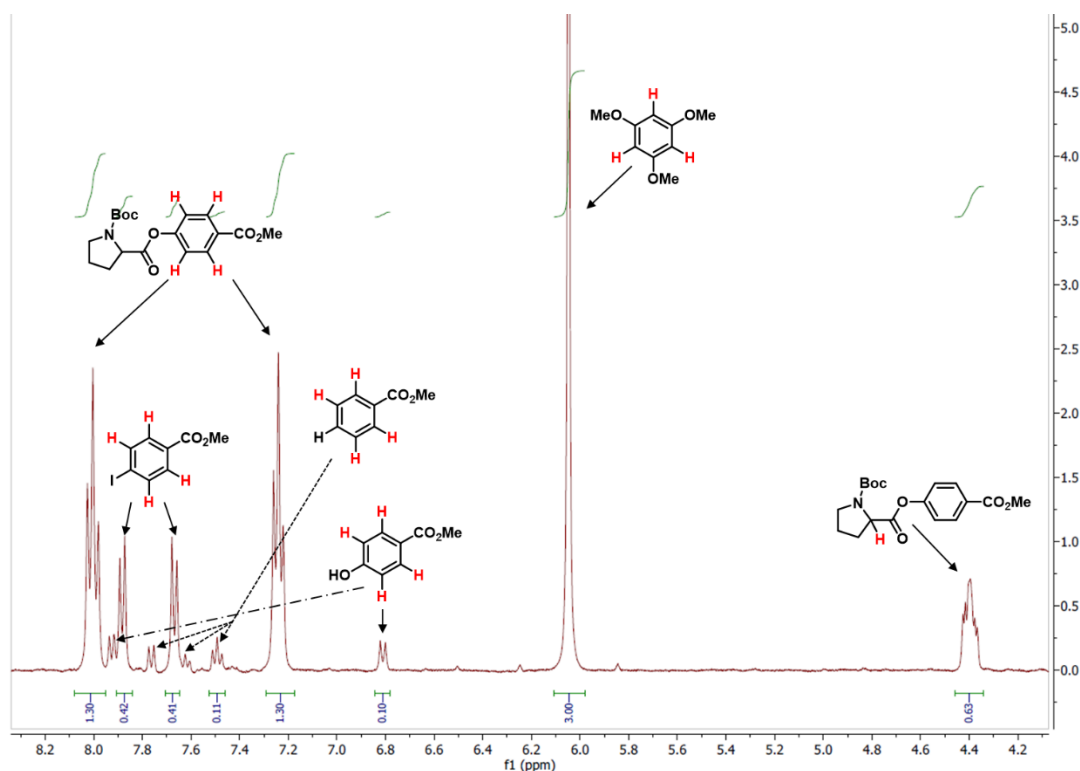
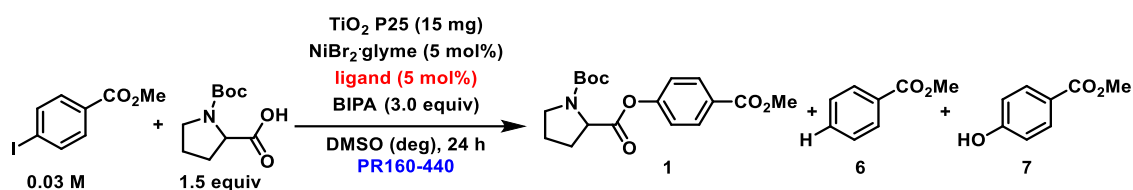
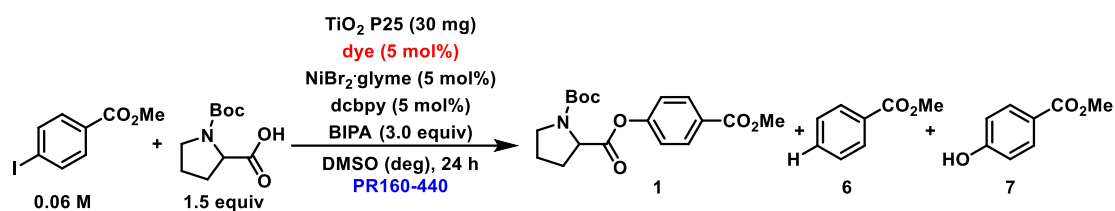


Figure S5.10. Representative ¹H-NMR spectrum of a crude reaction mixture for determining NMR yields in the DSMP catalyzed C-O arylation.

Table S5.3. Ligand screening in absence of a dye using the 440 nm LED setup.^a

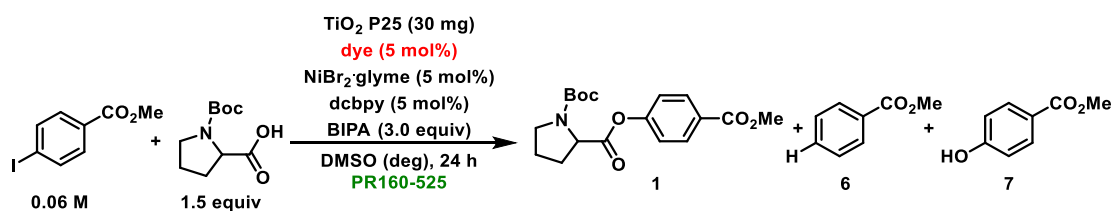
Entry	Ligand	Conversion [%] ^b	1 [%] ^c	6 [%] ^c	7 [%] ^c
1		29	24	n.d.	n.d.
2		17	8	n.d.	n.d.
3		16	12	n.d.	n.d.
4		12	7	n.d.	n.d.
5		10	0	n.d.	n.d.
6		8	0	n.d.	n.d.

^aReaction conditions: methyl 4-iodobenzoate (95.1 μmol), *N*-Boc proline (140.7 μmol), NiBr₂·glyme (4.6 μmol), ligand (4.6 μmol), BIPA (285.4 μmol), TiO₂ (15 mg), DMSO (anhydrous, 3 mL), 440 nm LED (50% power), 24 h. ^bConversion of methyl 4-iodobenzoate determined by ¹H-NMR using 1,3,5-trimethoxybenzene as internal standard. ^cNMR yields determined by ¹H-NMR using 1,3,5-trimethoxybenzene as internal standard. n.d. = not detected. BIPA = *N*-*tert*-butylisopropylamine. glyme = 1,2-dimethoxyethane. deg = degassed

Table S5.4. Dye screening using the 440 nm LED setup.^a

Entry	Dye	Conversion [%] ^b	1 [%] ^c	6 [%] ^c	7 [%] ^c
1	--	37	33	n.d.	traces
2	Fluorescein sodium	76	48	16	traces
3	Rose bengal	42	25	9	traces
4	Brilliant blue R	29	5	18	n.d.
5	Rhodamin B	26	traces	12	n.d.
6	Coumarin 343	15	n.d.	10	n.d.
7	Alizarin red S	9	n.d.	4	n.d.
8	Bromophenol blue	6	n.d.	n.d.	traces
9	Congo red	3	n.d.	n.d.	n.d.
10	Catechol	0	n.d.	n.d.	n.d.
11	Methyl orange	0	n.d.	n.d.	n.d.

^aReaction conditions: methyl 4-iodobenzoate (190.3 μmol), *N*-Boc proline (285.4 μmol), dye (9.5 μmol), NiBr₂·glyme (9.5 μmol), dcbpy (9.5 μmol), BIPA (570.8 μmol), TiO₂ (30 mg), DMSO (anhydrous, 3 mL), 440 nm LED (50% power), 24 h. ^bConversion of methyl 4-iodobenzoate determined by ¹H-NMR using 1,3,5-trimethoxybenzene as internal standard. ^cNMR yields determined by ¹H-NMR using 1,3,5-trimethoxybenzene as internal standard. dcbpy = 2,2'-bipyridine-4,4'-dicarboxylic acid. n.d. = not detected. BIPA = *N*-*tert*-butylisopropylamine. glyme = 1,2-dimethoxyethane. deg = degassed

Table S5.5. Dye screening using the 525 nm LED setup.^a

Entry	Dye	Conversion [%] ^b	1 [%] ^c	6 [%] ^c	7 [%] ^c
1	--	0	n.d.	n.d.	n.d.
2	Fluorescein sodium	47	29	12	1
3	Rhodamin B	23	9	10	n.d.
4	Rose bengal	21	7	10	n.d.
5	Coumarin 343	7	traces	traces	n.d.
6	Congo red	1	n.d.	n.d.	n.d.
7	Methyl orange	0	n.d.	n.d.	n.d.
8	Alizarin red S	0	n.d.	n.d.	n.d.
9	Brilliant blue R	0	n.d.	n.d.	n.d.
10	Catechol	0	n.d.	n.d.	n.d.
11	Bromophenol blue	0	n.d.	n.d.	n.d.

^aReaction conditions: methyl 4-iodobenzoate (190.3 μmol), *N*-Boc proline (285.4 μmol), dye (9.5 μmol), $\text{NiBr}_2 \cdot \text{glyme}$ (9.5 μmol), dcbpy (9.5 μmol), BIPA (570.8 μmol), TiO_2 (30 mg), DMSO (anhydrous, 3 mL), 525 nm LED (50% power), 24 h. ^bConversion of methyl 4-iodobenzoate determined by $^1\text{H-NMR}$ using 1,3,5-trimethoxybenzene as internal standard. ^cNMR yields determined by $^1\text{H-NMR}$ using 1,3,5-trimethoxybenzene as internal standard. dcbpy = 2,2'-bipyridine-4,4'-dicarboxylic acid. n.d. = not detected. BIPA = *N*-tert-butylisopropylamine. glyme = 1,2-dimethoxyethane. deg = degassed

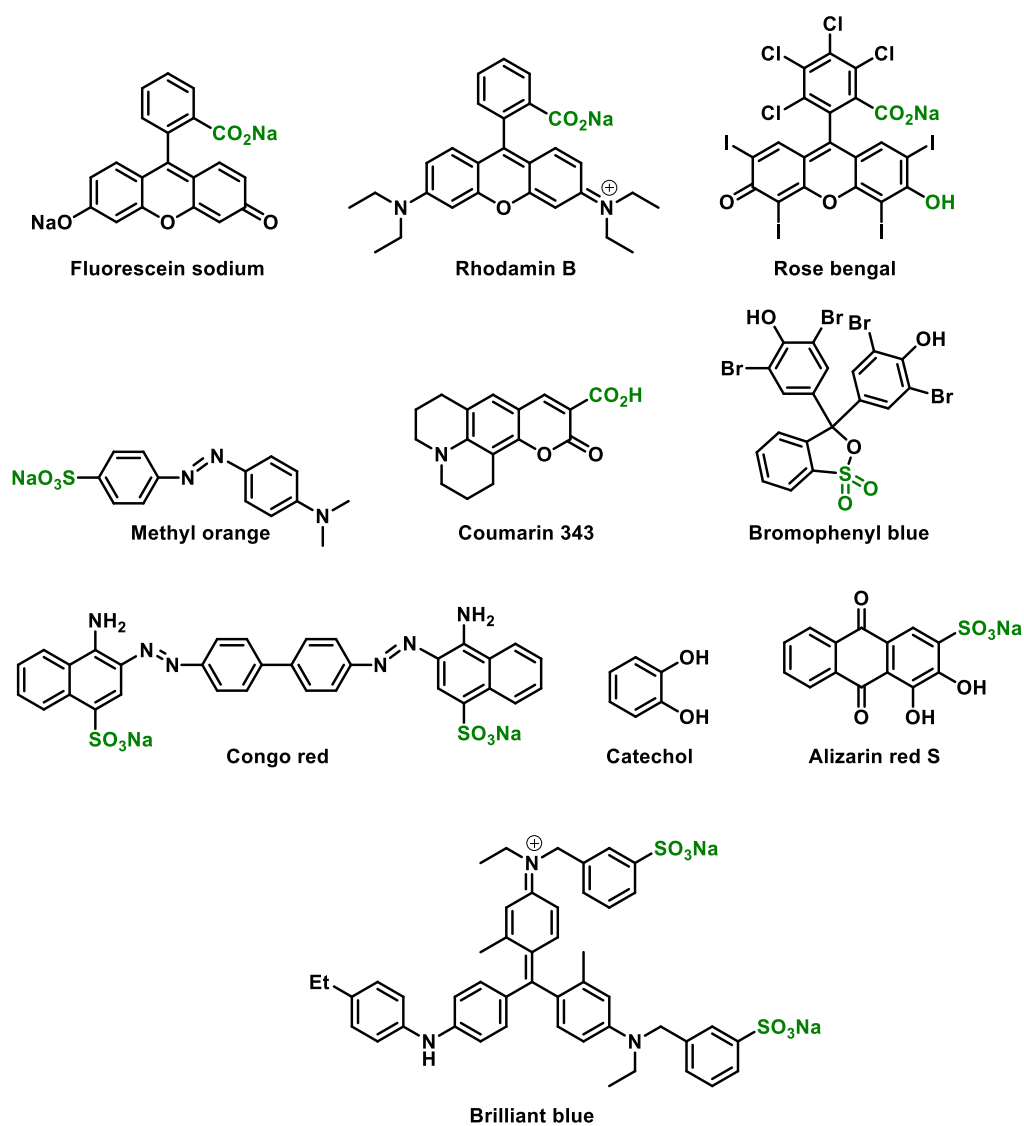
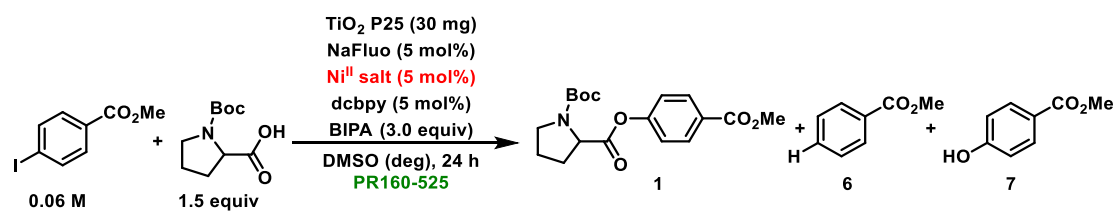


Figure S5.11. Structures of dyes that were tested for experiments using the 440 and 525 nm setup. The functionalities that bind to the surface hydroxyl groups of TiO₂ are marked in green.

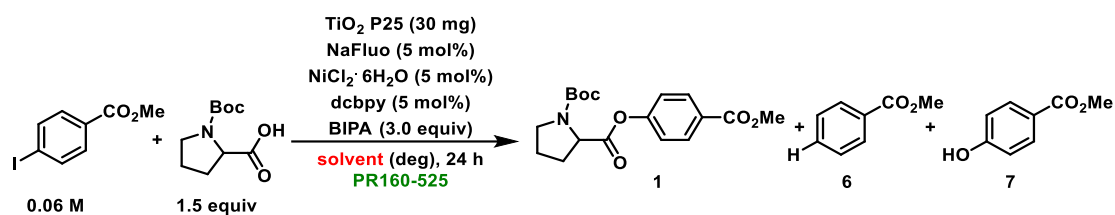
Table S5.6. Screening of Ni^{II} salts using the 525 nm LED setup.^a

Entry	Ni ^{II} source	Conversion [%] ^b	1 [%] ^c	6 [%] ^c	7 [%] ^c
1	NiBr ₂ ·glyme	40	20	11	traces
2	NiCl ₂ ·glyme	38	19	12	traces
3	Ni(OAc) ₂ ·4H ₂ O	38	14	10	traces
4	NiCl ₂ ·6H ₂ O	32	15	10	traces
5	NiBr ₂ ·3H ₂ O	12	n.d.	8	n.d.

^aReaction conditions: methyl 4-iodobenzoate (190.3 μmol), *N*-Boc proline (285.4 μmol), Fluorescein sodium (9.5 μmol), NiBr₂·glyme (9.5 μmol) and dcbpy (9.5 μmol) in DMSO (anhydrous, 3 mL), BIPA (570.8 μmol), TiO₂ (30 mg), 525 nm LED (50% power), 24 h.

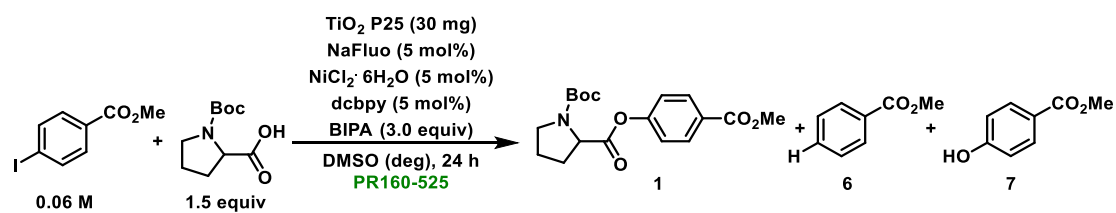
^bConversion of methyl 4-iodobenzoate determined by ¹H-NMR using 1,3,5-trimethoxybenzene as internal standard. ^cNMR yields determined by ¹H-NMR using 1,3,5-trimethoxybenzene as internal standard. NaFluo = Fluorescein sodium. dcbpy = 2,2'-bipyridine-4,4'-dicarboxylic acid. n.d. = not detected. BIPA = *N*-*tert*-butylisopropylamine. glyme = 1,2-dimethoxyethane. deg = degassed

Although NiBr₂·glyme and NiCl₂·glyme showed best results, NiCl₂·6H₂O was used for further experiments. This nickel source is significantly cheaper and more convenient to handle, as NiBr₂·glyme and NiCl₂·glyme are hygroscopic. Methyl 4-acetoxybenzoate was occasionally observed in case of Ni(OAc)₂·4H₂O as side-product. This resulted from the C-O arylation of the aryl iodide with the acetate anion of Ni(OAc)₂·4H₂O.

Table S5.7. Solvent screening using the 525 nm LED setup.^a

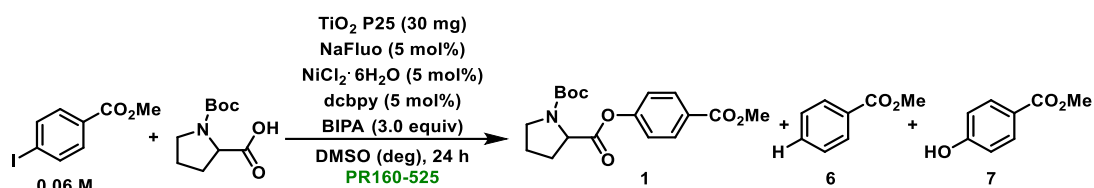
Entry	Solvent	Conversion [%] ^b	1 [%] ^c	6 [%] ^c	7 [%] ^c
1	DMSO	52	27	13	traces
2	DMAc	50	24	12	traces
3	MeCN	10	6	3	traces
4	Diglyme	10	7	3	n.d.
5	THF	9	3	traces	traces
6	Dioxane	8	4	4	n.d.
7	DCM	6	n.d.	n.d.	n.d.
8	Acetone	2	n.d.	n.d.	n.d.

^aReaction conditions: methyl 4-iodobenzoate (190.3 μmol), *N*-Boc proline (285.4 μmol), Fluorescein sodium (9.5 μmol), NiCl₂·6H₂O (9.5 μmol) and dcbpy (9.5 μmol) in solvent (anhydrous, 3 mL), BIPA (570.8 μmol), TiO₂ (30 mg), 525 nm LED (50% power), 24 h. ^bConversion of methyl 4-iodobenzoate determined by ¹H-NMR using 1,3,5-trimethoxybenzene as internal standard. ^cNMR yields determined by ¹H-NMR using 1,3,5-trimethoxybenzene as internal standard. NaFluo = Fluorescein sodium. dcbpy = 2,2'-bipyridine-4,4'-dicarboxylic acid. n.d. = not detected. BIPA = *N*-*tert*-butylisopropylamine. glyme = 1,2-dimethoxyethane. deg = degassed

Table S5.8. Optimization of lamp power using the 525 nm LED setup.^a

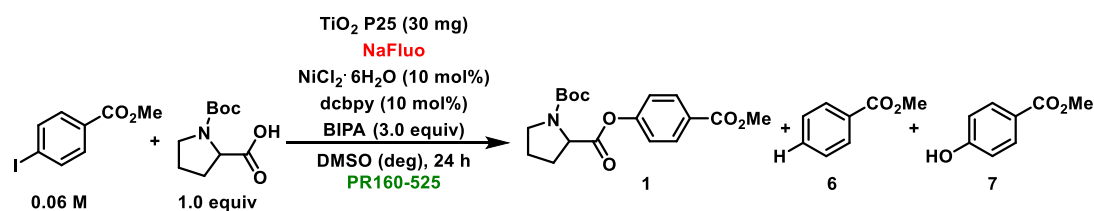
Entry	Lamp power [%]	Conversion [%] ^b	1 [%] ^c	6 [%] ^c	7 [%] ^c
1	50	52	27	13	traces
2	25	43	27	9	traces

^aReaction conditions: methyl 4-iodobenzoate (190.3 μmol), *N*-Boc proline (285.4 μmol), Fluorescein sodium (9.5 μmol), NiCl₂·6H₂O (9.5 μmol) and dcbpy (9.5 μmol) in solvent (anhydrous, 3 mL), BIPA (570.8 μmol), TiO₂ (30 mg), 525 nm LED, 24 h. ^bConversion of methyl 4-iodobenzoate determined by ¹H-NMR using 1,3,5-trimethoxybenzene as internal standard. ^cNMR yields determined by ¹H-NMR using 1,3,5-trimethoxybenzene as internal standard. NaFluo = Fluorescein sodium. dcbpy = 2,2'-bipyridine-4,4'-dicarboxylic acid. n.d. = not detected. BIPA = *N*-*tert*-butylisopropylamine. deg = degassed

Table S5.9. Optimization of the equivalents of *N*-Boc proline using the 525 nm LED setup.^a

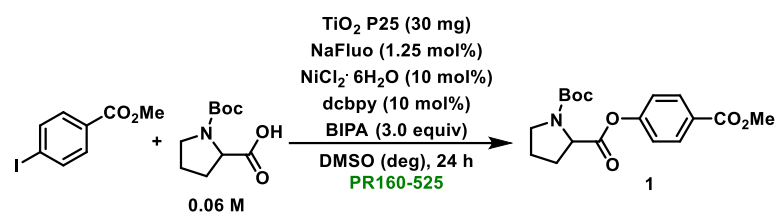
Entry	<i>N</i> -Boc proline [equiv]	Conversion [%] ^b	1 [%] ^c	6 [%] ^c	7 [%] ^c
1	1.0	30	20	7	traces
2	1.5	30	17	8	traces
3	2.0	22	13	8	traces
4	2.5	22	10	8	n.d.

^aReaction conditions: methyl 4-iodobenzoate (190.3 μmol), *N*-Boc proline, Fluorescein sodium (9.5 μmol), NiCl₂·6H₂O (9.5 μmol) and dcbpy (9.5 μmol) in DMSO (anhydrous, 3 mL), BIPA (570.8 μmol), TiO₂ (30 mg), 525 nm LED (25% power), 24 h. ^bConversion of methyl 4-iodobenzoate determined by ¹H-NMR using 1,3,5-trimethoxybenzene as internal standard. ^cNMR yields determined by ¹H-NMR using 1,3,5-trimethoxybenzene as internal standard. NaFluo = Fluorescein sodium. dcbpy = 2,2'-bipyridine-4,4'-dicarboxylic acid. n.d. = not detected. BIPA = *N*-tert-butylisopropylamine. deg = degassed

Table S5.10. Optimization of the amount of fluorescein sodium using the 525 nm LED setup.^a

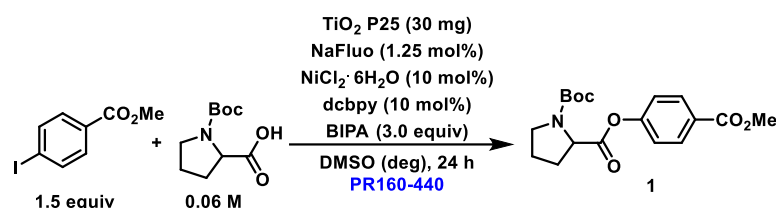
Entry	NaFluo [mol%]	Conversion [%] ^b	1 [%] ^c	6 [%] ^c	7 [%] ^c
1	2.50	56	41	7	3
2	2.00	66	52	7	5
3	1.50	79	64	6	4
4	1.25	77	66	6	5
5	1.00	74	64	5	4
6	0.75	47	40	traces	traces
7	0.50	40	35	traces	traces

^aReaction conditions: methyl 4-iodobenzoate (190.3 μmol), N-Boc proline (190.3 μmol), Fluorescein sodium, NiCl₂·6H₂O (19.0 μmol) and dcbpy (19.0 μmol) in DMSO (anhydrous, 3 mL), BIPA (570.8 μmol), TiO₂ (30 mg), 525 nm LED (25% power), 24 h. ^bConversion of methyl 4-iodobenzoate determined by ¹H-NMR using 1,3,5-trimethoxybenzene as internal standard. ^cNMR yields determined by ¹H-NMR using 1,3,5-trimethoxybenzene as internal standard. NaFluo = Fluorescein sodium. dcbpy = 2,2'-bipyridine-4,4'-dicarboxylic acid. n.d. = not detected. BIPA = *N*-*tert*-butylisopropylamine. deg = degassed

Table S5.11. Optimization of the amount of *N*-Boc proline using the 525 nm LED setup.^a

Entry	Methyl 4-iodobenzoate [equiv]	1 [%] ^b
1	1.5	76
2	1.0	66

^aReaction conditions: methyl 4-iodobenzoate, *N*-Boc proline (190.3 μmol), Fluorescein sodium (2.4 μmol), NiCl₂·6H₂O (19.0 μmol) and dcbpy (19.0 μmol) in DMSO (anhydrous, 3 mL), BIPA (570.8 μmol), TiO₂ (30 mg), 525 nm LED (25% power), 24 h. ^bNMR yields determined by ¹H-NMR using 1,3,5-trimethoxybenzene as internal standard. NaFluo = Fluorescein sodium. dcbpy = 2,2'-bipyridine-4,4'-dicarboxylic acid. n.d. = not detected. BIPA = *N*-tert-butylisopropylamine. deg = degassed

Table S5.12. Optimized conditions and control studies using the 440 nm setup.^a

Entry	Deviation from standard conditions	1 [%] ^b
1	none	95
2	UV filter ^c	80
3	no NaFluo	15
4	no NaFluo, UV filter ^c	n.d.
5	no TiO ₂	25
6	no TiO ₂ , UV filter ^d	20
7	No dcbpy	n.d.
8	no NiCl ₂ ·6H ₂ O	n.d.
9	no light	n.d.
10	no degassing	n.d.
11	no BIPA	n.d.

Reaction conditions: methyl 4-iodobenzoate (285.4 μmol), *N*-Boc proline (190.3 μmol), Fluorescein sodium (2.4 μmol), NiCl₂·6H₂O (19.0 μmol) and dcbpy (19.0 μmol) in DMSO (anhydrous, 3 mL), BIPA (570.8 μmol), TiO₂ (30 mg), 440 nm LED lamp (25% power), 24 h. ^bNMR yields determined by ¹H-NMR using 1,3,5-trimethoxybenzene as internal standard. ^cReactions were carried out with a 425 nm cut-off filter (See Figure S5.12) between the light source and the reaction vessel NaFluo = Fluorescein sodium. dcbpy = 2,2'-bipyridine-4,4'-dicarboxylic acid. n.d. = not detected. BIPA = *N*-tert-butylisopropylamine. deg = degassed

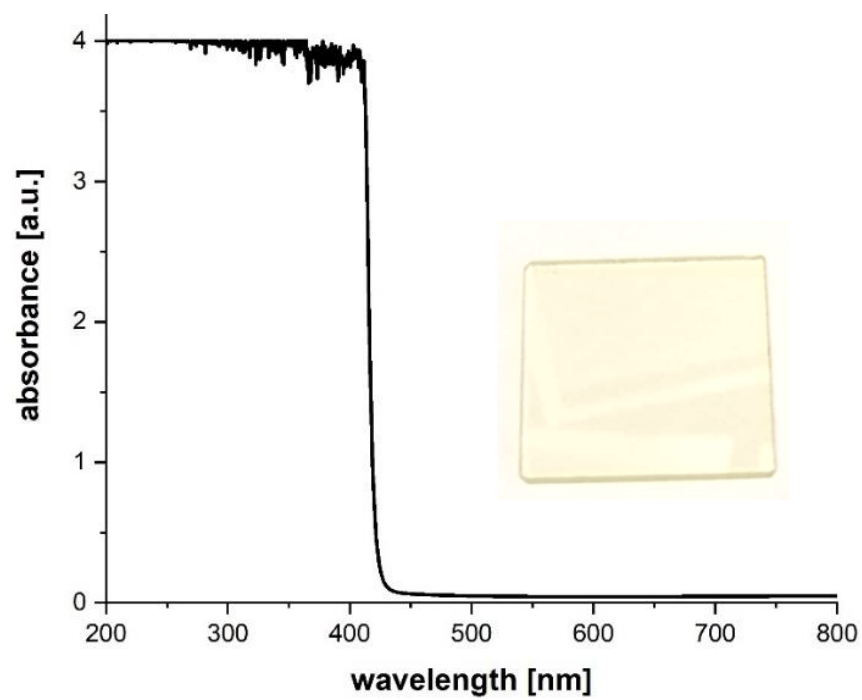
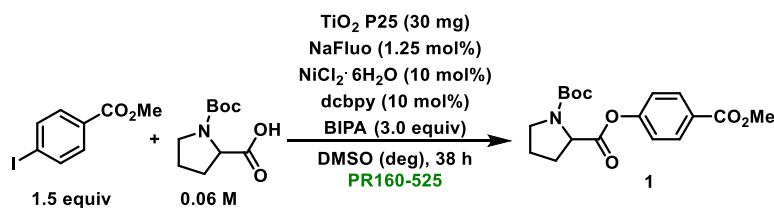


Figure S5.12. Absorption spectrum of the 425 nm cut-off filter that was used for control studies using the PR160-440 setup.

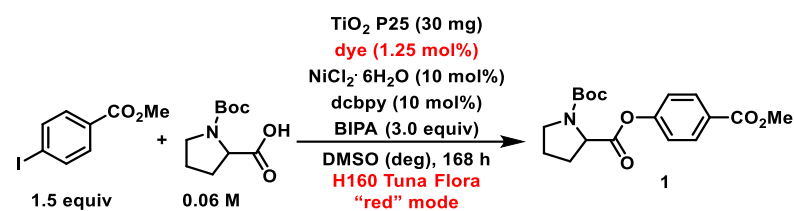
Table S5.13. Optimized conditions and control studies using the 525 nm setup.^a

Entry	Deviation from standard conditions	1 [%] ^b
1	none	97
2	DSMP prepared <i>ex situ</i> ^c	62
3	0.1 mol% NaFluo	90
4	1 mol% NiCl ₂ ·6H ₂ O & dcbpy	97
5	0.1 mol% 1 mol% NiCl ₂ ·6H ₂ O & dcbpy	n.d.
6	1 mol% NaFluo 2 mol% NiCl ₂ ·6H ₂ O % dcbpy	50
7	no TiO ₂	n.d.
8	no NaFluo	n.d.
9	no dcbpy	traces
10	no NiCl ₂ ·6H ₂ O	n.d.
11	no light	n.d.
12	no degassing	n.d.
13	no BIPA	n.d.

^aReaction conditions: methyl 4-iodobenzoate (285.4 μmol), *N*-Boc proline (190.3 μmol), Fluorescein sodium (2.4 μmol), NiCl₂·6H₂O (19.0 μmol) and dcbpy (19.0 μmol) in DMSO (anhydrous, 3 mL), BIPA (570.8 μmol), TiO₂ (30 mg), 525 nm LED (25% power), 38h.

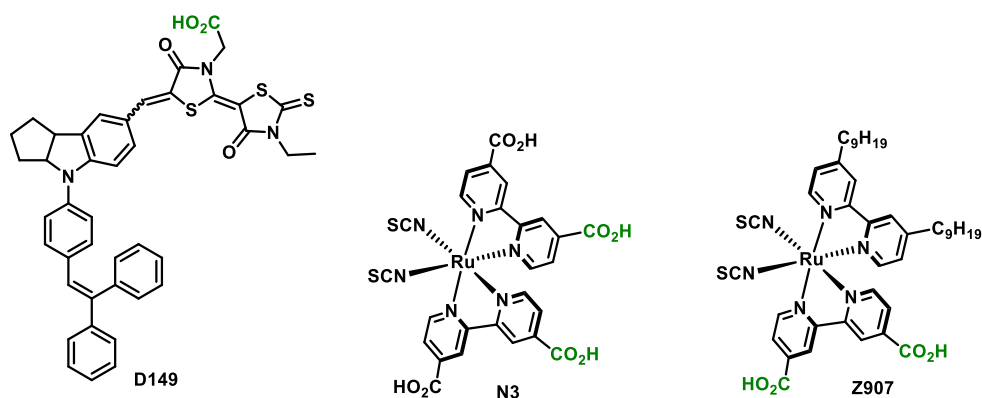
^bNMR yields determined by ¹H-NMR using 1,3,5-trimethoxybenzene as internal standard.

^ccontains ~1 mol% of NaFluo, ~2 mol% of NiCl₂·6H₂O and ~2 mol% of dcbpy. NaFluo = Fluorescein sodium. dcbpy = 2,2'-bipyridine-4,4'-dicarboxylic acid. n.d. = not detected. BIPA = *N*-*tert*-butylisopropylamine. deg = degassed

Table S5.14. Dye screening using the 666 nm setup.^a

Entry	Dye	Variation	1 [%] ^b
1	N3	--	95
2	N3	No TiO_2	n.d.
3	Z907	--	29
4	D149	--	n.d.

^aReaction conditions: methyl 4-iodobenzoate (285.4 μmol), *N*-Boc proline (190.3 μmol), Fluorescein sodium (2.4 μmol), $\text{NiCl}_2 \cdot 6\text{H}_2\text{O}$ (19.0 μmol) and dcbpy (19.0 μmol) in DMSO (anhydrous, 3 mL), BIPA (570.8 μmol), TiO_2 (30 mg), 666 nm LED (100% power), 168h. ^bNMR yields determined by $^1\text{H-NMR}$ using 1,3,5-trimethoxybenzene as internal standard. NaFluo = Fluorescein sodium. dcbpy = 2,2'-bipyridine-4,4'-dicarboxylic acid. n.d. = not detected. BIPA = *N*-tert-butylisopropylamine. deg = degassed

**Figure S5.13.** Structures of dyes that were tested for experiments using the 666 nm setup. The functionalities that bind to the surface hydroxyl groups of TiO_2 are marked in green.

5.5.3.2 Experimental procedure for the optimized C-O arylation using *in situ* generation of DSMPs.

An oven dried vial (19 x 100 mm) equipped with a stir bar was charged with TiO₂ P25 (90 mg), *N*-Boc proline (122.7 mg, 570.0 μmol, 1.0 equiv), methyl 4-iodobenzoate (224.1 mg, 855.1 μmol, 1.5 equiv), fluorescein sodium or N3 (7.1 μmol, 1.25 mol%), NiCl₂·6H₂O (13.6 mg 57.1 μmol, 10 mol%) and 2,2'-bipyridine-4,4'-dicarboxylic acid (dcbpy, 13.9 mg 57.1 μmol, 10 mol%). Subsequently, DMSO (anhydrous, 6 mL) and *N*-tert-butylisopropylamine (BIPA, 271 μL, 1.71 mmol, 3 equiv) were added and the vial was sealed with a septum and Parafilm. The reaction mixture was sonicated for 5-10 min followed by stirring for 5 min to obtain a fine dispersion. The mixture was then degassed by bubbling Argon for 10 min. The mixture was irradiated using the 525 (fluorescein sodium) or 666 nm LED setup (N3) with rapid stirring (1400 rpm). After the respective reaction time, one equivalent of 1,3,5-trimethoxybenzene (internal standard, 96 mg, 570 μmol) was added and the mixture was stirred for 5 min. An aliquot of the reaction mixture (~200 μL) was filtered, diluted with DMSO-d₆ and subjected to ¹H-NMR analysis to determine NMR yields. Thereafter, the NMR sample was combined with the reaction mixture. The reaction mixture was diluted with H₂O (40 mL) and extracted with dichloromethane (3 x 30 mL). The combined organic phases were washed with brine (50 mL), dried over Na₂SO₄ and concentrated. The product was purified by flash column chromatography (SiO₂, Hexane/EtOAc elution gradient of 0-20%) on a Grace Reveleris system using a 12 g cartridge. In some cases, mixed fractions containing small amounts of the phenol byproduct and the desired product were observed. These could be easily purified by a basic extraction (DCM and 0.5 M NaOH), followed by drying the organic phase over Na₂SO₄ and solvent evaporation to maximize the reaction yield. The title compound was isolated as a yellowish solid.

Using fluorescein sodium and the 525 nm setup:

Reaction time: 38 h

Isolated yield: 90% (179.2 mg, 512.9 μmol)

Using N3 and the 666 nm setup:

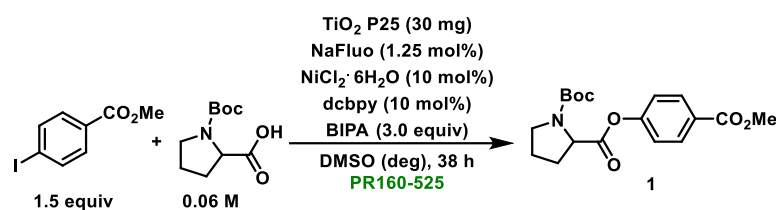
Reaction time: 168 h

Isolated yield: 92% (183.2 mg, 524.4 μmol)

1-(tert-butyl) 2-(4-(methoxycarbonyl)phenyl) pyrrolidine-1,2-dicarboxylate 1: ^1H NMR (400 MHz, CDCl_3) rotameric mixture, δ 8.03 (m, 2H), 7.15 (m, 2H), 4.50 (dd, $J = 8.6, 4.3$ Hz, 0.4H), 4.42 (dd, $J = 8.7, 4.3$ Hz, 0.6H), 3.88 (m, 3H), 3.61 – 3.38 (m, 2H), 2.45 – 2.25 (m, 1H), 2.16 (m, 1H), 2.10 – 1.86 (m, 2H), 1.42 (m, 9H). ^{13}C NMR (151 MHz, CDCl_3) rotameric mixture, signals for minor rotamer are enclosed in parenthesis δ (170.86) 170.82, (166.01) 165.88, 154.15 (153.88), 153.15, 130.93 (130.80), 127.52 (127.36), (121.22) 121.86, 80.00 (79.80), 58.88 (58.79), 51.93 (51.87), (46.34) 46.15, 30.71 (29.66), 28.09, (24.25) 23.43. HRMS (ESI) m/z calcd for $\text{C}_{18}\text{H}_{23}\text{NNaO}_6$ [(M+Na) $^+$] 372.1423, found 372.1417.

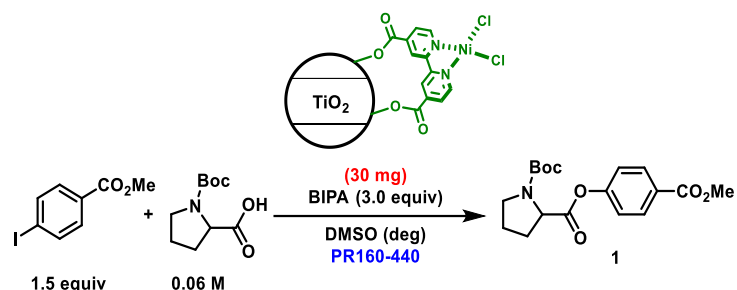
These data are in full agreement with those previously published in the literature.⁶

5.5.3.3 C-O arylation with different aryl halides

Table S5.15. C-O arylation of different aryl halides using the 525 nm setup.^a

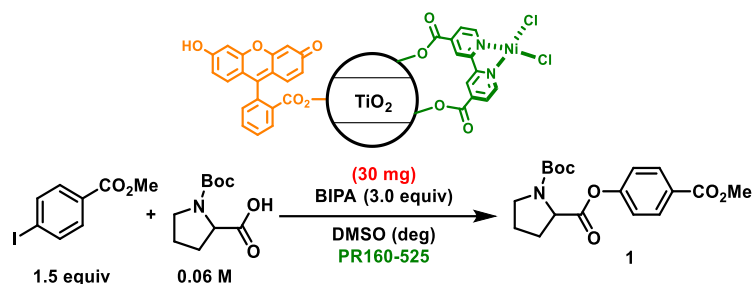
Entry	Deviation from standard conditions	1 [%] ^b
1	none	97
2	4-iodobenzonitrile	89
3	4-iodotoluene	n.d.

^aReaction conditions: methyl 4-iodobenzoate (285.4 μmol), *N*-Boc proline (190.3 μmol), Fluorescein sodium (2.4 μmol), NiCl₂·6H₂O (19.0 μmol) and dcbpy (19.0 μmol) in DMSO (anhydrous, 3 mL), BIPA (570.8 μmol), TiO₂ (30 mg), 525 nm LED (25% power), 38h. ^bNMR yields determined by ¹H-NMR using 1,3,5-trimethoxybenzene as internal standard. NaFluo = Fluorescein sodium. dcbpy = 2,2'-bipyridine-4,4'-dicarboxylic acid. n.d. = not detected. BIPA = *N*-*tert*-butylisopropylamine. deg = degassed

5.5.3.4 Experiments using *ex situ* prepared catalysts.**Table S5.16.** C-O arylation with an nickel complex immobilized on TiO₂ (*ex situ* preparation), using the 440 nm setup.^a

Entry	t [h]	1 [%] ^c
1	38	29
2	168	67

^aReaction conditions: methyl 4-iodobenzoate (285.4 μmol), *N*-Boc proline (190.3 μmol), TiO₂-NiCl₂-dcbpy (30 mg) in DMSO (anhydrous, 3 mL), BIPA (570.8 μmol), 440 nm LED (25% power), 38 h. ^cNMR yields determined by ¹H-NMR using 1,3,5-trimethoxybenzene as internal standard. dcbpy = 2,2'-bipyridine-4,4'-dicarboxylic acid. n.d. = not detected. BIPA = *N*-*tert*-butylisopropylamine. deg = degassed

Table S5.17. C-O arylation with an *ex situ* prepared DSMP and reference systems using the 525 nm setup.^a

Entry	Catalyst	t [h]	1 [%] ^b
1	Fluo-TiO ₂ -NiCl ₂ ·dcbpy	38	63
2	Fluo-TiO ₂ + NiCl ₂ ·dcbpy ^c	24	63
3	Fluo-TiO ₂ + NiCl ₂ ·dtbbpy ^c	24	27

^aReaction conditions: methyl 4-iodobenzoate (285.4 μmol), *N*-Boc proline (190.3 μmol), NaFluo-TiO₂-NiCl₂·dcbpy (30 mg) in DMSO (anhydrous, 3 mL), BIPA (570.8 μmol), TiO₂ (30 mg), 525 nm LED (25% power), 38 h. ^bNMR yields determined by ¹H-NMR using 1,3,5-trimethoxybenzene as internal standard. The nickel salt and the ligand were added separately (19.0 μmol). NaFluo = Fluorescein sodium. dcbpy = 2,2'-bipyridine-4,4'-dicarboxylic acid. dtbbpy = 4,4'-di-*tert*-butyl-2,2'-dipyridyl. n.d. = not detected. BIPA = *N-tert*-butylisopropylamine. deg = degassed

5.4.4 C-S cross-coupling

5.5.4.1 Experiments using *ex situ* prepared catalysts.

5.5.4.1.1 Optimization studies using in situ generation of DSMPs.

An oven dried vial (19 x 100 mm) equipped with a stir bar was charged with TiO₂ P25 (30 mg), methyl 4-iodobenzoate (1 equiv), methyl 3-mercaptopropionate (2 equiv), a dye (1.25 mol%), NiBr₂·3H₂O (10 mol%), and the ligand (10 mol%). Subsequently, MeCN (anhydrous, 3 mL) and *N*-tert-butylisopropylamine (BIPA, 3 equiv) were added, and the vial was sealed with a septum and Parafilm. The reaction mixture was sonicated for 5-10 min followed by stirring for 5 min to obtain a fine dispersion. The mixture was then degassed by bubbling Argon for 10 min. The mixture was irradiated with the respective LED lamps with rapid stirring (1400 rpm). After the respective reaction time, one equivalent of 1,3,5-trimethoxybenzene was added. An aliquot of the reaction mixture (~200 μL) was filtered, diluted with DMSO-d₆ and subjected to ¹H-NMR analysis. For a representative NMR spectrum, see **Fehler! Verweisquelle konnte nicht gefunden werden.**

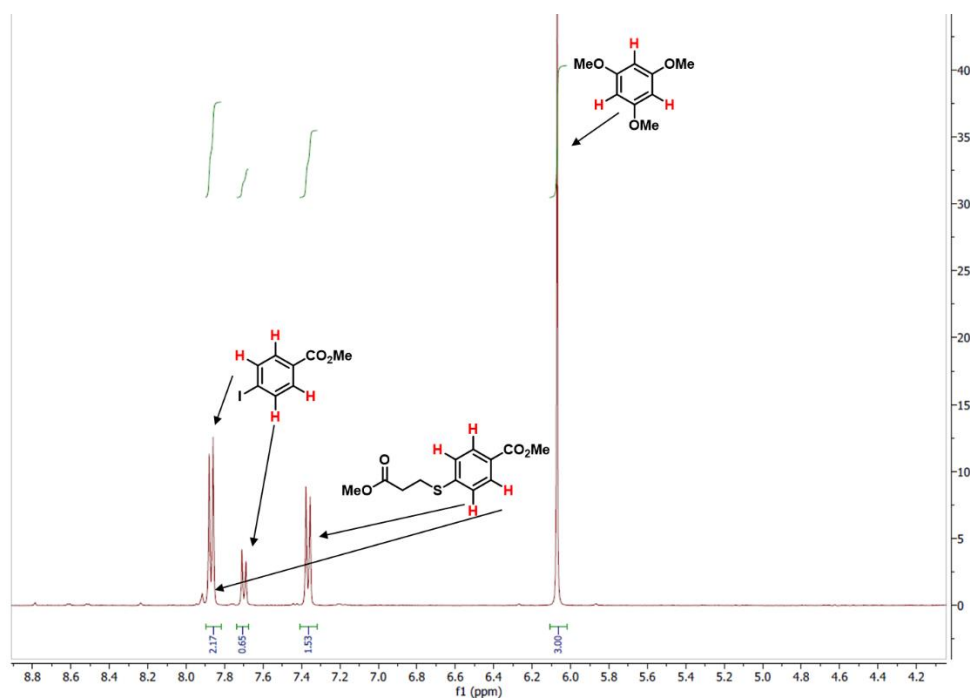
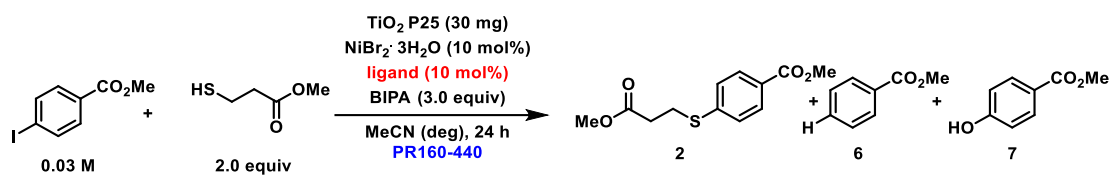
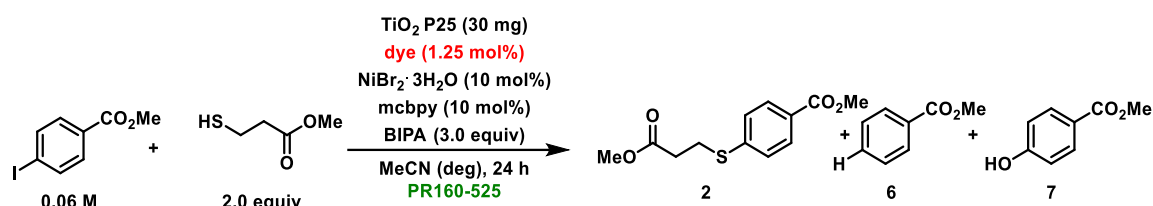


Figure S5.14. Representative ¹H-NMR spectrum of a crude reaction mixture for determining NMR yields in the C-S arylation.

Table S5.18. Ligand screening in absence of a dye using the 440 nm LED setup.^a

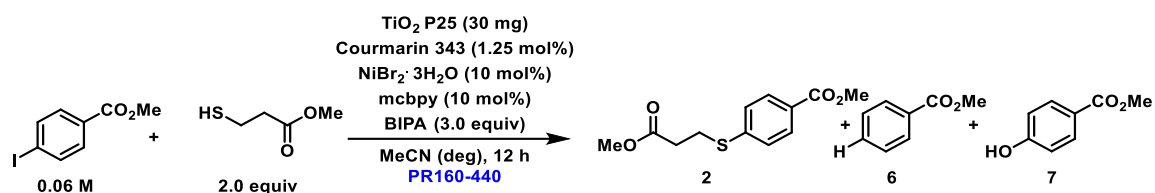
Entry	Ligand	Conversion [%] ^b	2 [%] ^c	6 [%] ^c	7 [%] ^c
1		86	84	n.d.	n.d.
2		32	32	n.d.	n.d.

^aReaction conditions: methyl 4-iodobenzoate (300.0 μmol), methyl 3-mercaptopropionate (600.0 μmol), NiBr₂·3H₂O (30.0 μmol), ligand (30.0 μmol), BIPA (900 μmol) in MeCN (3 mL), and TiO₂ (30 mg), 440 nm LED (50% power), 24 h. ^bConversion of methyl 4-iodobenzoate determined by ¹H-NMR using 1,3,5-trimethoxybenzene as internal standard. ^cNMR yields determined by ¹H-NMR using 1,3,5-trimethoxybenzene as internal standard. BIPA = *N*-*tert*-butylisopropylamine. n.d. = not detected. deg = degassed

Table S5.19. Dye screening using the 525 nm LED setup.^a

Entry	Dye	Conversion [%] ^b	2 [%] ^c	6 [%] ^c	7 [%] ^c
1	--	18	18	n.d.	n.d.
2	Coumarin 343	quant	99	n.d.	n.d.
3	Rose bengal	91	91	n.d.	n.d.
4	Rhodamin B	47	45	n.d.	n.d.
5	Brilliant blue R	5	n.d.	n.d.	n.d.
6	Alizarin red S	5	5	n.d.	n.d.
7	Methyl orange	4	n.d.	n.d.	n.d.
8	Congo Red	4	n.d.	n.d.	n.d.
9	Bromophenol blue	0	n.d.	n.d.	n.d.
10	Fluorescein sodium	0	n.d.	n.d.	n.d.

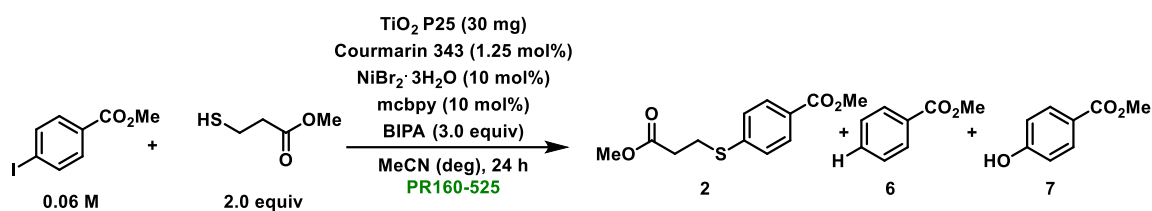
^aReaction conditions: methyl 4-iodobenzoate (190.3 μmol), methyl 3-mercaptopropionate (380.5 μmol), dye (2.4 μmol), NiBr₂·3H₂O (19.0 μmol) TiO₂ (30 mg), and mcbpy (19.0 μmol), BIPA (570.8 μmol) in MeCN (3 mL), 525 nm LED (50% power), 24 h. ^bConversion of methyl 4-iodobenzoate determined by ¹H-NMR using 1,3,5-trimethoxybenzene as internal standard. ^cNMR yields determined by ¹H-NMR using 1,3,5-trimethoxybenzene as internal standard. For structures of the dyes, see **Fehler! Verweisquelle konnte nicht gefunden werden.** BIPA = *N*-*tert*-butylisopropylamine. mcbpy = 4'-methyl-2,2'-bipyridine-4-carboxylic acid. n.d. = not detected. deg = degassed. quant = quantitative.

Table S5.20. Optimized conditions and control studies using using the 440 nm LED setup.^a

Entry	Deviation from standard conditions	Conversion [%] ^b	Yields [%] ^c		
			2 [%] ^c	6 [%] ^c	7 [%] ^c
1	--	quant	99	n.d.	n.d.
2	no degassing	40	35	n.d.	n.d.
3	no Coumarin 343	21	19	n.d.	n.d.
4	no BIPA	20	19	n.d.	n.d.
5	no light	5	n.d.	n.d.	n.d.
6	no NiBr ₂ ·3H ₂ O	4	traces	n.d.	n.d.
7	no TiO ₂	3	n.d.	n.d.	n.d.
8	no mcbpy	0	n.d.	n.d.	n.d.

^aReaction conditions: methyl 4-iodobenzoate (190.3 μmol), methyl 3-mercaptopropionate (380.5 μmol), coumarin 343 (2.4 μmol), NiBr₂·3H₂O (19.0 μmol) and mcbpy (19.0 μmol), BIPA (570.8 μmol) in MeCN (3 mL), TiO₂ (30 mg), 440 nm LED (50% power), 12 h.

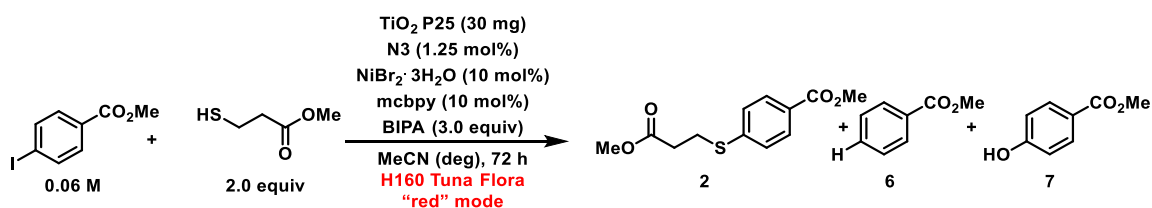
^bConversion of methyl 4-iodobenzoate determined by ¹H-NMR using 1,3,5-trimethoxybenzene as internal standard. ^cNMR yields determined by ¹H-NMR using 1,3,5-trimethoxybenzene as internal standard. BIPA = *N-tert*-butylisopropylamine. mcbpy = 4'-methyl-2,2'-bipyridine-4-carboxylic acid. n.d. = not detected. deg = degassed. quant = quantitative.

Table S5.21. Optimized conditions and control studies using the 525 nm LED setup.^a

Entry	Deviation from				
	standard conditions	Conversion [%] ^b	2 [%] ^c	6 [%] ^c	7 [%] ^c
1	--	quant.	99	n.d.	n.d.
2	no degassing	40	37	n.d.	n.d.
3	no BIPA	18	17	n.d.	n.d.
4	no Coumarin 343	17	17	n.d.	n.d.
5	no NiBr ₂ ·3H ₂ O	8	traces	n.d.	n.d.
6	no TiO ₂	6	traces	3	n.d.
7	no light	5	n.d.	n.d.	n.d.
8	no mcbpy	0	n.d.	n.d.	n.d.

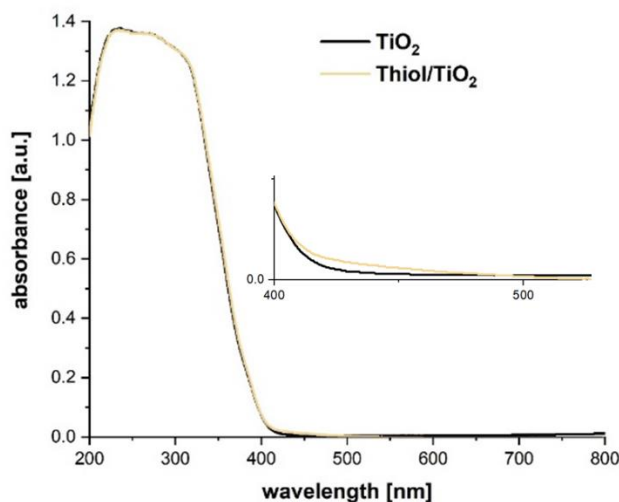
^aReaction conditions: methyl 4-iodobenzoate (190.3 μmol), methyl 3-mercaptopropionate (380.5 μmol), Coumarin 343 (2.4 μmol), NiBr₂·3H₂O (19.0 μmol) and mcbpy (19.0 μmol), BIPA (570.8 μmol) in MeCN (3 mL), TiO₂ (30 mg), 525 nm LED (50% power), 24 h.

^bConversion of methyl 4-iodobenzoate determined by ¹H-NMR using 1,3,5-trimethoxybenzene as internal standard. ^cNMR yields determined by ¹H-NMR using 1,3,5-trimethoxybenzene as internal standard. BIPA = *N*-*tert*-butylisopropylamine. mcbpy = 4'-methyl-2,2'-bipyridine-4-carboxylic acid. n.d. = not detected. deg = degassed. quant = quantitative.

Table S5.22. Optimized conditions and control studies using the 666 nm setup.^a

Entry	Deviation from		Conversion [%] ^b	2 [%] ^c	6 [%] ^c	7 [%] ^c
	standard	conditions				
1	--		quant	99	n.d.	n.d.
2	no TiO ₂		20	20	n.d.	n.d.
3	no N3		10	10	n.d.	n.d.

^aReaction conditions: methyl 4-bromobenzoate (190.3 μmol), methyl 3-mercaptopropionate (380.5 μmol), N3 (2.4 μmol), NiBr₂·3H₂O (19.0 μmol) and mcbpy (19.0 μmol) BIPA (570.8 μmol) in MeCN (3 mL), TiO₂ (30 mg), 666 nm LED (100% power), 72 h. ^bConversion of methyl 4-iodobenzoate determined by ¹H-NMR using 1,3,5-trimethoxybenzene as internal standard. ^cNMR yields determined by ¹H-NMR using 1,3,5-trimethoxybenzene as internal standard. BIPA = *N-tert*-butylisopropylamine. mcbpy = 4'-methyl-2,2'-bipyridine-4-carboxylic acid. n.d. = not detected. deg = degassed. quant = quantitative.

**Figure S5.15.** UV/Vis absorption spectra of TiO₂ (black) and 3-mercaptopropionate-TiO₂ (yellow).

The absorption spectrum of TiO₂ P25 is extended to visible light due to surface complexation of the thiol starting material⁷. This effect is responsible for background reactions.

5.5.4.1.2 Experimental procedure for the optimized C-S arylation using in situ generation of DSMPs.

An oven dried vial (19 x 100 mm) equipped with a stir bar was charged with TiO₂ P25 (90 mg), methyl 4-iodobenzoate (149.37 mg, 570.0 μmol, 1.0 equiv), methyl 3-mercaptopropionate (126.3 μL, 1.14 mmol, 2.0 equiv), Coumarin 343 or N3 (7.1 μmol, 1.25 mol%), NiBr₂·3H₂O (15.5 mg, 57.0 μmol, 10 mol%) and 4'-methyl-2,2'-bipyridine-4-carboxylic acid (12.2 mg, 57.0 μmol, 10 mol%). Subsequently, MeCN (anhydrous, 6 mL) and *N*-tert-butylisopropylamine (BIPA, 271 μL, 1.71 mmol, 3 equiv) were added and the vial was sealed with a septum and Parafilm. The reaction mixture was sonicated for 5-10 min followed by stirring for 5 min to obtain a fine dispersion. The mixture was then degassed by bubbling Argon for 10 min. The mixture was irradiated using the 525 (fluorescein sodium) or 666 nm LED setup (N3) with rapid stirring (1400 rpm). After the respective reaction time, one equivalent of 1,3,5-trimethoxybenzene (internal standard 96 mg, 570 μmol) was added and the mixture was stirred for 5 min. An aliquot of the reaction mixture (~200 μL) was filtered, diluted with DMSO-d₆ and subjected to ¹H-NMR analysis. Thereafter, the NMR sample was combined with the reaction mixture, diluted with H₂O (40 mL) and extracted with ethyl acetate (3 x 30 mL). The combined organic phases were washed with aqueous NaOH (1 M, 2x40 ml) and brine (40 mL), dried over Na₂SO₄ and concentrated. The product was purified by flash column chromatography (SiO₂, Hexane/EtOAc elution gradient of 0-10%) on a Grace Reveleris system using a 12 g cartridge. The title compound was isolated as a white solid.

Using Coumarin 343 and the 525 nm setup:

Reaction time: 24 h

Isolated yield: 95% (135.7 mg, 533.6 μmol)

Using N3 and the 666 nm setup:

Reaction time: 72 h

Isolated yield: 96% (137.3 mg, 540.0 μmol)

Methyl 4-((3-methoxy-3-oxopropyl)thio)benzoate 2: ¹H NMR (400 MHz, CDCl₃) δ 7.93 (d, J = 8.6 Hz, 2H), 7.31 (d, J = 8.6 Hz, 2H), 3.89 (s, 3H), 3.69 (s, 3H), 3.25 (t, J = 7.4 Hz, 2H), 2.68 (t, J = 7.4 Hz, 2H). ¹³C NMR (101 MHz, CDCl₃) δ 171.98, 166.68, 142.68, 130.18,

127.41, 127.17, 52.21, 52.08, 33.83, 27.38. HRMS-EI (m/z) [M*]⁺ calcd for C₁₂H₁₄O₄S: 254.0613; found: 254.0617.

These data are in full agreement with those previously published in the literature.⁸

5.5.5 C-S cross-coupling

5.5.5.1 Optimization studies using *in situ* generation of DSMPs.

General experimental procedure for screening experiments *via in situ* DSMP preparation. An oven dried vial (19 x 100 mm) equipped with a stir bar was charged with TiO₂ P25 (30 mg), methyl 4-bromobenzoate (1 equiv), pyrrolidine (3 equiv), a dye, NiBr₂·3H₂O (10 mol%), and a ligand (10 mol%). Subsequently, dimethylacetamide (anhydrous, 3 mL) was added and the vial was sealed with a septum and Parafilm. The reaction mixture was sonicated for 5-10 min, followed by stirring for 5 min to obtain a fine dispersion. The mixture was then degassed by bubbling Argon for 10 min. The mixture was irradiated with the respective LED lamps with rapid stirring (1400 rpm). After the respective reaction time, one equivalent of 1,3,5-trimethoxybenzene was added. An aliquot of the reaction mixture (~200 μL) was filtered, diluted with DMSO-d₆ and subjected to ¹H-NMR analysis. For a representative NMR spectrum, see Figure S5.16. **Fehler! Verweisquelle konnte nicht gefunden werden..**

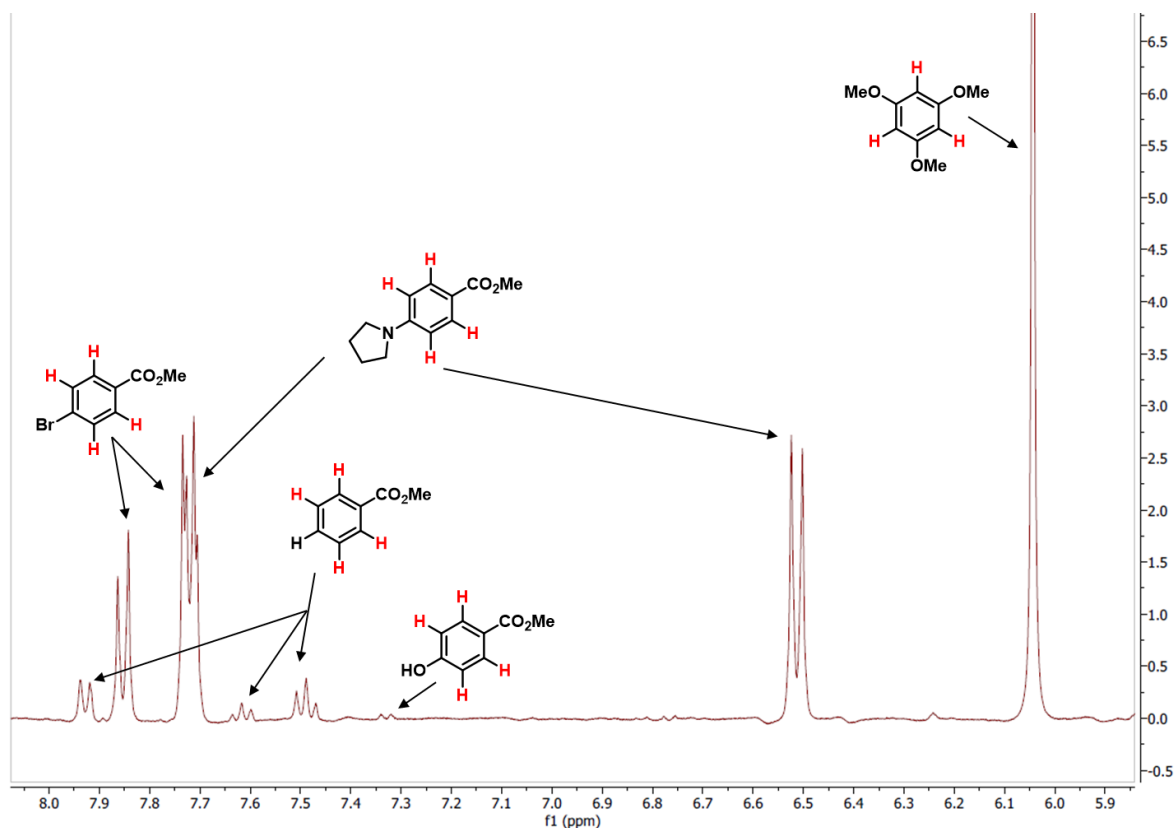
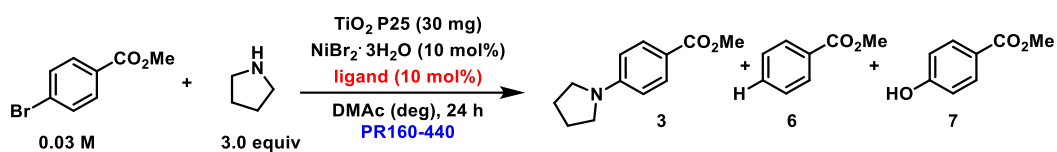
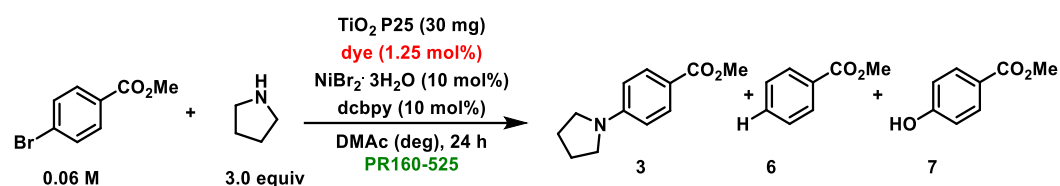


Figure S5.16. Representative ¹H-NMR spectrum of a crude reaction mixture for determining NMR yields in the C-N arylation.

Table S5.23. Ligand screening in absence of a dye using the 440 nm LED setup.^a

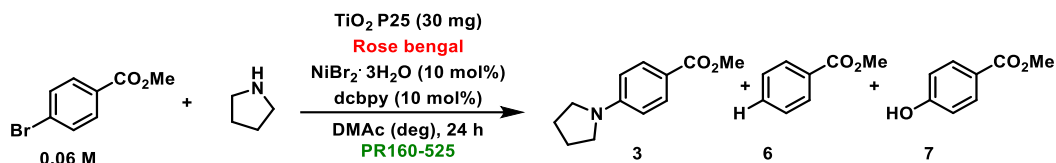
Entry	Ligand	Conversion [%] ^b	3 [%] ^c	6 [%] ^c	7 [%] ^c
1		89	78	3	traces
2		88	62	10	3

^aReaction conditions: methyl 4-bromobenzoate (300.0 μmol), pyrrolidine (900.0 μmol), NiBr₂·3H₂O (30.0 μmol) and ligand (30.0 μmol) in DMAc (3 mL), TiO₂ (30 mg), 440 nm, LED (50% power), 24 h. ^bConversion of methyl 4-bromobenzoate determined by ¹H-NMR using 1,3,5-trimethoxybenzene as internal standard. ^cNMR yields determined by ¹H-NMR using 1,3,5-trimethoxybenzene as internal standard. DMAc = dimethylacetamide.

Table S5.24. Dye screening using the 525 nm LED setup.^a

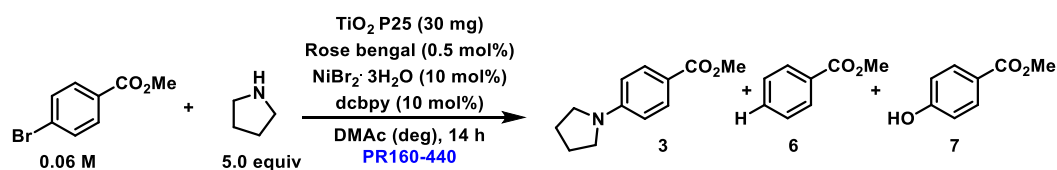
Entry	Dye	Conversion [%] ^b	3 [%] ^c	6 [%] ^c	7 [%] ^c
1	--	2	n.d.	n.d.	n.d.
2	Rose bengal	56	43	7	n.d.
3	Coumarin 343	50	32	14	n.d.
4	Rhodamin B	15	3	traces	n.d.
5	Fluorescein sodium	10	traces	6	n.d.
6	Bromophenol blue	7	n.d.	n.d.	n.d.
7	Congo red	5	n.d.	n.d.	n.d.
8	Alizarin red S	4	n.d.	n.d.	n.d.
9	Brilliant blue R	2	n.d.	n.d.	n.d.
10	Catechol	0	n.d.	n.d.	n.d.
14	Methyl orange	0	n.d.	n.d.	n.d.

^aReaction conditions: methyl 4-bromobenzoate (190.3 μmol), pyrrolidine (570.8 μmol), dye (2.4 μmol), $\text{NiBr}_2 \cdot 3\text{H}_2\text{O}$ (19.0 μmol) and dcbpy (19.0 μmol) in DMAc (3 mL), TiO_2 (30 mg), 525 nm LED (50% power), 24 h. ^bConversion of methyl 4-bromobenzoate determined by ¹H-NMR using 1,3,5-trimethoxybenzene as internal standard. ^cNMR yields determined by ¹H-NMR using 1,3,5-trimethoxybenzene as internal standard. For structures of the dyes, see **Fehler! Verweisquelle konnte nicht gefunden werden.** dcbpy = 2,2'-bipyridine-4,4'-dicarboxylic acid. DMAc = dimethylacetamide. n.d. = not detected. deg = degassed.

Table S5.25. Optimization of the amount of dye and equivalents of pyrrolidine using the 525 nm setup.^a

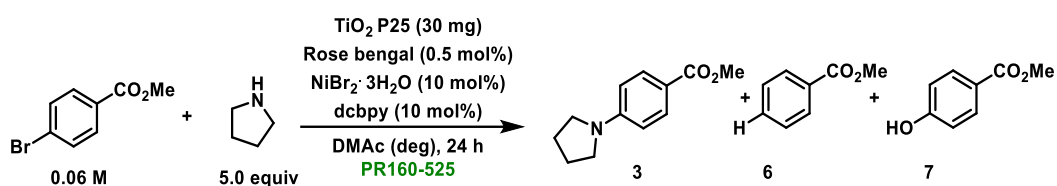
Entry	variations	Conversion [%] ^b	3 [%] ^c	6 [%] ^c	7 [%] ^c
1	0.50 mol% dye + 5 equiv pyrrolidine	quant	98	traces	n.d.
2	0.63 mol% dye + 5 equiv pyrrolidine	quant	85	6	n.d.
3	0.63 mol% dye + 3 equiv pyrrolidine	67	58	10	traces

^aReaction conditions: methyl 4-bromobenzoate (190.3 μmol), pyrrolidine, NiBr₂·3H₂O (19.0 μmol), Rose bengal, and dcbpy (19.0 μmol) in DMAc (3 mL), TiO₂ (30 mg), 525 nm LED (50% power), 24 h. ^bConversion of methyl 4-bromobenzoate determined by ¹H-NMR using 1,3,5-trimethoxybenzene as internal standard. ^cNMR yields determined by ¹H-NMR using 1,3,5-trimethoxybenzene as internal standard. dcbpy = 2,2'-bipyridine-4,4'-dicarboxylic acid. DMAc = dimethylacetamide n.d. = not detected. deg = degassed. quant = quantitative.

Table S5.26. Optimized conditions and control studies using the 440 nm setup.^a

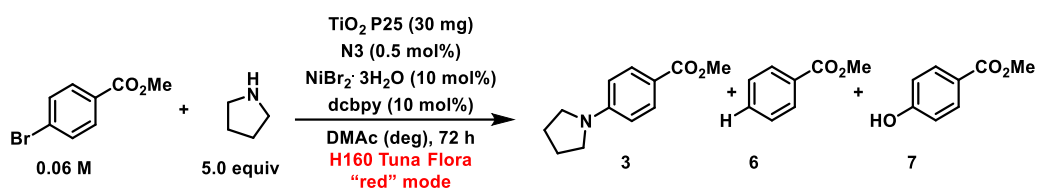
Entry	Deviation from				
	standard conditions	Conversion [%] ^b	3 [%] ^c	6 [%] ^c	7 [%] ^c
1	--	quant	99	traces	n.d.
2	no dcbpy	67	65	n.d.	n.d.
3	no Rose Bengal	20	19	n.d.	n.d.
4	no light	2	n.d.	n.d.	n.d.
5	no NiBr ₂ ·3H ₂ O	0	n.d.	n.d.	n.d.
6	no TiO ₂	0	n.d.	n.d.	n.d.
7	no degassing	0	n.d.	n.d.	n.d.

^aReaction conditions: methyl 4-bromobenzoate (190.3 μmol), pyrrolidine (951.6 μmol), Rose Bengal (1.0 μmol), NiBr₂·3H₂O (19.0 μmol) and dcbpy (19.0 μmol) in DMAc (3 mL), TiO₂ (30 mg), 440 nm blue LED (50% power) for 14 h. ^bConversion of methyl 4-bromobenzoate determined by ¹H-NMR using 1,3,5-trimethoxybenzene as internal standard. ^cNMR yields determined by ¹H-NMR using 1,3,5-trimethoxybenzene as internal standard. dcbpy = 2,2'-bipyridine-4,4'-dicarboxylic acid. DMAc = dimethylacetamide n.d. = not detected. deg = degassed. quant = quantitative

Table S5.27. Optimized conditions and control studies using the 525 nm setup.^a

Entry	Deviation from				
	standard conditions	Conversion [%] ^b	3 [%] ^c	6 [%] ^c	7 [%] ^c
1	--	quant	99	traces	n.d.
2	no dcbpy	70	69	n.d.	n.d.
3	no Rose Bengal	2	traces	n.d.	n.d.
4	no light	2	n.d.	n.d.	n.d.
5	no NiBr ₂ ·3H ₂ O	0	n.d.	n.d.	n.d.
6	no TiO ₂	0	n.d.	n.d.	n.d.
7	no degassing	0	n.d.	n.d.	n.d.

^aReaction conditions: methyl 4-bromobenzoate (190.3 μmol), pyrrolidine (951.4 μmol), Rose Bengal (1.0 μmol), NiBr₂·3H₂O (19.0 μmol) and dcbpy (19.0 μmol) in DMAc (3 mL), TiO₂ (30 mg), 525 nm LED (50% power), 24 h. ^bConversion of methyl 4-bromobenzoate determined by ¹H-NMR using 1,3,5-trimethoxybenzene as internal standard. ^cNMR yields determined by ¹H-NMR using 1,3,5-trimethoxybenzene as internal standard. dcbpy = 2,2'-bipyridine-4,4'-dicarboxylic acid. DMAc = dimethylacetamide n.d. = not detected. deg = degassed. quant = quantitative

Table S5.28. Optimized conditions and control studies using the 666 nm setup.^a

Entry	Deviation from				
	standard conditions	Conversion [%] ^b	3 [%] ^c	6 [%] ^c	7 [%] ^c
1	--	quant.	95	4	n.d.
2	no TiO ₂	2	n.d.	n.d.	n.d.
3	No N3	3	n.d.	n.d.	n.d.

^aReaction conditions: methyl 4-bromobenzoate (190.3 μmol), pyrrolidine (951.4 μmol), Rose Bengal (1.0 μmol), NiBr₂·3H₂O (19.0 μmol) and dcbpy (19.0 μmol) in DMAc (3 mL), TiO₂ (30 mg), 666 nm red LED (100% power), 72 h. ^bConversion of methyl 4-bromobenzoate determined by ¹H-NMR using 1,3,5-trimethoxybenzene as internal standard. ^cNMR yields determined by ¹H-NMR using 1,3,5-trimethoxybenzene as internal standard. dcbpy = 2,2'-bipyridine-4,4'-dicarboxylic acid. DMAc = dimethylacetamide n.d. = not detected. deg = degassed. quant = quantitative

5.5.5.2 Experimental procedure for the optimized C-N arylation using in situ generation of DSMPs.

An oven dried vial (19 x 100 mm) equipped with a stir bar was charged with TiO₂ (90 mg), pyrrolidine (121.6 mg, 142.7 μ l, 1.71 mmol, 5.0 equiv), and 4-bromomethylbenzoate (122.6 mg, 570.0 μ mol, 1.0 equiv), Rose Bengal or N3 (2.9 μ mol, 0.50 mol%), NiBr₂·3H₂O (57.0 μ mol, 10 mol%) and 2,2'-bipyridine-4,4'-dicarboxylic acid (57.0 μ mol, 10 mol%). Subsequently, DMAc (anhydrous, 6 mL) was added and the vial was sealed with a septum and Parafilm. The reaction mixture was sonicated for 5-10 min followed by stirring for 5 min to obtain a fine dispersion. The mixture was then degassed by bubbling Argon for 10 min. The mixture was irradiated using the 525 (Rose Bengal) or 666 nm LED setup (N3) with rapid stirring (1400 rpm). After the respective reaction time, one equivalent of 1,3,5-trimethoxybenzene (internal standard 96 mg, 570 μ mol) was added and the mixture was stirred for 5 min. An aliquot of the reaction mixture (~200 μ L) was filtered, diluted with DMSO-d₆ and subjected to ¹H-NMR analysis. Thereafter, the NMR sample was combined with the reaction mixture, diluted with H₂O (40 mL) and extracted with ethyl acetate (3 x 30 mL). The combined organic phases were washed with H₂O (40 mL), NaHCO₃ solution (40 ml) and brine (40 mL), dried over Na₂SO₄ and concentrated. The product was purified by flash column chromatography (SiO₂, Hexane/EtOAc elution gradient of 0-10%) on a Grace Reveleris system using a 12 g cartridge. The title compound was isolated as a white solid.

Using Rose Bengal and the 525 nm setup:

Reaction time: 72 h

Isolated yield: 94% (109.9 mg, 535.8 μ mol)

Using N3 and the 666 nm setup:

Reaction time: 72 h

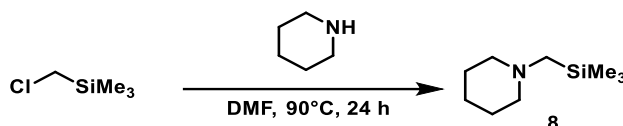
Isolated yield: 96% (112.2 mg, 547,0 μ mol)

1-(4-methylbenzoate)pyrrolidine 3: ¹H NMR (400 MHz, CDCl₃) δ 7.90 (d, *J* = 8.7 Hz, 2H), 6.47 (d, *J* = 8.7 Hz, 2H), 3.84 (s, 3H), 3.42 – 3.09 (m, 4H), 2.05 – 1.86 (m, 4H). ¹³C NMR (101 MHz, CDCl₃) δ 167.76, 150.95, 131.49, 116.37, 110.76, 51.55, 47.62, 25.58. HRMS (ESI-TOF) *m/z* calcd. for C₁₂H₁₆NO₂ [(M+H)⁺]: 206.1176; found: 206.1187.

These data are in full agreement with those previously published in the literature.⁹

5.5.6 C-C cross-coupling

5.5.6.1 Synthesis of 1-((trimethylsilyl)methyl)piperidine



A 100 mL round bottom flask equipped with a stir bar was charged with (chloromethyl)trimethylsilane (3.07 g, 25 mmol, 1 equiv), DMF (25 mL) and piperidine (6.38 g, 7.41 mL, 75 mmol, 3.0 equiv). The mixture was heated to 90°C in an oil bath (overnight) under an argon atmosphere. Reaction progress was assessed by NMR. When the reaction was completed, the mixture was cooled to room temperature and was diluted with deionized H₂O (~50 mL). The mixture was extracted with Et₂O (75 mL). The layers were separated, and the aqueous layer was extracted with Et₂O (2 × 50 mL). The combined organic layers were washed with deionized H₂O (2 × 100 mL) and brine (150 mL). The organic layer was dried (Na₂SO₄), and the solvent was removed. Further purification was accomplished by vacuum distillation (bp 60-62 °C @ 1 mmHg) giving clear colorless oil (2.57 g, 60%).

1-((trimethylsilyl)methyl)piperidine 8: ¹H NMR (400 MHz, CDCl₃) δ. 0.02 (s, 9H), 1.29 -1.38 (m, 2H), 1.47 -1.56 (m, 4H), 1.85 (s, 2H), 2.19 -2.38 (m, 4H). ¹³C NMR (101 MHz, CDCl₃) δ -0.97 (CH₃), 23.96 (CH₂), 26.45 (CH₂), 51.82 (CH₂), 58.58 (CH₂). HRMS (ESI-TOF) m/z calcd. for C₉H₂NSi [(M+H)⁺]: 172.1516; found: 172.1515.

These data are in full agreement with those previously published in the literature.⁴

5.5.6.2 Optimization studies using *in situ* generation of DSMPs.

General experimental procedure for screening experiments *via in situ* DSMP preparation. An oven dried vial (19 x 100 mm) equipped with a stir bar was charged with TiO₂ P25 (30 mg), 4-bromobenzonitrile (1 equiv), 1-((trimethylsilyl)methyl)piperidine (1.2 equiv), a dye (1.25 mol%), NiBr₂·glyme (10 mol%), and a ligand (10 mol%). Subsequently, the solvent (anhydrous, 3 mL) was added and the vial was sealed with a septum and Parafilm. The reaction mixture was sonicated for 5-10 min followed by stirring for 5 min to obtain a fine dispersion. The mixture was then degassed by bubbling Argon for 10 min. The mixture was irradiated with the respective LED lamps with rapid stirring (1400 rpm). After the respective reaction time, an aliquot of the reaction mixture (~200 μL) was extracted with diethyl ether and the solvent was removed. The remaining reaction mixture, diluted with CDCl₃ and subjected to ¹H-NMR analysis to determine substrate-to-product ratios. For a representative NMR spectrum, see Figure S5.17.

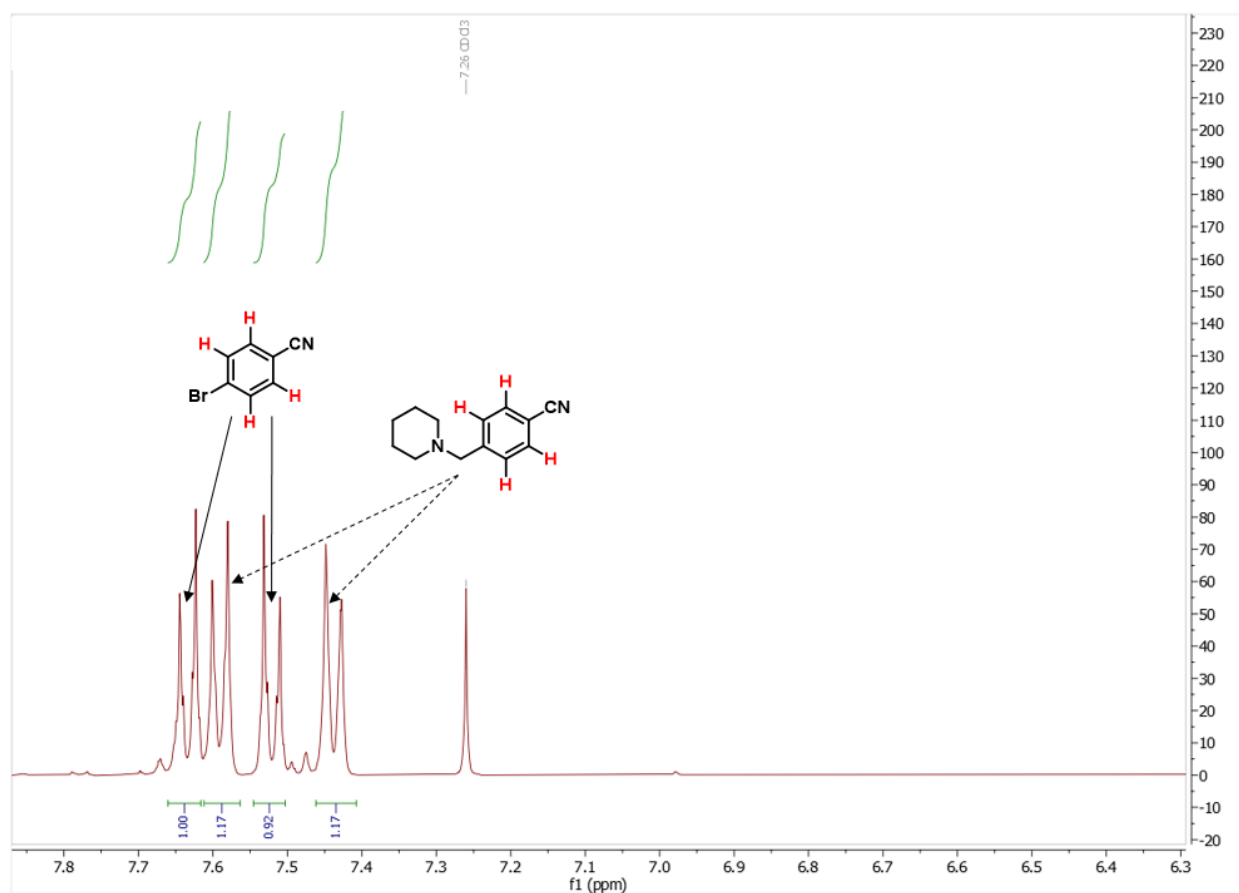
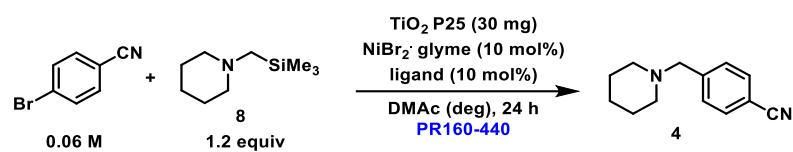
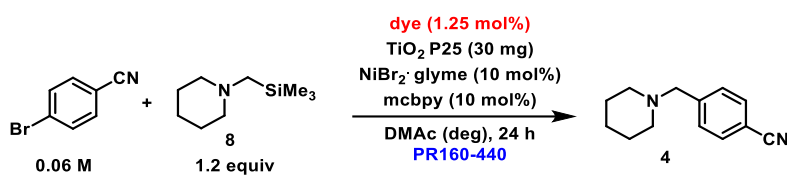


Figure S5.17. Representative ¹H-NMR spectrum of a crude reaction mixture for determining substrate-to-product ratios yields in the C-C cross-coupling.

Table S5.29. Ligand screening in absence of a dye using the 440 nm LED setup.^a

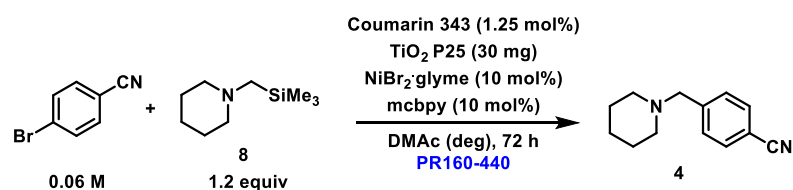
Entry	Ligand	Ar-Br:4 ^b
1		19:1
2		1:0

^aReaction conditions: 4-bromobenzonitrile (190.3 μmol), 1-((trimethylsilyl)methyl)piperidine (228.3 μmol), $\text{NiBr}_2 \cdot 3\text{H}_2\text{O}$ (19.0 μmol) and ligand (19.0 μmol) in DMAc (3 mL), TiO_2 (30 mg), 440 nm LED (100% power), 24 h. ^bDetermined by ¹HNMR. DMAc = dimethylacetamide. glyme = 1,2-dimethoxyethane. n.d. = not detected. deg = degassed.

Table S5.30. Dye screening using the 440 nm LED setup.^a

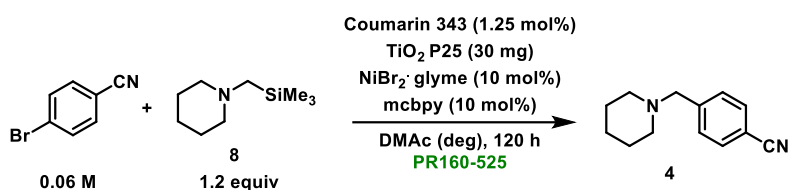
Entry	Sensitizer	Ar-Br: 4 ^b
1	Coumarin 343	1.8:1
2	Rose bengal	1.4:1
3	Rhodamin B	3:1
4	Fluorescein sodium	3.4:1

^aReaction conditions: 4-bromobenzonitrile (190.3 μ mol), 1-((trimethylsilyl)methyl)piperidine (228.3 μ mol), Sensitizer (1.25 mol%), NiBr₂·glyme (19.0 μ mol) and mcbpy (19.0 μ mol) in DMAc (3 mL), TiO₂ (30 mg), 440 nm LED (100% power), 24 h. ^bDetermined by ¹HNMR. For structures of the dyes, see **Fehler! Verweisquelle konnte nicht gefunden werden.** DMAc = dimethylacetamide. glyme = 1,2-dimethoxyethane. mcbpy = 4'-methyl-2,2'-bipyridine-4-carboxylic acid. n.d. = not detected. deg = degassed.

Table S5.31. Optimized conditions and control studies using the 440 nm setup.^a

Entry	Deviation from standard conditions	Ar-Br: 4 ^b
1	--	0:1
2	no mcbpy	4:1
3	no Coumarin 343	10:1
4	no light	1:0
5	no TiO ₂	9:1
6	no NiBr ₂ ·glyme	1:0
7	no degassing	13:1

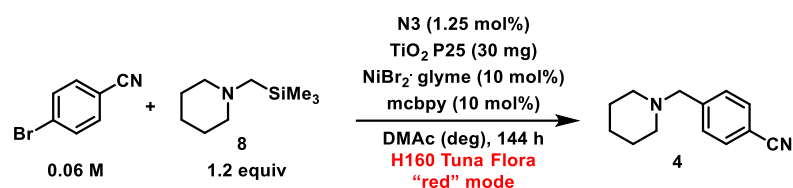
^aReaction conditions: 4-bromobenzonitrile (190.3 μmol), 1-((trimethylsilyl)methyl)piperidine (228.3 μmol), Coumarin 343 (1.25 mol%), NiBr₂·glyme (19.0 μmol) and mcbpy (19.0 μmol) in DMAc (3 mL), TiO₂ (30 mg), 440 nm LED (100% power), 72 h. ^bDetermined by ¹HNMR. DMAc = dimethylacetamide. glyme = 1,2-dimethoxyethane. mcbpy = 4'-methyl-2,2'-bipyridine-4-carboxylic acid. n.d. = not detected. deg = degassed.

Table S5.32. Optimized conditions and control studies using the 525 nm setup.^a

Entry	Deviation from standard conditions	Ar-Br:4 ^b
1	none	0:1
2	no mcbpy	7:1
3	no Coumarin 343	1:0
4	no light	1:0
5	no TiO ₂	12:1
6	no NiBr ₂ ·glyme	1:0
7	no degassing	19:1

^aReaction conditions: 4-bromobenzonitrile (190.3 μmol), 1-((trimethylsilyl)methyl)piperidine (228.3 μmol), Coumarin 343 (1.25 mol%), NiBr₂·glyme (19.0 μmol) and mcbpy (19.0 μmol) in DMAc (3 mL), TiO₂ (30 mg), 525 nm LED (100% power), 120 h.

^bDetermined by ¹HNMR. DMAc = dimethylacetamide. glyme = 1,2-dimethoxyethane. mcbpy = 4'-methyl-2,2'-bipyridine-4-carboxylic acid. n.d. = not detected. deg = degassed.

Table S5.33. Optimized conditions and control studies using the 666 nm setup.^a

Entry	Deviation from standard conditions	Ar-Br: 4 ^b
1	none	0:1
2	no N3	1:0
3	no TiO ₂	1:0

^aReaction conditions: 4-bromobenzonitrile (190.3 μmol), 1-((trimethylsilyl)methyl)piperidine (228.3 μmol), N3 (1.25 mol%), NiBr₂·glyme (19.0 μmol) and mcbpy (19.0 μmol) in DMAc (3 mL), TiO₂ (30 mg), 666 nm LED (100% power), 144 h. ^bDetermined by ¹HNMR. DMAc = dimethylacetamide. glyme = 1,2-dimethoxyethane. mcbpy = 4'-methyl-2,2'-bipyridine-4-carboxylic acid. n.d. = not detected. deg = degassed.

5.5.6.3 Experimental procedure for the optimized C-C coupling using *in situ* generation of DSMPs.

An oven dried vial (19 x 100 mm) equipped with a stir bar was charged with TiO₂ (30 mg), 1-((trimethylsilyl)methyl)piperidin (139.8 μ L, 685.0 μ mol, 1.2 equiv), 4-bromobenzonitrile (103.9 mg, 570.0 μ mol, 1.0 equiv), Coumarin 343 (7.1 μ mol, 1.25 mol%), NiBr₂·glyme (57.0 μ mol, 10 mol%) and 4'-methyl-2,2'-bipyridine-4-carboxylic acid (57.0 μ mol, 10 mol%). Subsequently, DMAc (anhydrous, 6 mL) was added and the vial was sealed with a septum and Parafilm. The reaction mixture was sonicated for 5-10 min followed by stirring for 5 min to obtain a dispersion. The mixture was then degassed by bubbling Argon for 10 min. The mixture was irradiated using the 440, 525 (Rose Bengal) or 666 nm LED setup (N3) with rapid stirring (1400 rpm). After the respective reaction time, an aliquot of the reaction mixture was extracted with diethyl ether. The solvent was removed and remaining reaction mixture diluted with CDCl₃ and subjected to ¹H-NMR analysis. Thereafter, the NMR sample was combined with the reaction mixture, diluted with H₂O (40 mL) and 2M NaOH (10 mL) and extracted with Et₂O (3 x 30 mL). The combined organic phases were washed with brine (50 mL), dried over Na₂SO₄ and concentrated. The product was purified by flash column chromatography (SiO₂, DCM/MeOH elution gradient of 0-2%) on a Grace Reveleris system using a 12 g cartridge. The title compound was isolated as a yellowish oil.

Using Coumarin 343 and the 440 nm setup:

Reaction time: 72 h

Isolated yield: 68% (77.7 mg, 388.0 μ mol)

Using Coumarin 343 and the 525 nm setup:

Reaction time: 120 h

Isolated yield: 75% (85.6 mg, 427.4 μ mol)

Using N3 and the 666 nm setup:

Reaction time: 144 h

Isolated yield: 81% (92.4 mg, 461.3 μ mol)

4-(Piperidin-1-ylmethyl)benzonitrile 4: ¹H NMR (400 MHz, CDCl₃) δ 7.60 (d, *J* = 8.2 Hz, 2H), 7.46 (d, *J* = 8.0 Hz, 2H), 3.52 (s, 2H), 2.46 - 2.29 (m, 4H), 1.64 - 1.51 (m, 4H), 1.50 - 1.38 (m, 2H). ¹³C NMR (101 MHz, CDCl₃) δ 144.79, 132.13, 129.66, 119.17, 110.80, 63.31,

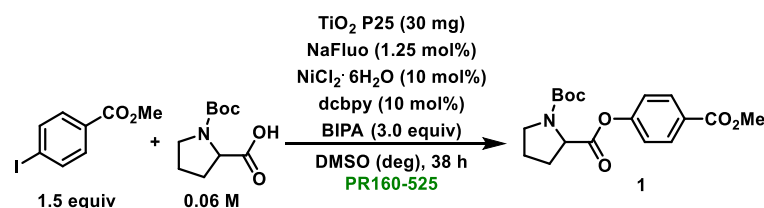
Supporting Information - Chapter 5

54.71, 26.01, 24.29. HRMS (ESI-TOF) m/z calcd. for $C_{13}H_{16}N_2 [(M+H)^+]$: 200.1386; found: 200.1397.

These data are in full agreement with those previously published in the literature.⁴

5.5.7 Catalyst recycling experiments

Experimental procedure for catalyst recycling experiments of the C-O arylation with the 525 nm setup using Fluo-TiO₂-NiCl₂·dcbpy generated *in situ*. An oven dried vial (19 x 100 mm) equipped with a stir bar was charged with TiO₂ P25 (30 mg), *N*-Boc proline (40.9 mg, 190.3 μmol, 1.0 equiv), methyl 4-iodobenzoate (74.8 mg, 285.4 μmol, 1.5 equiv), fluorescein sodium (2.4 μmol, 1.25 mol%), NiCl₂·6H₂O (4.5 mg 19.0 μmol, 10 mol%) and 2,2'-bipyridine-4,4'-dicarboxylic acid (dcbpy, 4.6 mg 19.0 μmol, 10 mol%). Subsequently, DMSO (anhydrous, 3 mL) and *N*-tert-butylisopropylamine (BIPA, 90.4 μL, 570.8 μmol, 3 equiv) were added and the vial was sealed with a septum and Parafilm. The reaction mixture was sonicated for 5-10 min followed by stirring for 5 min to obtain a fine dispersion. The mixture was then degassed by bubbling Argon for 10 min. The mixture was irradiated using the 525 nm LED setup with rapid stirring (1400 rpm). After the respective reaction time, the reaction mixture was centrifuged and washed twice with 3 mL DMSO. The remaining DSMPs was lyophilized overnight and reused in the next reaction

Table S5.34. Catalyst Recycling experiments of the C-O arylation with the 525 nm setup using an *in situ* generated DSMP.^a

Entry	Cycle	1 [%] ^c
1	1	95
2	2	67
3	3	58
4	4	26
5	5	n.d.
6	+NaFluo (1.25 mol%) ^d	98
7	+NiCl ₂ ·6H ₂ O (10 mol%) ^e	75

^aReaction conditions: methyl 4-iodobenzoate (285.4 μmol), *N*-Boc proline (190.3 μmol), Fluorescein sodium (2.4 μmol), NiCl₂·6H₂O (19.0 μmol) and dcbpy (19.0 μmol) in DMSO (anhydrous, 3 mL), BIPA (570.8 μmol), TiO₂ (30 mg), 525 nm LED (25% power), 38h. ^bConversion of methyl 4-iodobenzoate determined by ¹H-NMR using 1,3,5-trimethoxybenzene as internal standard. ^cNMR yields determined by ¹H-NMR using 1,3,5-trimethoxybenzene as internal standard. ^dFluorescein sodium (2.4 μmol) was added to a reaction mixture using the material recovered from entry 5. ^eThe nickel salt (19.0 μmol) was added to a reaction mixture using the material recovered from entry 5. NaFluo = Fluorescein sodium. dcbpy = 2,2'-bipyridine-4,4'-dicarboxylic acid. n.d. = not detected. BIPA = *N*-*tert*-butylisopropylamine. deg = degassed

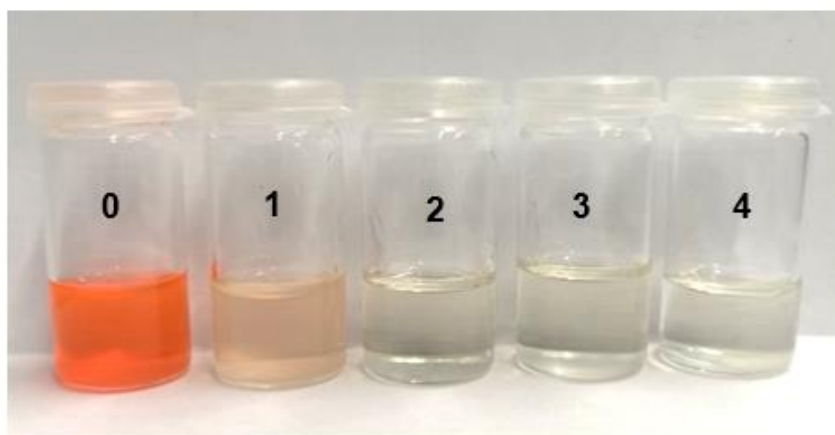


Figure S5.18. Reaction mixtures (see Table S5.34) by centrifugation.

Table S5.35. ICP-OES measurements of the nickel content the DSMP and the recovered DSMP after 5 cycles.

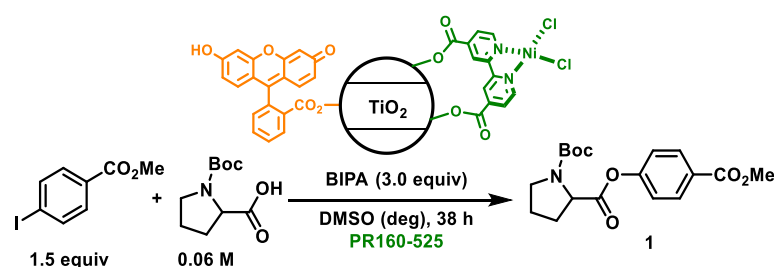
Sample	Ni [mg/g catalyst]
TiO ₂	0.02
Fluo-TiO ₂ -NiCl ₂ -dcbpy (<i>in situ</i>)	7.43
Fluo-TiO ₂ -NiCl ₂ -dcbpy (after) ^a	0.71

^aFluo-TiO₂-NiCl₂-dcbpy after 5 reaction cycles

Experimental procedure for catalyst recycling experiments of the C-O arylation with the 525 nm setup using Fluo-TiO₂-NiCl₂-dcbpy generated *in ex situ*.

An oven dried vial (19 x 100 mm) equipped with a stir bar was charged with TiO₂ P25 (30 mg), *N*-Boc proline (40.9 mg, 190.3 μmol, 1.0 equiv), methyl 4-iodobenzoate (74.8 mg, 285.4 μmol, 1.5 equiv) and Fluo-TiO₂-NiCl₂-dcbpy (for preparation, see section 2). Subsequently, DMSO (anhydrous, 3 mL) and *N*-tert-butylisopropylamine (BIPA, 90.4 μL, 570.8 μmol, 3 equiv) were added and the vial was sealed with a septum and Parafilm. The reaction mixture was sonicated for 5-10 min followed by stirring for 5 min to obtain a fine dispersion. The mixture was then degassed by bubbling Argon for 10 min. The mixture was irradiated using the 525 nm LED setup with rapid stirring (1400 rpm). After the respective reaction time, the reaction mixture was centrifuged and washed twice with 3 mL DMSO. The remaining DSMPs was lyophilized overnight and reused in the next reaction.

Table S5.36. Catalyst Recycling experiments of the C-O arylation with the 525 nm setup using an *ex situ* prepared DSMP.^a



Entry	Cycles	1 [%] ^c
1	<i>ex situ</i> prepared	63
2	1	21
3	2	4

^aReaction conditions: methyl 4-iodobenzoate (285,4 μmol), *N*-Boc proline (190.3 μmol) in DMSO (anhydrous, 3 mL), BIPA (570.8 μmol), catalyst (30 mg; for preparation procedure see 2.1), 525 nm LED (25% power), 38h.

^bConversion of methyl 4-iodobenzoate determined by ¹H-NMR using 1,3,5-trimethoxybenzene as internal standard. ^cNMR yields determined by ¹H-NMR using 1,3,5-trimethoxybenzene as internal standard. dcbpy = 2,2'-bipyridine-4,4'-dicarboxylic acid. n.d. = not detected. BIPA = *N*-tert-butylisopropylamine. deg = degassed

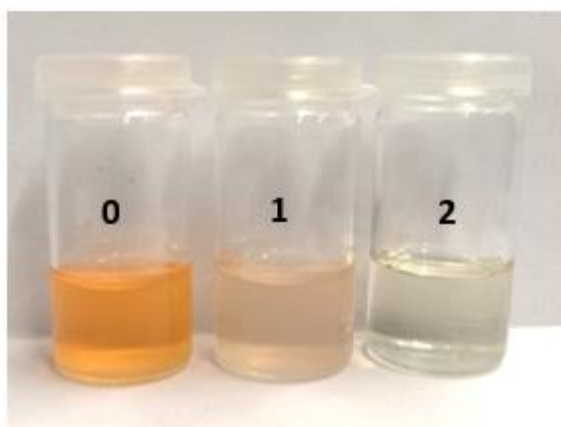


Figure S5.19. Reaction mixtures (see Table S5.36) after catalyst separation by centrifugation.

Table S5.37. ICP-OES measurements of the nickel content on the new and recovered catalyst

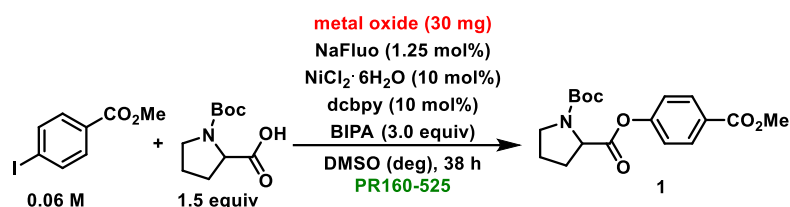
Sample	Ni [mg/g catalyst]
TiO ₂	0.02
Fluo-DSMP (<i>ex situ</i>)	6.50
Fluo-DSMP (after) ^a	1.66
Fluo-TiO ₂	0.041
TiO ₂ -NiCl ₂ ·dcbpy	5.45

^aFluo-TiO₂-NiCl₂·dcbpy after 5 reaction cycles

5.5.8 Experiments with insulating metal oxides and diffusion controlled metallaphotocatalysis.

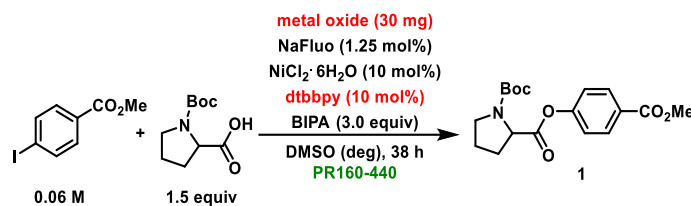
The reactions were carried out according to the optimized experimental procedures for the individual couplings using different metal oxides and ligands.

Table S5.38. C-O cross-couplings with different metal oxides using the 525 nm setup.^a



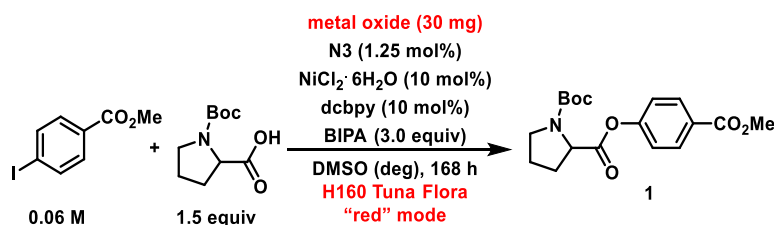
Entry	Metal oxide	1 [%] ^b
1	TiO ₂	97
2	SiO ₂	50
3	Al ₂ O ₃	39
4	ZnO	33
5	-	n.d.

^aReaction conditions: methyl 4-iodobenzoate (285.4 μmol), *N*-Boc proline (190.3 μmol), Fluorescein sodium (2.4 μmol), NiCl₂·6H₂O (19.0 μmol) and dcbpy (19.0 μmol), BIPA (570.8 μmol), and metal oxide (30 mg) in DMSO (anhydrous, 3 mL), 525 nm LED (25% power) for 38h. ^bNMR yields determined by ¹H-NMR using 1,3,5-trimethoxybenzene as internal standard. NaFluo = Fluorescein sodium. dcbpy = 2,2'-bipyridine-4,4'-dicarboxylic acid. n.d. = not detected. BIPA = *N*-*tert*-butylisopropylamine. deg = degassed

Table S5.39. C-O cross-couplings with different metal oxides and a non-binding nickel complex using the 525 nm setup.^a

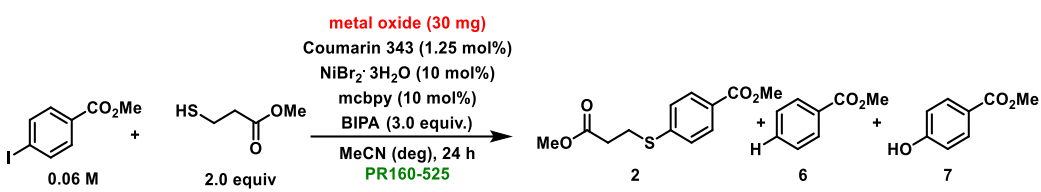
Entry	Metal oxide	1 [%] ^b
1	TiO ₂	65
2	SiO ₂	n.d.
3	Al ₂ O ₃	n.d.
4	ZnO	traces
5	-	n.d.

^aReaction conditions: methyl 4-iodobenzoate (285.4 μmol), *N*-Boc proline (190.3 μmol), Fluorescein sodium (2.4 μmol), NiCl₂·6H₂O (19.0 μmol), dtbbpy (19.0 μmol), BIPA (570.8 μmol), and metal oxide (30 mg) in DMSO (anhydrous, 3 mL), 525 green LED (25% power) for 38h. ^bNMR yields determined by ¹H-NMR using 1,3,5-trimethoxybenzene as internal standard. NaFluo = Fluorescein sodium. dtbbpy = 4,4'-di-*tert*-butyl-2,2'-dipyridyl. n.d. = not detected. BIPA = *N*-*tert*-butylisopropylamine. deg = degassed

Table S5.40. C-O cross-couplings with different metal oxides using the 666 nm setup.^a

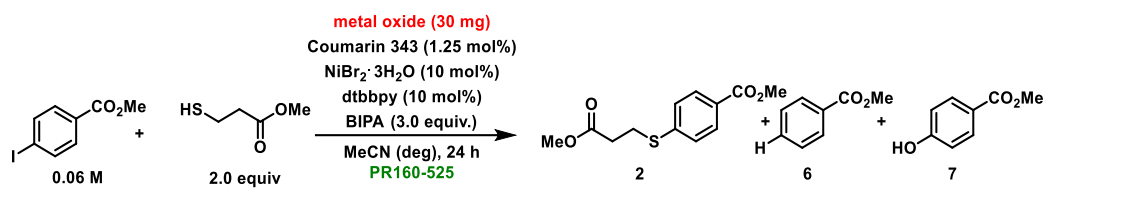
Entry	Metal oxide	1 [%] ^c
1	TiO ₂	95
2	SiO ₂	48
3	Al ₂ O ₃	37

^aReaction conditions: methyl 4-iodobenzoate (285.4 μmol), *N*-Boc proline (190.3 μmol), Fluorescein sodium (2.4 μmol), NiCl₂·6H₂O (19.0 μmol) and dcbpy (19.0 μmol) in DMSO (anhydrous, 3 mL), BIPA (570.8 μmol), semiconductor (30 mg), 666 nm LED (100% power) for 168h. ^cNMR yields determined by ¹H-NMR using 1,3,5-trimethoxybenzene as internal standard. NaFluo = Fluorescein sodium. dcbpy = 2,2'-bipyridine-4,4'-dicarboxylic acid. n.d. = not detected. BIPA = *N*-*tert*-butylisopropylamine. deg = degassed

Table S5.41. C-S cross-couplings with different metal oxides using the 525 nm setup.^a


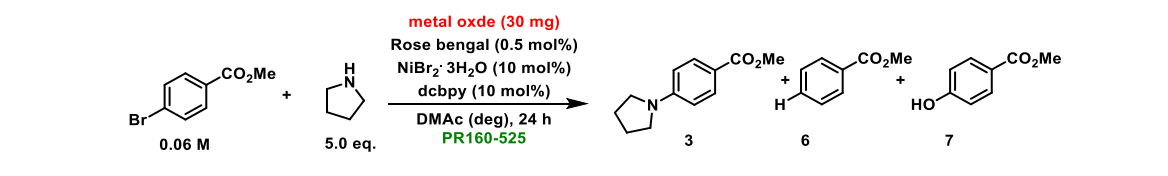
Entry	Metal oxide	2 [%] ^b	6 [%] ^b	7 [%] ^b
1	TiO ₂	99	n.d.	n.d.
2	Al ₂ O ₃	99	n.d.	n.d.
3	SiO ₂	48	n.d.	n.d.
4	-	traces	n.d.	n.d.

^aReaction conditions: methyl 4-bromobenzoate (190.3 μ mol), methyl 3-mercaptopropionate (380.5 μ mol), Coumarin 343 (2.4 μ mol), NiBr₂·3H₂O (19.0 μ mol), mcbpy (19.0 μ mol) and metal oxide (30 mg) in MeCN (3 mL), 525 nm LED (50% power) for 24 h. ^bNMR yields determined by ¹H-NMR using 1,3,5-trimethoxybenzene as internal standard. BIPA = *N-tert*-butylisopropylamine. mcbpy = 4'-methyl-2,2'-bipyridine-4-carboxylic acid. n.d. = not detected. deg = degassed. quant = quantitative.

Table S5.42. C-S cross-couplings with different metal oxides and a non-binding nickel complex using the 525 nm setup.^a


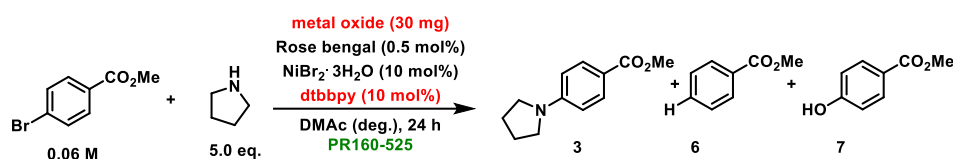
Entry	Metal oxide	2 [%] ^b	6 [%] ^b	7 [%] ^b
1	TiO ₂	80	n.d.	n.d.
2	Al ₂ O ₃	10	n.d.	n.d.
3	SiO ₂	5	n.d.	n.d.
4	-	traces	n.d.	n.d.

^aReaction conditions: methyl 4-bromobenzoate (190.3 μmol), methyl 3-mercaptopropionate (380.5 μmol), Coumarin 343 (2.4 μmol), NiBr₂·3H₂O (19.0 μmol), dtbbpy (19.0 μmol) and metal oxide (30 mg) in MeCN (3 mL), 525 green LED (50% power) for 24 h. ^bNMR yields determined by ¹H-NMR using 1,3,5-trimethoxybenzene as internal standard. BIPA = *N*-*tert*-butylisopropylamine. dtbbpy = 4,4'-di-*tert*-butyl-2,2'-dipyridyl. n.d. = not detected. deg = degassed. quant = quantitative.

Table S5.43. C-N cross-couplings with different metal oxides using the 525 nm setup.^a


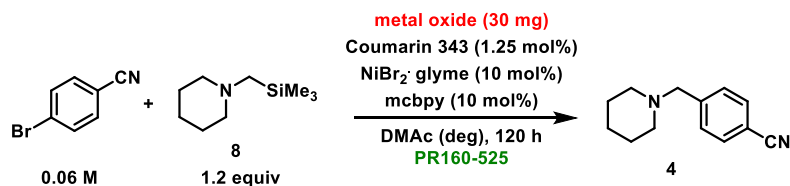
Entry	Metal oxide	3 [%] ^b	6 [%] ^b	7 [%] ^b
1	TiO ₂	99	n.d.	n.d.
2	Al ₂ O ₃	99	n.d.	n.d.
3	SiO ₂	48	n.d.	n.d.
4	-	n.d.	n.d.	n.d.

^aReaction conditions: methyl 4-bromobenzoate (190.3 μmol), pyrrolidine (951.4 μmol), Rose Bengal (0.5 mol%), NiBr₂·3H₂O (19.0 μmol) and dcbpy (19.0 μmol) in DMAc (3 mL), metal oxide (30 mg), 525 nm green LED (50% power) for 24 h. ^bConversion of methyl 4-bromobenzoate determined by ¹H-NMR using 1,3,5-trimethoxybenzene as internal standard. ^cNMR yields determined by ¹H-NMR using 1,3,5-trimethoxybenzene as internal standard. dcbpy = 2,2'-bipyridine-4,4'-dicarboxylic acid. DMAc = dimethylacetamide. n.d. = not detected. deg = degassed. quant = quantitative.

Table S5.44. C-N cross-couplings with different metal oxides and a non-binding nickel complex using the 525 nm setup.^a

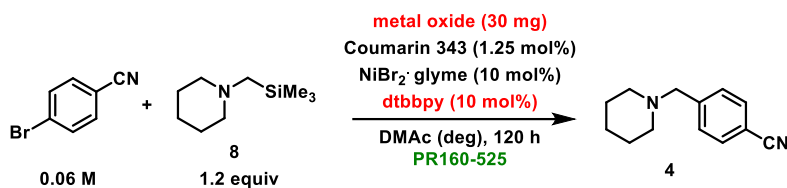
Entry	Metal oxide	3 [%] ^b	6 [%] ^b	7 [%] ^b
1	TiO ₂	12	n.d.	n.d.
2	Al ₂ O ₃	n.d.	n.d.	n.d.
3	SiO ₂	n.d.	n.d.	n.d.
4	-	n.d.	n.d.	n.d.

^aReaction conditions: methyl 4-bromobenzoate (190.3 μmol), pyrrolidine (951.4 μmol), Rose Bengal (0.5 mol%) NiBr₂·3H₂O (19.0 μmol) and dtbbpy (19.0 μmol), metal oxide (30 mg), in DMAc (3 mL), 525 nm LED (50% power) for 24 h. ^bNMR yields determined by ¹H-NMR using 1,3,5-trimethoxybenzene as internal standard. dtbbpy = 4,4'-di-tert-butyl-2,2'-dipyridyl. DMAc = dimethylacetamide n.d. = not detected. deg = degassed. quant = quantitative

Table S5.45. C-C cross-couplings with different metal oxides using the 525 nm setup.^a

Entry	Metal oxide	Ar-Br:4 ^b
1	TiO ₂	0:1
2	Al ₂ O ₃	1.5:1
3	SiO ₂	1.6:1
4	-	1:traces

^aReaction conditions: 4-bromobenzonitrile (190.3 μmol), 1-((trimethylsilyl)methyl)piperidine (228,3 μmol), N3 (1.25 mol%), NiBr₂·glyme (19.0 μmol) metal oxide (30 mg), and mcbpy (19.0 μmol) in DMAc (3 mL), 666 nm LED (100% power), 144 h. ^bDetermined by ¹HNMR. DMAc = dimethylacetamide. glyme = 1,2-dimethoxyethane. mcbpy = 4'-methyl-2,2'-bipyridine-4-carboxylic acid. n.d. = not detected. deg = degassed.

Table S5.46. C-C cross-couplings with different metal oxides and a non-binding nickel complex using the 525 nm setup.^a

Entry	semiconductor	Ar-Br:4 ^b
1	TiO ₂	0:1
2	Al ₂ O ₃	1:0
3	SiO ₂	1:0
4	-	1:0

^aReaction conditions: 4-bromobenzonitrile (190.3 μmol), 1-((trimethylsilyl)methyl)piperidine (228.3 μmol), N3 (1.25 mol%), NiBr₂·glyme (19.0 μmol) metal oxide (30 mg), and mcbpy (19.0 μmol) in DMAc (3 mL), 666 nm LED (100% power), 144 h. ^bDetermined by ¹HNMR. DMAc = dimethylacetamide. glyme = 1,2-dimethoxyethane. dtbbpy = 4,4'-di-tert-butyl-2,2'-dipyridyl. n.d. = not detected. deg = degassed.

5.5.9 Spectrophotometric titrations

Incremental amounts of NiCl₂·dcbpy or NiCl₂·dtbbpy were added while the concentration of Fluo-TiO₂ or Fluo-SiO₂ was kept constant. The fluorescence signals were corrected for re-absorption effects at the excitation wavelength and quantitatively analyzed.

Spectrophotometric titrations were conducted to analyze the electronic interactions between Fluo-MO (with MO = TiO₂ or SiO₂) and a nickel complex (NiCl₂·dcbpy or NiCl₂·dtbbpy) dispersed in DMSO. To this end, the absorption and emission features were monitored in dispersions with a constant concentration of Fluo-MO upon adding varying amounts of a nickel complex. The prominent absorption feature related to Fluo-MO with a maximum at 521 nm diminishes gradually upon stepwise addition of a nickel complex. The Fluo-MO related fluorescence, excited at 505 nm, is gradually quenched upon addition of the nickel complex (Fig. S27). The I₀/I relationship shows linear trends in all experiments except for the titration of Fluo-TiO₂ with NiCl₂·dcbpy, where a drastic increase of the slope was observed for NiCl₂·dcbpy concentrations > 7.3 × 10⁻⁷ M. A positive deviation from the initial linear relationship is typically described as mixed static and dynamic quenching, i.e. complex formation occurs to a certain degree. Association were determined from the linear parts of the I₀/I relationships and are summarized in Table S5.47.

Table S5.47. Association constants determined by spectrophotometric titrations.

	K_{ass} (dynamic) L mol⁻¹	K_{ass} (static) L mol⁻¹
Fluo-TiO ₂ - NiCl ₂ ·dcbpy	6.2 × 10 ⁶	6.2 × 10 ⁷
Fluo-TiO ₂ - NiCl ₂ ·dtbbpy	6.2 × 10 ⁶	
Fluo-SiO ₂ - NiCl ₂ ·dcbpy	1.5 × 10 ⁵	
Fluo-SiO ₂ - NiCl ₂ ·dtbbpy	7.0 × 10 ⁴	

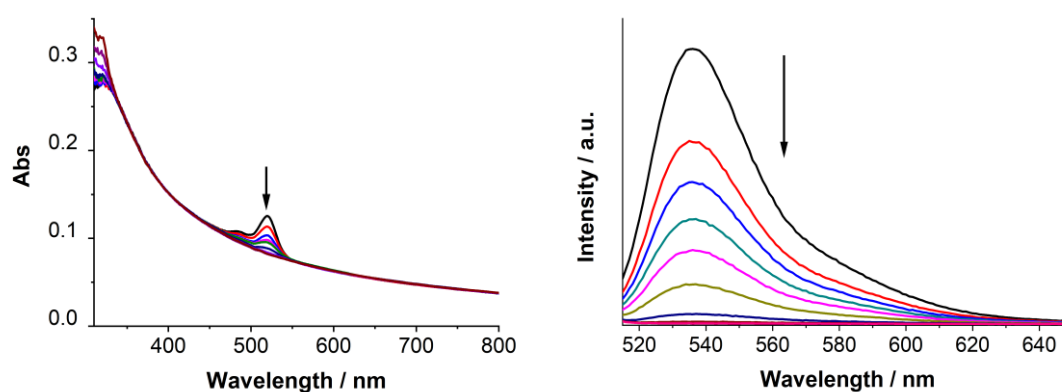


Figure S5.20. Left: absorption spectra of Fluo-TiO₂ dispersed in DMSO during the course of a titration with NiCl₂·dcbpy (black to purple, 0 – 2.6 × 10⁻⁶ M); Right: steady-state fluorescence spectra of Fluo-TiO₂ dispersed in DMSO during the course of a titration with NiCl₂·dcbpy (black to purple, 0 – 2.6 × 10⁻⁶ M);

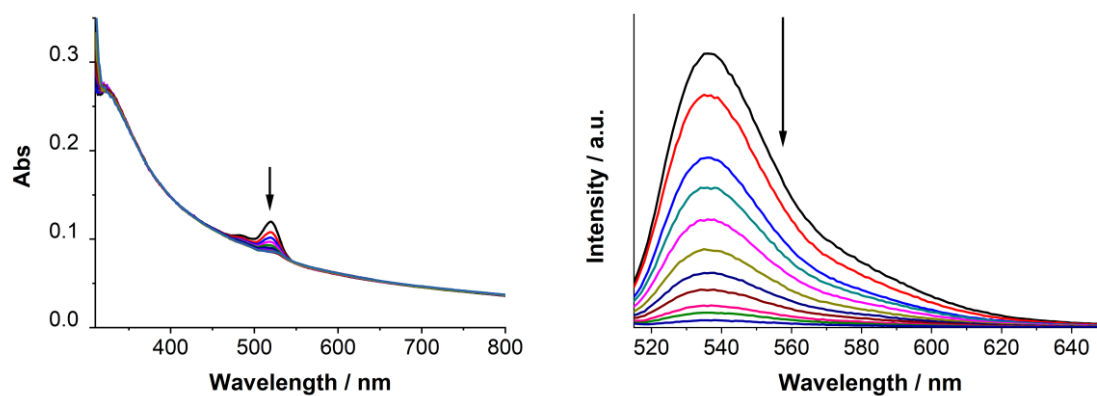


Figure S5.21. Left: absorption spectra of Fluo-TiO₂ dispersed in DMSO during the course of a titration with NiCl₂·dtbbpy (black to purple, 0 – 2.6 × 10⁻⁶ M); Right: steady-state fluorescence spectra ($\lambda_{\text{ex}} = 505$ nm) of Fluo-TiO₂ dispersed in DMSO during the course of a titration with NiCl₂·dtbbpy (black to purple, 0 – 2.6 × 10⁻⁶ M).

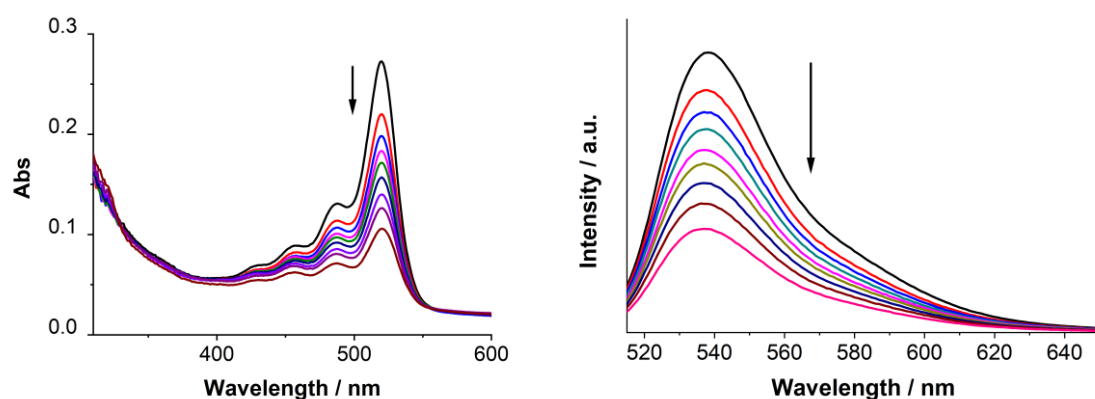


Figure S5.22. Left: absorption spectra of Fluo-SiO₂ dispersed in DMSO during the course of a titration with NiCl₂·dcbpy (black to purple, 0 – 1.6 × 10⁻⁶ M); Right: steady-state fluorescence spectra ($\lambda_{\text{ex}} = 505$ nm) of Fluo-SiO₂ dispersed in DMSO during the course of a titration with NiCl₂·dcbpy (black to purple, 0 – 1.6 × 10⁻⁶ M).

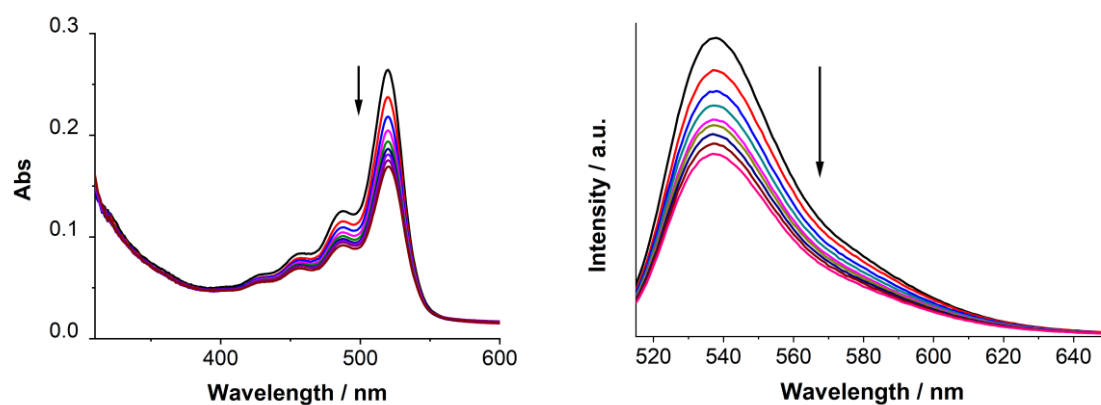


Figure S5.23. Left: absorption spectra of Fluo-SiO₂ dispersed in DMSO during the course of a titration with NiCl₂·dtbbpy (black to purple, 0 – 1.6 × 10⁻⁶ M); Right: steady-state fluorescence spectra ($\lambda_{\text{ex}} = 505$ nm) of Fluo-SiO₂ dispersed in DMSO during the course of a titration with NiCl₂·dtbbpy (black to purple, 0 – 1.6 × 10⁻⁶ M).

5.5.10 Comparison of metallaphotocatalyst systems for the C-O arylation of cinnamic acid.

An oven dried vial (19 x 100 mm) equipped with a stir bar was charged with *trans* cinnamic acid (84.5 mg, 570 μmol , 1.0 equiv), 4-iodobenzotrifluoride (125.6 μL , 855 μmol , 1.5 equiv), $\text{NiCl}_2 \cdot 6\text{H}_2\text{O}$ (57 μmol , 10 mol%) and 2,2'-bipyridine-4,4'-dicarboxylic acid (57 μmol , 10 mol%).

Three different homogeneous photocatalysts ($\text{Ir}[\text{dF}(\text{Me})\text{ppy}]_2(\text{dtbbpy})\text{PF}_6$ (5.17 μmol , 1.00 mol%), $\text{Ir}[\text{dF}(\text{CF}_3)\text{ppy}]_2(\text{dtbbpy})\text{PF}_6$ (5.17 μmol , 1.00 mol%), $\text{Ir}(\text{ppy})_3$ (5.17 μmol , 1.00 mol%) and the DSMP system (Fluorescein sodium (7.14 μmol , 1.25 mol%) + TiO_2 (90 mg)) were studied in individual reactions. DMSO (anhydrous, 6 mL) and *N*-tert-butylisopropylamine (BIPA, 271 μL , 1.2 mmol, 3 equiv) were added and the vial was sealed with a septum and Parafilm. The reaction mixture was sonicated for 5-10 min followed by stirring for 5 min to obtain a fine dispersion of the solids. The mixture was then degassed by bubbling Argon for 10 min. The mixture was irradiated with the respective LED lamp with rapid stirring (1400 rpm). After the respective reaction time, one equivalent of 1,3,5-trimethoxybenzene (internal standard 96 mg, 570 μmol) was added and the mixture was stirred for 5 min. An aliquot of the reaction mixture (~200 μL) was filtered, diluted with CDCl_3 , extracted with 1M HCl and subjected to $^1\text{H-NMR}$ analysis. For representative NMR spectra, see Figure S5.24.

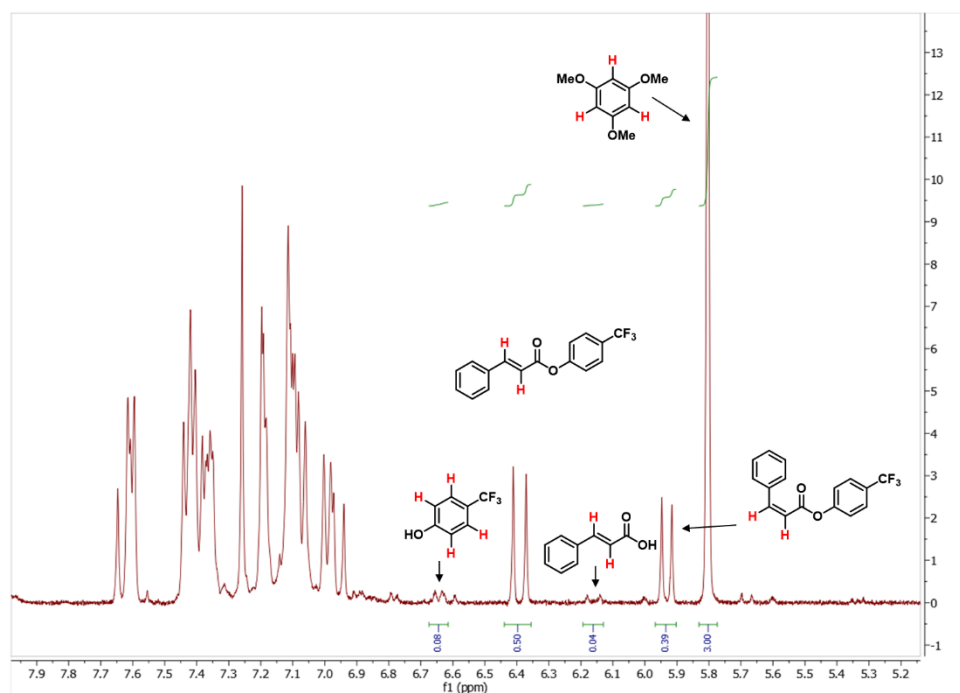


Figure S5.24. Representative $^1\text{H-NMR}$ spectrum of a crude reaction mixture for determining NMR yields in the DSMP catalyzed C-O arylation of cinnamic acid.

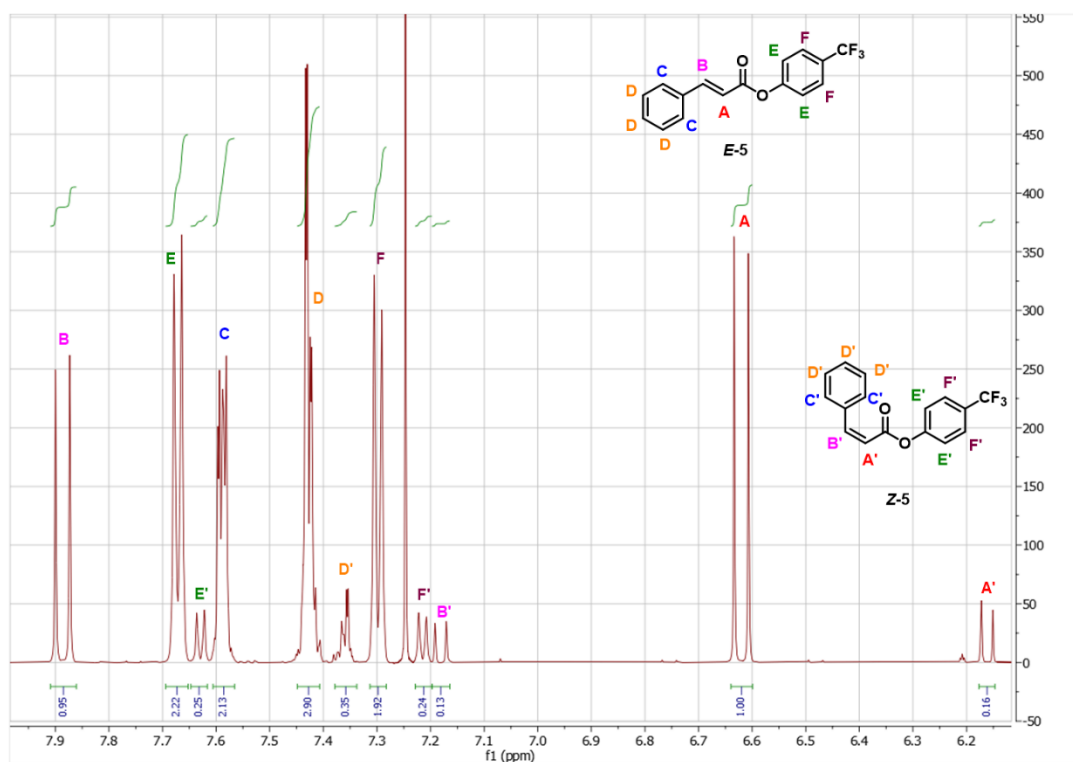
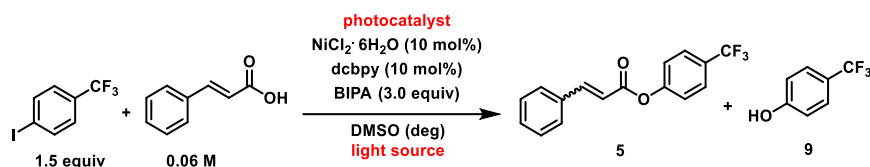


Figure S5.25. Representative $^1\text{H-NMR}$ spectrum of a crude reaction mixture of *E*- and *Z*-cinnamic acid.

Table S5.48. Comparison of metallaphotocatalyst systems for the C-O arylation of cinnamic acid.^a

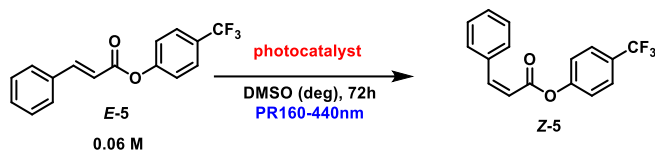
Entry	photocatalyst	Light source	Time	<i>E</i> -5	<i>Z</i> -5	9
		[nm]	[h]	[%] ^c	[%] ^c	[%] ^c
1	TiO ₂ (30 mg) + NaFluo (1.25 mol%)	525	72	95	n.d.	3
2	TiO ₂ (30 mg) + NaFluo (1.25 mol%)	440	35	74	24	6
3	Ir[dF(Me)ppy] ₂ (dtbbpy))PF ₆ (1.00 mol%)	440	1	52	36	9
4	Ir[dF(CF ₃)ppy] ₂ (dtbpy))PF ₆ (1.00 mol%)	440	1	48	38	16
5	Ir(ppy) ₃ (1.00 mol%)	440	1	70	22	20
6	Ir(ppy) ₃ (1.00 mol%)	525	2	76	22	6

^aReaction conditions: 4-Iodobenzotrifluoride (285.4 μmol), *trans*-cinnamic acid (190.3 μmol), Ir catalyst (1.90 μmol), Fluorescein sodium (2.4 μmol), TiO₂ (30 mg), NiCl₂·6H₂O (19.0 μmol) and dc bpy (19.0 μmol) in DMSO (anhydrous, 3 mL), BIPA (570.8 μmol), 440 nm blue LED (100% power) at RT. ^cNMR yields determined by ¹H-NMR using 1,3,5-trimethoxybenzene as internal standard. ^d525 nm LED (100%) instead of 440 nm LED. NaFluo = Fluorescein sodium. dc bpy = 2,2'-bipyridine-4,4'-dicarboxylic acid. BIPA = *N*-*tert*-butylisopropylamine. n.d. = not detected. deg = degassed

The reaction from 5.48, Entry 1 was isolated on a larger scale for product characterization: An oven dried vial (19 x 100 mm) equipped with a stir bar was charged with *trans* cinnamic acid (84.5 mg, 570 μmol , 1.0 equiv), 4-iodobenzotrifluoride (125.6 μL , 855 μmol , 1.5 equiv), $\text{NiCl}_2 \cdot 6\text{H}_2\text{O}$ (13.6 mg, 57 μmol , 10 mol%), 2,2'-bipyridine-4,4'-dicarboxylic acid (dcbpy, 13.9 mg, 57 μmol , 10 mol%), fluorescein sodium (7.14 μmol , 1.25 mol%), and TiO_2 (90 mg). DMSO (anhydrous, 6 mL) and *N*-tert-butylisopropylamine (BIPA, 271 μL , 1.2 mmol, 3 equiv) were added and the vial was sealed with a septum and Parafilm. The reaction mixture was sonicated for 5-10 min followed by stirring for 5 min to obtain a fine dispersion of the solids. The mixture was then degassed by bubbling Argon for 10 min. The mixture was irradiated with the respective LED lamp with rapid stirring (1400 rpm). After the respective reaction time, one equivalent of 1,3,5-trimethoxybenzene (internal standard 96 mg, 570 μmol) was added and the mixture was stirred for 5 min. An aliquot of the reaction mixture (~200 μL) was filtered, diluted with CDCl_3 , extracted with 1M HCl and subjected to ^1H -NMR analysis. The NMR sample was combined with the reaction mixture, diluted with H_2O (40 mL) and extracted with dichloromethane (3 x 30 mL). The combined organic phases were washed with brine (50 mL), dried over Na_2SO_4 and concentrated. The product was purified by flash column chromatography (SiO_2 , Hexane/EtOAc elution gradient of 0-20%) on a Grace Reveleris system using a 12 g cartridge. The title compound was isolated as a white solid in 90% yield (Reaction time: 72 h, 149.92 mg, 513.0 μmol).

***E*-4-(Trifluoromethyl)phenyl cinnamate *E*-5:** ^1H NMR (400 MHz, CDCl_3) δ . 7.92 (d, J = 16.0 Hz, 1H), 7.69 (d, J = 8.4 Hz, 2H), 7.61 (dt, J = 6.7, 2.3 Hz, 2H), 7.45 (dd, J = 5.1, 2.0 Hz, 3H), 7.32 (d, J = 8.2 Hz, 2H), 6.65 (d, J = 16.0 Hz, 1H). ^{13}C NMR (101 MHz, CDCl_3) δ 164.92, 153.42, 147.53, 134.05, 131.10, 129.17, 128.51, 128.26 (s, J = 32.74 Hz), 126.89 (q, J = 3.8 Hz), 125.39 (s, J = 272.17 Hz), 122.27, 116.7. ^{19}F NMR (377 MHz, CDCl_3) δ -62.21 ppm. HRMS-EI (m/z) $[\text{M}^*]^+$ calcd for $\text{C}_{16}\text{H}_{11}\text{F}_3\text{O}_2$: 292.0711; found: 292.0718.

These data are in full agreement with those previously published in the literature.¹⁰

Table S5.49. Control studies isomerization of 4-(Trifluoromethyl)phenyl cinnamate.^a

Entry	photocatalyst	<i>E</i> -5 : <i>Z</i> -5 ^c
1	--	1 : 0.16
2	-- ^d	1:0
3	NaFluo (1.25 mol%)	1 : 0.11
4	TiO ₂ (30 mg)	1 : 0.12

^aReaction conditions: *E*-4-(Trifluoromethyl)phenyl cinnamate (190.3 μmol), Fluorescein sodium (2.4 μmol), TiO₂ (30 mg), in DMSO (anhydrous, 3 mL), 440 nm blue LED (100% power), 72h. ^c Determined by ¹HNMR. NaFluo = Fluorescein sodium. n.d. = not detected. deg = degassed. ^d525 nm LED (100% power), 72h.

5.5.1 References

1. Neuthe, K.; Bittner, F.; Stiemke, F.; Ziem, B.; Du, J.; Zellner, M.; Wark, M.; Schubert, T.; Haag, R., Phosphonic acid anchored ruthenium complexes for ZnO-based dye-sensitized solar cells. *Dyes Pigments* **2014**, *104*, 24-33.
2. Shigeta, Y.; Kobayashi, A.; Yoshida, M.; Kato, M., Crystal Engineering of Vapochromic Porous Crystals Composed of Pt(II)-Diimine Luminophores for Vapor-History Sensors. *Crys. Growth. Des.* **2018**, *18* (6), 3419-3427.
3. Brown, H. C.; Kanth, J. V. B.; Dalvi, P. V.; Zaidlewicz, M., Molecular Addition Compounds. 15. Synthesis, Hydroboration, and Reduction Studies of New, Highly Reactive tert-Butyldialkylamine-Borane Adducts. *J. Org. Chem.* **1999**, *64* (17), 6263-6274.
4. Remeur, C.; Kelly, C. B.; Patel, N. R.; Molander, G. A., Aminomethylation of Aryl Halides Using α -Silylamines Enabled by Ni/Photoredox Dual Catalysis. *ACS Catal.* **2017**, *7* (9), 6065-6069.
5. <https://www.kessil.com/photoreaction/index.php>
6. Pieber, B.; Malik, J. A.; Cavedon, C.; Gisbertz, S.; Savateev, A.; Cruz, D.; Heil, T.; Zhang, G.; Seeberger, P. H., Semi-heterogeneous Dual Nickel/Photocatalysis using Carbon Nitrides: Esterification of Carboxylic Acids with Aryl Halides. *Angew. Chem. Int. Ed.* **2019**, *58* (28), 9575-9580.
7. Gisbertz, S.; Pieber, B., Heterogeneous Photocatalysis in Organic Synthesis. *ChemPhotoChem* **2020**, *4*, 1-21.
8. Cavedon, C.; Madani, A.; Seeberger, P. H.; Pieber, B., Semiheterogeneous Dual Nickel/Photocatalytic (Thio)etherification Using Carbon Nitrides. *Org. Lett.* **2019**, *21* (13), 5331-5334.
9. Gisbertz, S.; Reischauer, S.; Pieber, B., Overcoming Limitations in Dual Photoredox/Nickel catalyzed C–N Cross-Couplings due to Catalyst Deactivation. *Nat. Catal.* **2020**, *3*, 611–620.
10. Ahlin, J. S. E.; Donets, P. A.; Cramer, N., Nickel(0)-Catalyzed Enantioselective Annulations of Alkynes and Arylenoates Enabled by a Chiral NHC Ligand: Efficient Access to Cyclopentenones. *Angew. Chem. Int. Ed.* **2014**, *53* (48), 13229-13233.

Supporting Information - Chapter 6

Recyclable, bifunctional metallaphotocatalysts for C-S cross-couplings

Reischauer, S.; Pieber, B.

ChemPhotoChem, **2021**, *5*, 716-720.

<https://doi.org/10.1002/cptc.202100062>

6.5 Supporting information

6.5.1 General remarks

Substrates, reagents, and solvents were purchased from commercial suppliers and used without further purification. Titanium dioxide Aeroxide P25 (Acros), Bismuth oxide powder (Fisher), Bismuth oxide nanopowder (Fisher) and Cadmiumsulfid powder (Aldrich) were used. CN-OA-m¹, mpg-CN², *N-tert*-butylisopropylamine (BIPA)³, and Ru(bpy)₂(dpbpy)⁴ were prepared according to literature procedures. LED lamps for photocatalytic experiments were purchased from Kessil Lightning.⁵ ¹H-, ¹³C-, and ³¹P spectra were recorded on an Ascend™ 400 spectrometer (400 MHz, Bruker) and a Varian 600 spectrometer (600 MHz, Agilent) at 298 K, and are reported in ppm relative to the residual solvent peaks. Peaks are reported as: s = singlet, d = doublet, t = triplet, q = quartet, m = multiplet or unresolved, with coupling constants in Hz. Purification of final compounds was carried out by flash chromatography on the Reveleris X2 Flash Chromatography System from GRACE using prepacked columns with 40 μm silica gel. Silica 60 M (0.04-0.063 mm). Silica gel (Sigma Aldrich) was used for dry loading of the crude compounds on the flash chromatography system. Centrifugation was carried out using an Eppendorf 5430 centrifuge. UV/Vis spectra of liquid samples were recorded using a UV-1900 spectrometer (Shimadzu). Diffuse reflectance UV/Vis spectra of powders were recorded on a Shimadzu UV-2600 spectrometer equipped with an integrating sphere. Inductively coupled plasma - optical emission spectrometry (ICP-OES) was carried out using a Horiba Ultra 2 instrument equipped with a photomultiplier tube detection system. Scanning electron microscopy (SEM) images were obtained on a LEO 1550-Gemini microscope. Energy-dispersive X-ray (EDX) investigations were conducted on a Link ISIS-300 system (Oxford Microanalysis Group) equipped with a Si(Li) detector and an energy resolution of 133 eV.

6.5.1.1. 440 nm setup

Experiments using blue light were carried out using a Kessil PR160L-440 LED (Figure S6.1). Two sealed reaction vessels were placed on a stirring plate 4.5 cm away from a single lamp. To avoid heating of the reaction mixture, a fan was used for cooling. All reactions were performed with maximum stirring speed.

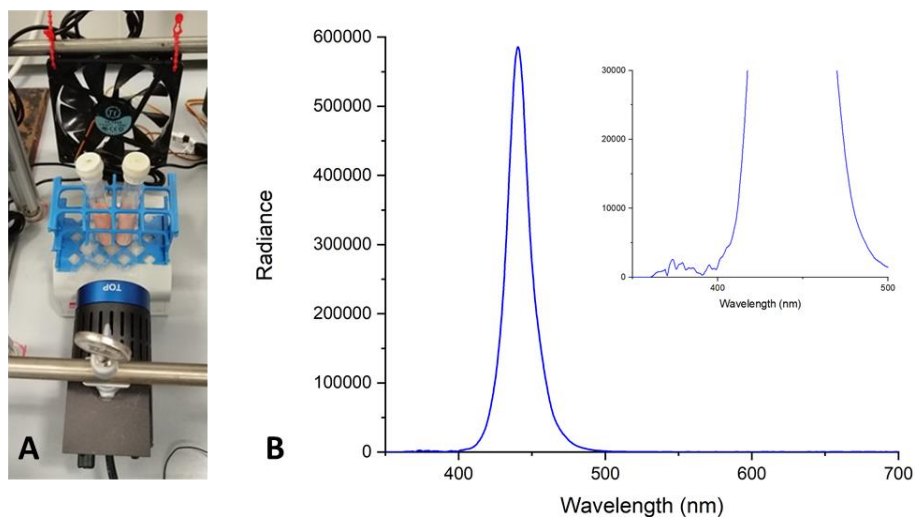


Figure S6.1. Setup for blue light experiments (A). Emission spectra of the Kessil PR160L-440 (B)

6.5.1.2. 525 nm setup

Experiments using green light were carried out using a Kessil PR160L-525 LED (Figure S6.2). Two sealed reaction vessels were placed on a stirring plate 4.5 cm away from a single lamp. To avoid heating of the reaction mixture, a fan was used for cooling. All reactions were performed with maximum stirring speed.

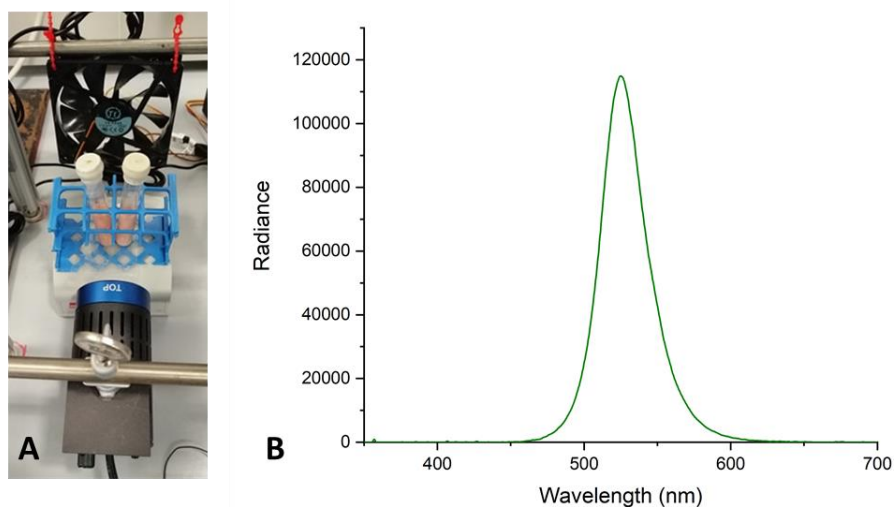


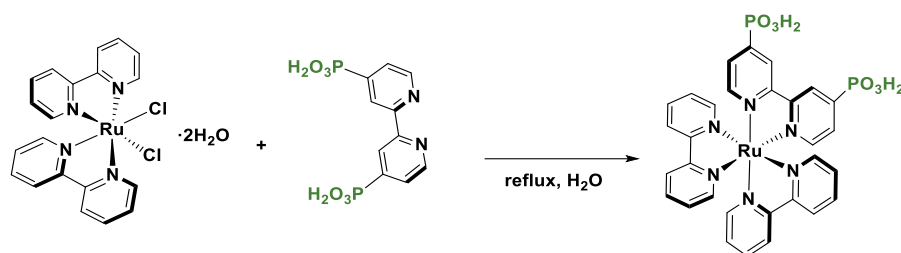
Figure S6.2. Setup for green light experiments (A). Emission spectra of the Kessil PR160L-525 (B).

6.5.2 Preparation of CN-OA-m

The synthesis for CN-OA-m was carried out using a slightly adapted version of the literature procedure (Scheme 6.1).¹ For each batch of the photocatalyst, urea (10 g, 166.5 mmol) and oxamide (0.5 g, 5.7 mmol) were mixed in 10 mL of H₂O to obtain a homogeneous mixture. After drying at 373 K, the resulting solids were grinded, transferred into a crucible with a cover and heated up in an air-oven with a heating rate of 4.3 K/min to 773 K. After keeping the mixture for 2 h at 773 K, the sample was allowed to cool to room temperature. Subsequently, KCl (3.3 g, 44.3 mmol) and LiCl (2.7 g, 63.7 mmol) were added and the solids were grinded to obtain a homogeneous mixture which was heated in an inert atmosphere (N₂ flow: 5 mL/min) to 823 K with a heating rate of 4.6 K/min. After keeping the mixture for 2 h at 823 K, the sample was allowed to cool to room temperature and the resulting solids were collected on a filter paper and washed with H₂O (3 x 100 mL). The resulting yellow material was dried at 373 K.

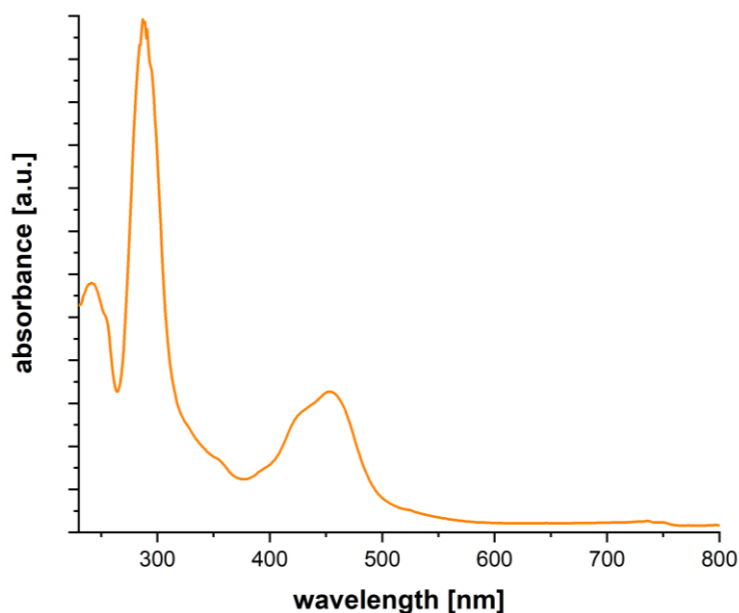
6.5.3 Preparation of mpg-CN

The synthesis for mpg-CN was carried out using the literature procedure.² Molten cyanamide (1g, 24 mmol) and 40% dispersion of 12 nm SiO₂ in water were mixed. The resulting mixture was transferred into a crucible with a cover and heated up in an air-oven with a heating rate of 4.3 °Cmin⁻¹ to 550°C. After keeping the mixture for 4h at 550°C, the sample was allowed to cool to room temperature. Then the sample was heated to 600°C for 10 h under static vacuum. Finally, the powder was treated with 4 M NH₄HF₂ to remove the silica template. The powder was separated by centrifugation, washed three times with water and twice with ethanol and dried in a 70°C oven for several hours.

6.5.4 Synthesis of Ru(bpy)₂(dpbpy)Scheme S6.1. Synthesis of Ru(bpy)₂(dpbpy)

RuCl₂bpy₂·2H₂O (21 mg, 0.041 mmol, 1.00 equiv.) was dissolved in water (15 mL) and [2,2'-bipyridine]-4,4'-diyl diphosphonic acid (dpbpy) (13 mg, 0.041 mmol, 1.0 equiv.) was added. The mixture was refluxed for 24 h. The solvent was removed in vacuo and acetone was added (8 mL). The resulting solution was stored at 7°C over night. The formed crystals were filtered and washed with cold acetone. The title compound was isolated as dark purple crystals (14.1 mg, 0.019 mmol, 47%).

Ru(bpy)₂(dpbpy): ¹H NMR (600 MHz, D₂O) δ 8.77 (d, *J* = 12.6 Hz, 2H), 8.54 (d, *J* = 8.3 Hz, 4H), 8.07 (t, *J* = 7.9 Hz, 4H), 7.94 (dd, *J* = 5.7, 3.3 Hz, 2H), 7.81 (dd, *J* = 13.8, 5.6 Hz, 4H), 7.58 (dd, *J* = 11.6, 5.8 Hz, 2H), 7.39 (t, *J* = 6.7 Hz, 4H). ³¹P (243 MHz, D₂O) δ 6.75.

Figure S6.3. UV-Vis spectrum of Ru(bpy)₂(dpbpy)

These data are in full agreement with those previously published in the literature.⁴

6.5.4 C–S cross coupling

6.5.4.1 Optimization studies using *in situ* generated bifunctional catalysts.

An oven dried vial (19 x 100 mm) equipped with a stir bar was charged with the respective semiconductor (5–30 mg, 1.67–10 mg/ml), methyl 4-iodobenzoate (49.79 mg, 190.3 μmol , 1.0 equiv), methyl 3-mercaptopropionate (42.1 μL , 380.5 μmol , 2.0 equiv), $\text{NiBr}_2 \cdot 3\text{H}_2\text{O}$ (2.59–5.18 mg, 9.5–19.0 μmol , 5–10 mol%), [2,2'-bipyridine]-4,4'-diyldiphosphonic acid (3.0–6.0 mg, 9.5–19.0 μmol , 5–10 mol%), optionally, $\text{Ru}(\text{bpy})_2(\text{dpbpy})$ (1.74 mg, 2.4 μmol , 1.25 mol%). Subsequently, MeCN (anhydrous, 3 mL) and *N*-tert-butylisopropylamine (BIPA, 150.7 μL , 951.5 μmol , 5 equiv) were added and the vial was sealed with a septum and Parafilm. The reaction mixture was sonicated for 5–10 min followed by stirring for 5 min to obtain a fine dispersion. The mixture was degassed by bubbling Argon for 10 min. The mixture was irradiated with the respective LED lamps with rapid stirring (1400 rpm). After the respective reaction time, one equivalent of 1,3,5-trimethoxybenzene (internal standard, 32 mg, 190.3 μmol , 1.0 equiv) was added. An aliquot of the reaction mixture (~200 μL) was filtered, diluted with DMSO-d_6 and subjected to $^1\text{H-NMR}$ analysis. For a representative NMR spectrum, see Figure S6.4.

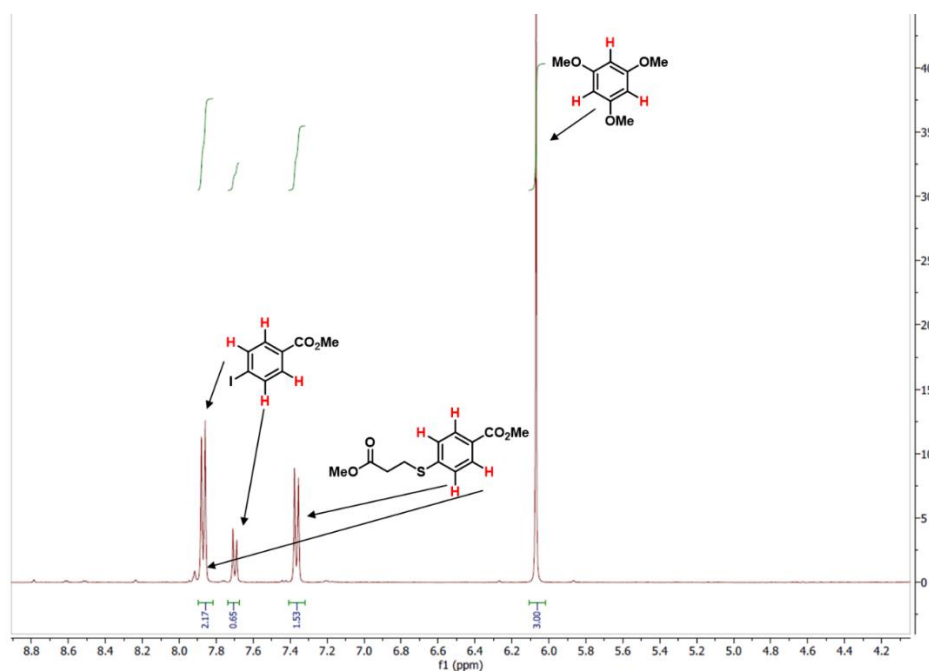
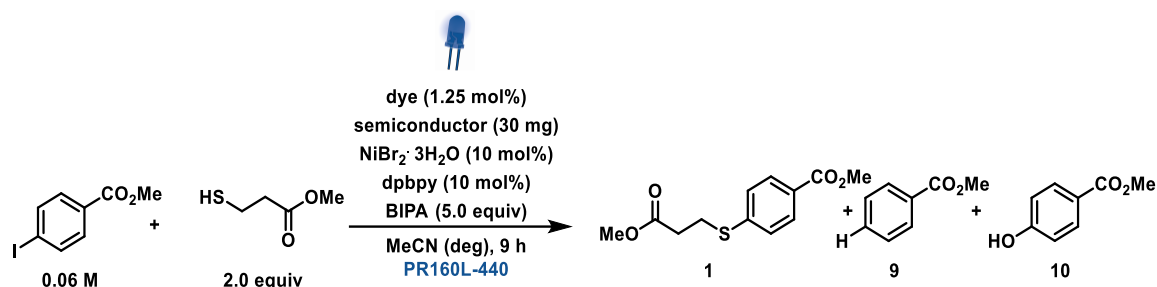


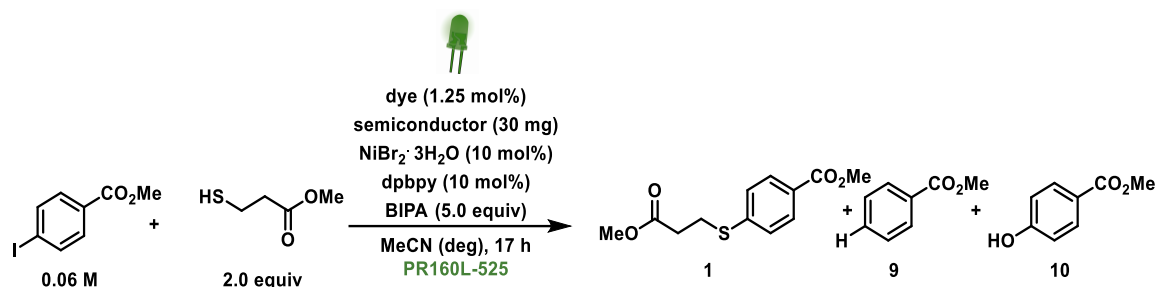
Figure S6.4. Representative $^1\text{H-NMR}$ spectrum of a crude reaction mixture for determining NMR yields in the C–S arylation.

6.5.4.2 Semiconductor screening

Table S6.1. Semiconductor screening using the 440 nm LED setup.^a

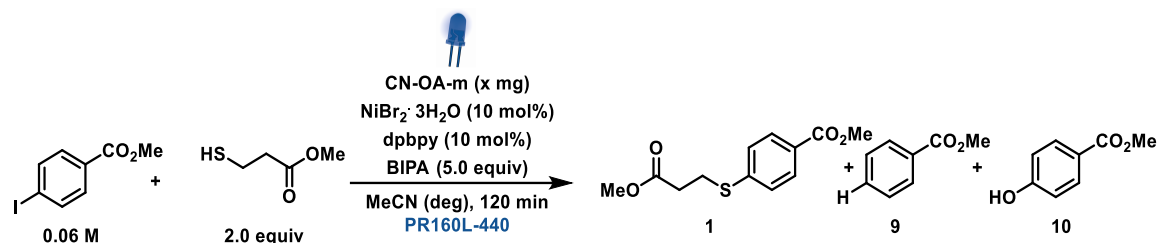
Entry	Semiconductor	Conversion [%] ^b	1 [%] ^c	9 [%] ^c	10 [%] ^c
1	CN-OA-m	quant.	99	n.d.	traces
2	mpg-CN	quant	99	n.d.	traces
3	TiO ₂	39	38	n.d.	traces
4	Ru(bpy) ₂ (dpbpy)-TiO ₂	quant	99	n.d.	traces
5	CdS	55	45	n.d.	traces
6	Bi ₂ O ₃	1	n.d.	n.d.	traces
7	Bi ₂ O ₃ nanopowder	2	n.d.	n.d.	traces

^aReaction conditions: methyl 4-iodobenzoate (190.3 μmol), methyl 3-mercaptopropionate (380.5 μmol), dye (2.4 μmol), NiBr₂·3H₂O (19.0 μmol), semiconductor (30 mg), dpbpy (19.0 μmol) and BIPA (951.5 μmol) in MeCN (3 mL), 440 nm LED (100% power), 9 h. ^bConversion of methyl 4-iodobenzoate determined by ¹H-NMR using 1,3,5-trimethoxybenzene as internal standard. ^cNMR yields determined by ¹H-NMR using 1,3,5-trimethoxybenzene as internal standard. BIPA = *N*-tert-butylisopropylamine. dpbpy = [2,2'-bipyridine]-4,4'-diylidiphosphonic acid. n.d. = not detected. deg = degassed. quant. = quantitative.

Table S6.2. Semiconductor screening using the 525 nm LED setup.^a

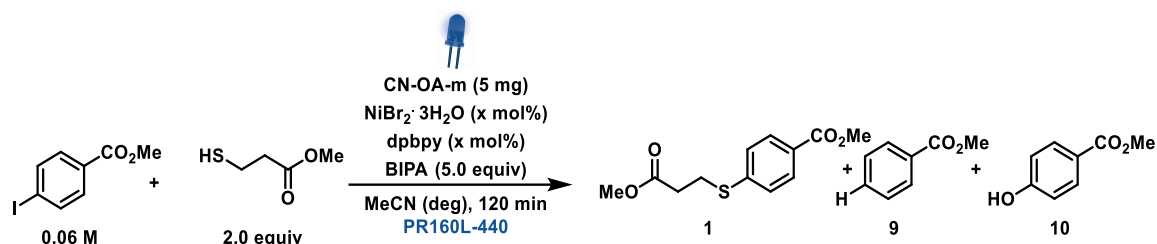
Entry	Semiconductor	Conversion [%] ^b	1 [%] ^c	9 [%] ^c	10 [%] ^c
1	CN-OA-m	quant.	99	n.d.	n.d.
2	CN-OA-m ^d	quant.	99	n.d.	n.d.
3	mpg-CN	5	4	n.d.	traces
4	TiO ₂	13	5	n.d.	traces
5	Ru(bpy) ₂ (dpbpy)-TiO ₂	71	69	n.d.	traces
6	CdS	21	20	n.d.	traces
7	Bi ₂ O ₃	2	n.d.	n.d.	traces
8	Bi ₂ O ₃ nanopowder	2	n.d.	n.d.	traces

^aReaction conditions: methyl 4-iodobenzoate (190.3 μmol), methyl 3-mercaptopropionate (380.5 μmol), dye (2.4 μmol), NiBr₂·3H₂O (19.0 μmol), semiconductor (30 mg), and dpbpy (19.0 μmol), BIPA (951.5 μmol) in MeCN (3 mL), 525 nm LED (100% power), 17 h. ^bConversion of methyl 4-iodobenzoate determined by ¹H-NMR using 1,3,5-trimethoxybenzene as internal standard. ^cNMR yields determined by ¹H-NMR using 1,3,5-trimethoxybenzene as internal standard. ^d10mg CN-OA-m were used. BIPA = *N-tert*-butylisopropylamine. dpbpy = [2,2'-bipyridine]-4,4'-diyldiphosphonic acid. n.d. = not detected. deg = degassed. quant. = quantitative.

6.5.4.3 CN-OA-m–NiBr₂·dpbpy (Cat 1)Table S6.3. Optimization of the amount of CN-OA-m using the 440 nm LED setup.^a

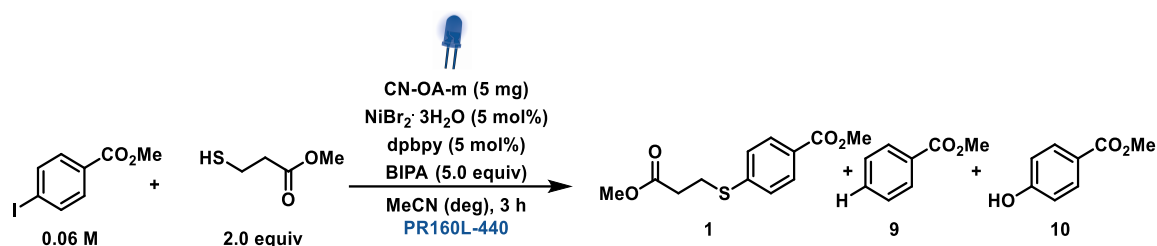
Entry	CN-OA-m	Conversion [%] ^b	1 [%] ^c	9 [%] ^c	10 [%] ^c
1	5 mg	90	91	n.d.	traces
2	5 mg ^d	quant.	99	n.d.	traces
3	10 mg	85	86	n.d.	n.d.
4	20 mg	85	85	n.d.	n.d.
5	30 mg	87	86	n.d.	n.d.

^aReaction conditions: methyl 4-iodobenzoate (190.3 μmol), methyl 3-mercaptopropionate (380.5 μmol), NiBr₂·3H₂O (19.0 μmol), CN-OA-m (x mg), dpbpy (19.0 μmol) and BIPA (951.5 μmol) in MeCN (3 mL), 440 nm LED (100% power), 2 h. ^bConversion of methyl 4-iodobenzoate determined by ¹H-NMR using 1,3,5-trimethoxybenzene as internal standard. ^cNMR yields determined by ¹H-NMR using 1,3,5-trimethoxybenzene as internal standard. ^d3 h reaction time. BIPA = *N-tert*-butylisopropylamine. dpbpy = [2,2'-bipyridine]-4,4'-diyldiphosphonic acid. n.d. = not detected. deg = degassed. quant. = quantitative.

Table S6.4. Optimization of the amount of NiBr₂·H₂O and ligand loading using the 440 nm LED setup.^a

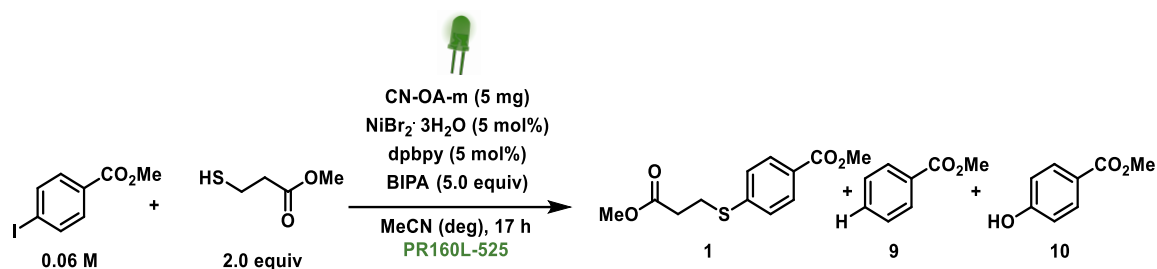
Entry	Ni & L	Conversion [%] ^b	1 [%] ^c	9 [%] ^c	10 [%] ^c
1	10 mol%	90	91	n.d.	traces
2	7.5 mol%	96	96	n.d.	traces
3	5 mol%	93	93	n.d.	traces
4	5 mol% ^d	quant.	99	n.d.	traces

^aReaction conditions: methyl 4-iodobenzoate (190.3 μmol), methyl 3-mercaptopropionate (380.5 μmol), NiBr₂·3H₂O, CN-OA-m (5 mg) dpbpy and BIPA (951.5 μmol) in MeCN (3 mL), 440 nm LED (100% power), 2 h. ^bConversion of methyl 4-iodobenzoate determined by ¹H-NMR using 1,3,5-trimethoxybenzene as internal standard. ^cNMR yields determined by ¹H-NMR using 1,3,5-trimethoxybenzene as internal standard. ^d3 h reaction time. BIPA = *N*-tert-butylisopropylamine. dpbpy = [2,2'-bipyridine]-4,4'-diylidiphosphonic acid. n.d. = not detected. deg = degassed. quant. = quantitative.

Table S6.5. Optimized conditions and control studies using the 440 nm setup.^a

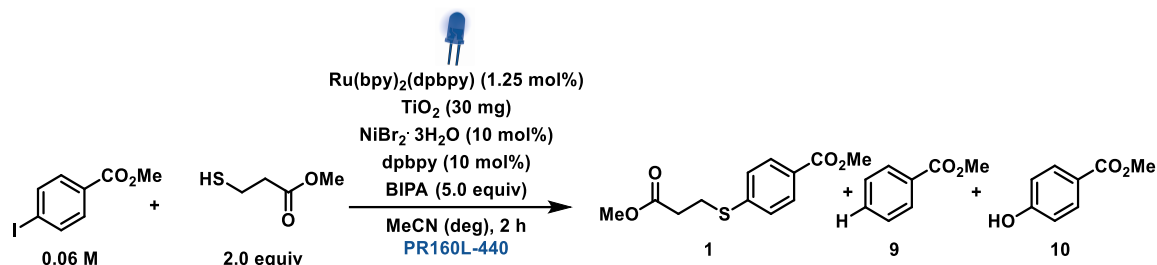
Entry	Deviation from				
	standard conditions	Conversion [%] ^b	1 [%] ^c	9 [%] ^c	10 [%] ^c
1	--	quant.	99	n.d.	n.d.
2	no CN-OA-m	4	n.d.	n.d.	n.d.
3	no dpbpy	6	n.d.	n.d.	n.d.
4	no NiBr ₂ ·3H ₂ O	16	16	n.d.	n.d.
5	no BIPA	3	n.d.	n.d.	n.d.
6	no degassing	6	2	n.d.	4
7	no light	2	n.d.	n.d.	n.d.

^aReaction conditions: methyl 4-iodobenzoate (190.3 μmol), methyl 3-mercaptopropionate (380.5 μmol), NiBr₂·3H₂O (9.5 μmol), CN-OA-m (5 mg) dpbpy (9.5 μmol) and BIPA (951.5 μmol) in MeCN (3 mL), 440 nm LED (100% power), 3 h. ^bConversion of methyl 4-iodobenzoate determined by ¹H-NMR using 1,3,5-trimethoxybenzene as internal standard. ^cNMR yields determined by ¹H-NMR using 1,3,5-trimethoxybenzene as internal standard. BIPA = *N-tert*-butylisopropylamine. dpbpy = [2,2'-bipyridine]-4,4'-diylidiphosphonic acid. n.d. = not detected. deg = degassed. quant. = quantitative.

Table S6.6. Optimized conditions and control studies using the 525 nm setup.^a

Entry	Deviation from standard conditions	Conversion [%] ^b	1 [%] ^c	9 [%] ^c	10 [%] ^c
1	--	quant.	99	n.d.	n.d.
2	methyl 4-bromobenzoate	14	11	n.d.	n.d.
3	no CN-OA-m	0	n.d.	n.d.	n.d.
4	no dpbpy	0	n.d.	n.d.	n.d.
5	no NiBr ₂ ·3H ₂ O	11	10	n.d.	n.d.
6	no BIPA	7	n.d.	n.d.	n.d.
7	no degassing	6	4	n.d.	traces
8	no light	5	n.d.	n.d.	traces

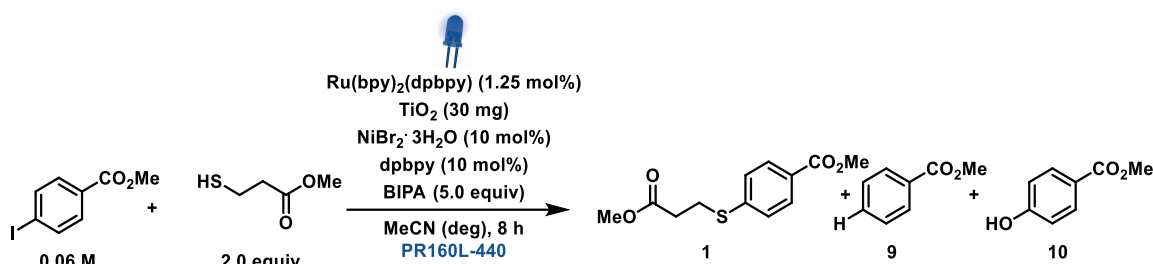
^aReaction conditions: methyl 4-iodobenzoate (190.3 μmol), methyl 3-mercaptopropionate (380.5 μmol), NiBr₂·3H₂O (9.5 μmol), CN-OA-m (5 mg) dpbpy (9.5 μmol) and BIPA (951.5 μmol) in MeCN (3 mL), 525 nm LED (200% power), 17 h. ^bConversion of methyl 4-iodobenzoate determined by ¹H-NMR using 1,3,5-trimethoxybenzene as internal standard. ^cNMR yields determined by ¹H-NMR using 1,3,5-trimethoxybenzene as internal standard. BIPA = *N*-*tert*-butylisopropylamine. dpbpy = [2,2'-bipyridine]-4,4'-diylidiphosphonic acid. n.d. = not detected. deg = degassed. quant. = quantitative.

6.5.4.4 Ru(bpy)₂(dpbpy)–TiO₂–NiBr₂·dpbpy (Cat 2)Table S6.7. Initial experiments using the 440 nm LED setup.^a

Entry	Variations	Conversion [%] ^b	1 [%] ^c	9 [%] ^c	10 [%] ^c
1	--	58	56	n.d.	n.d.
2	8h	quant.	99	n.d.	traces
3	no TiO ₂	15	15	n.d.	traces

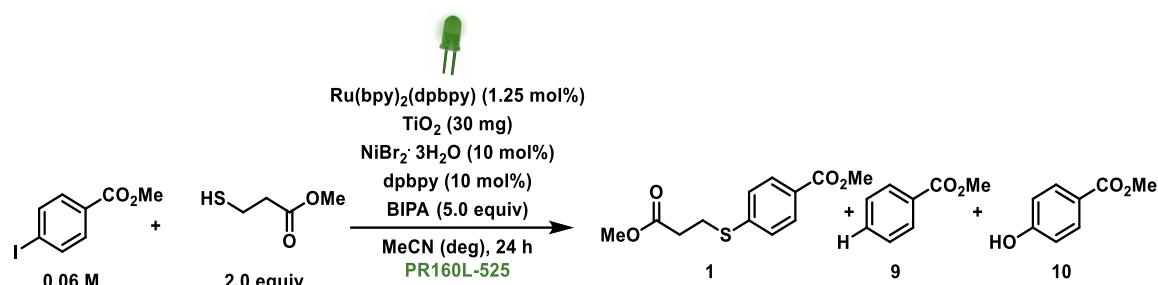
^aReaction conditions: methyl 4-iodobenzoate (190.3 μmol), methyl 3-mercaptopropionate (380.5 μmol), NiBr₂·3H₂O (19.0 μmol), Ru(bpy)₂(dpbbpy) (1.25mol%), TiO₂ (30 mg) dpbpy (19.0 μmol) and BIPA (951.5 μmol) in MeCN (3 mL), 440 nm LED (100% power), 2 h.

^bConversion of methyl 4-iodobenzoate determined by ¹H-NMR using 1,3,5-trimethoxybenzene as internal standard. ^cNMR yields determined by ¹H-NMR using 1,3,5-trimethoxybenzene as internal standard. BIPA = *N-tert*-butylisopropylamine. dpbpy = [2,2'-bipyridine]-4,4'-diylidiphosphonic acid. n.d. = not detected. deg = degassed. quant. = quantitative.

Table S6.8. Optimized conditions and control studies using the 440 nm setup.^a

Entry	Deviation from standard conditions	Conversion [%] ^b	1 [%] ^c	9 [%] ^c	10 [%] ^c
1	--	quant.	99	n.d.	traces
2	no TiO ₂	43	39	n.d.	traces
3	no dye	72	71	n.d.	traces
4	no dpbpy	2	n.d.	n.d.	traces
5	no NiBr ₂ ·3H ₂ O	20	traces	n.d.	traces
6	no BIPA	2	n.d.	n.d.	traces
7	no degassing	4	traces	n.d.	traces
8	no light	3	n.d.	n.d.	traces

^aReaction conditions: methyl 4-iodobenzoate (190.3 μmol), methyl 3-mercaptopropionate (380.5 μmol), dye (2.4 μmol), NiBr₂·3H₂O (19.0 μmol), TiO₂ (30 mg) dpbpy (19.0 μmol) and BIPA (951.5 μmol) in MeCN (3 mL), 440 nm LED (100% power), 8 h. ^bConversion of methyl 4-iodobenzoate determined by ¹H-NMR using 1,3,5-trimethoxybenzene as internal standard. ^cNMR yields determined by ¹H-NMR using 1,3,5-trimethoxybenzene as internal standard. BIPA = *N-tert*-butylisopropylamine. dpbpy = [2,2'-bipyridine]-4,4'-diyldiphosphonic acid. n.d. = not detected. deg = degassed. quant. = quantitative.

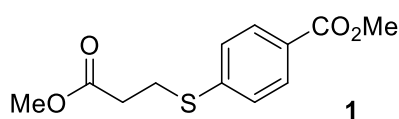
Table S6.9. Optimized conditions and control studies using the 525 nm setup.^a

Entry	Deviation from standard conditions	Conversion [%] ^b	1 [%] ^c	9 [%] ^c	10 [%] ^c
1	--	quant.	99	n.d.	traces
2	no TiO ₂	25	23	n.d.	traces
3	No dye	3	n.d.	n.d.	traces
4	no dpbbp	2	n.d.	n.d.	traces
5	no NiBr ₂ ·3H ₂ O	10	traces	n.d.	traces
6	no BIPA	5	n.d.	n.d.	traces
7	no degassing	2	n.d.	n.d.	traces
8	no light	0	n.d.	n.d.	traces

^aReaction conditions: methyl 4-iodobenzoate (190.3 μmol), methyl 3-mercaptopropionate (380.5 μmol), dye (2.4 μmol), NiBr₂·3H₂O (19.0 μmol), TiO₂ (30 mg), dpbbp (19.0 μmol) and BIPA (951.5 μmol) in MeCN (3 mL), 525 nm LED (200% power), 24 h. ^bConversion of methyl 4-iodobenzoate determined by ¹H-NMR using 1,3,5-trimethoxybenzene as internal standard. ^cNMR yields determined by ¹H-NMR using 1,3,5-trimethoxybenzene as internal standard. BIPA = *N*-tert-butylisopropylamine. dpbbp = [2,2'-bipyridine]-4,4'-diylidiphosphonic acid. n.d. = not detected. deg = degassed. quant. = quantitative.

6.5.4.5 General procedure for the C–S arylation of thiols

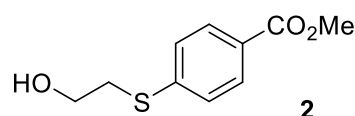
An oven dried vial (19 x 100 mm) equipped with a stir bar was charged with CN-OA-m (15 mg, 1.67 mg/g), aryl iodide (570.0 μmol , 1.0 equiv), thiol (1.14 mmol, 2.0 equiv), $\text{NiBr}_2 \cdot 3\text{H}_2\text{O}$ (7.75 mg, 28.5 μmol , 5 mol%) and [2,2'-bipyridine]-4,4'-diylidiphosphonic acid (9.0 mg, 28.5 μmol , 5 mol%). Subsequently, MeCN (anhydrous, 6 mL) and *N*-tert-butylisopropylamine (BIPA, 452 μL , 2.85 mmol, 5 equiv) were added and the vial was sealed with a septum and Parafilm. The reaction mixture was sonicated for 5-10 min followed by stirring for 5 min to obtain a fine dispersion. The mixture was degassed by bubbling argon for 10 min. The mixture was irradiated using the 440 nm or 525 nm LED setup with rapid stirring. After the respective reaction time, one equivalent of 1,3,5-trimethoxybenzene (internal standard, 96 mg, 570 μmol , 1.0 equiv) was added and the mixture was stirred for 5 min. An aliquot of the reaction mixture (~200 μL) was filtered, diluted with DMSO-d_6 and subjected to $^1\text{H-NMR}$ analysis. The NMR sample was combined with the reaction mixture, diluted with H_2O (40 mL) and extracted with ethyl acetate (3 x 30 mL). The combined organic phases were washed with aqueous NaOH (1 M, 2x40 mL) and brine (40 mL), dried over Na_2SO_4 and concentrated. The product was purified by flash column chromatography (SiO_2 , Hexane/EtOAc) on a Grace Reveleris system using a 12 g cartridge.



Methyl 4-((3-methoxy-3-oxopropyl)thio)benzoate 1: From methyl 4-iodobenzoate (149.37 mg, 570.0 μmol , 1.0 equiv) and methyl 3-mercaptopropionate (126.3 μL , 1.14 mmol, 2.0 equiv). The title compound was isolated after irradiation for 17 hours in 94% yield (136.3 mg, 533.8 μmol) as white solid using an elution gradient of 0-5% of ethyl acetate in hexane.

$^1\text{H NMR}$ (400 MHz, CDCl_3) δ 7.94 (d, $J = 8.6$ Hz, 2H), 7.32 (d, $J = 8.6$ Hz, 2H), 3.90 (s, 3H), 3.70 (s, 3H), 3.25 (t, $J = 7.4$ Hz, 2H), 2.69 (t, $J = 7.4$ Hz, 2H). $^{13}\text{C NMR}$ (101 MHz, CDCl_3) δ 172.02, 168.82, 142.70, 130.21, 127.46, 127.23, 52.25, 52.11, 33.87, 27.43.

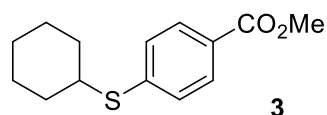
These data are in full agreement with those previously published in the literature.⁶



Methyl 4-((2-hydroxyethyl)thio)benzoate. From methyl 4-iodobenzoate (149.37 mg, 570.0 μmol , 1.0 equiv) and 2-mercaptoethanol (80.08 μL , 1.14 mmol, 2.0 equiv). The title compound was isolated after irradiation for 3 hours in 63% yield (75.5 mg, 356 μmol) as white solid using an elution gradient of 0-25% of ethyl acetate in hexane.

^1H NMR (400 MHz, CDCl_3) δ 7.90 (d, $J = 8.5$ Hz, 2H), 7.31 (d, $J = 8.5$ Hz, 2H), 3.88 (s, 3H), 3.81 (t, $J = 6.2$ Hz, 2H), 3.18 (t, $J = 6.2$ Hz, 2H), 2.45 (m, 1H). ^{13}C NMR (101 MHz, CDCl_3) δ 166.85, 142.66, 130.12, 127.28, 127.19, 60.51, 52.24, 35.34.

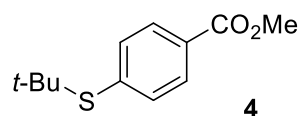
These data are in full agreement with those previously published in the literature.⁶



Methyl 4-(cyclohexylthio)benzoate. From methyl 4-iodobenzoate (149.37 mg, 570.0 μmol , 1.0 equiv) and cyclohexanethiol (139.68 μL , 1.14 mmol, 2.0 equiv). The title compound was isolated after irradiation for 18 hours in 64% yield (91.5 mg, 365 μmol) as colorless oil using an elution gradient of 0-5% of ethyl acetate in hexane.

^1H NMR (400 MHz, CDCl_3) δ 7.91 (d, $J = 8.5$ Hz, 2H), 7.33 (d, $J = 8.5$ Hz, 2H), 3.89 (s, 3H), 3.32 – 3.24 (m, 1H), 2.06 – 1.98 (m, 2H), 1.82 – 1.75 (m, 2H), 1.67 – 1.58 (m, 1H), 1.47 – 1.20 (m, 5H). ^{13}C NMR (101 MHz, CDCl_3) δ 166.94, 143.15, 129.99, 128.52, 127.16, 52.18, 45.11, 33.19, 26.06, 25.79.

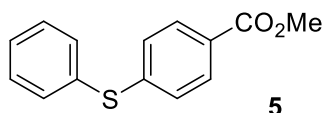
These data are in full agreement with those previously published in the literature.⁶



Methyl 4-(tert-butylthio)benzoate. From methyl 4-iodobenzoate (149.37 mg, 570.0 μmol , 1.0 equiv) and *tert*-butyl mercaptan (128.72 μL , 1.14 mmol, 2.0 equiv). The title compound was isolated after irradiation for 18 hours in 59% yield (75.03 mg, 336 μmol) as colorless oil using an elution gradient of 0-3% of ethyl acetate in hexane.

^1H NMR (400 MHz, CDCl_3) δ 7.98 (d, $J = 9.0$ Hz, 2H), 7.59 (d, $J = 9.0$ Hz, 2H), 3.92 (s, 3H), 1.31 (s, 9H). ^{13}C NMR (101 MHz, CDCl_3) δ 166.91, 139.12, 136.96, 130.21, 129.59, 52.38, 46.92, 31.21.

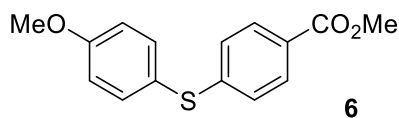
These data are in full agreement with those previously published in the literature.⁶



Methyl 4-(phenylthio)benzoate. From methyl 4-iodobenzoate (149.37 mg, 570.0 μmol , 1.0 equiv) and thiophenol (117.24 μL , 1.14 mmol, 2.0 equiv). The title compound was isolated after irradiation for 18 hours in 82% yield (105.1 mg, 468 μmol) as white solid using an elution gradient of 0-5% of ethyl acetate in hexane.

^1H NMR (400 MHz, CDCl_3) δ 7.92 (d, $J = 8.5$ Hz, 2H), 7.55 – 7.47 (m, 2H), 7.44 – 7.35 (m, 3H), 7.23 (d, $J = 8.5$ Hz, 2H), 3.91 (s, 3H). ^{13}C NMR (101 MHz, CDCl_3) δ 166.73, 144.47, 133.77, 132.42, 130.16, 129.72, 128.74, 127.61, 127.52, 52.15.

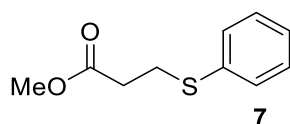
These data are in full agreement with those previously published in the literature.⁶



Methyl 4-((4-methoxyphenyl)thio)benzoate. From methyl 4-iodobenzoate (149.37 mg, 570.0 μmol , 1.0 equiv) and 4-methoxybenzenethiol (140.42 μL , 1.14 mmol, 2.0 equiv). The title compound was isolated after irradiation for 18 hours in 78% yield (122.21 mg, 445 μmol) as white solid using an elution gradient of 0-5% of ethyl acetate in hexane.

^1H NMR (400 MHz, CDCl_3) δ 7.85 (d, $J = 8.6$ Hz, 2H), 7.47 (d, $J = 8.9$ Hz, 2H), 7.07 (d, $J = 8.6$ Hz, 2H), 6.94 (d, $J = 8.9$ Hz, 2H), 3.87 (s, 3H), 3.84 (s, 3H). ^{13}C NMR (101 MHz, CDCl_3) δ 166.83, 160.68, 146.49, 136.85, 130.03, 126.75, 125.84, 121.61, 115.41, 55.48, 52.09.

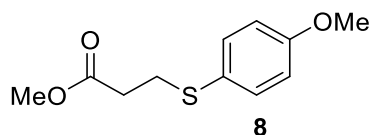
These data are in full agreement with those previously published in the literature.⁶



Methyl 3-(phenylthio)propanoate. From methyl iodobenzene (63.89 μL , 570.0 μmol , 1.0 equiv) and methyl 3-mercaptopropionate (126.3 μL , 1.14 mmol, 2.0 equiv). The title compound was isolated after irradiation for 3 hours in 73% yield (81.9 mg, 417 μmol) as white solid using an elution gradient of 0-5% of ethyl acetate in hexane.

^1H NMR (400 MHz, CDCl_3) δ 7.39 (m, 2H), 7.32 (t, $J = 15.5$ Hz, 2H), 7.23 (t, $J = 15.5$ Hz, 1H), 3.70 (s, 3H), 3.19 (t, $J = 14.8$ Hz, 2H), 2.65 (t, $J = 14.8$ Hz, 2H). ^{13}C NMR (101 MHz, CDCl_3) δ 172.25, 135.26, 130.17, 129.11, 126.66, 51.90, 34.29, 29.10.

These data are in full agreement with those previously published in the literature.⁷



Methyl 3-((4-methoxyphenyl)thio)propanoate. From methyl 4-iodoanisole (133.61 mg, 570.0 μmol , 1.0 equiv) and methyl 3-mercaptopropionate (126.3 μL , 1.14 mmol, 2.0 equiv). The title compound was isolated after irradiation for 18 hours in 70% yield (90.82 mg, 401 μmol) as white solid using an elution gradient of 0-5% of ethyl acetate in hexane.

^1H NMR (400 MHz, CDCl_3) δ 7.35 (d, $J = 8.8$ Hz, 2H), 6.83 (d, $J = 8.8$ Hz, 2H), 3.77 (s, 3H), 3.65 (s, 3H), 3.03 (t, $J = 14.5$ Hz, 2H), 2.55 (t, $J = 14.5$ Hz, 2H). ^{13}C NMR (101 MHz, CDCl_3) δ 172.32, 159.39, 134.23, 125.12, 114.69, 55.36, 51.78, 34.42, 31.12.

These data are in full agreement with those previously published in the literature.⁷

6.5.4.6 *Ex situ* preparation of the bifunctional catalysts

6.5.4.6.1 CN-OA-m–NiBr₂·dpbpy (Cat 1)

CN-OA-m (15 mg) was dispersed in 9 mL MeCN and sonicated for 5 min. Then, NiBr₂·3H₂O (7.75 mg, 28.5 μmol, 5 mol%) and [2,2'-bipyridine]-4,4'-diyldiphosphonic acid (9.0 mg, 28.5 μmol, 5 mol%) were added and the mixture was again sonicated for 10 min. The mixture was stirred overnight and the solid material was separated by centrifugation. After washing with MeCN and separation by centrifugation (2x), the material was lyophilized overnight.



Figure S6.5. Unfunctionalized CN-OA-m (A) and CN-OA-m–NiBr₂·dpbpy (Cat 1) (B). Structure of NiBr₂·dcbpy (C). The functionalities that bind to the surface of CN-OA-m are marked in green.

The amount of immobilized NiBr₂·3H₂O and dpbpy ([2,2'-bipyridine]-4,4'-diyldiphosphonic acid) was determined by ICP-OES (Table S6.10). The white powder has a nickel content of 21.1 mg g⁻¹, which corresponds to 1.8 μmol of NiBr₂·3H₂O (0.98 mol%) and a phosphorus content of 71.2 mg g⁻¹ (5.7 μmol, 3 mol%).

Table S6.10. Nickel and phosphorus content of CN-OA-m–NiBr₂·dpbpy (Cat 1) and CN-OA-m determined by ICP-OES analysis

Sample	Ni [mg/g catalyst]	P [mg/g catalyst]
CN-OA-m	0.02	0.01
Cat 1	21.1	71.2

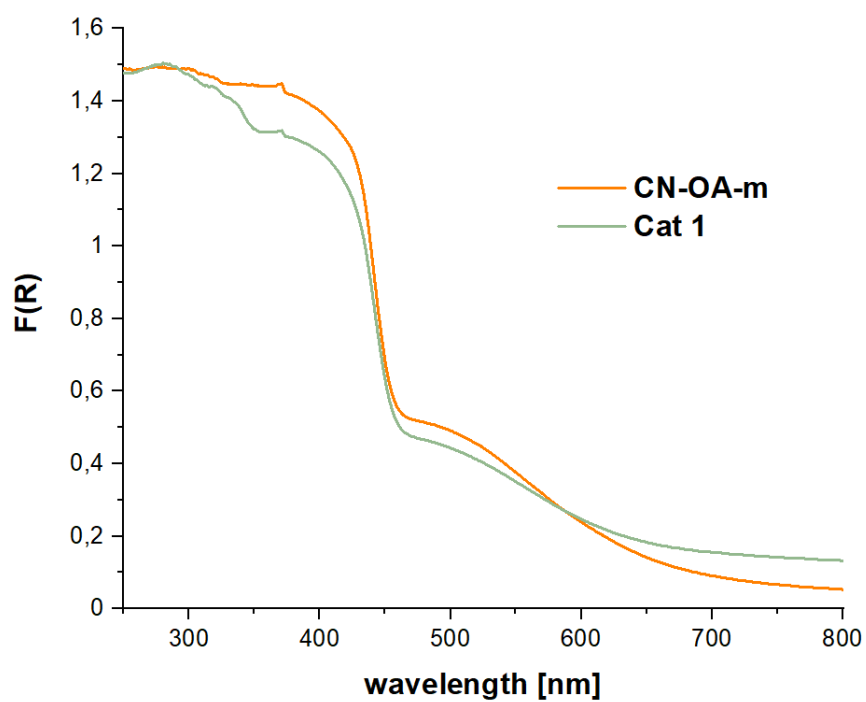


Figure S6.6. Diffuse reflectance UV/Vis spectra of **Cat 1** and unfunctionalized CN-OA-m.

SEM images of the unfunctionalized CN-OA-m and **Cat 1** showed a porous texture that was not altered during functionalization (Figure S6.7).

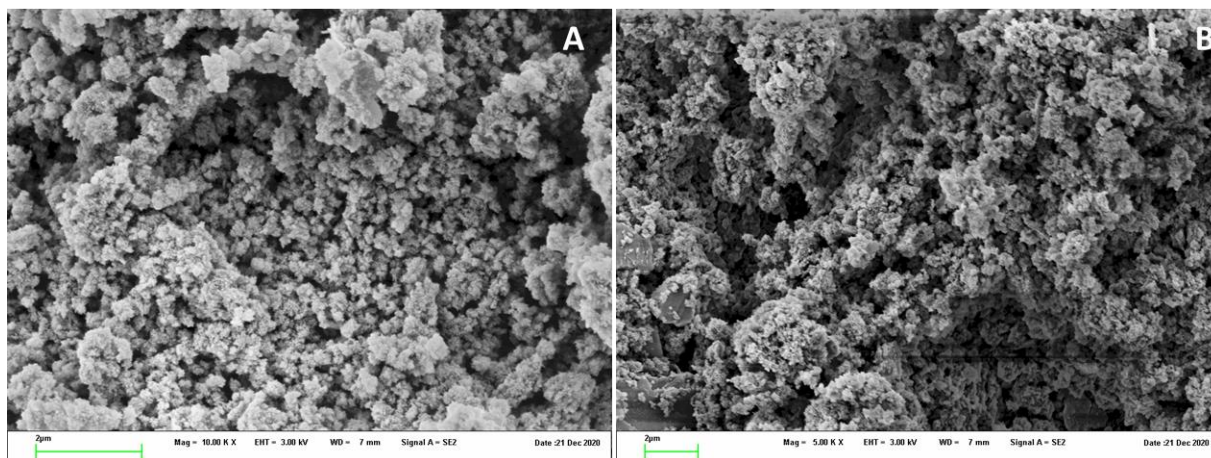
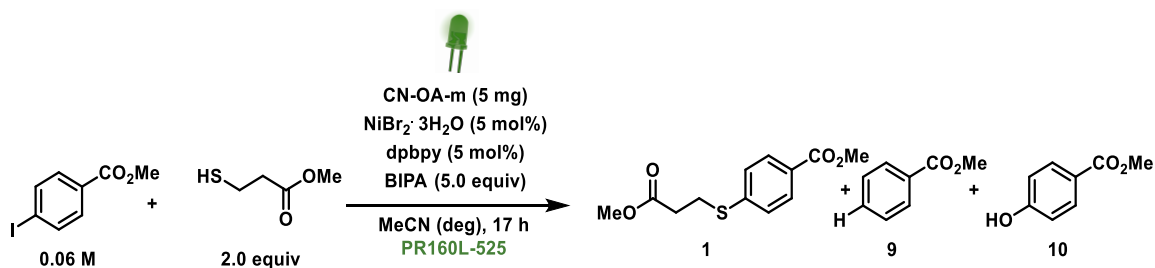


Figure S6.7. SEM images of CN-OA-m (A) and **Cat 1** (B).

Table S6.11. EDX elemental composition of Cat 1 and CN-OA-m.

Sample	% w/w C	% w/w N	% w/w O	% w/w P	% w/w K	% w/w Br	% w/w Ni
CN-OA-m	24.34	52.39	7.06	0.06	11.05	0.10	0.02
CN-OA-m- NiBr ₂ ·dcbpy	32.31	34.62	15.92	6.02	4.20	3.47	3.46

Table S6.12. Comparison of the *ex situ* and *in situ* method for the title reaction using the 525 nm setup.^a

Entry	Deviation from standard conditions	Conversion [%] ^b	1 [%] ^c	9 [%] ^c	10 [%] ^c
1	--	quant.	99	n.d.	n.d.
2	Cat 1 prepared <i>ex situ</i>	quant.	99	n.d.	n.d.

^aReaction conditions: methyl 4-iodobenzoate (190.3 μmol), methyl 3-mercaptopropionate (380.5 μmol), NiBr₂·3H₂O (9.5 μmol), CN-OA-m (5 mg) dpbpy (9.5 μmol) and BIPA (951.5 μmol) in MeCN (3 mL), 525 nm LED (200% power), 17 h. ^bConversion of methyl 4-iodobenzoate determined by ¹H-NMR using 1,3,5-trimethoxybenzene as internal standard. ^cNMR yields determined by ¹H-NMR using 1,3,5-trimethoxybenzene as internal standard. BIPA = *N-tert*-butylisopropylamine. dpbpy = [2,2'-bipyridine]-4,4'-diylidiphosphonic acid. n.d. = not detected. deg = degassed. quant. = quantitative.

6.5.4.6.2 Ru(bpy)₂(dpbpy)–TiO₂–NiBr₂·dpbpy (Cat 2)

TiO₂ P25 (90 mg) was dispersed in 9 mL MeCN and sonicated for 5 min. Ru(bpy)₂(dpbpy) (5.19 mg, 7.13 μmol, 1.25 mol%), NiBr₂·3H₂O (15.5 mg, 57.0 μmol, 10 mol%) and [2,2'-bipyridine]-4,4'-diylidiphosphonic acid (18.0 mg, 57.0 μmol, 10 mol%) were added and the mixture was again sonicated for 10 min. The mixture was stirred overnight and the solid material was separated by centrifugation. After washing with MeCN and separation by centrifugation (2x), the material was lyophilized overnight.

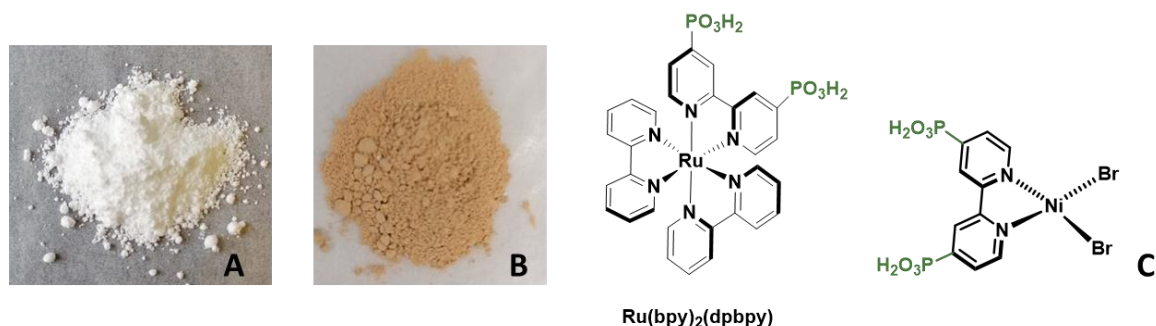


Figure S6.8. Unfunctionalized TiO₂ P25 (A) and Ru(bpy)₂(dpbpy)–TiO₂–NiBr₂·dpbpy (Cat 2) (B). Structure of Ru(bpy)₂(dpbpy) and NiBr₂·dpbpy (C). The functionalities that bind to the surface of TiO₂ are marked in green.

The nickel and phosphorus content of the material was determined by ICP-OES (Table 6.16). The brown powder has a nickel content of 4.18 mg g⁻¹, which corresponds to 2.14 μmol of NiBr₂·3H₂O (1.16 mol%), 4.59 mg g⁻¹ ruthenium and a phosphorus content of 32.2 mg g⁻¹.

Table S6.13. Nickel, ruthenium and phosphorus content of Ru(bpy)₂(dpbpy)–TiO₂–NiBr₂·dpbpy (Cat 2) and unfunctionalized TiO₂ determined by ICP-OES analysis

Sample	Ru [mg/g catalyst]	Ni [mg/g catalyst]	P [mg/g catalyst]
TiO ₂	0.02	0.02	0.02
Cat 2	4.59	4.18	32.2

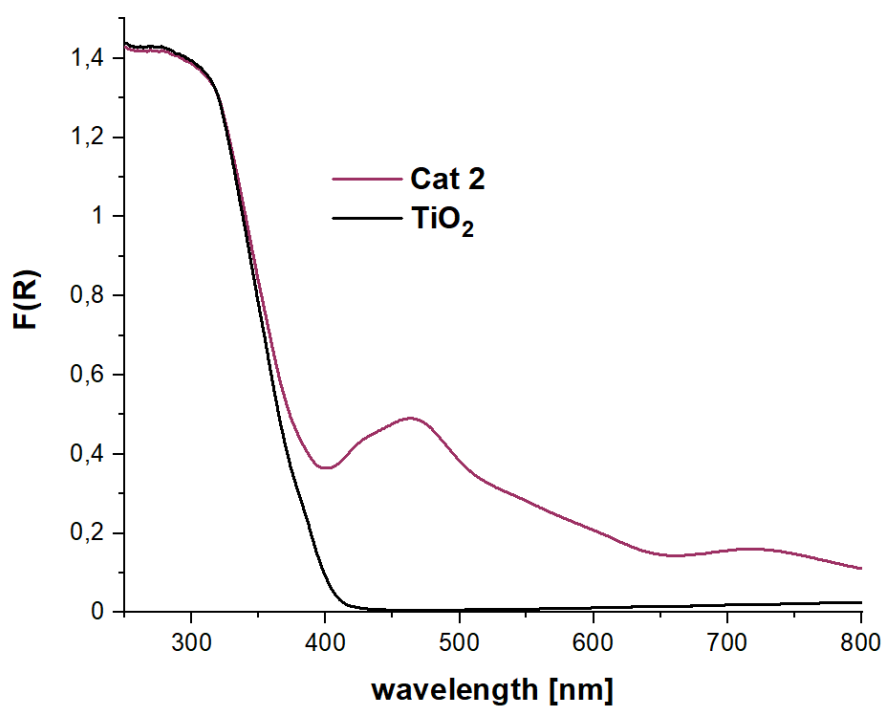


Figure S6.9. Diffuse reflectance UV/Vis spectra of Ru(bpy)₂(dpbbpy)-TiO₂-NiBr₂·dpbbpy (**Cat 2**) and unfunctionalized TiO₂ P25.

SEM images of Ru(bpy)₂(dpbbpy)-TiO₂-NiBr₂·dpbbpy (**Cat 2**) and unfunctionalized TiO₂ P25 showed a porous texture that was not altered during functionalization process (Figure S6.10).

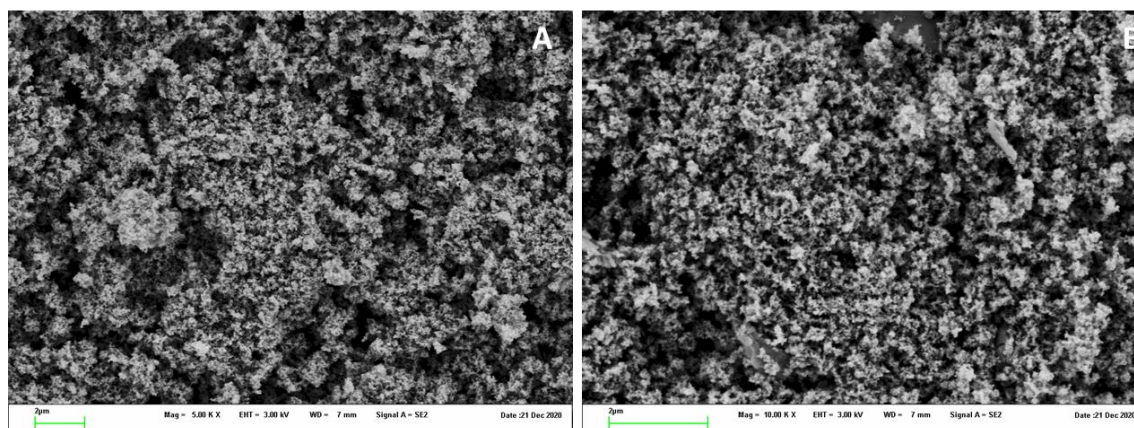
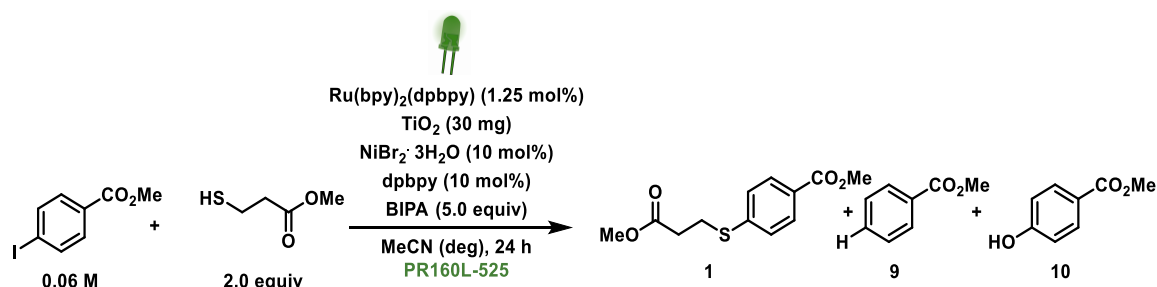


Figure S6.10. SEM images of TiO₂ P 25 (A) and Ru(bpy)₂(dpbbpy)-TiO₂-NiBr₂·dpbbpy (**Cat 2**) (B)

Table S6.14. EDX elemental composition of Ru(bpy)₂(dpbpy)-TiO₂-NiBr₂·dpbpy (Cat 2) and unfunctionalized TiO₂ P25.

Sample	% w/w C	% w/w O	% w/w P	% w/w Ti	% w/w Ni	% w/w Br
TiO ₂	4.00	48.96	0.02	46.91	0.11	0.02
Cat 2	28.20	50.01	4.41	15.22	0.62	1.56

Table S6.15. Comparison of the *ex situ* and *in situ* method for the title reaction using the 525 nm setup.^a

Entry	Deviation from standard conditions	Conversion [%] ^b	1 [%] ^c	9 [%] ^c	10 [%] ^c
1	--	quant.	99	n.d.	traces
2	Cat 2 prepared <i>ex situ</i>	66	60	n.d.	traces

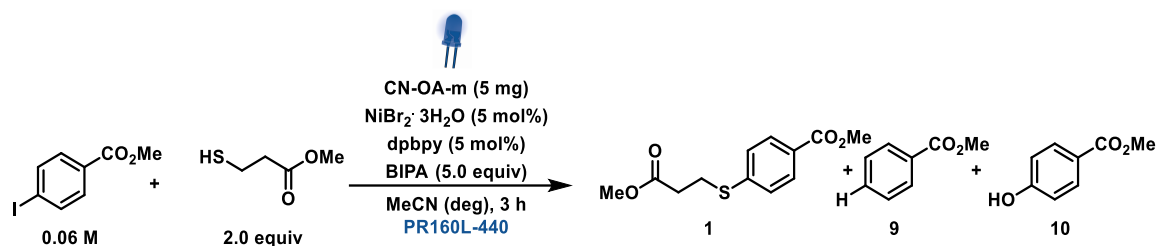
^aReaction conditions: methyl 4-iodobenzoate (190.3 μmol), methyl 3-mercaptopropionate (380.5 μmol), dye (2.4 μmol), NiBr₂·3H₂O (19.0 μmol), CN-OA-m (10 mg) dpbpy (19.0 μmol) and BIPA (951.5 μmol) in MeCN (3 mL), 525 nm LED (200% power), 24 h. ^bConversion of methyl 4-iodobenzoate determined by ¹H-NMR using 1,3,5-trimethoxybenzene as internal standard. ^cNMR yields determined by ¹H-NMR using 1,3,5-trimethoxybenzene as internal standard. BIPA = *N*-tert-butylisopropylamine. dpbpy = [2,2'-bipyridine]-4,4'-diylidiphosphonic acid. n.d. = not detected. deg = degassed. quant. = quantitative.

6.5.4.7 Catalyst recycling

6.5.4.7.1 CN-OA-m-NiBr₂·dpbpy (Cat 1)

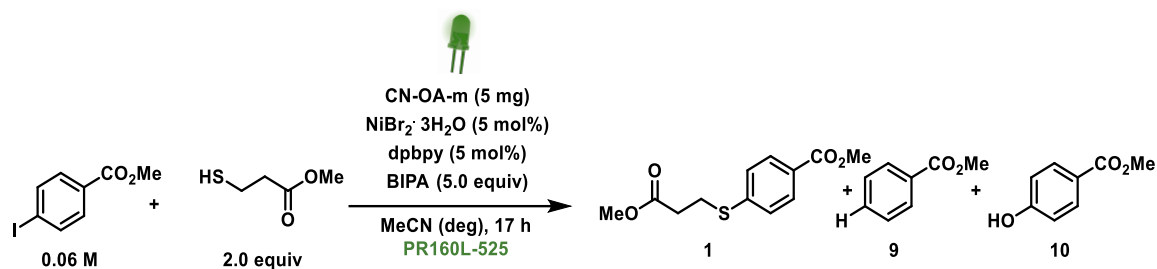
Experimental procedure for catalyst recycling experiments of the C–S arylation with the 440 nm or 525 nm setup using CN-OA-m-NiBr₂·dpbpy (Cat 1) generated *in situ*.

An oven dried vial (19 x 100 mm) equipped with a stir bar was charged with the respective CN-OA-m (5 mg, 1.67 mg/ml), methyl 4-iodobenzoate (49.79 mg, 190.3 μmol, 1.0 equiv), methyl 3-mercaptopropionate (42.1 μL, 380.5 μmol, 2.0 equiv), NiBr₂·3H₂O (2.59, 9.5 μmol, 5 mol%) and [2,2'-bipyridine]-4,4'-diyldiphosphonic acid (3.0 mg, 9.5 μmol, 5 mol%). Subsequently, MeCN (anhydrous, 3 mL) and *N*-tert-butylisopropylamine (BIPA, 150.7 μL, 951.5 μmol, 5 equiv) were added and the vial was sealed with a septum and Parafilm. The reaction mixture was sonicated for 5-10 min followed by stirring for 5 min to obtain a fine dispersion. The mixture was then degassed by bubbling Argon for 10 min. The mixture was irradiated using the 440 or 525 nm LED setup for the respective reaction time with rapid stirring (1400 rpm). After the respective reaction time, the reaction mixture was centrifuged and washed twice with 3 mL MeCN. The remaining catalyst was lyophilized and reused in the next reaction.

Table S6.16. Catalyst recycling (Cat 1) in the C–S coupling using the 440 nm setup.^a

Entry	Cycle	Conversion [%] ^b	1 [%] ^c	9 [%] ^c	10 [%] ^c
1	1	quant.	99	n.d.	traces
2	2	quant.	95	n.d.	traces
3	3	quant.	99	n.d.	traces
4	4	quant.	99	n.d.	traces
5	5	quant.	99	n.d.	traces
6	6	quant.	99	n.d.	traces
7	7	90	88	n.d.	traces

^aReaction conditions: methyl 4-iodobenzoate (190.3 μmol), methyl 3-mercaptopropionate (380.5 μmol), NiBr₂·3H₂O (9.5 μmol), CN-OA-m (5 mg), and dpbpy (9.5 μmol), BIPA (951.5 μmol) in MeCN (3 mL), 440 nm LED (100% power), 3 h. ^bConversion of methyl 4-iodobenzoate determined by ¹H-NMR using 1,3,5-trimethoxybenzene as internal standard. ^cNMR yields determined by ¹H-NMR using 1,3,5-trimethoxybenzene as internal standard. BIPA = *N*-*tert*-butylisopropylamine. dpbpy = [2,2'-bipyridine]-4,4'-diyldiphosphonic acid. n.d. = not detected. deg = degassed. quant. = quantitative.

Table S6.17. Catalyst recycling (Cat 1) in the C–S coupling using the 525 nm setup.^a

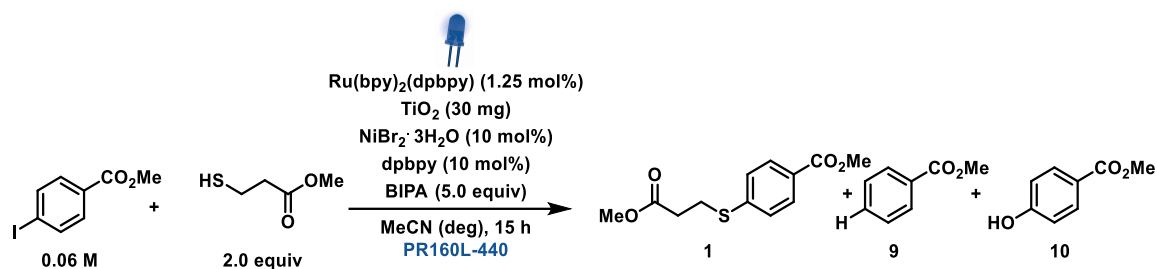
Entry	Cycle	Conversion [%] ^b	1 [%] ^c	9 [%] ^c	10 [%] ^c
1	1	quant.	99	n.d.	traces
2	2	quant.	99	n.d.	traces
3	3	quant.	99	n.d.	traces
4	4	quant.	99	n.d.	traces
5	5	quant.	95	n.d.	traces
6	6	quant.	99	n.d.	traces
7	7	quant.	96	n.d.	traces

^aReaction conditions: methyl 4-iodobenzoate (190.3 μmol), methyl 3-mercaptopropionate (380.5 μmol), NiBr₂·3H₂O (9.5 μmol), CN-OA-m (5 mg), and dpbpy (9.5 μmol), BIPA (951.5 μmol) in MeCN (3 mL), 525 nm LED (200% power), 17 h. ^bConversion of methyl 4-iodobenzoate determined by ¹H-NMR using 1,3,5-trimethoxybenzene as internal standard. ^cNMR yields determined by ¹H-NMR using 1,3,5-trimethoxybenzene as internal standard. BIPA = *N*-*tert*-butylisopropylamine. dpbpy = [2,2'-bipyridine]-4,4'-diyldiphosphonic acid. n.d. = not detected. deg = degassed. quant. = quantitative.

6.5.4.7.1 Ru(bpy)₂(dpbpy)-TiO₂-NiBr₂·dpbpy (Cat 2)

Experimental procedure for catalyst recycling experiments of the C-S arylation with the 440 nm or 525 nm setup using Ru(bpy)₂(dpbpy)-TiO₂-NiBr₂·dpbpy (Cat 2) generated *in situ*.

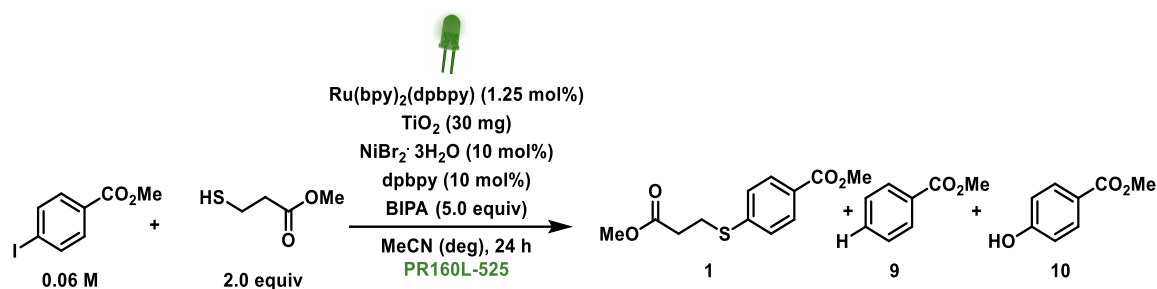
An oven dried vial (19 x 100 mm) equipped with a stir bar was charged with the respective TiO₂ P25 (30 mg, 10 mg/ml), methyl 4-iodobenzoate (49.79 mg, 190.3 μmol, 1.0 equiv), methyl 3-mercaptopropionate (42.1 μL, 380.5 μmol, 2.0 equiv), NiBr₂·3H₂O (5.18 mg, 19.0 μmol, 10 mol%), [2,2'-bipyridine]-4,4'-diylidiphosphonic acid (6.0 mg, 19.0 μmol, 10 mol%) and Ru(bpy)₂(dpbpy) (1.74 mg, 2.4 μmol, 1.25 mol%). Subsequently, MeCN (anhydrous, 3 mL) and *N*-tert-butylisopropylamine (BIPA, 150.7 μL, 951.5 μmol, 5 equiv) were added and the vial was sealed with a septum and Parafilm.. The reaction mixture was sonicated for 5-10 min followed by stirring for 5 min to obtain a fine dispersion. The mixture was then degassed by bubbling Argon for 10 min. The mixture was irradiated using the 440 or 525 nm LED setup with rapid stirring (1400 rpm). After the respective reaction time, the reaction mixture was centrifuged and washed twice with 3 mL MeCN. The remaining catalyst was lyophilized and reused in the next reaction.

Table S6.18. Catalyst recycling (Cat 2) in the C–S coupling with the 440 nm setup.^a

Entry	Cycle	Conversion [%] ^b	1 [%] ^c	9 [%] ^c	10 [%] ^c
1	1	quant.	99	n.d.	traces
2	2	quant.	99	n.d.	traces
3	3	quant.	99	n.d.	traces
4	4	quant.	99	n.d.	traces
5	5	quant.	99	n.d.	traces
6	6	quant.	99	n.d.	traces
7	7	quant.	97	n.d.	traces

^aReaction conditions: methyl 4-iodobenzoate (190.3 μmol), methyl 3-mercaptopropionate (380.5 μmol), Ru(bpy)₂(dpbbp) (2.4 μmol), NiBr₂·3H₂O (19.0 μmol), TiO₂ (30 mg), and dpbbp (19.0 μmol), BIPA (951.5 μmol) in MeCN (3 mL), 440 nm LED (100% power), 15 h.

^bConversion of methyl 4-iodobenzoate determined by ¹H-NMR using 1,3,5-trimethoxybenzene as internal standard. ^cNMR yields determined by ¹H-NMR using 1,3,5-trimethoxybenzene as internal standard. BIPA = *N-tert*-butylisopropylamine. dpbbp = [2,2'-bipyridine]-4,4'-diylidiphosphonic acid. n.d. = not detected. deg = degassed. quant. = quantitative.

Table S6.19. Catalyst recycling (Cat 2) in the C–S coupling with the 525 nm setup.^a

Entry	Cycle	Conversion [%] ^b	1 [%] ^c	9 [%] ^c	10 [%] ^c
1	1	quant.	99	n.d.	traces
2	2	quant.	99	n.d.	traces
3	3	quant.	99	n.d.	traces
4	4	quant.	99	n.d.	traces
5	5	quant.	95	n.d.	traces
6	6	quant.	97	n.d.	traces
7	7	quant.	97	n.d.	traces

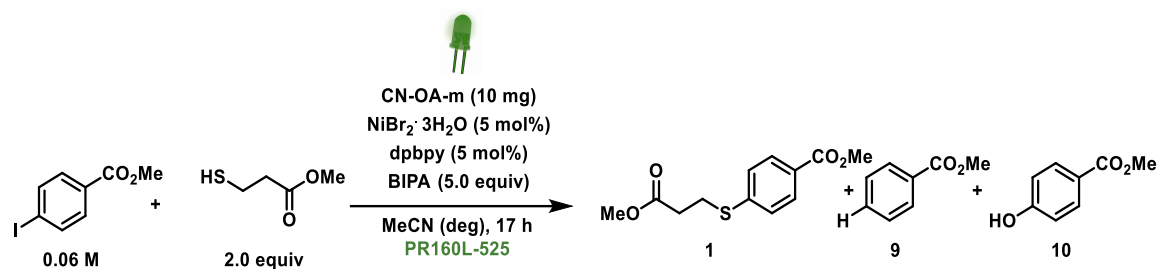
^aReaction conditions: methyl 4-iodobenzoate (190.3 μmol), methyl 3-mercaptopropionate (380.5 μmol), Ru(bpy)₂(dpbpy) (2.4 μmol), NiBr₂·3H₂O (19.0 μmol), TiO₂ (30 mg) and dpbpy (19.0 μmol), BIPA (951.5 μmol) in MeCN (3 mL), 525 nm LED (200% power), 24 h.

^bConversion of methyl 4-iodobenzoate determined by ¹H-NMR using 1,3,5-trimethoxybenzene as internal standard. ^cNMR yields determined by ¹H-NMR using 1,3,5-trimethoxybenzene as internal standard. BIPA = *N-tert*-butylisopropylamine. dpbpy = [2,2'-bipyridine]-4,4'-diylidiphosphonic acid. n.d. = not detected. deg = degassed. quant. = quantitative.

6.5.4.8 Catalyst recycling (Cat 1) in the C–S coupling including ICP-OES analysis

Experimental procedure for catalyst recycling experiments of the C–S arylation with 525 nm setup using CN-OA-m–NiBr₂·dpbpy (Cat 1) generated *in situ*.

An oven dried vial (19 x 100 mm) equipped with a stir bar was charged with the respective CN-OA-m (5 mg, 1.67 mg/ml), methyl 4-iodobenzoate (49.79 mg, 190.3 μmol, 1.0 equiv), methyl 3-mercaptopropionate (42.1 μL, 380.5 μmol, 2.0 equiv), NiBr₂·3H₂O (2.59, 9.5 μmol, 5 mol%) and [2,2'-bipyridine]-4,4'-diyldiphosphonic acid (3.0 mg, 9.5 μmol, 5 mol%). Subsequently, MeCN (anhydrous, 3 mL) and *N*-tert-butylisopropylamine (BIPA, 150.7 μL, 951.5 μmol, 5 equiv) were added and the vial was sealed with a septum and Parafilm. The reaction mixture was sonicated for 5-10 min followed by stirring for 5 min to obtain a fine dispersion. The mixture was then degassed by bubbling Argon for 10 min. The mixture was irradiated using the 525 nm LED setup for the respective reaction time with rapid stirring (1400 rpm). After the respective reaction time, the reaction mixture was centrifuged and washed twice with 3 mL MeCN. The remaining catalyst was lyophilized and reused in the next reaction. After each cycle the catalyst was analyzed by ICP-OES (see Table S6.19).

Table S6.20. Catalyst recycling (Cat 1) in the C–S coupling with the 525 nm setup.^a

Entry	Cycle	Conversion [%] ^b	1 [%] ^c	9 [%] ^c	10 [%] ^c
1	1	quant.	99	n.d.	traces
2	2	quant.	99	n.d.	traces
3	3	quant.	99	n.d.	traces
4	4	quant.	99	n.d.	traces
5	5	quant.	99	n.d.	traces
6	6	95	94	n.d.	traces
7	7	quant.	99	n.d.	traces
8	8	96	95	n.d.	traces
9	9	96	96	n.d.	traces
10	10	98	98	n.d.	traces

^aReaction conditions: methyl 4-iodobenzoate (380.6 μ mol), methyl 3-mercaptopropionate (761.2 μ mol), NiBr₂·3H₂O (19 μ mol), CN-OA-m (10 mg), and dpbpy (19 μ mol), BIPA (1.9 mmol) in MeCN (3 mL), 525 nm LED (200% power), 17 h. ^bConversion of methyl 4-iodobenzoate determined by ¹H-NMR using 1,3,5-trimethoxybenzene as internal standard. ^cNMR yields determined by ¹H-NMR using 1,3,5-trimethoxybenzene as internal standard. BIPA = *N*-*tert*-butylisopropylamine. dpbpy = [2,2'-bipyridine]-4,4'-diylidiphosphonic acid. n.d. = not detected. deg = degassed. quant. = quantitative.

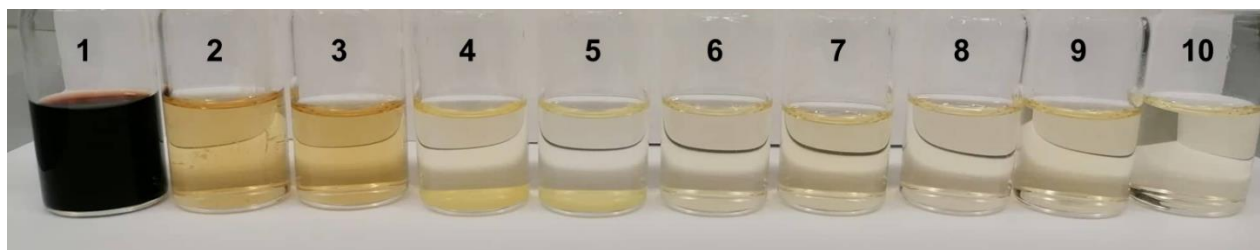


Figure S6.11. Solutions after centrifugation after each reaction cycle.

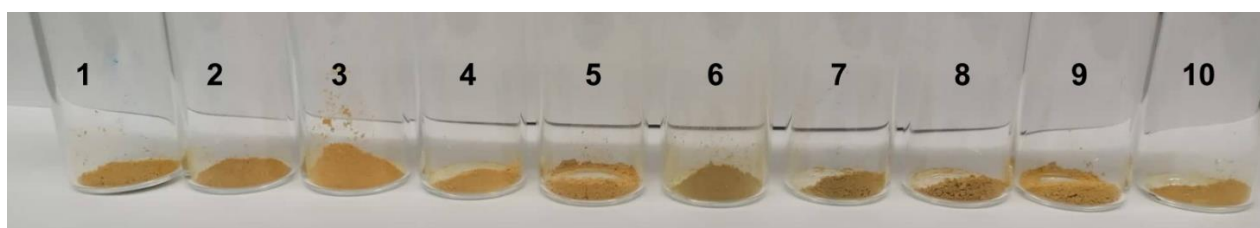


Figure S6.12. Cat 1 after centrifugation, washing and lyophilization after each reaction cycle.

Table S6.21. Nickel and phosphorus content of unfunctionalized CN-OA-m, and CN-OA-m-NiBr₂·dpbpy (Cat 1) after each recycling experiment (ICP-OES analysis).

Sample	Ni [mg/g catalyst]	Corresponds to NiBr ₂ ·3H ₂ O [mol%]	P [mg/g catalyst]	Corresponds to dpbpy [mol%]
CN-OA-m	0.02	--	0.01	--
cycle 1	2.65	0.12	52.2	2.22
cycle 2	2.63	0.12	47.8	2.03
cycle 3	2.47	0.11	44.6	1.89
cycle 4	1.83	0.08	43.6	1.85
cycle 5	2.38	0.11	45.3	1.92
cycle 6	2.92	0.14	42.0	1.78
cycle 7	2.67	0.12	47.8	2.03
cycle 8	1.95	0.09	47.0	2.00
cycle 9	2.43	0.11	41.6	1.77
cycle 10	1.94	0.09	42.9	1.82

SEM images of the unfunctionalized CN-OA-m and **Cat 1** showed a porous texture that was not altered during the recycling study.

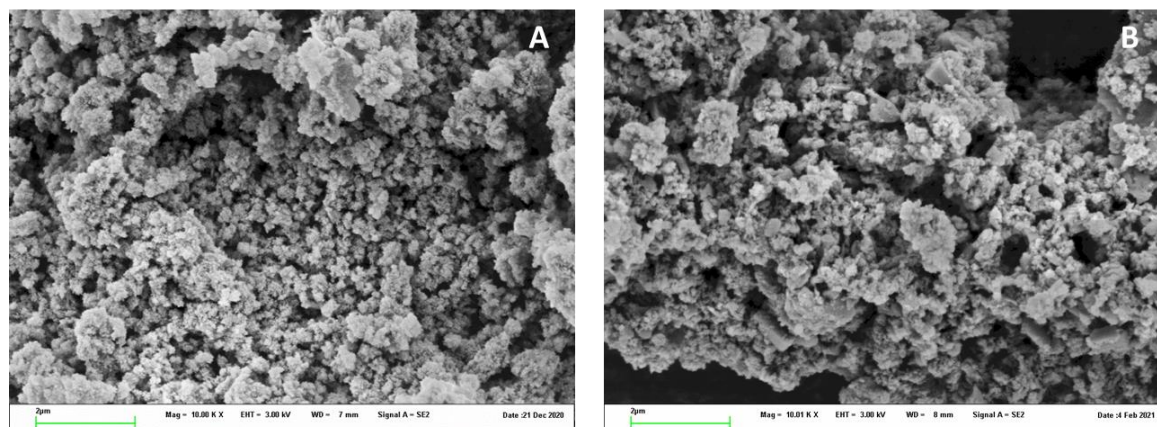
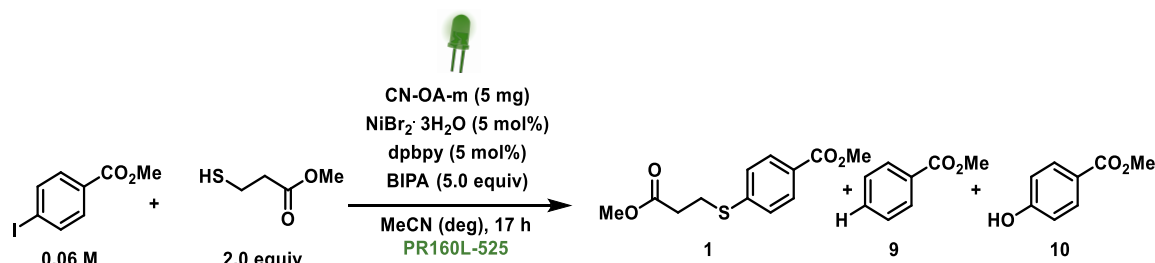
**Figure S6.13.** SEM images of CN-OA-m (A) and Cat 1 (B) after ten reaction cycles.

Table S6.22. EDX elemental composition of CN-OA-m and Cat 1 after ten cycles.

Sample	% w/w	% w/w	% w/w	% w/w	% w/w	% w/w	% w/w
	C	N	O	P	K	Br	Ni
CN-OA-m	24.34	52.39	7.06	0.06	11.05	0.10	0.02
CAT 1 after 10 cycles	30.35	28.37	23.27	5.37	5.72	3.61	0.84

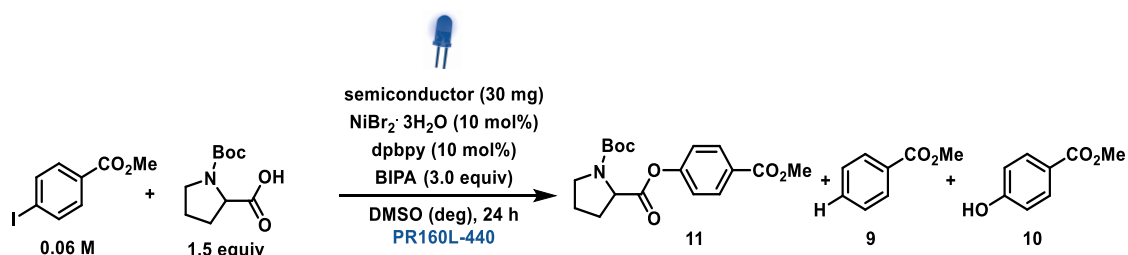
Table S6.23. Comparison of the C–S cross coupling with Cat 1 using the conditions described in Table S6.21 and using the Ni/P content that was measured after the recycling experiments using the 525 nm setup.^a

Entry	Deviation from standard conditions	Conversion [%] ^b	1 [%] ^c	9 [%] ^c	10 [%] ^c
1	--	quant.	99	n.d.	n.d.
2	0.1 mol% NiBr ₂ ·3H ₂ O and 1.9 mol% dpbpy	quant.	99	n.d.	n.d.

^aReaction conditions: methyl 4-iodobenzoate (190.3 μmol), methyl 3-mercaptopropionate (380.5 μmol), NiBr₂·3H₂O (9.5 μmol), CN-OA-m (5 mg) dpbpy (9.5 μmol) and BIPA (951.5 μmol) in MeCN (3 mL), 525 nm LED (200% power), 17 h. ^bConversion of methyl 4-iodobenzoate determined by ¹H-NMR using 1,3,5-trimethoxybenzene as internal standard. ^cNMR yields determined by ¹H-NMR using 1,3,5-trimethoxybenzene as internal standard. BIPA = *N-tert*-butylisopropylamine. dpbpy = [2,2'-bipyridine]-4,4'-diylidiphosphonic acid. n.d. = not detected. deg = degassed. quant. = quantitative.

6.5.5 Other cross-coupling reactions

6.5.5.1 C–O cross coupling

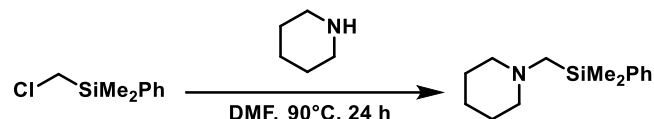
Table S6.24. Comparison of different semiconductorss for the C–O arylation of *N*-Boc proline with 5-bromobenzoate using the 440 nm LED setup.^a

Entry	Semiconductor	Conversion [%] ^b	11 [%] ^c	9 [%] ^c	10 [%] ^c
1	TiO ₂	2	n.d.	n.d.	n.d.
2	CN-OA-m	1	n.d.	n.d.	n.d.
3	mpg-CN	3	traces	n.d.	n.d.
4	Ru-TiO ₂	1	n.d.	n.d.	n.d.
5	Bi ₂ O ₃	1	n.d.	n.d.	n.d.
6	Bi ₂ O ₃ nanopowder	3	n.d.	n.d.	n.d.
7	CdS	2	n.d.	n.d.	n.d.
8	Ir(ppy) ₃ ^d	2	n.d.	n.d.	n.d.

Reaction conditions: methyl 4-iodobenzoate (285.4 μmol), *N*-Boc proline (190.3 μmol), dye (2.4 μmol), NiCl₂·6H₂O (19.0 μmol), dpbpy (19.0 μmol), semiconductor (30 mg) and BIPA (570.8 μmol) in MeCN (anhydrous, 3 mL) 440 nm LED lamp (50% power), 24 h. ^bConversion of methyl 4-iodobenzoate determined by ¹H-NMR using 1,3,5-trimethoxybenzene as internal standard. ^cNMR yields determined by ¹H-NMR using 1,3,5-trimethoxybenzene as internal standard. ^d2 mol% Ir(ppy)₃. BIPA = *N*-*tert*-butylisopropylamine. dpbpy = [2,2'-bipyridine]-4,4'-diylidiphosphonic acid. n.d. = not detected. deg = degassed.

6.5.5.2 C–C (silane) cross-coupling

Synthesis of 1-((Dimethyl(phenyl)silyl)methyl)piperidine

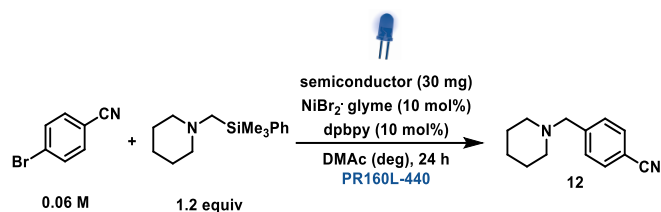


Scheme S6.2. Synthesis of 1-((Dimethyl(phenyl)silyl)methyl)piperidine

A 100 mL round bottom flask equipped with a stir bar was charged with ((chloromethyl)dimethylphenyl)silane (4.73 g, 25 mmol, 1 equiv), DMF (25 mL) and piperidine (6.38 g, 7.41 mL, 75 mmol, 3.0 equiv). The mixture was heated to 90°C in an oil bath (overnight) under an argon atmosphere. The reaction progress was assessed by NMR. Upon completion, the mixture was cooled to room temperature and was diluted with H₂O (~50 mL). The mixture was extracted with Et₂O (75 mL). The layers were separated, and the aqueous layer was extracted with Et₂O (2 × 50 mL). The combined organic layers were washed with deionized H₂O (2 × 100 mL) and brine (150 mL). The organic layer was dried (Na₂SO₄), and the solvent was removed. Further purification was accomplished by vacuum distillation (bp 60-62 °C @ 1 mmHg) giving clear colorless oil (3.02 g, 52%).

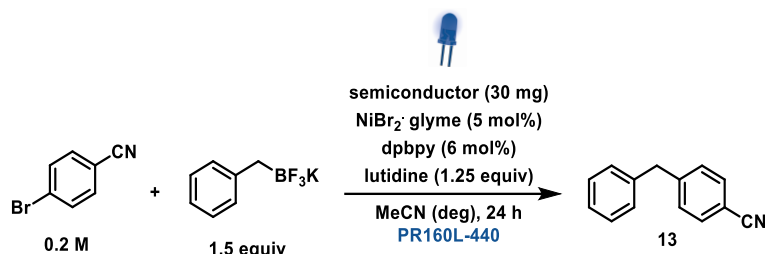
1-((Dimethyl(phenyl)silyl)methyl)piperidine: ¹H NMR (400 MHz, CDCl₃) δ. 0.36 (s, 6H), 1.30 -1.39 (m, 2H), 1.49 -1.59 (m, 4H), 2.15 (s, 2H), 2.28 -2.38 (m, 4H), 7.33-7.37 (m, 3H), 7.54-7.59 (m, 2H). ¹³C NMR (101 MHz, CDCl₃) δ -2.40, 23.87, 26.31, 50.73, 58.60, 127.86, 139.01, 133.76, 139.50

These data are in full agreement with those previously published in the literature.⁸

Table S6.25. Comparison of different semiconductors for the C–C cross-coupling of 1-((Dimethyl(phenyl)silyl)methyl)piperidine and 4-bromobenzonitril using the 440 nm LED setup.^a

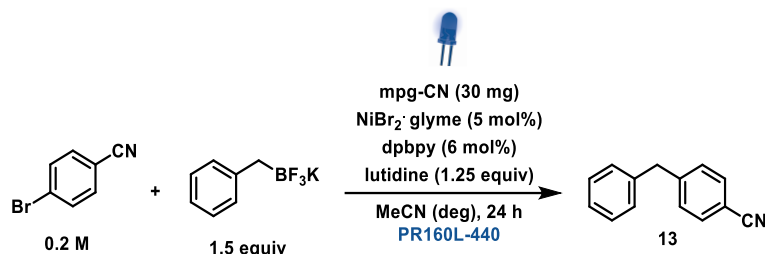
Entry	Semiconductor	ArBr:12 ^b
1	TiO ₂	1:0
2	CN-OA-m	1:0
3	mpg-CN	1:0
4	Ru-TiO ₂	1:0
5	Bi ₂ O ₃	1:0
6	Bi ₂ O ₃ nanopowder	1:0
7	CdS	1:0
8	(Ir[dF(CF ₃)ppy] ₂ (dtbpy))PF ₆	1:0

^aReaction conditions: 4-bromobenzonitrile (190.3 μmol), 1-((Dimethyl(phenyl)silyl)methyl)piperidine (228.3 μmol), dye (1.25 mol%), NiBr₂·glyme (19.0 μmol), dpbpy (19.0 μmol) and semiconductor (30 mg) in DMAc (3 mL), 440 nm LED (100% power), 24 h. ^bDetermined by ¹HNMR. ^c2 mol% (Ir[dF(CF₃)ppy]₂(dtbpy))PF₆. DMAc = dimethylacetamide. glyme = 1,2-dimethoxyethane. dpbpy = [2,2'-bipyridine]-4,4'-diylidiphosphonic acid. deg = degassed.

6.5.5.3 C–C (BF₃K) cross-coupling**Table S6.26.** Comparison of different semiconductors for the C–C cross-coupling of potassium benzyltrifluoroborate and 4-bromobenzonitrile using the 440 nm LED setup.

Entry	Semiconductor	Conversion [%] ^b	13 [%] ^c
1	TiO ₂	1	n.d.
2	CN-OA-m	2	n.d.
3	mpg-CN	29	25
4	Ru-TiO ₂	3	n.d.
5	Bi ₂ O ₃	3	n.d.
6	Bi ₂ O ₃ nanopowder	3	n.d.
7	CdS	3	n.d.

^aReaction conditions: 4-bromobenzonitrile (0.2 mmol), potassium benzyl trifluoroborate (0.3 mmol), NiBr₂·glyme (5 mol%), dpbpy (6 mol%), 2,6-lutidine (0.25 mmol) and semiconductor (30 mg) in MeCN (anhydrous, 1 mL), 440 nm LED (50% power), 24h. ^bConversion of methyl 4-iodobenzoate determined by ¹H-NMR using 1,3,5-trimethoxybenzene as internal standard. ^cNMR yields determined by ¹H-NMR using 1,3,5-trimethoxybenzene as internal standard. BIPA = *N*-*tert*-butylisopropylamine. dpbpy = [2,2'-bipyridine]-4,4'-diyldiphosphonic acid. n.d. = not detected. deg = degassed.

C–C (BF₃K): Recycling with mpg-CNTable S6.27. C–S recycling study with mpg-CN as a semiconductor using the 440 nm LED setup.^a

Entry	Conversion [%] ^b	13 [%] ^c
1	27	25
2	2	0

^aReaction conditions: 4-bromobenzonitrile (0.2 mmol), potassium benzyl trifluoroborate (0.3 mmol), NiBr₂·glyme (5 mol%) and dpbpy (6 mol%), 2,6-lutidine (0.25 mmol) and CN (30 mg) in MeCN (anhydrous, 1 mL), 440 nm LED (50% power), 24h. ^bConversion of methyl 4-iodobenzoate determined by ¹H-NMR using 1,3,5-trimethoxybenzene as internal standard. ^cNMR yields determined by ¹H-NMR using 1,3,5-trimethoxybenzene as internal standard. BIPA = *N*-*tert*-butylisopropylamine. dpbpy = [2,2'-bipyridine]-4,4'-diyldiphosphonic acid. n.d. = not detected. deg = degassed. quant. = quantitative.

The reaction mixture turned black after the second cycle and no product formation could be observed.

6.5.1 References

1. Zhang, G.; Li, G.; Lan, Z.-A.; Lin, L.; Savateev, A.; Heil, T.; Zafeiratos, S.; Wang, X.; Antonietti, M., Optimizing Optical Absorption, Exciton Dissociation, and Charge Transfer of a Polymeric Carbon Nitride with Ultrahigh Solar Hydrogen Production Activity. *Angew. Chem., Int. Ed.* **2017**, *129* (43), 13630-13634.
2. Goettmann, F.; Fischer, A.; Antonietti, M.; Thomas, A., Chemical Synthesis of Mesoporous Carbon Nitriles Using Hard Templates and Their Use as a Metal-Free Catalyst for Friedel–Crafts Reaction of Benzene. *Angew. Chem. Int. Ed.* **2006**, *45* (27), 4467-4471.
3. Brown, H. C.; Kanth, J. V. B.; Dalvi, P. V.; Zaidlewicz, M., Molecular Addition Compounds. 15. Synthesis, Hydroboration, and Reduction Studies of New, Highly Reactive tert-Butyldialkylamine–Borane Adducts. *J. Org. Chem.* **1999**, *64* (17), 6263-6274.
4. Neuthe, K.; Bittner, F.; Stiemke, F.; Ziem, B.; Du, J.; Zellner, M.; Wark, M.; Schubert, T.; Haag, R., Phosphonic acid anchored ruthenium complexes for ZnO-based dye-sensitized solar cells. *Dyes Pigments* **2014**, *104*, 24-33.
5. <https://www.kessil.com/photoreaction/index.php>
6. Cavedon, C.; Madani, A.; Seeberger, P. H.; Pieber, B., Semiheterogeneous Dual Nickel/Photocatalytic (Thio)etherification Using Carbon Nitriles. *Org. Lett.* **2019**, *21* (13), 5331-5334.
7. Greed, S.; Briggs, E. L.; Idiris, F. I. M.; White, A. J. P.; Lücking, U.; Bull, J. A., Synthesis of Highly Enantioenriched Sulfonimidoyl Fluorides and Sulfonimidamides by Stereospecific Sulfur–Fluorine Exchange (SuFEx) Reaction. *Chem. Eur. J.* **2020**, *26* (55), 12533-12538.
8. Remeur, C.; Kelly, C. B.; Patel, N. R.; Molander, G. A., Aminomethylation of Aryl Halides Using α -Silylamines Enabled by Ni/Photoredox Dual Catalysis. *ACS Catal.* **2017**, *7* (9), 6065-6069.

Supporting Information - Chapter 7

Carbon dot/TiO₂ nanocomposites as photocatalysts for metallaphotocatalytic carbon–heteroatom cross-couplings

Zhao Z., Reischauer, S.; Pieber, B., Delbianco M.

Green Chem., **2021**, *23*, 4524-4530.

<https://doi.org/10.1039/D1GC01284C>

7.5 Supporting information

7.5.1 General materials and methods

All substrates, reagents, and solvents were obtained from commercial suppliers and were used without further purification unless otherwise noted. All light-emitting diode (LED) lamps were purchased from Kessil Lighting (<https://www.kessil.com/science/index.php>). Analytical thin layer chromatography (TLC) was performed on pre-coated TLC-sheets, ALUGRAM Xtra SIL G/UV₂₅₄ sheets (Macherey-Nagel) and visualized with 254 nm light or staining solutions followed by heating. Purification of final compounds was carried out by flash chromatography on the Reveleris X2 Flash Chromatography System from GRACE using prepacked columns with 40 µm silica gel. Silica 60 M (0.04-0.063 mm) silica gel (Sigma Aldrich) was used for dry loading of the crude compounds on the flash chromatography system. Carbon dots (CDs) were synthesized using a domestic microwave (SEVERIN). Centrifugation of CDs and CD/titanium dioxide (TiO₂ P25) nanocomposites were carried out using an Eppendorf 5810R centrifuge and an Eppendorf 5430 centrifuge, respectively. NMR spectra were recorded on an Ascend™ 400 (400 MHz, Bruker) spectrometer, and are reported in ppm relative to the residual solvent peaks. Peaks are reported as: s = singlet, d = doublet, t = triplet, q = quartet, m = multiplet or unresolved, with coupling constants in Hz. Infrared (IR) spectra were recorded on a Perkin-Elmer FT-IR spectrometer (Spectrum 100). The morphologies of CDs were observed using transmission electron microscopy (TEM, Zeiss EM 912Ω). The prepared CDs were diluted with distilled water to suitable concentrations and then deposited onto carbon-coated copper grids. After drying at room temperature, the samples were imaged. The morphologies and elemental composition of CD/TiO₂ P25 nanocomposites were measured using scanning electron microscopy and energy dispersive X-ray spectroscopy (SEM-EDX, LEO 1550 system). The freeze-dried CD/TiO₂ P25 nanocomposites were suspended in distilled water and sonicated for 5 min. The resulting suspension was deposited on the silicon substrate and coated with Au. After drying at room temperature, the samples were imaged. Fluorescence spectra of CDs were measured using a microplate reader (SpectraMax M5, Molecular Devices). Absorption spectra of CDs and CD/TiO₂ P25 nanocomposites were collected using a Shimadzu UV-1900 (solutions), or a Shimadzu UV-2600 spectrometer equipped with an integrating sphere (solids). X-ray diffraction (XRD) spectrum was measured with a Bruker D8 Advanced X-ray diffractometer with Cu Kα radiation. Zeta potential was measured with

a dynamic light scattering instrument (DLS, Zetasizer Nano, Malvern). Photoluminescence lifetime was measured using the time-correlated single photon counting technique (TCSPC, FluoTime 250, fluorescence lifetime spectrometer). Inductively coupled plasma - optical emission spectrometry (ICP-OES) was carried out using a Horiba Ultra 2 instrument equipped with a photomultiplier tube detection system.

7.5.2 Synthesis of CDs

The carbohydrate carbon source was dissolved in ultrapure H₂O (20 mL) in a conical flask (300 mL). The doping agent was added and the mixture was agitated to yield a homogenous solution. The flask was transferred into a domestic microwave in a fume hood and heated at 700 W for the respective time. The crude mixture was cooled for 10 min before ultrapure H₂O (40 mL) was added. The resulting solution was filtered through a filter paper and centrifuged at 8000 rpm for 0.5 h through Amicon® Ultra-15 centrifugal filter units. The filtrate was lyophilized to yield the desired CDs.

Table S7.1. Summary of the conditions used for the synthesis of the CDs.

Entry	CD	Carbon source (mmol/mL)	Doping agent (mmol/mL)	Time / min
1	CD1	GlcN·HCl (0.12)	β-Ala (0.13)	3
2	CD2 ^a	GlcN·HCl (0.15)	1,3-Diaminobenzene (0.17)	3
3	CD3		l-Cys (0.25)	3
4	CD4	GlcN·HCl (0.23)	PEG (0.25)	9
5	CD5		Gly (0.25)	3
6	CD6	Glc (0.12)		4.5
7	CD7	GlcNAc (0.12)		4.5
8	CD8	Gal (0.12)	β-Ala (0.13)	4.5
9	CD9	Lac (0.12)		4.5
10	CD10	Pullulan (25 mg/mL)		5

^aThe doping agent was first dissolved in MeOH (10 mL) and then added to the aqueous solution (20 mL) of carbon source. GlcN·HCl = glucosamine hydrochloride. Glc = glucose. GlcNAc = *N*-acetylglucosamine. Gal = galactose. Lac = D-lactose. β-Ala = β-alanine. l-Cys = l-cysteine. PEG = poly(ethylene glycol) (average M_n 400). Gly = glycine.

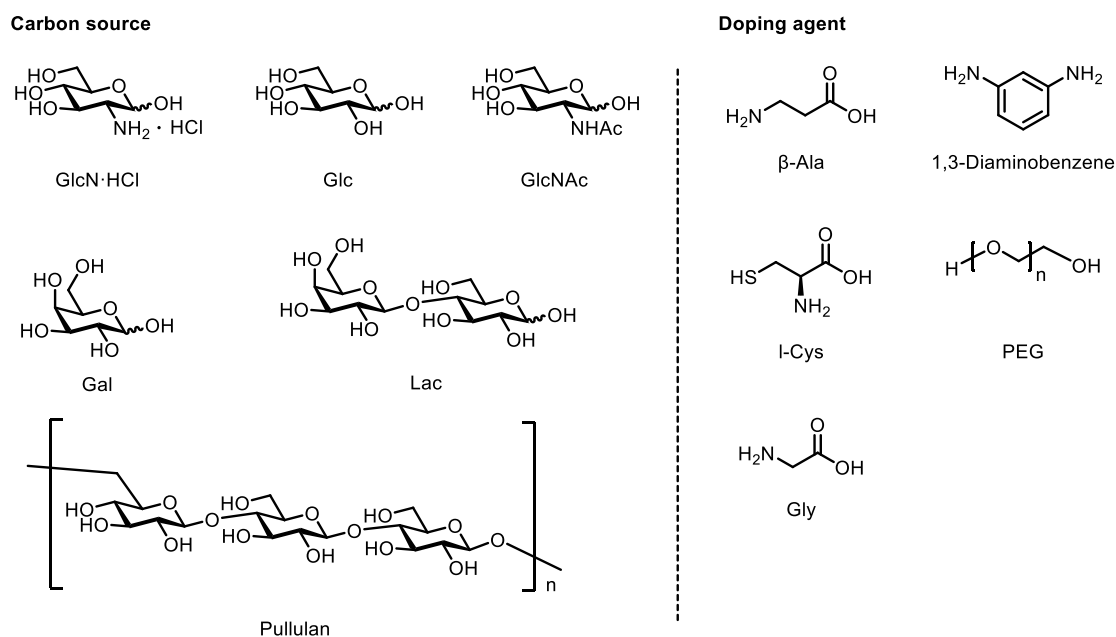


Figure S7.1. Chemical structures of carbon sources and doping agents used for CD synthesis.

7.5.3 Preparation of CD/TiO₂ P25 nanocomposites

TiO₂ P25 (120 mg) was dispersed in ultrapure H₂O (80 mL) in a round-bottom flask. The respective amount of CDs was added to prepare nanocomposites with different CD-to-TiO₂ P25 mass ratios. The mixture was shielded from light and stirred for 24 h at room temperature. The resulting CD/TiO₂ nanocomposites were centrifuged at 5000 rpm for 15 min and further washed two times with ultrapure H₂O. The nanocomposites were lyophilized to afford a light brown powder. The amount of CDs immobilized on the TiO₂ P25 surface was determined using UV-Vis absorption spectroscopy.

Table S7.2. Conditions used for the preparation of the CD/TiO₂ nanocomposites.

Entry	CD	CD-to-TiO ₂ P25 mass ratio	CD Immobilization (weight % (CD/nanocomposite))
1	CD1	1 : 20	1.5
2		1 : 10	1.8
3		1 : 4	2.4
4		1 : 1	5.0
5		4 : 1	8.1
6		1 : 1 (CD-to-SiO ₂)	1.6
7	CD2	1 : 1	- ^a
8	CD3	1 : 1	2.5

9	CD4	1 : 1	13.6
10	CD5	1 : 1	3.4
11	CD6	1 : 1	3.7
12	CD7	1 : 1	11.9
13	CD8	1 : 1	3.0
14	CD9	1 : 1	11.4
15	CD10	1 : 1	27.2

^aQuantification by UV-Vis was not possible due to the formation of side-products in the solution that affected the measurements.

7.5.4 Characterization of CDs

7.5.4.1 CD1

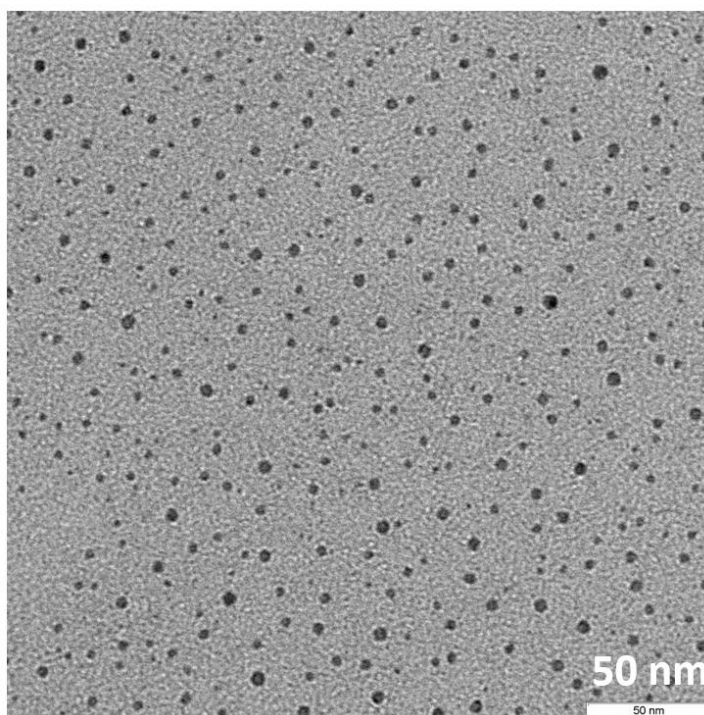


Figure S7.2. TEM image of CD1.

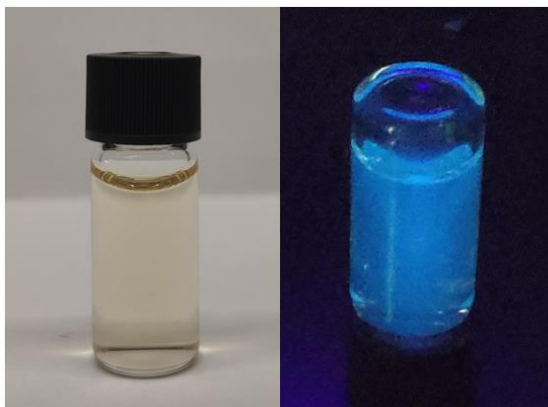


Figure S7.3. Photographs of an aqueous solution of **CD1** in daylight (left) and under UV light irradiation ($\lambda_{\text{ex}} = 366 \text{ nm}$, right).

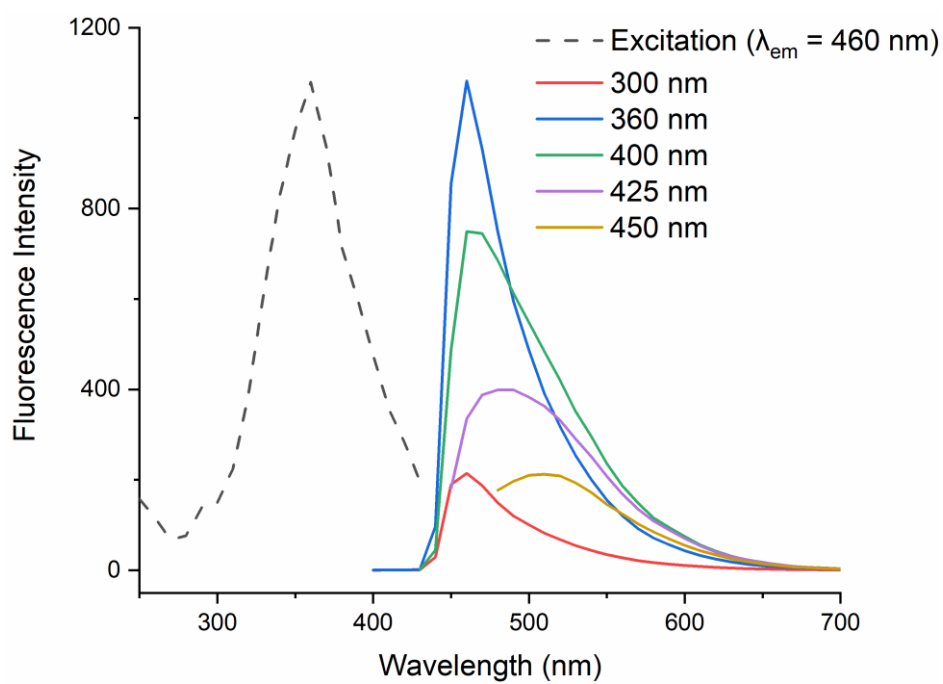


Figure S7.4. Excitation ($\lambda_{\text{em}} = 460 \text{ nm}$) and emission spectra of **CD1** recorded upon excitation with different excitation wavelengths (H_2O , 298 K).

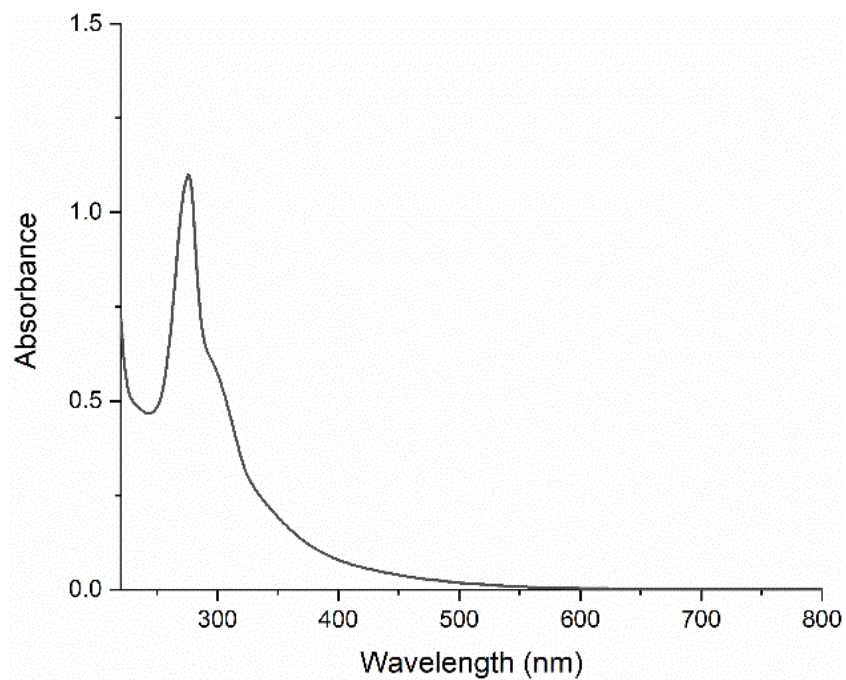


Figure S7.5. Absorption spectrum of **CD1** (H₂O, 298 K).

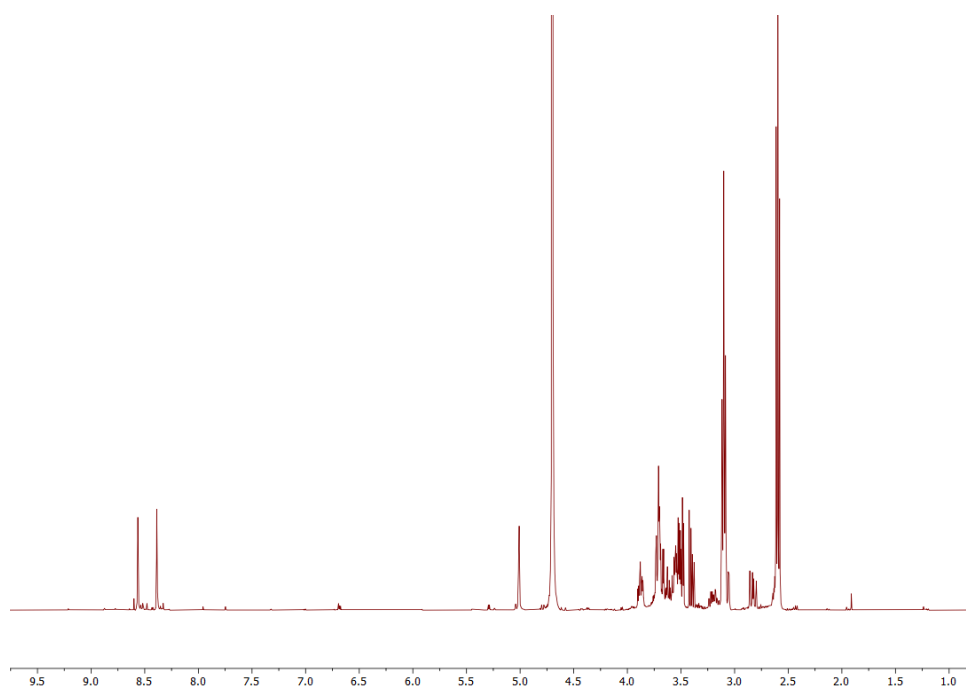


Figure S7.6. ¹H NMR spectrum of **CD1** in D₂O (400 MHz). The spectrum is in agreement with previously reported data,¹ indicating the presence of the β-alanine on **CD1** surface.

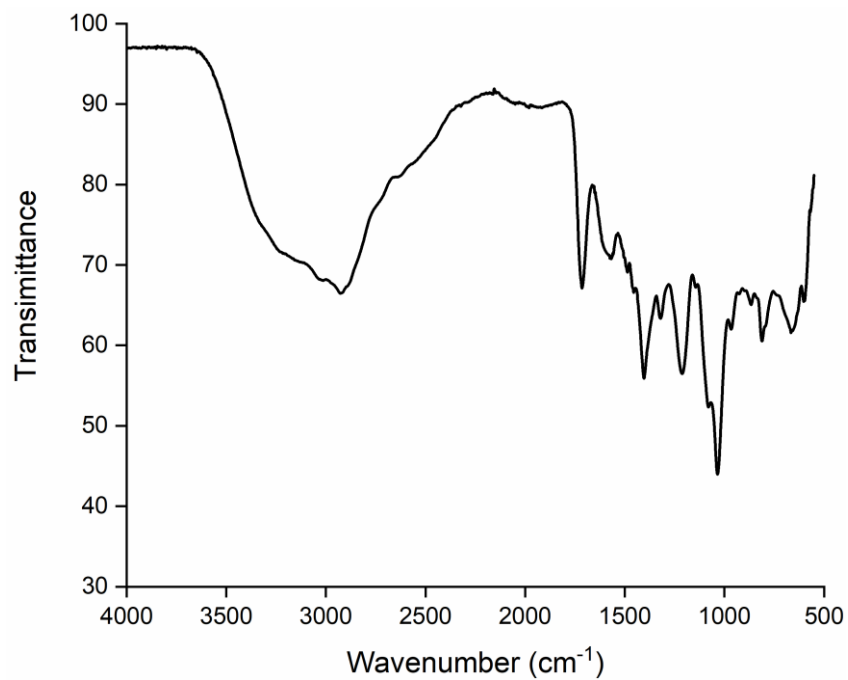


Figure S7.7. IR spectrum of **CD1**. Key features: 2927 cm⁻¹ (O-H); 1715 cm⁻¹ (C=O).

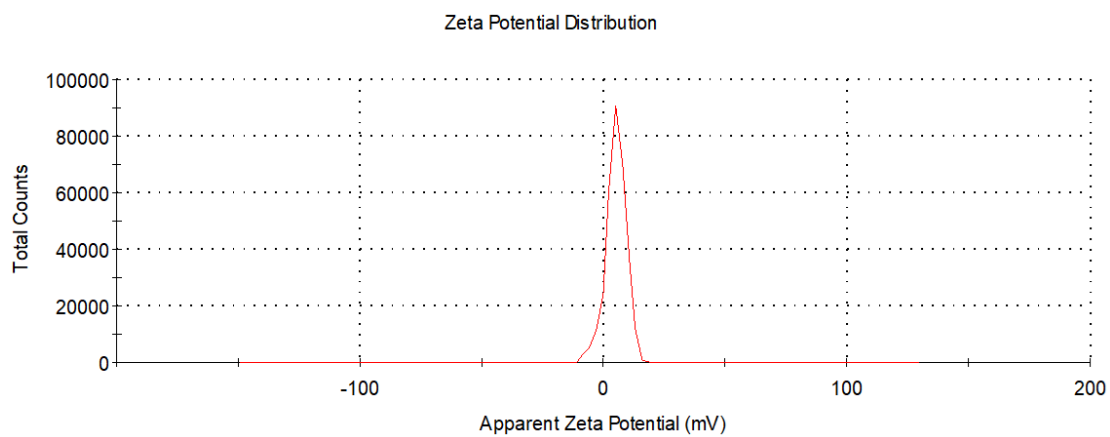


Figure S7.8. Zeta potential of **CD1** (-11.1 to +18.7 mV, H₂O, 298 K).

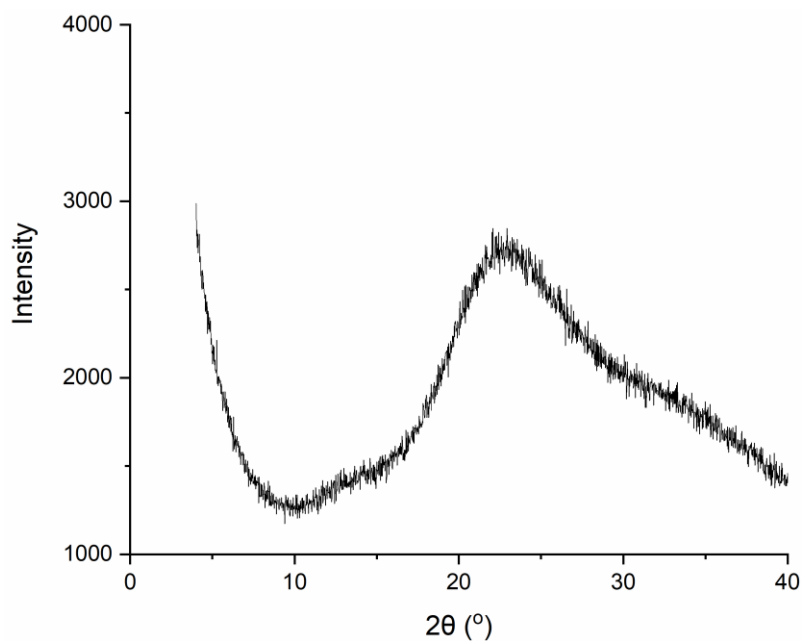
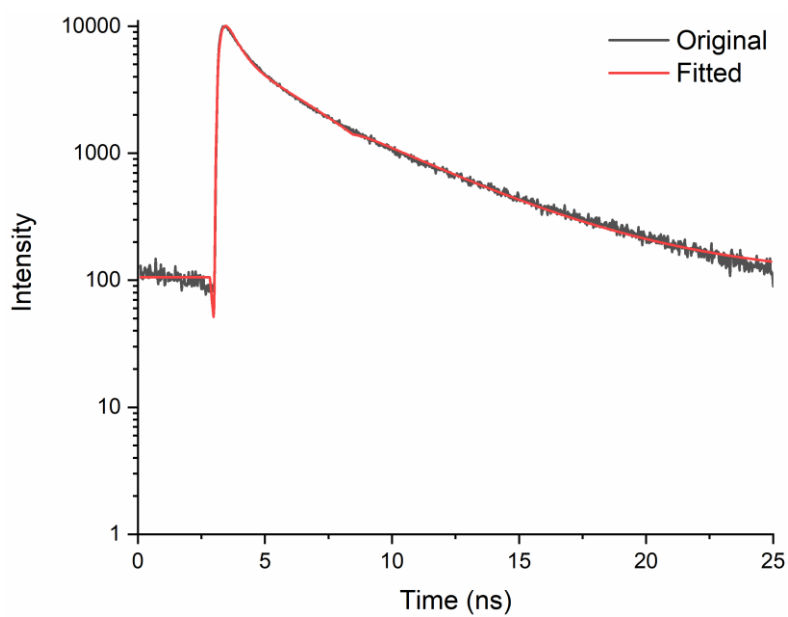


Figure S7.9. Powder XRD profile of **CD1** confirming its amorphous nature.

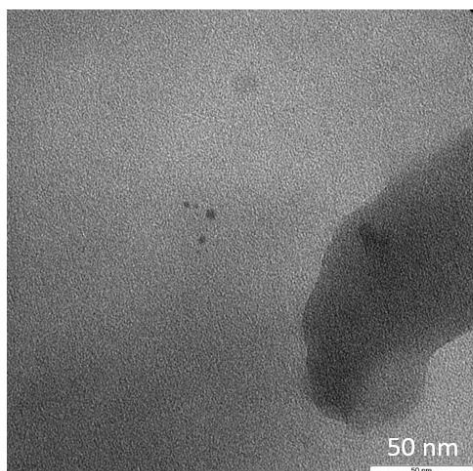


A_1	A_2	τ_1 (ns)	τ_2 (ns)
10.49	6.131	0.451	4.454

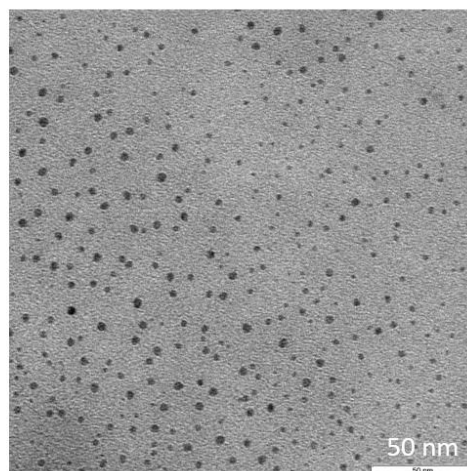
Figure S7.10. Photoluminescence lifetime of **CD1** (H₂O, 298 K).

7.5.4.2 Characterization of CD2-CD10

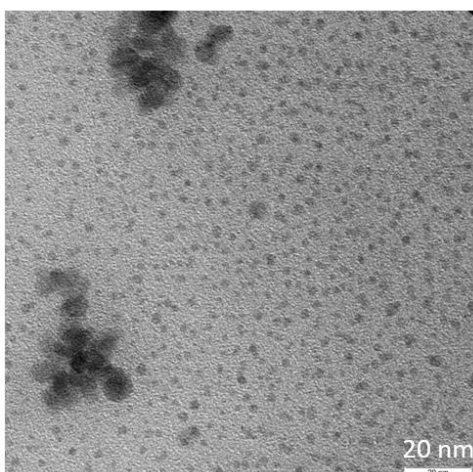
CD2



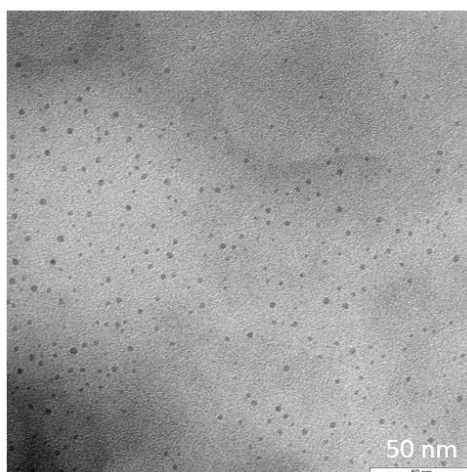
CD3



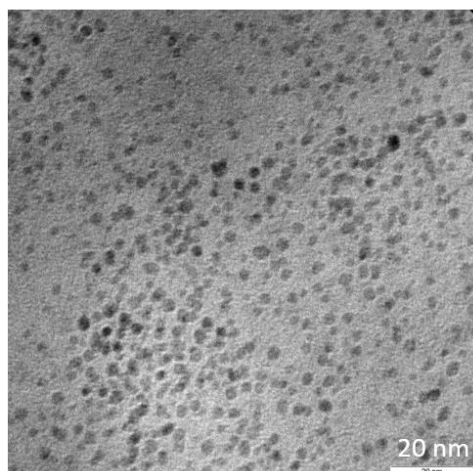
CD4



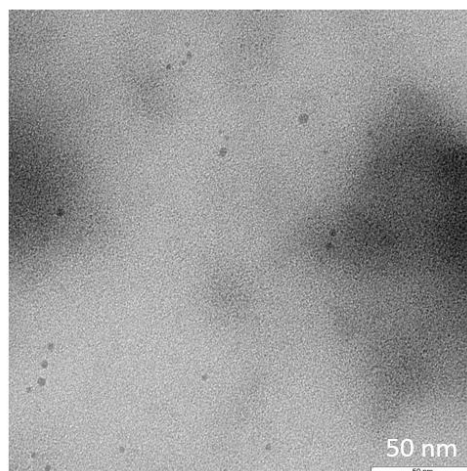
CD5



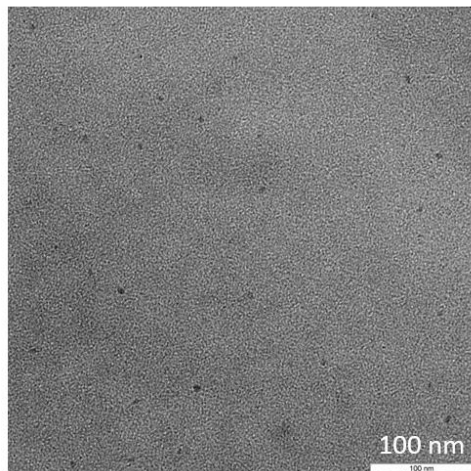
CD6



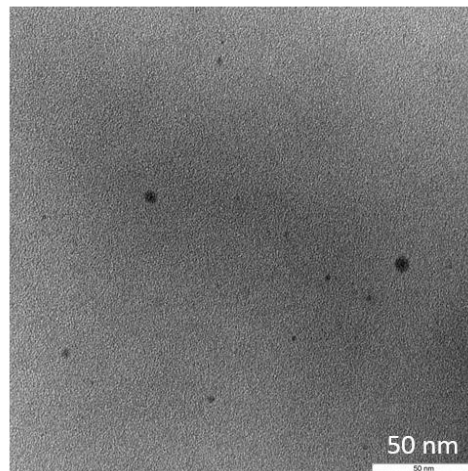
CD7



CD8



CD9



CD10

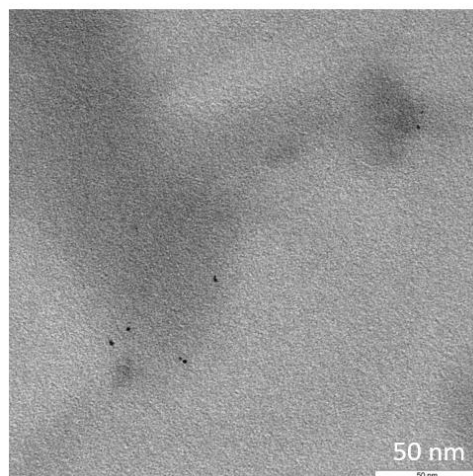


Figure S7.11. TEM images of CD2, CD3, CD4, CD5, CD6, CD7, CD8, CD9 and CD10.

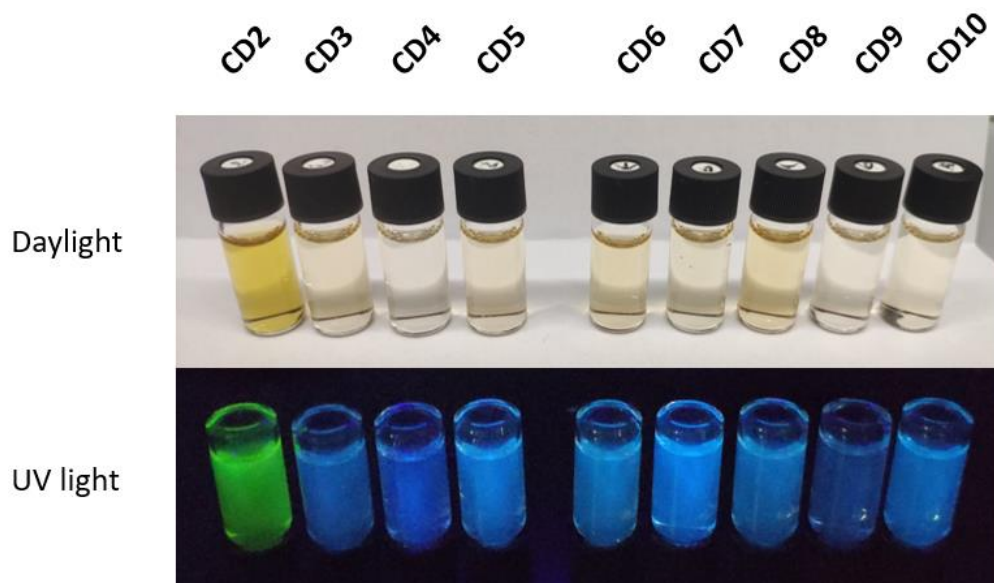
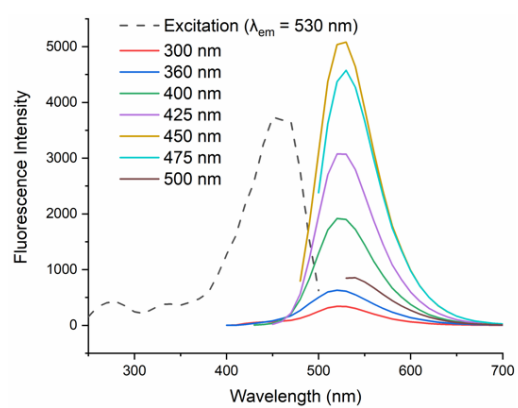
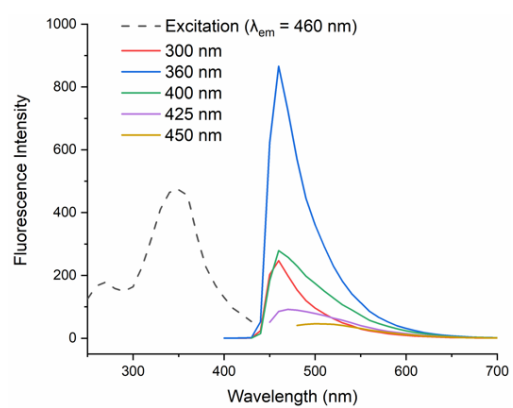


Figure S7.12. Photographs of aqueous solutions of **CD2**, **CD3**, **CD4**, **CD5**, **CD6**, **CD7**, **CD8**, **CD9** and **CD10** in daylight and under UV light irradiation ($\lambda_{\text{ex}} = 366 \text{ nm}$).

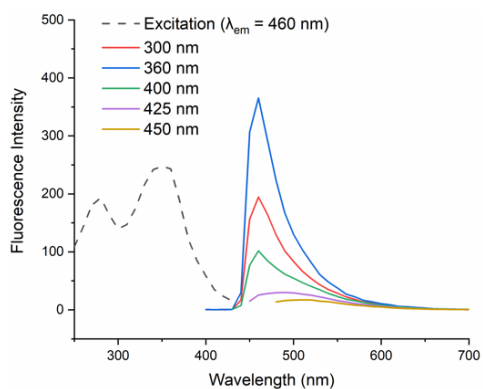
CD2



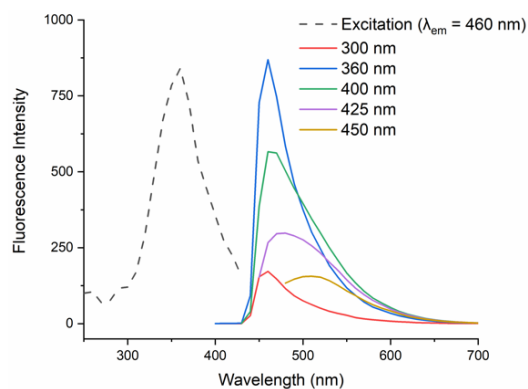
CD3



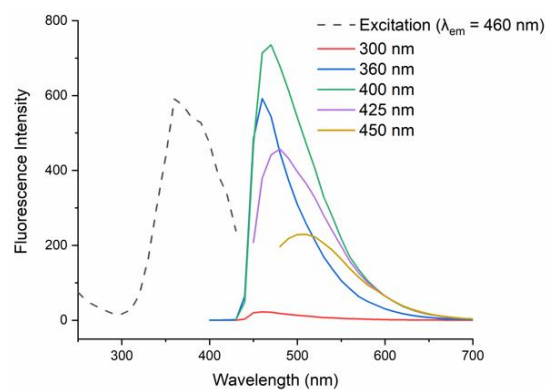
CD4



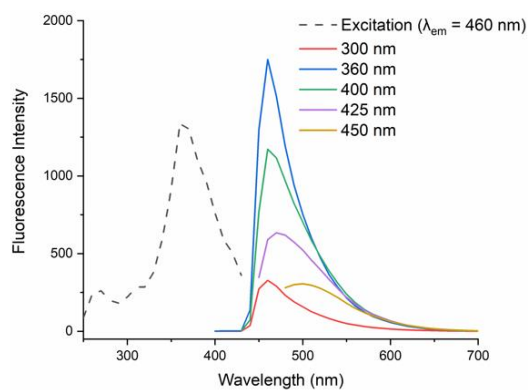
CD5



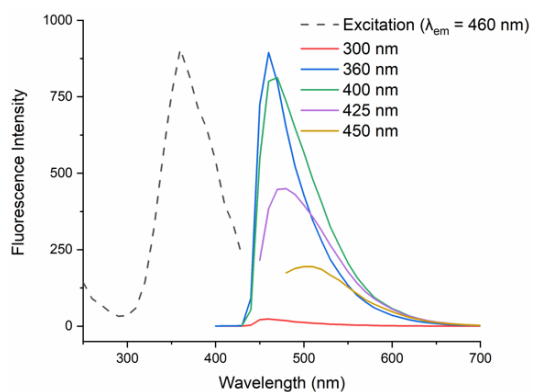
CD6



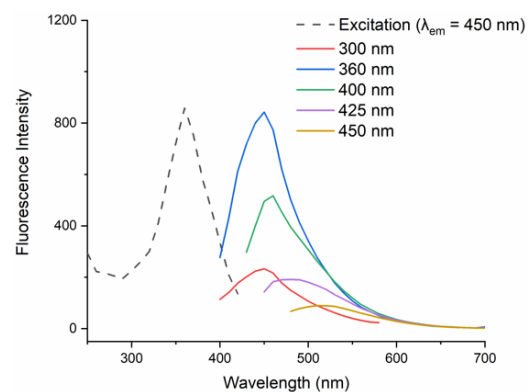
CD7



CD8



CD9



CD10

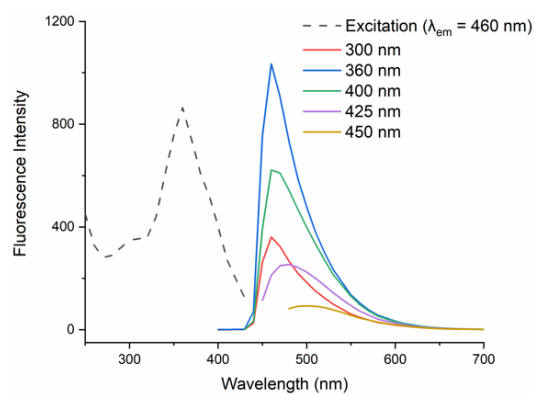
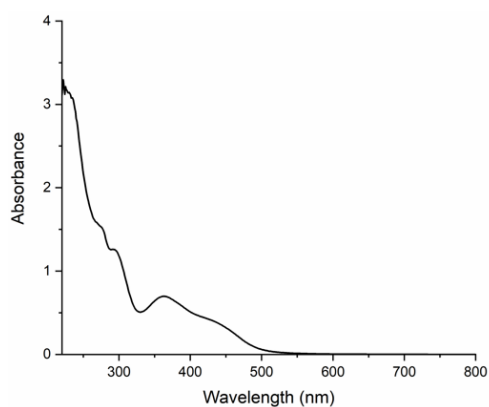
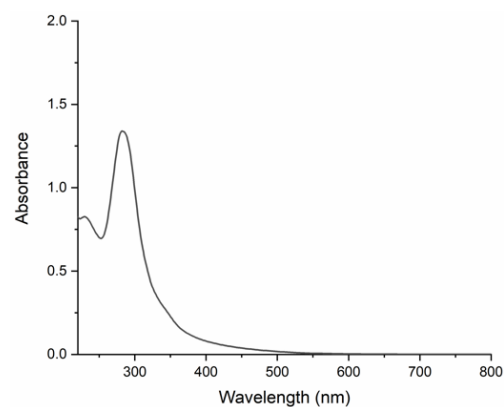


Figure S7.13. Excitation and emission spectra of **CD2**, **CD3**, **CD4**, **CD5**, **CD6**, **CD7**, **CD8**, **CD9** and **CD10** recorded upon excitation with different excitation wavelengths (H₂O, 298 K).

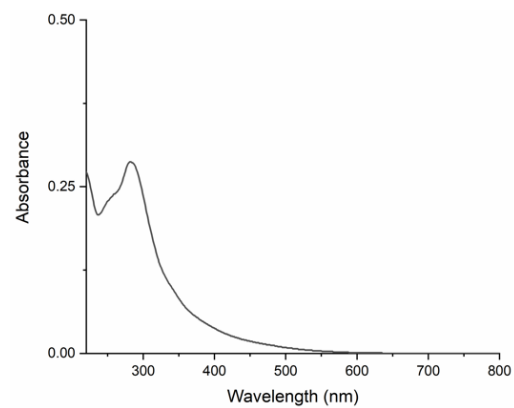
CD2



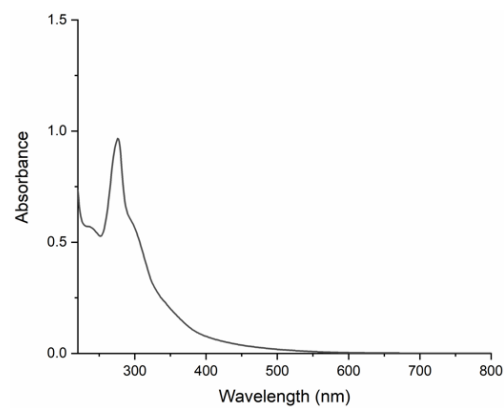
CD3



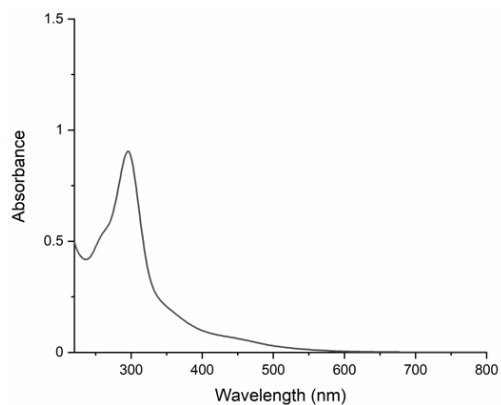
CD4



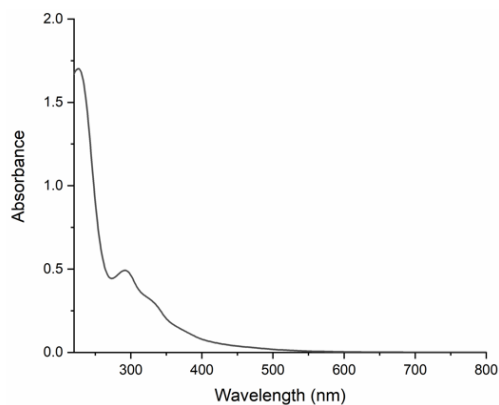
CD5



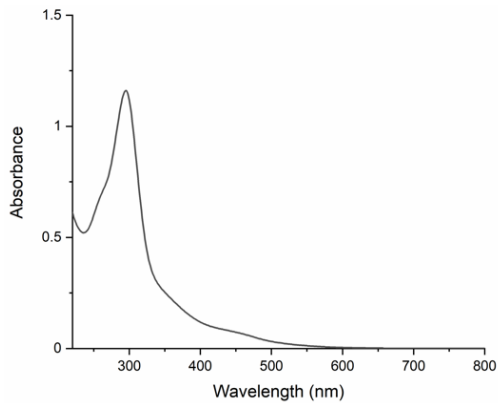
CD6



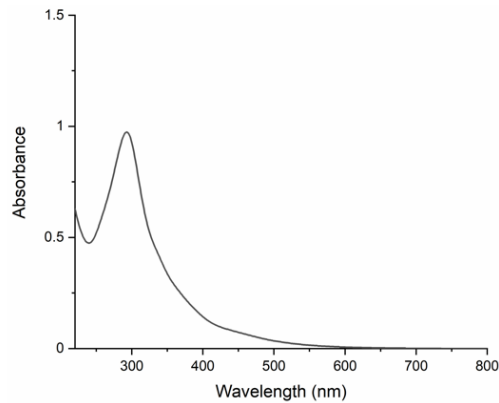
CD7



CD8



CD9



CD10

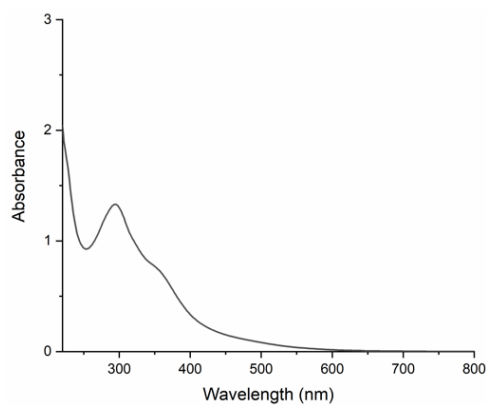
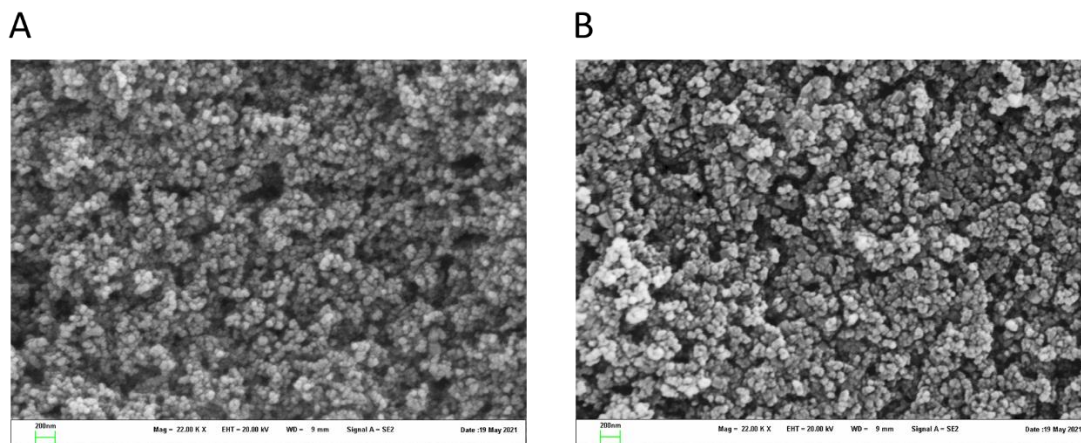


Figure S7.14. Absorption spectra of CD2, CD3, CD4, CD5, CD6, CD7, CD8, CD9 and CD10 (H₂O, 298 K).

7.5.5 Characterization of CD/TiO₂ nanocomposites7.5.5.1 CD1/TiO₂

Sample	C	O	Ti	Ni
CD1/TiO ₂	23.86	59.04	17.15	0
CD1/TiO ₂ (after)	32.75	60.79	6.26	0.23

Figure S7.15. SEM image and elemental composition of CD1/TiO₂ P25 nanocomposite (A) and CD1/TiO₂ P25 nanocomposite after the catalytic reaction (B). All values are given as atomic %.

Table S7.3. ICP-OES measurements of the nickel content of CD1/TiO₂ P25 nanocomposite and CD1/TiO₂ P25 nanocomposite after the catalytic reaction.

Sample	Ni (mg/g)
CD1/TiO ₂	0.016
CD1/TiO ₂ (after)	24.8

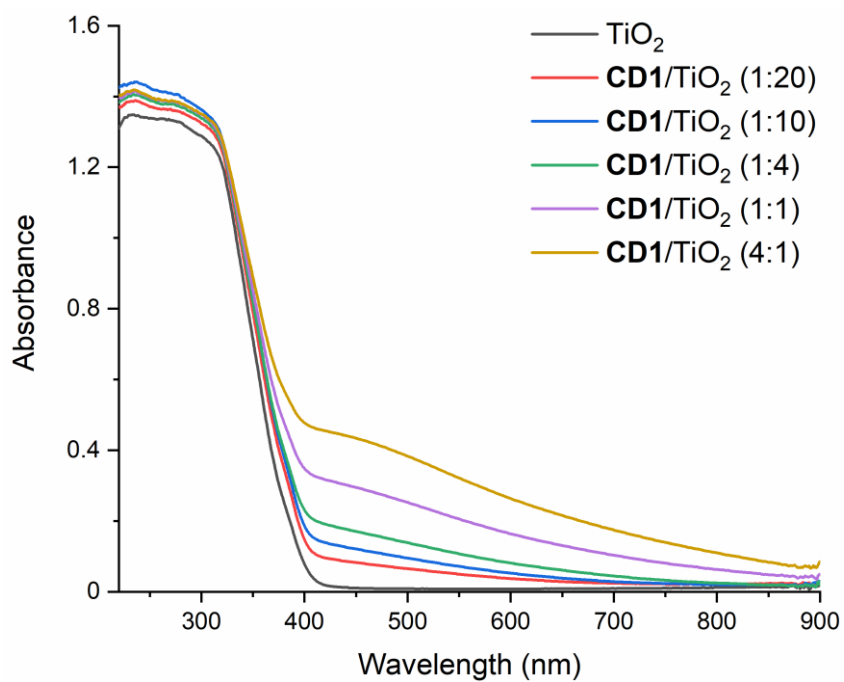


Figure S7.16. Absorption spectra (solid state) of CD1/TiO₂ nanocomposites prepared using different CD1-to-TiO₂ P25 mass ratios.

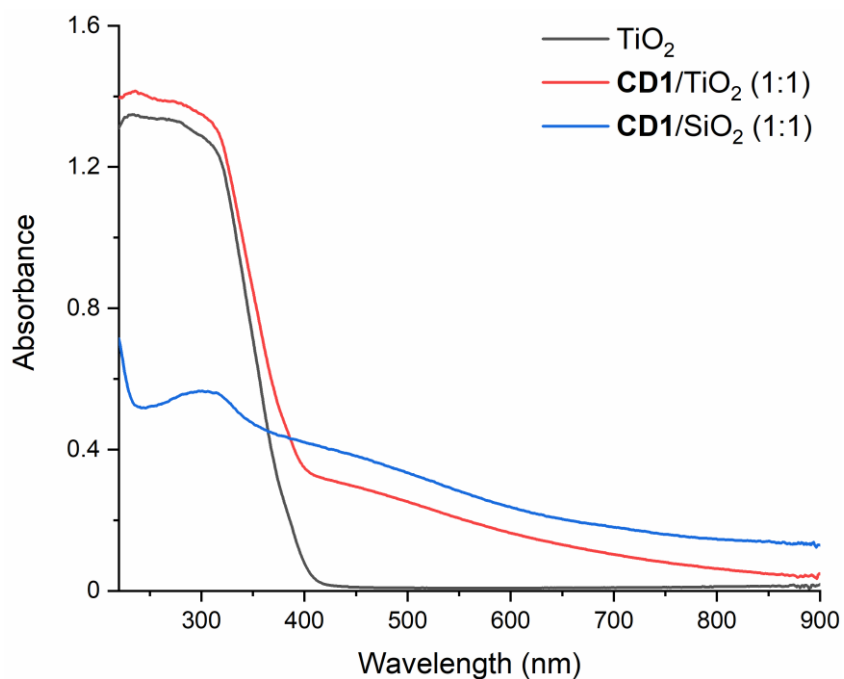
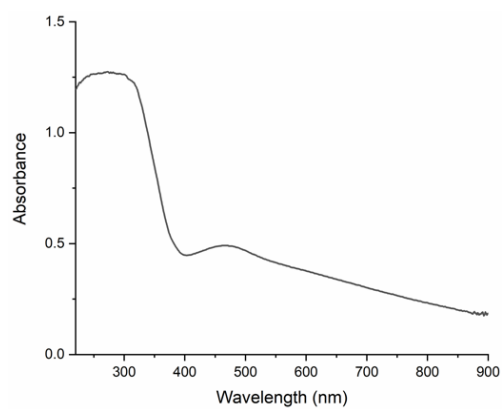


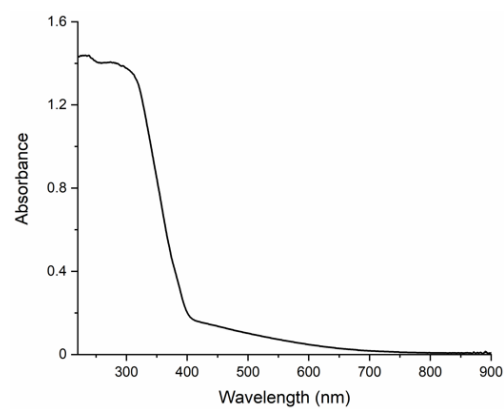
Figure S7.17. Absorption spectra (solid state) of CD1/TiO₂ and CD1/SiO₂ nanocomposites (mass ratio = 1:1).

7.5.5.2 Characterization of nanocomposites prepared using CD2-CD10

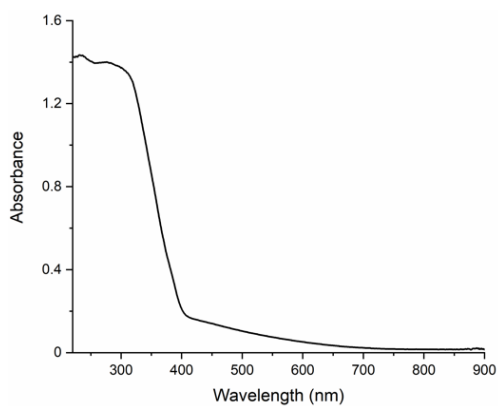
CD2/TiO₂



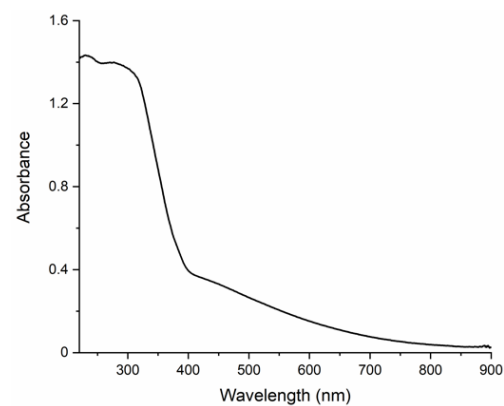
CD3/TiO₂



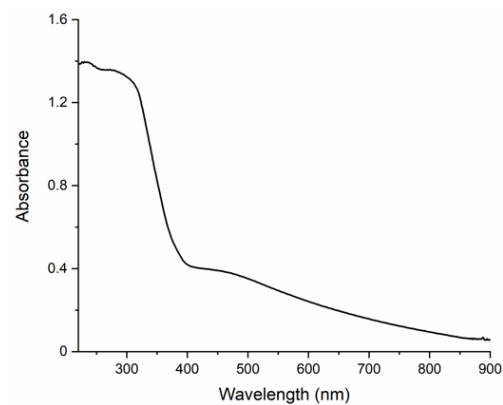
CD4/TiO₂



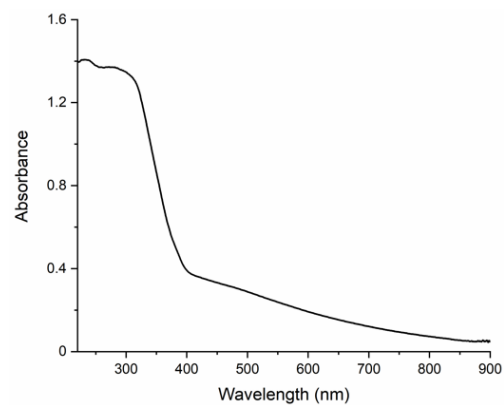
CD5/TiO₂



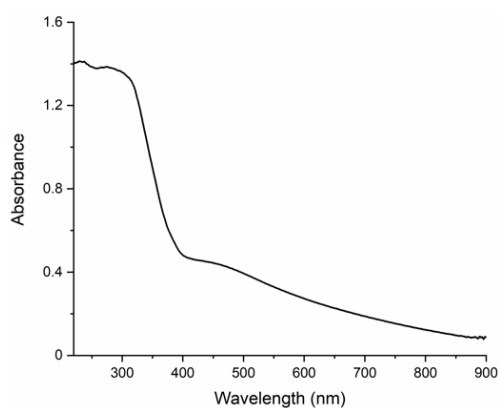
CD6/TiO₂



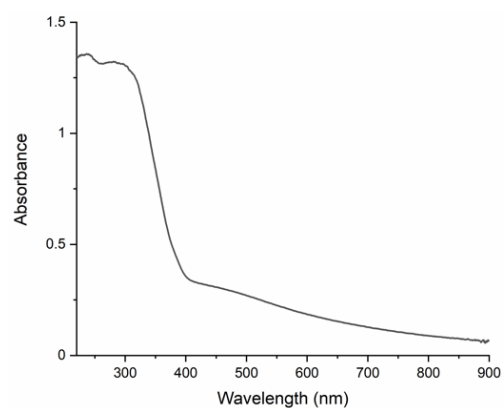
CD7/TiO₂



CD8/TiO₂



CD9/TiO₂



CD10/TiO₂

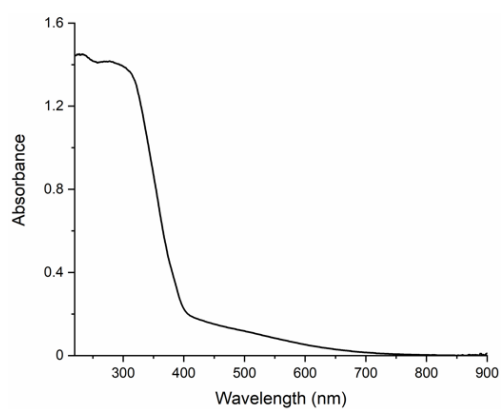


Figure S7.18. Absorption spectra (solid state) of CD2/TiO₂, CD3/TiO₂, CD4/TiO₂, CD5/TiO₂, CD6/TiO₂, CD7/TiO₂, CD8/TiO₂, CD9/TiO₂ and CD10/TiO₂ nanocomposites.

7.5.6 Cross-coupling reaction

Setup for blue light experiments.¹ Two vials were placed in the middle of the stirring plate (4.5 cm away from single lamp). The reaction was irradiated with a single blue LED lamp (Kessil PR160L-440). The fan was used to avoid possible heating of the reaction mixture.



Figure S7.19. Image of the setup using a single blue LED lamp.

Setup for green light experiments.¹ Two vials were placed in the middle of the stirring plate (4.5 cm away from each lamp). The reaction was irradiated with two green LED lamps (Kessil PR160L-525). The fan was used to avoid the possible heating of the reaction mixture.

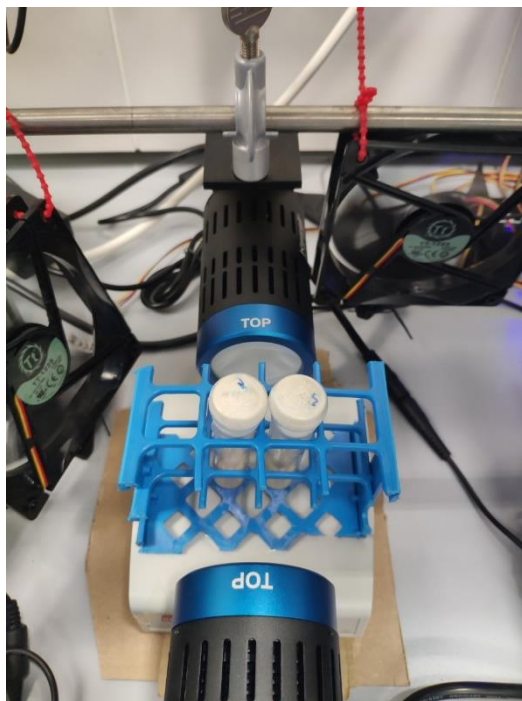
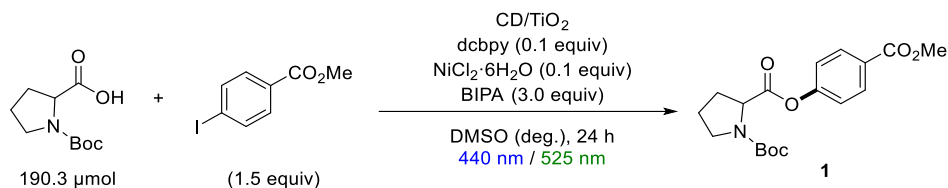


Figure S7.20. Image of the setup using two green LED lamps.

7.5.6.1 C-O arylation of Boc-Pro-OH



General experimental procedure. Boc-Pro-OH (*N*-(*tert*-butoxycarbonyl)-L-proline, 41.0 mg, 190.3 μmol), methyl 4-iodobenzoate (74.8 mg, 285.4 μmol) and the respective CD/TiO₂ nanocomposite (Table S7.4) were added to an oven-dried glass vial equipped with a stir bar. Subsequently, a DMSO solution (3 mL) of dcbpy (2,2'-bipyridine-4,4'-dicarboxylic acid, 4.7 mg, 19.0 μmol), NiCl₂·6H₂O (nickel(II) chloride hexahydrate, 4.5 mg, 19.0 μmol), and BIPA (*N*-*tert*-butylisopropylamine, 90.5 μL, 570.8 μmol) were added. The glass vial was sealed with a septum and Parafilm. The reaction mixture was stirred and sonicated for 10 min to obtain a fine dispersion and subsequently degassed with Argon for 10 min. The vial was then irradiated with the respective LED lamps at room temperature for the respective time. 1,3,5-Trimethoxybenzene (32.0 mg, 190.3 μmol) was added as internal standard to determine NMR yields. An aliquot of the resulting mixture (~250 μL) was filtered through a syringe filter, diluted with DMSO-d₆ (~250 μL) and subjected to ¹H-NMR analysis.

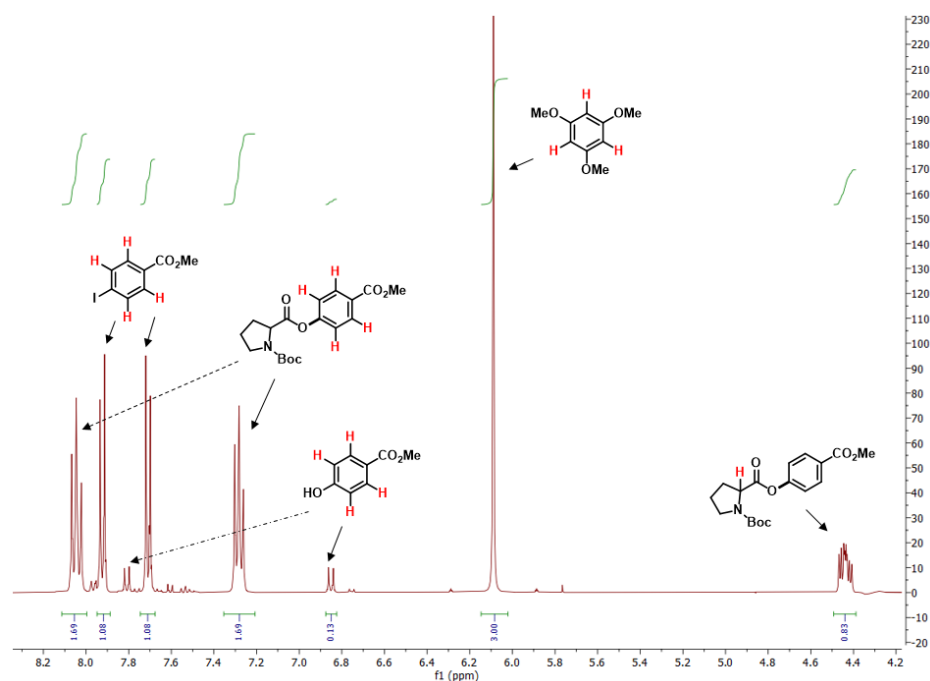


Figure S7.21. Representative ¹H-NMR spectrum of the crude reaction mixture to determine yields by ¹H-NMR analysis using 1,3,5-trimethoxybenzene as internal standard (DMSO-d₆, 400 MHz).

Table S7.3. Summary of the CD/TiO₂ nanocomposites used in the photocatalyzed C-O cross-coupling of Boc-Pro-OH with methyl 4-iodobenzoate.

Entry	Nanocomposite	Initial CD-to-TiO ₂ P25 mass ratio ^[a]	CD Immobilization ^[b] (weight % (CD/nanocomposite))	Amount ^[c] / mg	
1	TiO ₂ P25	-	-	30.0	
2	CD1	-	-	30.0	
3	CD1/TiO₂	1 : 20	1.5	30.5	
4		1 : 10	1.8	30.5	
5		1 : 4	2.4	30.8	
6		1 : 1	5.0	31.6	
7		4 : 1	8.1	32.6	
8		1 : 1 (CD-to-SiO ₂)	1.6	30.5	
9		CD2/TiO₂	1 : 1	-	30.0
10		CD3/TiO₂	1 : 1	2.5	30.8
11	CD4/TiO₂	1 : 1	13.6	34.7	
12	CD5/TiO₂	1 : 1	3.4	31.1	
13	CD6/TiO₂	1 : 1	3.7	31.1	
14	CD7/TiO₂	1 : 1	11.9	34.1	
15	CD8/TiO₂	1 : 1	3.0	30.9	
16	CD9/TiO₂	1 : 1	11.4	33.9	
17	CD10/TiO₂	1 : 1	27.2	41.2	

[a] CD-to-TiO₂ P25 mass ratio used for the preparation of the nanocomposite. [b] Weight % of CD immobilized on TiO₂ as calculated by UV-Vis spectroscopy. [c] Amount of nanocomposite used in the C-O arylation of Boc-Pro-OH.

Procedure to obtain the isolated yield. An oven-dried vial (19 x 100 mm) equipped with a stir bar was charged with **CD1**/TiO₂ (63.2 mg), Boc-Pro-OH (82 mg, 380.6 μmol, 1.0 equiv), methyl 4-iodobenzoate (149.6 mg, 571 μmol, 1.5 equiv), NiCl₂·6H₂O (9 mg, 38 μmol, 10 mol%) and dcbpy (9.3 mg, 38 μmol, 10 mol%). Subsequently, DMSO (anhydrous, 6 mL) and BIPA (180.9 μL, 1.14 mmol, 3.0 equiv) were added and the vial was sealed with a septum and Parafilm. The reaction mixture was sonicated for 5-10 min followed by stirring for 5 min to obtain a fine dispersion. The mixture was then degassed by bubbling Argon for 10 min. The mixture was irradiated using the 440 nm setup with rapid stirring (1400 rpm). After 40 h, one equivalent of 1,3,5-trimethoxybenzene (internal standard, 64 mg, 380 μmol) was added and the mixture was stirred for 5 min. An aliquot of the reaction mixture (~200 μL) was filtered, diluted with DMSO-d₆ and subjected to ¹H-NMR analysis to determine the NMR yield (90%). Thereafter, the NMR sample was combined with the reaction mixture. The reaction mixture was diluted with H₂O (40 mL) and extracted with dichloromethane (3 x 30 mL). The combined organic phases were washed with brine (50 mL), dried over Na₂SO₄ and concentrated. The product was purified by flash column chromatography (SiO₂, Hexane/EtOAc elution gradient of 0-20%) on a Grace Reveleris system using a 12 g cartridge. In some cases, mixed fractions containing small amounts of the phenol byproduct and the desired product were observed. These could be easily purified by a basic extraction (DCM and 0.5 M NaOH), followed by drying the organic phase over Na₂SO₄ and solvent evaporation to maximize the reaction yield. The title compound was isolated as a yellowish solid.

Isolated yield: 84% (111.5 mg, 319 μmol)

1-(tert-butyl) 2-(4-(methoxycarbonyl)phenyl) pyrrolidine-1,2-dicarboxylate 1: ¹H NMR (400 MHz, CDCl₃) rotameric mixture, δ 8.04 (m, 2H), 7.16 (m, 2H), 4.49 (dd, *J* = 8.6, 4.4 Hz, 0.4H), 4.43 (dd, *J* = 8.7, 4.3 Hz, 0.6H), 3.87 (m, 3H), 3.66 – 3.39 (m, 2H), 2.42 – 2.26 (m, 1H), 2.19 – 2.09 (m, 1H), 2.07 – 1.86 (m, 2H), 1.44 (m, 9H). ¹³C NMR (151 MHz, CDCl₃) rotameric mixture, signals for minor rotamer are enclosed in parenthesis δ (171.21) 171.16, (166.37) 166.23, 154.51 (154.23), 153.68, 131.29 (131.15), 127.87 (127.71), (121.57) 121.20, 80.36, (80.16), 59.23 (59.14), 52.28 (52.21), (46.69) 46.50, 31.06 (30.01), 28.45, (24.60) 23.77.

The data are in full agreement with those previously published in the literature².

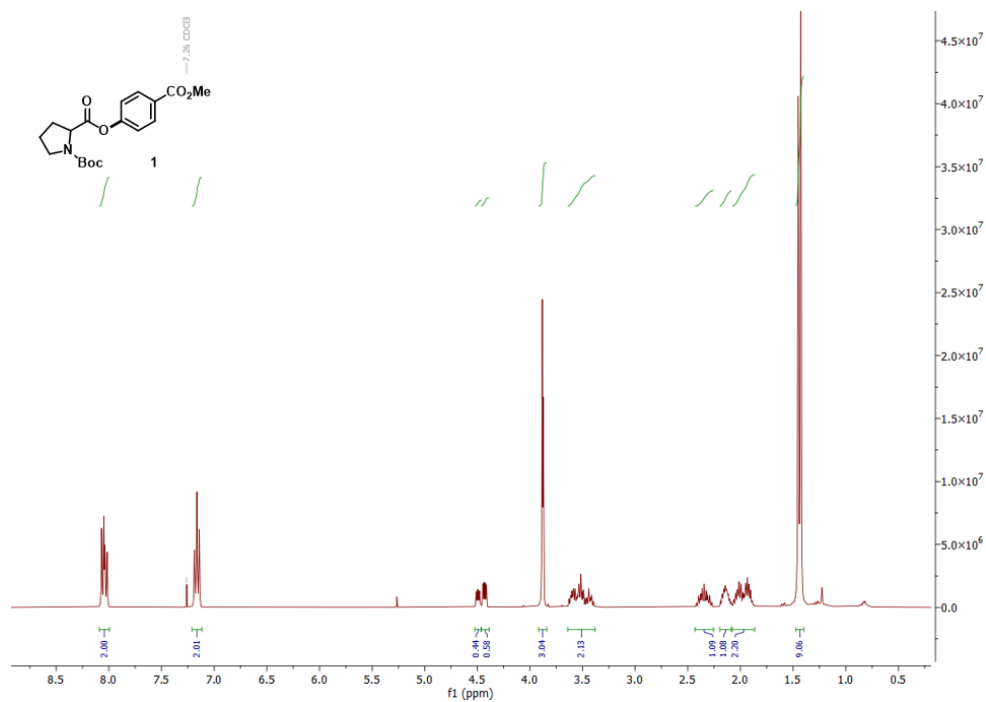
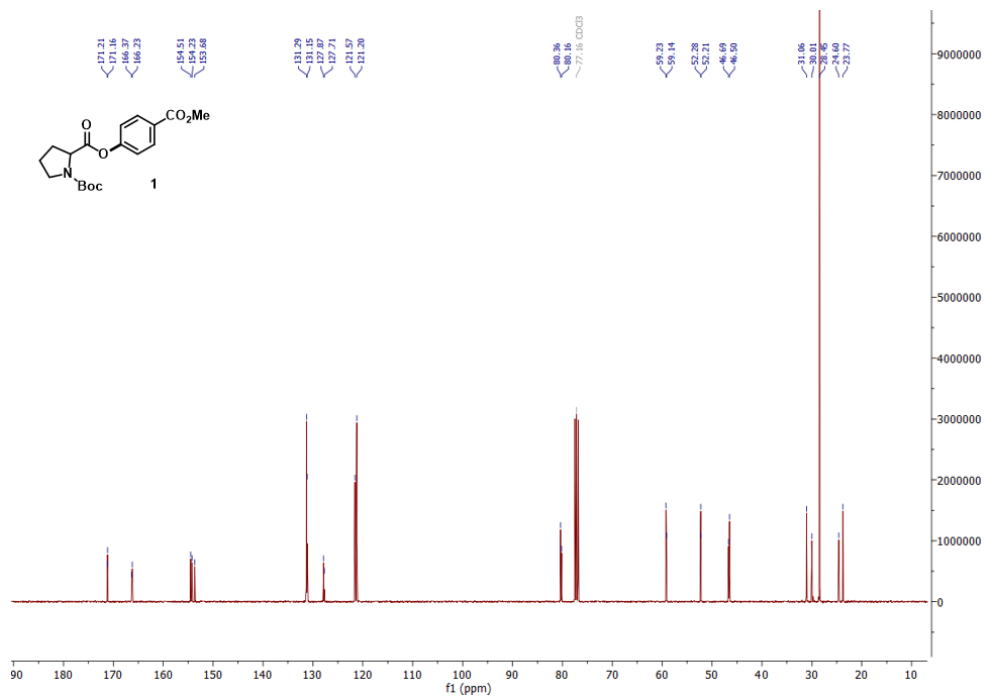
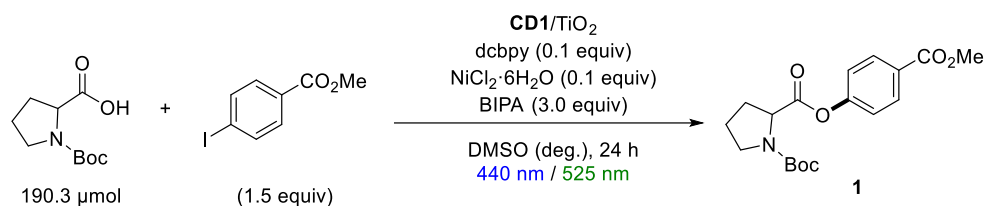
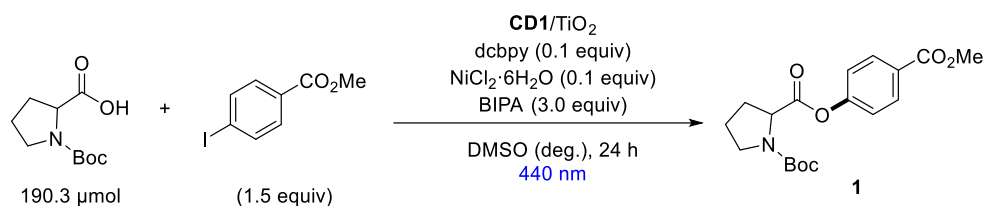
Figure S7.22. ¹H-NMR spectrum of compound 1 (CDCl₃, 400 MHz).Figure S7.23. ¹³C-NMR spectrum of compound 1 (CDCl₃, 151 MHz).

Table S7.4. Screening of **CD1**/TiO₂ nanocomposites prepared using different **CD1**-to-TiO₂ P25 mass ratios for the metallaphotocatalytic C-O arylation of Boc-Pro-OH with methyl 4-iodobenzoate.

Entry	CD1-to-TiO ₂ P25 mass ratio ^[a]	1 [%] ^[b]	1 [%] ^[c]
1	1 : 20	52	8
2	1 : 10	64	10
3	1 : 4	80	19
4	1 : 1	83	22
5	1 : 1^[d]	84	-
6	4 : 1	70	14

[a] CD-to-TiO₂ P25 mass ratio used for the preparation of the nanocomposite. Reaction conditions: methyl 4-iodobenzoate (285.4 μmol), Boc-Pro-OH (190.3 μmol), NiCl₂·6H₂O (19.0 μmol) and dcbpy (19.0 μmol) in DMSO (anhydrous, 3 mL), BIPA (570.8 μmol), **CD1**/TiO₂, 24 h. NMR yields were determined by ¹H-NMR using 1,3,5-trimethoxybenzene as internal standard. [b] 440 nm LED lamp (50% power). [c] 525 nm LED lamp (200% power). [d] **CD1**/TiO₂ stored at room temperature for 26 weeks. deg. = degassed.

Table S7.5. Screening of different amount of **CD1**/TiO₂ nanocomposites for the metallaphotocatalytic C-O arylation of Boc-Pro-OH with methyl 4-iodobenzoate.

Entry	CD1/TiO ₂ / mg	1 [%]
1	20	85
2	10	70
3	5	63
4	1	49
5	0	7

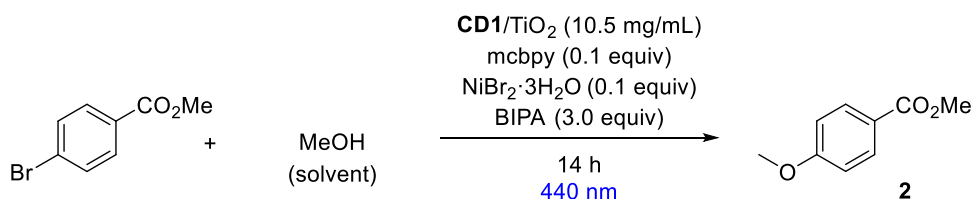
Reaction conditions: methyl 4-iodobenzoate (285.4 μmol), Boc-Pro-OH (190.3 μmol), NiCl₂·6H₂O (19.0 μmol) and dcbpy (19.0 μmol) in DMSO (anhydrous, 3 mL), BIPA (570.8 μmol), **CD1**/TiO₂, 440 nm LED lamp (50% power), 24 h. NMR yields were determined by ¹H-NMR using 1,3,5-trimethoxybenzene as internal standard. deg. = degassed.

7.5.6.2 C-O arylation of MeOH

An oven-dried vial (19 x 100 mm) equipped with a stir bar was charged with CD1/TiO₂ (15.8 mg), methyl 4-bromobenzoate (20.47 mg, 95.2 μmol, 1.0 equiv), NiBr₂·3H₂O (nickel(II) bromide trihydrate, 2.6 mg, 9.5 μmol, 10 mol%) and mcbpy (4'-methyl-2,2'-bipyridine-4-carboxylic acid, 2.1 mg, 9.5 μmol, 10 mol%). Subsequently, MeOH (anhydrous, 1.5 mL) and BIPA (45 μL, 285.6 μmol, 3.0 equiv) were added and the vial was sealed with a septum and Parafilm. The reaction mixture was sonicated for 5-10 min followed by stirring for 5 min to obtain a fine dispersion. The mixture was then degassed by bubbling Argon for 10 min. The mixture was irradiated using the 440 nm LED setup with rapid stirring (1400 rpm). After 14 h, one equivalent of 1,3,5-trimethoxybenzene (internal standard, 16 mg, 95.2 μmol) was added and the mixture was stirred for 5 min. An aliquot of the reaction mixture (~200 μL) was filtered, diluted with DMSO-d₆ and subjected to ¹H-NMR analysis. The product was identified by spiking the crude reaction mixture with a pure sample of the desired product.

The data are in full agreement with those previously published in the literature.³

Table S7.6. C-O arylation of methanol using CD1/TiO₂ and the 440 nm LED setup.



Entry	Conversion [%] ^[a]	2 [%]
1	quant.	93

Reaction conditions: methyl 4-bromobenzoate (95.2 μmol), NiBr₂·3H₂O (9.5 μmol), mcbpy (9.5 μmol) and BIPA (285.6 μmol) in MeOH (1.5 mL), CD1/TiO₂ (15.8 mg), 440 nm LED lamp (100% power), 14 h. NMR yields determined by ¹H-NMR using 1,3,5-trimethoxybenzene as internal standard. [a] Conversion of methyl 4-bromobenzoate determined by ¹H-NMR using 1,3,5-trimethoxybenzene as internal standard. quant. = quantitative.

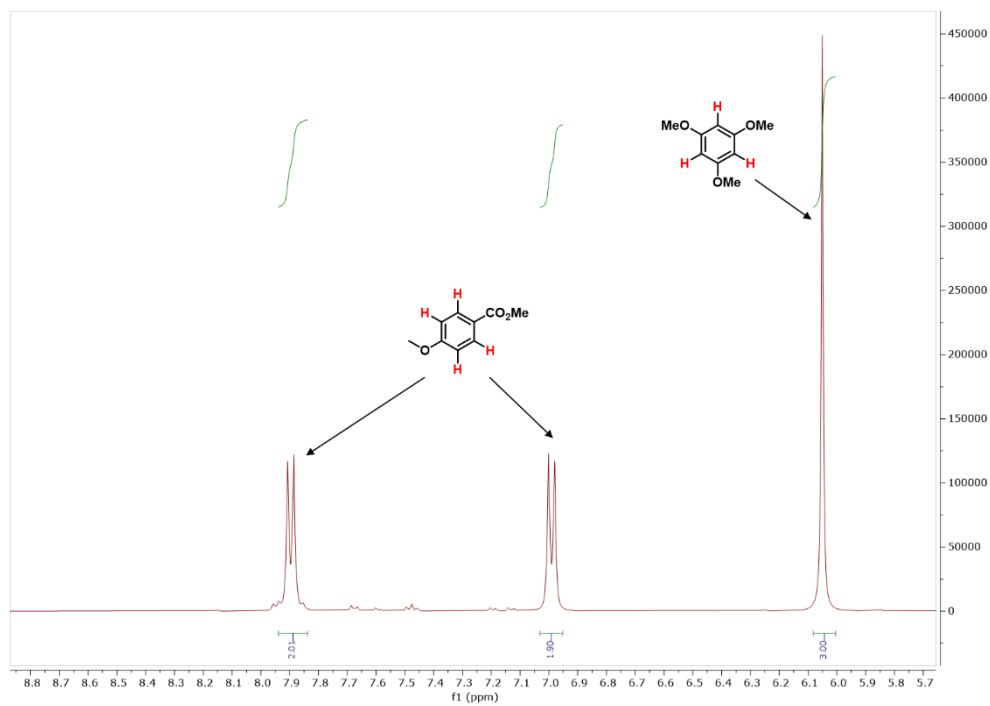


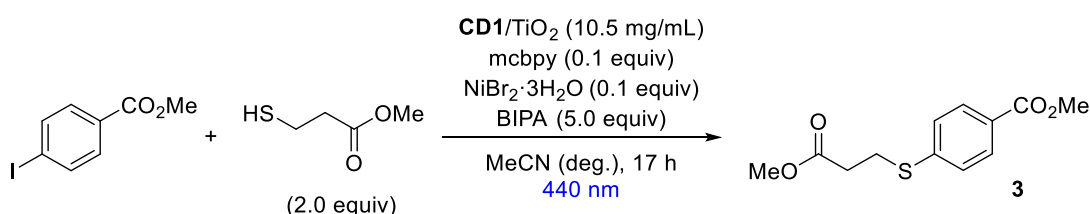
Figure S7.24. Representative ¹H-NMR spectrum of a crude reaction mixture for determining NMR yields in the C-O arylation of methanol (DMSO-d₆, 400 MHz).

7.5.6.3 C-S arylation of methyl 3-mercaptopropionate

An oven-dried vial (19 x 100 mm) equipped with a stir bar was charged with **CD1**/TiO₂ (31.6 mg), methyl 4-iodobenzoate (49.87 mg, 190.3 μmol, 1.0 equiv), methyl 3-mercaptopropionate (45.2 μL, 380.5 μmol, 2.0 equiv), NiBr₂·3H₂O (5.2 mg, 19 μmol, 10 mol%) and mcbpy (4.2 mg, 19 μmol, 10 mol%). Subsequently, MeCN (anhydrous, 3 mL) and BIPA (150.8 μL, 951.5 μmol, 5.0 equiv) were added and the vial was sealed with a septum and Parafilm. The reaction mixture was sonicated for 5-10 min followed by stirring for 5 min to obtain a fine dispersion. The mixture was then degassed by bubbling Argon for 10 min. The mixture was irradiated using the 440 nm LED setup with rapid stirring (1400 rpm). After 17 h, one equivalent of 1,3,5-trimethoxybenzene (internal standard, 32 mg, 190.3 μmol) was added and the mixture was stirred for 5 min. An aliquot of the reaction mixture (~200 μL) was filtered, diluted with DMSO-d₆ and subjected to ¹H-NMR analysis. The product was identified by spiking the crude reaction mixture with a pure sample of the desired product.

The data are in full agreement with those previously published in the literature.³

Table S7.7. C-S arylation of methyl 3-mercaptopropionate using **CD1**/TiO₂ and the 440 nm LED setup.



Entry	Conversion [%] ^[a]	3 [%]
1	quant.	98

Reaction conditions: methyl 4-iodobenzoate (190.3 μmol), methyl 3-mercaptopropionate (380.5 μmol), NiBr₂·3H₂O (19.0 μmol), mcbpy (19.0 μmol) and BIPA (951.5 μmol) in MeCN (3 mL), **CD1**/TiO₂ (31.6 mg), 440 nm LED lamp (50% power), 17 h. NMR yields determined by ¹H-NMR using 1,3,5-trimethoxybenzene as internal standard. [a] Conversion of methyl 4-iodobenzoate determined by ¹H-NMR using 1,3,5-trimethoxybenzene as internal standard. deg. = degassed. quant. = quantitative.

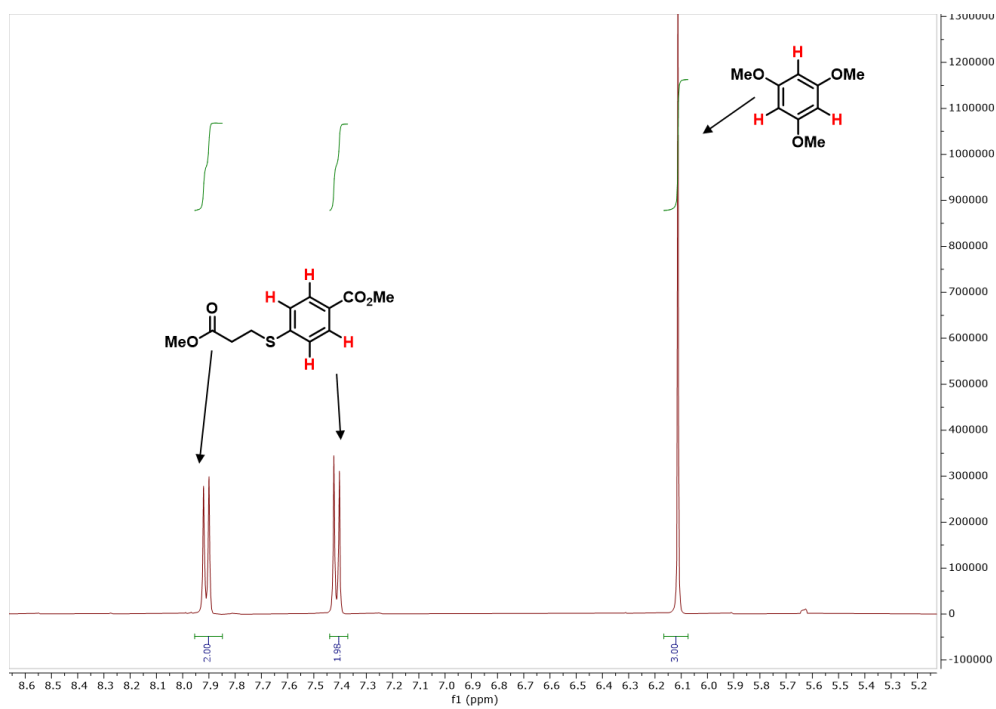


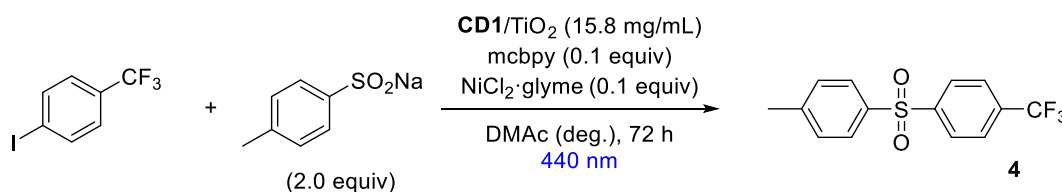
Figure S7.25. Representative ¹H-NMR spectrum of a crude reaction mixture for determining NMR yields in the C-S arylation of methyl 3-mercaptopropionate (DMSO-d₆, 400 MHz).

7.5.6.4 C-S arylation of sodium *p*-toluensulfinate

An oven-dried vial (19 x 100 mm) equipped with a stir bar was charged with **CD1**/TiO₂ (31.6 mg), 4-iodobenzotrifluoride (14.7 μL, 100 μmol, 1.0 equiv), sodium *p*-toluensulfinate (38.8 mg, 200 μmol, 2.0 equiv), NiCl₂·glyme (nickel(II) chloride ethylene glycol dimethyl ether complex, 2.2 mg, 10 μmol, 10 mol%) and mcbpy (2.1 mg, 10 μmol, 10 mol%). Subsequently, DMAc (dimethylacetamide, anhydrous, 2 mL) was added and the vial was sealed with a septum and Parafilm. The reaction mixture was sonicated for 5-10 min followed by stirring for 5 min to obtain a fine dispersion. The mixture was then degassed by bubbling Argon for 10 min. The mixture was irradiated using the 440 nm LED setup with rapid stirring (1400 rpm). After 72 h, one equivalent of 1,3,5-trimethoxybenzene (internal standard, 16.8 mg, 100 μmol) was added and the mixture was stirred for 5 min. An aliquot of the reaction mixture (~200 μL) was filtered, diluted with DMSO-d₆ and subjected to ¹H-NMR analysis. The product was identified by spiking the crude reaction mixture with a pure sample of the desired product.

The data are in full agreement with those previously published in the literature.⁴

Table S7.8. C-S arylation of sodium *p*-toluensulfinate using **CD1**/TiO₂ and the 440 nm LED setup.



Entry	Conversion [%] ^[a]	4 [%]
1	quant.	55

Reaction conditions: 4-iodobenzotrifluoride (100 μmol), sodium *p*-toluensulfinate (200 μmol), NiCl₂·glyme (10 μmol) and mcbpy (10 μmol) in DMAc (2 mL), **CD1**/TiO₂ (31.6 mg), 440 nm blue LED lamp (100% power), 72 h. NMR yields determined by ¹H-NMR using 1,3,5-trimethoxybenzene as internal standard. [a] Conversion of 4-iodobenzotrifluoride determined by ¹H-NMR using 1,3,5-trimethoxybenzene as internal standard. deg. = degassed. quant. = quantitative.

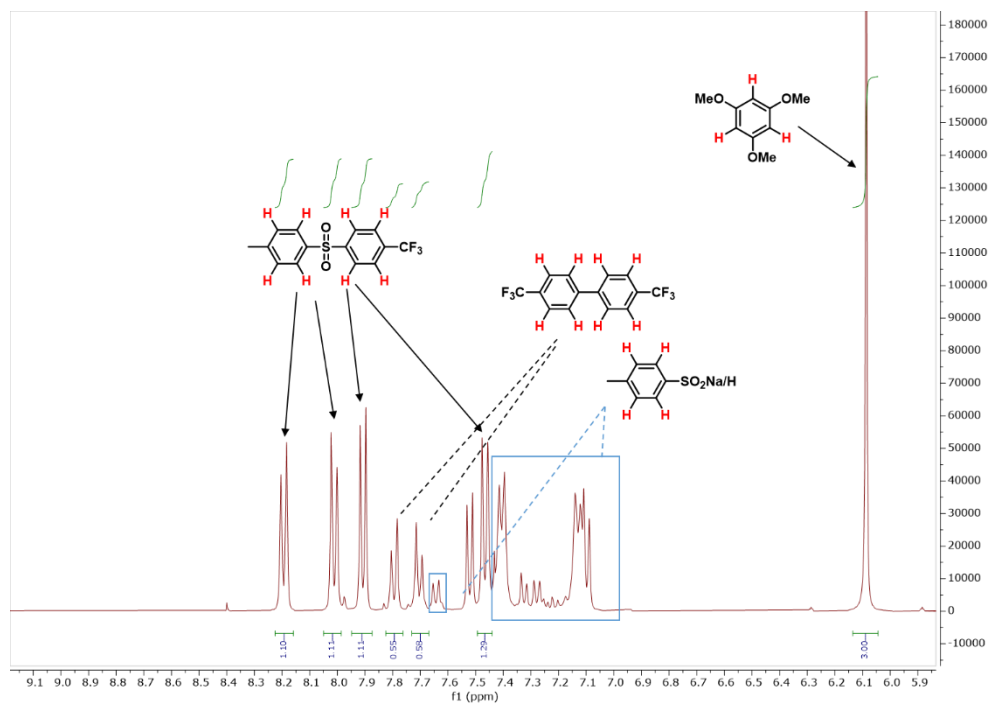


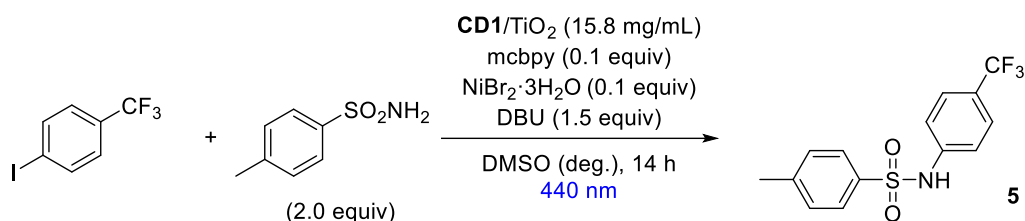
Figure S7.26. Representative $^1\text{H-NMR}$ spectrum of a crude reaction mixture for determining NMR yields in the C-S arylation of sodium *p*-toluenesulfinate (DMSO- d_6 , 400 MHz).

7.5.6.5 C-N arylation of *p*-toluensulfonamide

An oven-dried vial (19 x 100 mm) equipped with a stir bar was charged with **CD1**/TiO₂ (31.6 mg), 4-iodobenzotrifluoride (14.7 μL, 100 μmol, 1.0 equiv), *p*-toluensulfonamide (34.2 mg, 200 μmol, 2.0 equiv), NiBr₂·3H₂O (2.7 mg, 10 μmol, 10 mol%), mcbpy (2.1 mg, 10 μmol, 10 mol%) and DBU (1,8-diazabicyclo[5.4.0]undec-7-en, 22.4 μL, 150 μmol, 1.5 equiv). Subsequently, DMSO (anhydrous, 2 mL) was added and the vial was sealed with a septum and Parafilm. The reaction mixture was sonicated for 5-10 min followed by stirring for 5 min to obtain a fine dispersion. The mixture was then degassed by bubbling Argon for 10 min. The mixture was irradiated using the 440 nm LED setup with rapid stirring (1400 rpm). After 14 h, one equivalent of 1,3,5-trimethoxybenzene (internal standard, 16.8 mg, 100 μmol) was added and the mixture was stirred for 5 min. An aliquot of the reaction mixture (~200 μL) was filtered, diluted with DMSO-d₆ and subjected to ¹H-NMR analysis. The product was identified by spiking the crude reaction mixture with a pure sample of the desired product.

The data are in full agreement with those previously published in the literature.⁵

Table S7.9. C-N arylation of *p*-toluensulfonamide using **CD1**/TiO₂ and the 440 nm LED setup.



Entry	Conversion [%] ^[a]	5 [%]
1	quant.	90

Reaction conditions: 4-iodobenzotrifluoride (100 μmol), *p*-toluensulfonamide (200 μmol), NiBr₂·3H₂O (10 μmol), mcbpy (10 μmol) and DBU (150 μmol) in DMSO (2 mL), **CD1**/TiO₂ (31.6 mg), 440 nm blue LED lamp (100% power), 14 h. NMR yields determined by ¹H-NMR using 1,3,5-trimethoxybenzene as internal standard. [a] Conversion of 4-iodobenzotrifluoride determined by ¹H-NMR using 1,3,5-trimethoxybenzene as internal standard. deg. = degassed. quant. = quantitative.

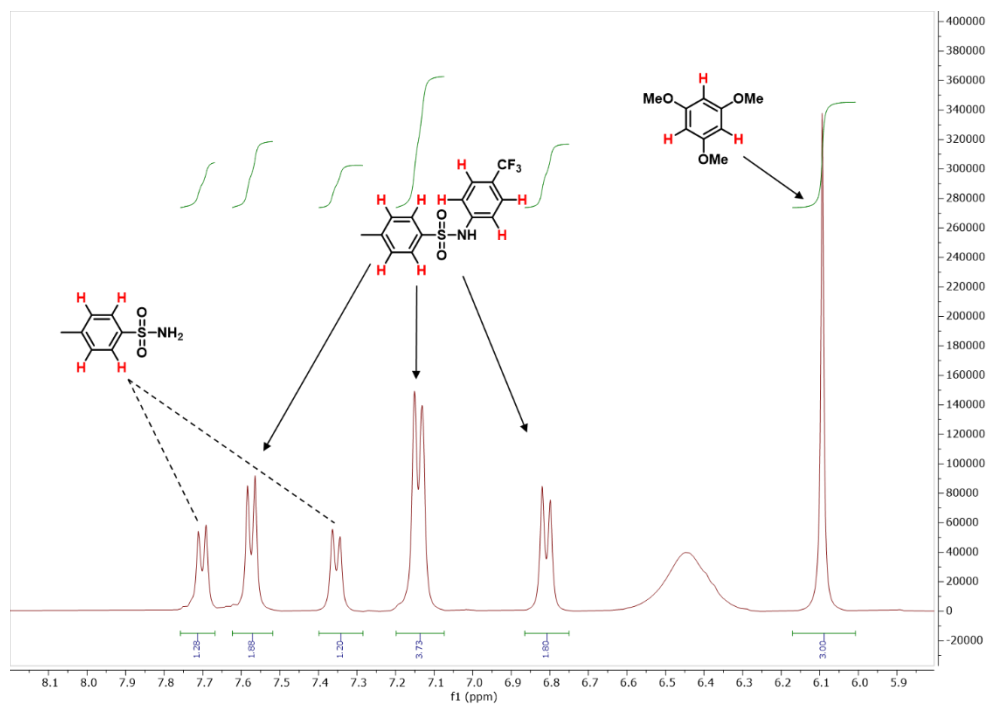


Figure S7.27. Representative ¹H-NMR spectrum of a crude reaction mixture for determining NMR yields in the C-N arylation of *p*-toluenesulfonamide (DMSO-d₆, 400 MHz).

7.5.7 Photobleaching experiments

The photocatalyst (CD1/TiO₂, 31.6 mg; Fluo (fluorescein)/TiO₂, 0.54 mg of Fluo and 30 mg of TiO₂) was added to an oven-dried glass vial equipped with a stir bar.² DMSO (1.5 mL) was added and the reaction mixture was stirred and sonicated for 10 min to obtain a fine dispersion. The vial equipped with an air balloon was then transferred into a dark fume hood and irradiated with a blue LED lamp (440 nm LED lamp, 50% power) at room temperature. After the respective time, Boc-Pro-OH (41.0 mg, 190.3 μmol), methyl 4-iodobenzoate (74.8 mg, 285.4 μmol), a DMSO solution (1.5 mL) of dcbpy (4.7 mg, 19.0 μmol), NiCl₂·6H₂O (4.5 mg, 19.0 μmol), and BIPA (90.5 μL, 570.8 μmol) were added. The glass vial was sealed with a septum and Parafilm. The reaction mixture was stirred and sonicated for 10 min to obtain a fine dispersion and subsequently degassed with Argon for 10 min. The vial was then irradiated with a blue LED lamp (440 nm LED lamp, 50% power) at room temperature for 24 h. 1,3,5-Trimethoxybenzene (32.0 mg, 190.3 μmol) was added as internal standard to determine NMR yields. An aliquot of the resulting mixture (~250 μL) was filtered through a syringe filter, diluted with DMSO-d₆ (~250 μL) and subjected to ¹H-NMR analysis.

7.5.8 Recycling experiments

Boc-Pro-OH (41.0 mg, 190.3 μmol), methyl 4-iodobenzoate (74.8 mg, 285.4 μmol) and **CD1**/TiO₂ nanocomposite (31.6 mg) were added to an oven-dried glass vial equipped with a stir bar. Subsequently, a DMSO solution (3 mL) of dcbpy (4.7 mg, 19.0 μmol), NiCl₂·6H₂O (4.5 mg, 19.0 μmol), and BIPA (90.5 μL , 570.8 μmol) were added. The glass vial was sealed with a septum and Parafilm. The reaction mixture was stirred and sonicated for 10 min to obtain a fine dispersion and subsequently degassed with Argon for 10 min. The vial was then irradiated with a blue LED lamp (440 nm LED lamp, 50% power) at room temperature. After 24 h, the reaction mixture was centrifuged and washed twice with DMSO (3 mL). The remaining nanocomposite was lyophilized overnight and reused in the next reaction. For the controlled studies, NiCl₂·6H₂O (4.5 mg, 19.0 μmol) or NiCl₂·6H₂O (4.5 mg, 19.0 μmol)/dcbpy (4.7 mg, 19.0 μmol) were added to the new reaction mixture.

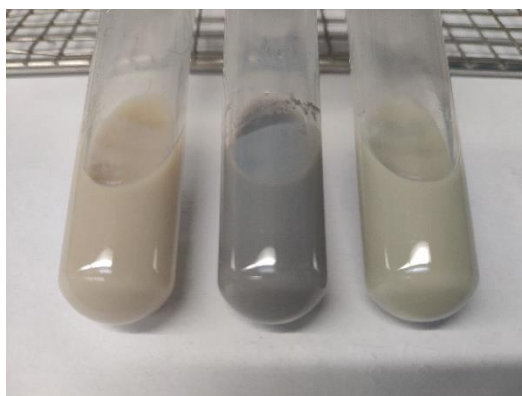


Figure S7.28. Photograph of the reaction mixture (+ none group, left; + NiCl₂·6H₂O group, middle; + NiCl₂·6H₂O/dcbpy, right) after C-O cross-coupling reaction (cycle 4).

7.5.9 References

1. Hill, S. A.; Benito-Alifonso, D.; Davis, S. A.; Morgan, D. J.; Berry, M.; Galan, M. C., Practical Three-Minute Synthesis of Acid-Coated Fluorescent Carbon Dots with Tuneable Core Structure. *Sci Rep* **2018**, *8* (1), 12234.
2. Reischauer, S.; Strauss, V.; Pieber, B., Modular, Self-Assembling Metallaphotocatalyst for Cross-Couplings Using the Full Visible-Light Spectrum. *ACS Catal.* **2020**, *10* (22), 13269-13274.
3. Cavedon, C.; Madani, A.; Seeberger, P. H.; Pieber, B., Semiheterogeneous Dual Nickel/Photocatalytic (Thio)etherification Using Carbon Nitrides. *Org. Lett.* **2019**, *21* (13), 5331-5334.
4. Yue, H.; Zhu, C.; Rueping, M., Cross-Coupling of Sodium Sulfinates with Aryl, Heteroaryl, and Vinyl Halides by Nickel/Photoredox Dual Catalysis. *Angew. Chem. Int. Ed.* **2018**, *57* (5), 1371-1375.
5. Ye, F.; Berger, F.; Jia, H.; Ford, J.; Wortman, A.; Börgel, J.; Genicot, C.; Ritter, T., Aryl Sulfonium Salts for Site-Selective Late-Stage Trifluoromethylation. *Angew. Chem. Int. Ed.* **2019**, *58* (41), 14615-14619.

List of abbreviations

ξ	Photon efficiency
τ	Excited state lifetime
λ	Wavelength
Φ	Quantum yield
ε	molar extinction coefficient
β -Ala	β -Alanine
$^1\text{O}_2$	Singlet oxygen
$^3\text{MLCT}$	Triplet excited state resulting from a metal-to-ligand charge transfer transition
4-CzIPN	1,2,3,5-Tetrakis(carbazol-9-yl)-4,6-dicyanobenzene
A	Electron acceptor
A	Absorbance
acac	Acetylacetonate
AaeUPO	<i>A. aegerita</i>
Acr	Acridiniums
An	Annihilator
ADH-A	Alcohol dehydrogenase
API	Active pharmaceutical ingredient
ARS	Alizarin red s (3,4-Dihydroxy-9,10-dioxo-9,10-dihydroanthracene-2-sulfonic acid)
ATRA	Atom transfer radical addition
BET	Brunauer-Emmett-Teller (surface area)
BINAP	2,2'-Bis(diphenylphosphino)-1,1'-binaphthyl
BIPA	<i>N-tert</i> -Butylisopropylamine
Boc-Pro-OH	<i>N-(tert</i> -Butoxycarbonyl)proline

BODIPY	Boron dipyrromethenes
BPI	Benzo[<i>ghi</i>]perylene monoimide
bpy	2,2'-Bipyridine
bpz	2,2'-Bipyrazine
BTMG	2- <i>tert</i> -Butyl-1,1,3,3-tetramethylguanidine
c	Concentration
CB	Conduction band
CD	Carbon dots
CMB-CN	Carbon nitride material from cyanuric acid, melamine and barbituric acid
CMP	Conjugated microporous polymer
CN	Carbon nitride
CN-OA-m	Carbon nitride based on urea and oxamide, synthesized in molten salt
COF	Covalent organic framework
ConPET	Consecutive photoinduced electron transfer
CSTR	continuous stirred tank reactor
CTF	Covalent triazine network
CV	Cyclic voltammetry
czbpy	5,5'-Dicarbazolyl-2,2'-bipyridyl
D	Electron donor
d	Doublet
DABCO	1,4-Diazabicyclo[2.2. 2]octane
DBU	1,8-Diazabicyclo[5.4.0]undec-7-ene
DCE	Dichloroethane
DCM	Dichloromethane
dcbpy	2,2'-bipyridine-4,4'-dicarboxylic acid

dF(CF ₃)ppy	2-(2,4-Difluorophenyl)-5-(trifluoromethyl)pyridine
diglyme	Diethylene glycol dimethyl ether
DHIMQ	6,7-dihydroxy-2-methylisoquinolinium
DIPEA	<i>N,N</i> -diisopropylethylamine
DMA or DMAc	<i>N,N</i> -Dimethylacetamide
DMAP	<i>N,N</i> -Dimethylaminopyridine
dme	Dimethyl ether
DMF	<i>N,N</i> -Dimethylformamide
dmg	Dimethylglyoxime
DMSO	Dimethylsulfoxide
donor*	Excited state participating in energy transfers
DDQ	2,3-dichloro-5,6-dicyano-1,4-benzoquinone
DMPU	<i>N,N'</i> -Dimethylpropyleneurea
DSP	Dye-sensitized photocatalyst
DSMP	Dye-sensitized metallaphotocatalysts
DSSC	Dye-sensitized solar cell
dtbbpy	4,4'-Di-tert-butyl-2,2'-bipyridine
E	Energy
EDA	Electron-donor acceptor (complex)
EdX	Energy-dispersive X-ray
EI	Electronic ionization
EnT	Energy transfer
EPR	Electron paramagnetic resonance spectroscopy
ESI	Electrospray ionization
ET	Electron transfer
EY	Eosin Y

FDPP	Furanyldiketopyrrolopyrrole
FTIR	Fourier-transform infrared spectroscopy
g-CN	Graphitic carbon nitride
glyme	1,2-Dimethoxyethane
HAADF	High-angle annular dark-field
HAT	Hydrogen atom transfer
HMDS	Hexamethyldisilazane
HOMO	Highest occupied molecular orbital
HPLC	High-performance liquid chromatography
HR-MS	High resolution mass spectrometry
ICP-OES	Inductively coupled plasma - optical emission spectroscopy
ISC	Intersystem crossing
Irspyy	<i>fac</i> -tris[2-(5'-sulfonatophenyl)pyridine]iridate(III) pentahydrate
k_d	Diffusion konstant
K-PHI	Potassium poly(heptazinie imide)
l	Optical path length of the light
LD	Laser diffraction
LED	Light emitting diode
LSC	Luminescent solar concentrators
LUMO	Lowest unoccupied molecular orbital
m	Multiplet
mcbpy	4'-methyl-2,2'-bipyridine-4-carboxylic acid
MeCN	Acetonitrile
MeOH	Methanol
MLCT	Metal-to-ligand charge transfer
MMA	Methyl methacrylate

MO	Metal oxide
MOF	Metal organic framework
mpg-CN	Mesoporous graphitic carbon nitride
MTBD	7-Methyl-1,5,7-triazabicyclo[4.4.0]dec-5-en
n.d.	Not detected
n.d.o.	Not determined due to overlapping peaks
Nafluo	Fluorescein sodium
Ni	Nickel
NIR	Near-infrared
NMR	Nuclear magnetic resonance spectroscopy
NP	Nanoparticle
OA	Oxidative Addition
OMs	Methanesulfonate
OTf	Trifluoromethanesulfonate
OTs	<i>para</i> -Toluensulfonate
PAH	Polycyclic aromatic hydrocarbons
PC	Photocatalyst
PC*	Excited state of the photocatalyst
PC ^{·+}	Photocatalyst after oxidative quenching
PC ^{·-}	Photocatalyst after reductive quenching
PDI	<i>N,N</i> -bis(2,6-diisopropylphenyl)perylene-3,4,9,10-bis(dicarboximide)
PdPc	Palladium(II) octabutoxyphthalocyanine
PET	Photoinduced electron transfer
PL	Photoluminescence
PRC	Photoredox catalysis
PSD	Particle size distribution

p-TSA	<i>para</i> -Toluensulfonic acid
Pt	Palladium
PtTBTNB	Platinum(II) tertraphenyltetranaphthoporphyrin
q	Quartet
QD	Quantum dot
quinuclidine	1-Azabicyclo[2.2.2]octane
RE	Reductive Elimination
Rhodamine B	9-(2-Carboxyphenyl)-3,6-bis(diethylamino)xanthyliumchlorid
Rh-6G	Rhodamine 6G
ROS	Reactive oxygen species
s	Singlet
S ₀	Singlet state
S ₁	Singlet excited state
SCE	Saturated calomel electrode
SEM	Scanning electron microscopy
sens	Sensitizer
SET	Single electron transfer
SMBR	Serial micro-batch reactor
STEM	Scanning transmission electron microscopy
t	Triplet
T ₁	Triplet excited state
TBADT	tetrabutylammoniumdecatungstate
TEM	Transmission electron microscopy
THF	Tetrahydrofurane
TLC	Thin layer chromatography
TMEDA	<i>N,N,N',N'</i> -tetramethylethylenediamine

TMP	2,2,6,6-tetramethylpiperidin
TMG	1,1,3,3-Tetramethylguanidine
TMSCN	Trimethylsilyl cyanide
Tol	Toluene
Ts	<i>para</i> -Toluensulfonyl
UPO	unspecific peroxygenase
UV	Ultraviolet
Vis	Visible
VB	Valence band
XPS	X-ray photoelectron spectroscopy
XRD	X-ray powder diffraction
Zn	Zink